

Space Photovoltaic Research and Technology 1995

1996049234

1+43

50386 - 50428

339 P

*Proceedings of the SPRAT XIV conference held at
NASA Lewis Research Center
Cleveland, Ohio
October 24-26, 1995*



NASA Conference Publication 3324

Space Photovoltaic Research and Technology 1995

*Proceedings of the SPRAT XIV Conference
held at and sponsored by NASA Lewis Research Center
Cleveland, Ohio
October 24-26, 1995*



National Aeronautics and
Space Administration

Office of Management

**Scientific and Technical
Information Program**

1996



Space Photovoltaic Research and Technology 1995

Table of Contents

| | |
|---|------------|
| <i>Contents</i> | <i>iii</i> |
| Foreword | <i>vi</i> |
| The Irving Weinberg Award | 1 |
| Session 1: <i>Invited papers</i> | |
| C.P. Bankston, R.B. Bennett and P.M. Stella Planetary and Deep-Space Requirements for Photovoltaic Solar Arrays | 2 |
| G. Strobl <i>et al.</i> Development of Advanced Si and GaAs Solar Cells for Interplanetary Missions | 10 |
| G.P. Summers Naval Research Laboratory's Programs in Advanced Indium Phosphide Solar Cell Development | 21 |
| C. Goodbody and R. Kimber The Defense Research Agency Photovoltaic Programme | 24 |
| T. Saga, Y. Kiyota, T. Matsutani, A. Suzuki, O. Kawasaki, T. Hisamatsu and S. Matsuda Japanese Photovoltaic Power Generation for Space Application | 31 |
| Session 2: <i>Multijunction Cells</i> | |
| E.M. Gaddy Cost Trade Between Multi-junction, GaAs and Silicon Solar Cells | 40 |
| P.K. Chiang, D.D. Krut and B.T. Cavicci The Progress of Large Area GaInP ₂ /GaAs/Ge Triple Junction Cell Development at Spectrolab | 47 |
| Y.C.M. Yeh and C.L. Chu Status of Multijunction Solar Cells | 57 |
| M.F. Vilela <i>et al.</i> InP tunnel Junctions for InGaAs/InP Tandem Solar Cells | 65 |

Session 3: Radiation Damage

| | | |
|---|---|-----|
| G.P. Summers, R.J. Walters, S.R. Messenger and E.A. Burke | The Role of Radiation Hard Solar Cells in Minimizing the Costs of Global Satellite Communications Systems | 71 |
| G. Rybicki <i>et al.</i> | High and Low Energy Proton Radiation Damage in p/n InP Solar Cells | 80 |
| R. Walters, G.P. Summers, S.R. Messenger and E.A. Burke | Correlation of Electron and Proton Irradiation-Induced Damage in InP Cells | 89 |
| S. Wojtczuk <i>et al.</i> | Diffusion Lengths in Irradiated n/p InP on Si Solar Cells | 95 |
| S. Messenger, H.L. Cotal, R.J. Walters and G.P. Summers | Electron and Proton Damage on InGaAs Solar Cells Having an InP Window Layer | 100 |
| A. Meulenberg | Photo-Recovery of Electron-Irradiated GaAs Solar Cells | 106 |

Session 4: Cell Technology

| | | |
|--|---|-----|
| L.C. DiNetta <i>et al.</i> | Initial Results for the Silicon Monolithically Interconnected Solar Cell Product | 114 |
| L. DiNetta and M.H. Hannon | Monolithically Interconnected GaAs Solar Cells: A New Interconnection Technology for High-Voltage Solar Cell Output | 122 |
| B. Chatterjee, W.C. Davis, S.A. Ringel and R. Hoffman, Jr. | Hydrogen Passivation of n+p and p+n Heteroepitaxial InP Solar Cells | 127 |
| R.E. Welser and L.J. Guido | The Growth of Low Bandgap InAs on (111)B GaAs Substrates | 137 |
| J. Moulot <i>et al.</i> | Three-layer Antireflection Coating for High Efficiency InP Solar Cells Using a Chemical Oxide as First Layer | 142 |
| M.H. Hannon, M.W. Dashiell, L.C. DiNetta, and A.M. Barnett | Lightweight, Light-trapped Thin GaAs Solar Cell for Spacecraft Applications: Progress and Results Update | 150 |

Session 5: Measurements

| | | |
|--|--|-----|
| J.R. Woodyard | Laboratory Instrumentation and Techniques for Characterizing Multi-junction Solar Cells for Space Applications | 158 |
| D.R. Burger and R.L. Mueller | Solar Cell Angle of Incidence Corrections | 168 |
| D.A. Scheiman, P. Jenkins, D.J. Brinker and J. Appelbaum | Low Intensity Low Temperature (LILT) Measurements and Coefficients on New Photovoltaic Structures | 178 |
| D.J. Brinker <i>et al.</i> | A Summary of the International Workshops on Space Solar Cell Calibration and Measurement Techniques | 186 |

Session 6: TPV and advanced concepts

| | | |
|--|---|-----|
| D. Chubb <i>et al.</i> | Review of Recent Thermophotovoltaic Research at Lewis Research Center | 191 |
| L.M. Fraas, J.E. Samaras, J.E. Avery and R. Ewell | Thermophotovoltaic Generators using Selective Metallic Emitters | 208 |
| Z.A. Shellenbarger, M.G. Mauk, L.C. DiNetta, and G.W. Charache | InGaAsSb/GaSb Thermophotovoltaic Cells | 215 |
| S. Wojtczuk | Multijunction InGaAs Thermophotovoltaic Power Converter | 223 |
| P.E. Simms, L.C. DiNetta, K.D. Cavanagh and M.A. Goetz | Gallium Phosphide Energy Converters | 231 |

Session 7: Assembly and Panels

| | | |
|----------------------------|--|-----|
| M.R. Brown <i>et al.</i> | Characterization Testing of MEASAT GaAs/Ge Solar Cell Assemblies | 237 |
| E.L. Ralph and E.B. Linder | Advanced Solar Panel Designs | 247 |
| A. Meulenberg | Space Qualification of UV and IR Reflecting Coverslides for GaAs Solar Cells | 257 |

Session 8: Flight Experiments and Space Plasma

| | | |
|---|---|-----|
| H. Curtis and D. Marvin | One Year of Flight Data From the PASP-Plus Experiment | 268 |
| V.A. Davis, B.M. Gardner, D.A. Guidice and P.S. Severance | Parasitic Collection by PASP-Plus Solar Arrays | 274 |
| D.A. Guidice | High Voltage Space Plasma Interactions on the PASP-Plus Test Arrays | 286 |
| W.R. Mackey | Preliminary Chaotic Model of Snapover on High Voltage Solar Cells | 296 |
| P.A. Jones and D.M. Murphy | A Linear Refractive Photovoltaic Concentrator Solar Array Flight Experiment | 304 |
| G.A. Landis and P. Jenkins | Development of a Solar Cell Dust Opacity Measurement Instrument for Mars Pathfinder | 313 |

Workshops

| | |
|---|-----|
| 1. Multijunction Cells | 318 |
| 2. Radiation Damage | 320 |
| 3. Characterization and Testing of New Solar Cell Types | 323 |
| 4. Solar Power Satellite | 325 |

| | |
|--------------------------|-----|
| List of Attendees | 328 |
|--------------------------|-----|

FOREWORD

Navid S. Fatemi
Essential Research, Inc.
NASA Lewis Research Center

The Fourteenth Space Photovoltaic Research and Technology (SPRAT XIV) Conference was held October 24-26, 1995 at the NASA Lewis Research Center, bringing together representatives of the space photovoltaic community from the U.S. , Europe, and Japan. In attendance were about 100 scientists, engineers, program managers, and others representing 21 commercial corporations, 7 government agencies, and 9 universities.

The latest results of research and development activities, commercialization plans, and flight data on photovoltaic power generation for space were presented at the meeting. During the course of the meeting, it became apparent that PV power generation needs of the near future will rest more with the commercial sector in general and the communication satellite industry in particular, than with the traditionally government-funded missions. This was indeed good news for the space PV community.

In addition, it was clear that advanced solar cell technologies such as GaAs on Ge, InP on Si or Ge, and multibandgap cells are rapidly gaining acceptance and utilization as viable cost-effective alternatives to the conventional Si technology. This fact gave more urgency to the discussions held by the attendees at the conference workshops dedicated to multibandgap cells, radiation resistance issues, characterization and testing of new cell types, and solar power satellites.

As with its predecessors, the invited papers, the contributed papers, and the summary of the workshops presented in this volume make it one of the most up-to-date compendia of space solar cell and array literature available anywhere.

In conclusion, I would like to thank all those who helped organize and run the conference. They are: publications chair, Geoffrey Landis; logistics chair, George Rybicki; social events chair, Karen Wester; secretarial and registration, Jenise Veris, Brunilda Quiñones, and Pat Wielinski; and finally Dennis Flood for his mentorship.

The Irving Weinberg Award

The fourteenth Space Photovoltaic Research and Technology executive committee has established the Irving Weinberg Award, in memory of Dr. Irving Weinberg, a leading contributor to the field of space photovoltaic research and development for most of his professional career. This award is to be given at every SPRAT meeting to persons who have made significant contributions to the field of space photovoltaics. This award is meant to be inclusive of all aspects of space photovoltaic research and technology, from fundamental investigations of semiconductor materials, to device improvements, and finally to innovations in hardware for actual mission applications. The recipient of the first Irving Weinberg award is Professor Chandra Goradia.

Professor Chandra Goradia

Professor Goradia received his M.Sc. degree in physics from the University of Bombay, India, in 1962. He then received his M.E.E. and Ph.D. degrees in electrical engineering from the University of Oklahoma, Norman, Oklahoma, in 1964 and 1967 respectively. Since 1967, he has been a faculty member in the Electrical Engineering Department of the Cleveland State University, where he has been a full professor since 1981.

Professor Goradia has conducted solar cell research since 1974. For the first five years, his research was concentrated on theoretical modeling, experimental fabrication and performance evaluation of the Vertical Multijunction silicon solar cells. Subsequently, inspired by and in collaboration with Dr. Irving Weinberg, he worked on the theoretical optimal design and performance prediction of a variety of space and terrestrial solar cells of different materials and geometries. These included the single- and double-connected silicon Tandem Junction Cell (TJC), high base resistivity conventional silicon nip cells, space GaAs concentrator cells, CuInSe_2 and CdTe thin film terrestrial cells, and InP space solar cells.

In 1988, professor Chandra Goradia established, jointly with his research colleague and wife, professor Manju Ghalla-Goradia, the NASA Lewis-funded Space Photovoltaic Research Center (SPRC) within the Electrical Engineering Department at Cleveland State University. They have been the co-directors of the SPRC since its inception.

Professor Goradia has published quite widely in the semiconductors and solar cells area and is the principal author or joint author of over seventy-five publications in journals and conference proceedings. Professor Goradia is also a Senior Member of the Institute of Electrical and Electronics Engineers (IEEE).

IN S1
50386

Planetary and Deep Space Requirements for Photovoltaic Solar Arrays¹

C. P. Bankston, R. B. Bennett, and P. M. Stella
Jet Propulsion Laboratory
California Institute of Technology
Pasadena, CA 91109

INTRODUCTION

In the past 25 years, the majority of interplanetary spacecraft have been powered by nuclear sources. However, as the emphasis on smaller, low cost missions gains momentum, more deep space missions now being planned have baselined photovoltaic solar arrays due to the low power requirements (usually significantly less than 100 W) needed for engineering and science payloads. This will present challenges to the solar array builders, inasmuch as planetary requirements usually differ from earth orbital requirements. In addition, these requirements often differ greatly, depending on the specific mission; for example, inner planets vs. outer planets, orbiters vs. flybys, spacecraft vs. landers, and so on. Also, the likelihood of electric propulsion missions will influence the requirements placed on solar array developers.

This paper will discuss representative requirements for a range of planetary and deep space science missions now in the planning stages. We have divided the requirements into three categories: Inner planets and the sun; outer planets (greater than 3 AU); and Mars, cometary, and asteroid landers and probes. Requirements for Mercury and Ganymede landers will be covered in the Inner and Outer Planets sections with their respective orbiters. We will also discuss special requirements associated with solar electric propulsion (SEP). New technology developments will be needed to meet the demanding environments presented by these future applications as many of the technologies envisioned have not yet been demonstrated. In addition, new technologies that will be needed reside not only in the photovoltaic solar array, but also in other spacecraft systems that are key to operating the spacecraft reliably with the photovoltaics.

GENERAL CONSIDERATIONS

Planetary and deep space scientific exploration is faced with the same programmatic requirements common to virtually all space programs in the 1990's, and beyond. These programs will face tightly constrained budgets that are often near \$100 million for the design, fabrication and integration of the spacecraft. Launch services costs must be kept to a minimum. Tight funding requires the payload system developer to produce mission hardware that is mass and volume efficient. The more capability which can be packaged in a small, light weight system the smaller and less expensive the launch vehicle that is required to boost it. Spacecraft and payload development cycles will frequently be only 2-3 years. This will demand that proven or accepted designs and technologies must be ready for implementation once project start is approved, since critical design reviews may be scheduled within three months of project start.

Accordingly, overlaying requirements associated with low mass, low cost systems will always be in place as part of the system trade-offs. This means that compact packaging and low mass structures conforming to launch vehicle restraints will be needed. In general, the highest efficiency cell technologies consistent with the cost constraints will be sought as planetary and deep space missions are usually power limited. Finally, short cycle times also require that

¹ The work described in this paper was performed by the Jet Propulsion Laboratory, California Institute of Technology, under contract with the National Aeronautics and Space Administration.

constituent components are readily available for rapid assembly and that vendor source agreements are in place.

Finally, beyond direct power system considerations, there are a host of ancillary spacecraft technology considerations for the described mission concepts. Such considerations play a key role in determining power system feasibility. Some of these considerations include fault tolerance and reliability requirements, on-board autonomous operations capability, power-down cruise capability, low-temperature tolerances and thermal control constraints, and power storage requirements and capabilities for off-sun events and pointing anomalies. While beyond the scope of the photovoltaic solar array requirements addressed in this paper, such considerations and the technologies needed to address them are enabling for application of photovoltaics in many of the applications described here, especially for those missions beyond the orbit of Mars.

INNER PLANETS AND THE SUN

Several inner body explorations are under study at the Jet Propulsion Laboratory. Missions being planned for exploration inside 1 AU include a Mercury lander and orbiter combination, and a "solar probe" to investigate solar regions within one-half of a solar radius. A mission to Venus is also under study, but has not identified exceptional technology demands that are beyond the need for rapid, low cost implementation with the best performance, lowest mass, and most compact packaging.

A mission to Mercury is now being planned for launch around 2010. It would consist of an orbiter carrying a separate lander package. The orbiter design life is one year following orbit insertion, while the lander will descend to the surface and would function for one Mercurian day (176 Earth days). Orbiter and lander power needs are 210 W and 25 W respectively. For both orbiter and lander, the thermal environments are extraordinary, where the solar flux at 0.4 AU is about 10^4 W/m². On the surface the subsolar temperature is 700K, with a black body emission from the surface of 530K. At night the lander temperature would drop to 90K. The high temperatures will require welded solar array construction along with many new array materials. These must also be capable of withstanding wide temperature swings in eclipse or the day/night cycle. Also, off-sun pointing performance of the baselined GaAs solar arrays will be required and characterization of the performance of the system at highly oblique angles (10°-25°) will be necessary. Solar radiation levels will require the use of heavy shielding. Note that a solar electric propulsion option is being considered for this mission; the advantages of such an approach are described in the SEP discussion below.

The solar probe mission (Figure 1) has the goal of making in situ measurements as far into the solar atmosphere (solar corona) as possible. Its perihelion is 4 solar radii where the spacecraft would be exposed to 3000 suns solar flux at 0.3 AU. For a solar powered mission, two solar arrays may be required. A large, low mass array would be required from launch outward to 5.2 AU, inasmuch as the spacecraft requires a gravity assist at Jupiter to place it on the desired trajectory. This array would also be utilized on the cruise inward to about 0.7 AU. The area of the large solar array will be determined by the requirement to provide 60 W at 5.2 AU for spacecraft survival. This array must perform under low intensity, low temperature conditions, and will be gimballed to provide pointing capability on and off sun as the spacecraft moves away and then returns. Low mass designs will be required, with flexible fold out panels. An inflatable structure is presently the baselined concept. This array would be jettisoned at about 0.7 AU (or at 400K) in favor of a second smaller panel for the region 0.7-0.3 AU. This would be a rigid panel with welded cells for survivability. This array will also require pointing off-sun as it approaches the sun. It is possible that the second array may not be necessary if the primary array can be feathered sufficiently and controllably to keep temperatures within a safe range. The characteristics of cell performance at highly oblique, yet high intensity, incident solar fluxes must be determined for the cells selected.

OUTER PLANETS

Very low-power missions to the outer solar system that have been studied include a Galilean orbiter and Ganymede lander combination, and a flight to the Kuiper belt. Also, a much higher powered mission to search for extra-solar planets is being considered that would perform its investigations from up to 5 AU. While onboard power requirements would be moderate, the low solar intensity will require very large array areas. For example, the solar intensity at 5 AU would be only 54 W/m² and even if as much as 25 percent can be converted (a high value) to electrical power, this would yield only 13.5 W/m² of array area. As a result, such missions will demand extremely compact packaging and low mass structures to conform to launch vehicle constraints. In turn, the large area, low mass designs will impact allowable spacecraft loads. Inflatable array structures, with and without concentration, and multi-band gap cells will be considered if available. In general, the highest efficiency cell technologies operable under low intensity, low temperature conditions will be needed.

For the Galilean orbiter, the spacecraft power required is 50-100W at Jupiter, equivalent to at least 2500 W at 1 AU. If radiation damage, either from solar flares, or trapped radiation in the Jovian belts is included, the 1 AU power level equivalent may be on the order of 4 kW. These arrays will require both early cruise off-sun pointing and reliable performance under low intensity, low light (LILT) conditions. The Ganymede lander will require only a few watts, but must operate in the average temperature range 150-170 K under the extreme low light and high radiation (100 kRad qualification level) conditions near Jupiter. The low light conditions would require stowage of an exceptionally large solar array in comparison to the lander. Furthermore, the difficulty in providing energy storage and thermal control under such conditions may make a radioisotope source necessary for the lander.

A "Kuiper Express" (Figure 2) is being studied to conduct reconnaissance of the primitive objects of the Kuiper Belt. Launch would take place after 2000 with a ten year cruise phase. Mission options include fly bys of Mars, an asteroid, Uranus, and Neptune in route. Solar electric propulsion via 6-2.5kW ion engines would be used out to 3 AU, with solar power continuing to provide at least 10 W out to 50 AU. An inflatable, "mini-dome" fresnel concentrator array has been baselined to meet the challenging power requirement in the low light conditions, while meeting packaging and mass constraints. Thus, significant technology challenges remain before these mission requirements can be met.

Finally, the search for extra solar planets with a spacecraft (Figure 3) at 5 AU has the goal of identifying the presence of planets within 10 parsecs. The spacecraft, a large aperture interferometric telescope, would require about 600W generated from varying sun angles under LILT conditions. Launch mass constraints dictate a solar array performance target of >200W/kg at 1 AU. The plan is for 2 single axis, articulated arrays for this special application. Inflatable array technology is presently baselined.

MARS, COMETARY, AND ASTEROID LANDERS AND PROBES

Most studies of other landers and probes usually focus on the Mars environment, since that planet is the one for which a series of landers and probes are planned well into the next century. Energy management on the Martian surface will be affected by the weather, latitude, and temperature swings during the day/night cycle. On the other hand, conditions on a comet or asteroid may provide different challenges. The surface density and composition of a comet are unknown to the extent that a probe could encounter rock, "sand", or ice.

The environment encountered by Mars landers depends significantly upon the latitude of the landing and weather conditions, particularly the likelihood of dust storms. Power levels vary from as low as milliwatts in a quiescent mode to near 1 watt for brief periods for a so-called

microlander/penetrator, up to 100 watts for more complex rovers or other science packages. Surface temperatures will likely range between 150K (night time at 70° south latitude) to 300K in the day time. Low mass, highly compact packaging will be essential for these systems. In addition, the probe may experience landing conditions ranging from a soft landing to shock loadings up to 10,000 g's for the case of a penetrator afterbody. These conditions might also be common to asteroid landings.

Surface weather conditions on Mars are of special concern due to the possibility of blowing dust. This will affect solar array performance either through obscuration of the sun or deposition of dust on the surface of the array. Optical depths of 3.6 have been measured by the Viking I lander and up to 6 are possible in low to middle latitudes, thus reducing the solar flux by as much as 85 percent. The Mars Pathfinder/Rover mission will carry a small experiment, supplied by NASA's Lewis Research Center, to determine the effects of dust on solar cells in the Martian environment at Ares Vallis(19°N, 32°W).

The use of solar arrays for a cometary lander (Figure 4) would present additional problems. A proposed lander for the Rosetta mission to the comet "Wirtanen" would require 1-10 W of power at about 3.25 AU. The surface temperatures are expected to be 130-150K with power requirements being sized to recharge batteries during a 15 hour rotation cycle. A comet lander system powered by a solar array may require that that rendezvous occur far enough from the sun such that the comet is relatively inactive to minimize the effects of dust or other debris contamination. Due to these issues, along with mass and volume constraints, no solar array system has yet been baselined for a comet lander mission.

SOLAR ELECTRIC PROPULSION

One of the more exciting applications for interplanetary photovoltaics is solar electric propulsion (SEP). Combining high power lightweight solar arrays with efficient ion propulsion will provide a multitude of benefits for future missions. For many missions the use of SEP will dramatically reduce flight times to distant targets. For others, the use of SEP will allow for increases in the spacecraft science mass. These benefits arise from the advantage of SEP in achieving high spacecraft velocities with a minimum of mass. These advantages are well understood by mission designers and the first New Millennium (NM) mission is planned to space qualify an SEP stage suitable for a wide range of small spacecraft missions.

Unlike conventional Earth orbiting spacecraft, where high powered array systems are combined with heavy battery storage systems, SEP stages will rely only on PV for propulsion, with no allocation for thrusting during non-illuminated periods. As a result, the solar array can be a significant fraction of the SEP mass and low mass array technology is directly applicable. SEP arrays may also serve a dual purpose for outbound missions, for as the array power drops with increasing solar distance, eventually being insufficient for propulsion stage operation, it is in most cases more than sufficient to power a small spacecraft. In this manner a well designed mission would utilize a single array for both propulsion and the spacecraft. This is the approach that will be followed for the first New Millennium flight. For the NM flight test, it will be critical to verify that the solar array is not degraded to any extent by metallic erosion products of the SEP thruster. Since the thruster operates best at high voltages, the NM array will be operated at approximately 100 V with down conversion used for the spacecraft (28 V) and up conversion used for the ion thruster (1000 V). Due to inefficiencies in the conversion process and the high power level required for the thruster, future efforts will attempt to design direct drive solar arrays that can operate at 1000 V and directly feed the propulsion stage. At present, these voltage levels have not been demonstrated with solar arrays and will be a formidable challenge. Concentrator solar arrays that require fewer cells are the most likely choices for such systems.

EXAMPLE SEP BENEFITS

An example of the advantages attributable to the use of SEP is in the Mercury Orbiter/Lander mission described previously. Optimum SEP trajectories, based on the performance of xenon ion "NSTAR" thrusters, with flight times between 600 and 880 days were developed. The spiral trajectories have flight times equal to or less than those required for multiple Venus and Mercury gravity assists. Launch opportunities exist approximately every four months. Various SEP system mass reductions were examined including an "advanced SEP" design which incorporates "TAL" (anode layer) thrusters.

Unlike the all chemical propulsion design, the maximum landed mass for an SEP-delivered system occurs for lander deployment from low circular orbits. The reason is that the ΔV required to circularize the orbit at Mercury is less than 10% of the total ΔV required for the mission (for the chemical mission option, the maximum orbiter and lander masses are delivered for Mercury orbits which are highly eccentric). In this case, the orbiter propellant savings associated with using a high eccentricity orbit do not compensate for the higher lander propellant loads.

Assuming major improvements in high- I_{sp} , high thrust, lightweight chemical propulsion, the Mercury orbiter/lander mission is extremely challenging and requires the use of low mass spacecraft systems. Advanced SEP offers the promise of significantly higher delivery masses and shorter flight times compared with the all chemical option.

CURRENT SPACECRAFT DEVELOPMENTS

Several photovoltaic powered planetary missions are in development or will begin development in fiscal year 1996. These include the Mars Pathfinder lander and rover mission, the Mars Global Surveyor orbiting mission, the Mars 1998 orbiter and lander mission, the Near Earth Asteroid Rendezvous (NEAR) mission, and the first New Millennium flight now planned for an asteroid and cometary rendezvous. These missions utilize advances in solar array technology that have emerged in recent years, especially the emergence of GaAs/Ge solar cells. The Applied Physics Laboratory's NEAR will be the first NASA planetary mission to launch with GaAs/Ge. The NEAR array will provide 1800 W at 1 AU and 400 W at 2.2 AU on its trajectory to the asteroid Eros. In addition, all of the planned Mars missions will utilize GaAs/Ge solar cells for the orbiter or lander, or both, in order to achieve the desired energy balance, especially when packaging has limited available surface area. This marks a clear transition to the acceptance of GaAs/Ge solar arrays for planetary missions.

The Mars Global Surveyor orbiter, to be launched in November of 1996, employs 2-GaAs/Ge and 2-Si panels to provide 667 W of power. It will collect a variety of data on Mars surface and atmospheric characteristics over a two year mission. Of particular note is the fact that the arrays will be utilized for aerobraking to circularize the orbit following insertion. This has resulted in special design considerations relating to thermal issues. The Mars Pathfinder Mission to be launched in December of 1996 employs GaAs/Ge for cruise, lander and a 6-wheeled rover vehicles. This mission is to be the first of a series of missions to place weather, seismological, and other monitoring and scientific instruments on the Martian surface. The lander array will provide about 200 W on clear days and the rover array 16 W. For the Mars 1998 mission, now in the early phase of development, the baseline now includes GaAs/Ge on an orbiter (1440 W), GaAs/Ge on a lander cruise array (470 W), and Si on a lander array (1440 W, all powers are BOL).

The first New Millennium flight plans to employ a linear concentrator array, supplied by the Ballistic Missile Defense Organization in partnership with NASA Lewis Research Center, with GaInP/GaAs/Ge, 2-junction, multi-bandgap solar cells. This mission will demonstrate solar electric propulsion for the first time in a planetary exploration environment. The array will provide 2.6 kW at 1 AU (BOL) to an NSTAR xenon ion thruster system. Approximately 200 W will be used by the

New Millennium spacecraft for engineering and science functions. The combined demonstration of concentrator array, multi-bandgap cells, and solar electric propulsion will open a new era in scientific exploration of deep space.

SUMMARY

We have provided a representative sampling of studies that provide a wide range of requirements for the future use of photovoltaic solar arrays in planetary and deep space scientific missions. These requirements represent major challenges for solar array technology developers. Inner planet missions face special thermal and possibly high radiation environments. Missions that would travel to more than 3 AU or beyond must perform under low intensity, low temperature conditions, also with the possibility of high radiation environments. A completely different set of requirements await solar arrays that must be landed on the surfaces of terrestrial planets or small planetary bodies, where dust and atmospheres, in addition to possible wide temperature cycles must be taken into account. Finally, requirements for low mass and compact packaging will require innovative structures and deployment techniques, such as inflatable systems, in order to meet launch vehicle constraints. Such concepts may also include innovative architectures like a combined power and telecommunications system using a deployable concentrator/antenna. If proven feasible, a "power antenna" system might enable a low power photovoltaic power source to be used at greater distances from the sun while meeting high science telemetry data rates. The realization of such innovative architectures will, of course, depend heavily on parallel advances in other spacecraft technologies. Spacecraft pointing, attitude control, thermal control, and fault tolerance requirements will be key drivers in the power system evolution to come.

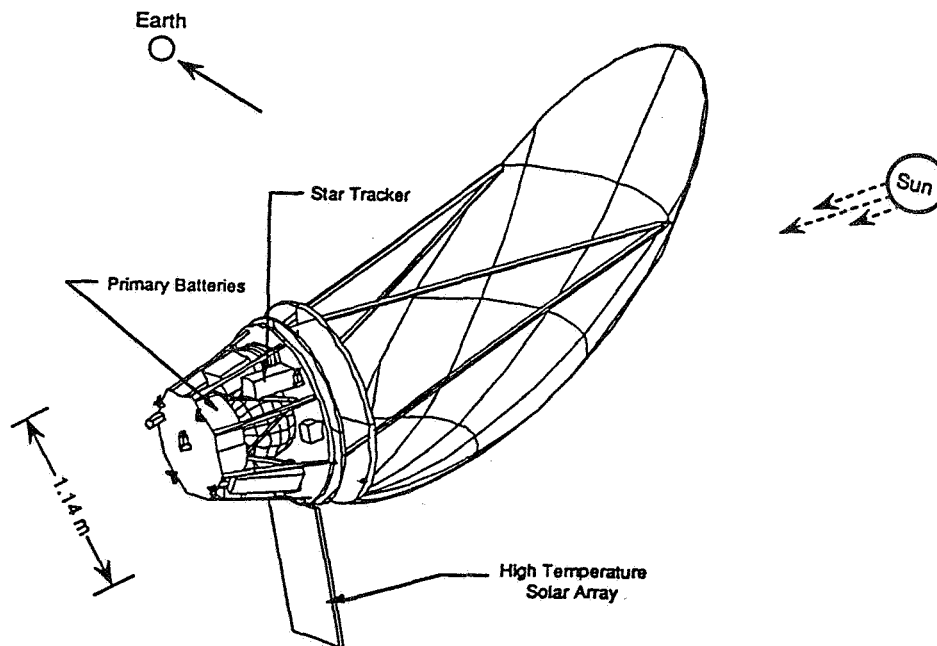


Figure 1. Solar Probe Spacecraft Concept

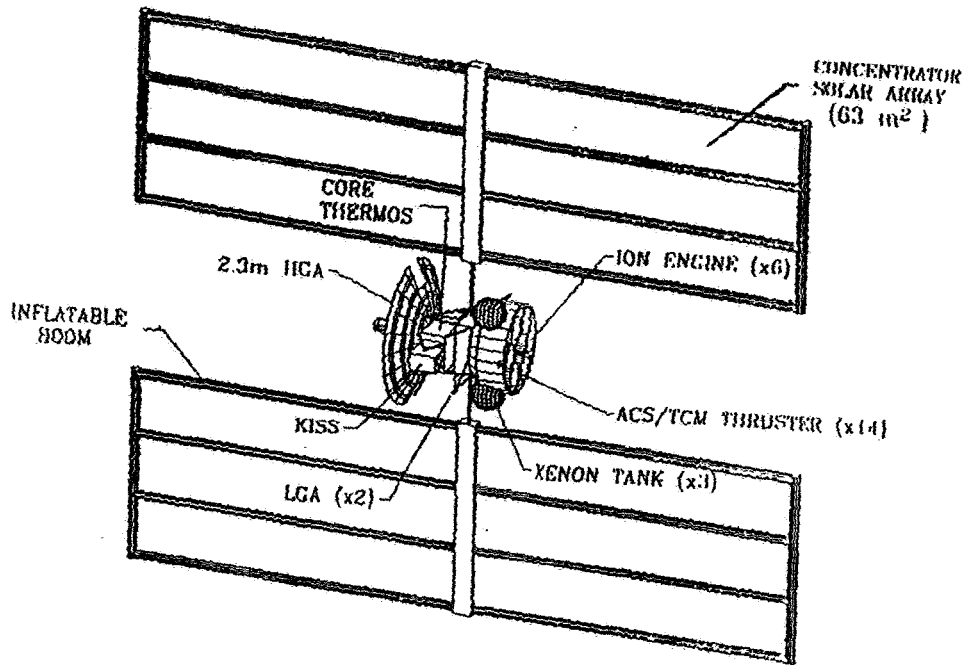


Figure 2. Kuiper Express Concept

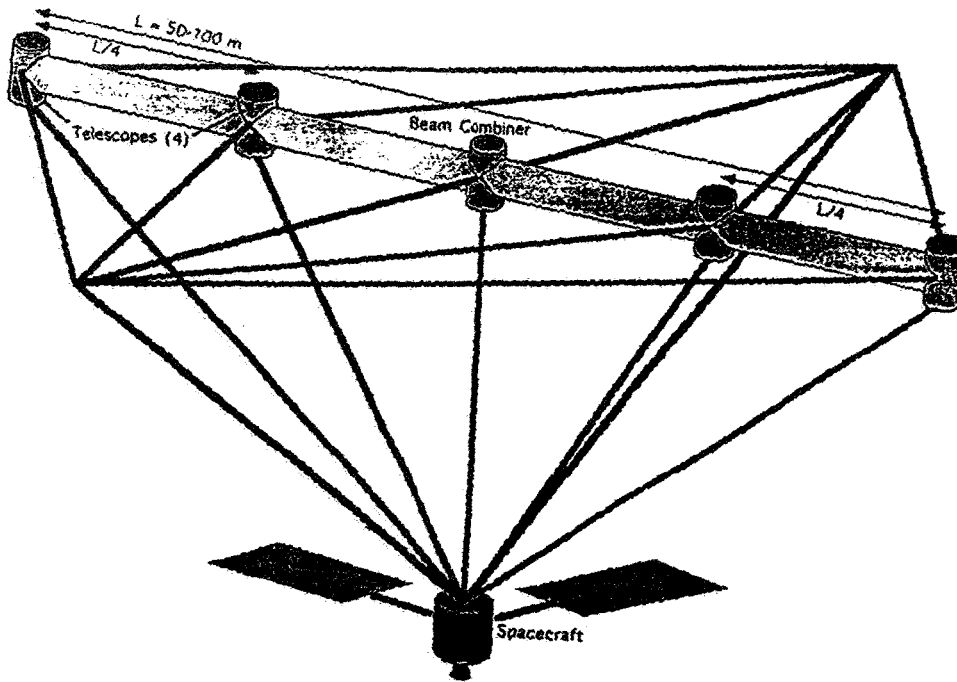


Figure 3. Extra Solar Planetary Search Spacecraft Concept

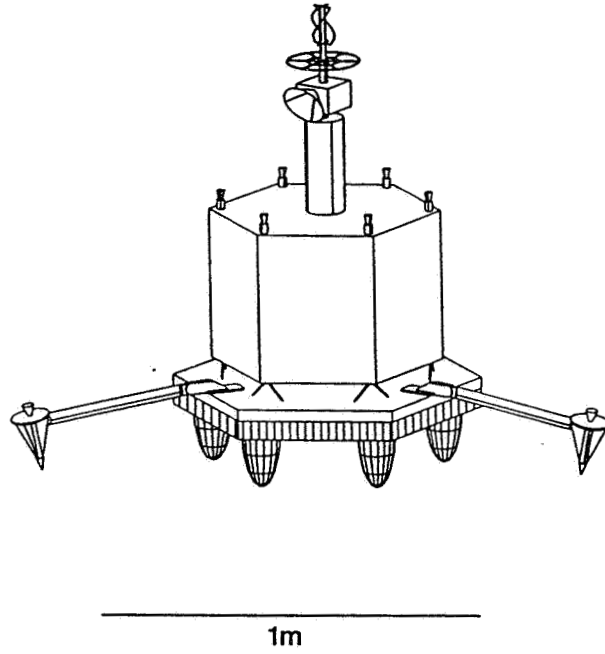


Figure 4. Comet Lander Concept

S2
IN - 50387

DEVELOPMENT OF ADVANCED SI AND GA AS SOLAR CELLS FOR INTERPLANETARY MISSIONS

G.Strobl¹, P.Uebele¹, R.Kern¹, K.Roy¹, C.Flores², R.Campesato², C.Signorini³, K.Bogus³, P.Cozi⁴

¹ASE, Heilbronn Germany; ²CISE spa, Milano Italy; ³ESA/ESTEC, Noordwijk The Netherlands; ⁴CRSC, Roma Italy.

Abstract

The deep space and planetary exploration project have been acquiring more and more importance and some of them are now well established both in ESA and NASA programs.

This paper presents the possibility to utilise both silicon and gallium arsenide solar cells as spacecraft primary power source for missions far from the Sun, in order to overcome the drawbacks related to the utilisation of radioisotope thermoelectric generators - such as cost, safety and social acceptance.

The development of solar cells for low illumination intensity and low temperature (LILT) applications is carried out in Europe by ASE (Germany) and CISE (Italy) in the frame of an ESA programme, aimed to provide the photovoltaic generators for ROSETTA: the cometary material investigation mission scheduled for launch in 2003. The LILT cells development and testing objectives are therefore focused on the following requirements: insolation intensity as low as 0.03 Solar Constant, low temperature down to -150 C and solar flare proton environment.

At this stage of development, after the completion of the technology verification tests, it has been demonstrated that suitable technologies are available for the qualification of both silicon and gallium arsenide cells and both candidates have shown conversion efficiencies over 25 % at an illumination of 0.03 SC and a temperature of -150 C. In particular, when measured at those LILT conditions, the newly developed "HI-ETA/NR-LILT" silicon solar cells have reached a conversion efficiency of 26.3 %, that is the highest value ever measured on a single junction solar cell.

A large quantity of both "HI-ETA/NR-LILT" silicon and "GaAs/Ge-LILT" solar cells are presently under fabrication and they will be submitted to a qualification test plan, including radiation exposure, in order to verify their applicability with respect to the mission requirements. The availability of two valid options will minimise the risk for the very ambitious scientific project.

The paper describes how the technical achievements have been possible with Si and GaAs LILT solar cells (including a comparison between measured and modelled I-V characteristics) and it presents the technology verification tests results.

1. Introduction

In the last few years, both in Europe and in U.S.A., considerable resources have been dedicated to the development of solar cells capable of good performances under low light intensity and low temperature conditions. The effort is motivated by the increasing scientific interest in space missions far from the sun. As a matter of fact, interplanetary explorations and cometary investigation projects are well established both in ESA and NASA scientific programmes.

Although the spacecraft primary power source in deep space could be provided by the Radioisotope Thermoelectric Generators (R.T.G.), the use of photovoltaic generators would be preferred because of a number of factors, like cost, safety, social acceptance and, as far as European Missions are concerned, non availability of R.T.G. technology in Europe.

The R. & D. programme "Solar cells for Low Intensity / Low Temperature (LILT) applications" was initiated by ESA in 1991 with the general aim of supporting future interplanetary projects and with an initial target for 0.1 Solar Constant (S.C.) and -100 C. LILT conditions. More recently, the LILT R. & D. programme has been finalised to a specific mission: ROSETTA, the ESA project for cometary investigation, due for launch in 2003. The ROSETTA baseline mission foresees 10 years lifetime and two options power requirements at 5,8 A.U. 260W and 680W respectively. The LILT cell development programme objectives have been consequently adapted to the ROSETTA LILT conditions, i.e. low intensity equivalent to 0.03 S.C. and temperature down to -150 C.

The ESA LILT cell R&D. programme consists of the parallel developments of two different technologies, silicon and gallium arsenide, and it is carried out by the co-operation of two European Companies: ASE, taking over the leadership of the programme, the silicon cell development and the whole characterisation work; CISE, executing the gallium arsenide development. Both the two technology developments have been based on existing space proven cell structures, initially characterised at LILT conditions and then modified in order to reduce the LILT degradation effects [2,3,4]. Subsequently, a technology verification test programme has been accomplished on the newly developed Si and Ga As LILT cells and, finally, 150 samples are presently under manufacturing.

2. Silicon solar cell development

2.1 HI-ETA/NR-LILT silicon solar cell

The interest in using silicon solar cells to power spacecrafts for interplanetary missions began over three decades ago. Anyhow, severe fill factor degradation effects under LILT conditions, occurring on a statistical basis and which could not be assessed from room temperature measurements, prevented silicon solar cells to be used under these particular conditions so far [1].

With the newly developed HI-ETA/NR-LILT silicon solar cell, it has been demonstrated for the first time that the detrimental effects of fill factor deterioration are suppressed, even more that the fill factor is increasing at low temperature as expected from Shockley's diode theory.

The HI-ETA/NR-LILT silicon solar cell structure, its LILT performance, fundamental LILT characterisation and first results obtained during technology verification testing have already been presented in previous papers [2,3,4]. Here a review of the main achievements will be given, recent results of electron irradiation test with HI-ETA/NR-LILT solar cells will be presented and another inherent design feature of HI-ETA/NR-LILT solar cells, namely an integrated Zener diode (IZD) for by-pass shunting will be discussed.

The HI-ETA/NR-LILT silicon solar cell has all the characteristic features of the standard HI-ETA technology, such as $10 \Omega\text{cm/CZ}$ base material, n^+/pp^+ structure, front and rear side oxide passivation, fine grid line pattern defined by photolithography, double layer antireflection coating, Al rear side reflector and space proven TiPdAg contact system. In addition, the HI-ETA/NR-LILT silicon solar cell has a non-reflective front surface realised by inverted pyramids for a high current output, it is equipped both with a planar structure including a p^+ - guard-ring channelstopper for eliminating edge channel currents and with heavy n^{++} - diffusion under the front contact grid for reducing diode loss currents caused by filamentary paths under the front contact metal. By these measures a high efficiency is achieved and the diode loss currents under LILT conditions are reduced resulting in no fill factor degradation.

Although the structure of the HI-ETA/NR-LILT silicon solar cell is more complicated than standard HI-ETA cells, it can be fabricated in a standard HI-ETA silicon solar cell production line.

The illuminated I-V characteristics of bare HI-ETA/NR-LILT silicon solar cells as measured under an insolation intensity of 0.11 SC and 0.037 SC in the temperature range of $+25^\circ\text{C}$ to -150°C are displayed in Figure 1. The measurements have been performed in a vacuum chamber with quartz window, where the samples could be cooled by liquid nitrogen and the insolation intensity of the solar simulator could be adjusted by a grey filter and the lamp current.

As can be realised from Figure 1, the current is decreasing at low temperature for both intensities due to an increase of energy gap E_g and a reduction in minority carrier lifetime τ [2]. The voltage strongly increases at low temperature due to a reduction of the diode saturation current J_0 which is varying with the square of the intrinsic carrier density n_i [5]. The most remarkable result is the fill factor behaviour at extreme LILT conditions. Even for an insolation intensity of only 0.037 SC and temperatures as low as -150°C with its very low photogenerated current there exists no fill factor degradation, since the diode loss currents are reduced to very low levels. Instead the fill factor is increasing at low temperature following Shockley's diode theory due to a reduction of the thermal voltage $U_T=kT$ in the exponential function of the diode equation [5].

The dark forward J-V characteristics of HI-ETA/NR-LILT and standard HI-ETA solar cells are displayed in Figure 2 and 3 as measured for varying temperatures between $+25^\circ\text{C}$ and -175°C and fitted with the well-known two diode model [2]. The two-diode model is consisting of two diodes in parallel with one following ideal Shockley's behaviour and the other taking into account recombination/generation currents within the space charge depletion region. From Figure 2 and 3 it can be realised that in case of HI-ETA/NR-LILT silicon solar cells the measured curves are very close to the theoretical ones, whereas for standard HI-ETA solar cells there are strong deviations especially in the low current, low temperature region. These deviations of measured dark J-V characteristics from modelled ones are responsible of the fill factor deterioration of standard HI-ETA solar cells under LILT conditions and have already been observed in previous work [6] ("flat spot" effect).

2.2 Integrated Zener Diode (IZD)

From standard silicon space solar cells it is known that in reverse bias conditions, e.g. in partially shadowed arrays, the solar cell may fail due to a non-reversible localised break-through of the pn-junction for voltages higher than 20V. This effect is well-known as the hot-spot phenomenon. Highly doped junctions, however, such as the n^+/p^+ (emitter/channelstopper) junction, exhibit a relatively large leakage current under low reverse bias voltages: this results in the reversible Zener break-through of HI-ETA/NR-LILT solar cells, displayed in Figure 4 as measured in dark and under AM0 illumination for temperatures varying from $+25^\circ\text{C}$ to -150°C . From the temperature behaviour of the Zener voltage U_z , which is in the range of 6 - 8 V, it can be deduced that avalanche break through is the responsible mechanism. Thus the

behaviour of HI-ETA/NR-LILT silicon solar cells in reverse bias is characterised by an integrated Zener diode (IZD) for by-pass shunting. The equivalent circuit can be inspected in Figure 5.

3. Ga As solar cell development

3.1. LILT GaAs solar cell structure

The GaAs solar cells were grown utilizing a MOCVD system working at a very low pressure (20 mbar) in order to improve the gas velocity and therefore the layer uniformity and to reduce the gas consumption. The sources for Ga, As and Al are trimethylgallium, arsine and trimethylaluminium. The dopants are silane and dimethylzinc. The basic structure of a GaAs LILT solar cell is illustrated in Figure 6.

The epitaxial GaAs layers can be grown on GaAs or on Ge substrates.

A GaAs LILT solar cell differs from a standard GaAs solar cell for these characteristics:

- very low doping level in the cell base
- high doping level in the cap layer
- antireflection coating deposition
- introduction of a i-layer into the junction

The impact of these items on the LILT performances will be explained in the following.

Low doping level in the base. The short circuit current of a solar cell decreases at low temperature because of the energy gap increasing. The temperature coefficient of the short circuit current is affected by the temperature behaviour of the hole diffusion length in the base region. As demonstrated [7], the temperature behaviour of the diffusion length depends on the doping level, in particular at low doping level the hole diffusion length increases as the temperature decreases. Therefore a doping level of $2 \times 10^{16} \text{cm}^{-3}$ was chosen for the base of LILT solar cells.

High doping level of the cap. The dominant mechanism for the ohmic conduction between GaAs and metal depends on the doping level of the semiconductor. In general there are three mechanisms of conduction: a) thermoionic emission (TE), b) thermoionic field emission (TFE), c) field emission (FE). The first two mechanisms are temperature dependent and at low temperature present a high contact resistance value. The FE mechanism is tunneling dominated and then temperature independent. In order to obtain a good contact for a LILT solar cell it is recommended that the FE mechanism dominates, then a high doping level of the cap layer is requested. For LILT solar cells a doping of $2 \times 10^{19} \text{cm}^{-3}$ was selected for the cap layer.

ARC deposition. The antireflection coating deposition technique affects the dark currents. The electron beam evaporation forces the tunneling and the generation-recombination currents to increase and lower open circuit voltage and FF were measured at low temperature and low intensity conditions. For these reasons, thermal evaporated coating (ZnS/MgF₂) was used for preliminary samples. This double antireflection coating is optimal for a bare GaAs solar cell operating at low temperature because of its low reflection in the UV part of the spectrum (in fact at low temperature the energy gap increases and shifts the spectral response towards higher energies).

i-layer. The dark currents of a GaAs solar cell at low temperature are affected by the tunneling of carriers through impurity states in the space charge region [2]. In order to limit the tunneling current, an undoped i-layer was introduced into the junction. The spacer thickness was varied from 12 nm to 35 nm. The effect of the thinner spacer was negligible because of the Zn diffusion during p-type layer growth. GaAs LILT solar cells were characterized in low temperature, low intensity conditions. Table I reports the performances in AM0, 0.11 - 0.03 suns and 25/-150 C for different GaAs samples with and without spacer in the p-n junction. The cells with spacer have higher FF at low temperature and low intensity. Thus this cell type is the most suitable one for LILT applications.

From Table I, it is possible to notice that GaAs/GaAs cells with 35 nm spacer exhibit very good LILT performances, an efficiency of 25.4% was reached at -150 C, 0.11 suns and an efficiency of 24.7% was reached at -150 C, 0.03 suns.

In order to understand the FF temperature behaviour and to extrapolate GaAs solar cells behaviour at LILT conditions, dark measurements at low temperature are necessary.

The experimental dark I-V curves of different GaAs samples were recorded and fitted using a triple diode model developed by CISE [4]; the introduction of the i-layer lowers the tunneling saturation current of one order of magnitude.

3.2 Comparison between GaAs/GaAs and GaAs/Ge LILT cells

Using the MOCVD technique it is possible to grow the GaAs epitaxial layers on GaAs or Ge substrates. Basically there are no differences in the performances of a LILT GaAs cell grown on GaAs or Ge substrate even if we expect for GaAs/Ge cells a conversion efficiency a little bit smaller than for the pure GaAs cell. The main advantages of growing on Ge are:

- lower cell cost;
- higher mechanical strength;
- lower thickness with the possibility to decrease it down to 100 μm ;
- lightweight solar cells, as a consequence of low thickness.

The main difficulty to transfer the LILT structure on a Ge substrate is to obtain a passive GaAs/Ge solar cell. The passivity means that the Ge substrate does not present neither a heterojunction with GaAs nor a diffused junction into Ge due to the different diffusion coefficient and solubility of Ga and As in the Ge. In fact, as demonstrated in [8], an active GaAs/Ge solar cell is not suitable for LILT application because of the difference between temperature coefficients of I_{sc} for the GaAs and the Ge junctions. Moreover an active GaAs/Ge cell shows a knee in the I-V curve under sunlight because of the imperfect matching of current between the two junctions.

From LILT characterization it is possible to determine if a GaAs/Ge cell is active or passive by means of the open circuit voltage temperature coefficient. In fact while for passive solar cells the V_{oc} temperature coefficient is equal to that of GaAs/GaAs cell (1.9-2.0 mV/C), for active GaAs/Ge solar cell the V_{oc} temperature coefficient exceeds 2.2 mV/C. The Ge contribution to the open circuit temperature coefficient, in an active cell, is quite variable and depends on the dark mechanism that dominates the dark I-V curve of the Ge junction.

The analysis of the voltage temperature coefficient is not a very precise method to decide if a cell is active or passive. In fact, according to our experience, if the Ge extravoltage is in the range of 10-30 mV, the temperature coefficient could be similar to that of a pure GaAs cell. For this category of cells the best way to decide the existence of a Ge P/N junction is to measure the cell voltage under a solar simulator, at the same current, using both a neutral filter and a short-wavelength pass filter.

Some high efficiency GaAs/Ge LILT solar cells were produced and measured. Table II reports the low temperature, low intensity characteristics of a GaAs/Ge solar cell. The efficiency of this cell in standard conditions was 20.9 %, AM0, the cell area is 2x4 cm². At low temperature (-150 C), 0.11 suns, the efficiency of this cell was 24.5 %. The passivity of the cell was verified by means of the open circuit voltage temperature coefficient that was similar to that of GaAs/GaAs solar cells, and by means of filters.

Some dark I-V curves of GaAs/Ge solar cells have been recorded. Figure 7 shows a comparison between dark I-V curves at room temperature and low temperature for GaAs/GaAs and GaAs/Ge solar cells. At low voltages, a strong contribution of the dark current is shown in GaAs/Ge solar cells while it is not noticeable in GaAs/GaAs solar cells. This contribution seems to be related to shunt paths across the junction. The shunt paths can be induced by dislocations originating at the cell edge during the dicing saw cutting process, while the GaAs cells are usually cleaved after scribing. A mesa etch before cell cutting could be the best solution to this problem.

3.3 Correlation between room and low temperature measurements

The electrical characterization of illuminated parameters of GaAs solar cells in low temperature, low intensity conditions, needs quite sophisticated apparatus to be made and it is time-consuming.

Then it is advisable to completely characterize only few samples under LILT conditions and identify a correlation method between room temperature and LILT performances.

In fact it is possible to predict the behaviour at low temperature and low intensity of short circuit current and open circuit voltage of a given sample, when the illuminated I-V performances and the dark curve at room condition are known.

In fact I_{sc} is linearly depending on the solar intensity and the temperature coefficient is well established. From the dark curve it is possible to estimate the V_{oc} at low intensity, and then applying the temperature coefficient for the open circuit voltage it is possible to predict the low temperature behaviour.

The estimation of FF and efficiency of the sample is much more complicated because the temperature coefficient of the FF differs from one sample to another. In order to have a preliminary evaluation of the LILT performances of a GaAs solar cell, the room temperature performances and the dark I-V curve at 300 K and 123 K are needed.

A computer code was developed that extrapolates the illuminated performances from the dark curves measurements.

Table III provides with a comparison between the LILT performances (directly measured under the solar simulator) and the values extrapolated from the dark curves for a GaAs LILT sample.

4 Technology verification testing

In parallel with the cell technology development work a wide range of testing activities has been performed with both 40 HI-ETA/NR-LILT and 40 GaAs-LILT solar cells and solar cell assemblies (SCA's) including front interconnector adherence, rear interconnector adherence, extended storage simulation, antireflection coating adherence, BOL performance and EOL performance measurements[4]. 1 MeV electron irradiations with fluences ranging from $10^{13}e/cm^2$ to $10^{15}e/cm^2$ have been performed at the Inter-faculty Reactor Institute of the Technical University in Delft/The Netherlands

In this paper the EOL performance data of HI-ETA/NR-LILT solar cell assemblies are presented in detail. The front and rear side silver interconnectors have been welded by using the parallel gap welding process and for glassing 100 μ m thick CMX coverglasses have been used.. Before electron irradiation, the HI-ETA/NR-LILT SCAs have been measured under low intensity illumination at room temperature, subsequently the 1 MeV electron irradiation has been carried out at room temperature and after electron irradiation the cells have been measured again under low intensity illumination at both room temperature and low temperature. The degradation data for the different electron irradiation dosages have been determined from different HI-ETA/NR-LILT SCAs of the same structure and the absolute low temperature EOL data of one SCA have been related with the absolute low temperature BOL data of another SCA in order to calculate the relative degradation behaviour.

In Figures 8 to 11 the relative degradation data of HI-ETA/NR-LILT SCAs measured during this electron irradiation experiment are displayed including absolute BOL values for open-circuit-voltage (V_{oc}), short-circuit-current density (J_{sc}), maximum power density (P_{max}), fill factor (FF) as measured under an insolation intensity of 0.11 AM0 and temperatures ranging from +25°C to -175°C.

Five LILT Ga As solar cells (three GaAs/GaAs and two GaAs/Ge) were dressed with silver plated molybdenum interconnectors and 150 μ m thick coverglasses and submitted to electron irradiation at Delft University. The cells were measured at LILT conditions before and after irradiation.

The electrical tests, carried out after irradiation, showed some incongruities, probably because of difficult measurement accuracy at very low intensities.

A new batch of Ga As samples has been submitted to electron irradiation and sent to Spasolab laboratory (Madrid, Spain) for electrical performance testing: the discussion on Ga As solar cell radiation hardness at LILT conditions shall be based on those measurement results, expected in November '95.

5. Conclusions and future work

The ESA R. & D. programme "Solar cells for Low Intensity / Low Temperature applications" is coming to a conclusion: suitable technologies are available for the qualification of both silicon and gallium arsenide (on germanium) LILT solar cells, according to the ROSETTA mission requirements.

The availability of two technologies will minimize the risk for the project.

With the newly developed HI-ETA/NR-LILT silicon solar cells it has been demonstrated for the first time that the fill factor deterioration which prevented silicon solar cells to be used under these conditions so far can be suppressed. In future work emphasis will be paid on raising the current especially at low temperature operation.

The LILT GaAs solar cell structures were optimized both on GaAs and Ge substrates using a small scale MOCVD Aixtron reactor. According to the experimental results, the highest efficiency can be obtained at LILT conditions with GaAs solar cells grown on GaAs substrates. The GaAs/Ge structure seems to be slightly affected by the lattice mismatch between the substrate and the grown layers. A test procedure was proposed to predict the LILT behaviour of GaAs solar cells avoiding time-consuming and expensive low temperature measurements.

100 HI-ETA/NR-LILT silicon solar cells and 50 LILT GaAs solar cells are being produced and will be ready by December 1995; a dedicated test plan has been defined, including: LILT electron and proton irradiation, I-V measurements at high intensities, LILT electrical performance measurements on large number of samples for statistical assessment.

Low temperature electron irradiation experiments have been set up, including in-situ electrical measurements without any warming-up annealing and, on this purpose, dedicated test facilities have been developed at the University of Paris.

The final part of the development and the additional work needed to achieve the qualification are expected to be carried out in the frame of the ROSETTA project.

TABLE I: LILT performances of bare GaAs/GaAs solar cells

| sample: moc88b | | AM0 performances | | Isc = 260.5 mA | | FF = .81 | | | |
|-----------------------|------------|-------------------------|-----------|-----------------------|------------|----------------------|-----------|-------------|--|
| without spacer | | 1 sun, 25 C | | Voc = 1037 mV | | Eff. = 19.8 % | | | |
| | | s.c.= 0.1092 | | | | s.c.= 0.0299 | | | |
| T | Voc | Isc | FF | Eff. | Voc | Isc | FF | Eff. | |
| (C) | | (mA) | | (%) | | (mA) | | (%) | |
| 25 | 926 | 28.45 | 0.736 | 16.40 | 847 | 7.8 | 0.740 | 15.11 | |
| 0 | 983 | 28 | 0.779 | 18.15 | 913 | 7.69 | 0.784 | 17.01 | |
| -50 | 1084 | 27.6 | 0.805 | 20.37 | 1017 | 7.6 | 0.815 | 19.46 | |
| -100 | 1182 | 27.3 | 0.841 | 22.95 | 1132 | 7.5 | 0.830 | 21.77 | |
| -130 | 1237 | 26.9 | 0.839 | 23.63 | 1193 | 7.38 | 0.825 | 22.44 | |
| -150 | 1272 | 26.65 | 0.842 | 24.14 | 1218 | 7.27 | 0.830 | 22.71 | |

| sample: d19a | | AM0 performances | | Isc = 264.7 mA | | FF = .81 | | | |
|---------------------|------------|-------------------------|-----------|-----------------------|------------|---------------------|-----------|-------------|--|
| spacer 30 sec | | 1 sun, 25 C | | Voc = 1039 mV | | Eff. =20.2 % | | | |
| | | s.c.= 0.1124 | | | | s.c.= 0.0327 | | | |
| T | Voc | Isc | FF | Eff. | Voc | Isc | FF | Eff. | |
| (C) | | (mA) | | (%) | | (mA) | | (%) | |
| 25 | 951 | 29.7 | 0.755 | 17.59 | 867 | 8.64 | 0.774 | 16.74 | |
| 0 | 1000 | 29.25 | 0.788 | 19.02 | 942 | 8.58 | 0.790 | 18.43 | |
| -50 | 1110 | 28.85 | 0.829 | 21.91 | 1042 | 8.5 | 0.815 | 20.83 | |
| -100 | 1211 | 28.3 | 0.847 | 23.93 | 1147 | 8.43 | 0.834 | 23.29 | |
| -130 | 1269 | 28.1 | 0.848 | 24.93 | 1210 | 8.28 | 0.831 | 24.04 | |
| -150 | 1300 | 27.8 | 0.851 | 25.37 | 1251 | 8.13 | 0.833 | 24.46 | |

| sample: d20A2 | | AM0 performances | | Isc = 263 mA | | FF = .81 | | | |
|----------------------|------------|-------------------------|-----------|----------------------|------------|---------------------|-----------|-------------|--|
| spacer 30 sec | | 1 sun, 25 C | | Voc = 1036 mV | | Eff. =20.1 % | | | |
| | | s.c.= 0.1114 | | | | s.c.= 0.0319 | | | |
| T | Voc | Isc | FF | Eff. | Voc | Isc | FF | Eff. | |
| (C) | | (mA) | | (%) | | (mA) | | (%) | |
| 20 | 962 | 29.3 | 0.764 | 17.92 | 868 | 8.4 | 0.759 | 16.03 | |
| 0 | 1001 | 28.8 | 0.793 | 19.03 | 926 | 8.28 | 0.789 | 17.53 | |
| -50 | 1111 | 28.6 | 0.813 | 21.51 | 1038 | 8.17 | 0.828 | 20.33 | |
| -100 | 1216 | 28.5 | 0.847 | 24.44 | 1149 | 8.08 | 0.855 | 22.99 | |
| -130 | 1256 | 28 | 0.842 | 24.65 | 1216 | 8.04 | 0.861 | 24.37 | |
| -150 | 1286 | 27.5 | 0.852 | 25.08 | 1254 | 7.94 | 0.856 | 24.70 | |

TABLE II: GaAs/Ge solar cell LILT characteristics

| Sample: GaAs/Ge C85A2 with ARC | | | | | | | | |
|---|----------|----------|---------|---------|------|---------|--------------|--------------|
| Performances AM0, 1 SC, 25 C : $I_{sc} = 264$ mA $V_{oc} = 1079$ mV FF=.79 Eff.= 20.9 | | | | | | | | |
| INSOLATION = 0.11 SC | | | | | | | | |
| T [C] | Voc [mV] | Isc [mA] | Vm [mV] | Im [mA] | FF | Eff [%] | dV/dT [mV/C] | dI/dT [uA/C] |
| 25 | 975 | 28.8 | 826 | 26.5 | 0.78 | 18.6 | - | - |
| 0 | 1023 | 28.5 | 865 | 26.3 | 0.78 | 19.3 | -1.92 | 12.0 |
| -50 | 1126 | 28.0 | 976 | 26.1 | 0.81 | 21.6 | -2.06 | 10.0 |
| -100 | 1223 | 27.7 | 1064 | 26.0 | 0.82 | 23.4 | -1.94 | 6.0 |
| -130 | 1278 | 26.9 | 1128 | 25.0 | 0.82 | 23.8 | -1.83 | 26.7 |
| -150 | 1309 | 26.9 | 1141 | 25.3 | 0.82 | 24.5 | -1.72 | 0.0 |
| INSOLATION = 0.03 SC | | | | | | | | |
| T [C] | Voc [mV] | Isc [mA] | Vm [mV] | Im [mA] | FF | Eff [%] | dV/dT [mV/C] | dI/dT [uA/C] |
| 22 | 905 | 9.3 | 745 | 8.5 | 0.75 | 16.7 | - | - |
| 0 | 953 | 9.1 | 803 | 8.3 | 0.77 | 17.6 | -2.18 | 9.1 |
| -50 | 1051 | 9.0 | 901 | 8.2 | 0.78 | 19.6 | -1.98 | 2.0 |
| -100 | 1145 | 8.9 | 982 | 8.2 | 0.79 | 21.3 | -1.88 | 2.0 |
| -130 | 1201 | 8.8 | 1042 | 8.1 | 0.80 | 22.3 | -1.87 | 3.3 |
| -150 | 1232 | 8.7 | 1065 | 8.0 | 0.80 | 22.5 | -1.74 | 5.0 |

TABLE III : Comparison of the predicted and measured values of a GaAs LILT solar cell

| LILT measurements | | | | | extrapolated values | | | |
|-------------------|---------------|---------------|-----|--------|---------------------|---------------|-----|--------|
| 0.11 suns | | | | | | | | |
| T(K) | V_{oc} (mV) | I_{sc} (mA) | FF | Eff(%) | V_{oc} (mV) | I_{sc} (mA) | FF | Eff(%) |
| 295 | 951 | 29.7 | .76 | 17.6 | 954 | 29.7 | .76 | 17.8 |
| 223 | 1110 | 28.8 | .83 | 21.9 | 1107 | 28.8 | .82 | 21.6 |
| 123 | 1300 | 27.8 | .85 | 25.4 | 1306 | 27.8 | .85 | 25.4 |
| 0.03 suns | | | | | | | | |
| 295 | 867 | 8.64 | .77 | 16.7 | 874 | 8.64 | .76 | 16.2 |
| 223 | 1042 | 8.5 | .82 | 20.8 | 1042 | 8.5 | .82 | 20.5 |
| 123 | 1251 | 8.1 | .83 | 24.1 | 1255 | 8.1 | .83 | 24.1 |

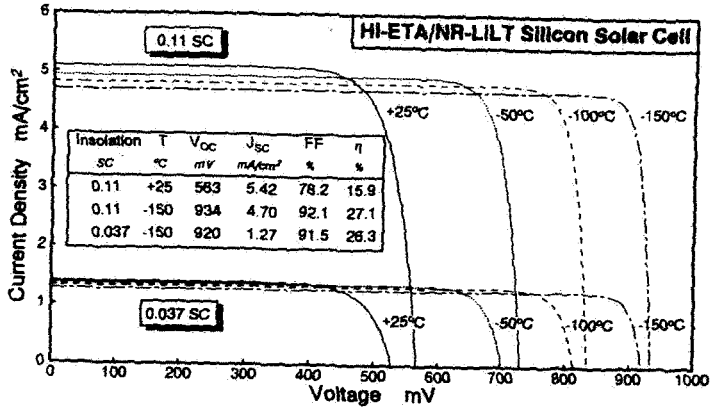


Figure 1: Illuminated I-V characteristics of bare HI-ETA/NR-LILT silicon solar cells (3.78cm*6.19cm) as measured under an insolation intensity of 0.11SC and 0.037SC in the temperature range of +25°C and -150°C.

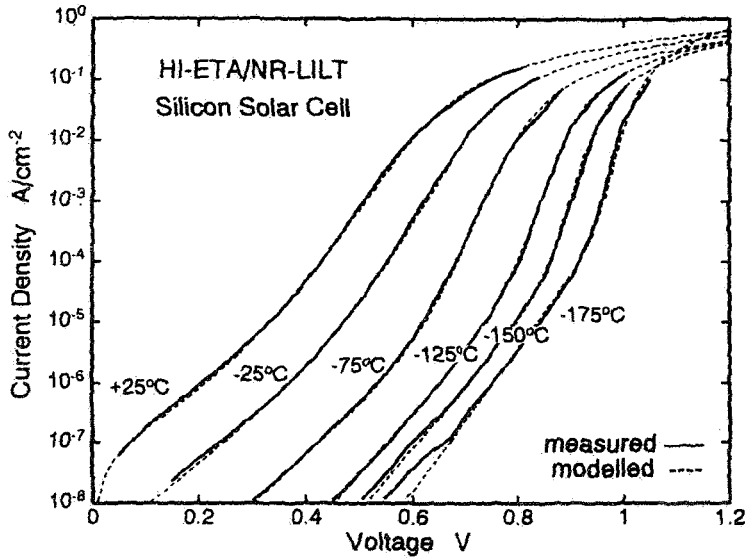


Figure 2: Measured dark J-V characteristics of HI-ETA/NR-LILT silicon solar cell (3.78cm*6.19cm) as a function of temperature with theoretical fit curves of double diode modelling.

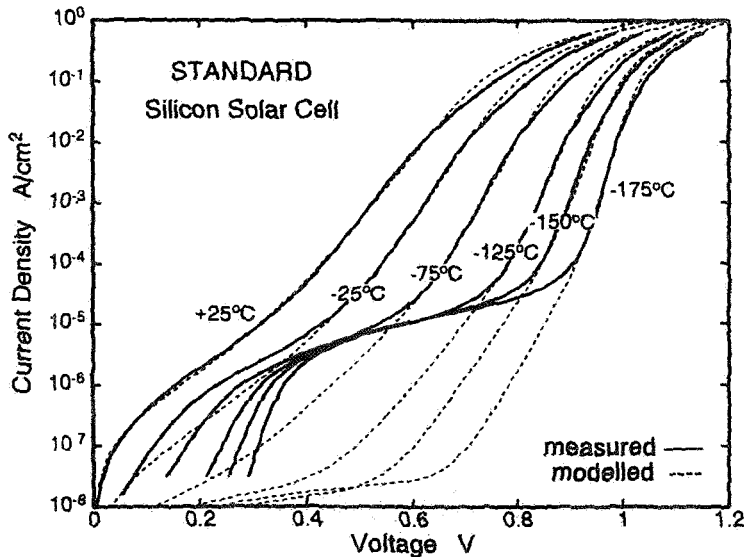


Figure 3: Measured dark J-V characteristics of standard HI-ETA silicon solar cell (3.78cm*6.19cm) as a function of temperature with theoretical fit curves of double diode modelling.

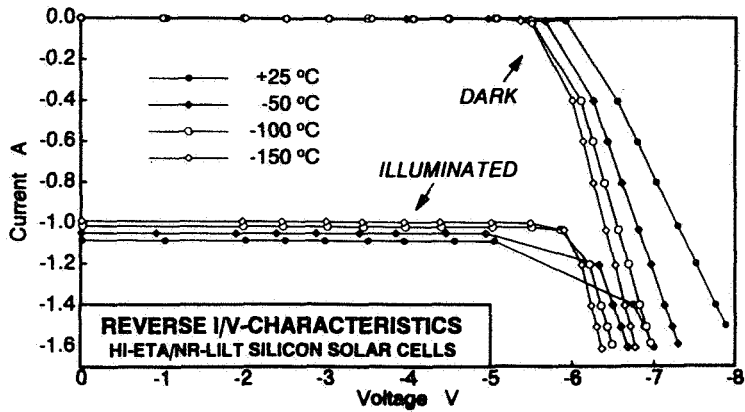


Figure 4: Dark reverse I-V characteristics of HI-ETA/NR-LILT silicon solar cells as measured in dark and under AM0 illumination for temperatures varying between +25°C and -150°C.

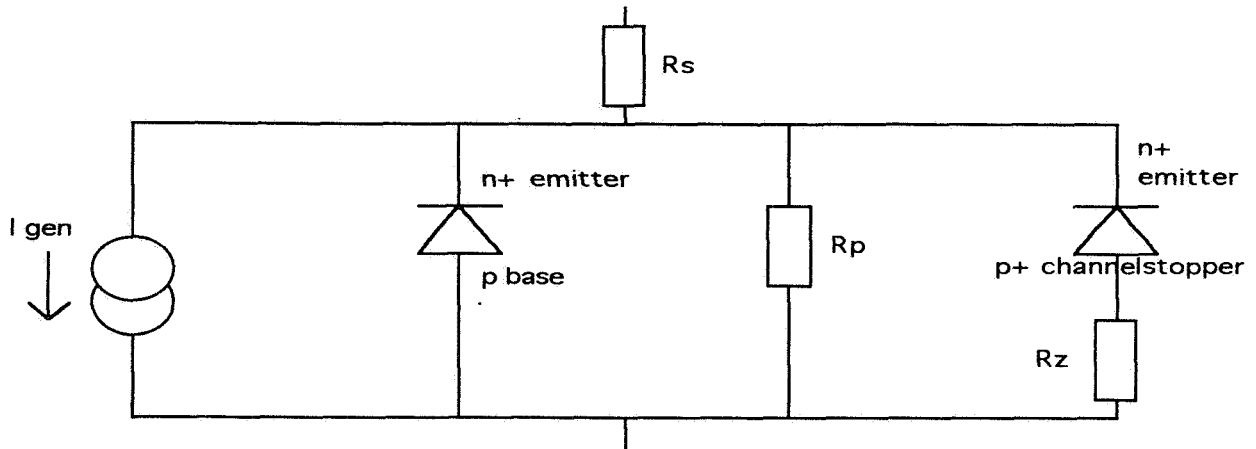


Figure 5: Equivalent circuit for I-V characteristics of HI-ETA/NR-LILT silicon solar cell with integrated Zener diode (IZD) for by-pass shunting.

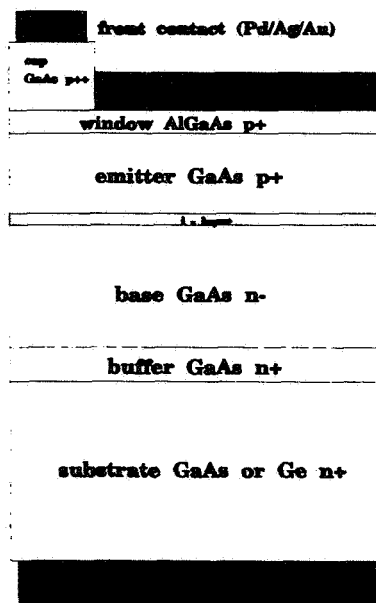


Figure 6: Ga As LILT solar cell structure.

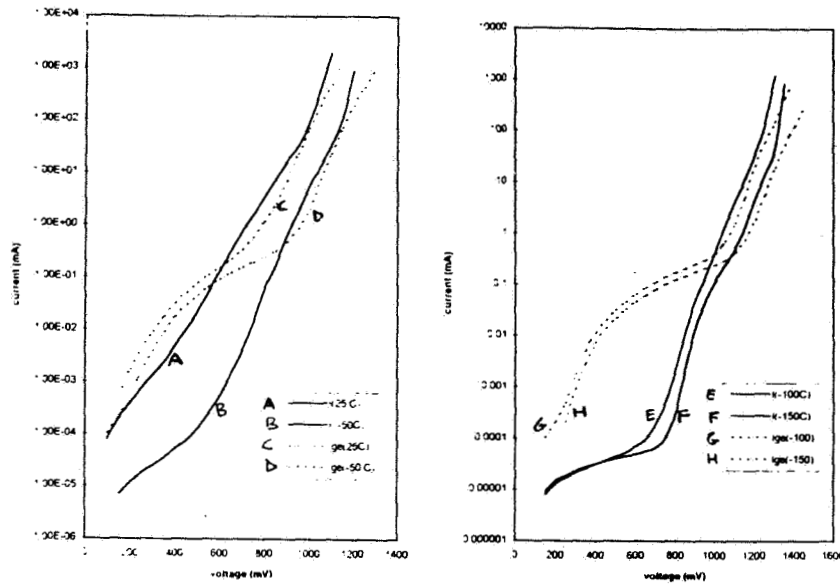


Figure 7: Dark I-V curves for GaAs/Ge and GaAs/GaAs solar cells.

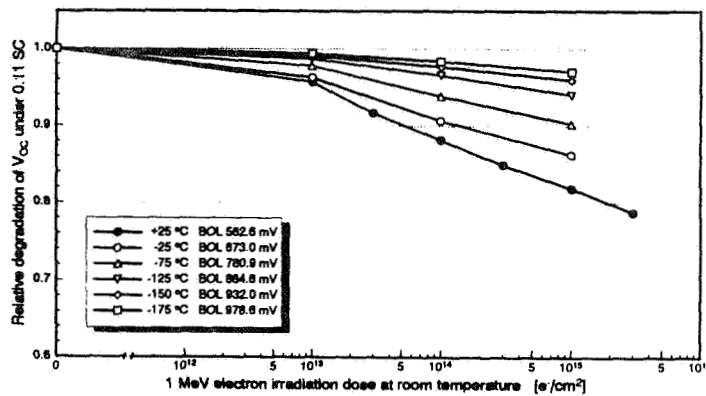


Figure 8: Degradation of open-circuit-voltage V_{OC} of HI-ETA-NR/LILT SCAs (3.78cm*6.19cm) with 100 μ m thick CMX coverglasses under LILT conditions after 1MeV electron irradiation at room temperature.

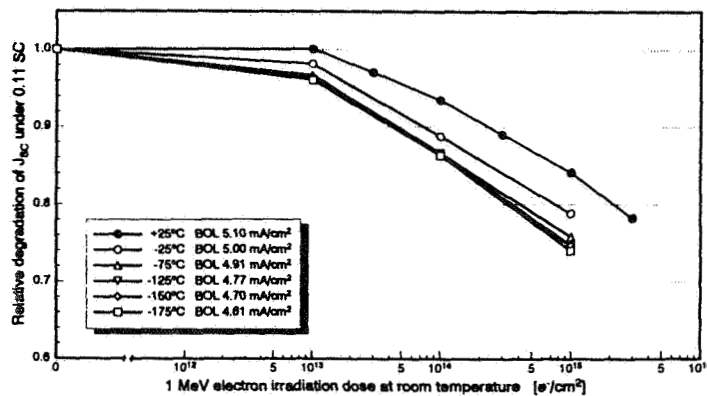


Figure 9: Degradation of short-circuit-current density J_{SC} of HI-ETA-NR/LILT SCAs (3.78cm*6.19cm) with 100 μ m thick CMX coverglasses under LILT conditions after 1MeV electron irradiation at room temperature

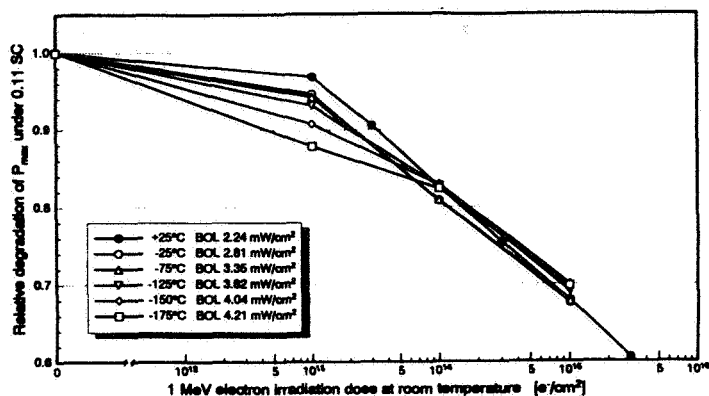


Figure 10: Degradation of maximum power density P_{max} of HI-ETA-NR/LILT SCAs (3.78cm*6.19cm) with 100 μ m thick CMX coverglasses under LILT conditions after 1MeV electron irradiation at room temperature

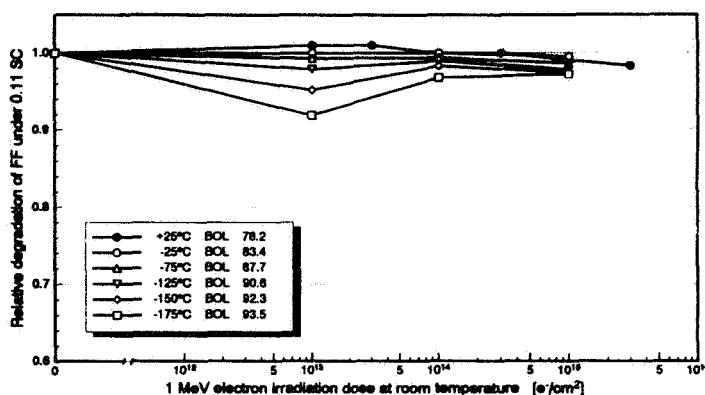


Figure 11: Degradation of fill factor FF of HI-ETA-NR/LILT SCAs (3.78cm*6.19cm) with 100 μ m thick CMX coverglasses under LILT conditions after 1MeV electron irradiation at room temperature

References

- [1] P.M.Stella, F.S.Pool, M.A.Nicolet, P.A.Iles, „PV technology for low intensity, low temperature (LILT) applications“, 1st WCPEC - World conference on photovoltaic energy conversion (1994)
- [2] G.Strobl, C.Flores, P.Uebele, R.Kern, R.Campesato, K.Roy, M.Martella, K.Bogus, Silicon and gallium arsenide solar cells for deep space missions“, Proceedings of ESPC-93 (ESA-WPP-054, European Space Power Conference, p.603-610)
- [3] G.Strobl, P.Uebele, R.Kern, K.Roy, C.Flores, R.Campesato, C.Signorini, K.Bogus, Silicon and gallium arsenide solar cells for low intensity, low temperature operation“, Proceedings of 1st WCPEC - World conference on photovoltaic energy conversion Vol.2,(1994), p.2124.
- [4] G.Strobl, P.Uebele, R.Kern, K.Roy, R.Campesato, C.Flores, C.Signorini, K.Bogus, High efficiency Si and GaAs solar cells for LILT applications“, Proceedings of ESPC - European Space Power Conference, (1995), pp.471-477.
- [5] H.J.Hovel, Semiconductors and Semimetals Vol.II, ed. by Willardson and Beer Solar Cells, Academic Press 1975
- [6] V.G.Weizer, J.D.Broder, On the cause of the flat-spot phenomenon observed in silicon solar cells at low temperature and low intensities“, J.Appl.Phys.,Vol.53,No.8, (1982), p.5926
- [7] R.Campesato, C.Flores, "Ga As solar cells for low temperature, low intensity applications“, Proceedings of ESPC - European Space Power Conference, (1991), p.759.
- [8] R.Campesato, C.Flores, "Effects of low temperature and intensity on Ga As and Ga As / Ge solar cells“, IEEE Transaction on Electron Devices, Vol.38, n.6, (June 1991).

S3
AN-50388

NAVAL RESEARCH LABORATORY'S PROGRAMS IN ADVANCED INDIUM PHOSPHIDE SOLAR CELL DEVELOPMENT

Geoffrey P. Summers
Naval Research Laboratory, Code 6615, Washington, DC 20375, and
Department of Physics, University of Maryland Baltimore County, Baltimore, MD 21228

INTRODUCTION

The Naval Research Laboratory (NRL) has been involved in the development of solar cells for space applications since the 1960s. It quickly became apparent in this work that radiation damage caused to solar cells by electrons and protons trapped by the earth's magnetic field would seriously degrade the power output of photovoltaic arrays in extended missions. Techniques were therefore developed to harden the cells by shielding them with coverglass, etc. Ultimately, however, there is a limit to such approaches, which is determined by the radiation response of the semiconductor material employed. A desire for high efficiency and radiation resistance led to the development of alternative cell technologies such as GaAs, which has since become the technology of choice for many applications. InP cells are currently the most radiation resistant, high efficiency, planar cells known.

NRL first sponsored InP solar cell technology in 1986, when Arizona State University was contracted to grow p/n cells by liquid phase epitaxy. NRL's interest in InP cells was generated by the results presented by Yamaguchi and his co-workers in the early 1980s on the remarkable radiation resistance of cells grown by diffusion of S into Zn doped p-type InP substrates. These cells also had beginning of life (BOL) efficiencies ~16%(AM0). Related to the radiation resistance of the cells was the fact that radiation-induced damage could be optically annealed by sunlight. Relatively large quantities of 1x2 cm² diffused junction cells were made and were used on the MUSES-A and the EXOS-D satellites. These cells were also available in the U.S. through NIMCO, and were studied at NRL and elsewhere. Workers at NASA Lewis became involved in research in InP cells about the same time as NRL.

SINGLE JUNCTION AND TANDEM CELLS GROWN ON InP SUBSTRATES

In 1987 a high level Navy sponsor became interested in InP cells, which led to a one year contract from NRL to Spire Corporation in 1988-89. The goals of this program were to produce large area (2x2 cm²) cells with BOL efficiencies >16%. The cells were to have space qualified contacts and antireflective (AR) coatings and to show a radiation resistance better than both single crystal GaAs and Si cells. The shallow homojunction technology which was developed in this program enabled cells to be made with AMO efficiencies >19%. More than 300 cells were eventually produced, many of which have been flown on space experiments such as PASP PLUS on the APEX satellite. These tests have confirmed the high radiation resistance of InP cells. NRL has published widely on the radiation response of these cells and also on radiation-induced defect levels detected by DLTS and other techniques.

During the late 1980s NRL began sending small amounts of funding to SERI (now NREL) for the development of tandem junction cells made by epitaxially growing an InP top cell (E_g~1.32 eV) on a lattice matched GaInAs bottom cell (E_g~0.73 eV). The cell was grown in both 3- and 2-terminal versions, with the latter requiring a connecting tunnel junction. This early work led in 1991 to a three year contract with NREL with the goals of producing large area (2x2 cm²), 2-terminal cells with high BOL efficiencies and with EOL efficiencies greater than

epitaxially grown, single junction InP cells. During the course of this program, several cells with AM0 efficiencies >22% were produced, but the funding ran out before the grid design and the AR coatings could be fully optimized. It was thought that with such optimization efficiencies close to 25% could have been readily achieved. In a 2-terminal tandem junction cell the photocurrent of both subcells has to be matched. Although this can be achieved relatively easily at BOL, superior radiation response for the cell requires that the current matching be maintained as both subcells degrade individually. Research at NRL showed that current matching in the subcells could be maintained to higher radiation levels by reducing the base doping of the GaInAs cell below the initial levels used ($\sim 5 \times 10^{17} \text{ cm}^{-3}$). Data were taken in these studies which will enable InP-GaInAs tandem cells to be grown in the future that can maintain current matching under AM0 light up to 1 MeV electron fluences $> 10^{16} \text{ cm}^{-2}$.

Five $2 \times 2 \text{ cm}^2$ tandem cells were provided to the U.K. DRA for the STRV 1b solar cell experiment and two of these cells were incorporated on the satellite. These were the only 2-terminal, tandem cells on the STRV experiment.

DEVELOPMENT OF CELLS GROWN ON Si and Ge SUBSTRATES

Both the single junction and the tandem junction cell development were very successful as research programs. However, it was realised that the high cost and relative brittleness of InP wafers meant that if InP cell technology were to become a viable space power source, the superior radiation resistance of InP would have to be combined with a cheaper and more robust substrate. The main technical challenge to this approach was to overcome the effect of the dislocations produced by the lattice mismatch at the interface of the two materials. Building on the success of the initial program, NRL secured funding from ONR to support a Phase 1 and 2 effort at Spire to produce InP on Si cells. The goals of this program were to produce cells as large as $2 \times 4 \text{ cm}^2$ with high BOL efficiencies and with EOL efficiencies comparable to InP homoepitaxial cells. Both cell polarities were investigated and several schemes for alleviating the $\sim 8\%$ lattice mismatch between InP and Si have been tried, including the use of GaInAs and GaInP grading layers. The best efficiencies to date ($\sim 13\%$ on a $2 \times 4 \text{ cm}^2$ cell) were achieved with n/p cells. It is hoped to continue this cell development into a Phase 3, with the goals of increasing the BOL efficiency and fabricating more than 400 $2 \times 4 \text{ cm}^2$ cells for assembly into two small power panels for the STRV 1 c/d satellite for launch in 1998.

As of the Phase 2 program at Spire, ONR/NRL sponsored a study with an independent contractor to evaluate the potential commercial market for InP/Si cells into the next decade. This study was completed in July of this year. The main conclusions of this study, which was made by Booz Allen & Hamilton, were that a niche market exists for InP/Si technology for missions that operate in high radiation environments. These would include several of the proposed global satellite communication systems such as Ellipso and Odyssey. Based on current and projected systems in these orbits, the addressable market for InP/Si technology by the year 2007 was estimated to be 15 kW per year. Outside the niche market the study found that InP/Si technology would have comparable performance and cost to GaAs/Ge.

In June of this year, NRL negotiated a contract with Applied Solar Energy Corporation as prime contractor, and with RTI and NREL as subcontractors, to develop a 2-terminal, InP-GaInAs tandem junction cell on a robust substrate. The goals of this program are essentially to produce a cell that substantially exceeds the efficiency of the InP/Si cell at all particle fluences. It has been decided that a Ge substrate will be used initially, although the possibility of eventually employing a Si substrate is included in the program. Because of the problem of auto-doping, the p/n polarity is preferable from an epitaxy viewpoint and one of the early successes in this program is that by carefully controlling the diffusion of Zn in a relatively thick p-type

emitter, RTI have produced single junction p/n InP cells with efficiencies >16%. It is thought that p/n cells can be grown eventually with efficiencies close to the best achieved in n/p cells. The proton response of InP and GaInAs single junction cells is the same for both p/n and n/p polarities, so there is much flexibility for the best ultimate cell geometry. It is hoped that this development program will last several years.

REMAINING CHALLENGES

Although NRL's InP cell development has been very successful, there are several technical challenges still remaining. The most elusive of these has been that the ready optical annealing of radiation-induced damage observed in diffused junction InP cells has never been fully reproduced in cells grown by epitaxy, even in cell structures that appear to be identical. Secondly, efforts to minimize the effects of dislocations produced in the heteroepitaxy of InP on Si and GaInAs on Ge cells have still not yet been fully explored. This problem needs to be tackled both by reducing the number of dislocations produced and by reducing the electrical effect of those remaining. The task of scaling up the InP/Si cell to much larger dimensions also still remains to be attempted, but there seems no reason in principle why cells as large as 8x8 cm² could not be grown if required. Finally, of course, cell structures have to be developed that can be produced in large quantities at a competitive cost.

The Defence Research Agency Photovoltaic Programme

C. Goodbody and R. Kimber

Defence Research Agency
Space Department
Farnborough
Hants, GU14 6TD
UK.

54

IN-50389

INTRODUCTION

The current DRA photovoltaic programme is funded mainly by the UK Ministry of Defence. The programme is aimed at research and development into the performance of new solar cells and array concepts. The core of the programme consists of studies to determine the potential benefits and disadvantages of using the different solar cell/array combinations on future MoD spacecraft. The main areas of interest are cost, mass, volume, lifetime, radiation hardness, area, reliability and when the relevant technologies are likely to reach maturity. The programme addresses two timeframes, 5-10 years and 10-15 years. This is backed up by an extensive programme of cell characterisation and environmental testing to provide data for the studies. When the opportunity arises flight experiments are conducted to verify the results from the ground testing and to demonstrate the performance in the real environment with all its synergistic effects.

SOLAR ARRAYS

The initial trade-off studies have looked at three typical missions, 3 and 6 kW GEO communications satellites and an 8.7 kW LEO remote sensing spacecraft, all powers being end of life. They have considered the impact of a range of cell types on conventional rigid arrays eg. the Fokker ARA and Aerospatiale GSR3 and on the conventional flexible array, eg. the TRW EOS and Spar Olympus. The 6 kW study has been reported in reference 1.

The LEO study involved the sizing for a single wing remote sensing spacecraft which would generate 8.7kW after 5 years. Six cell types were involved in the study: Si BSR, Si BSFR, Si HiETA, GaAs/Ge and GaInP/GaAs/Ge tandem cell. These cells were assumed to be laydown onto conventional flexible and conventional rigid substrates and the salient parameters for each array design were calculated (mass, area of wing, cost of protoflight array and recurring cost). In the case of the tandem cell, educated estimates were made of the likely performance and cost once the cell is fully qualified. Figures 1 and 2 illustrate the cost and mass for the rigid and flexible respectively. (The estimated costs are relative for comparative purposes only).

The 3kW GEO conventional flexible and rigid array study considered a number of advanced cell technologies in two timeframes:

In the Medium term (5-10 years), the cells used in the study were the Silicon high efficiency and III-V high efficiency cells. The study showed that at the power level of 3kW the mass of a rigid array using the III-V cells were substantially lower than for Silicon (55kg, GaInP/GaAs against 100kg, Si HiETA). The flexible array showed no advantages, being heavier and more expensive in most cases.

In the Long term (10-15 years), the cells used in this study were the advanced thin Silicon, ultrathin III-V, multijunctions and thin film low efficiency CIS, CdTe and α -Si. Due to the long timeframe the cell cost and operating performance could be only roughly estimated. However the study showed that in terms of cost, the thin film cells could effect substantial savings at array level in comparison with the higher efficiency cells.

SOLAR CELLS

New solar cells, as they become available from the manufacturers, are being acquired and subjected to qualification and environmental tests to determine likely in-orbit losses (2). This is to verify manufacturers claims and provide specific performance data for use in the solar array trade off studies. The environmental testing is primarily electron and proton irradiations performed at AEA Technology (UK Atomic Energy Authority). A dedicated facility has been developed for the proton irradiation of solar cells and is being used on a collaborative programme with Phillips Laboratory that has just commenced.

PROTON IRRADIATION FACILITY

The facility is based on the AEA Technology, 7 MV Tandem Van de Graaff accelerator, and consists of a well characterised source of protons with a dose rate range of 10^6 to 10^9 protons $\text{cm}^{-2} \text{s}^{-1}$, providing an energy range of 2-10 MeV on the target plane. The proton beam is scattered using a thin foil to provide irradiation over a large area. Reproducibility of exposure dose is better than 5%, and the energy of the protons to better than 1%, with an energy distribution at the target plane of typically 150 keV. The proton intensity distribution across the target plate is currently uniform to $\pm 10\%$. This can be made better by moving further away from the scattering foil but with a reduction in dose rate.

A new target chamber has been developed to allow the irradiation of cells under a wide range of conditions: unidirectional or isotropic irradiation, at different temperatures -170°C to $+150^\circ\text{C}$, with or without illumination, with or without the cells electrically active. Provision has also been made for a solar simulator to allow the in-situ measurement of the cells, see figures 3 and 4. The target plate was designed to accommodate a number of single cells or strings, in any arrangement, to a maximum size of 110mm square. Gas nitrogen and or liquid nitrogen is passed through the plate to control the temperature. Typical temperature stabilities observed to date are $+100 \pm 1^\circ\text{C}$; $-100 \pm 2^\circ\text{C}$. The target plate is driven by a computer- controlled stepper motor and may be set at any angle in 360 degrees, in steps of 0.9 degrees, to the beam, or oscillated with a selected angular velocity profile to simulate isotropic conditions.

Secondary energy reducing foils, of increasing thickness, can be placed between the scattered proton flux and the cell to reduce the incident proton energy from 10 MeV to 2 MeV in 1MeV steps. With increasing foil thickness the proton energy distribution increases, to the extent that it is possible to simulate the proton spectra between 1 and 10 MeV for different orbits rather than treating it as discrete energies. With the inclusion of even thicker foils and/or dropping the initial proton energy it will be possible to subject cells to spectra of keV protons, which can be characterised, but not discrete energies.

FLIGHT EXPERIMENTS

UoSAT-5

UoSAT-5 satellite was launched into a 770 km Sun Synchronous orbit on the 16th July 1991 on an Ariane 4 launcher as a secondary payload to ERS-1. One of the payloads is the DRA solar cell experiment. The experiment consists of the I-V measurement of various types of silicon, gallium arsenide and indium phosphide solar cells from the UK, Europe and the USA. Results have been presented before, references 3,4. The experiment continues to work with data being collected every 3 months. Figure 5 shows a comparison of the short circuit current of 2 GaAs cells on the experiment, one with a conventional adhesive bonded 200 μm CMG coverglass and the other with the same coverglass but teflon bonded to the cell by Pilkington Space Technology. The degradation in current is less than 1% and there is no significant difference between the 2 cells.

STRV-1A/B

STRV-1A/B were launched on 17 June 1994 into a geostationary transfer orbit, GTO, (200x36000 km), figure 6 shows STRV-1A. Unfortunately the solar cell technology experiment (Ref 5) on board suffered a major failure with its sun overhead detectors during launch. Attempts to overcome this problem have failed resulting in no meaningful I-V data being obtained. The only positive result from the experiment is the temperature difference between two GaAs cells. One cell has a conventional AR coated CMG coverglass and the other has an early version of the Pilkington Infra-Red rejection coating for Silicon on the coverglass. Even though this coating is for a Silicon cell and not fully optimised nor designed for operation on a spin stabilised satellite such as STRV, this cell is running 6 °C cooler than the cell with the conventional AR coating.

On STRV-1B we are able to monitor the current of the solar panels at the operating point of 28V. The data from the panels has been corrected for temperature, Earth-Sun distance and solar aspect angle by Dr Dean Marvin of the Aerospace Corporation. Figure 7 shows the degradation of the current at 28V for the 4 panels. For the -Y, -X and +Y panels, all GaAs/Ge, the actual degradation was approximately agreeing with the prediction up to 300 days and then deviates. After 450 days the panels have degraded by approximately 8% compared to the predicted 10%. However, for the +X panel, which is GaAs/GaAs, the actual degradation is slightly worse than predicted up to 300 days and then converges with the predicted degradation curve. The GaAs/Ge panels were typically 18.5% efficient at beginning of life compared to 19.8% for the GaAs/GaAs panel. Radiation monitors on A and B are indicating that the radiation environment is less severe than predicted by the AE8 and AP8 environment models and so the GaAs/Ge results are not unexpected. The GaAs/GaAs result is probably due to the cell structure, giving higher initial performance but softer radiation characteristics.

In this year's work programme the existing Surrey Satellite Technology design of the measurement electronics package is being reviewed to identify all the short comings and potential modes of failure. A new design is being developed to overcome these. This will then followed by the manufacture of a breadboard model that can be fully tested to ensure correct, reliable operation. This is to give confidence for any future flight of a solar cell experiment.

LABORATORY

To support the cell/panel characterisation and environmental testing programme the DRA maintains a comprehensive test laboratory. This is subject to a continual programme of equipment upgrades to improve the quality of the measurements and meet new testing requirements. We are currently in the process of developing a new close spectral match simulator for the testing of multi-junction solar cells. Figure 8 shows the spectrum of the basic simulator design, giving a very good Class A spectrum. The simulator uses a compact Xenon arc lamp and an incandescent lamp with simple filtering. Work is now ongoing to modify this spectrum to produce the close match design. In addition to measuring multi-junction cells it is intended that the Close Match simulator will be used to generate primary standard reference cells.

FUTURE WORK

Solar Arrays

The above solar array trade off studies will be repeated as and when more cell data becomes available, to verify the assumptions made or to correct them as necessary. New data will be derived from in-house testing, DRA flight experiments, from manufacturers and also from the exchange of information through conferences and collaborations. The studies will also be extended to include new solar arrays designs, eg. Able's Ultraflex and the Linear Concentrator array and new concept arrays.

Solar Cells

The solar cell testing programme will continue as new and/or better cells become available from manufacturers. We also intend to shortly commence a long term UV irradiation programme on a range of cell types.

Flight Experiments

The flight of STRV-1C/D is currently in the planning stage, proposed launch end of 1998 into GTO. We are currently looking into the possibility of the re-flight of the solar cell experiment, determining costs and looking for collaborators on the experiment. The opportunity also exists for the flight of small panels of advanced high power cells, with the current being monitored at the operating point as on STRV-1B. It is hoped that the flight, if it occurs, will be backed up by a comprehensive ground based radiation test programme to allow accurate estimates of the degradation to be made for comparison with the actual in-flight degradation. The possibility of flying strings of advanced cells as an experiment on the proposed Skynet-4F Communications satellite is also being investigated.

Laboratory

In addition to the introduction of the close spectral match simulator, work will be undertaken to automate the measurement of cell I-V and spectral responses. The intention is to have the cells on most test programmes to be hard wired onto a substrate (removing any possibility of handling and probe damage), with connection of the cells to the electronic load through a 20 channel multiplexer. All of the measurement conditions, light intensity, measurement block temperature and cell selection is to be controlled via computer. The required sequence of measurements will then be programmed in removing the need for operator intervention and hence reduce testing costs.

CONCLUSIONS

The DRA photovoltaic programme is wide ranging in its activities, providing an independent assessment of new solar cell and array technologies in development around the World, for our MoD customer. Further activities are planned in these areas to meet the future requirements of MoD spacecraft.

REFERENCES

1. R. Kimber, C. Goodbody, "Cell types for Geostationary Array Applications", 4th European Space Power Conference, SP369, Poitiers, France, Sept 1995.
2. C. Goodbody, R. Kimber, "Achieving the optimum solar array size for spacecraft", 29th Intersociety Energy Conversion Engineering Conference, Monterey, CA, USA, Aug 1994.
3. C. Goodbody, "The UoSAT-5 Solar cell experiment - First year in orbit", Proc. XII Space Photovoltaic Research and Technology Conference, Cleveland, Ohio, USA, Oct 1992.
4. C. Goodbody, "The UoSAT-5 solar cell experiment", 3rd European Space Power Conference, WPP-054, Graz, Austria, Aug 1993.
5. C. Goodbody, N.Monekosso, "The STRV-1 A & B Solar Cell Experiment", Proc. 23rd IEEE Photovoltaic Specialists Conference, Louisville, KY, USA, May 1993.

© British Crown Copyright, 1995 /DRA.

Published with permission of the Controller of Her Britannic Majesty's Stationary Office.

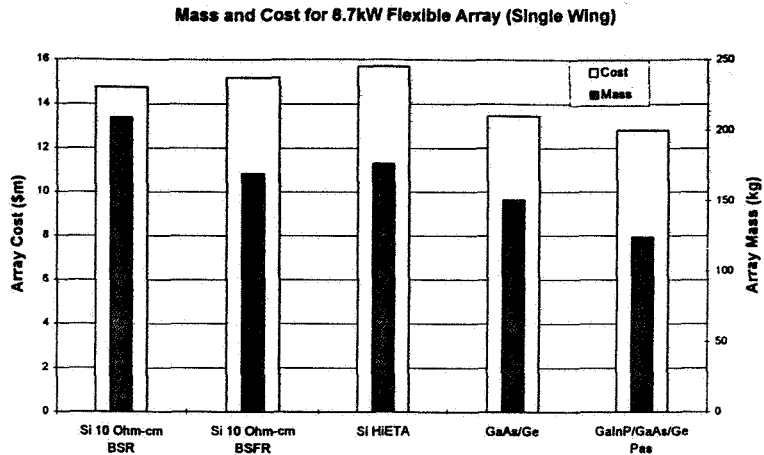


Figure 1. Comparison of Array Mass & Costs for LEO Flexible Array

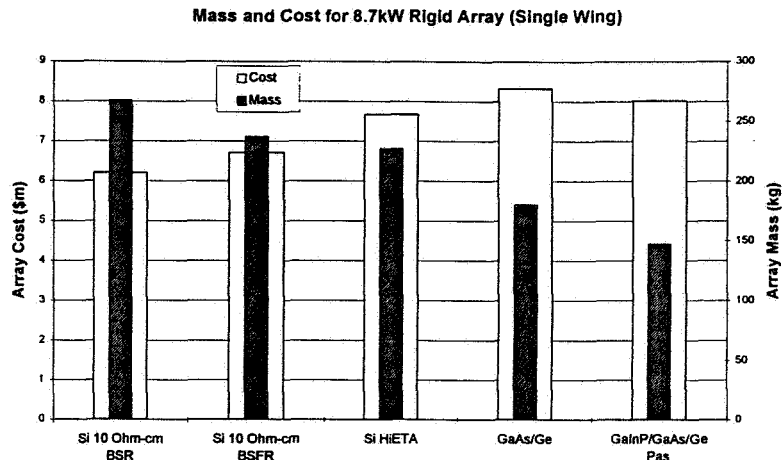


Figure 2. Comparison of Array Mass & Costs for LEO Flexible Array

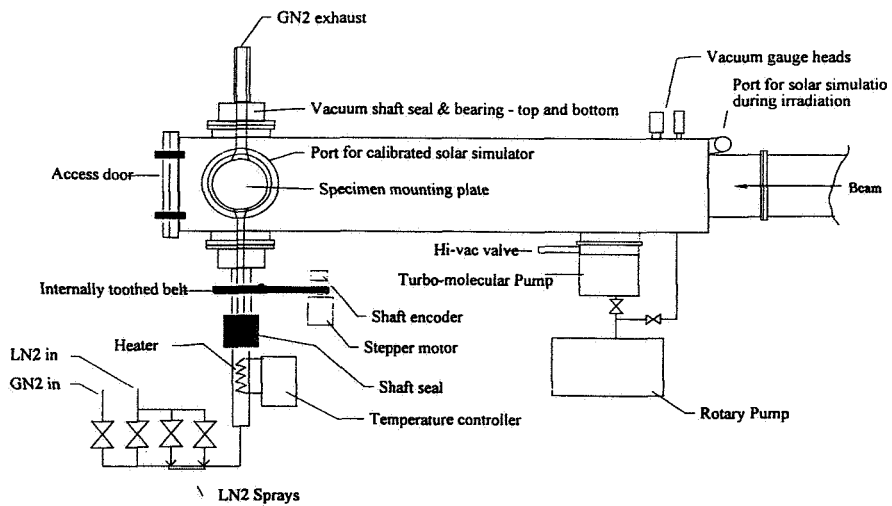


Figure 3. Schematic of Proton Irradiation Chamber.

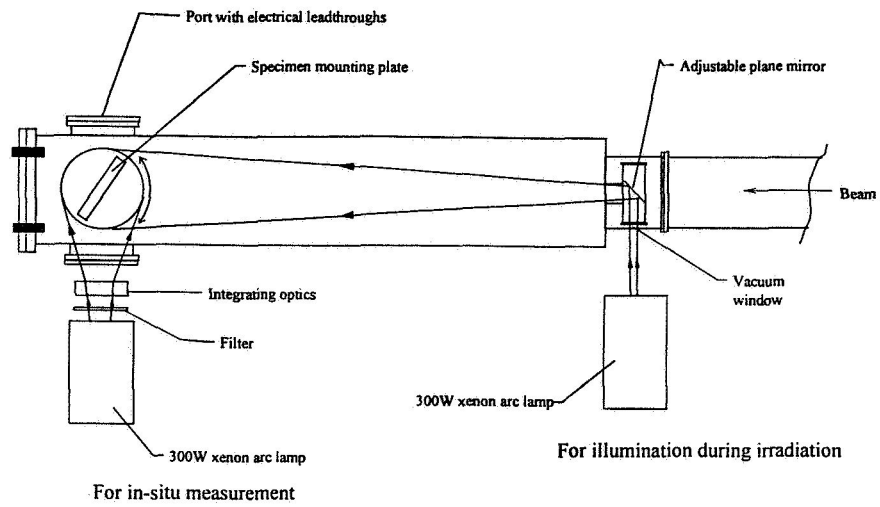


Figure 4. Schematic of Proton Irradiation Chamber.

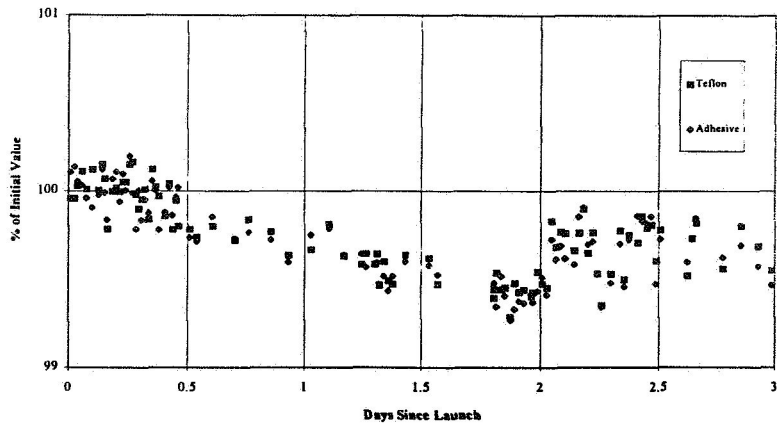


Figure 5. Comparison of the Isc of GaAs cells with Adhesive and Teflon bonded coverglasses: Flying on the UoSAT-5 solar cell experiment

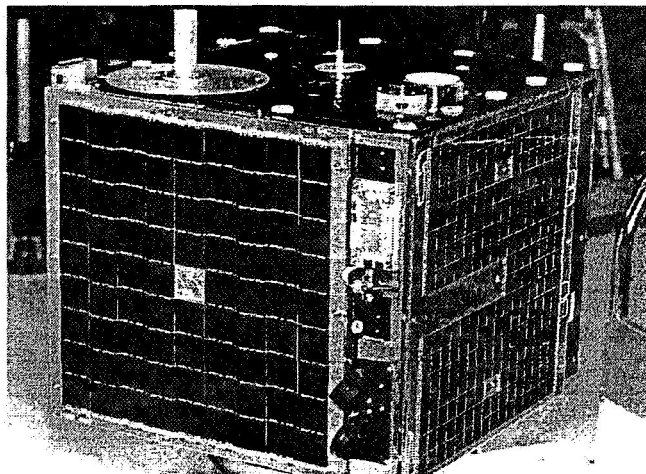


Figure 6 : STRV-1A.

STRV-1B SOLAR PANELS

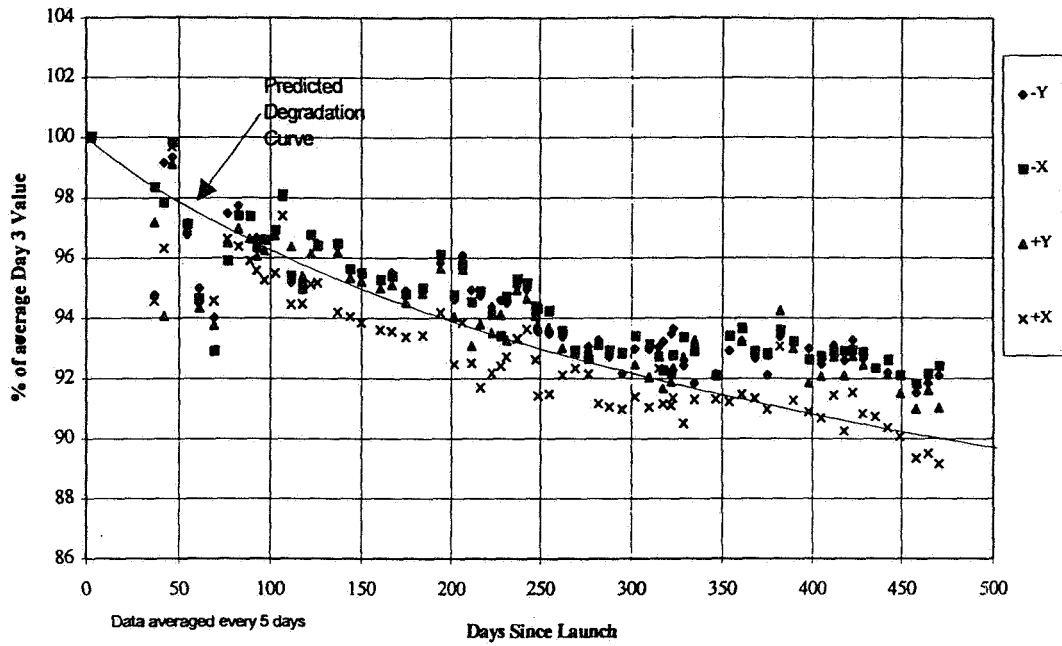


Figure 7. STRV-1B Solar Panels : Degradation of the Current generated at 28V with time in orbit, Normalised to the Average Day 3 value.

CLASS A Simulator

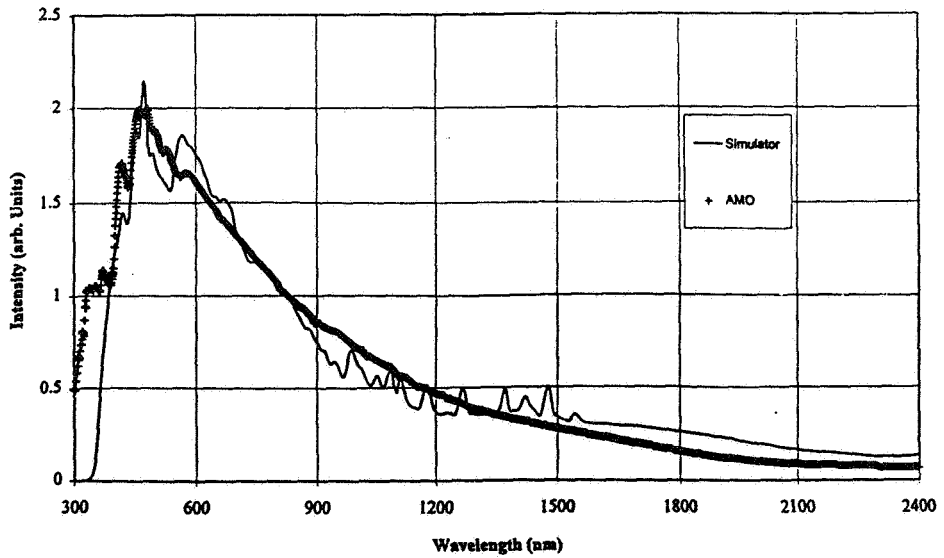


Figure 8. Spectrum of AMO Class A simulator in development

S5
IN-50390

JAPANESE PHOTOVOLTAIC POWER GENERATION FOR SPACE APPLICATION

T. Saga, Y. Kiyota, T. Matsutani, A. Suzuki, O. Kawasaki*, T. Hisamatsu* and S. Matsuda*

SHARP Corporation

282-1 Hajikami, Shinjo-cho, Kitakatsuragi-gun, Nara 639-21, Japan

* National Space Development Agency of Japan(NASDA)
2-1-1 Sengen, Tsukuba-shi, Ibaraki-ken 305, Japan

ABSTRACT

This paper describes Japanese activities on mainly silicon solar cell research, development and applications. The high efficiency thin silicon solar cells and the same kinds of solar cells with integrated bypass function (IBF cells) were developed and qualified for space applications. The most efficient cells (NRS/LBSF cells) showed average 18% at AM0 and 28°C conditions. After electron irradiation, NRS/BSF cells showed higher efficiency than NRS/LBSF cells. The IBF cells do not suffered high reverse voltage and can survive from shadowing. The designs and characteristics of these solar cell are presented. In the last section, our future plan for the solar cell calibration is presented.

INTRODUCTION

Silicon solar cells have been used as the most popular electrical power source for spacecrafts over thirty years. They have been in the advantages of high reliability, low mass and low cost compared to other solar cells for many years. The performance of silicon solar cells had increased from 10% efficiency in the early 1960's to 15% in the end of 1980's. NASDA and SHARP have continued to develop Si solar cells with higher efficiency, higher radiation resistance and lower mass. We developed the ultrathin 50 μ m BSFR cells in 1980's. The ultrathin solar cells have been used for JERS-1 and ETS-VI and the solar cell monitor (SCM) on ETS-V showed their excellent radiation performance (Ref.1). However the spacecraft have made a demand of higher power from year to year. GaAs solar cells have been expected to supplant Si solar cells. Although the GaAs solar cells have high efficiency and high radiation resistance, they have also the disadvantages of high mass, high fragility and high material cost resulted from the source limits which will become very important factor considering the future large scale space application, for example, space stations or space platforms. We thought the high efficiency Si solar cells compared favourably to the GaAs solar cells could be realized and the development was started in 1990. We have finished the developments of several types of high efficiency Si solar cells in 1995. They are 100 μ m thick NRS/LBSF (Non Reflective Surface/Localized Back Surface Field) cells with about 18% efficiency, NRS/BSF (Non Reflective Surface/Back Surface Field) cells with about 17% and NRS/LBSF & NRS/BSF cells with IBF. First, the solar cell applications for NASDA satellites are introduced, then the designs and characteristics of these advanced

Si cells are presented and discussed. Our activities for the universal calibration system of space solar cells are also introduced in the last section of this paper.

SOLAR CELL APPLICATIONS

The historical solar cell applications for NASDA satellites are shown in Table 1. This table shows the application and trends in development of several kinds of solar cells for space. The solar cells except high efficiency Si solar cells shown in Table 1 were introduced at the SPRAT XII (Ref. 2). The $10\Omega\text{cm}$ NRS/BSF cells have been brought into mass production for ADEOS-II program and the $2\Omega\text{cm}$ NRS/BSF cells with IBF are studying to be adopted for OICETS program. The NRS/BSF cells will use the blue red reflective (BRR) coverglasses made by OCLI to reduce the cell solar absorptivities and the operational temperature of solar array.

HIGH EFFICIENCY SILICON CELLS

Schematic drawings of the NRS/LBSF cell and NRS/BSF cell are shown in Figure 1 and Figure 2 respectively. Their designs are the same except two differences. The NRS/LBSF cell has a locally diffused P^+ back surface field layer and a planar PN junction. On the other hand, the NRS/BSF has a normal P^+ back layer and a normal PN junction. Both solar cells have $20\mu\text{m}$ squared inverted pyramids on the cell active area to reduce light reflection loss and the SiO_2 passivation layers on the front and back surfaces to reduce surface recombination loss of minority carriers. Direction of the inverted pyramids was declined by 45 degrees to the cell edge to minimize a risk of open failure of a string. The NRS/LBSF cell was made from only $2\Omega\text{cm}$ Si substrates because the fill factor of the $10\Omega\text{cm}$ NRS/LBSF cell was lower than the $2\Omega\text{cm}$ NRS/LBSF cell (Ref. 3). The NRS/BSF cells were made from $2\Omega\text{cm}$ and $10\Omega\text{cm}$ Si substrates and both cells showed each advantage for different radiation conditions. The typical electrical parameters and solar absorptivities of three types of high efficiency cells are given in Table 2. The NRS/LBSF cells showed the highest efficiency (average 18.0%) of three kinds of cells. The NRS/BSF cells showed lower efficiency (average 17.0 to 17.3%) than the NRS/LBSF cell. We measured reverse saturation currents J_{01} and J_{02} of these cells using two diodes model and ND filters method. The NRS/LBSF cell gave lower J_{01} ($6 \times 10^{-13}\text{A/cm}^2$) by about one third and a little lower J_{02} ($7 \times 10^{-9}\text{A/cm}^2$) than the NRS/BSF cell ($J_{01}: 1.8 \times 10^{-12}\text{A/cm}^2$, $J_{02}: 1.0 \times 10^{-8}\text{A/cm}^2$). In generally the localized BSF is necessary to get high open circuit voltage (low J_{01}) and the planar PN junction is necessary to get large fill factor (low J_{02}). But the planar PN junction did not improve the fill factor of the NRS/BSF cell and was not necessary for them. We found that the planar PN junction decreased J_{02} and was effective to increase the fill factor of the NRS/LBSF cell with low J_{01} but not effective for the NRS/BSF cell with relatively high J_{01} . Solar absorptivities of these cells were about 0.85 and lower by about 0.05 than those of the conventional textured cells. The improvement was resulted from the introduction of the SiO_2 passivation back layer.

The results of 1MeV electron irradiation to these solar cells are shown in Figure 3. The NRS/LBSF cells showed larger degradation than the NRS/BSF cells and conventional BSFR

cells with the same thickness in the low fluence range (less than $1 \times 10^{14} \text{e/cm}^2$). On the other hand, the NRS/BSF cells showed smaller degradation rate than the conventional BSFR cells. The $2 \Omega \text{cm}$ NRS/BSF cells showed higher power at lower fluences than $1 \times 10^{14} \text{e/cm}^2$ compared to the $10 \Omega \text{cm}$ NRS/BSF cells. The $10 \Omega \text{cm}$ NRS/BSF cells showed the highest power at higher fluence range than $1 \times 10^{14} \text{e/cm}^2$. These results suggest the radiation characteristics of NRS/BSF cell is dominated mainly by the bulk damage and the damage of Si/SiO₂ interface is added to the bulk damage in the NRS/LBSF cell (Ref 4). The back Si/SiO₂ interface of the NRS/LBSF cell is susceptible to the electron irradiation and increase J_{01} rapidly and decrease open circuit voltages of the NRS/LBSF cells. The radiation characteristics of NRS/BSF cells were similar to that of the conventional BSFR cell. The inverted pyramid surface made more minority carriers near to the PN junction than the flat surface and even the normal pyramid surface. They improved the cell radiation characteristics (Ref. 5). These high efficiency cells showed about 20% higher power than $200 \mu\text{m}$ BSR cells used for geostationary satellites at their EOL (1MeV electron fluence of $1 \times 10^{15} \text{e/cm}^2$).

The NRS/LBSF cells will be applicable to the satellites with low radiation at low altitude or with short mission lives. The NRS/BSF cells will have wide space applications due to their high radiation resistance and relatively low costs.

HIGH EFFICIENCY SILICON CELL WITH IBF

A Schematic drawing of the high efficiency Si cell with IBF is shown in Figure 4. The idea of IBD (integrated bypass diode) to protect the solar cell from the hot spot due to cell shadowing was studied in 1970's (Ref. 6). However the IBD cell needed a small diode integrated in a solar cell and a special interconnection. It needed necessarily high cost and did not become popular. The IBF (integrated bypass function) is a simple idea to protect the solar cell from the cell failure due to shadowing. The IBF cell has many small dots of P⁺ diffused layer in the front N⁺ diffused layer. The P⁺ dots are formed by the same boron diffusion as the back surface P⁺ diffusion and form high doped P⁺N⁺ junctions in the N⁺ diffused layer. Therefore the IBF cells need only a small amount of additional cost compared to the usual cells. Because the high doped P⁺N⁺ junctions can flow much more reverse current compared to the cell PN junction and more current than the cell short circuit current at low reverse voltage (about -3V), the IBF cell does not suffered a high reverse voltage and can survive from shadowing. As the reverse current increases in proportion to the total length of P⁺N⁺ junctions, we can easily control the reverse characteristics of the cell without a remarkable power loss (Ref. 5). Considering the temperature effects of the reverse I-V characteristics (the reverse current decreases with temperature increase), we think the avalanche breakdowns of P⁺N⁺ junctions are being induced at low voltages in the IBF cells.

The typical reverse I-V characteristics of a $2 \times 2 \text{cm}^2$ IBF cell is shown in Figure 5. The NRS/LBSF and NRS/BSF cells with IBF were developed and qualified for space application. The electrical parameters of them are shown in Table 3. The efficiencies of the NRS/LBSF cell and NRS/BSF cell with IBF were lower by 0.8% and 0.3% respectively than those of the same kinds of usual cells. The specification of reverse current was determined to be more than 0.2 A per $2 \times 2 \text{cm}^2$ at the reverse voltage of -3 V using the electrical and thermal

simulations of solar array with the IBF cells. The radiation characteristics of the IBF cells were almost the same as those of the same kinds of usual cells. The reverse characteristics of the IBF cells were hardly changed by 1 MeV electron irradiation to 3×10^{11} e/cm². The temperature coefficients of the electrical parameters and solar absorptivities of them were almost the same as those of the same kinds of usual cells.

The reverse bias tests using NRS/BSF cells with IBF were successfully performed using the test configuration shown in Figure 6. The test results showed the IBF cells did not suffer hot spots or PN junction failures. We think the IBF cells are useful to realize the solar array with a simple design, high reliability and less cost which have cell shadowing problems.

FUTURE PLAN FOR SOLAR CELL CALIBRATION

We have proposed the solar simulator calibration method of space solar cells to the space agencies in the world. The solar simulator method is shown in Figure 7. The advantages of the solar simulator method are as follows;

1. A large number of cells can be calibrated in a short period.
2. Cells can be calibrated regardless of weather or environmental contamination.
3. Cells can be calibrated at relatively low cost.

The solar simulator calibration value and the balloon flight calibration value of a solar cell was compared. The difference between our calibration value and the balloon flight calibration value was 1.1% to 2.2 % using spectral irradiance of WMO (World Meteorological Organization). And we calculated confidence intervals from these results to analyze the uncertainty of this method. A very small value of total confidence interval (0.25%) indicates that the solar simulator method is highly accurate systematically. The accuracy of the solar simulator method is comparable with the balloon flight calibration method. We believe that the solar simulator method can be applied to the primary calibration of Si solar cells and are going to prepare the ISO draft standards on space solar cell calibration.

CONCLUSIONS

New high efficiency silicon solar cells with efficiencies of 17% and 18% (AM0, 1 sun) were qualified for space use and their characteristics were clarified. The NRS/LBSF cell gave the highest efficiency at BOL condition. But the NRS/BSF cells showed higher radiation resistances than the NRS/LBSF cells. Both cells gave about 20% higher efficiencies than 200 μ m thick BSR cells used for geostationary satellites at their EOL condition (1MeV electron fluence of 1×10^{15} e/cm²).

The design, characteristics and test results of the IBF cells were presented. By forming small P⁺ dots in the N⁺ diffused layer, the reverse characteristics of the cells could be controlled without remarkable power losses. The IBF cells would contribute to

realize the solar array with a simple design, high reliability and less cost.

The advantages of the solar simulator calibration method were presented. We are going to prepare the ISO draft standards and expect this method will be accepted as primary calibration of Si solar cells by ISO in future.

REFERENCES

1. O. Kawasaki et al, "NASDA's Space Solar Cell -Ground Test Data and Flight Data-", Proc. 1994 IEEE 1st World Conference on Photovoltaic Energy Conversion", 1994, P.2224
2. S. Matsuda et al, "NASDA Activities in Space Solar Power System Research, Development and Applications", Proc. of the XII Space Photovoltaic Research and Technology Conference (SPRSAT XII), 1992, P. 318
3. T. Hisamatsu et al, "Electrical Properties of Thin Silicon Space Solar Cells", Proc. 7th International Photovoltaic Science and Engineering Conference, 1993, P.573
4. T. Hisamatsu et al, "Advanced Thin Silicon Space Solar Cell", Pro. 4th European Space Power Conference, 1995, P. 371
5. T. Katsu et al, "Development of High Efficiency Silicon Space Solar Cells", Proc. 1994 IEEE 1st World Conference on Photovoltaic Energy Conversion", 1994, P. 2133
6. H. S. Rauschenbach, "Solar Cell Array Design Handbook", Van Norstrand Reinhold Company, 1980, P. 300

Table 1 Solar Cell Applications of NASDA Satellites

| | ETS-V | CS-3a CS-3b | GMS-4 | MOS-1b | BS-3a BS-3b | JERS-1 | ETS-VI | GMS-5 | ADEOS | COMETS | OICETS | ADEOS-2 |
|-----------------------|-----------|------------------------|---------------------------------|-----------|------------------------|-----------|--------------|---------------------|--------------|--------------|---------------------|----------------------|
| Lanch Date | 87. 8. 27 | 88. 2. 19 88. 9. 16 | 89. 9. 6 | 90. 2. 7 | 90. 8. 28 91. 2. 25 | 92. 2. 11 | 94 SUMMER | 95 WINTER | 96 WINTER | 97 WINTER | 98 SUMMER | 99 WINTER |
| Satellite Shape | Box | Cylindrical | Cylindrical | Box | Box | Box | Box | Cylindrical | Box | Box | Box | Box |
| Satellite Weight | 550Kg | 550Kg | 325Kg | 740Kg | 550Kg | 1340Kg | 2000Kg | 345Kg | 3500Kg | 2000Kg | 500Kg | 3500Kg |
| Satellite Life | 1.5y | 7y | 5y | 2y | 7y | 2y | 10y | 5y | 3y | 3y | 1y | 5y |
| Satellite Power (EOL) | 845W | 628W | 265W | 540W | 1482W | 2053W | 4100W | - | 4500W | 5400W | 1320W | 5000W |
| Solar Cell Type | Si BSFR | GaAs | Si BSFR | Si BSF | Si BSR | Si BSFR | Si BSFR | Si BSFR | Si BSFR | GaAs | Si NRS/BSF 2Ω cm | Si NRS/BSF 10Ω cm |
| Solar Cell Size | 2cm × 4cm | 2cm × 2cm | 6. 2cm × 2. 2cm* 2cm × 2cm*2 | 2cm × 4cm | 2cm × 4cm | 2cm × 4cm | 2cm × 4cm | 2. 43cm × 6. 2cm | 2cm × 4cm | 2cm × 4cm | 4cm × 6cm | 2cm × 4cm |
| Solar Cell Thickness | 280 μm | 280 μm | 200 μm*1 280 μm*2 | 280 μm | 200 μm | 50 μm | 50 μm | 200 μm | 100 μm | 200 μm | 100 μm | 100 μm |
| Cover- grass | CMX150 | CMS150 | OCL1 150 μm | CMS150 | OCL1 150 μm | AS100 | AS50 | OCL1 150 μm | AS100 | AS100 | OCL1 AR100 μm | OCL1 BRR100 μm |

*1 : main array
*2 : charge array

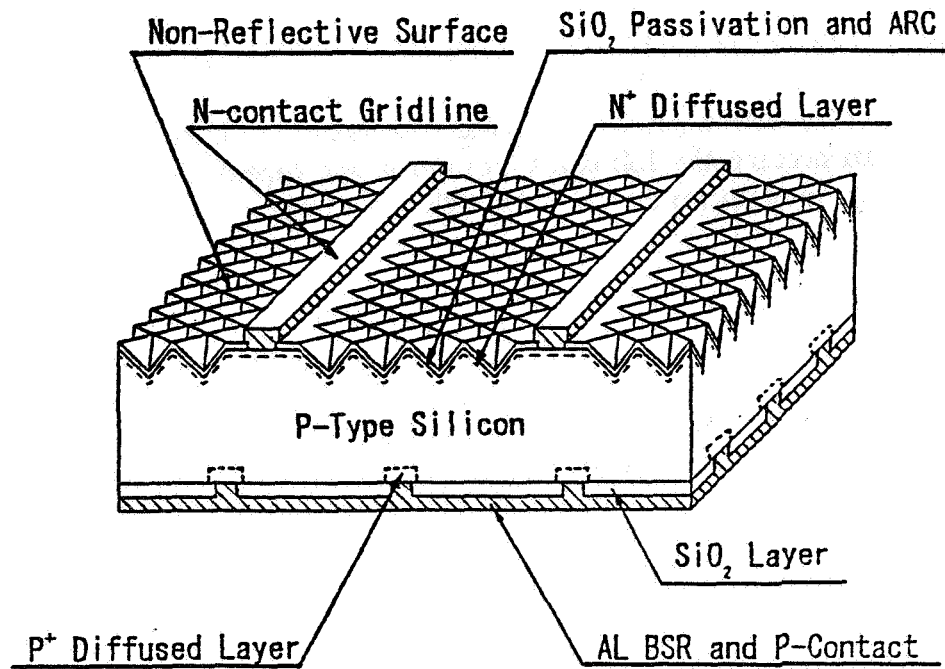


Fig.1 Schematic Drawing of NRS/LBSF Cell

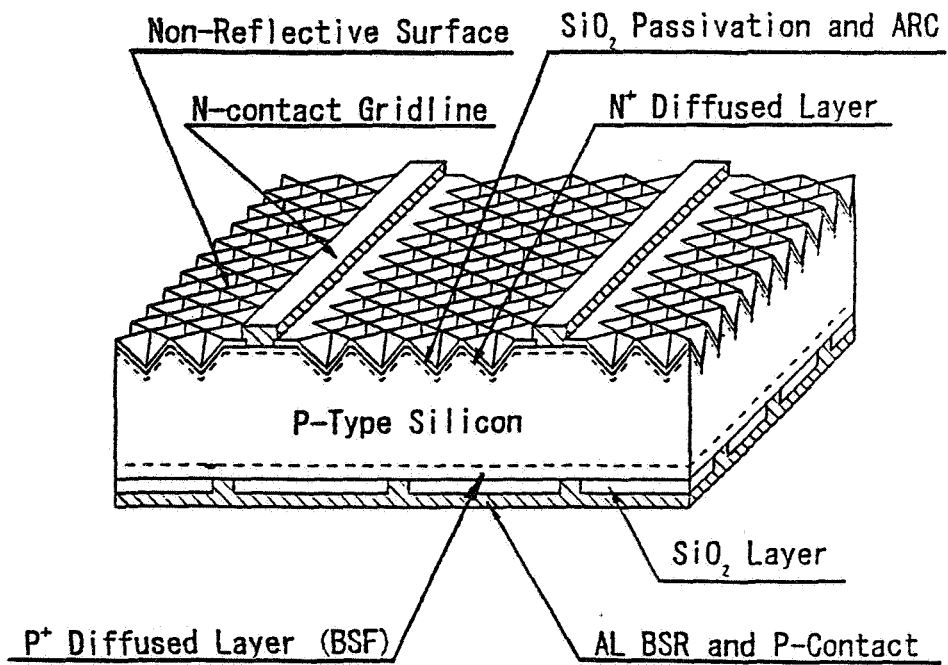


Fig.2 Schematic Drawing of NRS/BSF Cell

Table 2 Typical Electrical Parameters and Absorptivities

| Cell Type | Resistivity (Ω cm) | Voc (mV) | Isc (mA) | FF | Pmax (mW) | Eff. (%) | α s |
|-----------|-------------------------------|-------------|-------------|------|--------------|-------------|------------|
| NRS/LBSF | 2 | 637 | 194 | 0.79 | 97.6 | 18.0 | 0.84 |
| NRS/BSF | 2 | 630 | 191 | 0.78 | 93.6 | 17.3 | 0.85 |
| NRS/BSF | 10 | 625 | 191 | 0.77 | 92.0 | 17.0 | 0.85 |

Note : AMO , 135.3mW/cm² , 28°C

Cell Size 2cm×2cm , 100 μ m thick

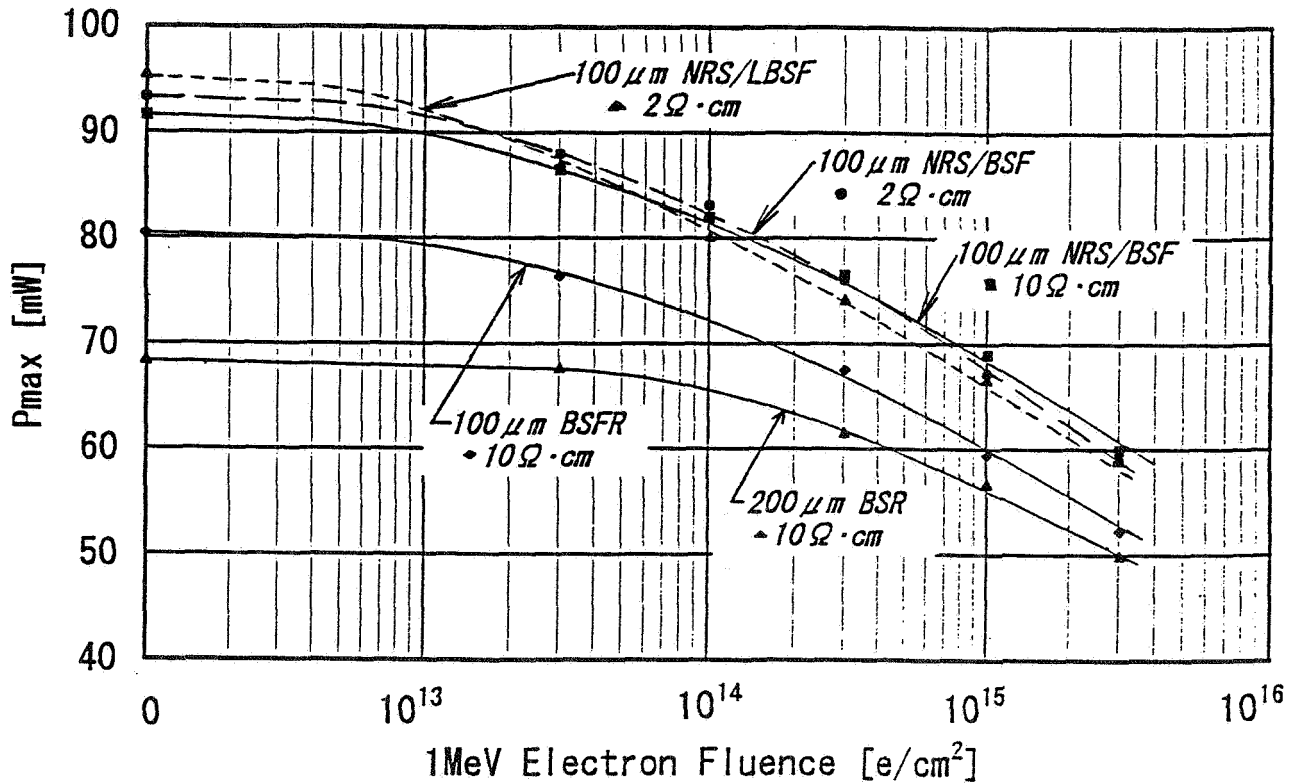


Fig. 3 Pmax Degradation of High Efficiency Cells and Conventional Cells

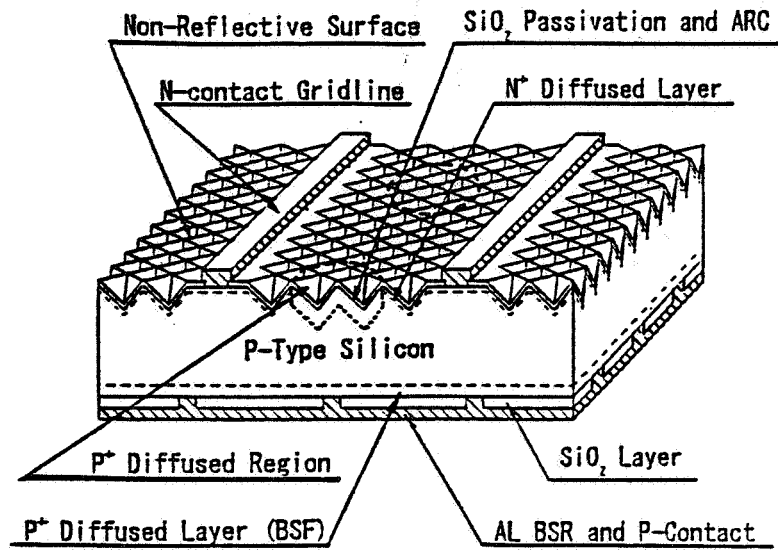


Fig.4 Schematic Drawing of NRS/BSF Cell with IBF

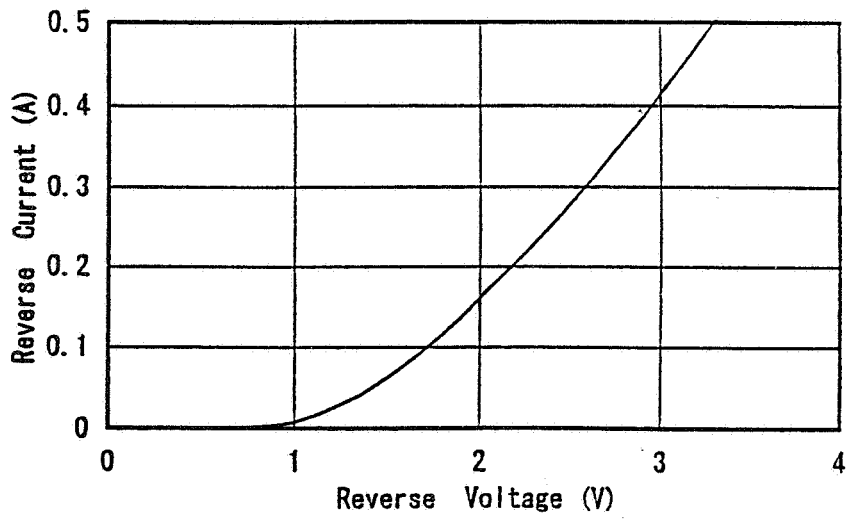


Fig.5 Typical Reverse I-V Characteristics of 2×2cm² IBF Cell

Table 3 Typical Electrical Parameters and Absorptivities

| Cell Type | Resistivity (Ω cm) | Voc (mV) | Isc (mA) | FF | Pmax (mW) | Eff. (%) | αs |
|-------------------|--------------------|----------|----------|------|-----------|----------|------|
| NRS/LBSF with IBF | 2 | 625 | 193 | 0.77 | 92.9 | 17.2 | 0.84 |
| NRS/BSF with IBF | 2 | 625 | 191 | 0.77 | 92.0 | 17.0 | 0.85 |
| NRS/BSF with IBF | 10 | 620 | 191 | 0.76 | 90.3 | 16.7 | 0.85 |

Note : AMO . 135.3mW/cm² , 28°C
 Cell Size 2cm×2cm , 100μm thick

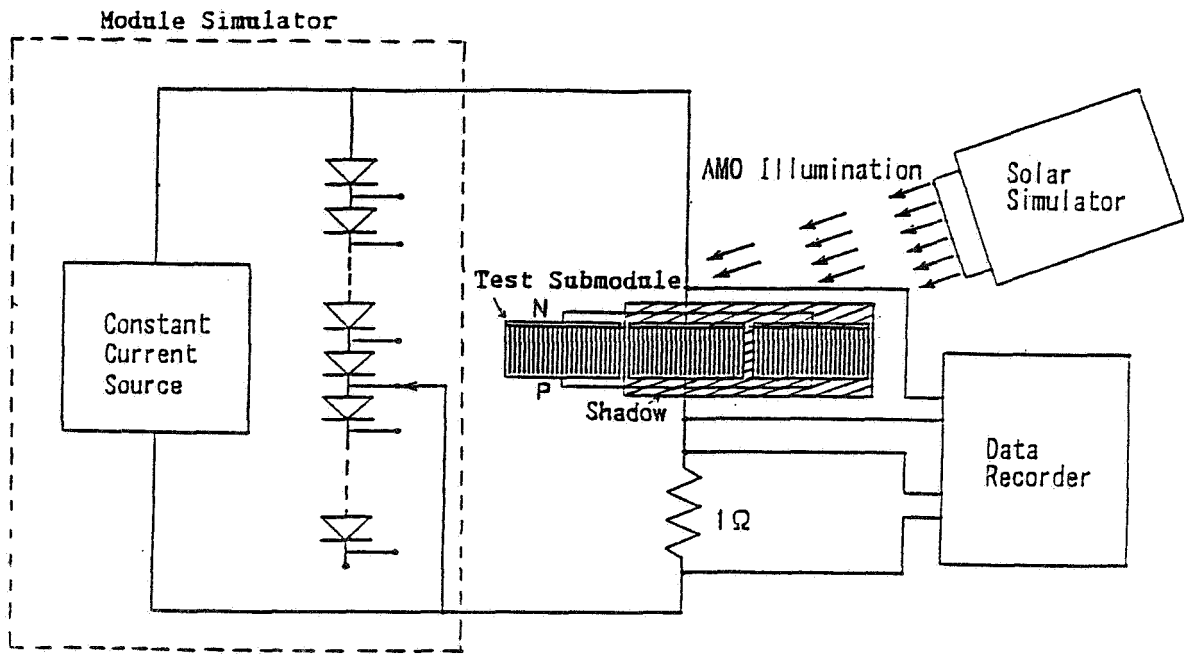


Fig. 6 Reverse Bias Test Configuration

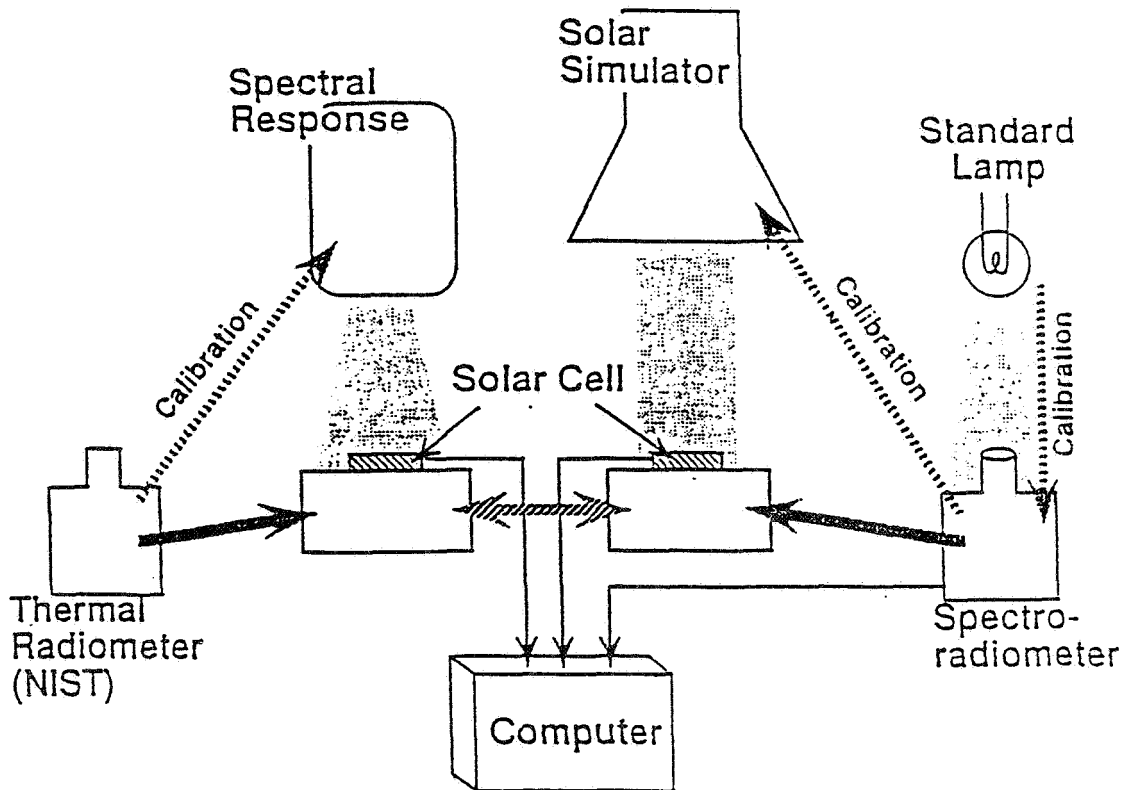


Fig. 7 Solar Simulator Calibration Method

IN
SO - 50391

COST TRADE BETWEEN MULTI-JUNCTION, GALLIUM ARSENIDE, AND SILICON SOLAR CELLS

Edward M. Gaddy
Goddard Space Flight Center
Greenbelt, MD 20771

Abstract

Multi-junction (MJ),¹ gallium arsenide (GaAs), and silicon (Si) solar cells have respective test efficiencies of approximately 24%, 18.5% and 14.8%. Multi-junction and gallium arsenide solar cells weigh more than silicon solar cells and cost approximately five times as much per unit power at the cell level.² A trade is performed for the TRMM spacecraft to determine which of these cell types would have offered an overall performance and price advantage to the spacecraft. A trade is also performed for the multi-junction cells under the assumption that they will cost over ten times that of silicon cells at the cell level. The trade shows that the TRMM project, less the cost of the instrument, ground systems and mission operations, would spend approximately \$552,000 dollars per kilogram to launch and support³ science in the case of the spacecraft equipped with silicon solar cells. If these cells are changed out for gallium arsenide solar cells, an additional 31 kilograms of science can be launched and serviced at a price of approximately \$90 thousand per kilogram. The weight reduction is shown to derive from the smaller area of the array and hence reductions in the weight of the array substrate and supporting structure.

If the silicon solar cells are changed out for multi-junction solar cells, an additional 45 kilograms of science above the silicon base line can be launched and supported at a price of approximately \$58,000 per kilogram. The trade shows that even if the multi-junction cells are priced over ten times that of silicon cells, a price that is much higher than projected, that the additional 45 kilograms of science are launched and serviced at \$180,000 per kilogram. This is still much less than the original \$552,000 per kilogram to launch and service the science. Data and qualitative factors are presented to show that these figures are subject to a great deal of uncertainty. Nonetheless, the benefit of the higher efficiency solar cells for TRMM is far greater than the uncertainties in the analysis.

Tradeoff Between Multi-Junction, GaAs, and Silicon Solar Cells

The TRMM spacecraft has actually already chosen gallium arsenide cells. These were selected in 1991, before multi-junction cells were remotely available, and just as adequate technical and price information on gallium arsenide cells was attainable. Thus what follows only estimates the relative value of the different types of solar cells to a spacecraft. The weight data used in this exercise, which includes more than just the weight of the cells e.g. the weight of the array's mechanical systems, is based on that which was originally estimated for silicon and gallium arsenide solar cells, with the estimates for the multi-junction cells scaled from the estimate for the gallium arsenide cells. Subsequently, the weight for the selected gallium arsenide array has increased due to an increase in the weight of the array mechanical systems. At least an equal, and probably a greater increase would have occurred for the silicon array. This means that the weight estimates for all the cell types should be higher than given in this paper and that the resulting trade between the cells, computed below, predicts a too small advantage for the more efficient cells.

The TRMM spacecraft is planned to be earth pointing and to fly at an initial altitude of 350 km and an inclination of 35°. For any of the solar cells, the spacecraft has two solar array wings and flies with the velocity vector perpendicular to a line drawn between the wings. From here, the designs depart. The multi-junction or gallium arsenide solar arrays can power the spacecraft with four panels or two panels per wing. The wings for the more efficient multi-junction cells are of course smaller than the wings for the gallium arsenide solar cells. The silicon

solar array needs twelve panels or six per wing. This means of course that the weight of the silicon panels is significantly greater. All of this is summarized in Table I.

Table I
TRMM Array Comparisons for a 2674 Watt at End of Life Array

| Parameter | Si | GaAs | MJ |
|--|---------------------|-------------------|---------------------|
| Weight of Cell Stack, Wiring, Connectors & Misc. | 48 kg | 47 kg | 38 kg |
| Array Area | 26.2 m ² | 18 m ² | 13.4 m ² |
| Array Temperature | 74 C | 87 C | 87 C |
| BOL Efficiency at Operating Temperature | 11.3% | 15.8% | 21.4% |
| EOL Efficiency at Operating Temperature | 9.4% | 13.3% | 18.0% |
| Number of Panels | 12 | 4 | 4 |
| Number of Panel Hinges | 20 | 4 | 4 |
| Number of Delay Actuators | 2 | 0 | 0 |
| Number of Potentiometers | 12 | 2 | 2 |
| Mechanical System Weight | 144 kg | 94 kg | 81 kg |
| Total Weight | 192 kg | 141 kg | 119 kg |

The cost of these three arrays, including test costs, even though the only test specifically called out is a deployment test, is summarized in Table II. With respect to the multi-junction solar cells some caution is in order. The price estimates used assume that the multi-junction solar cells are mature and is derived by using a ratio of .86 between gallium arsenide and multi-junction cell arrays on a basis of power produced.⁴ This ratio will not hold for the first several multi-junction solar cell arrays produced. As a result, the price for the multi-junction cell array in Table II is too low for the first few multi-junction arrays. This underestimate is taken into account later.

Table II
TRMM Solar Array Cost Comparison

| Component | Si Cost (\$) | GaAs Cost (\$) | MJ Cost (\$) |
|--|------------------|------------------|------------------|
| Cell Stack, Wiring, Connectors & Misc. | 2,470,000 | 4,200,000 | 3,620,000 |
| Panel Substrate | 436,600 | 300,000 | 223,333 |
| Panel Hinges & Boom | 200,000 | 80,000 | 80,000 |
| Delay Actuators | 70,000 | 0 | 0 |
| Potentiometers | 3,000 | 500 | 500 |
| Deployment Test | 150,000 | 75,000 | 75,000 |
| Total | 3,329,600 | 4,655,500 | 3,998,833 |

Table II does not show the price advantage of the multi-junction and gallium arsenide solar arrays to the spacecraft. This is because these arrays offer substantial weight reductions, see Table I, and some of this reduction can increase the amount of science that the spacecraft can carry hence increasing the cost effectiveness of the spacecraft. Below, this advantage is estimated first for the gallium arsenide and then the multi-junction cells.

Value of GaAs Array Weight Reduction on Spacecraft Science

From Table I, the gallium arsenide array is 51 kilograms less than the silicon array. Not all of the 51 kilograms can go into science. Some of the weight must go into the various spacecraft systems that support the increase in science. Such systems are increased in weight in rough proportion to the percentage weight increase in science. The amount of increase is computed using equations (1) through (6). Some spacecraft systems, those whose size is primarily determined by the spacecraft weight, remain unaffected by the increase in science. These systems are attitude control, propulsion, structure and thermal.

The equations (1) through (6) and their solutions account for the effect of the spacecraft systems that increase in weight. These equations predict an increase in the weight of the solar array as well as other spacecraft systems. The solar array weight increases, as do the other subsystem weights, to support the increase in the science capability. This means that the GaAs array will have to be more powerful than the silicon array. The data in Tables I and II do not reflect this. To obtain final costs for the spacecraft array this change in array and other subsystem costs is accounted for later in the paper. In equations (1) through (6), the variables INSTR, CDH, COMM, HGAS, ELEC, PWR, and SA are respectively the weights of the scientific instruments; command and data handling, communications, high gain antenna, electrical, power exclusive of the solar array, and solar array systems on the spacecraft with the silicon array. The variables ΔCDH, ΔCOMM, ΔHGAS, ΔELEC, ΔPWR and ΔSA are the increases in the weights of the respective systems as a result of the additional capability they must have to serve the additional science when the silicon array is replaced by a gallium arsenide array. The variable CF is the fraction of the command and data handling system that is used to support science. This fraction is obtained because about 13.85 kb/sec are used for the spacecraft while about 169.80 kb/sec are used for the instruments. This same fraction is used for the communications and high gain antenna. The variable PF is the fraction of power that is used by the instruments in normal operation, in this case 382 watts out of the total spacecraft wattage of 938.5 watts. SF is the fraction of weight by which the solar array increases when there is an increase in the array's power producing capability. In this case it means that the solar array increases .863% for every 1.0% increase in the array's power producing capability. The six equations imply that the capability of the spacecraft systems is proportional to weight. Although this is a reasonable approximation, it is not necessarily the case. For the greatest accuracy, each spacecraft subsystem would have to be redesigned for the increased capability and then its weight reestimated. In the context of this paper, the resources to do this are not available and the approximation used is good enough.

- (1) $CF * CDH (51 - \Delta CDH - \Delta COMM - \Delta PWR - \Delta ELEC - \Delta HGAS - \Delta SA) / INSTR = \Delta CDH,$
- (2) $CF * COMM (51 - \Delta CDH - \Delta COMM - \Delta PWR - \Delta ELEC - \Delta HGAS - \Delta SA) / INSTR = \Delta COMM,$
- (3) $CF * HGAS (51 - \Delta CDH - \Delta COMM - \Delta PWR - \Delta ELEC - \Delta HGAS - \Delta SA) / INSTR = \Delta HGAS,$
- (4) $PF * ELEC (51 - \Delta CDH - \Delta COMM - \Delta PWR - \Delta ELEC - \Delta HGAS - \Delta SA) / INSTR = \Delta ELEC,$
- (5) $PF * PWR (51 - \Delta CDH - \Delta COMM - \Delta PWR - \Delta ELEC - \Delta HGAS - \Delta SA) / INSTR = \Delta PWR,$
- (6) $SF * PF * SA (51 - \Delta CDH - \Delta COMM - \Delta PWR - \Delta ELEC - \Delta HGAS - \Delta SA) / INSTR = \Delta SA,$

INSTR = 633 kg
 CDH = 83.0 kg
 COMM = 32.4 kg
 HGAS = 81.8 kg
 ELEC = 263. kg
 PWR = 172. kg
 SA = 141. kg

CF = .918
 PF = .407
 SF = .863

Solving these equations yields the following results:

$$\begin{aligned}\Delta CDH &= 3.74 \text{ kg,} \\ \Delta COMM &= 1.46 \text{ kg,} \\ \Delta HGAS &= 3.68 \text{ kg,} \\ \Delta ELEC &= 5.25 \text{ kg,} \\ \Delta PWR &= 3.43 \text{ kg,} \\ \Delta SA &= 2.43 \text{ kg,} \\ \\ \text{Total} &= 20.0 \text{ kg.}\end{aligned}$$

The above results mean that the spacecraft can accommodate $51 - 20 = 31$ kg of additional science. A value for this increased science can be computed as follows. The launch costs for the TRMM spacecraft are approximately \$116.8 million and the spacecraft costs, excluding instrument, ground systems, and mission operations, are approximately \$232.7 million. This means that the total costs to get the science to orbit, and to support it with the spacecraft are \$349.5 million. This figure must be increased because the capability and complexity of some of the subsystems has increased. Using the results of equations (1) through (6) as shown in Table III, leads to a price increase of \$2.8 million. Again, this assumption is a reasonable approximation, but not completely accurate.

The scientific instruments weigh 633 kilograms (The TRMM spacecraft itself will weigh approximately 3,512 kilograms). This means that the launch costs for the original scientific payload are \$552,000 per kilogram. On this basis the launch and support of the additional 31 kilograms cost about \$17.1 million. This far exceeds the price of the more expensive gallium arsenide solar cells. Another measure of this is that the added 31 kilograms cost \$2.8 million or \$90,000 per kilogram to launch and support, about a factor of 5 less than the first 633 kilograms on a per weight basis. Another measure is that the silicon powered spacecraft launches 633 kilograms of science at a cost of \$552,000 per kilogram. The gallium arsenide spacecraft launches 664 kilograms of science at a cost of \$531,000 per kilogram.

This analysis underestimates, to a degree, the value of the gallium arsenide solar cells. For example in the power and electrical systems, the predicted increase in weight is assumed to be directly proportional to the increased power requirement. This is not the case; the power system weight will go up somewhat less than the linear increase predicted. The analysis, in another way, overestimates the value of the gallium arsenide solar cells. This is because the value of the first 633 kilograms of science is undoubtedly higher on a per weight basis than the value of the next 31 kilograms. The analysis also overestimates the value of the gallium arsenide cells in that their use resulted in an atypical reduction in the complexity of the solar array. This made the gallium arsenide cells look "better" than they would be on average.

Most importantly, this analysis presumes a clean possibility to organize and plan the spacecraft to the optimum. This is plainly not the case. For example, the satellite weight becomes a much more critical parameter as the spacecraft weight is about to be too heavy for the planned launch vehicle and to bump the spacecraft to the next larger vehicle. As another example, the power system weight is heavily dependent on batteries whose weight and size are not readily available in the exact optimum size. In addition, the design of spacecraft is such that subsystems are frequently not completely optimized for many reasons, one of which is just to get the heritage and known price of a previously existing subsystem. Furthermore, most of the GSFC spacecraft fly instruments and technology that have not been flown before or even done before. As a result, the spacecraft must carry rather significant weight contingencies. In short, the business of fabricating a spacecraft such as TRMM involves a great deal of intuitive judgment and a high degree of uncertainty. It is messy. Nonetheless, averaged over a large number of spacecraft, the predictions made here have merit in assigning value to the weight saved by a solar array and serve as a guide as to whether more efficient solar cells have value.

The history of TRMM illustrates the uncertainties of the predictions made above and the messiness of planning a unique spacecraft. On TRMM the gallium arsenide solar cells were selected, but the saved weight went into added fuel to keep the spacecraft aloft for the required time rather than into the scientific payload. Subsequently, the atmospheric models used to evaluate the decay of the spacecraft orbit changed, so the additional fuel was no longer necessary to meet mission requirements.

Table III
Cost of Spacecraft Systems for TRMM in Millions of Dollars

| Item (An asterisk indicates that subsystem price changes with solar cell price) | Cost With Si Array | Cost With GaAs Array | Cost With MJ Array |
|---|--------------------|----------------------|--------------------|
| Test | 4.7 | 4.7 | 4.7 |
| Structure | 12.6 | 12.6 | 12.6 |
| Deployables | 7.0 | 7.0 | 7.0 |
| Optical Alignment | .7 | .7 | .7 |
| Gimbal | 2.8 | 2.8 | 2.8 |
| ACS | 15.2 | 15.2 | 15.2 |
| *Power (Exclusive of Array) | 7.3 | 7.4 | 7.5 |
| Array | 3.3 | 4.7 | 4.1 |
| Thermal Design | 3.5 | 3.5 | 3.5 |
| Thermal Contamination | 1.6 | 1.6 | 1.6 |
| Thermal Coatings | .3 | .3 | .3 |
| Reaction Control System | 5.3 | 5.3 | 5.3 |
| *Electrical including I & T | 21.4 | 21.8 | 22.0 |
| *C & DH | 11.0 | 11.5 | 11.7 |
| Software | 2.1 | 2.1 | 2.1 |
| *Communications | 6.0 | 6.3 | 6.4 |
| Subtotal | 104.8 | 107.6 | 107.4 |
| Software Management | 1.8 | 1.8 | 1.8 |
| System Engineering | 4.9 | 4.9 | 4.9 |
| Project Support | 4.1 | 4.1 | 4.1 |
| Instruments (\$73.2) | N/A | N/A | N/A |
| P.A. | 5.5 | 5.5 | 5.5 |
| Ground Systems(\$25.2) | N/A | N/A | N/A |
| Mission Operations(\$3.7) | N/A | N/A | N/A |
| MPS (Center Tax-Overhead) | 26.9 | 26.9 | 26.9 |
| Subtotal | 148.0 | 150.8 | 150.6 |
| Contingency | 9.0 | 9.0 | 9.0 |
| Civil Servants | 75.7 | 75.7 | 75.7 |
| Total | 232.7 | 235.5 | 235.3 |

Value of MJ Array Weight Reduction on Spacecraft Science

The methodology used in this section is the same as that used in the previous section. From Table I, the multi-junction cell array is 73 kilograms less than the silicon array. Again, not all of the 73 kilograms can go into science. The spacecraft system weights will increase per the equations below. The variables have the same meaning and the constants have the same values as in equations (1) through (6) except for SA which is given its value below.

$$\begin{aligned}CF*CDH & (73-\Delta CDH-\Delta COMM-\Delta PWR-\Delta ELEC-\Delta HGAS-\Delta SA) / INSTR = \Delta CDH, \\CF*COMM & (73-\Delta CDH-\Delta COMM-\Delta PWR-\Delta ELEC-\Delta HGAS-\Delta SA) / INSTR = \Delta COMM, \\CF*HGAS & (73-\Delta CDH-\Delta COMM-\Delta PWR-\Delta ELEC-\Delta HGAS-\Delta SA) / INSTR = \Delta HGAS, \\PF*ELEC & (73-\Delta CDH-\Delta COMM-\Delta PWR-\Delta ELEC-\Delta HGAS-\Delta SA) / INSTR = \Delta ELEC, \\PF*PWR & (73-\Delta CDH-\Delta COMM-\Delta PWR-\Delta ELEC-\Delta HGAS-\Delta SA) / INSTR = \Delta PWR, \\SF*PF*SA & (73-\Delta CDH-\Delta COMM-\Delta PWR-\Delta ELEC-\Delta HGAS-\Delta SA) / INSTR = \Delta SA,\end{aligned}$$

$$SA = 119 \text{ kg}$$

Solving these equations yields the following results:

$$\begin{aligned}\Delta CDH & = 5.39 \text{ kg}, \\ \Delta COMM & = 2.10 \text{ kg}, \\ \Delta HGAS & = 5.31 \text{ kg}, \\ \Delta ELEC & = 7.57 \text{ kg}, \\ \Delta PWR & = 4.95 \text{ kg}, \\ \Delta SA & = 2.95 \text{ kg},\end{aligned}$$

$$\text{Total} = 28.3 \text{ kg}.$$

This means that the spacecraft can accommodate $73 - 28 = 45$ kg of additional science. The total costs to get the science to orbit, support it, and send raw data back are computed as \$235 million in Table III. This figure includes the increased capability and complexity of some of the subsystems due to the increase in science. Again the launch and support costs for the original scientific payload are \$552,000 per kilogram. On this basis the additional 45 kilograms cost about \$24.8 million to launch and support the spacecraft. Once again this far exceeds the price of the more expensive solar cell array. The solar array makes the added 45 kilograms available at \$2.6 million or \$57,000 per kilogram, an order of magnitude less than the first 633 kilograms on a per weight basis.

Sensitivity Analysis

That the cost of the first several multi-junction solar arrays would be significantly greater than that quoted in Table II and Table III was mentioned earlier. Making the assumption that this price is twice that given for gallium arsenide cells in Table III will give a notion of how sensitive this analysis is to the price of the arrays. This assumption is quite conservative even for the first few multi-junction arrays in that if the entire difference is due to cell cost, the multi-junction cells should be about an order of magnitude more expensive than gallium arsenide cells. This price difference cannot begin to be predicted. The material cost of the multi-junction cells should be quite close to that of gallium arsenide solar cells. The capital equipment used to produce them should be the same as for gallium arsenide cells. The labor used to produce multi-junction cells may be slightly greater than gallium arsenide cells in that the multi-junctions must stay longer in the reactor that grows additional cell layers. The major difference may well be that the multi-junction cells will have a lower yield than the gallium arsenide cells or that some sort of protection against reverse bias will have to be added; but in short, the price estimate from reference 1 appears reasonable. The first few arrays may be much more expensive because the cells may well give "teething problems" of an as yet unknown nature. This means that the manufacturer will face possible losses that will cause a significant protective increase in price. A factor of two is more than adequate to cover contingencies.

Making an assumption of a factor of two in array price will change the analysis as follows. If the multi-junction solar array is priced at twice that of the gallium arsenide array as well as increased in power output to support additional science, it will cost \$9.6 million rather than the \$4.1 million shown in Table III. This means that overall cost to the project will rise \$5.5 million to \$8.1 million from the \$2.6 million given in the preceding analysis. This is \$180,000

per kilogram; still substantially less than the \$552,000 per kilogram cost to launch and service the science with a silicon array.

Range of Validity of the Analysis

This results of this analysis depend on the higher efficiency solar cells to reduce the mechanical weight of the solar array substantially. This is true with an array such as TRMM that has relatively heavy substrates, and mechanical deployment and positioning systems. The analysis may lose validity if the cells can no longer leverage their efficiency advantage to cut array mechanical systems weight.

There are two types of arrays where the analysis in this paper may not hold true. The first is a body mounted array on spinning spacecraft. If such a spacecraft can obtain adequate power with the area available on its body with the use of silicon arrays, the use of higher efficiency cells would be counterproductive because the higher efficiency cells are heavier. The second type of array for which the analysis may be invalid is a deployable array such as the Advanced Photovoltaic Solar Array (APSA)⁵ or Solar Array Flight Experiment (SAFE)⁶ or the Hubble Space Telescope Array⁷. For these arrays, the reduction of weight with the increasing efficiency of cells is not necessarily achievable because most of the mechanical weight of these arrays is in the blanket storage and deployment mechanisms. Changing to a more efficient cell will have little effect on reducing this mechanical weight. This issue is quantitatively discussed by Ralph⁸ who uses only the launch cost per unit weight. In this case, the analysis still favors the higher efficiency cells.

Conclusions

From this study, both gallium arsenide and multi-junction solar cells offer significant cost advantages to spacecraft having deployable arrays. Gallium arsenide solar cells offer increases in the scientific payload at about \$90,000 per kilogram and multi-junction solar cells offer increases in the scientific payload at about \$ 58,000 per kilogram. This compares to the payload that costs \$533,000 to launch and support. The magnitude of this advantage is dependent on the higher efficiency cells to reduce the mechanical and structural weights of the solar array through a reduction in the array's area.

¹ P. K. Chiang, et al, "Large Area GaInP₂/GaAs Tandem Cell Development for Space Power Systems," *Twenty-Third Photovoltaic Specialists Conference*, 1993, pp. 659-664.

² Gene Ralph, "High Efficiency Solar Cell Arrays System Tradeoffs," *IEEE First World Conference on Photovoltaic Energy Conversion*, 1994, Hawaii, Figure 1, p.1998.

³ Throughout this paper the term "support" means to provide the scientific instrument with environmental protection from the space environment, to keep it at acceptable temperatures and to send the data it produces to earth in readable form. In short, the services provided by the spacecraft.

⁴ Gene Ralph, "High Efficiency Solar Cell Arrays System Tradeoffs," p. 1998.

⁵ Paul Stella and Richard Kurland, "Thin Film GaAs for Space--Moving Out of the Laboratory," *Twenty-Third Photovoltaic Specialists Conference*, 1993, pp. 21-26.

⁶ "Solar Array Flight Experiment," Final Report, LMSC-F087173, under Contract NAS-8-31352, April 1986.

⁷ Lothar Gerlach, "The Solar-Power Generator for the Hubble Space Telescope," *ESA Journal*, vol. 14, no. 2, 1990, pp. 149-168.

⁸ Gene Ralph, "High Efficiency Solar Cell Arrays System Tradeoffs," Figure 7, p. 2000

S7
M-50392

THE PROGRESS OF LARGE AREA GaInP₂/GaAs/Ge TRIPLE-JUNCTION CELL DEVELOPMENT AT SPECTROLAB¹

P. K. Chiang, D. D. Krut and B. T. Cavicchi
Spectrolab Inc.,
Sylmar, California

ABSTRACT

This paper describes the successful demonstration of high efficiency, large area monolithic triple-junction, n on p, GaInP₂/GaAs/Ge cells. The highest open circuit voltage and cell efficiency (cell size: 2 cm x 2 cm) measured to date are 2.573 V and 23.3%, respectively, under 1 sun, AM0 illumination. A very uniform distribution of cell efficiency across a 3" diameter wafer is also achieved. The temperature coefficient and 1 MeV electron irradiation results are obtained. We have incorporated a triple-junction cell in the 1995 JPL balloon flight. The I-V result obtained from the balloon flight and the solar simulators are compared. Finally, we have fabricated more than 50, 2 cm x 2 cm triple-junction cell-interconnect-cover (CIC) assemblies. The highest CIC efficiency is 23.2%. No degradation in CIC performance after 100, -120 °C to +140 °C thermal cycles was observed.

INTRODUCTION

The GaInP₂/GaAs/Ge monolithic multi-junction cell is an attractive technology for space applications due to its high efficiency and radiation hardness. Ge is a low cost (compared to GaAs or InP) substrate available in 100 mm wafer diameters sufficiently rugged for thin, large area cell fabrication. In past years, Spectrolab has demonstrated dual-junction cell efficiencies up to 24.2% (cell size: 0.5 cm x 0.5 cm) under 1x, AM0 illumination on Ge substrates [1]. Concurrently, we have modeled a triple junction version of the cell utilizing the Ge as a voltage booster. Model results indicated with the inclusion of a third junction in the Ge substrate, the cell efficiency will have an additional 2% to 2.5% (absolute efficiency) increase.

Under this U.S. Air Force development contract, the objective has been to demonstrate proof-of-concept triple junction devices and to deliver cells with a goal of 24% efficiency. The ultimate objectives are (1) to demonstrate a 26.5% cell efficiency and (2) to extend the growths to larger reactors capable of supporting volume production. In this work, we have utilized a multiple wafer reactor to grow the triple-junction GaInP₂/GaAs/Ge cells. The highest efficiency achieved to date is 23.3% for a cell measuring 2 cm x 2 cm. We have also achieved a very uniform distribution of cell efficiencies across 3" diameter wafers. Average cell efficiency of 22.8% across the 3" diameter wafer indicates large area cells, up to 4 x 6 cm² across 3" wafer are possible. Cells have been characterized by electron irradiation.

¹ This Work is supported by the Department of the Air Force and Managed by Phillips Laboratory, Space Power and Thermal Management Division, under Phillips Laboratory contract no. F33615-91-2146.

tion stability (1 MeV), and temperature coefficient measurements for both dual and triple-junction cells. The results indicate the difference in absolute efficiency between these two devices is 2% at an operating temperature of 54 °C.

In addition, we have incorporated a triple-junction cell in the JPL balloon flight 1995. The same cell was also measured by NREL and Spectrolab. The efficiency measured from the balloon flight is 0.7% and 1.9% (relative efficiency) lower than what measured by NREL and Spectrolab, respectively.

Finally, we have fabricated more than 50 triple junction welded CICs. The highest CIC efficiency is 23.2%. The average efficiency for the 50 CICs (CIC size: 2 cm x 2 cm) was 22.0% and is very comparable to that which was measured on the bare cells (average cell efficiency is 22.1%) before they were fabricated into CICs. Several CICs were subjected to a 100 thermal cycle test with the temperature varying from -120 °C to +140 °C in each cycle. No degradation was observed for this test.

GaInP₂/GaAs/Ge TRIPLE-JUNCTION CELL RESULTS

GaInP₂/GaAs/Ge Triple-Junction Performance Modeling

In this work we first performed modeling to calculate the minimum achievable efficiency in the triple-junction cell in the high volume production environment. Our approach has been to combine what we have already demonstrated on the dual-junction with conservatively modeled performance for the Ge bottom cell. The triple-junction cell structure shown in Fig. 1 consists of a dual-junction GaInP₂/GaAs interconnected to the Ge bottom cell through a second GaAs tunnel junction. The resultant I-V curve for a triple-junction GaInP₂/GaAs/Ge cell is shown in Fig. 2. The expected minimum average efficiency at beginning-of-life (BOL) is 26.5%. Previous work on the electron irradiation of Ge cells demonstrated a low rate of current and voltage loss up to high fluence levels [2,3]. At an EOL fluence of 1×10^{15} , 1 MeV electrons/cm², the Ge cell will continue to function as a voltage booster and the triple-junction cell will have an efficiency greater than 21%.

GaInP₂/GaAs/Ge Triple-Junction Solar Cell Fabrication

The cell structure utilized in this work has been shown in Fig. 1. The thickness of the emitter and base layers in GaInP₂ cell were 0.1-0.15 μm and 0.4-0.48 μm, respectively. The carrier concentration in the emitter of both cells was $1-3 \times 10^{18}$ cm⁻³. The base of the top cell was doped to a level of $1-3 \times 10^{17}$ cm⁻³, while a base doping of the $3-6 \times 10^{16}$ cm⁻³ was targeted in the GaAs cell to maximize EOL current collection. A high bandgap AlInP₂ layer was used to passivate the front of the GaInP₂ cell; the back surface was passivated in this cell with an AlGaInP layer. A GaInP₂ layer was used for the window on the GaAs cell. An AlGaAs (or GaInP₂) was used for the GaAs cell back surface passivation. The Ge bottom cell active junction was formed by As diffusion into a p-type Ge substrate.

The GaInP₂/GaAs/Ge triple-junction cells were grown on 3-inch diameter Ge substrates. The grown wafers show mirror like shiny surface morphology. Cells were then processed into a 2 cm x 2 cm cell size using standard single junction GaAs/Ge producing procedures. After processing, cells were evaluated by light I-V measurements. Since current in these cells is limited by the top two cells, the X-25 simulator intensity was set with JPL balloon flight GaInP₂ and GaAs (filtered by GaInP₂) standard.

The highest efficiency measured to date is 23.3% (AM0, 28 °C) for a 2 cm x 2 cm cell. As shown in Fig. 3 the open circuit voltage (V_{oc}), short circuit current (I_{sc}), and fill factor (FF) are 2.573 V, 58.06 mA and 86.1%, respectively. To our knowledge this is the first, and the highest efficiency reported for, an n/p GaInP₂/GaAs/Ge triple junction cell.

Figure 4 shows the best measured cell efficiency distribution for cells grown on a 3 inch diameter substrate. The cell efficiencies, with an average of 22.8% (1x, AM0), were uniformly distributed across the wafer. The average Voc, Isc and FF, were measured at 2.549 V, 58.1 mA and 84.7%, respectively, in this wafer. Good cell uniformity across the 3 inch diameter wafer indicates large area, 4 cm x 6 cm cells could be fabricated. The spectral response was measured using light bias at different wavelength. The external quantum efficiency (Q.E.) of the three subcells are clear from the data in Fig. 5. After integration of the external Q.E. with AM0 spectrum we obtained a much higher current in the Ge cell and confirmed that the current triple-junction cell performance is limited by the top two cells.

GaInP₂/GaAs/Ge Triple-Junction Solar Cell Characterization

Electron Irradiation Test Results

In this test we irradiated a small quantity of bare cells. The electron energy and fluence used in this test were 1.0 MeV and 1E15 e/cm², respectively. After the irradiation, cells were re-measured with X-25 simulator. Due to a lack of balloon flight standard, for end-of-life (EOL), the X-25 simulator intensity was set with JPL balloon flight GaInP₂ and GaAs (filtered by GaInP₂) standard cells for BOL.

The light I-V results for the irradiated cells are summarized in Table 1. Voc1, Isc1, FF1 and Eff1 are the open circuit voltage, short circuit current, fill factor and efficiency, respectively, for BOL. Voc2, Isc2, FF2 and Eff2 are the results for EOL. Average Voc, Isc, FF and Eff ratios for cells measured at EOL to BOL are 92.4%, 81.1%, 99.2% and 74.4%, respectively. Since the ratio of Isc is very close to that measured in GaAs single junction cells, we concluded that the EOL performance of triple-junction cell is limited by the degradation of GaAs cell. In order to verify this, we performed spectral response measurements on these cells. As shown in Fig. 6 the external Q.E. for both GaInP₂ and GaAs cells degraded at EOL. The ratio of integrated current for EOL to BOL are approximately 93% and 80%, respectively, for the GaInP₂ and GaAs cells, which confirms that the EOL performance of current triple-junction cell is limited by the degradation of the GaAs cell. Recently, we have improved the GaAs single junction cell electron irradiation performance. We will incorporate this into the triple junction cell growths and expect a better EOL performance in optimized triple junction cells.

GaInP₂/GaAs/Ge Triple-Junction Cell Temperature Coefficient Measurement

Several triple-junction cells have been used for the temperature coefficient measurements. Light I-V measurements were performed at four different temperatures (10, 28, 50 and 80 °C). The open circuit voltage decreases with increasing temperature is shown in Fig. 7. The decrease in the Voc is due to the increasing dark currents. The rate of decrease of Voc with temperature is 6.07 mV/°C. For comparison, the temperature coefficient of 3.99 mV/°C for the dual-junction cell is also plotted in the same figure.

The short circuit current increases with increasing temperature is shown in Fig. 8. The improvement in Isc with increasing temperature is due mostly to the shift in the absorption edge of three cells. The rate of increase of short circuit current density with temperature is 0.0162 mA/cm²/°C.

The efficiency decreases with increasing temperature for both dual and triple-junction cells are shown in Fig. 9. The rate of decrease of Eff with temperature are 0.040 and 0.053 %/°C (absolute), respectively, for dual and triple-junction cells. This figure also clearly shows the difference between these two devices is 2% at an operating temperature of 54 °C, as we previously reported [1].

GaInP₂/GaAs/Ge Triple-Junction Cell Balloon Flight Measurement Results

Triple junction device measurements are performed using Spectrolab's modified X-25 simulator. The simulator contains an attachment with a movable set of filters that allow trimming simulator's spectral content to achieve proper color balance between the GaInP₂ top cell to GaAs middle cell with respect to the set of balloon flight standards.

Device 2T110A4 was measured using this simulator with appropriate set of top and middle cell standards. This cell was also measured at NREL using multi-source filtering attachment. In addition to Spectrolab and NREL measurements, Cell 2T110A4 was mounted onto the standard JPL balloon package and flown on the 1995 balloon flight. The results and temperature corrected results are shown in Table 2.

Measurement differences between Spectrolab ground and balloon measurements are less than 2%. Most of the error is in the voltage measurement, rather than I_{sc} and fill factor. This error may be related to the difference in temperature coefficients of the measured cell and the values measured for other devices (presented in this paper). Similarly, the difference between NREL and Spectrolab measurements is less than 2%. Good agreements in measured currents between three measurements show that terrestrial measurements of multijunctions within 1% are possible.

GaInP₂/GaAs/Ge TRIPLE-JUNCTION CIC RESULTS

In this work, we have successfully fabricated full CIC structures. In order to meet the delivery requirement, fifty bare cells with an average efficiency of 22.1% were selected for the CIC fabrications. Silver straps were used to weld to the top metal contact of the cells. Three mil thick, CMX glasses were cut to the size of the cells and cemented to the surfaces of the cells. After fabrication, light I-V were re-measured. The highest efficiency measured to date is 23.2% (AM0, 28 °C) for a 2 cm x 2 cm CIC. The Voc, I_{sc}, FF are 2.564 V, 57.76 mA and 86.3%, respectively. The average efficiency for these 50 CICs is 22.0%, which is very comparable to the average bare cell efficiency of 22.1% before they were fabricated into the CICs.

Several CICs were subjected to a 100 thermal cycle test. In this test, the temperature varied from -120 °C to +140 °C at the rate of 15 °C/min in each cycle. After the test, they were re-measured. The I-V results are very close to what were measured before the thermal cycle test indicating no degradation occurred during this thermal cycle test.

CONCLUSIONS

GaInP₂/GaAs/Ge triple-junction cells have been successfully demonstrated. The best cell efficiency of 23.3% AM0, 28 °C) is the highest reported efficiency for this device. With optimization, these cells are capable of providing a minimum average efficiency of 26.5% in volume production. The electron irradiation of first few cells yielded average P/P₀ at 0.744. This performance is limited by the GaAs middle cell. With optimization the P/P₀ in this device is expected to improve to 0.80 at 1.0 MeV (1E15 e/cm²) electron irradiation. We have completed temperature coefficient measurements shown 2% absolute efficiency difference between the dual and triple-junction cells at operating temperature of 54 °C. Finally, the triple junction CICs were successfully fabricated indicating the "transparency" of the product to standard Spectrolab's welded panel fabrication process. The best CIC (2 cm x 2 cm) efficiency is 23.2%. No degradation in CICs was observed after thermal cycle testing.

REFERENCES

- [1] P.K. Chiang et. al., "Large area GaInP₂/GaAs/Ge multijunction solar cells for space applications", Proc. 1st world conf. on PV energy conversion, 1994, pp. 2120-2123.
- [2] R. Venkatasubramanian et. al., "High temperature performance and radiation resistance of high efficiency Ge and Si_{0.07}Ge_{0.93} solar cells on lightweight Ge substrates", Proc. 22nd IEEE PVSC, 1991, pp.85-89.
- [3] D. D. Krut et. al., "The development of Ge bottom cell for monolithic and stacked multijunction applications", Proc. 22nd IEEE PVSC, 1991, pp. 90-92.

Table 1 Light I-V test results for BOL and EOL

| | Voc1 (V) | Voc2 (V) | Ratio | Isc1 (mA) | Isc2 (mA) | Ratio | FF1 (%) | FF2 (%) | Ratio | Eff1 (%) | Eff2 (%) | Ratio |
|----------|-------------|-------------|-------|--------------|--------------|-------|------------|------------|-------|-------------|-------------|-------|
| 2T101A-5 | 2.524 | 2.324 | 0.921 | 60.68 | 49.10 | 0.809 | 81.16 | 81.08 | 0.999 | 22.5 | 16.8 | 0.744 |
| 2T110A-5 | 2.526 | 2.342 | 0.927 | 60.66 | 49.35 | 0.814 | 83.67 | 82.42 | 0.985 | 23.2 | 17.3 | 0.743 |
| Avg: | 2.525 | 2.333 | 0.924 | 60.67 | 49.23 | 0.811 | 82.42 | 81.75 | 0.992 | 22.9 | 17.0 | 0.744 |

Table 2 Triple Junction Cell Testing Results

| | Spectrolab Measurement (ASTM AM0) | JPL Balloon | | NREL (WRRL AM0) |
|-----|--------------------------------------|--------------------|----------------------|---------------------|
| | Measured at 28°C | Measured at 53.5°C | Corrected to 28°C | Measured at 25°C |
| Isc | 58.47 mA | 59.98 mA | 58.83 mA | 58.97 mA |
| Voc | 2.541 V | 2.355 V | 2.510 V | 2.553 V |
| Eff | 22.95% | 21.15% | 22.51% | 22.6% |
| FF | 83.94% | 81.96% | ----- | 83.89% |

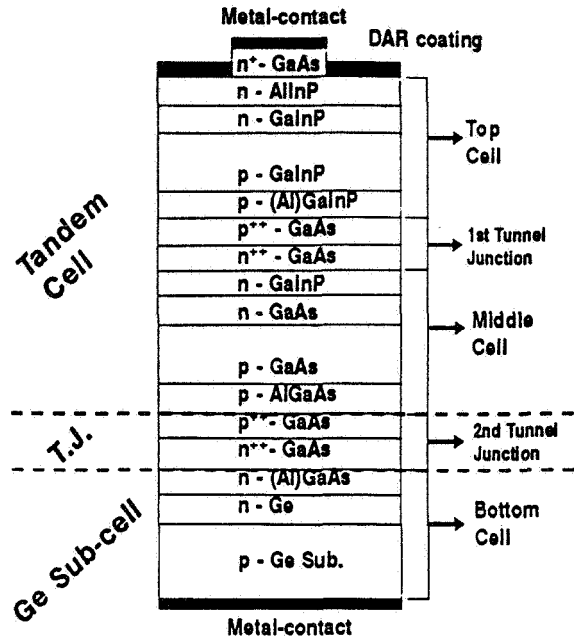


Fig. 1. Cross-section of a triple-junction cell

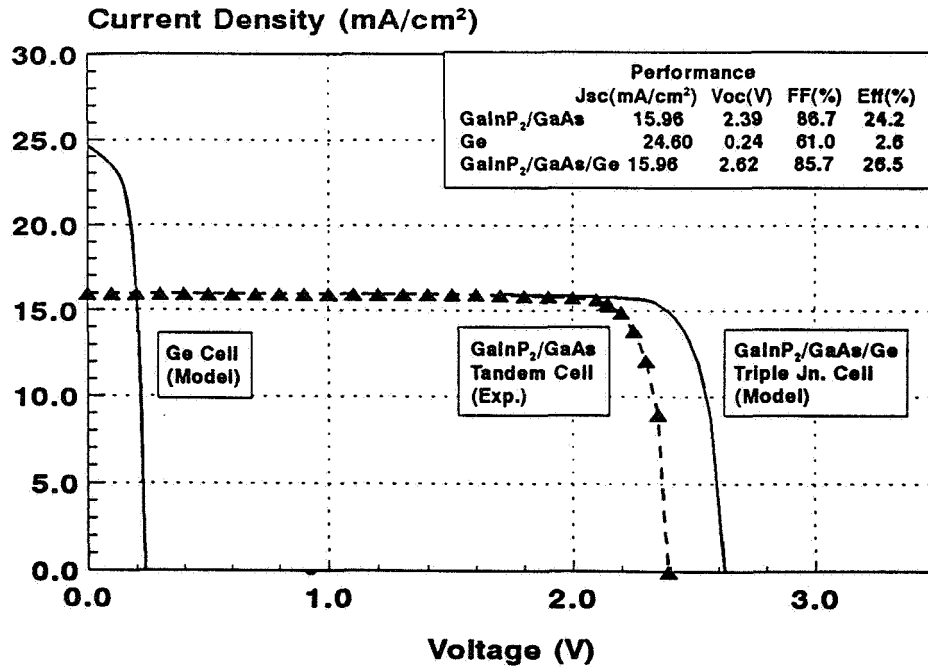


Fig. 2. Modeled BOL performance of proposed n/p GaInP₂/GaAs/Ge monolithic triple-junction cell (AM0 28 °C)

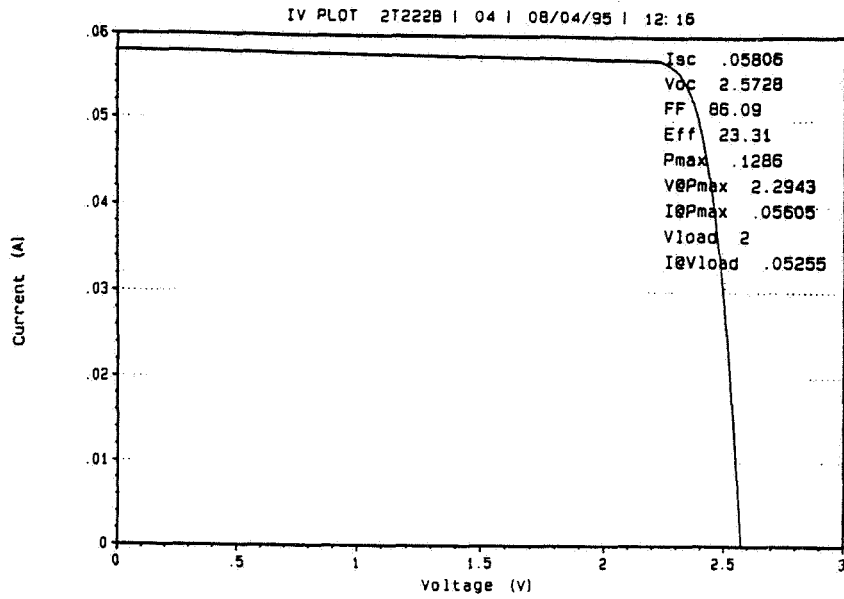
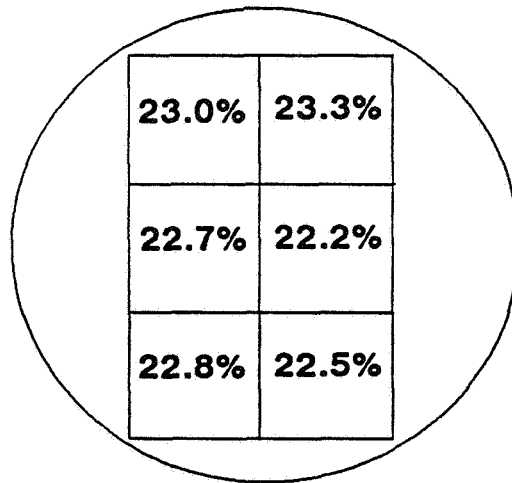


Fig. 3. I-V curve for the highest efficiency GaInP₂/GaAs/Ge triple junction cell



**Sub: 3" Diameter p-Ge
(Cell Area: 4.078 cm²)**

Fig. 4. Efficiency distribution of triple-junction cells across a 3" diameter substrate

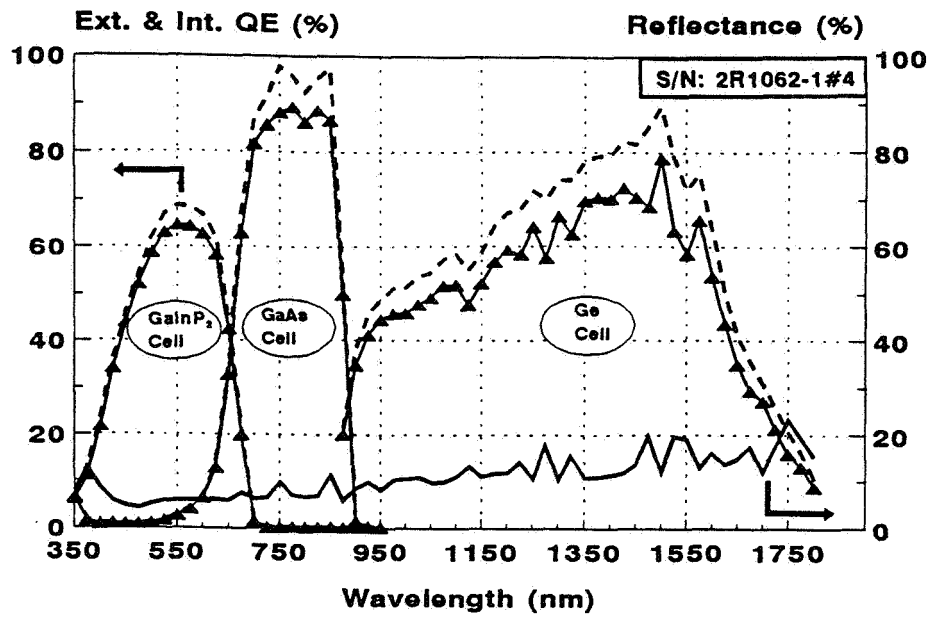


Fig. 5. External quantum efficiency and reflectance of a triple-junction cell

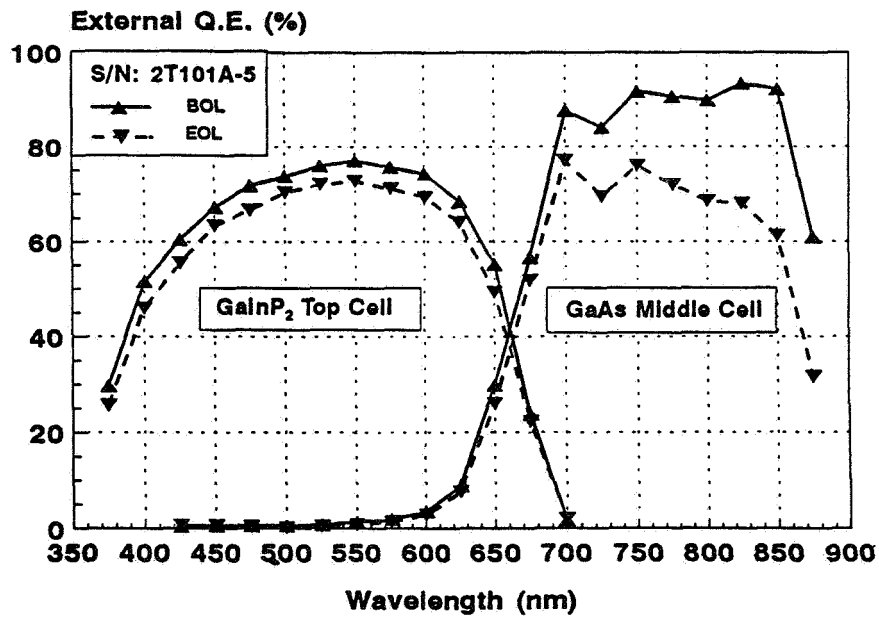


Fig. 6. External quantum efficiency of a GaInP₂/GaAs/Ge triple junction cell measured before and after electron irradiation

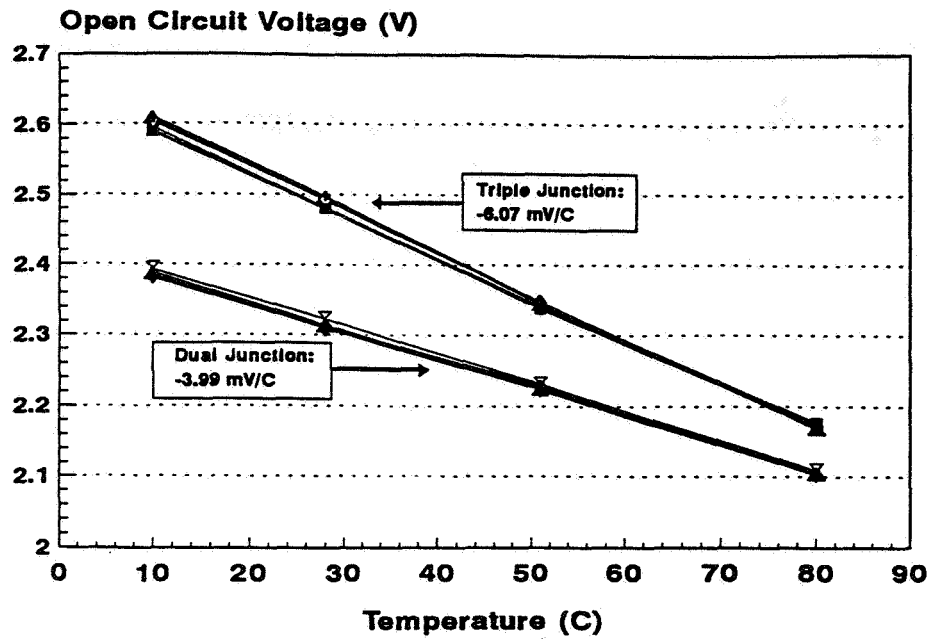


Fig. 7. Open circuit voltage of dual and triple-junction cells as a function of temperature

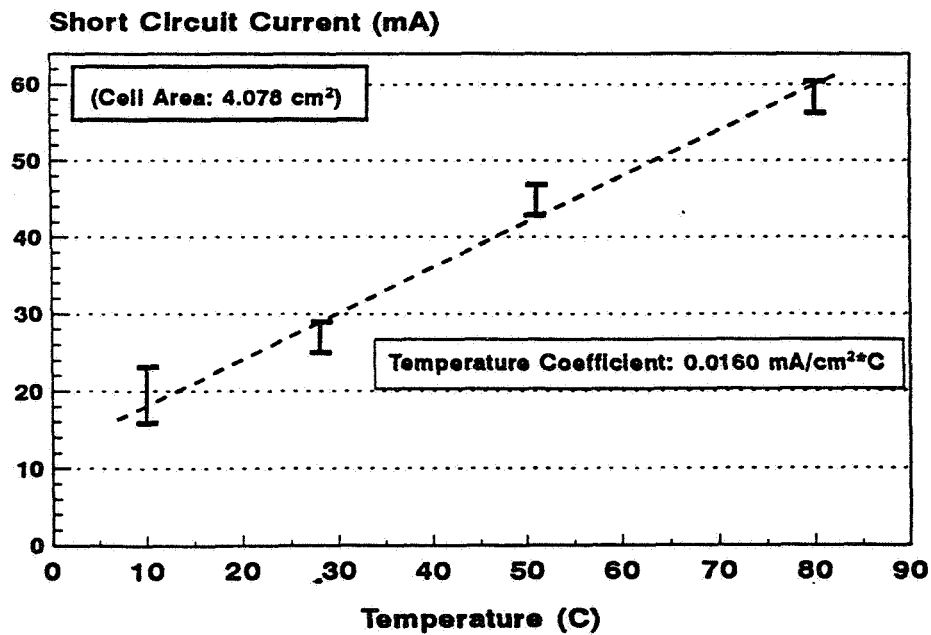


Fig. 8. Short circuit current of triple junction cell as a function of temperature. (note: vertical bar in each temperature represents the range of measurements in three cells)

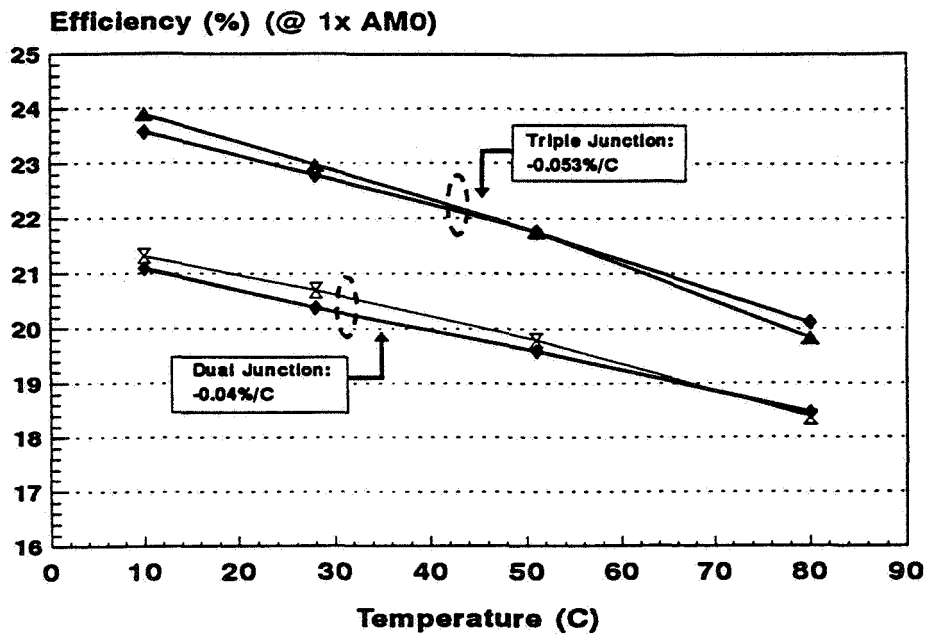


Fig. 9. Efficiency of dual and triple-junction cells as a function of temperature

58
IN- 50393

STATUS OF MULTIJUNCTION SOLAR CELLS

Y.C. M Yeh and C.L. Chu
Applied Solar Energy Corporation
15251 Don Julian Rd.
City of Industry, CA 91745-1002

INTRODUCTION

This paper describes Applied Solar's present activity on Multijunction space cells. We have worked on a variety of MJ cells, both monolithic and mechanically stacked. In recent years, most effort has been directed to GaInP₂/GaAs monolithic cells, grown on Ge substrates, and the status of this cell design will be reviewed here.

Purpose of Work

MJ cells are in demand to provide satellite power because of the acceptance of the overwhelming importance of high efficiency to reduce the area, weight and cost of space PV power systems. The need for high efficiencies has already accelerated the production of GaAs/Ge cells, with efficiencies 18.5-19%. When users realized that MJ cells could provide higher efficiencies (from 22% to 26%) with only fractional increase in costs, the demand for production MJ cells increased rapidly.

The main purpose of the work described is to transfer the MOCVD growth technology of MJ high efficiency cells to a production environment, providing all the space requirements of users.

TECHNICAL APPROACH

The feasibility of the high efficiency MJ cells considered here, was demonstrated primarily by an NREL group under Dr. Jerry Olsen. The challenge is to transfer this MJ cell to production status. This required validation that large area MJ cells could be fabricated evaluation of the relative merits of P/N and N/P configurations, and demonstration that Ge substrates could replace GaAs, to provide larger area, thin MJ cells.

The main technical challenges for MJ cells result from the larger numbers of cell design options (10-12 layers) and from the controlled MODVD procedures required for uniform multilayer growth over substrates.

The approach used is to systematically vary the various layers using design of experiment methods to optimize the layers for high efficiency. These tests are made in a large capacity MOCVD reactor to validate that these optimization procedures can be achieved at production levels. Production operation includes the need to upgrade the toxic disposal (involving both P and As) and establishing of maintenance schedules to provide round-the-clock operation, to meet user delivery schedules.

There is one other important factor in control of the growth procedures. The BOL cell efficiency depends on the current match between the GaInP₂ and GaAs cells, and is highest when the sub-cell currents are equal. However, because radiation degrades the subcells at different rates, (usually the GaAs cell degrades faster when exposed to only the longer wavelengths transmitted by the the GaInP₂ cell), in order to meet typical space mission requirements, it is necessary to modify the growth procedures to over-match the GaAs cell. Although this reduces the BOL efficiency slightly, the EOL efficiency is improved. We have investigated this tailoring of radiation performance, including steps to increase the radiation resistance of the GaAs sub cell, and have validated a model which allows prediction and monitoring tests that ensure than large numbers of MJ cells have consistent EOL performance, meeting specific flight conditions.

For MJ cells, the contact requirements are not excessive . The higher internal impedance of the cell allows very low series resistance (high CFF) to be obtained with low metal shading (~ 3%). The requirements for bondability contact adhesion and minimization of interaction between the contact metallization and the MJ cell structure can be fulfilled using experience gained on GaAs/Ge cells. We are continuing to evaluate possible improved metallization schemes. For MJ cells, there is only slight decrease in CFF resulting from the larger grid path length on larger size substrates.

The AR coatings need modification, to ensure the correct match for 2J (and 3J cells).

To control and monitor MJ cell performance, we have developed a set of inline characterization tests. A major requirement is that the solar simulators used can replicate the AM0 spectrum for all cells in the stack, and over the whole cell area. We are using two-light simulators, one an existing Hoffman simulator, the other a Xe light simulator, with added optical filters. We are also modifying a large area pulsed solar simulator for testing strings and panels made from MJ cells. The simulator coefficient is checked by radiometers, and also using balloon-flown subcells or secondary standards to calibrate simulator.

The I-V data are analyzed in detail to extract the performance of the overall cell and of the subcells.

Other tests include:

- Visual check of surface morphology of MOCVD grown layers. (This follows procedures developed successfully with GaAs/Ge cells)
- Detailed analysis of illuminated I-V performance
- Spectral analysis of individual cell output
- C-V Polaron profiling, to derive the impurity concentration and thickness of the main layers, usually the emitter and base of the subcells.
- X-ray diffraction to check the lattice spacing and strain
- Spectral reflectance to check solar absorptance and AR coatings

For tests of external cell features, (contact strength, temperature cycling, humidity etc.) the usual QA equipment and procedures are used.

RESULTS ACHIEVED

The initial efficiency goal (21.5 - 22%) has been achieved for large area cells (over 4 cm², up to 36 cm²), grown in a large production MOCVD reactor.

As mentioned above, the major factor in achieving high efficiency for large area MJ cells is not to correct for the slight loss in CFF resulting from longer grid length, but the need to optimize all the critical layer growth parameters over larger areas.

Figures 1 and 2 show AM0 I-V curves for two cells of different area. The radiation performance has been modeled. Figures 3 and 4 show the performance of dual-junction cells for a range of 1 MeV fluences, as a function of the subcell current mismatch. Figure 5 shows some experimental radiation data for dual junction cells, plotted with the model predictions.

Figures 6 and 7 shows some in-line characterization results, the measurement of the spectral response of each subcell, and the deviation of the bandgap of the GaInP₂ cell.

These MJ cells have successfully passed the space qualification tests shown in Table1.

Present efforts continue to increase the yield for cells made under production conditions.

DEVELOPMENT WORK

In addition to the on-line yield improvements, several other areas of MJ cell development are proceeding at Applied Solar, to meet future production requirements.

Enhanced Dual Junction Cells

Work is proceeding to develop dual-junction cells with enhanced output. This involves improving the passivation at several cell interfaces, and also some fine-tuning of the growth parameters. The design of the enhanced output cells (minimum average goal 24%) will also ensure that the cells meet specified radiation exposures.

Triple-Junction Cells

The user-demands for GaAs/Ge cells led to the requirement that the GaAs/Ge interface should be photovoltaically inactive, and the growth procedures were defined to tender this interface inactive.

For MJ cells, it is easier to provide matching current in a Ge cell under a 2J cell, and work has proceeded to add a third (Ge) cell under the dual junction cell. In the best case, this should further increase efficiency to 26%, with no penalty in radiation resistance, and minimum increase in temperature coefficients.

Applied Solar has continued work begun (with RTI) on making dual junction monolithic cells from AlGaAs &or GaInAsP) cells grown on Ge cells. We are re-evaluating the options for forming Ge cells, which retain best performance after exposure to the full growth sequence of GaAs and GaInP₂ cells.

On a NASA-Lewis SBIR, in Phase I we studied the options available to include Ge PN junctions. The methods adjustment of the growth parameters to form the PN junction in-situ (the method used to make GaAs/Ge cells with active interface), or preforming Ge PN cells, by epitaxial growth, or by ion implantation or diffusion. We have established that high emitter doping density ($>5 \times 10^{18} \text{ cm}^{-3}$) is needed to ensure effective PN junctions in P/N structures after As in-diffusion occurs during growth of the GaAs cell.

We are also studying the many impurity interactions that take place across the GaAs/Ge interface during the growth schedule.

We have established that the quality of present N-Ge substrates can provide matching current when illuminated under the dual-junction layers. The main emphasis is on maximizing the Voc and CFF of the Ge cell under the same illumination conditions.

Other MJ Cells

We have begun work (with NREL and RTI) on an NRL contract, to investigate MJ cells (InP/InGaAs) grown on Ge substrates. The goal of this contract is to provide high EOL performance. The main technical emphasis is to optimize the cell performance by growing intermediate layers with increasing lattice spacing on the Ge substrates to reduce the effects of the lattice mismatch between Ge and the other two cell materials.

We are also continuing to explore the methods developed with RTI, on mechanically stacked MJ cells with improved cell-cell bonding methods. This option allows cells with suitable bandgaps but widely varying lattice spacings to be combined effectively.

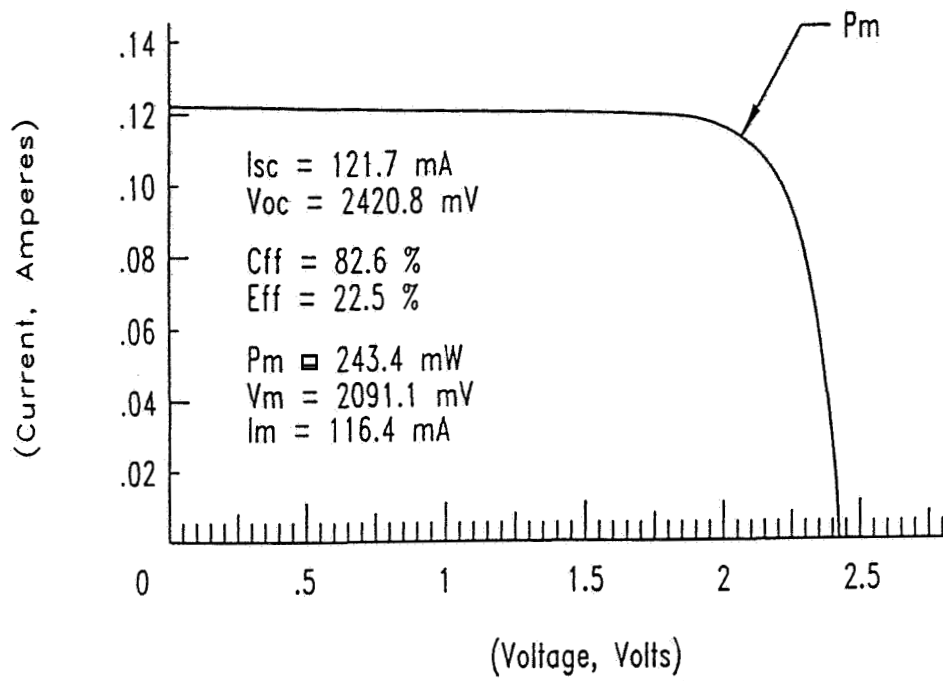
SUMMARY

This paper described Applied Solar's current activity in MJ cells. The goals are to meet increased user demands for higher efficiency large area space cells, at production levels. We have described the production build up of dual junction cells, primarily in demonstrating growth of all the DJ cell layers in a large throughput MOCVD reactor. We have also established effective in-line characterization, analysis and testing methods. Space-qualified post-growth process methods have been demonstrated.

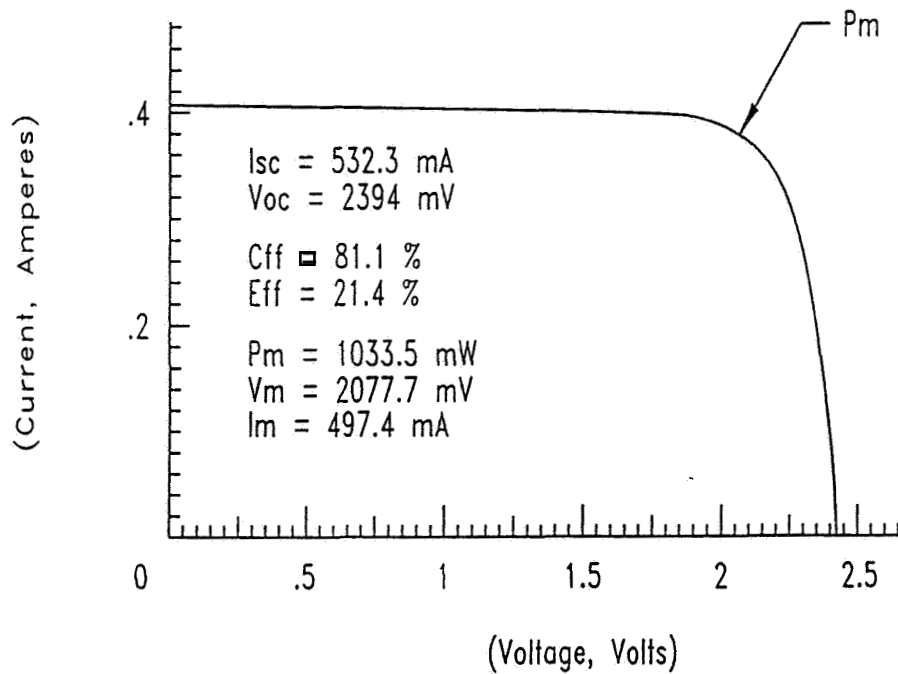
We outlined work to enhance DJ cells, and to add a third junction. We also described work on some associated MJ cell designs.

Table I Space Qualification Tests Completed

| TEST | CONDITIONS |
|--------------------------|--|
| PARTICULATE RADIATION | PROTON ENERGY: 200 KeV FLUENCES 1E + 11 TO 1E + 13 e/cm ² ELECTRON ENERGY: 1-MeV FLUENCES 3E+13 TO 3E + 15 e/cm ² |
| UV RADIATION | 550 - SUN-HOURS AT 1-SUN AMO |
| HUMIDITY | 95% AT 45°C FOR 30 DAYS |
| OPTICAL PROPERTIES | ABSORPTIVITY = 0.89, EMISSIVITY = 0.85 WITH OCLI 0213 GLASS COVERSLIDE |
| WELDABILITY | FRONT/BACK CONTACT 45° PULL, 350 GRAMS |
| SOLDERABILITY | FRONT/BACK CONTACT 45° PULL, 600 GRAMS |
| ANGLE OF INCIDENCE | 0° TO 80° SUN ANGLE AT ROOM AMBIENT |
| REVERSE BIAS SOAK | 30-MINS DARK REVERSE AT 120°C, 1.67 X 1 _{sc} |
| REVERSE BIAS CYCLING | > 25,000 CYCLES AT 120°C, 1.67 X 1 _{sc} |
| TEMPERATURE COEFFICIENTS | 28°C TO 120°C, 0 TO 3E +15, 1-MeV ELECTRONS |
| THERMAL CYCLING | 5,000 CYCLES FROM -110°C TO 120°C |



**Figure 1 I-V Data (AM0, 28°C) for
 Dual-Junction Cell, Area 8 cm²**



**Figure 2 I-V Data (AM0, 28°C) for
 Dual Junction Cell, Area ~ 36 cm²**

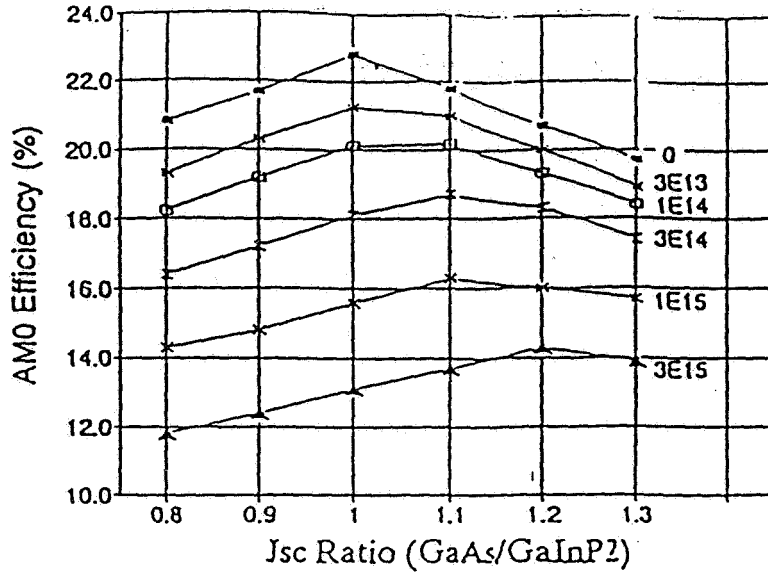


Figure 3 Influence of Current Mismatch on AMO Efficiency of a Dual Junction Cell Exposed to Several 1 MeV Electron Fluences

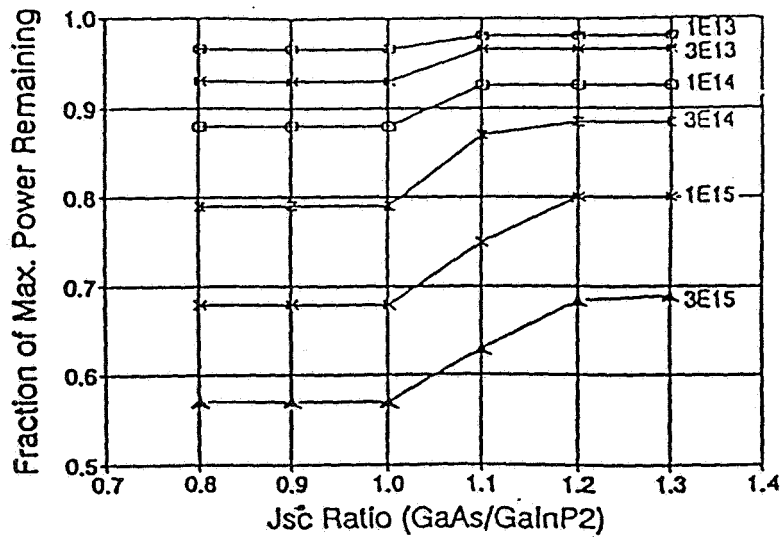


Figure 4 Influence of Current Mismatch on Fraction of Power Remaining, for a Dual-Junction Cell Exposed to Several 1 MeV Electron Fluences

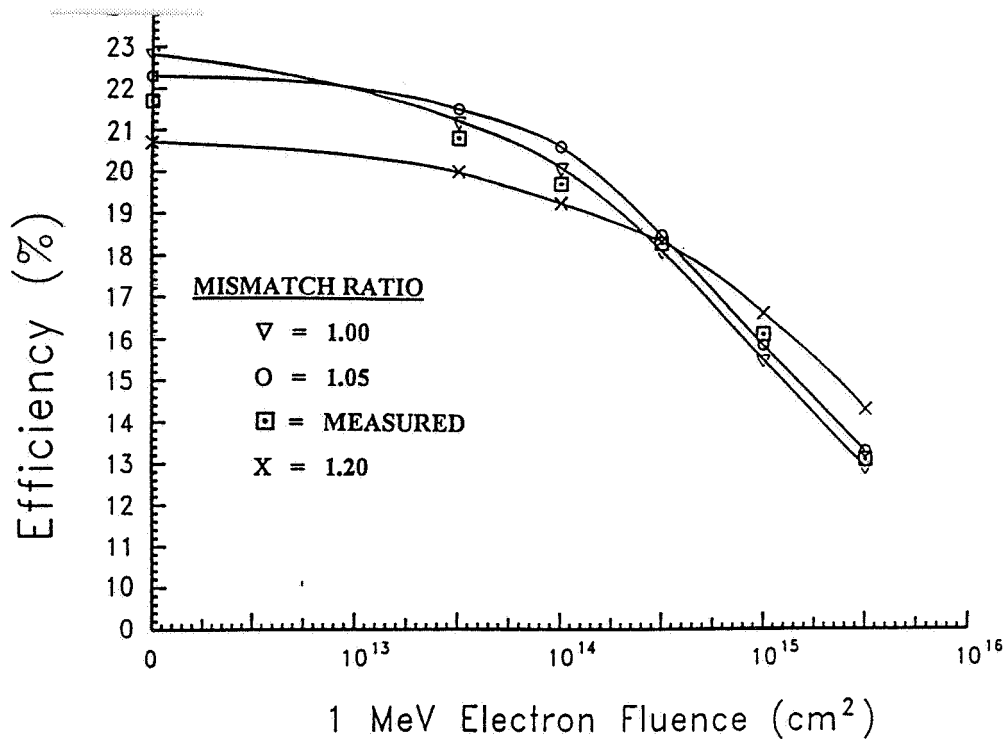


Figure 5 Radiation Performance of Dual-Junction Cell [Modeled and Experimental]

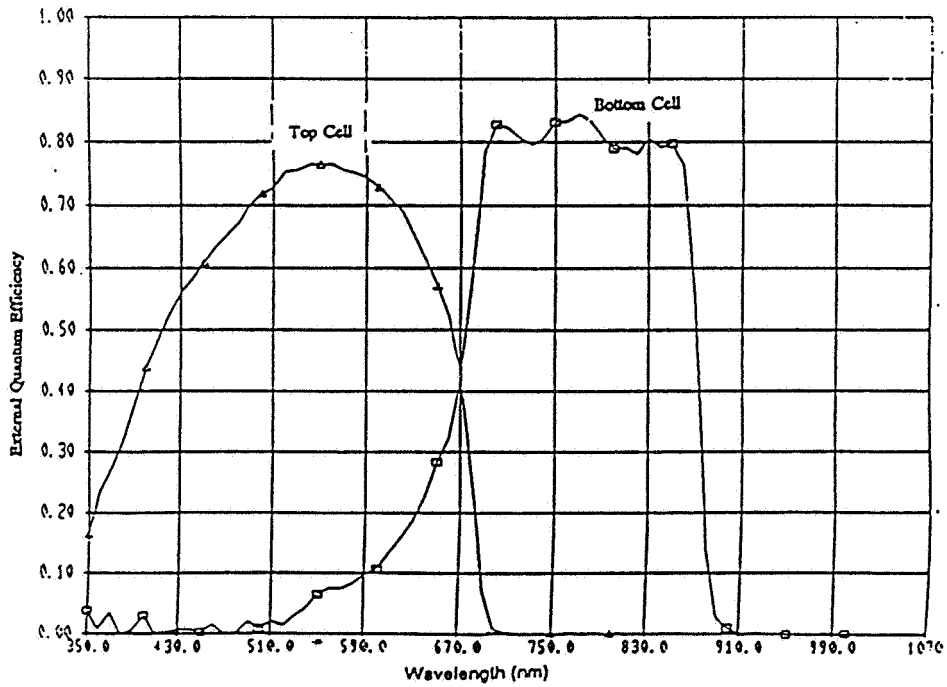


Figure 6 Spectral Response of Dual-Junction Cell

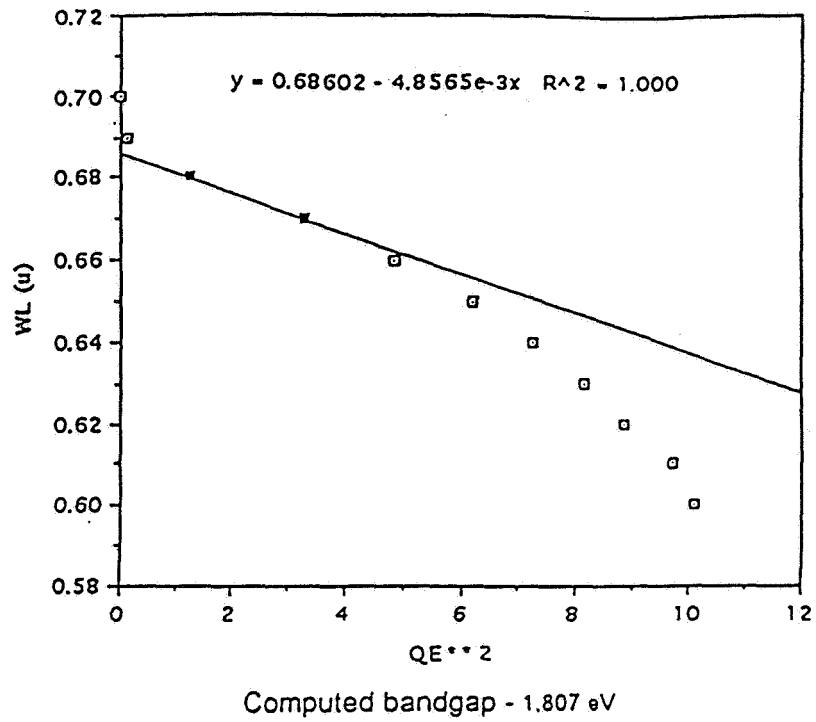


Figure 7 Bandgap of GaInP₂ Derived From Spectral Response

S9
IN-50394

InP tunnel junctions for InP/InGaAs tandem solar cells⁽¹⁾

M. F. VILELA^a, N. MEDELICI^b, A. BENSAOULA^b, A. FREUNDLICH^a, and P. RENAUD^a

^a Space Vacuum Epitaxy Center, University of Houston, Houston, TX 77204-5507

^b Also International Stellar Technologies, Inc., 9209 Hilldale St., Houston TX USA 77055

We report, for the first time, an epitaxially grown InP p⁺/n⁺⁺ tunnel junction. A diode with peak current densities up to 1600 A/cm² and maximum specific resistivities (V_p/I_p - peak voltage to peak current ratio) in the range of 10⁻⁴ Ω·cm² is obtained. This peak current density is comparable to the highest results previously reported for lattice matched In_{0.53}Ga_{0.47}As tunnel junctions. Both results were obtained using chemical beam epitaxy (CBE). In this paper we discuss the electrical characteristics of these tunnel diodes and how the growth conditions influence them.

1. Introduction

The drive for higher photovoltaic efficiency has led the technology away from single-junction cells and toward multiple-bandgap (tandem) cells. These multi-bandgap devices can be better matched to the solar spectrum. In this approach, cells of different bandgaps are placed optically in series, either during the growth process (monolithic tandems) or by being joined together after individual processing (mechanically stacked tandems). With regards to production costs and compatibility with current panel fabrication standards, the monolithic approach is superior.

InP solar cells have shown higher radiation resistance than the more traditional solar cells such as Si and GaAs, and are ideally suited for space applications. Due to their potential high efficiency, InP/InGaAs tandem solar cells seem to be the ideal doublet for both space and terrestrial applications.

Chemical Beam Epitaxy (CBE) has been shown to be a powerful technology for the growth of phosphorus-based compounds. Moreover, CBE permits reproducible and precise control over the layer composition and doping and has demonstrated growth of complex heterostructures with interfaces below one monolayer fluctuation. Therefore, CBE appears to be the technique of choice for solar cells such as the two-terminal multi-junction InP/InGaAs.

The key to achieving very high conversion efficiencies for monolithically integrated tandem solar cells is realizing stable and optically transparent tunnel junctions. We have recently demonstrated In_{0.53}Ga_{0.47}As tunnel junctions with very high peak current densities on InP, GaAs, and Si substrates using CBE. Growing InP layers on top of these tunnel junctions did not degrade them [1]. However, InGaAs tunnel diodes absorb a significant portion of the low energy photons thus limiting the efficiency of the tandem device. In this work we report the first realization of an InP tunnel junction with a peak current density of 1600 A/cm². The InP tunnel junction is utilized to provide the crystallographically compatible and optically transparent ohmic interconnect between the InP and InGaAs solar cells.

2. Experimental growth

Epitaxial runs were accomplished in a Riber CBE 32 system using Trimethyl-Indium (TMI), Triethyl-Gallium (TEG), and pre-cracked Arsine (AsH₃) and Phosphine (PH₃) as growth precursors. Solid Beryllium and Silicon were used as p and n doping sources respectively.

Be-doped p-InGaAs with net hole concentrations varying from $7.2 \times 10^{17} \text{ cm}^{-3}$ to $2 \times 10^{20} \text{ cm}^{-3}$ and Si-doped n-InGaAs with net electron concentrations varying from $1 \times 10^{17} \text{ cm}^{-3}$ to $2 \times 10^{20} \text{ cm}^{-3}$ were achieved; more details on these results can be found in reference [2].

(1) This work was supported by the following State of Texas Advanced Technology and Research Programs: #93-03652-224, #93-03652-236, #93-03652-243, #93-03652-260. The work at I.S.T. Inc. was supported by NASA SBIR Program #NASW-4093.

The InP layers were grown at temperatures ranging from 753K (480°C) to 803K (530°C) and growth rates varying from 0.5 $\mu\text{m/hr}$ to 1 $\mu\text{m/hr}$. Be-doped p-InP with net hole concentrations varying from $2 \times 10^{19} \text{ cm}^{-3}$ to $1 \times 10^{18} \text{ cm}^{-3}$ and Si-doped n-InP with net electron concentrations varying from $1 \times 10^{18} \text{ cm}^{-3}$ to $4 \times 10^{17} \text{ cm}^{-3}$ were achieved.

The InP beryllium doping study shows that the p-type carrier concentration levels vary with Be source temperature, the growth temperature and growth rate, Fig. 1. A similar behavior was observed for Be-doped InGaAs layers grown by CBE [3]. A drastic drop in the carrier concentration for higher Be source temperatures was observed; the same behavior exists for Be-doped InP epilayers grown in our laboratory by molecular beam epitaxy (MBE). The threshold for this drop seems to be related to other growth parameters. For example, at a growth rate of 1 $\mu\text{m/hr}$ and a growth temperature of 783K (510°C), the maximum doping level reached was for a Be source at 1203K (930°C). Using a growth rate of 0.75 $\mu\text{m/hr}$ and the same growth temperature of 783K (510°C), the maximum doping level was reached for a Be source at 1153K (880°C).

Fig. 1 shows that the carrier concentration is more sensitive to growth temperature than to growth rate. For instance, a change in the growth rate from 1 to 0.75 $\mu\text{m/hr}$ (2.78 to 2.08 \AA/s) only slightly increases the hole concentration, from $4 \times 10^{18} \text{ cm}^{-3}$ to $5 \times 10^{18} \text{ cm}^{-3}$; this difference is within the experimental error. However, if the growth temperature is decreased by 45 K (from 828K (555°C) to 783K (510°C)) the doping level increases from $5 \times 10^{17} \text{ cm}^{-3}$ to $1 \times 10^{18} \text{ cm}^{-3}$.

The Be source activation energy was determined to be 3.0 eV.

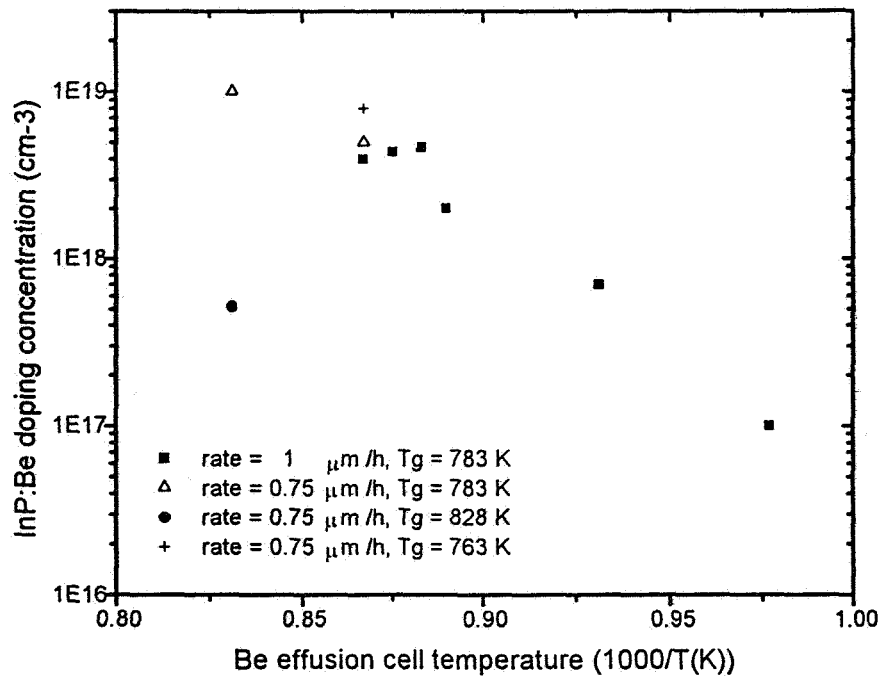


Fig. 1: Hole concentration in InP as a function of the Beryllium source temperature.

Fig. 2 shows the electron concentration as a function of the Si effusion cell temperature. High and low electron concentrations were obtained. The electron concentration was found to be minimally sensitive to both the growth temperature and the growth rate.

The silicon activation energy was found to be 7.57 eV.

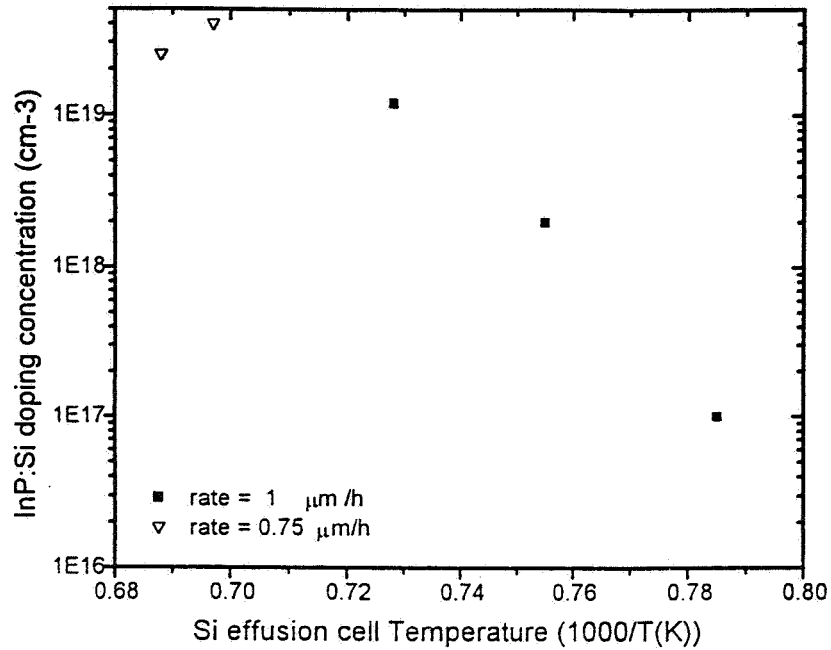


Fig. 2: Electron concentration in InP as a function of the Silicon source temperature.

3. Photovoltaic results

The CBE technique is expected to allow the realization of tunnel junctions with superior properties. Those devices require both degenerately doped semiconductor layers and low interdiffusion of doping species in the narrow (~20 nm) space charge region of the junction. This is possible since high quality InP and InGaAs layers can be grown at much lower temperatures than those required in more conventional techniques, such as liquid phase epitaxy (LPE) and metallorganic vapor phase epitaxy (MOVPE).

In previous reports [1,2] we have reported In_{0.53}Ga_{0.47}As tunnel junctions with peak current densities of up to 1015 A/cm² using CBE. In_{0.53}Ga_{0.47}As tunnel junctions grown on GaAs and Si substrates which yield peak current densities as high as 560 A/cm² were also demonstrated [1], see Table 1. We would like to point out two major results of that work. First, the peak current densities reached by those diodes were the highest ever reported for this kind of tunnel diode. Second, and most important, those characteristics were unchanged even after subsequent growth of a thick (3 μm) InP solar cell at high growth temperature (>833K (560°C)), representing more than 2 hours of growth. We summarize our In_{0.53}Ga_{0.47}As tunnel diodes results in Table 1.

Table 1
InGaAs Tunnel Diodes

| substrate | peak current A/cm ² | resistivity (x10 ⁻⁴)Ω-cm ² | annealing |
|-----------|-----------------------------------|--|----------------|
| InP | 1015 | 2.5 | No |
| GaAs | 452 | 4 | No |
| Si | 560 | 4.8 | No |
| InP* | 580 | 3.14 | No |
| InP** | 860 | 2.9 | 2 hr (> 560°C) |

* tunnel diode belongs to the same wafer used for **.

** half wafer used in * was reloaded in the growth chamber and had an additional InP solar cell grown on it.

Our preliminary work on the growth of InP and InGaAs solar cells resulted in photovoltaic converters with AM1.5 efficiencies equal to 18% for InP and 10.2% for In_{0.53}Ga_{0.47}As. We have also fabricated InP/InGaAs tandem devices which were grown using a 0.1 μm thick InGaAs tunnel diode as the interconnect. The tunnel diodes are shown to provide a low resistivity ohmic contact, even at simulated high concentration sunlight. The open circuit voltage of the tandem device is the sum of the InP and InGaAs individual cell voltages. The spectral response of this tandem revealed minimal sensitivity for photons with energies between 1.4 eV and 0.75 eV. This is due to photon absorption in the InGaAs tunnel diode. The use of very thin tunnel diodes should minimize this absorption. However, Wanlass et al [4] showed, by using MOVPE, that the use of ultra-thin tunnel diodes precludes using this tandem technology for high concentration applications, because the degradation of the tunnel diode electrical characteristics.

We summarize our photovoltaic results in Table 2.

Table 2
Photovoltaic Performances

| Solar Cell (AM1.5 values) | Voc V | Jsc mA/cm ² | FF % | η % |
|------------------------------|----------|---------------------------|---------|--------|
| InP | 0.81 | 28 | 80 | 18.1 |
| InGaAs | 0.25 | 60 | 62 | 10.2 |
| InP/InGaAs tandem* | 1.2 | 60 | 82 | --- |
| InP/InGaAs tandem | 1.0 | 8 | 76 | 6.3 |

* - under concentrated light; Voc - open circuit voltage; Jsc - short circuit current density; FF - fill factor; η - efficiency; AM1.5 - air mass 1.5.

4. InP tunnel diodes devices

The samples grown in this study are simple InP p⁺/n⁺⁺ junctions. In order to investigate the evolution of the tunnel characteristics for tandem solar cell applications, all samples have an additional InP p-type layer grown, which simulates the InP top solar cell in the actual tandem device (the thickness was determined by computer modeling [5]). The growth is terminated with an In_{0.53}Ga_{0.47}As p-type contact layer. The complete structure is shown in Fig. 3. For all samples analyzed, the n-doped InP layer characteristics were kept constant, with the Si doping at N_D - N_A = 1 × 10¹⁹ cm⁻³, a thickness of 750 Å, a growth temperature (T_g) of 783K (510 °C), and a growth rate (r_g) of 1 μm/hr. Only the p+ layer growth parameters were varied. Fig. 4 shows the I-V characteristics of a device, CBE 399, exhibiting a peak current density of 1,600 A/cm². This tunnel junction imposes a voltage drop on the tandem device in the microvolt range, for a sunlight concentration of 100x (AM0 spectrum).

The Be-doped InP layer for this device was grown under the following conditions: T_g = 773K (500°C); r_g = 0.75 μm/hr; and T_{Be} = 1153K (880°C). The doping level in this layer, as extracted from the Hall measurements, is N_A - N_D = 7 × 10¹⁸ cm⁻³. To our knowledge this is the first demonstration of an epitaxially-grown InP tunnel diode.

The dependence of the tunneling characteristics on the Be-doped InP layer growth parameters was investigated. The tunneling characteristics are completely lost if, taking the growth conditions of the sample CBE 399 as reference (see Table 3), we increase the growth temperature by 30K (from 773K (500°C) to 813K (530°C)), or if we increase the growth rate by 33% (from 0.75 to 1 μm/hr (2.08 to 2.78 Å/s)), or if the Be source temperature rises beyond the threshold, as explained in the section 2. The results are summarized in Table 3. The samples shown in the table were selected to stress the level of growth control required in order to achieve tunnel diodes with superior properties. More studies are necessary to figure out the mechanisms controlling the diffusion and/or the incorporation of Be in InP.

The doping levels of both layers composing tunnel diode CBE-399, as deduced from our Hall measurement calibration graphs, were: 7 × 10¹⁸ cm⁻³ for the p layer (see Fig. 1) and 1 × 10¹⁹ cm⁻³ for the n layer (see Fig. 2). Those doping concentrations give an effective doping level, N* = N_A × N_D / (N_A + N_D), of 4 × 10¹⁸ cm⁻³. The theoretical expression developed by Kane [6] (see Vilela et al [2]), correlating the effective doping level and peak current in tunnel diodes, predicts a peak current of less than 200 A/cm². However, the

1,600 A/cm² peak current density exhibited by CBE-399 demands an effective doping level of 8×10^{18} cm⁻³, at least 2×10^{19} cm⁻³ for each adjacent layer in the CBE 399 device. In other words, the theoretical calculation implies that one or both doping layer levels in that tunnel junction are underestimated. Also, the 1,600 A/cm² peak current value shows a minimal interdiffusion between both layers. Indeed, if Be or Si were fast diffusing elements in CBE grown InP material, tunnel diodes heated to 803K (530°C) for 20 minutes, as CBE-399 was, would show peak current densities much lower than 1,600 A/cm².

Secondary Ion Mass Spectrometry (SIMS) profiles will be performed in this device, in order to address this discrepancy between theory and experiment.

Table 3
InP Tunnel Diodes Growth Parameters Effects of the Be doped InP layers.

| SAMPLE | Growth Temp. °C | Growth Rate µm/h | Be Temp. °C | Peak Current A/cm ² |
|---------|--------------------|---------------------|----------------|-----------------------------------|
| CBE 399 | 500 | 0.75 | 880 | 1,600 |
| CBE 469 | 500 | 1 | 880 | No (B) |
| CBE 449 | 530 | 0.75 | 880 | No (Z) |
| CBE 407 | 500 | 0.75 | 920 | No (S) |

For all the samples the n⁺⁺-doped (silicon) InP layer characteristics were fixed at a $N_D - N_A = 1 \times 10^{19}$ cm⁻³, thickness of 750 Å, a growth temperature (T_g) of 783K (510°C) and a growth rate (r_g) of 1 µm/hr. No - means no tunnel characteristics presented.

(Z) means Zener, (B) means Backward or (S) means Simple diode.

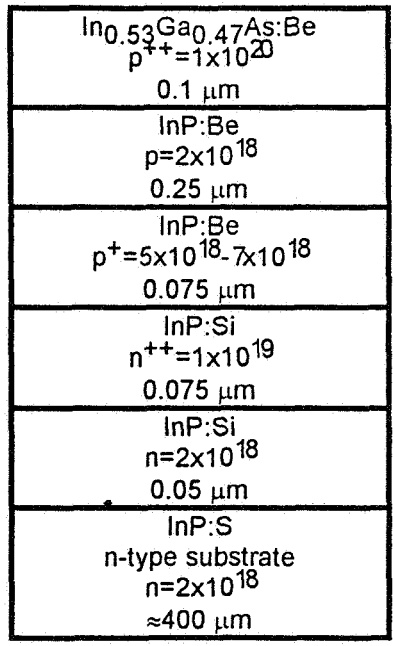


Fig. 3: Schematic representation of the InP tunnel diode studied in this work.

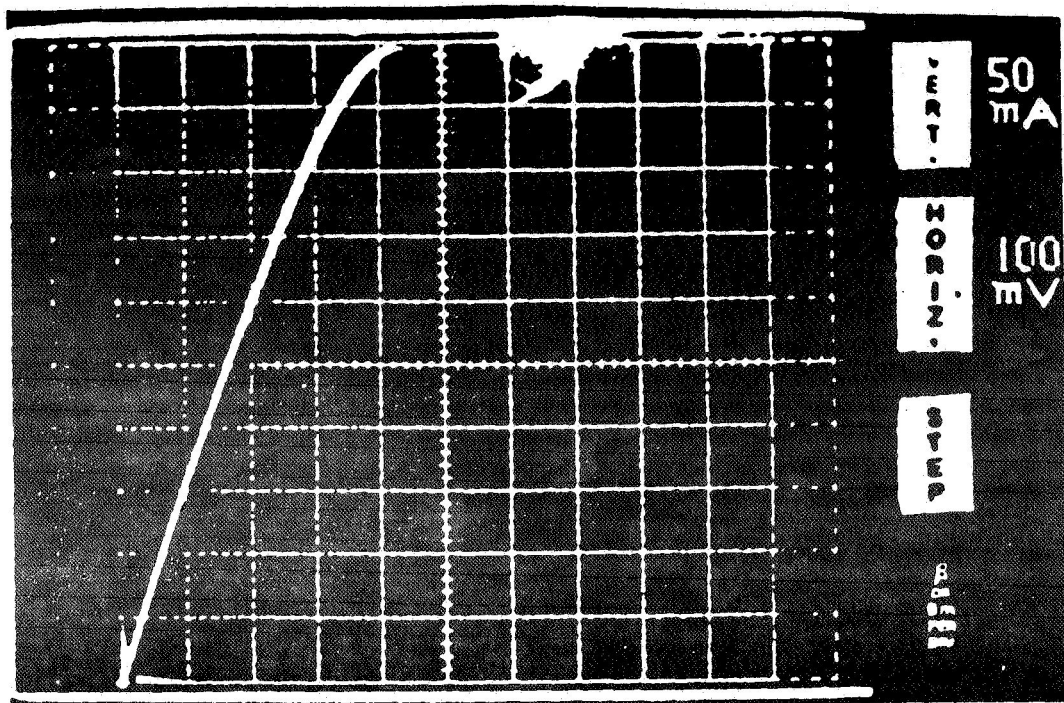


Fig. 4: I-V characteristic of an InP tunnel junction (mesa 200 μm in diameter) fabricated on InP substrate. This tunnel diode has a cap layer simulating the InP solar cell growth during the tandem fabrication (20 min growth at 803K (530°C)).

5. Conclusion

In summary, using Chemical Beam Epitaxy, we have demonstrated the fabrication of InP tunnel diodes with very high peak current densities (up to 1600 A/cm^2). This peak current is one of the highest ever reported for tunnel junctions fabricated with III-V compounds. This realization should allow the growth of InP/InGaAs tandem solar cells with optically transparent and electrically compatible interconnects for concentrator applications. This tunnel junction induces a voltage drop in the microvolt range for a concentration of $100\times$ AM0. We are currently working toward the fabrication of such monolithically integrated InGaAs/InP tandem solar cells. We have also demonstrated the drastic influence of the growth rate and growth temperature on the tunneling characteristics of these devices. Finally, the absence of any degradation in InP tunnel diodes subjected to the growth of a top InP solar cell, combined with the efficiencies reached by our single solar cells (InP and InGaAs in Table. 2), make CBE the ideal technology for the fabrication of high performance InGaAs/InP tandem solar cells.

The authors would like to thank Alex Ignatiev for helpful discussions, David Moore for the legibility of this text and Ping-chi (Pablo) Chang for his assistance during CBE growth.

6. References

- [1] A. Freundlich, M. F. Vilela, A. Bensaouia and N. Medelci, Proc. 23rd IEEE-PV Conf. (1993) 644.
- [2] M. F. Vilela, A. Freundlich, A. Bensaouia and N. Medelci, 5th International Conference on InP and Related Materials, Paris, France, IEEE Catalog #93CH3276 (1993) 227.
- [3] R. A. Hamm, M. B. Panish, R. N. Nottenburg, Y. K. Chen, and Humphrey; Appl. Phys. Lett. 54 (25) (1989) 2586
- [4] M. W. Wanlass, J. S. Ward, K. A. Emery and T. J. Coutts, Proc. 23rd IEEE-PV Conf. (1993) 621.
- [5] P. Renaud, M. F. Vilela, A. Freundlich, N. Medelci and A. Bensaouia; Proc. of the XII Space Photovoltaic Research And Technology Conference (SPRAT XII), Cleveland (1994) 141.
- [6] E. O. Kane; J. Appl. Phys. 32 (1961) 83.

SIO
IN-50355

THE ROLE OF RADIATION HARD SOLAR CELLS IN MINIMIZING THE COSTS OF GLOBAL SATELLITE COMMUNICATION SYSTEMS

Geoffrey P. Summers
Code 6615, Naval Research Laboratory, Washington, DC 20375 and
Department of Physics
University of Maryland Baltimore County, Baltimore, MD 21228

Robert J. Walters
Code 6615, Naval Research Laboratory, Washington, DC 20375

Scott R. Messenger and Edward A. Burke,
SFA, Inc., Landover, MD 20785

INTRODUCTION

An analysis embodied in a PC computer program is presented, which quantitatively demonstrates how the availability of radiation hard solar cells can help minimize the cost of a global satellite communications system. An important distinction between the currently proposed systems, such as Iridium, Odyssey and Ellipsat, is the number of satellites employed and their operating altitudes. Analysis of the major costs associated with implementing these systems shows that operation at orbital altitudes within the earth's radiation belts (10^3 to 10^4 km) can reduce the total cost of a system by several hundred percent [1,2], so long as radiation hard components including solar cells can be used. A detailed evaluation of the predicted performance of photovoltaic arrays using several different planar solar cell technologies is given, including commercially available Si and GaAs/Ge, and InP/Si which is currently under development.

Several examples of applying the program are given, which show that the end of life (EOL) power density of different technologies can vary by a factor of ten for certain missions. Therefore, although a relatively radiation-soft technology can usually provide the required EOL power by simply increasing the size of the array, the impact upon the total system budget could be unacceptable, due to increased launch and hardware costs. In aggregate, these factors can account for more than a 10% increase in the total system cost. Since the estimated total costs of proposed global-coverage systems range from \$1B to \$9B, the availability of radiation-hard solar cells could make a decisive difference in the selection of a particular constellation architecture.

EMERGING SATELLITE COMMUNICATION SYSTEMS

The first satellite communication systems deployed provided mainly point-to-point communications, although connection to mobile handsets was possible where cellular systems were available. The new systems are designed to provide global communication services directly to maritime and land-mobile terminals in addition to fixed communication centers. To provide global coverage, some of these systems plan to orbit as many as 840 satellites (Teledesic). The orbital altitudes selected range from low earth orbit (LEO, 1000 km or less) to geostationary earth orbit (GEO, 35,793 km). Medium earth orbits (MEO) are used to designate altitudes between these extremes and would include highly elliptical orbits (HEO). The geostationary orbit, initiated with INTELSAT I in 1965, has been widely used for global communications. However, the propagation delay (0.6 seconds for a typical international

connection), high latitude shadowing effects, the power required for the up-link and the possibility of catastrophic system failure due to the loss of a single satellite, have led to the development of alternative LEO and MEO systems.

THE OPTIMUM ALTITUDE

The total cost of deploying a global satellite communications system is a strong function of altitude. The requirement for global coverage defines the minimum number of satellites required as a function of altitude. The number decreases by a factor of about 25 in moving from LEO to GEO. On the other hand launch costs increase markedly as the altitude increases. When communication systems costs are calculated based upon satellite cost per kg and launch cost per kg, a shallow minimum in the cost curve is found at altitudes between 2,000 and 10,000 km. Fig. 1 shows typical estimates for launch costs and the total mass of satellites in orbit plotted versus altitude. The total mass is the product of the number of satellites and their individual mass. Launch costs are taken from the TRW Space data Book and are an average for several launch vehicles, including various configurations of the Titan IV, and the shuttle.

The exact location of the minimum in the cost curve is sensitive to relatively small changes in the detailed parameters of a given system especially when details about satellite capability are included, e.g. the number of communication channels, the type of data transmitted, etc. A general estimate of system costs based on Fig. 1 are compared with actual cost estimates for individual systems in Fig. 2. As can be seen all of the data indicate that below 2,000 km the costs of these systems increase precipitously. A curve similar to Fig. 2 has also been discussed by Logston [1].

There are a number of other reasons why a MEO system is a favored configuration. These include lower life-cycle costs than LEO because of fewer satellites (and ground stations for some systems), less potential for launch failures than LEO, shorter transmission delay than GEO, higher elevation angles than LEO or GEO, and less frequent handoffs than LEO [3].

The major obstacle to establishing cost-effective MEO systems is the fact that the earth's radiation belts reach a maximum intensity in this region. Of electronic satellite components, solar cells are particularly vulnerable to radiation damage because of the necessity to maximize their exposure to the sun. The availability of radiation hard solar cells are therefore critical to achieving the potential benefits of MEO operation.

SELECTING AN OPTIMUM SOLAR ARRAY FOR A MEO COMMUNICATIONS SYSTEM

In order to compare different array technologies and to optimize the implementation of a given technology, many different factors must be accounted for [4]. The computer program developed for this purpose calculates the EOL power density of solar arrays taking into account the cell geometry, coverglass thickness, support frame, electrical interconnects, electrical harness, adhesive, and packing density. The EOL power density can be determined for any altitude from LEO to GEO, and for equatorial to polar planes of inclination. The mission duration can be varied over the entire range planned for the proposed satellite systems. An algorithm is included in the program for determining the degradation of cell efficiency due to proton and electron irradiation for different solar cell technologies [5] using the data given in the Solar Cell Radiation Handbook [6]. Solar flare effects can also be included.

The program can be used to determine the optimum configuration for any cell technology as a function of a particular orbit and a specified mission life. Consequently, it is possible to compare the expected performance of all kinds of cells including those that are currently available and those that are expected to be available in the near future. The critical factor from

the cost point of view is the EOL power density in watts per kilogram. This can be translated directly into cost. Factors such as beginning of life (BOL) efficiency and even the cost per cell are found to have a much weaker impact on the final cost of the system.

RESULTS OF THE ANALYSIS

An example of the results obtained with the program is shown in Fig. 3 for three different solar cell technologies: Si, GaAs/Ge, and InP/Si. It will be shown below that if the array support material is kept the same, the single most important variable is the coverglass thickness. In Fig. 3, the optimum coverglass thickness for each technology for orbits in the radiation belts has been used. The values for the remaining parameters such as the cell thickness, the support frame and the mission life were made identical. It can be seen that the InP/Si technology surpasses all others in EOL power density even though the BOL efficiency was equal to or less than the other two technologies. The difference was especially noticeable in orbits in the radiation belts where the InP/Si EOL power density exceeds those of the other technologies by 50 to 300%.

In Fig.4 we show that there is an optimum coverglass thickness for each technology if the EOL power density is to be maximized for a particular mission. For operation in the radiation belts, the optimum thickness for InP/Si is ~12 mils, whereas for GaAs/Ge it is ~30 mils and for Si ~20 mils. Slightly different curves would be obtained for different missions.

The sensitivity of the cell types to factors such as BOL efficiency and substrate thickness has also been examined. These factors are not as readily changed as coverglass thickness but can be expected to improve as cell development continues. Results appear in Figs. 5 and 6. In Fig. 5 the EOL power density is given versus the BOL efficiency. These curves were derived assuming that as-grown and radiation-induced defects have the same effect on cell efficiency. For silicon, the BOL efficiency has no effect on EOL power density over the full range studied for this particular mission. Some improvement is obtained for InP/Si and GaAs/Ge up to about 15%, but little enhancement in EOL power density occurs beyond that point. InP/Si is markedly superior to the others for BOL values ranging from 10 to 25%. Fig. 6 shows that the EOL power density is relatively insensitive to cell thickness. As was found for BOL efficiency, the relative ranking of the different technologies is not changed as cell thickness varies from 2 to 16 mils.

Some insight into the contribution of the various factors to the EOL power density can be obtained by examining their relative weights for typical input values. Results for the three technologies are given in Table I for the particular mission used for Figs 3 - 6.

Table I
Percentage Contributions of Major Elements to the Total Array Weight

| | InP/Si | GaAs/Ge | Si |
|--------------|--|---------------------------------------|---------------------------------------|
| | 12 mil glass 12 mil cell 14% BOL | 30 mil glass 8 mil cell 18% BOL | 20 mil glass 4 mil cell 14% BOL |
| Frame | 59.7 | 43.4 | 60.2 |
| Glass | 19.4 | 33.7 | 31.6 |
| Cells | 19.1 | 21.1 | 2.9 |
| Elect. Harn. | 1.8 | 1.7 | 1.8 |

As can be seen in Table 1, the largest single contributor to the total weight of all the arrays is the honeycomb frame holding the cells. It should be noted that in addition to structural support, the frame plays an important role in shielding the cells from the underside, contributing the equivalent of a 30 mil coverglass. Unlike efficiency and cell thickness, the array material can be changed relatively easily. Results of substituting a flex array with 1/10 the density of a honeycomb are shown in Fig. 7.

Fig. 7 shows that marked improvement occurs in the EOL power density of the InP/Si technology as a result of using the flex array. The influence upon the other two cell types is marginal. The reason for the difference is the radiation hardness of the InP/Si cell. Note that the shielding effect of the substrate has been taken into account for InP/Si and GaAs/Ge in Fig. 7, but not for the ~4 mil thick Si cells, because it has such a small effect.

SUMMARY

We have examined the various factors which influence the EOL power density for three different planar solar cell technologies. The performance of the InP/Si technology in the middle of the radiation belts was found to exceed those of alternative technologies by a substantial margin. Factors such as BOL efficiency and cell thickness did not strongly influence the results. However, the density of the array support frame has a marked effect on the result.

To achieve the same total power output as the InP/Si technology, the mass of the more vulnerable solar arrays would have to be increased by as much as 450%. The additional hardware and the associated launch costs add significantly to the cost of the total system. Technical problems introduced by the larger arrays can further magnify the costs. The availability of radiation-hard solar cells, therefore, could make a decisive difference in the selection of a particular constellation architecture when total system costs are measured in billions of dollars.

ACKNOWLEDGEMENTS

This work was supported in part by the Office of Naval Research. The authors would like to acknowledge the assistance of Harvey B. Serreze of Spire Corporation with the computer programming.

REFERENCES

1. T. Logston, "Mobile Communication satellites", McGraw-Hill, 1995.
2. W.W. Wu et al., "Mobile Satellite Communications", Proc. IEEE, 82, 1431-1448, 1994.
3. N.D. Hulkower, "An Update on The Mobile Communications Scene", IEEE Communications Chapter Boston, MA, 14 Sept. 1995.
4. S. Bailey and G. Landis, "Use of Advanced Solar Cells for Commercial Communication Satellites", IEEE Proc. 1st World Conference on Photovoltaic Energy Conversion, Hawaii, Dec. 1994, pp 2002-2005.
5. G.P. Summers, R.J. Walters, M.A. Xapsos, E.A. Burke, S.R. Messenger, P. Shapiro and R.L. Statler, "A New Approach to Damage Prediction for Solar Cells Exposed to Different

Radiations", IEEE Proc. 1st World Conference on Photovoltaic Energy Conversion, Hawaii, Dec. 1994, pp 2068-2073.

6. H.Y. Tada, J.R. Carter, B.E. Anspaugh and R.G. Downing, in "The Solar Cell radiation Handbook", JPL Publication 82-69 , 1982 and B.E. Anspaugh, "Solar Cell Radiation Handbook - Addendum 1: 1982 - 1988", JPL Publication 82-69, Addendum 1, 1989.

GLOBAL MOBILE SATELLITE COMMUNICATION SYSTEMS
Cost Determining Factors as a Function of Altitude

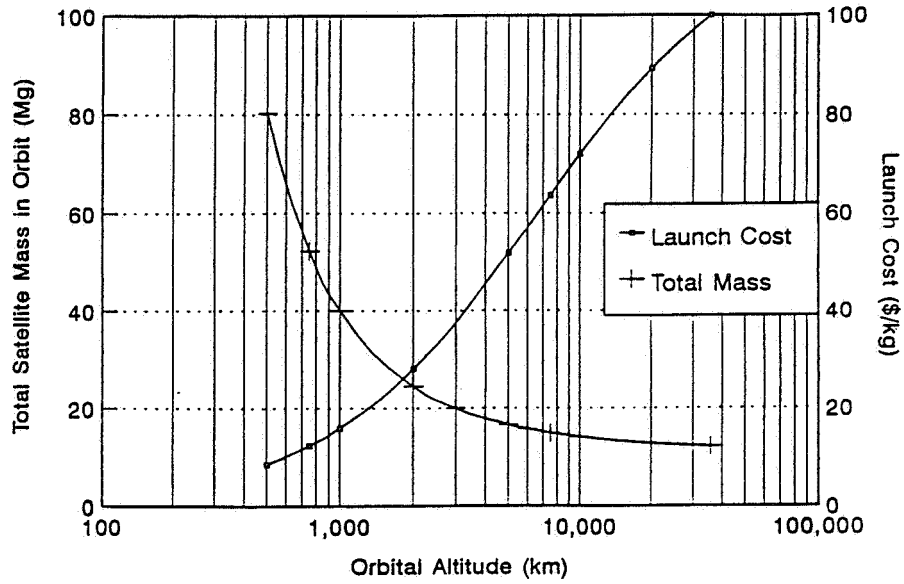


Fig.1 The total mass of a global mobile communication satellite system and the launch cost per kilogram, both as a function of orbital altitude.

GLOBAL MOBILE SATELLITE COMMUNICATION SYSTEMS
Cost vs Orbital Altitude

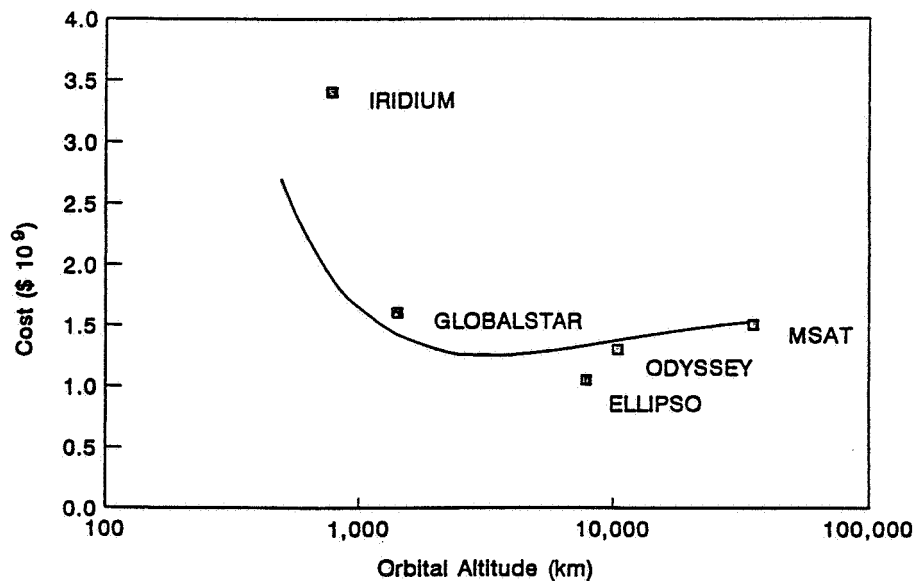


Fig.2 The estimated total cost of a global mobile satellite communication system as a function of orbital altitude, based on inputs such as the total mass of the system and launch costs. Actual estimated costs by proposers of several commercial systems are also shown.

EOL SOLAR ARRAY POWER DENSITY vs ALTITUDE
 10 Year Mission - Circular Orbit - 60° Inclination

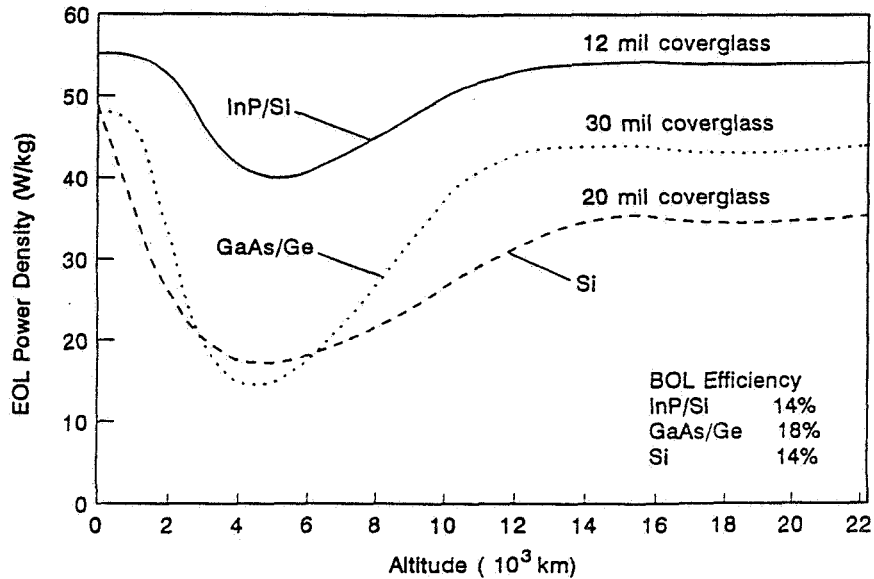


Fig. 3 End of life (EOL) power density as a function of orbital altitude for arrays of InP/Si, GaAs/Ge and Si solar cells for a 10 year mission in a circular orbit with a 60° angle of inclination. A standard Al honeycomb array material has been used in each case.

EOL POWER DENSITY vs COVERGLASS THICKNESS
 5 Year Mission - 7400 km Circular Orbit - 60° Inclination

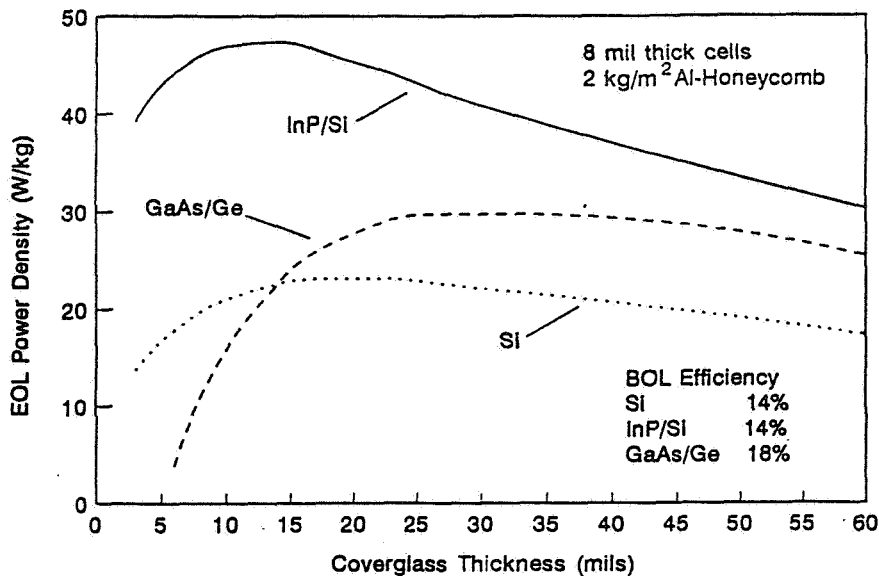


Fig. 4 End of life (EOL) power density vs coverglass thickness for arrays of InP/Si, GaAs/Ge and Si solar cells, for a 5 year mission in a 7,400 km circular orbit with a 60° angle of inclination. This is an orbit in the heart of the earth's radiation belts.

EOL POWER DENSITY vs BOL EFFICIENCY
 5 Year Mission - 7400 km Circular Orbit - 60° Inclination

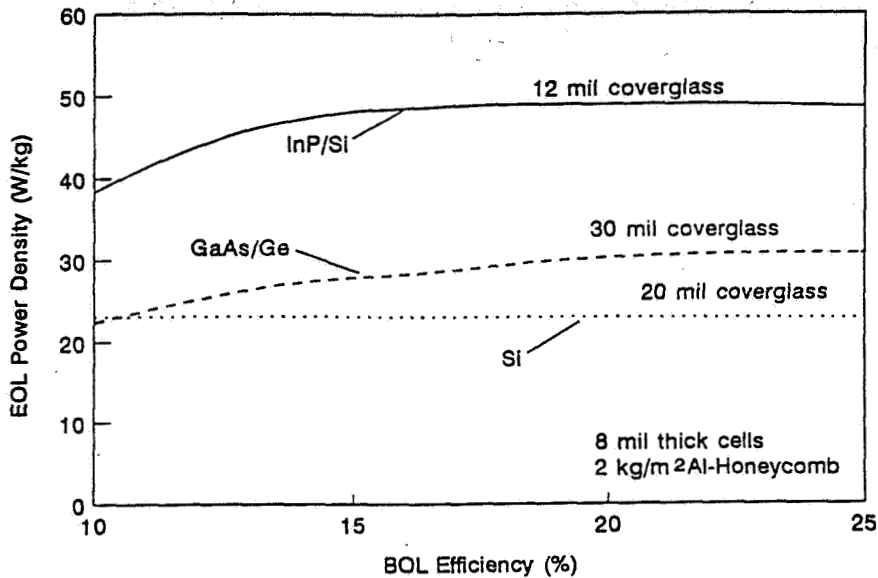


Fig. 5 End of life (EOL) power density vs beginning of life (BOL) efficiency for arrays of InP/Si, GaAs/Ge and Si solar cells, for a 5 year mission in a 7,400 km circular orbit with a 60° angle of inclination. Note that the optimum coverglass thickness has been used for each cell technology.

EOL POWER DENSITY vs SOLAR CELL THICKNESS
 5 Year Mission - 7400 km Circular Orbit - 60° Inclination

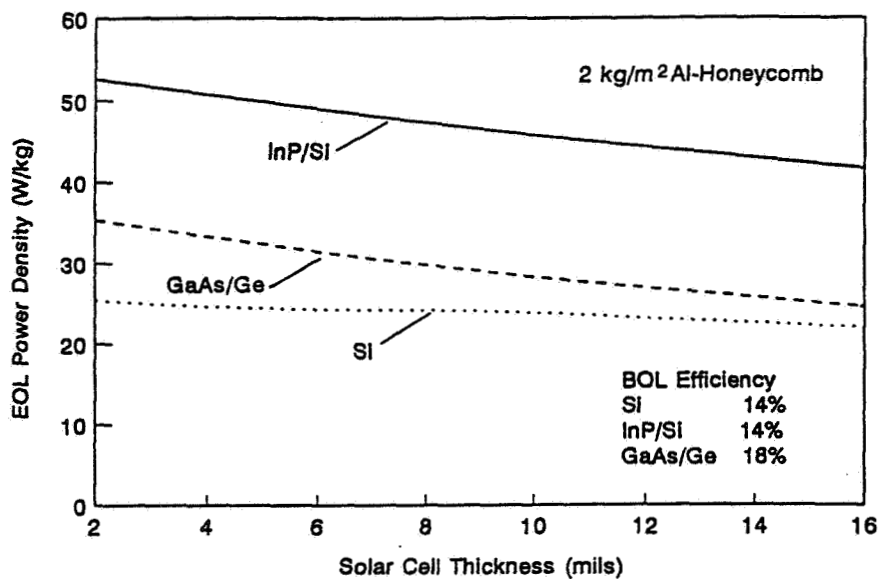


Fig. 6 End of life (EOL) power density vs cell thickness for arrays of InP/Si, GaAs/Ge and Si solar cells, for a 5 year mission in a 7,400 km circular orbit with a 60° angle of inclination.

EOL SOLAR ARRAY POWER DENSITY vs ALTITUDE
 10 Year Mission - Circular Orbit - 60° Inclination
 Flex Array - 0.2 kg/m²

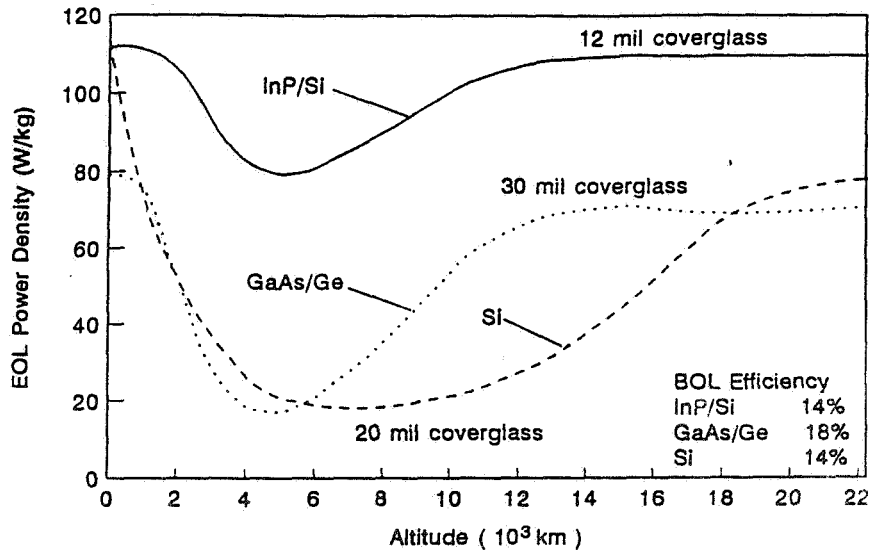


Fig. 7 End of life (EOL) power density as a function of orbital altitude for arrays of InP/Si, GaAs/Ge and Si solar cells, for a 10 year mission in a circular orbit with a 60° angle of inclination. A flex array material has been used in each case. Compare this figure with Fig.3 to see the effect of the lighter array material.

High and Low Energy Proton Radiation Damage in p/n InP MOCVD Solar Cells

317
IN-50396

George Rybicki and Irv Weinberg
Photovoltaic Branch
NASA Lewis Research Center, Cleveland, Ohio.

Dave Scheiman
NYMA Inc. Brookpark, Ohio

Carlos Vargas-Aburto and Roberto Uribe
Kent State University, Kent, Ohio

Abstract

InP p+/n/n+ solar cells, fabricated by metal organic chemical vapor deposition, (MOCVD) were irradiated with 0.2 MeV and 10 MeV protons to a fluence of $10^{13}/\text{cm}^2$. The power output degradation, IV behavior, carrier concentration and defect concentration were observed at intermediate points throughout the irradiations. The 0.2 MeV proton-irradiated solar cells suffered much greater and more rapid degradation in power output than those irradiated with 10 MeV protons. The efficiency losses were accompanied by larger increases in the recombination currents in the 0.2 MeV proton-irradiated solar cells. The low energy proton irradiations also had a larger impact on the series resistance of the solar cells. Despite the radiation induced damage, the carrier concentration in the base of the solar cells showed no reduction after 10 MeV or 0.2 MeV proton irradiations and even increased during irradiation with 0.2 MeV protons. In a deep level transient spectroscopy (DLTS) study of the irradiated samples, the minority carrier defects H4 and H5 at $E_v + 0.33$ and $E_v + 0.52$ eV and the majority carrier defects E7 and E10 at $E_c - 0.39$ and $E_c - 0.74$ eV, were observed. The defect introduction rates for the 0.2 MeV proton irradiations were about 20 times higher than for the 10 MeV proton irradiations. The defect E10, observed here after irradiation, has been shown to act as a donor in irradiated n-type InP and may be responsible for obscuring carrier removal. The results of this study are consistent with the much greater damage produced by low energy protons whose limited range causes them to stop in the active region of the solar cell.

Introduction

A near record AM0 efficiency InP solar cell of 19.1% was achieved through MOCVD growth of a homoepitaxial InP p+/n/n+ structure.(1) This type of structure has the potential to simplify the growth of heteroepitaxial InP cells on Si by eliminating the problem of counter doping of the base region in the InP on Si n on p cells. Electron irradiation testing of MOCVD InP p/n cells has also shown that they have superior radiation resistance to MOCVD InP n/p cells. (2)

Several phenomena are observed in irradiation studies of n-type InP that may contribute to its improved radiation resistance. It has been observed that carrier concentration in n-type InP, rather than decreasing, increases after electron and proton irradiation.(3,4) This phenomenon, which we shall call carrier enhancement, has been observed only in pn diodes in which the p region was zinc doped. (5) Furthermore, this effect is correlated with a specific defect through the use of DLTS. (3) In contrast, it has been shown that the carrier concentration in p-type InP decreases after either proton or electron irradiation.(6,7) In the present study we observe the effects of high and low energy proton irradiations on the defect structure and carrier concentration in the n-type region of the diode. In particular we focus our attention on the radiation effects which involve low energy protons whose range is such that they stop within the active n-type region of the pn diode. We concern ourselves mainly with the defect structures,

possible carrier enhancements and the differences in the effects of low and high energy particles on the series resistance and performance of InP p⁺/n/n⁺ solar cells. It is of particular interest to observe the effects of carrier enhancement on the performance of the solar cells.

Experimental

The diodes and solar cells used in this study were fabricated by MOCVD at the Spire Corporation under contract with NASA Lewis. The cell configuration, dopants, and concentrations are shown in Figure 1. Cell performance was measured in the calibration laboratory of the Photovoltaic Branch at NASA Lewis, using a Spectrolab X-25 xenon arc solar simulator and a flight-calibrated InP standard cell. The low energy proton irradiations were performed at the University of Michigan's Ion Beam Laboratory and the high energy proton irradiations were performed in the tandem Van de Graaff accelerator of Western Michigan University. Spectral response and IV measurements were made prior to the irradiations and at each step throughout. Carrier concentrations were measured using the capacitance-voltage (CV) technique. The concentration and energy levels of the radiation-induced defects were measured by DLTS. The concentration of defects have been corrected for incomplete trap filling (8), and the energy levels have been corrected for the Frenkel-Poole effect. (9)

Results and Discussion

The pre-irradiation performance parameters of the p on n cells are given in Table 1.

| | J _{SC} (ma/cm ²) | V _{OC} (mV) | Fill Factor % | Efficiency % |
|---------|---------------------------------------|----------------------|---------------|--------------|
| 0.2 MeV | 23.6 | 851.4 | 84.7 | 12.41 |
| 10 MeV | 22.5 | 854.9 | 85.2 | 11.95 |

Table 1. Pre-irradiation cell performance parameters

The performance of these cells was clearly not state of the art. As indicated before, cells of up to 19.1 % have been fabricated in this configuration.(1) The cells used in this study were produced as part of a development program; therefore, growth and cell design parameters had not yet been optimized. The post irradiation cell performance parameters are given as a function of fluence in Table 2. The normalized efficiency as a function of fluence in presented in Figure 2.

| Energy (MeV) | 0.2 | 0.2 | 0.2 | 10 | 10 | 10 |
|--------------------------|--------------|----------------------|----------------------|--------------|----------------------|----------------------|
| Fluence cm ⁻² | efficiency % | I _{sc} (ma) | V _{oc} (mV) | efficiency % | I _{sc} (ma) | V _{oc} (ma) |
| 0 | 12.41 | 23.6 | 851 | 11.95 | 22.5 | 855 |
| 10 ¹¹ | 8.37 | 19.8 | 772 | 11.81 | 22.4 | 852 |
| 10 ¹² | 4.85 | 14.5 | 649 | 10.45 | 21.4 | 828 |
| 10 ¹³ | 2.75 | 10.8 | 545 | 7.90 | 19.0 | 755 |

Table 2. Pre and Post Irradiation cell performance parameters

The dramatic difference in damage rates is immediately evident. The low energy protons produce far more degradation than the 10 MeV protons. The reason is that the range and damage production rate of the two particles differ dramatically. The 10 MeV proton has a projected range of 497 um and will pass

completely through the active region of the cell. The 0.2 MeV proton however has a projected range of 1.56 μm and will stop inside the active region of the cell. (10) An incident proton produces maximum damage at the end of its track and, since the 0.2 MeV proton stops in the active region of the solar cell it produces a greater number of defects in this region of the cell. The low energy proton thus produces a much greater amount of degradation. The degradation is dominated by a reduction in short circuit current in the 0.2 MeV cells but is comparable in open circuit voltage and short circuit current in the 10 MeV irradiated cells. This is also related to the differences in damage production of the two particles. Although the 0.2 and 10 MeV irradiations both increased the dark currents, the 0.2 MeV proton irradiations had a greater effect by more strongly reducing the diffusion length and thus reducing the current collected. This effect is clearly visible in the external quantum efficiency curves given in Figure 3.

Figure 3 shows the external quantum efficiency of the unirradiated and irradiated cells. The 0.2 MeV proton irradiations had a more pronounced effect on the quantum efficiency. The 10 MeV irradiations produced a relatively uniform degradation in output as a function of wavelength. The 0.2 MeV irradiations, however, produced a larger degradation in the red end of the spectrum. This reflects the strong effects of the 0.2 MeV protons in reducing the diffusion lengths in the cells. The quantum efficiency in the red portion of the spectrum, where the light is absorbed more weakly, and thus penetrates to a deeper depth, is more strongly affected by the low energy protons which have a greater effect in reducing the diffusion length of photogenerated carriers.

The 10 MeV proton radiation resistance of the p/n/n+ MOCVD solar cells versus n/p MOCVD solar cells (2) and diffused junction n/p solar cells(11), is shown in Figure 4. The radiation resistance of the p/n/n+ cells in this study is better than that of the n/p MOCVD configuration but is still not as good as that of the diffused junction cells. The starting efficiencies of all three cells however, were not the same and so although the results suggest that the p/n MOCVD configuration is better than the n/p MOCVD configuration, the data must be viewed cautiously. The variations in radiation resistance between the diffused junction and MOCVD n/p configurations has been the subject of some study. (12) The differences in performance between MOCVD and diffused junction cells have to do with the annealing of defects in the diffused cells. In the diffused junction cells the radiation induced defects anneal easily during operation and the power output recovers, while in MOCVD cells, the defects, as identified by DLTS, anneal out, cell power output recovery is not observed, or at least not to the same extent. (12) The variation in radiation resistance between cells based on n and p type InP materials may also have to do with the introduction rate of the defects. It has been demonstrated that the introduction rate of defects is lower in n type than in p type materials. (13,14) An absence of radiation induced carrier removal may also help improve the radiation resistance in n type InP.(3)

Carrier concentration data for the irradiated samples are presented in Figure 5. It can be seen that not only is carrier removal not observed after proton irradiation but that the carrier concentration increases slightly in the case of 10 MeV irradiations, and strongly in the 0.2 MeV irradiations. The lack of carrier removal has been previously observed in n-type InP and has been correlated with a radiation induced defect. (3) As the 0.2 MeV protons have a higher defect production rate than the 10 MeV protons, they produce a larger increase in carrier concentration.

IV curves were also taken throughout irradiations and cell parameters were measured. The data is presented in Table 3 . The series resistance as a function of fluence is plotted in Figure 6.

From the data it can be seen that the 0.2 MeV proton irradiations produce a larger increase in the recombination currents in the solar cells. The differences produced in series resistance as shown in Figure 6, became more pronounced at higher fluences. The recombination current is related to the defect concentration in the depletion region and the 0.2 MeV protons produce more defects in this region and thus a greater increase in recombination currents. In the case of the low energy protons the degradation in the diffusion current is slightly higher than the degradation in the recombination current. This indicates significant damage in the depletion region, emitter and base. In the case of the 10 MeV irradiations the degradation in the recombination current is very limited, but much greater in the diffusion

| Energy (MeV) | 0.2 | 0.2 | 0.2 | 10 | 10 | 10 |
|-----------------------------|--------------------------------------|--------------------------------------|----------------------|--------------------------------------|--------------------------------------|----------------------|
| Fluence (cm ⁻²) | J ₀₁ (A/cm ²) | J ₀₂ (A/cm ²) | R _s (ohm) | J ₀₁ (A/cm ²) | J ₀₂ (A/cm ²) | R _s (ohm) |
| 0 | 3.2 x 10 ⁻¹⁷ | 5.3x10 ⁻¹⁴ | 0.49 | 5.85x10 ⁻¹⁸ | 1.17x10 ⁻¹² | 0.51 |
| 10 ¹¹ | 1.85x10 ⁻¹¹ | 1.08x10 ⁻⁹ | — | 5.91x10 ⁻¹⁸ | 2.22x10 ⁻¹² | 0.52 |
| 10 ¹² | 1.5 x 10 ⁻¹¹ | 5.5 x 10 ⁻⁸ | 0.56 | 1.04x10 ⁻¹⁷ | 7.84x10 ⁻¹² | 0.63 |
| 10 ¹³ | 1.2 x 10 ⁻⁹ | 1.75x10 ⁻⁸ | 1.7 | 9.09x10 ⁻¹² | 7.11x10 ⁻¹¹ | 0.61 |

Table 3. Pre and Post Irradiation IV Data

current . This suggests that little damage is produced in the emitter and the depletion region by the 10 MeV protons and that most of the damage occurs in the base. This again is a result of the high damage production rate of the low energy protons which stop in the active region of the solar cell as opposed to the high energy protons which pass through the cell or produce damage deeper in the base of the cell.

The series resistance of the solar cells was also more strongly affected by the low energy protons but the effect was pronounced only at the highest fluence. This effect occurs at the same point where the carrier concentration increase was observed in the low energy proton irradiated samples. It is apparent that the carrier concentration increase, which has been related to the presence and concentration of a radiation induced defect (3), does not reduce the series resistance or benefit cell performance. The increase in carrier concentration has not been observed in the 10 MeV proton irradiated cells due to the lower defect introduction rates of the 10 MeV protons.

DLTS was used to study the defect spectra and to measure the defect introduction rates in the samples. The DLTS spectra are shown in Figures 7 through 11. A preirradiation analysis showed that no deep levels were present in the samples. The defect concentrations were measured throughout the experiments and the introduction rates calculated. The data appears in Tables 4 and 5.

| Fluence, ϕ (cm ⁻²) | 1 x 10 ¹¹ | 5 x 10 ¹¹ | 1 x 10 ¹² | 1 x 10 ¹³ |
|--|-------------------------------|--------------------------------|--------------------------------|--------------------------------|
| N _T (cm ⁻³) E7 | 1.08 x 10 ¹⁴ ± 0.1 | 3.65 x 10 ¹⁴ ± 0.16 | 5.87 x 10 ¹⁴ ± 0.20 | 8.67 x 10 ¹⁵ ± 0.41 |
| N _T (cm ⁻³) H4 | — | 1.55 x 10 ¹⁴ ± 0.1 | 2.96 x 10 ¹⁴ ± 0.08 | — |
| N _T (cm ⁻³) H5 | — | 1.06 x 10 ¹⁴ | 3.08 x 10 ¹⁴ ± 0.28 | — |
| N _T (cm ⁻³) E10/11 | — | — | — | 4.88 x 10 ¹⁵ ± 0.41 |
| N _T / ϕ (cm ⁻³) E7 | 1080 | 730 | 587 | 865 (873) |
| N _T / ϕ (cm ⁻¹) H4 | — | 310 | 296 | — (296) |
| N _T / ϕ (cm ⁻¹) H5 | — | 212 | 308 | — (308) |
| N _T / ϕ (cm ⁻¹) E10/11 | — | — | — | 488 (488) |

Table 4. Defect Concentrations and Introduction rates in 0.2 MeV Proton Irradiated InP (Numbers in parenthesis are a least squares fit of all N_T vs. ϕ data.)

| Fluence, ϕ (cm ⁻²) | 1 x 10 ¹¹ | 1 x 10 ¹² | 1 x 10 ¹³ |
|--------------------------------------|----------------------|--------------------------------|--------------------------------|
| N_T (cm ⁻³) E7 | — | 6.48 x 10 ¹³ ± 0.53 | 5.24 x 10 ¹⁴ ± 0.21 |
| N_T (cm ⁻³) H4 | — | 2.92x 10 ¹³ ± 0.28 | 1.82 x 10 ¹⁴ ± 0.08 |
| N_T (cm ⁻³) H5 | — | 1.56 x 10 ¹³ ± 0.41 | 1.22 x 10 ¹⁴ ± 0.13 |
| N_T (cm ⁻³) E10/11 | — | — | 7.79x10 ¹³ ± 0.40 |
| N_T/ϕ (cm ⁻¹) E7 | | 64.8 | 52.4 (51.8) |
| N_T/ϕ (cm ⁻¹) H4 | — | 29.2 | 18.2 (17.7) |
| N_T/ϕ (cm ⁻¹) H5 | — | 15.6 | 12.2 (12.1) |
| N_T/ϕ (cm ⁻¹)E10/11 | — | — | 7.8 (7.8) |

Table 5. Defect Concentration and Introduction Rates in 10 MeV Proton Irradiated InP (Numbers in parenthesis are a least squares fit of all N_t vs. ϕ data.)

The post irradiation DLTS analysis revealed the presence of two deep levels in the minority carrier spectra and three deep levels in the majority carrier spectra. Only two of the majority levels could be resolved in both the high and low energy proton irradiations, the first, $E_c-0.37$ eV is referred to in the literature as E7.(5) The second level was found considerably deeper in the gap at $E_c-0.74$ eV, and is known as E10 or E11, (4,5). An additional level, E9 at $E_c-0.64$ eV was observed after the 10 MeV proton irradiations but it could not be clearly resolved in the 0.2 MeV spectra and no systematic study of this defect was performed. The defect E7 is associated with an antisite vacancy pair, ($V_{In}-P_{In}$). (17) The defect E10/11 is correlated with a displacement in the P sublattice of InP and thought to be a complex between this displacement induced defect and an intrinsic defect or impurity. (3)

The relative concentrations of the two defects in the majority carrier DLTS spectrum in the case of the 0.2 MeV irradiations is not in agreement with some of the results in the literature, ie. E7 not E10/11 is the defect with the largest introduction rate.(5) This however is a result of the metastable nature of the defect E7. The defect E7 is the major defect in the spectrum known as the B configuration, which results from cooling the sample under reverse bias.(17)

The minority carrier spectra in both high and low energy proton irradiations showed two deep levels at $E_v+0.29$ and $E_v+0.52$ eV, referred to in the literature as H4 and H5.(15). The defect H4 is thought to be a displacement on the P sublattice of InP, possibly P_{In} . H5 is thought to be a complex of a defect and a dopant impurity, $V_{In}-Zn$ or $P_{In}-Zn$, as evidenced by the strong dependence of its introduction rate on the dopant concentration. (18) The minority carrier spectra shown here in which H4 is the defect with the highest introduction rate, is in agreement with the spectra published in the literature.(15)

The defect introduction rates were calculated from a least squares fit of the defect concentration versus particle fluence. The data are shown graphically in Figures 11 and 12. The data presented in the graphs corresponds to a least squares fit of all data up to the highest fluence at which reliable data could be extracted, the final value calculated in this manner is presented in parenthesis in the highest fluence column. This was a particular problem in the case of minority carrier analysis after 0.2 MeV irradiations at the highest fluences. A high concentration of defects can affect the quality of a DLTS analysis by introducing leakage currents, increasing series resistance or by producing very high defect concentrations. (16) In the

case of the lowest fluence 10 MeV irradiations the defect concentrations were below the detection limit of our instrument. The variation in defect introduction rates calculated with each additional data point is illustrative of the error which might be introduced by estimating introduction rates from a single data point, a practice which is common in the literature. This estimation however was necessary in this case for the calculation of the defect E10/11 which required scans up to 400K due to its large activation energy. Intermediate measurements were not made in this case to avoid annealing out the radiation damage.

The defect introduction rates measured here are very much higher in the case of the 0.2 MeV protons than for the 10 MeV protons and both are considerably higher than those measured for 1 MeV electrons. (6,13) An attempt was made to correlate the defect introduction rates with the energy loss rates of the particles in the material. The great majority of the energy loss of a high energy particle incident on a material is by ionization of the lattice atoms, but a small fraction is lost producing lattice atomic displacements. The energy lost by atomic displacement can be estimated using TRIM. (10) The software predicted that the 0.2 MeV protons would produce 25 times as much damage as the 10 MeV protons. In comparing the introduction rates observed here, the ratio of defect introduction rates for 0.2 MeV to 10 MeV for the defects H4 and H7 is roughly 16, but for the defect H5 it is exactly the 25 predicted. Thus there seems to be a reasonable correlation between the predicted energy loss and defect introduction rates.

The exception to this observation is the relationship in the introduction rates of E10/11 in the two cases above, the prediction is a ratio of 25 but the observed ratio is 63. The reason behind this discrepancy may be related to the nature of the defect E10/11. This defect has only been found in p/n junction diodes where the p dopant is zinc, it has not been found in irradiated Schottky barrier diodes. (5,13) Thus, it is theorized that the formation of E10/11 requires the participation of Zn in the n-type material from the diffusion front tail produced during the formation of the pn junction. (5) The introduction rate of E10/11 was also found to depend strongly on electron energy, leading one to believe that Zn atoms ejected into or implanted into the n region of the diode by proton irradiation may enhance the formation rate of E10/11. (5) In this case the low energy proton irradiations may have caused a large redistribution of the Zn due to the large number of displacements they cause in the junction region, as compared to the 10 MeV protons and 1 MeV electrons. The 0.2 MeV protons thus produced an anomalously high defect introduction rate for E10/11 by implanting more Zn into the n-type region of the diodes.

The superior radiation resistance of the p/n-type InP solar cells may be related to the defect introduction rates. In this study the introduction rate of the dominant majority carrier defect E10 in n-type InP was about 8 per 10 MeV proton. The defect introduction rate for the dominant majority carrier defect H4 in p-type InP was found to be approximately 90 per 10 MeV proton. (12) The lower defect introduction rate in n-type InP may contribute to enhanced radiation resistance in p/n InP solar cells. This finding is an agreement with previous authors who found the same relationship in electron irradiated InP.(13,14)

Conclusions

The 0.2 and 10 MeV proton irradiations produced dramatically different rates of degradation in the p/n/n+ InP solar cells studied. The relative rates of damage were correlated with the different ranges and damage production rates of the two particles. The low energy protons stopped in the active region of the cell and produced a dramatic decrease in efficiency, dominated by a decrease in the diffusion length of photogenerated carriers. The 10 MeV protons produced degradation dominated by an increase in dark currents in the cell. The MOCVD p/n/n+ InP solar cell configuration studied here showed better radiation resistance than the MOCVD n/p configuration in the literature. Studies of the radiation damage showed that the lack of carrier removal in n-type InP was not the reason for the enhanced radiation resistance, as increases in series resistance and no cell performance recovery as observed to attend this phenomenon. A DLTS study of the defects showed no significant differences in the defect spectra generated by low and high energy proton irradiation, or differences with the 1 MeV electron irradiation spectra in the literature, but that the low energy protons produced 15 to 60 times as many defects as the high energy protons. The defect introduction rate for the dominant majority carrier defect in n-type InP was found to be

lower than that in p-type InP, in agreement with the findings on electron irradiated materials. This fact may contribute to the superior radiation resistance in n-type InP materials.

Acknowledgements

The authors would like to acknowledge the help of Dr. Stephen Ferguson, from Western Michigan University and Dr. Victor Rotberg of the Michigan Ion Beam Laboratory of the University of Michigan for their help with the proton irradiations reported in this work. One of us (C.V.-A.) would also like to acknowledge partial support for this work from Wilberforce University, under subgrant number NCC3-281, and from NASA LeRC, under grant numbers: NAG3-946 and NAG3-1726.

References

1. C. Keavney, V. Haven and S. Vernon, Proc. 21st. IEEE Photovoltaics Specialist Conference, p.141 (1990).
2. C. Keavney, R. Walters and P. Drevinsky, J. Appl. Phys., **73**, 60 (1993).
3. A. Sibile, Appl. Phys. Lett., **48**, 593 (1986).
4. I. Weinberg, G. Rybicki, C.Vargas-Aburto, R. Jain and D. Scheiman, Proc. Of the XIII Space Photovoltaics Research and Technology Conference, p. 147 (1994).
5. J. Benton, M. Levinson, A. Macrander, H. Temkin and L. Kimerling, Appl. Phys. Lett, **45**, 567 (1984).
6. I. Weinberg, C. Swartz and P. Drevinsky, J. Appl. Phys., **72**, 5509 (1992).
7. G. Rybicki and C. Zorman, J. Appl. Phys., **75**, 3187 (1994).
8. Y. Zohta and M. Watanabe, J. Appl. Phys., **53**, 1809 (1982).
9. G. Vincent, A.Chantre and D. Bois, J. Appl. Phys., **50**, 5484 (1979).
10. J. Ziegler, J. Biersack and U. Littmark, "The Stopping and Range of Ions in Solids", (Pergamon Press, New York, NY,1985).
11. I. Weinberg, C. Swartz, R. Hart and M. Yamaguchi, Proc. Of the 5th. European Symposium on Photovoltaic Generators in Space", ESA SP267, p. 415 (1986).
12. R. Walters, S. Messenger, G. Summers, E. Burke and C. Keavney, Proc. 22nd. IEEE Photovoltaics Specialist Conference, p. 1560 (1991).
13. M. Levinson, J. Benton, H. Temkin and L. Kimerling, Appl. Phys. Lett., **40**, 990 (1983).
14. M. Levinson, H. Temkin and W. Bonner, J. Elec. Matls. , **12**, 423 (1983).
15. A. Sibile and J. Bourgoin, Appl. Phys. Lett., **41**, 956 (1982).
16. D. Schroder, *Semiconductor Material and Device Characterization*, (Wiley Interscience, NY, NY, 1990), p. 336.
17. J. Wager and J. Van Vechten, Phys. Rev .B., **32**, 5251 (1985).
18. M. Yamaguchi and K. Ando, J. Appl. Phys., **60**, 935 (1986).

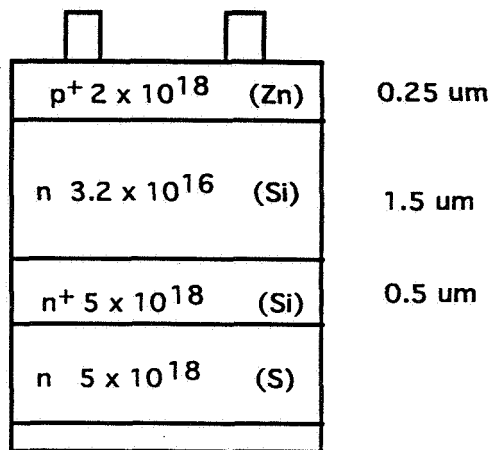


Figure 1. Details of InP cell configuration

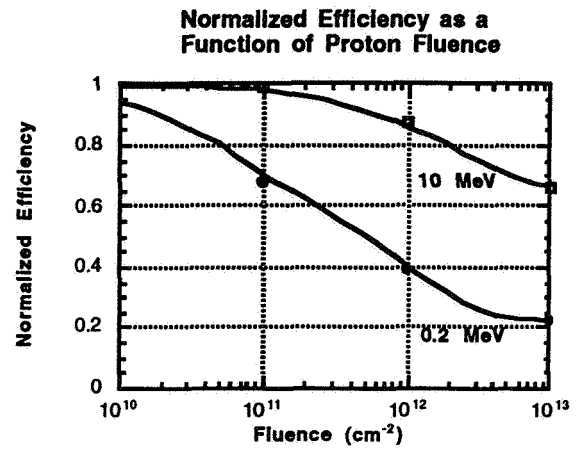


Figure 2. Normalized efficiency as a function of proton fluence.

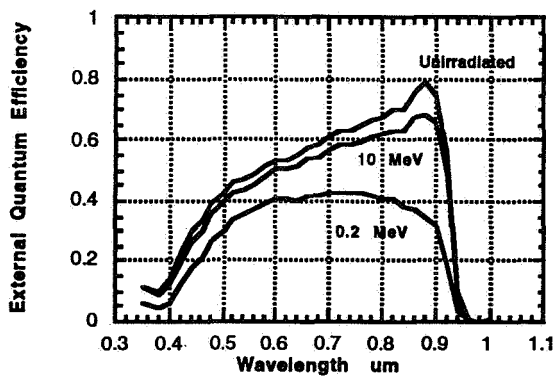


Figure 3. External quantum efficiency of cells, unirradiated and irradiated to 10¹²/cm²

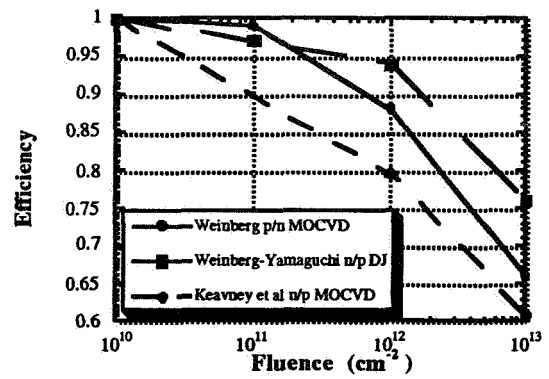


Figure 4. Normalized efficiency of various cells after 10 MeV irradiations.

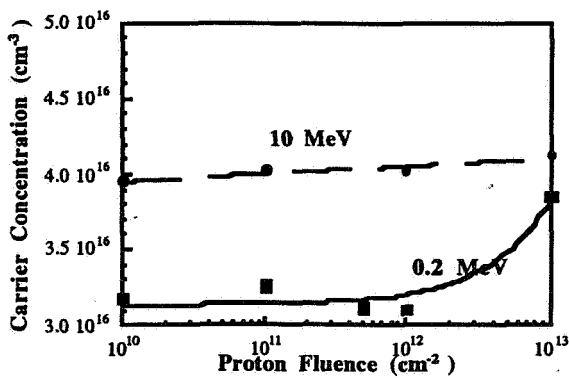


Figure 5. Carrier concentration as a function of proton fluence.

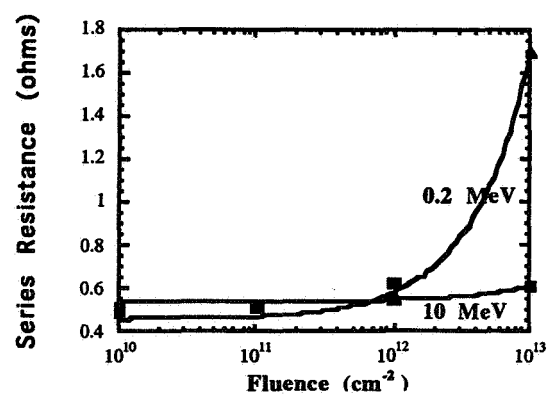


Figure 6. Series resistance as a function of proton fluence.

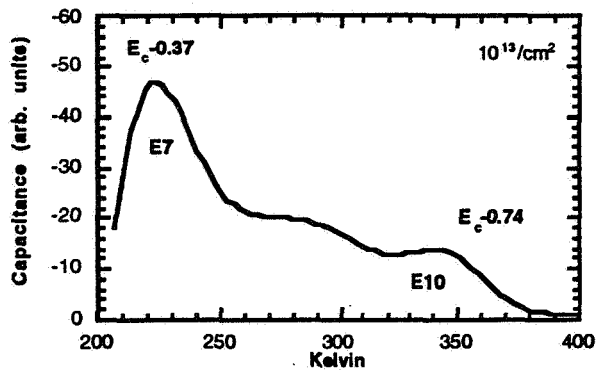


Figure 7. Majority carrier DLTS spectrum of 0.2 MeV proton irradiated InP.

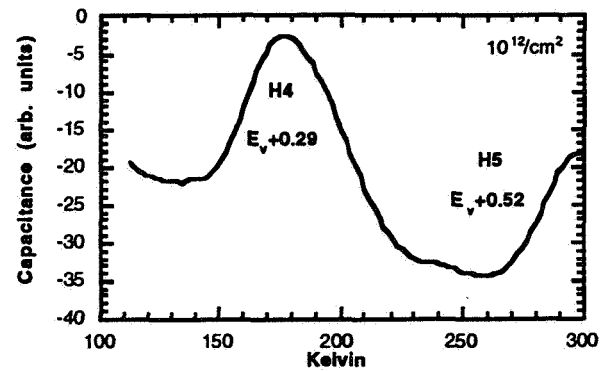


Figure 8. Minority carrier DLTS spectrum of 0.2 MeV proton irradiated InP.

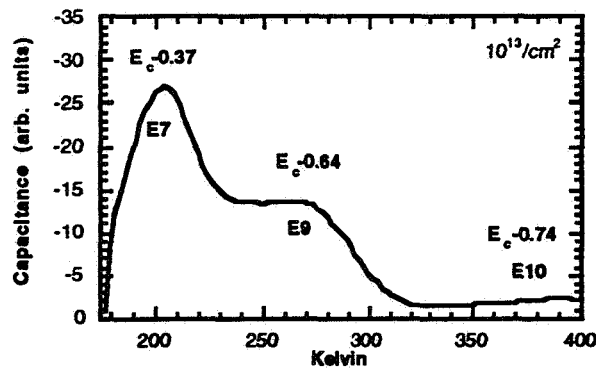


Figure 9. Majority carrier DLTS spectrum of 10 MeV proton irradiated InP.

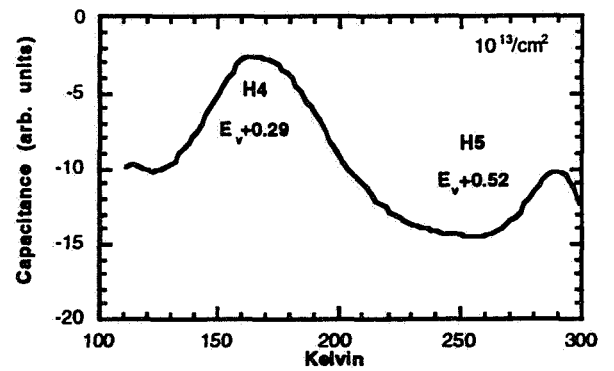


Figure 10. Minority carrier DLTS spectrum of 10 MeV proton irradiated InP.

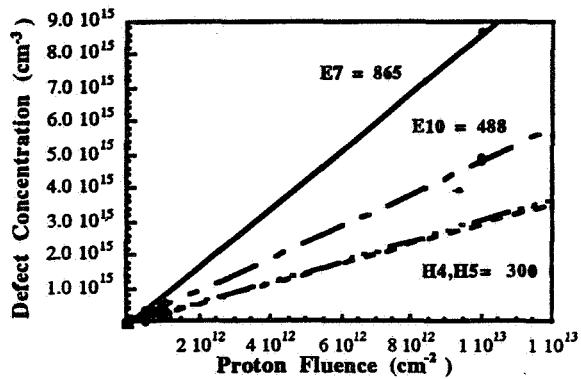


Figure 11. Defect introduction rates in 0.2 MeV proton irradiated InP.

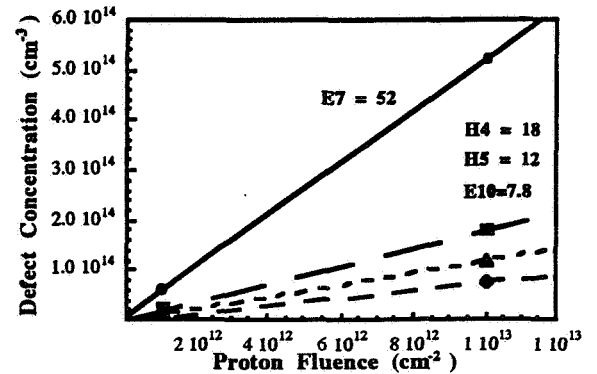


Figure 12. Defect introduction rates in 10 MeV proton irradiated InP

S12
IN-50397

Correlation of Electron and Proton Irradiation-Induced Damage in InP Solar Cells

Robert J. Walters

Naval Research Laboratory, Code 6615, Washington, DC 20375

Geoffrey P. Summers

Naval Research Laboratory, Code 6615, Washington, DC 20375, and
Department of Physics, University of Maryland Baltimore County, Baltimore, MD 21228

Scott R. Messenger and Edward A. Burke

SFA, Inc., Landover, MD 20785

ABSTRACT

The measured degradation of epitaxial shallow homojunction n^+p InP solar cells under 1 MeV electron irradiation is correlated with that measured under 3 MeV proton irradiation based on "displacement damage dose". The measured data is analyzed as a function of displacement damage dose from which an electron to proton dose equivalency ratio is determined which enables the electron and proton degradation data to be described by a single degradation curve. It is discussed how this single curve can be used to predict the cell degradation under irradiation by any particle energy. The degradation curve is used to compare the radiation response of InP and GaAs/Ge cells on an absolute damage energy scale. The comparison shows InP to be inherently more resistant to displacement damage deposition than the GaAs/Ge.

INTRODUCTION

When determining the best solar cell technology for a particular space flight mission, accurate prediction of solar cell performance in a space radiation environment is essential. The current methodology used to make such predictions requires extensive experimental data measured under both electron and proton irradiation. Due to the rising cost of accelerators and irradiation facilities, such data sets are expensive to obtain. Moreover, with the rapid development of novel cell designs, the necessary data is often not readily available. Therefore, a method for predicting cell degradation based on limited data would be most useful. Such a method has been developed at the Naval Research Laboratory based on damage correlation using "displacement damage dose" which is the product of the non-ionizing energy loss (NIEL) and the particle fluence.¹ Displacement damage dose is a direct analog of the ionization dose used to correlate the effects of ionizing radiations. In this method, the performance of a solar cell in a complex radiation environment can be predicted from data on a single proton energy and two electron energies, or one proton energy, one electron energy, and Co^{60} gammas. Summers et al.² have used this method to accurately predict the data measured by Anspaugh³ on GaAs/Ge solar cells under a wide range of electron and proton energies. In the present paper, the method is applied to InP solar cells using data measured under 1 MeV electron and 3 MeV proton irradiations, and the calculations are shown to agree well with the measured data.

In addition to providing accurate damage predictions, this method also provides a basis for quantitative comparisons of the performance of different cell technologies. The performance of the present InP cells is compared to that published for GaAs/Ge cells. The results show InP to be inherently more resistant to displacement energy deposition than GaAs/Ge.

EXPERIMENTAL NOTES

The 1 MeV electron irradiations were performed using the Van De Graff accelerator at the National Institute of Standards and Technology (NIST). The 3 MeV proton irradiations were performed using the Pelletron accelerator at the Naval Surface Warfare Center (NSWC) in White Oak, MD. In both cases the beam current was kept low enough so that no sample heating occurred during irradiation. The irradiations were done at room temperature, in the dark, and at open circuit. For the electron irradiations, dosimetry was achieved with a Faraday cup and current integrator. The proton fluences were determined by collecting all the charge striking the sample holder through a current integrator.

An Oriel 1000W Xe arc lamp solar simulator with AM0 filtering was used for PV measurements. The lamp intensity was adjusted to 1 sun, AM0 using an InP reference cell calibrated by Keith Emery at the National Renewable Energy Laboratory (NREL). Current-voltage (IV) curves were measured using two Keithley 617 electrometers and a Kepco 50-2M bipolar amplifier.

The solar cells studied here are n⁺p shallow homojunctions grown epitaxially by metalorganic chemical vapor deposition (MOCVD) on p-type InP wafers doped with Zn. The cells were grown by Spire Corporation under contract to the Naval Research Laboratory. The cell base was 3μm thick with Zn as the dopant atom. The emitter was 300 Å thick with Si or Se as the dopant atom. The cells were square, and 0.5 cm on a side. The total area of 0.25 cm² was used in all calculations.

CORRELATING 1 MeV ELECTRON AND 3 MeV PROTON DAMAGE

For the present study, the degradation of some InP solar cells under 1 MeV electron and others under 3 MeV proton irradiation has been measured. The irradiations were done incrementally with the cells being characterized after each fluence increment. The measured degradation of the cell maximum power (P_{max}) under both irradiations is shown in figure 1. Since 3 MeV protons are more damaging, i.e. have a larger NIEL, than 1 MeV electrons, the data sets are separated along the fluence axis. The goal is to correlate these data so that the degradation can be described by a single curve. In the present method, the first step is to convert the fluence values to displacement damage dose by multiplying by the appropriate NIEL value. The calculated NIEL values for electrons and protons over a wide energy range incident on Si, GaAs, and InP are tabulated in reference 2. From these tables, the NIEL for 1 MeV electrons incident on InP is 3.348×10^{-5} (MeV cm²/g) and that for 3 MeV protons is 2.031×10^{-2} (MeV cm²/g). The resultant plot of the degradation of P_{max} vs displacement damage dose is shown in figure 2.

As can be seen in figure 2, analyzing the degradation data as a function of displacement damage dose greatly reduces the separation of the electron and proton data sets. The next step in correlating the data is to determine an electron to proton dose equivalency ratio (R_{ep}). R_{ep} is defined as the ratio of the dose along the 1 MeV electron degradation curve to the dose along the 3 MeV proton degradation curve

which cause equal cell degradation. For the present data, $R_{ep} = 4.12$. By dividing the dose values of the 1 MeV electron data by this ratio, the electron and proton degradation data are correlated (figure 3). The reason that the electron and proton data do not initially correlate when plotted as a function of displacement damage dose (i.e why $R_{ep} \neq 1$) is that electron damage coefficients in p-type InP do not vary linearly with NIEL as will be discussed below.

Now that the degradation data has been properly correlated, a characteristic degradation curve for these InP solar cells can be determined. This curve is determined by fitting the correlated data to the following expression:

$$P_{max}(D_d) = A - C \log\left(1 + \frac{D_d}{D_x}\right)$$

$D_d \equiv$ displacement damage dose (1)

$A, C, D_x \equiv$ constants

which is essentially the degradation equation given in the Solar Cell Radiation Handbook⁴ except that, here, the parameters are functions of displacement damage dose instead of particle fluence. For the present data sets, these constants were determined: $A = 24.3$ (mW/cm²), $C = 4.87$ (mW/cm²), and $D_x = 1.79 \times 10^9$ (MeV/g). The fit is shown as a solid line in figure 3.

CALCULATING THE CELL RESPONSE TO OTHER IRRADIATIONS

Given the characteristic degradation equation, the response of these InP cells to any other irradiation can be calculated. This is possible because radiation damage in semiconductors can be related to NIEL. In the case of proton irradiation of p-type InP, the damage coefficients have been found to vary linearly with NIEL⁵⁻⁷. Therefore, the degradation of these InP cells under any proton irradiation can be calculated by simply dividing the dose range of equation (1) by the appropriate NIEL.

The case of electron irradiation of p-type InP is more complicated. The fact that the measured electron and proton degradation data do not directly correlate when plotted as a function of displacement damage dose (figure 2) indicates that the electron damage coefficients in p-type InP do not vary linearly with NIEL. It has been found in p-type Si and GaAs that the electron damage coefficients vary with the square of the NIEL^{1,5}. Preliminary results indicate the same to be true for p-type InP⁸, but more data is needed to confirm this. Once the dependence on NIEL is established, the degradation under any electron and proton irradiation can be calculated from the characteristic equation.

COMPARISON OF THE PERFORMANCE OF InP AND GaAs/Ge SOLAR CELLS

By applying the displacement damage dose concept, the response of a particular solar cell to irradiation by a spectrum of particle energies can be expressed in a single curve. Therefore, this method of analysis provides a basis for comparing the radiation response of different solar cell technologies on an absolute scale. As an example, the response of GaAs/Ge solar cells can be compared with the response of the InP cells studied here. In reference 2, a characteristic degradation curve was determined for GaAs/Ge solar cells based on measurements made by Anspaugh³. This curve is reproduced in figure 4 along with the characteristic degradation curve for InP solar cells derived here. The InP curve lies above

the GaAs/Ge curve. This indicates that InP solar cells are intrinsically more radiation resistant than GaAs/Ge solar cells to displacement damage energy.

SUMMARY

The measured degradation of epitaxial shallow homojunction n^+p InP solar cells under 1 MeV electron and 3 MeV proton irradiation has been correlated based on displacement damage dose. From the correlated data a characteristic degradation curve for these InP cells has been derived which can be used to calculate the cell response under any particle irradiation. Therefore, through this damage correlation method, the cell response to irradiation by any spectrum of particles can be calculated from a minimum of experimental data. The characteristic equation has also been used to compare the radiation response of these InP cells with that published for GaAs/Ge solar cells. The comparison shows these InP cells to be inherently more resistant to displacement energy deposition than GaAs/Ge cells.

REFERENCES

- 1 G.P. Summers, E.A. Burke, and M.A. Xapsos, "Displacement Damage Analogs to Ionizing Radiation Effects", *Radiation Measurements*, **24**, No. 1, 1-8 (1995).
- 2 G.P. Summers, R.J. Walters, M.A. Xapsos, E.A. Burke, S.R. Messenger, P. Shapiro, and R.L. Statler, "A New Approach to Damage Prediction for Solar Cells Exposed to Different Radiations", *IEEE Proc. 1st World Conference on Photovoltaic Energy Conversion, Waikoloa, Hawaii, Dec 5-9, 1994*, p. 2068-2073.
- 3 B.E. Anspaugh, "Proton and Electron Damage Coefficients for GaAs/Ge Solar Cells", *IEEE Proc. 22nd Photovoltaic Spec. Conf., Las Vegas, NV, Oct.*, p1593 (1991)
- 4 H.Y. Tada, J.R. Carter, B.E. Anspaugh, and R.G. Downing, "The Solar Cell Radiation Handbook", JPL Publication 82-69, 1982.
- 5 G.P. Summers, E.A. Burke, P. Shapiro, S.R. Messenger, and R.J. Walters, "Damage Correlation in Semiconductors Exposed to Gamma, Electron, and Proton Radiations", *IEEE Trans. Nuc. Sci.*, **40**, 1300-1306, Dec (1993)
- 6 T. Takamoto, H. Okazaki, H. Takamura, M. Ura, M. Ohmori, M. Yamaguchi, S. Ikegami, H. Arai, T. Hayashi, A. Ushirokawa, K. Takahashi, M. Koubata, and A. Ohnishi, "InP Solar Cells for Space Applications", *Technical Digest of the International PVSEC-5, Kyoto, Japan*, p547, (1990)
- 7 M. Yamaguchi, T. Hayashi, A. Ushirokawa, K. Takahashi, T. Takamoto, H. Okazaki, M. Ohmori, S. Ikegami, and H. Arai, "Analysis of Space Flight Data of InP Solar Cells in EXOS-D Orbit", *IEEE Proc. 22nd Photovoltaic Spec. Conf., Las Vegas, NV, Oct.*, (1991)
- 8 S.R. Messenger, "Electron and Gamma - Induced Displacement Damage Effects in InP Semiconductors Devices", Ph.D. Dissertation, Univ. of Maryland Baltimore County, 1995

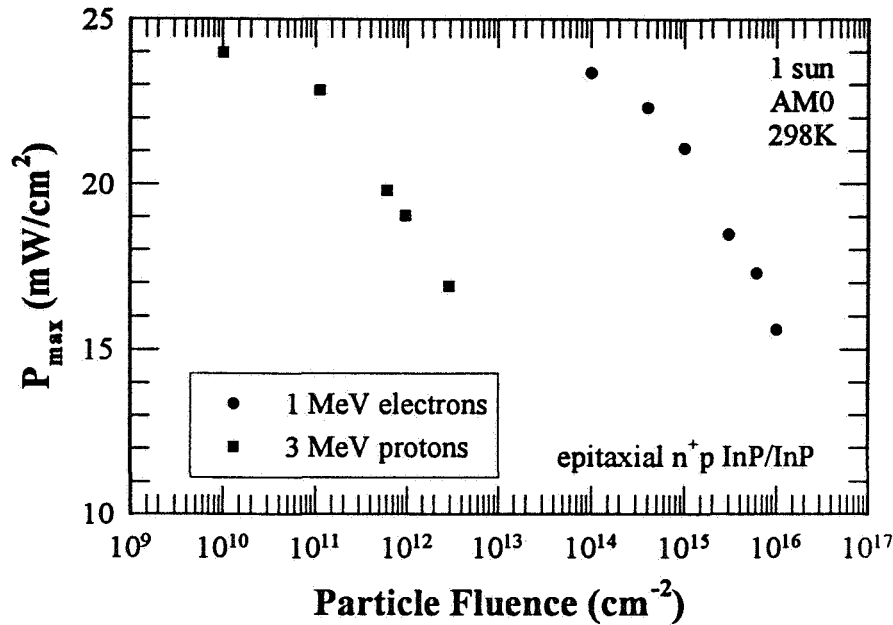


FIGURE 1: Measured degradation of the maximum power of epitaxial shallow homojunction n^+p InP solar cells under 1 MeV electron and 3 MeV proton irradiation. Since 3 MeV protons have a larger NIEL value than 1 MeV electrons, the data is separated along the fluence axis. The goal of the present analysis is to correlate these data.

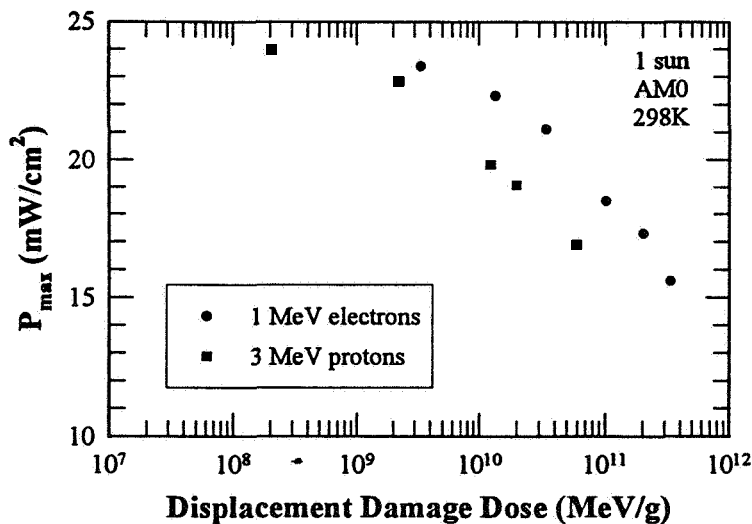


FIGURE 2: Measured degradation of the maximum power of epitaxial shallow homojunction n^+p InP solar cells under 1 MeV electron and 3 MeV proton irradiation plotted as a function of displacement damage dose. These are the same data as in figure 1 except that the fluence has been converted to displacement damage dose by multiplying by the calculated NIEL value for each particle energy. Analyzing the degradation data as a function of displacement damage dose brings the degradation curves much closer together.

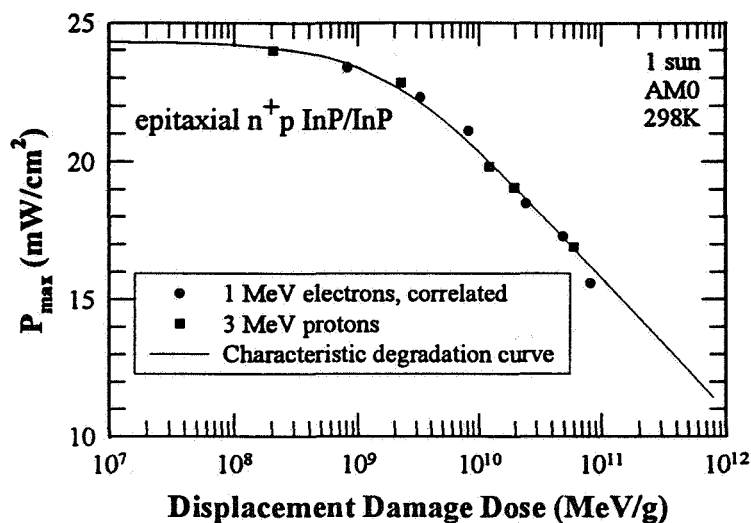


FIGURE 3: Correlation of the measured 1 MeV electron and 3 MeV proton irradiation damage. By applying the R_{ep} value of 4.12 to the data of figure 2, the degradation data is correlated. The degradation under electron and proton irradiation can now be described by a single degradation curve given by equation (1). The solid line is a fit of the correlated data to equation (1).

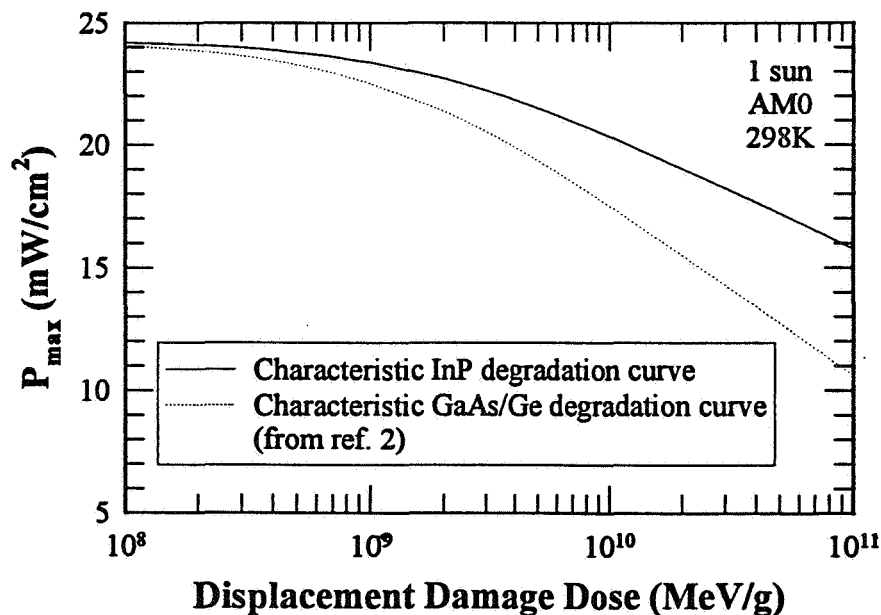


FIGURE 4: Comparison of the radiation response of GaAs/Ge and InP solar cells. Since the displacement damage dose damage correlation method allows the solar cell degradation under irradiation by electrons and protons of any energy to be described by a single curve, it provides a basis for the comparison of the performance of different cell technologies on an absolute scale. These data show that InP is inherently more resistant to displacement damage deposition than GaAs/Ge.

DIFFUSION LENGTHS IN IRRADIATED N/P InP-on-Si SOLAR CELLS

Steven Wojtczuk and Claudia Colerico
Spire Corporation
Bedford, MA 01730-2396

Geoffrey P. Summers and Robert J. Walters
Naval Research Laboratory
Washington, DC 20375

Edward A. Burke
Independent Consultant
Woburn, MA 01801

S13
/N-50398

OVERVIEW

Indium phosphide (InP) solar cells were made on silicon (Si) wafers (InP/Si) by to take advantage of both the radiation-hardness properties of the InP solar cell and the light weight and low cost of Si wafers. The InP/Si cell application is for long duration and/or high radiation orbit space missions. Spire has made N/P InP/Si cells¹ of sizes up to 2 cm by 4 cm with beginning-of-life (BOL) AM0 efficiencies over 13% (one-sun, 28C). These InP/Si cells have higher absolute efficiency and power density after a high radiation dose than gallium arsenide (GaAs) or silicon (Si) solar cells after a fluence of about 2×10^{15} 1 MeV electrons/cm². In this work, we investigate the minority carrier (electron) base diffusion lengths in the N/P InP/Si cells. A quantum efficiency model was constructed for a 12% BOL AM0 N/P InP/Si cell which agreed well with the absolutely measured quantum efficiency and the sun-simulator measured AM0 photocurrent (30.1 mA/cm²). This model was then used to generate a table of AM0 photocurrents for a range of base diffusion lengths. AM0 photocurrents were then measured for irradiations up to 7.7×10^{16} 1 MeV electrons/cm² (the 12% BOL cell was 8% after the final irradiation). By comparing the measured photocurrents with the predicted photocurrents, base diffusion lengths were assigned at each fluence level. A damage coefficient K of 4×10^{-8} and a starting (unirradiated) base electron diffusion length of 0.8 μm fits the data well. The quantum efficiency was measured again at the end of the experiment to verify that the photocurrent predicted by the model (25.5 mA/cm²) agreed with the simulator-measured photocurrent after irradiation (25.7 mA/cm²).

QUANTUM EFFICIENCY MODEL

The quantum efficiency model used, described well by Hovel², breaks up the total quantum efficiency into three components. The first is from the cell emitter. In an N/P InP cell, the emitter is very thin (300Å) to limit light absorbed in the emitter which is subjected to a high front surface recombination loss (1×10^7 cm/s). The emitter (hole) diffusion length is in almost all conceivable cases larger than the emitter thickness. Therefore, the model results are virtually independent of emitter diffusion length. Emitter diffusion lengths of 10, 1, 0.1, or 0.05 μm give the same result as far as the quantum efficiency and the AM0 photocurrent are concerned since all of these lengths are in excess of the 300Å emitter thickness. This non-sensitivity of the photocurrent to emitter diffusion length makes the study of the base diffusion length much easier.

The second component that contributes to the quantum efficiency is the NP junction depletion space charge region (SCR). In the NP InP cell the emitter is very heavily doped ($> 1e19/cm^3$) so that a one-sided step junction approximation is used to calculate the zero-bias SCR width in the base (doping $3e17/cm^3$), which is about 630\AA . To first order, the model assumes that any carriers photogenerated in the SCR are immediately collected and this component does not depend on either base or emitter diffusion lengths.

The third model component is from the base region of the solar cell, and the model is essentially similar to that of the emitter (but of opposite polarity and minority carrier types). The surface recombination velocity at the back of the $3\mu\text{m}$ thick cell was taken to be $1e4\text{ cm/s}$, but the results are very insensitive to this value, since the base diffusion lengths are all less than $1\mu\text{m}$ and very little is collected from $3\mu\text{m}$ away from the junction.

Figure 1 shows (black dots) the measured quantum efficiency of a 1 cm^2 12% InP/Si cell before irradiation. The AM0 photocurrent from the measured quantum efficiency and I-V measurements at one-sun on a sun simulator (set with a NASA-calibrated InP reference cell) agreed (30.1 mA). The quantum efficiency data were non-linear least squares fitted to the model using the Marquandt-Levenberg algorithm. The model fit is shown as the uppermost solid line, and when integrated against the AM0 power spectrum, gives a photocurrent of 30.3 mA , in close agreement with the measured data. The base (electron) diffusion length extracted at this point was $0.8\mu\text{m}$. The cell had not yet been irradiated; the diffusion length is lower than in homoepitaxial InP due to dislocation defects from the 8% lattice-mismatch in the heteroepitaxial InP/Si cell.

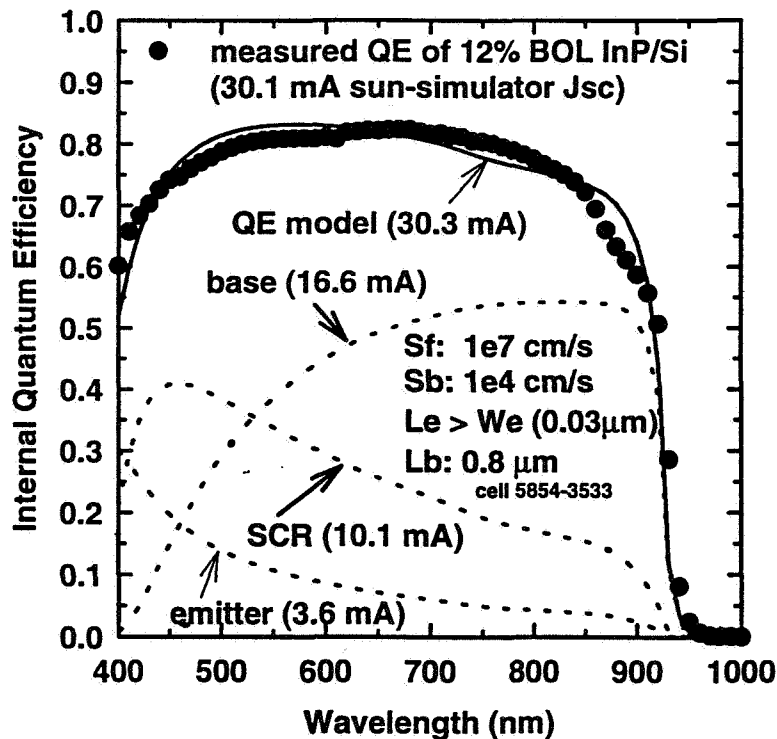


Figure 1 Measured (black dots) and model (solid line) quantum efficiency before irradiation for a 12% N/P InP/Si cell. Solid line (equivalent to 30.3 mA AM0) is the sum of the three dotted lines, representing contributions from the base (16.6 mA), depletion space-charge region (SCR) (10.1 mA), and the emitter (3.6 mA). An electron base diffusion length of $0.8\mu\text{m}$ fit the data.

DIFFUSION LENGTH DETERMINATION

Using the above quantum efficiency (QE) model, the predicted photocurrent was obtained versus the base diffusion length (Figure 2). This curve is then used to estimate the diffusion length from the measured photocurrent. The key to our experiment is the assumption the emitter diffusion length, when irradiated, is always larger than the 300Å emitter thickness, and that the space charge region is to first-order constant under irradiation. With these assumptions, the base component of the quantum efficiency curve dominates the photocurrent degradation with irradiation (the other components stay relatively constant).

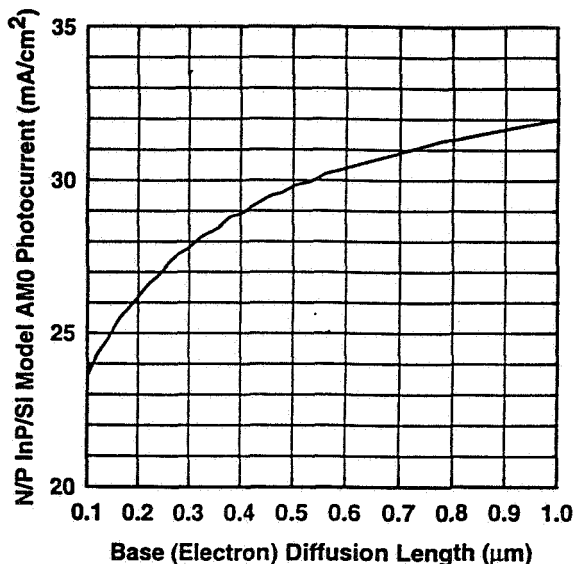


Figure 2 Model AMO photocurrent for an N/P InP/Si cell vs. base electron diffusion length.

The AMO I-Vs for the 12% AMO BOL N/P InP/Si cell were measured from no irradiation to an equivalent fluence of 7.7×10^{16} 1 MeV electrons/cm², where the efficiency was 8%. The cells were irradiated by alpha particles from a 1 mCi Am-241 source. This alpha source is small, self contained, and delivered an equivalent fluence of 7.7×10^{16} 1 MeV electrons/cm² in only 333 hours. Damage in InP from alphas is accurately converted into 1 MeV electron equivalent fluence using the non-ionizing energy loss (NIEL) method^{3,4}. For the source-cell distance used, the 3.9 MeV alpha flux was calculated as 1.03×10^6 α/cm²/s. The calculated equivalent 1 MeV electron flux was 6.45×10^{10} electrons/cm²/s. Table I shows the equivalent 1 MeV fluence, the measured photocurrent, and the base diffusion lengths obtained from Figure 2.

Table I Fluence vs. Measured AMO Photocurrent and Estimated Base Diffusion Lengths

| Eqv. 1 MeV Electron Fluence #/cm ² | AMO Photocurrent mA/cm ² | Base (Electron) Diffusion Length (μm) |
|--|--|--|
| 0 | 30.1 | 0.8 |
| 1.2 E 14 | 29.9 | 0.8 |
| 1.4 E 15 | 29.5 | 0.7 |
| 1.7 E 16 | 26.8 | 0.4 |
| 3.8 E 16 | 25.8 | 0.3 |
| 7.7 E 16 | 25.7 | 0.3 |

A standard empirical model for diffusion length versus fluence⁵ was fit using Table I data (Fig.3). The model parameters are the unirradiated electron diffusion length L_0 ($0.8\mu\text{m}$, Fig. 1) and K , the damage coefficient ($4\text{e-}8$). The fit is good except at the highest fluence; this may be due to radiation damage carrier removal effects changing the width of the space charge region; this effect was not included in our modeling.

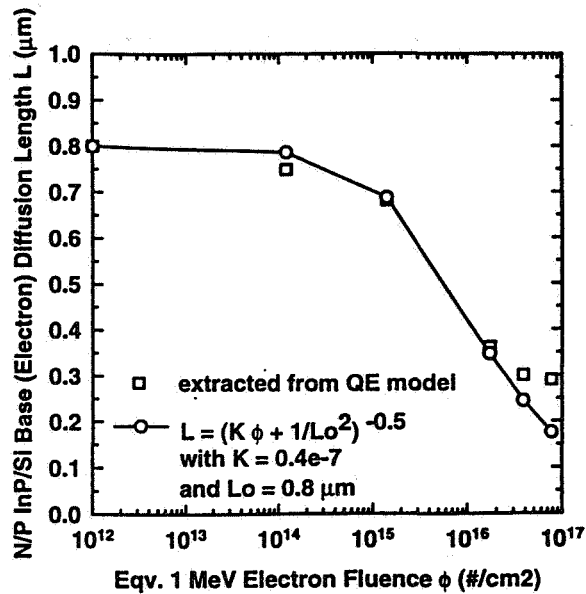


Figure 3 Estimated base electron diffusion length vs. fluence for an N/P InP/Si cell

We could not measure the quantum efficiency after every irradiation due to some scheduling issues. However, to confirm the QE model used in calculating Figures 1 and 2 and the diffusion lengths in Table I was still accurate after heavy irradiation, we measured the cell after the irradiations were all completed. The data is shown in Figure 4. The fit still agrees reasonably well with the measured sun-simulator photocurrent.

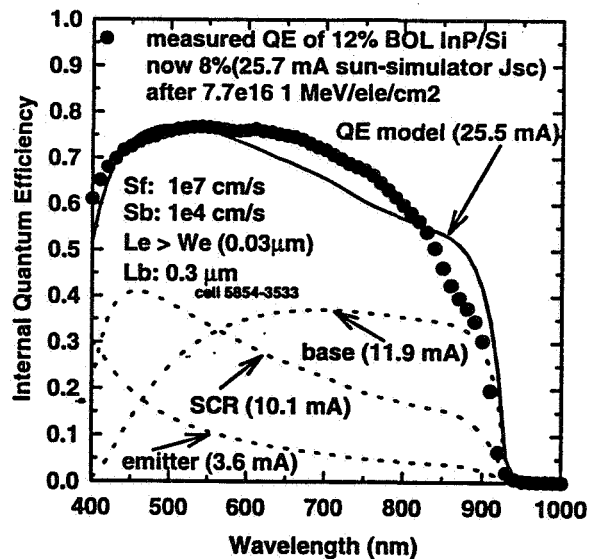


Figure 4 Measured (black dots) and model (solid line) quantum efficiency after $7.7\text{e}16$ 1 MeV electrons (12% BOL N/P InP/Si cell is now 8%). Solid line (equivalent to 25.5 mA AM0) is the sum of the three dotted lines, representing contributions from the base (11.9 mA), depletion space-charge region (SCR) (10.1 mA), and the emitter (3.6 mA). An electron base diffusion length of $0.3\mu\text{m}$ fit the data.

CONCLUSIONS

The minority carrier (electron) diffusion length in the P-type base of a 1 cm² N/P InP/Si cell starts at about 0.8μm (measured 12% AM0 efficiency, 30.1 mA photocurrent) before any irradiation, and drops to about 0.3μm after an extremely high 7.7e16 1 MeV electron fluence (measured 8% AM0 efficiency, 25.7 mA photocurrent). Except at possibly the highest fluence tested, it seems that the emitter and space-charge region contributions to the quantum efficiency and photocurrent may vary only a little in these thin emitter (300Å) cells, with most of the degradation caused by decreased photocollection from the base of the cell.

REFERENCES

1. S.J. Wojtczuk, N.H. Karam, P. Gouker, P. Colter, S.M. Vernon, G.P. Summers, R.L. Walters and R. Statler, "Development of InP Solar Cells on Inexpensive Si Wafers," *Proc. of 1st WCPEC (24th IEEE PVSC)*, 1994, pp. 1705-1708.
2. H.J. Hovel, *Solar Cells*, Vol.11 Semiconductors and Semimetals, Academic, 1975, pp. 17-20.
3. G.P. Summers, E.A. Burke, P. Shapiro, S.R. Messenger, and R.J. Walter, "Damage Correlations in Semiconductors Exposed to Gamma, Electron and Proton Radiations", *IEEE Trans. Nuclear Science*, **40**, 1993, pp. 1372-1379.
4. G.P. Summers, R.J. Walters, M.A. Xapsos, E.A. Burke, S.R. Messenger, P. Shapiro, and R.L. Statler, "A New Approach to Damage Prediction for Solar Cells Exposed to Different Radiations", *Proc. of 1st WCPEC (24th IEEE PVSC)*, 1994, pp. 2068-2073.
5. H.Y. Tada, J.R. Carter, B.E. Anspaugh, and R.G. Downing, *Solar Cell Radiation Handbook, 3rd Ed.*, JPL Publication 82-69, p. 3-19.

ELECTRON AND PROTON DAMAGE IN $\text{In}_{0.53}\text{Ga}_{0.47}\text{As}$ SOLAR CELLS
HAVING AN InP WINDOW LAYER

Scott R. Messenger
SFA, Inc.
Landover, MD 20785

Hector L. Cotal and Robert J. Walters
Naval Research Laboratory
Code 6615, Washington, DC 20375

Geoffrey P. Summers
Naval Research Laboratory
Code 6615, Washington, DC 20375
and
Department of Physics
University of Maryland Baltimore County
Baltimore, MD 21228

314-
IN-50399

ABSTRACT

As part of a continuing NRL program to optimize the space radiation resistance of InP/ $\text{In}_{0.53}\text{Ga}_{0.47}\text{As}$ tandem solar cells, $\text{In}_{0.53}\text{Ga}_{0.47}\text{As}$ (referred to as InGaAs below) solar cells were irradiated with 1 MeV electrons and with 3 MeV protons. The cells were grown with a 3 μm n-InP window layer to mimic the top cell in the tandem cell configuration for both AMO solar absorption and radiation effects. The results have been plotted against "displacement damage dose" which is the product of the nonionizing energy loss (NIEL) and the particle fluence. A characteristic radiation damage curve is then obtained for predicting the effect of all particles and energies.

Air mass zero (AMO), one sun solar illumination IV measurements were performed on the irradiated InGaAs solar cells and a characteristic radiation degradation curve was obtained using the solar cell conversion efficiency as the model parameter. Also presented are data comparing the radiation response of both n/p and p/n InGaAs solar cells. For the solar cell efficiency, the radiation degradation was found to be independent of the sample polarity.

INTRODUCTION

The InP/ $\text{In}_{0.53}\text{Ga}_{0.47}\text{As}$ tandem solar cell appears to be a promising solar cell technology for use in severe space radiation environments, primarily due to the known superior radiation resistance of the InP top cell. Several reports on both the tandem cell design and radiation response have been presented previously. One sun, AMO, conversion efficiencies as high as 21.1% and 22.2% at 25°C were measured for monolithic, two-terminal tandems with total areas of $\sim 4 \text{ cm}^2$ and $\sim 1 \text{ cm}^2$, respectively, for unoptimized cells(ref.1). The efficiency could be increased to $\sim 26\%$ when fully optimized(ref.1). Several radiation studies have shown that the InP/InGaAs tandem cell displays superior radiation resistance(refs.2,3). A new program is now underway involving NRL, ASEC, RTI and NREL to grow the InP/InGaAs tandem cell on Ge substrates, thereby greatly increasing cell durability and decreasing cost. Several cell designs are being considered, including both n/p and p/n polarities. Since Ge is an n-dopant in both InP and InGaAs, the n/p configuration will have to include an additional tunnel junction between the substrate and the bottom cell of the tandem.

To optimize the radiation degradation of InP/InGaAs, the radiation response of each component cell, as well as combined in the tandem configuration, must be investigated. Furthermore, current-matching between the subcells under irradiation is necessary while still maintaining the open circuit voltages. Otherwise, current-limiting conditions set in and the tandem cell current would then be controlled by the less radiation resistant subcell current. The optimization of each subcell can be achieved using such quantities as doping concentrations and layer thicknesses(refs.2,3).

The radiation degradation of InP cells due to electrons and protons of several different energies for both the n/p and p/n polarities have been reported(refs.4-6). Also, the radiation degradation of n/p and p/n InGaAs solar cells to 1 MeV electron irradiation has been reported(refs.7,8). The radiation response of the two-terminal InP/InGaAs tandem cell (on InP substrates) in the n/p configuration under both 1 MeV electron and 3 MeV proton irradiations have been reported (BOL efficiency ~20% on a 4 cm² cell)(refs.2,3). The results showed that the InGaAs cell was the limiting subcell. Therefore, increasing the radiation response of the InGaAs subcell is imperative for increasing the radiation response of the tandem cell.

This paper reports experimental results of both 1 MeV electron and 3 MeV proton irradiations on InGaAs solar cells. Cells of both the n/p and p/n polarities were irradiated, with the p/n cells having only 1 MeV electron irradiation exposure. The results obtained from the 1 MeV electron and 3 MeV proton irradiations were compared using "displacement damage dose", thus giving another example of how useful this technique is in predicting the damage in any radiation environment(refs.10,11). A single radiation degradation curve will be presented which fully describes displacement damage effects in InGaAs solar cells. Several base carrier concentrations were also considered in an attempt to optimize the cell radiation response to 1 MeV electrons.

EXPERIMENTAL DETAILS

The irradiations were performed on two different InGaAs cell structures both grown by MOCVD. InGaAs solar cells of the n/p polarity (A = 13.6 mm²) were fabricated by the Research Triangle Institute (RTI) while the p/n cells (A = 25 mm²) were grown by the National Energy Renewable Laboratory (NREL). Both cell types had a base doping concentration of 2x10¹⁷ cm⁻³. The complete cell structures are given in references 7 and 8. An InP window layer was grown on both cell polarities to mimic the tandem cell.

The 1 MeV electron irradiations were performed using a Van de Graaff accelerator either at NASA Goddard in Greenbelt, MD or at the National Institute of Standards and Technology (NIST) in Gaithersburg, MD, while the 3 MeV proton irradiations were performed using a Pelletron either at NRL or the Naval Surface Warfare Center (NSWC) in White Oak, MD. In all cases, the beam currents were kept low enough to avoid significant sample heating during irradiation. This is important, especially in InP, since both thermal and injection annealing during irradiation can occur.

Current-voltage (IV) measurements were performed both in the dark and under one sun, AM0 solar illumination using a Spectrolab X25 solar simulator at 298K. A silicon reference cell was measured on a Lear jet and then extrapolated to AM0 courtesy of NASA Lewis. The simulator intensity was then set for a measurement on InGaAs. The IV measurements were performed using HP34401A multimeters and a Kepco 36-1.6M bipolar amplifier, with full experiment automation achieved through IEEE-488 GPIB operation with a QuickBasic program. The measurement errors are expected to be less than 1%.

CORRELATION OF 1 MeV ELECTRON AND 3 MeV PROTON DAMAGE

Figure 1 shows the radiation results for 1 MeV electrons and 3 MeV protons on n/p InGaAs solar cells. The normalized solar cell efficiency is plotted as a function of the particle fluence. The data will be analyzed in terms of displacement damage dose. To calculate the displacement damage dose, the fluences are multiplied by the respective nonionizing energy loss (NIEL) values for the particle and energy in question. The NIEL values for 1 MeV electrons and 3 MeV protons in InGaAs are 2.88x10⁻⁵ and 2.33x10⁻² MeVcm²/g, respectively. The method of calculating NIEL values has been outlined in several prior publications(refs.11,12). Figure 2 shows the data from Figure 1 plotted as a function of displacement damage dose. It can be seen that the curves are much closer together when presented in this manner. The next step in the correlation is to

determine the electron to proton dose equivalency ratio (R_{ep}) as described in reference 9. R_{ep} is defined as the ratio of the dose along the 1 MeV electron degradation curve to the dose along the 3 MeV proton degradation curve which cause equal cell degradation. For the present data, R_{ep} is found to be 2. By dividing the dose values of the 1 MeV electron data by this ratio, the electron and proton degradation data are correlated as is also shown in Figure 2.

Now we have a characteristic degradation curve for radiation damage in n/p InGaAs solar cells. To describe this radiation damage quantitatively, an equation very similar to the one given in the Solar Cell Radiation Handbook is shown (for the solar cell conversion efficiency (η) as an example):

$$\eta(D_d) = A - C \log \left(1 + \frac{D_d}{D_x} \right), \quad (1)$$

where A , C , and D_x are the fitting parameters and D_d is the displacement damage dose. The degradation as a function of *displacement damage dose* is the difference between this equation and the one given in the Solar Cell Radiation Handbook. Upon a numerical data fit, the following values for the constants were determined: $A = 4.76$ (%), $C = 1.353$ (%), and $D_x = 1.433 \times 10^8$ (MeV/g). The solid line in Figure 2 shows the characteristic degradation curve for n/p InGaAs given by Eq. (1).

CELL POLARITY EFFECT ON EFFICIENCY DEGRADATION WITH 1 MeV ELECTRONS

InGaAs solar cells of the p/n polarity fabricated by NREL were also irradiated with 1 MeV electrons. The radiation results for the solar cell conversion efficiency are shown in Figure 3, where the efficiency degradation of cells having different polarities for the same base dopant concentration ($2 \times 10^{17} \text{cm}^{-3}$) are plotted as a function of 1 MeV electron fluence. A complete analysis, using the other solar cell parameters as well as dark IV data, is currently underway. It can be seen from Fig. 3 that the cell efficiency degradation is independent of cell polarity. This behavior is different than that reported for InP and Si(ref.13).

CONCLUSION

Having a characteristic degradation curve as a function of displacement damage dose is greatly beneficial in the prediction of cell response in different radiation environments. It also makes comparison straightforward with other cell technologies. Using this curve, one can predict the response of the cell in any radiation environment by simply calculating the NIEL of the cell material for the particle and energy of interest. A spectrum of particle energies, such as that produced by a Co^{60} source, can also be handled quite simply(ref. 13). This characteristic curve also aids in the absolute comparison of results from different cell technologies. As an example, the comparison of the degradation of n/p InP homojunction and GaAs/Ge solar cells is given in the paper by Walters et al. in these proceedings. It is shown that InP degrades less than GaAs/Ge for any displacement damage dose.

The polarity independence of solar cell efficiency degradation of InGaAs is an important result in the design of the InP/InGaAs tandem cell. The polarity independence gives us considerable flexibility in optimizing the final design for the InP/InGaAs tandem cell.

REFERENCES

1. M.W. Wanlass, J.S. Ward, K.A. Emery, A. Duda, and T.J. Coutts, "Improved Large-Area, Two-Terminal InP/In_{0.53}Ga_{0.47}As Tandem Solar Cells", Proceedings of the 1st IEEE World Conference on Photovoltaic Energy Conversion, Waikoloa, HI, 1994, pp. 1717-19.
2. H.L. Cotal, R.J. Walters, S.R. Messenger, and G.P. Summers, "Performance of Proton- and Electron-Irradiated, Two-Terminal, Monolithic InP/In_{0.53}Ga_{0.47}As Tandem Solar Cells", Proceedings of the 1st IEEE World Conference on Photovoltaic Energy Conversion, Waikoloa, HI, 1994, pp. 2088-95.
3. H.L. Cotal, R.J. Walters, G.P. Summers, and S.R. Messenger, "Electron Irradiation of Two-Terminal, Monolithic InP/In_{0.53}Ga_{0.47}As Tandem Solar Cells", J. Appl. Phys. **77**, 2173 (1995).
4. C.J. Keavney, R.J. Walters, and P.J. Drevinsky, "Optimizing the Radiation Resistance of InP Solar Cells: Effect of Dopant Density and Cell Thickness", J. Appl. Phys. **73**, 60 (1993).
5. I. Weinberg, G.C. Rybicki, C. Vargas-Aburto, D. Scheiman, "Performance, Defect Behavior, and Carrier Enhancement in Low Energy, Proton Irradiated p⁺nn⁺ InP Solar Cells", Proceedings of the 13th Space Photovoltaic Research and Technology Conference, NASA Lewis Research Center, Cleveland, OH, 1989, pp. 149-58.
6. S.R. Messenger, R.J. Walters, M.J. Panunto, and G.P. Summers, "Radiation Effects on p⁺n Junctions Grown by MOCVD", Proceedings of the 13th Space Photovoltaic Research and Technology Conference, NASA Lewis Research Center, Cleveland, OH, 1994, pp. 167-80.
7. R.J. Walters, G.J. Shaw, G.P. Summers, and S.R. Messenger, "The Effect of Base Dopant Level and Thickness on the Radiation Response of Ga_{0.47}In_{0.53}As Solar Cells", Proceedings of the 5th IEEE International Conference on Indium Phosphide and Related Materials, Paris, France, 1993, pp. 600-4.
8. S.R. Messenger, R.J. Walters, H.L. Cotal, and G.P. Summers, "Radiation Degradation in In_{0.53}Ga_{0.47}As Solar Cells", Proceedings of the 6th IEEE International Conference on Indium Phosphide and Related Materials, Santa Barbara, CA, 1994, pp. 504-7.
9. G.P. Summers, R.J. Walters, M.A. Xapsos, E.A. Burke, S.R. Messenger, P. Shapiro, and R.L. Statler, "A New Approach to Damage Prediction for Solar Cells Exposed to Different Radiations", Proceedings of the 1st IEEE World Conference on Photovoltaic Energy Conversion, Waikoloa, HI, 1994, pp. 2068-75.
10. G.P. Summers, E.A. Burke, P. Shapiro, R. Statler, S.R. Messenger, and R.J. Walters, "The Use of Displacement Damage Dose to Correlate Degradation in Solar Cells Exposed to Different Radiations", Proceedings of the 13th Space Photovoltaic Research and Technology Conference, NASA Lewis Research Center, Cleveland, OH, 1994, pp. 197-201.
11. G.P. Summers, E.A. Burke, R.J. Walters, G.J. Shaw, P. Shapiro, R. Statler, and S.R. Messenger, "A General Method for Predicting Radiation Damage to Solar Cells in the Space Environment", Proceedings of the 23rd IEEE Photovoltaic Specialists Conference, Louisville, KY, 1991, pp.1426-31.
12. G.P. Summers, E.A. Burke, P. Shapiro, S.R. Messenger, and R.J. Walters, "Damage Correlations in Semiconductors Exposed to Gamma, Electron and Proton Radiations", IEEE Trans. Nucl. Sci. **40**, 1372 (1993).
13. S.R. Messenger, "Electron and Gamma-Induced Displacement Damage Effects in InP Semiconductor Devices", Ph.D. Dissertation, University of Maryland Baltimore County, 1995.

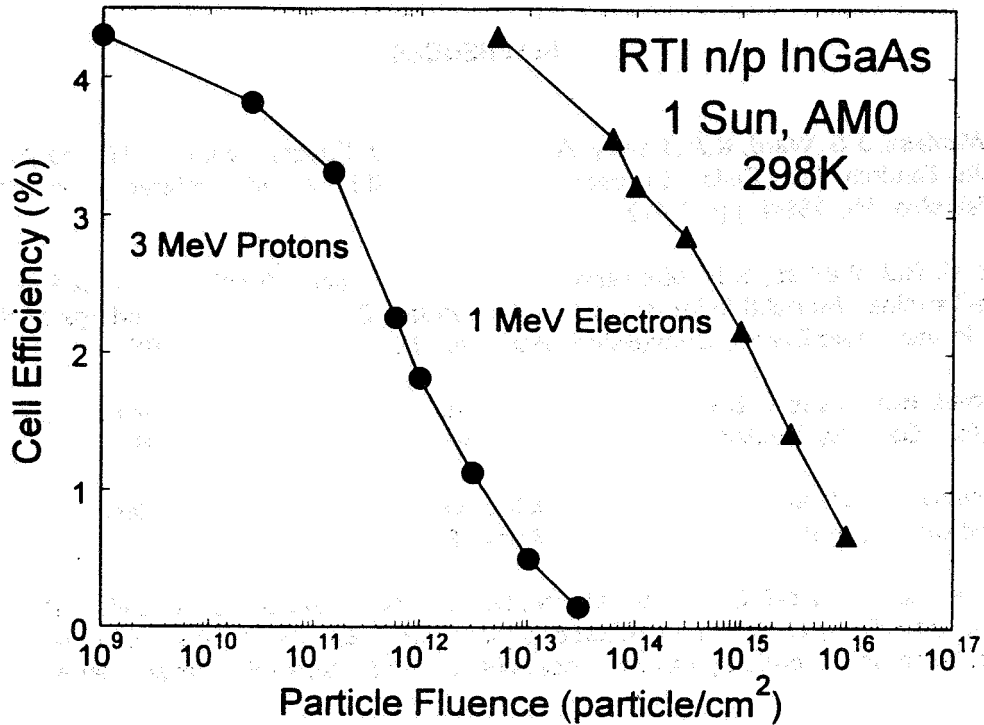


Figure 1 Degradation in n/p InGaAs solar cell efficiency (1 sun, AM0) due to 3 MeV proton and 1 MeV electron irradiation as a function of particle fluence.

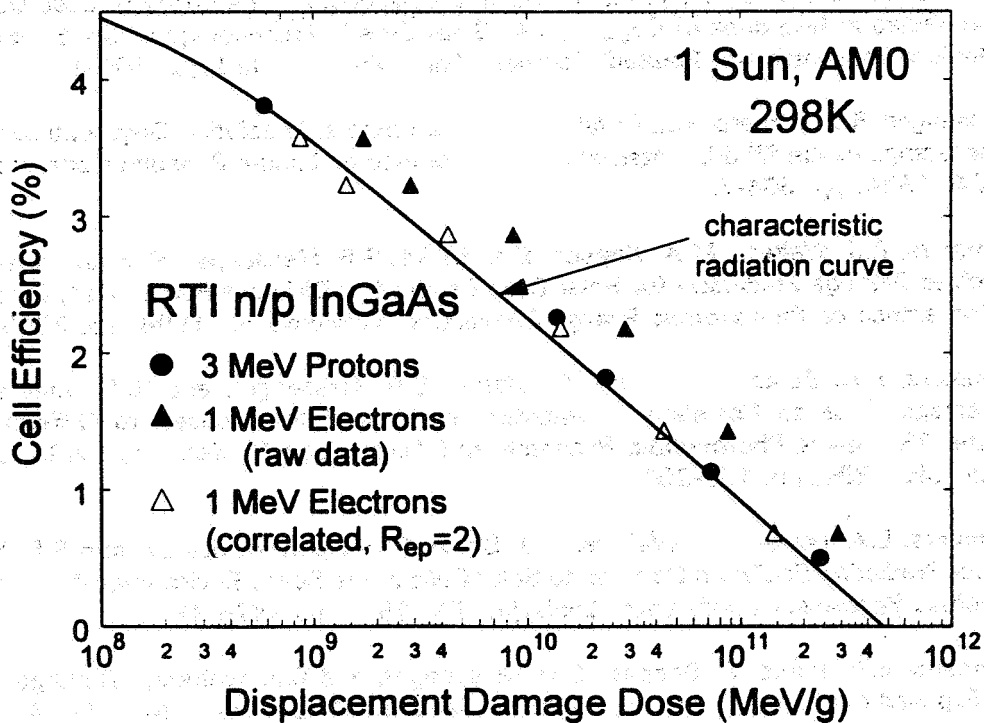


Figure 2 Data from Fig. 1 plotted as a function of displacement damage dose. The 1 MeV electron data is correlated with the 3 MeV proton data using the factor R_{ep} and a characteristic radiation curve is obtained.

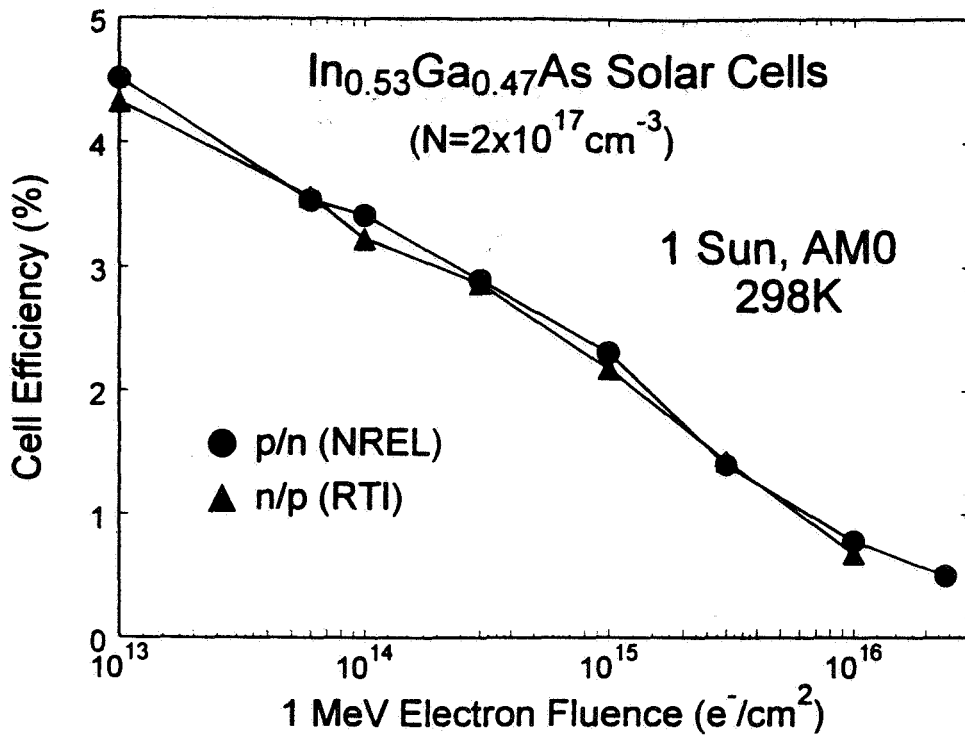


Figure 3 Efficiency degradation of n/p and p/n InGaAs solar cells. The degradation is shown to be polarity independent.

Photo-Recovery of Electron-Irradiated GaAs Solar Cells¹

Andrew Meulenberg (301-926-3609)
Consultant
Gaithersburg, MD 20855

S15
IN-50400

ABSTRACT

The first long-term (3000 hours) UV testing of unirradiated and 1 MeV electron-irradiated GaAs/Ge solar cells, with multilayer-coated coverslides to reduce operating temperature, has produced some unexpected results. The cells used for this series of tests displayed a much higher radiation degradation than that predicted based on JPL Solar Cell Radiation Handbook data. Covered cells degraded more than did bare cells and use of multilayer-coated coverslides further increased the radiation degradation in short-circuit current (I_{sc}).

Electron radiation damage to these GaAs solar cells anneals at 40°C when exposed to ~1 sun AM0 UV light sources. The effect appears to be linear with time (~1% of I_{sc} per 1000 UVSH), has not yet saturated (at 3000 hours), and may not saturate until recovery of electron damage is complete. If electron, and perhaps proton damage, to GaAs solar cells recovers totally with extended exposure to sunlight, the financial implications to the satellite community are immense. This effect must be confirmed by further laboratory and flight data.

NOTATION

Coverslide Coatings:

- ARR = antireflecting
- IRR = infrared (IR) reflecting
- UVR = ultraviolet (UV) reflecting
- BRR = blue-red reflecting (UVR on front; IRR on back)
- DSR = double-sided coated coverslides (coating contains both UVR and IRR in the same narrow-band-pass multilayer coating)
- SSR = single-sided coated coverslides (coating contains both UVR and IRR in the same narrow-band-pass multilayer coating)

INTRODUCTION

Five types of coverslide coatings (see notation above), designed for GaAs solar cells, have been tested as part of a NASA-sponsored, space-flight qualification for Blue-Red-Reflecting (BRR), multi-layer-coated, coverslides. Covered cells have been tested for degradation from the humidity, thermal, solar UV, and radiation environments representative of near-earth orbits (1). Coverslides and solar cells were characterized at each step of the test to identify the variation within the components and the reasons for changes observed with each step. As a control on the UV test, several covered INTELSAT-6 silicon solar cells (designated as I-6) were included.

Solar cells change their spectral response with particulate irradiation. In the case of GaAs cells, the response degradation is highest at the UV and IR ends of the spectrum. This is just where the BRR filters have their greatest impact; so, it was anticipated that GaAs cells with BRR filters might degrade less under irradiation than would the same cells without filters. Therefore, a set of solar cells from this test was irradiated to explore this hypothesis and to provide data for space-radiation-damage predictions. Since extended UV exposure of preirradiated GaAs cells has not been reported, we used available silicon solar cell data as the only potential guide.

¹ This paper is based on work performed at COMSAT Laboratories under contract from Goddard Space Flight Center. The final analysis and paper presented here was funded by Hi^π Consultants.

Silicon solar cells have demonstrated an effect called "Photo-Redegradation." This effect shows up in cells that have been electron irradiated and then exposed to light for an extended period: the cells degrade beyond the point that was measured right after irradiation. When first discovered and studied in depth (in the late '70s), the effect was determined to saturate rather quickly and to appear primarily in float-zone refined material. The procedure developed at the time was to anneal and stabilize the cells after irradiation with an overnight bake at 60°C under flood-lamp illumination.

In recent years, photo-redegradation has also been observed in crucible-grown silicon material, when solar cells have undergone UV testing after 1 MeV-electron irradiation and stabilization (2,3). With this background, the decision was made to run a comparison of irradiated and unirradiated GaAs solar cells in the same UV test to determine if a similar effect existed in this material as well. This paper describes the electron-irradiation and subsequent UV-exposure results.

ELECTRON IRRADIATION

One (1) MeV electron irradiations of the GaAs solar cells were carried out at the National Institutes of Standards and Technology. Cells were irradiated, in various combinations, at 2, 4, and 4x10¹⁴ e-/cm² to provide data points at 2, 4, 6, 8, and 10x10¹⁴ e-/cm² levels. Selected cells were removed from the test at different points to provide UV-irradiation test samples at the radiation levels more likely to be encountered in common missions (4-6x10¹⁴ e-/cm²). The primary purpose of the electron irradiation was to provide irradiated samples for the UV test. However, useful data for the particular GaAs/Ge cells provided for the test was anticipated. The total number of cells was limited; therefore, no coverslide group had many cells included. In addition to the normally covered cells in the test, some bare cells and cells with the coverslides on backwards were also included in an attempt to isolate damage effects and mechanisms in the electron- and UV-irradiated cells.

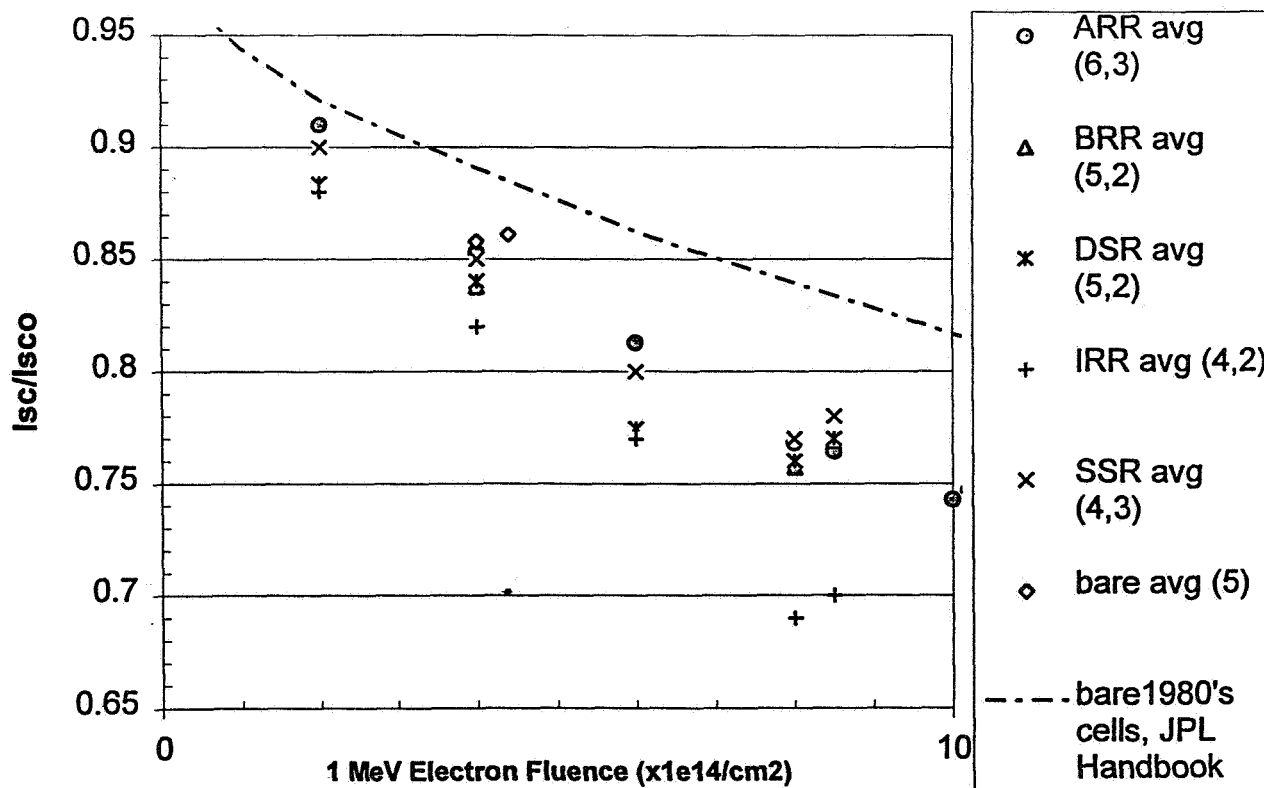


Figure 1 Relative Degradation of Short Circuit Current for 1 MeV Electron Irradiated GaAs Cells

Figure 1 indicates the effects of coverslide type on the electron irradiated cells. This plot compares the average degradation in short circuit current (I_{sc}) relative to the unirradiated cell current (I_{sc0}). The numbers beside each coverslide type indicate the total number of cells irradiated in each group and the number irradiated beyond 4×10^{14} e-/cm² respectively (e.g., 5,2 indicates 2 out of 5 cells were irradiated past 4×10^{14} e-/cm²). The data plotted at "4.5" and "8.5" $\times 10^{14}$ e-/cm² are values remeasured after a ~24 hour, 60°C, thermal anneal following the irradiations to 4 and 8×10^{14} e-/cm² respectively.

The dashed curve in Figure 1 is taken from the JPL Solar Cell Radiation Handbook, Addendum 1: 1982-1988 and represents bare GaAs/Ge solar cells from this period. The curve is quite different from the present covered-cell data, both in slope and degradation level, and thus indicates the danger of depending upon previous data for projections in a developing technology.

A basis for some of these differences might reside in the damage profile of covered cells versus that of bare cells. Back scattering of electrons from the surface layer (<5 μm thick) of silicon can reduce the damage in this surface layer by more than 20% compared to that in the subsurface material or in the surface layer with coverslide applied. In silicon solar cells, this has little effect, since bulk damage to the cell dominates and the damage in most of this region (which is 100-300 μm thick) is independent of coverslide. In GaAs solar cells, with a total active volume of less than 6 microns thickness and a higher average atomic number, the backscattering effect and the effect on cells are both greater. If a 30% effect is assumed for the backscattering in GaAs cells, the ARR covered cell data at $2E14$ is in better agreement with the JPL data for bare cells. However, the correction is inadequate at the higher fluences (the difference in slopes also eliminates a simple dosimetry error). Furthermore, bare cell results from this batch, irradiated at $4E14$, also were significantly lower than the JPL data.

Another reason, suggested for the higher than predicted electron-induced degradation, is the possibility that the Ge substrate is not inactive, as designed, and current may be collected from this region. With irradiation, loss of this Ge contribution to the I_{sc} would be greater than the loss from the GaAs. The problem with this explanation is that cells with IR reflectors would be less sensitive to this effect. As seen below, this is contrary to the experimentally observed results. Therefore, the full high-degradation slope of the present cells, cannot be attributed to dosimetry, to damage profile problems, or to the Ge substrate alone.

The second important feature of the data in Figure 1 is the difference between the IRR-coated coverslides and the others. The IRR data, which consists of one cell irradiated to 2 and 6×10^{14} e-/cm², two cells at 4×10^{14} e-/cm², and one cell at 4 and 8×10^{14} e-/cm², is internally consistent and clearly different from all but one individual cell in the 4 other groups of cells. Values of I_{sc} for the three cells, irradiated to 4×10^{14} e-/cm², are within ± 0.03 . Cell variation is therefore not enough to explain the difference with the other coverslide types. The data does not depend upon coverslide orientation. No explanation for the high electron degradation of the IRR coverslides relative to the other covered cells is offered at this time, beyond the possibility that the coatings used are susceptible to electron damage.

ULTRA-VIOLET DEGRADATION

The UV degradation results illustrated in Figure 2 are represented by the relative short-circuit current (UV test data divided by the initial data, I / I_0 , where I_0 is the data point taken at the beginning of the UV test) normalized against the relative I_{sc} of the control cells. The normalized relative currents ($I/I_0 / I_{sc}/I_{sc0}$) thus compensate for any changes in solar-simulator output intensity and spectrum experienced during a scan of the test and control cells. (The initial data point, I_0 , is artificially placed at 1.2 UVSH to provide a starting point on the log scale and to indicate that some UV exposure takes place during all of the initial measurements prior to beginning the UV test exposure.)

Most of the cells in this second of two UV tests had their coverslides reversed (and indicated in the figures by -r) to determine the effects of filtering the UV light through the coverslide (the DSR double-sided coverslides did not change with inversion), therefore relative values, not absolute values of change are to be considered in the analysis.

The most unexpected feature of Figure 2 is the recovery in I_{sc} experienced by the pre-irradiated cells. Since the unirradiated cells (no-rad) follow the expected UV degradation profiles, recovery of the irradiated GaAs/Ge cells is neither experimental error nor is it associated with the coverslides. The DSR and SSR cell results in the figure clearly show a reproducible recovery of the electron-irradiated cells relative to the non-irradiated cells during extended UV exposure. The data indicate that the extended UV exposure anneals the electron damage at about 1% per 1000 hours. Recovery curves therefore are generated by adding the UVSH times 10^{-5} to the unirradiated cell values at a given time (e.g., at 1000 UVSH, add 0.01). In figure 3, curves are provided to indicate the predicted level of recovery in I_{sc} for the pre-irradiated cells.

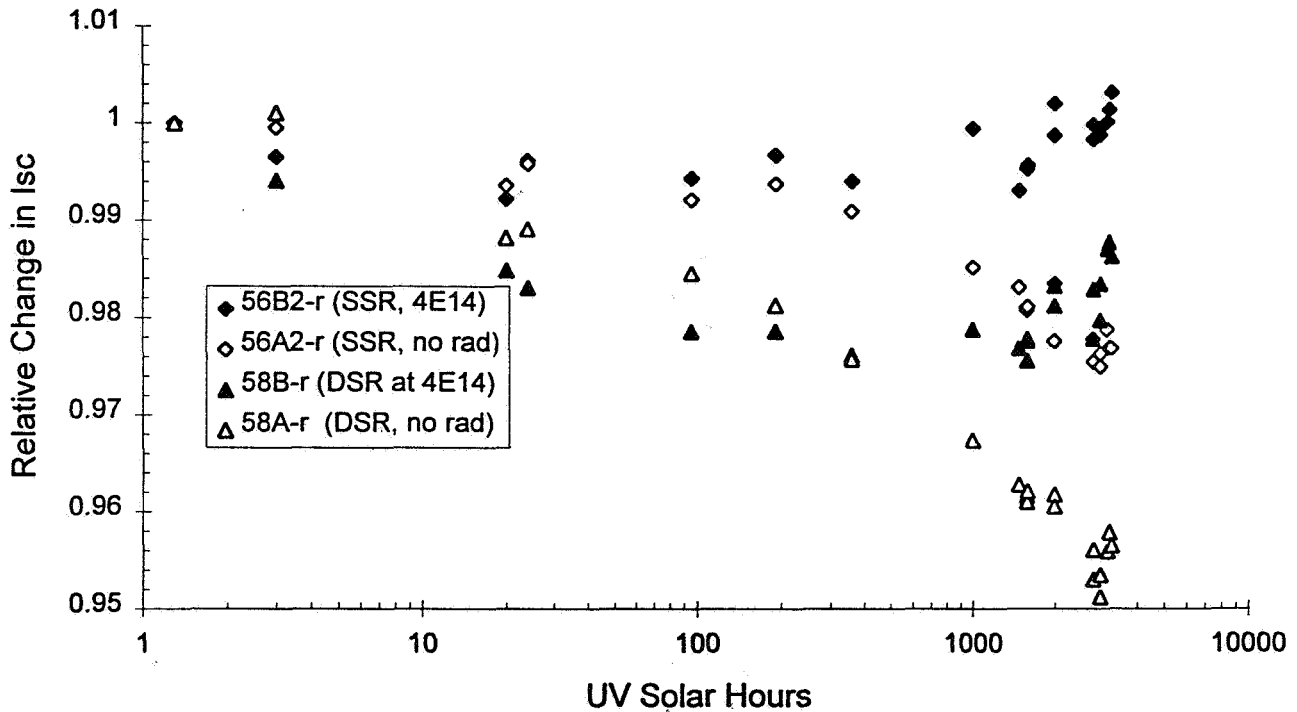


Figure 2. UV Degradation and Electron-Irradiation Recovery for SSR and DSR Covered GaAs Solar Cells in Test 2.

The UV degradation results in Figure 3 are those of Figure 2 with the addition of recovery curves and BRR cells from the same test. This time, the unirradiated cell data are represented by fitted curves, rather than by data points, to remove some clutter. UV degradation control cells were provided by inclusion of INTELSAT-6 cells that have been reproducible and well-characterized in past UV tests.

It is clear that qualitatively the pre-irradiated DSR and SSR covered cell data in Figure 3 follow the "DSR + recovery" and "SSR + recovery" curves quite well. However, the irradiated BRR cells fit the "GaAs + recovery" curve, rather than the expected "BRR + recovery" curve. The "GaAs + recovery" curve assumes only recovery from electron irradiation and no UV degradation (the predicted curve for BRR covered cells would be close to that of the irradiated "SSR + recovery" curve, since the BRR and SSR UV degradation curves are so close). The high peak values (~ 1.025) are unexpected for a recovering irradiated-BRR cell since more than 2% UV degradation has been observed in both Test 1 and Test 2 for unirradiated-BRR cells. These cells therefore appear to have an unusually high recovery from electron irradiation (4-5% at 3000 UVSH, rather than 3%).

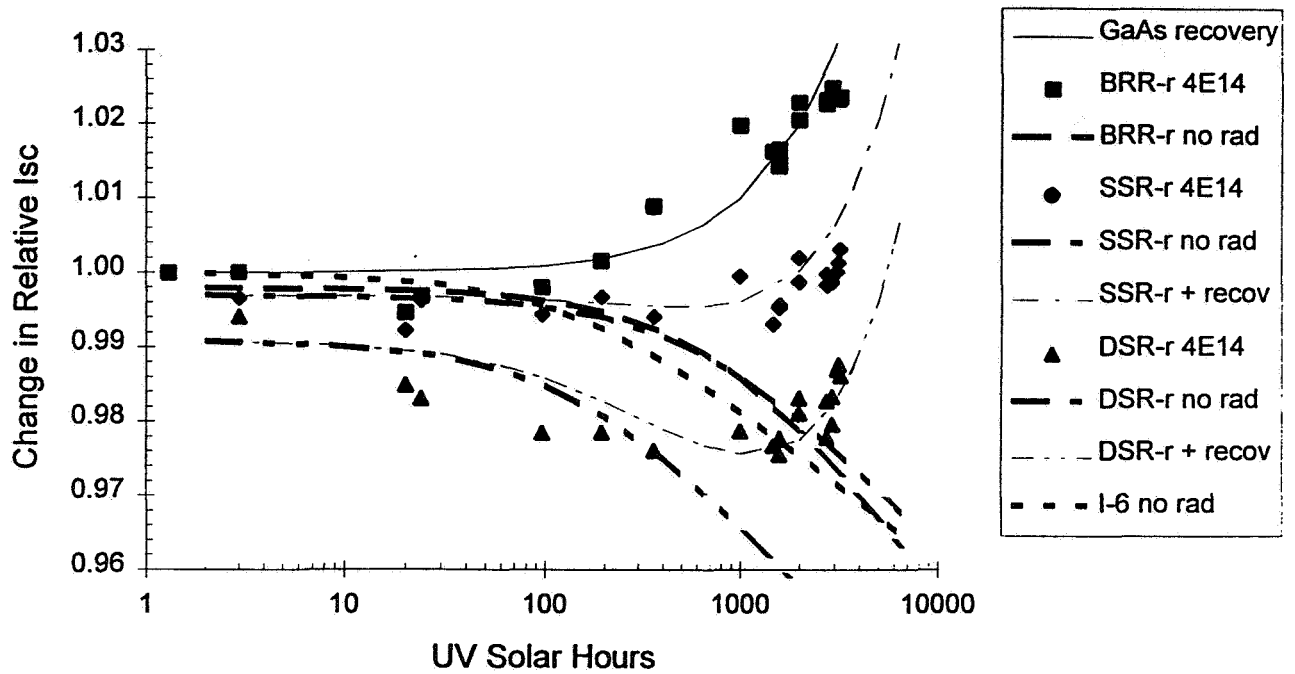


Figure 3. UV Degradation and Electron-Irradiation Recovery for BRR, SSR, and DSR Covered GaAs Solar Cells in Test 2.

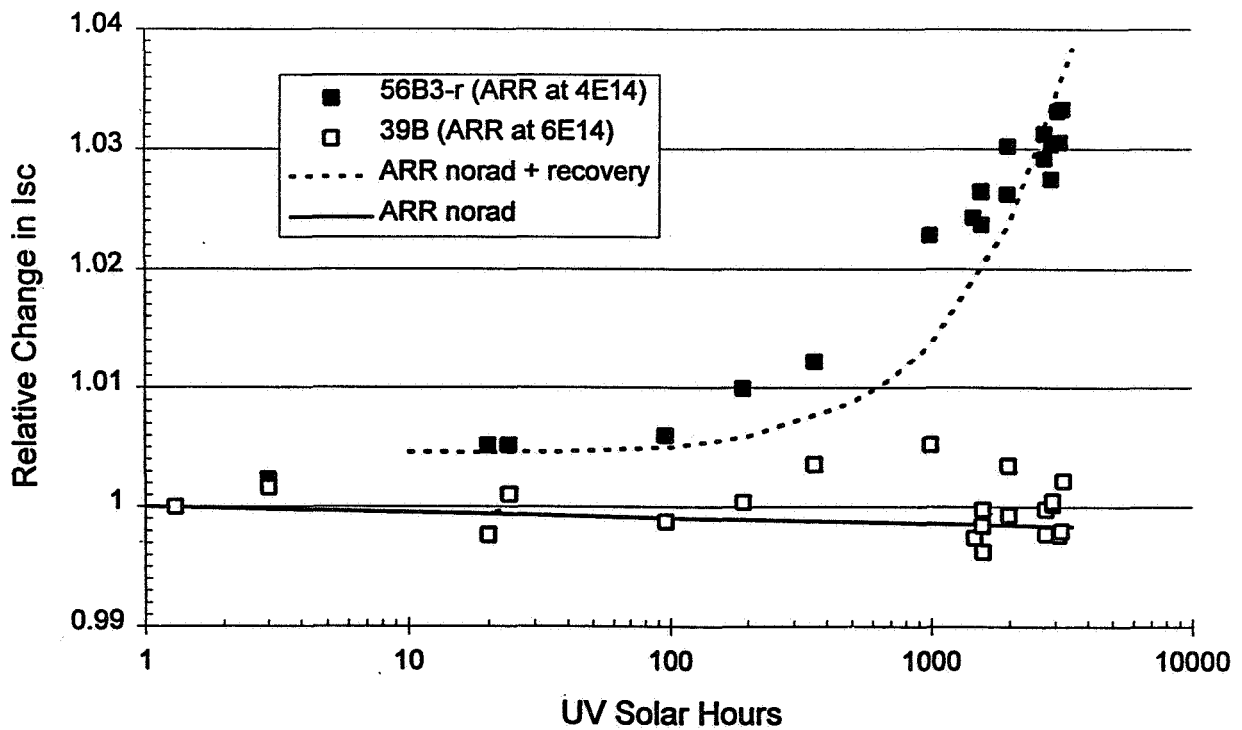


Figure 4. UV Degradation and Electron-Irradiation Recovery for ARR Covered GaAs Solar Cells in Test 2.

Figure 4 displays the ARR covered cells in the same format as used in Figure 3. The unirradiated ARR covered cell data (from Test 1) shows little UV degradation (Reference 1 data suggests 0.2% loss for a set of ARR cells). The ARR covered cell (with reversed coverslide) irradiated to $4E14$ 1 MeV electrons shows a recovery characteristic of those in Figure 2. The fit is even better if the "ARR + recovery" curve is raised by ~ 0.005 . This offset could be from statistical variation in the first measurement; or, it could be real and a result of a rapid UV induced change in refractive index of the optically mismatched system of adhesive and coverslide AR coating (matched to air, not adhesive).

While the "ARR at $4E14$ " data in Figure 4 are not fitted as well to the "ARR + recovery" curve as were the DRR and SSR data, the pattern is consistent with the estimated recovery formula. The "ARR at $6E14$ " cell cannot be forced to fit the recovery model. This cell starts the expected recovery in Isc beyond 100 UVSH; however, the "ARR + $6E16$ " data deviates dramatically from the recovery curve beyond 1000 UVSH hours². This is clearly not the behavior identified in the earlier cells. The fact that the two ARR cells in Figure 4 had their coverslides applied oppositely would not account for the observed difference in recovery. The 50% higher electron fluence of the one cell is not expected to be significant; yet, the same effect is seen in Figure 5 for the IRR cells.

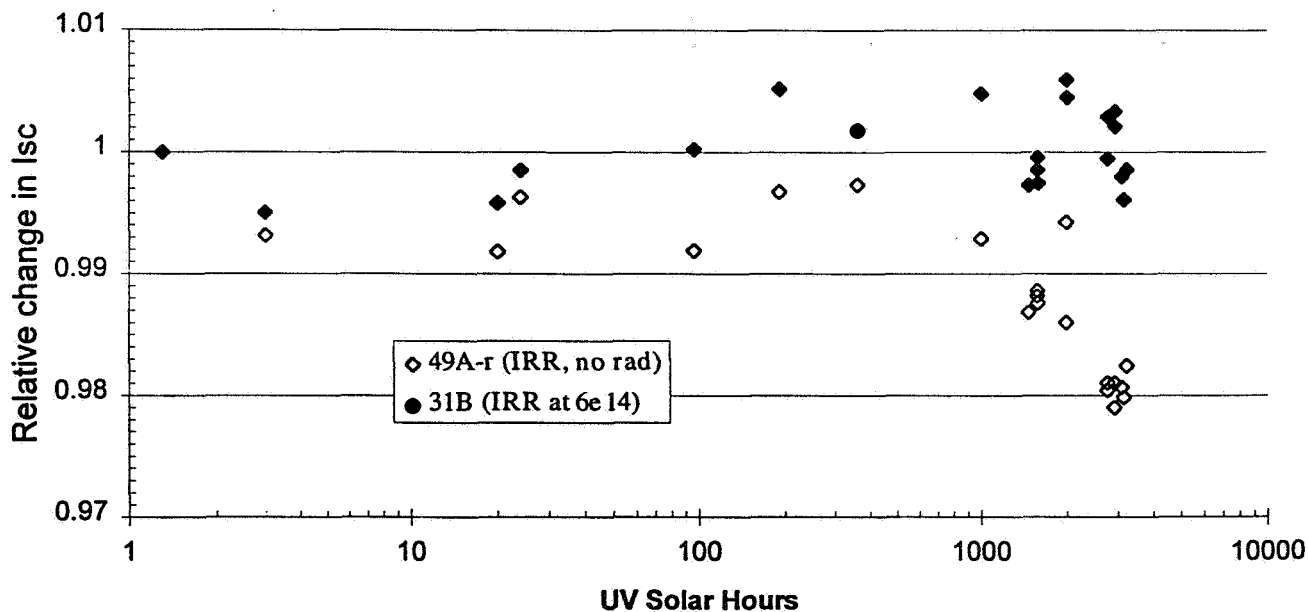


Figure 5. UV Degradation and Electron-Irradiation Recovery for IRR Covered GaAs Solar Cells in Test 2.

The irradiated IRR covered cell in Figure 5, with correctly oriented coverslide at 3000 UVSH, shows only a 0 - 1.5% increase in Isc relative to the unirradiated IRR-covered cells in Test 11. In that test, the unirradiated IRR data varied between 0 and 1% below the initial value. The "IRR at $6E14$ " cell mimics the "ARR + $6E14$ " data of Figure 4 in that it displays an initial recovery followed by a drop in Isc recovery beyond 1000 UVSH. Thus the 50% increase in prior electron-irradiation fluence appears to be significant. This fluence dependence is unexplained at this point; unless the higher electron irradiation of the GaAs begins formation of a different defect type that predisposes the material to subsequent UV degradation.

The unirradiated IRR cell in Figure 5, with inverted coverslide, shows a significantly higher UV degradation than do the cells with correctly oriented IRR coverslides in Reference 1 (2% vs. 0 - 1% at 3000 UVSH). If this result is a consequence of the unfiltered UV exposure to the multilayer coating, then the implication is that these layers are more sensitive to energetic radiation (UV with $\lambda < 0.35 \mu\text{m}$ or 1 MeV electrons) than to the lower energy

² The deviation begins earlier, if the 1000 UVSH data is lowered by 0.5%, or later, if the data cluster at 1500 UVSH is raised by 0.5%. Such a potential offset in the data points is seen in all of the figures and would be a consequence of the normalization.

UV that passes through the CMG coverslide. This sensitivity to energetic radiation could explain the higher loss in I_{sc} of the IRR-covered cells from the electron irradiation than that observed for the other cells in the same test.

The plotted data in Figures 2-5 include a correction, mentioned for Test 2, in the appendix of Reference 1, that consists of reducing the initial control cell data by 1%. Without this correction, the normalized values shown (other than the initial values) would be 1% lower. Figure 6 displays the unilluminated control cells on a linear plot to emphasize the later portion of the test where a deviation is noted between the different cell types. Since the cell I_{sc} values are self normalized, the ~1% offset in the initial point raises all of the other data points toward 1.01. The 100% line is an average of the GaAs control cell data beyond the initial point.

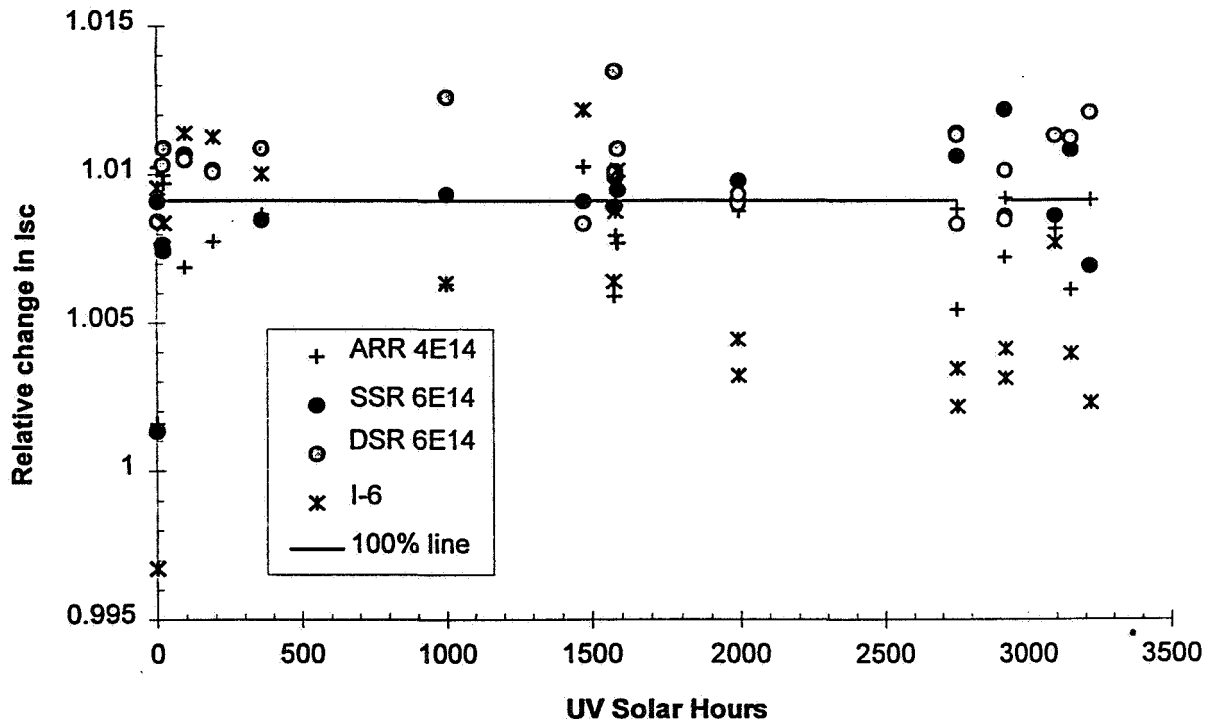


Figure 6. Self-Normalized Control-Cell Data for Test 2 of the Experiment

The GaAs control cells have been electron irradiated, but not exposed to UV. An important question concerns the long-term recovery of these cells when exposed to 40°C and vacuum but no intense light beyond the short periods of I-V test measurements. Examination of the data in Figure 6 indicates that the I-6 cell has degraded relative to the GaAs control cells. (For this reason, it was removed from the control cell average.) However, the "ARR at 4E14" cell has degraded less than the "DSR and SSR at 6E14" control cells. Initially, the I-6 degradation had been attributed to scattered UV light affecting the sensitive silicon cell optical stack. However, the ARR cell is the least UV sensitive of the GaAs cells. Therefore, scattered UV could not be a valid explanation. Recovery of electron damage is greater for the 4E14 cells than for the 6E14 cells after 1000 UVSH. Data at the lower UV exposure points is too confused by other effects to allow comment. There is no other data on thermal-vacuum recovery of these cells, so this must be high on the list of possibilities to be considered.

If thermal vacuum recovery is real for the electron-irradiated GaAs cells, then, the normalization procedure should be based on the I-6 cell rather than the irradiated GaAs cells in Figure 6. the consequences of such a renormalization would be an increase in I_{sc} of all the data by ~0.5% at 2-3000 UVSH. Such a change would generally improve the fit to the recovery model, reduce the apparent UV degradation of unirradiated cells, and result in a saturation, rather than a turnover, in the 6E14 cell data beyond 1000 UVSH. It would also indicate that the recovery of electron damage to GaAs cells will occur with or without light; but, it will be accelerated by the presence of photo-generated minority carriers.

DISCUSSION

While variations exist in the individual cells and coverslides of this program and the sample size is small, detailed analysis of the components and combined structures has allowed an understanding of the loss mechanisms to be expected from the space environmental effects. Nevertheless, there are two things to consider in this postulation of photo-recovery for electron irradiated GaAs solar cells

1. The measured electron-induced damage in the GaAs/Ge solar cells involved in this test was higher than expected.
 - The degradation in I_{sc} of the solar cells in this test was significantly higher than that seen in prior data (>14% vs. ~11% at 4×10^{14} 1 MeV electrons/cm² and >22% vs. 16% at 8×10^{14} /cm²).
 - The covered cells degraded further than did the bare cells of this test (2 - 8% more in I_{sc} / I_{sc0} at 8×10^{14} /cm²).
2. Since the test from which the photo-recovery data has been extracted was not designed with this study in mind, the data is limited and statistics are poor. Nevertheless:
 - A significant photo-recovery effect has been seen in 5 out of 7 electron-irradiated cells that were exposed to extended UV illumination. (The other two cells, that displayed less recovery, had been exposed to a 50% higher radiation fluence.)
 - None of the many unirradiated cells in the two tests showed any recovery beyond their initial values with extended UV exposure.
 - Three out of three irradiated GaAs control cells, that were exposed to the same handling, measurements, and thermal-vacuum environment (but not to the UV source), showed much less recovery. Light is therefore critical to the rate and perhaps to the magnitude of the effect, but not necessarily the only source of the effect.

In summary:

- The initial electron degradation for I_{sc} of these recovering cells was ~15%.
- No cells from this batch showed >1% recovery after irradiation when exposed to a floodlamp and 60°C for ~24 hours.

The long-term photo-recovery is a significant portion of the total electron damage (~3 out of 15%). Nevertheless, it has so far only brought the cells back to the level observed in the JPL irradiated GaAs solar cells.

A question remains: are we seeing a recovery of the basic GaAs radiation damage or only a recovery of the excess damage? Longer-term testing and analysis will be required to properly address this question and others on the generality of the effect.

REFERENCES

1. A. Meulenber, "Space Qualification of UV and IR Reflecting Coverslides for GaAs Solar Cells," Proc. of the 14th Space Photovoltaic Research and Technology Conference, NASA / LeRC, Cleveland, OH, October 24-26, 1995
2. A. Meulenber, "UV Testing of INTELSAT VII, VIIa, and VIII Solar Cells," Proceedings of the 13th Space Photovoltaic Research and Technology Conference, NASA / LeRC, Cleveland, OH, June 14-16, 1994
3. A. Meulenber, "UV Testing of Solar Cells; Effects of Anti-Reflective Coating, Prior Irradiation, and UV Source," Proceedings of the 12th Space Photovoltaic Research and Technology Conference, NASA / LeRC, Cleveland, OH, 1992

510
AN-50401

INITIAL RESULTS FOR THE SILICON MONOLITHICALLY INTERCONNECTED SOLAR CELL PRODUCT[†]

L. C. DiNetta, K. P. Shreve, J. E. Cotter, S. Sun, and A. M. Barnett
AstroPower, Inc.
Newark, DE 19716-2000

ABSTRACT

This proprietary technology is based on AstroPower's electrostatic bonding and innovative silicon solar cell processing techniques. Electrostatic bonding allows silicon wafers to be permanently attached to a thermally matched glass superstrate and then thinned to final thicknesses less than 25 μm . These devices are based on the features of a thin, light-trapping silicon solar cell: high voltage, high current, light weight (high specific power) and high radiation resistance. Monolithic interconnection allows the fabrication costs on a per Watt basis to be roughly independent of the array size, power or voltage, therefore, the cost effectiveness to manufacture solar cell arrays with output powers ranging from milliwatts up to four watts and output voltages ranging from 5 to 500 volts will be similar. This compares favorably to conventionally manufactured, commercial solar cell arrays, where handling of small parts is very labor intensive and costly. In this way, a wide variety of product specifications can be met using the same fabrication techniques. Prototype solar cells have demonstrated efficiencies greater than 11%. An open-circuit voltage of 5.4 volts, fill factor of 65%, and short-circuit current density of $28\text{mA}/\text{cm}^2$ at AM1.5 illumination are typical. Future efforts are being directed to optimization of the solar cell operating characteristics as well as production processing. The monolithic approach has a number of inherent advantages, including reduced cost per interconnect and increased reliability of array connections. These features make this proprietary technology an excellent candidate for a large number of consumer products.

INTRODUCTION

The monolithically interconnected solar cell (MISC) array benefits from the advantages afforded by thin solar cell design technology. AstroPower has been developing thin, electrostatically bonded silicon solar cells for a variety of applications. Specifically, the advantages and benefits of any thin solar cell technology can be summarized as below.

ADVANTAGES

- X Minority carrier diffusion length required to be two times the layer thickness permitting efficient operation from poor quality or degraded lifetime material.
- X The thin device design opportunity allows high open-circuit voltage.
- X Light trapping leads to good light absorption.
- X Good carrier collection leads to high short-circuit current.

RESULTING IN

- ✓ High Specific Power
 - ✓ High Efficiency
 - ✓ High Degree of Radiation Tolerance
-

In addition to the previously stated advantages, the integration of the monolithic interconnection technique allows for a number of inherent benefits. These are enhanced reliability of interconnections, lower I^2R losses, and minimization of the impact of shorts and opens in a deployed array.

[†] This research is supported by BMDO and managed by USASSDC through a current SBIR program, contract #DASG60-95-C-0007.

HIGH PERFORMANCE DESIGN

This thin electrostatically bonded solar cell structure incorporates a number of features that will enhance its efficiency. They include: a thin base layer, high base doping, light trapping and front and back surface passivation. The thin base layer can be highly doped thereby increasing the output voltage without paying a penalty in collection efficiency; i.e. current is maintained while the voltage is increased. This is due to the reduced dependence of collection efficiency on minority carrier lifetime for thin silicon solar cells. This same effect reduces the solar cell array's dependence on lifetime reducing damage caused by radiation. The degradation characteristics of thin silicon solar cells are expected to be comparable to GaAs and InP solar cells.

The back of the thinned silicon solar cell is micro-machined using an orientation-dependent etch to produce random pyramids in the surface. A back surface reflector is then deposited, so that the long wavelength light that enters the silicon is totally internally reflected by the textured back surface and planar front surface. It is possible to obtain optical thicknesses in the thin silicon that approach twenty times the actual thickness. Light trapping has been demonstrated in thin silicon structures with textured back surfaces [1, 2]. Light-trapping is incorporated into the array structure by the use of randomly-oriented pyramids etched into the back surface. The pyramids will cause light incident on the back surface to be reflected oblique to the plane parallel with the front. This will trap weakly absorbed light by total internal reflection at the top surface. Light-trapping allows the effective thickness to be much thicker than the actual thickness of the device. A reflective metal such as gold or silver evaporated onto the back surface will make the back surface nearly 100% reflective.

Another contribution to a high open circuit voltage is from the reduced recombination volume of the thin solar cell. This will require front and back surface passivation, which can be achieved with a thermal oxide on the front of the device, and a PECVD silicon nitride or silicon dioxide layer on the back. Fill factor improvements can be achieved because low resistivity silicon base layers can be employed in this solar cell design. This reduces the series resistance of the base layer in comparison to the high resistivity base layers currently in use for silicon space solar cells.

Surface passivation is achieved by forming a thermally grown silicon dioxide layer on the front surface before the electrostatic bonding step. Also, a thermal oxide is grown on the back side, since the glass/silicon laminate can withstand high temperatures. Passivating silicon oxides can also be deposited onto the back by plasma-enhanced chemical vapor deposition (PECVD), although thermally grown oxides are preferred.

Electrical isolation of the array elements is achieved by an orientation selective chemical etch process called "V-groove" etching. The groove is etched completely through the silicon layer after it has been bonded to the glass and thinned to a nominal thickness of 30 microns. The glass superstrate provides both mechanical support and electrical isolation.

Re-interconnection is provided by forming ohmic contacts on the side-walls of the V-grooves, which have been formed so that the base-layer of one array element is exposed on one side of the V-groove and the emitter of the adjacent array element is exposed on the other side of the V-groove. Thus, by depositing a metal layer in the groove, series interconnection is achieved. The wrap-around emitter is formed by solid-state diffusion after the bonding, thinning and V-groove processes. Utilizing a high-temperature process compatible glass superstrate is critical to forming the wrap-around emitter.

Parasitic losses are minimized by the device design. All contacts are formed on the back side of the solar cell array, therefore losses due to shading are minimized and can approach zero. Shunt conductance losses, which have been characteristic of previous monolithic array designs, will also be minimized by careful selection of contact metals and by complete element-to-element isolation provided by the V-groove and glass superstrate. Series resistance losses will be minimized by proper selection of the device geometry or by the incorporation of grid lines on the emitter and/or base. Modeling predicted losses of less than 5% due to shading and series resistance losses for optimized array geometries. (Shading and series resistance losses of production solar cells are typically greater than 10%.)

HIGH RADIATION TOLERANCE

Radiation damage is the primary degradation mechanism of silicon solar cells deployed in space and results in reduced performance with time and depends on the particular orbit and exposure level. The gradual degradation in solar cell performance is due to the reduction in the minority-carrier lifetime that results from cumulative damage to the crystal lattice. One approach to increasing silicon solar cell radiation tolerance has been to reduce the silicon base thickness as much as possible. Although silicon solar cells formed on free standing, thinned wafers are presently available, their minimum thickness is limited to 65 μ m due to handling and yield concerns.

Improvements in the radiation tolerance of silicon solar cells can occur if the active layers are thinner (20-35 μ m).

Modeling and experimental data showing the efficiency degradation of candidate space solar cells as a function of 1 MeV electron fluence is shown in Figure 1. Thin, light trapped, silicon solar cells have a theoretical radiation resistance similar to InP solar cells and better radiation resistance than GaAs/Ge solar cells. Experimental and theoretical values for a 4-mil thick silicon solar cell are shown to verify the model.

Because the absorber (base) layer is very thin, the solar cells will be extremely insensitive to changes in minority-carrier lifetime caused by irradiation. The efficiency of the array is roughly independent of the minority-carrier diffusion length until it is less than the thickness of the absorber layer. For silicon base layers on the order of 25 μ m or less, this is equivalent to a minority-carrier lifetime of 250 nanoseconds (as-grown, non-irradiated silicon typically has a lifetime greater than 10 microseconds). In contrast, present high-performance silicon solar cells require minority-carrier lifetimes on the order of 1 millisecond. This thinned silicon array design reduces the minority-carrier lifetime requirement by more than a factor of one-thousand. This design will substantially increase radiation tolerance and significantly extend the useful life of silicon solar cells deployed in space.

RELIABILITY

Due to the higher voltage attainable by the monolithically interconnected solar cell the I^2R array losses will be minimized for any bus voltage when compared to conventional silicon solar cells. Utilizing a higher voltage also results in a weight savings at the

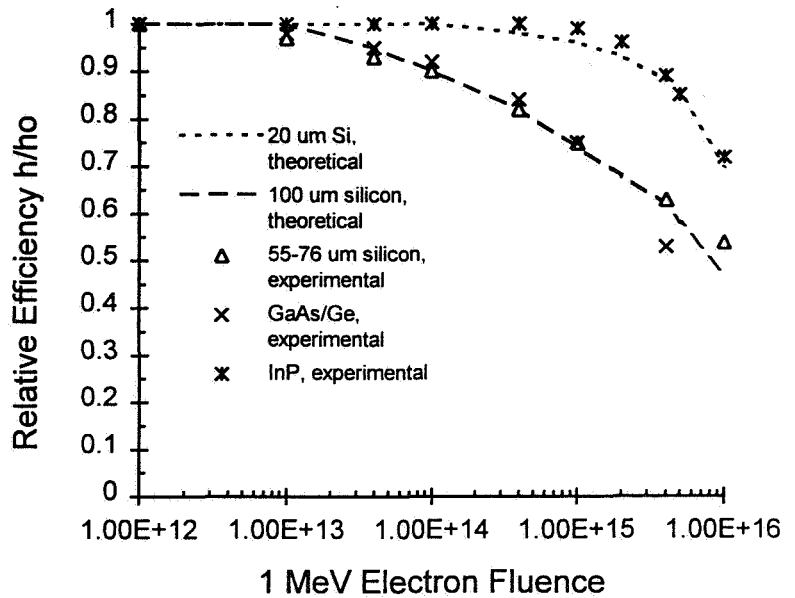


Figure 1: Radiation resistance of space solar cells [3, 4, 5].

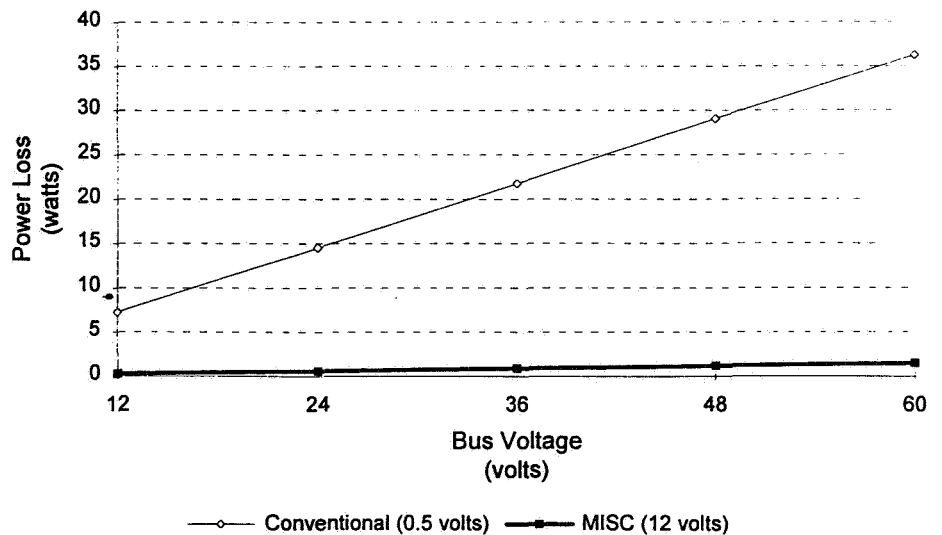


Figure 2: Solar cell voltage effect on power loss.

array level from the smaller quantity of high current carrying wire necessary for solar cell interconnection and the reduced dependence on stringing of low voltage devices to achieve the needed bus voltage.

This monolithic interconnection technique offers several additional advantages compared to conventional array interconnection technologies for space applications. The reliability of the array is enhanced by reducing the complexity of the interconnections [6], and monolithically interconnected solar cell arrays offers potentially higher yield compared to conventional array manufacturing processes such as welding [7] or soldering. Typical yield reductions in standard array interconnection are the result of breakage due to either mechanical or thermal stress.

Another reliability benefit from the high voltage device is the resultant lower power loss from shorts, opens, and impact damage at the array level. If the monolithically interconnected solar cells are operated either at the bus voltage or some factor of the bus voltage, loss of a single solar cell within a string will have minimal impact on the array power generation when compared to typical silicon solar cells. This is shown in Figure 2 using, for instance, a nominal 0.5 volt silicon solar cell and a 12 volt monolithically interconnected silicon solar cell. As is shown the power loss is quite dramatic due to the loss of a string of devices as compared to a single or a few devices when the string of devices becomes disabled.

EXPERIMENTAL RESULTS

The long term goals of this program are to develop and manufacture lightweight, radiation hard, high performance, high voltage solar cells for advanced space power systems and the terrestrial market. Results from initial prototype solar cell testing are discussed in the following sections.

I-V CHARACTERISTICS

Device #56 is a 27-micron thick device that is electrostatically bonded to an alkali free high temperature Corning glass. This device consists of twelve monolithically series interconnected segments. The I-V curve is shown in Figure 3.

Fill factor is limited to 61.5% by the high series resistance and low shunt resistance. Shunt resistance is approximately 20 ohm/cm² and has limited both J_{mp} and V_{mp} of this device. High series resistance is the other limiting factor of this device. Figure 4 shows the gray I-V response. It is evident from this curve that the device is largely limited by the low shunt resistance. The total series resistance of #56 can be approximated from the slope of the light I-V curve in the forward bias region near V_{oc} . It is estimated at 150 ohms total for this device and is the major contributor to the low fill-factor. This resistance is made up of an emitter component, a bulk or base component and a metallization component. The modeling of this structure indicates that both the emitter and bulk components contribute significantly to the high overall R_{series} value. Lower resistivity bulk material is needed, in addition to a lower R_{sheet} emitter value. The device operation will be optimal when bulk material resistivity is approximately 0.3 ohm-cm, and emitter R_{sheet} value is approximately 45 - 50 ohms/square.

A second device, #28, is 28-microns thick and is processed similarly to the previous

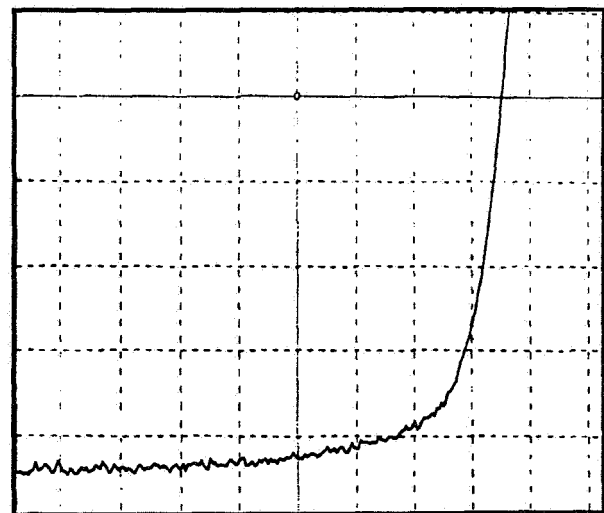


Figure 3. Light I-V curve #56.

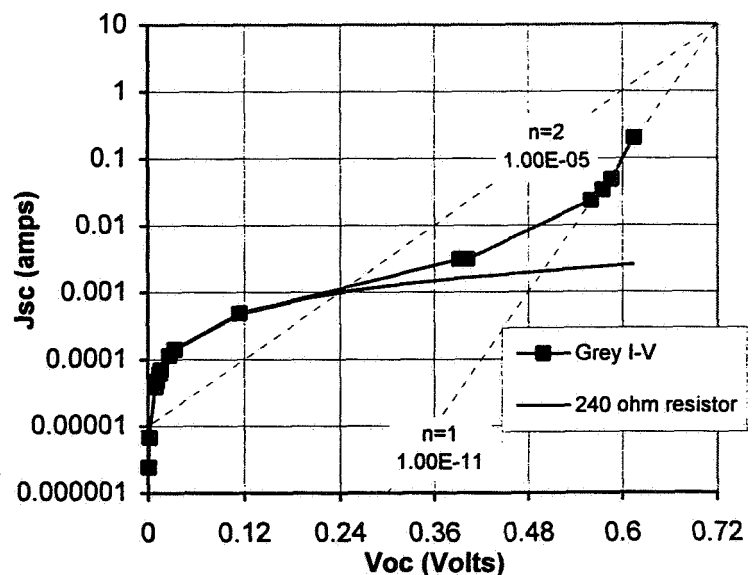


Figure 4. Gray I-V curve (#56).

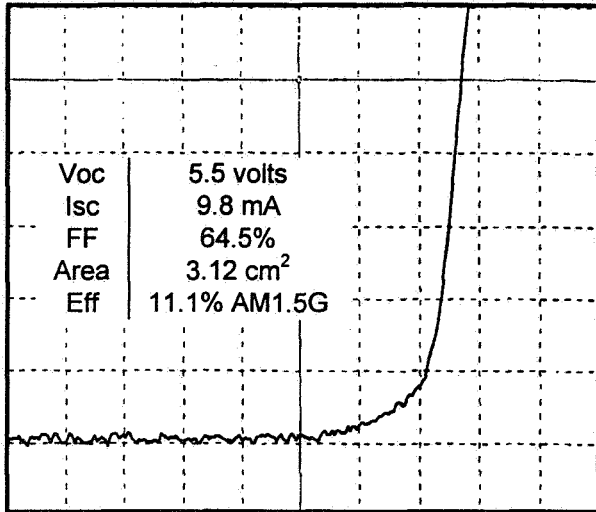


Figure 5. Light I-V response (28)

solar cell. Refer to Figure 5 for the light I-V characteristics and Figure 6 for the gray I-V characteristics. Fill factor has improved to 64.5% due to reduced I²R losses in the base.

Performance of #28 shows improvements over #56 which can be attributed to the use of more heavily doped bulk material. The bulk resistivity is approximately optimal at 0.3 ohm-cm, but the emitter R_{sheet} is nearly the same as #56 at 130 ohms/square, which is nearly three times the ideal value. The gray I-V curve, Figure 6, indicates good shunt resistivity (23k ohms total) and reasonable J_{01} and J_{02} values of 5×10^{-12} and 1×10^{-7} , respectively, for a silicon diode. The series resistance has improved to 110 ohms. Total series resistance is still limiting the fill-factor of this device, and improvements will be gained with the use of more heavily doped emitters.

SPECTRAL RESPONSE

Quantum efficiency measurements, Figure 7 and 8, indicate reasonable material quality after the non-optimized high temperature post bond processing. The silicon-glass laminate is subjected to a high temperature processing step and stress related degradation of the material quality would be expected to degrade the blue response of the solar cell. Previous work with electrostatically bonded silicon solar cells has shown that excellent blue response can be attained and that there are no detrimental effects from the bonding step itself or at post bond processing temperatures below 900°C. Experiments are being conducted to reduce the temperature of this processing step and to improve the front surface passivation which should result in significantly improved blue response.

At greater than 500 nm, both of these devices compare favorably to control samples fabricated on the same quality starting material. Furthermore, the effective diffusion length, which is derived from the long wavelength response is 195 microns and 93 microns. This demonstrates a light trapping coefficient of greater than 7 and 3 respectively. Inconsistencies in the effective diffusion length can be remedied by optimizing the solar cell processing and carefully controlling the starting material specifications as related to specific process parameters.

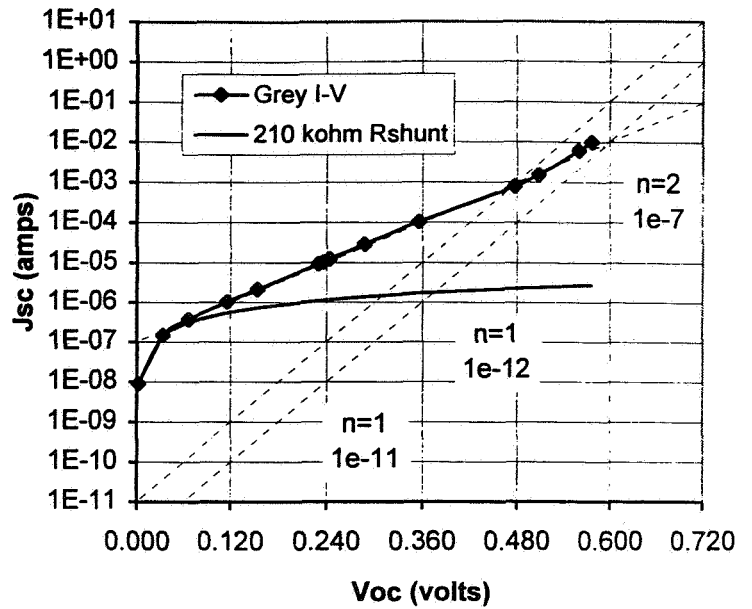


Figure 6. Gray I-V curve (FZ28).

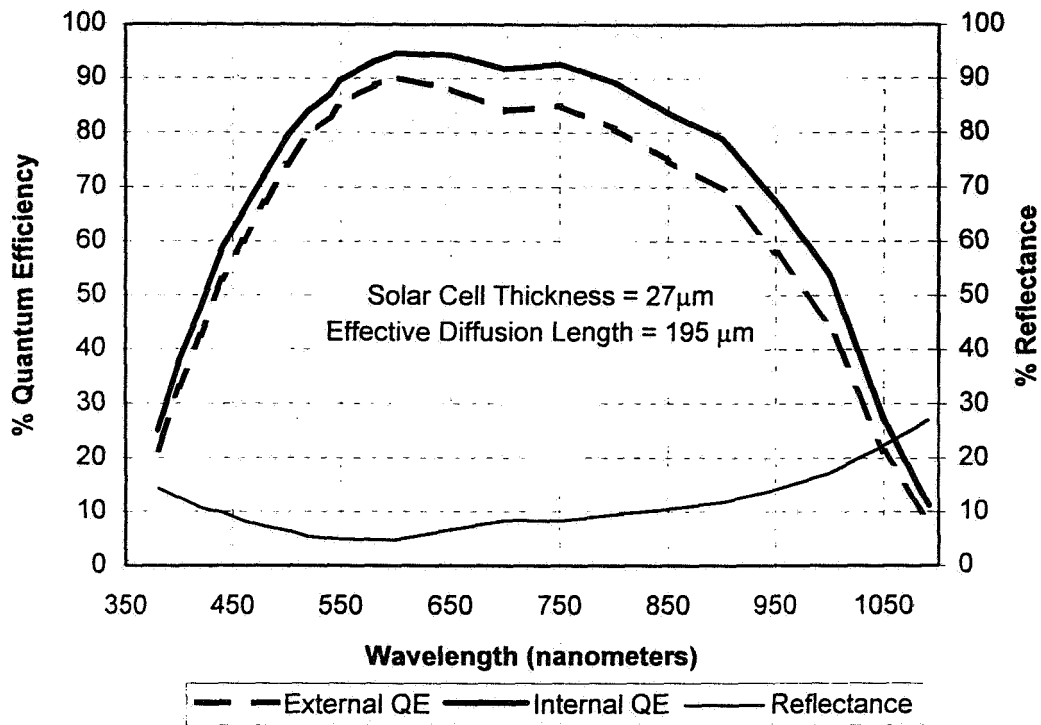


Figure 7. Spectral response curves of MISC device #56

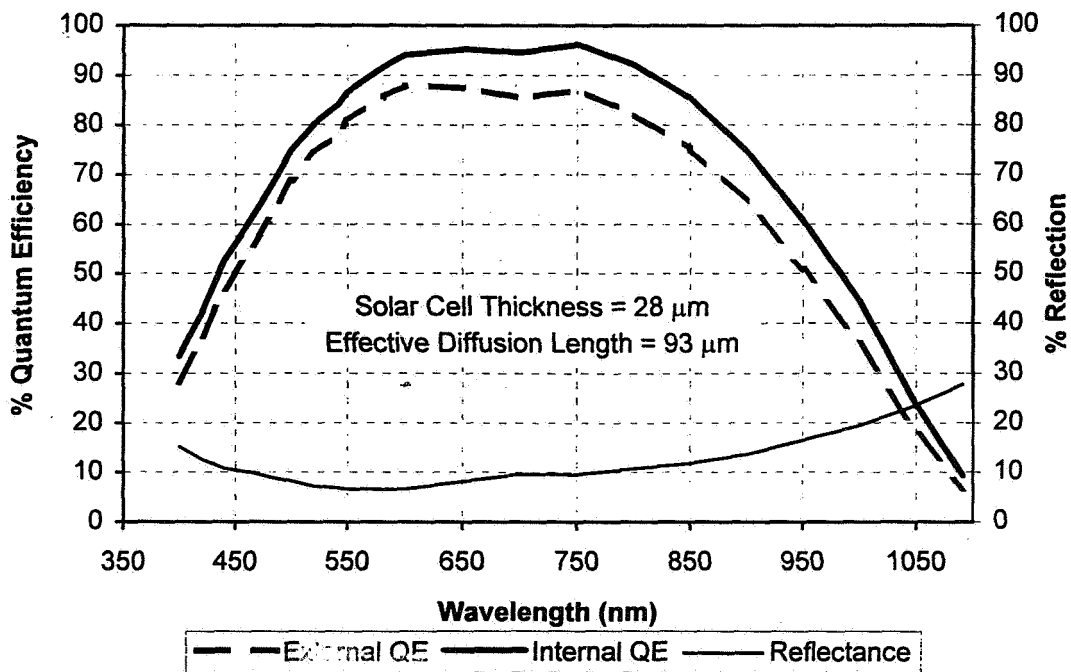


Figure 8. Spectral response curves of MISC device #28

HIGH TEMPERATURE SURVIVABILITY

High temperature survivable glass/silicon laminates are necessary to enable post bond processing and long term operational stability. Upper temperature survivability limits have been evaluated for electrostatically bonded silicon to Corning's 1737 glass structures. Interfacial degradation has been observed at approximately 70°C below the specified softening point of the specified glass. The upper limit of the 1737 glass bonded to silicon is approximately 900°C and is related to the softening point of the glass. High temperature survivability of Pyrex glass bonded to silicon was found to be approximately 750°C. Both of these upper limits were approximately 70°C below the accepted softening point values for the glasses. In order to increase the temperature survivability of the glass bonded silicon, a higher softening point glass was formulated specifically for this work and evaluated. This glass formulation was used to electrostatically bond to silicon and has shown good survivability to 900°C. The projected upper temperature survivability of this bonded glass is approximately 950°C.

High temperature survivability and optical transmission tests were conducted using various commercially available space quality ceria doped glasses and other glass compounds including a custom formulated ceria doped glass. Ceria doping is important in the space environment to prevent darkening of the solar cell coverglass due to ionizing radiation over the projected lifespan of the satellite. The ceria, although imparting some initial tint to these glasses, makes them more stable and inhibits the formation of color centers.

A high temperature survivable, custom ceria doped glass was formulated successfully by Sem-Com for our experiments. This glass has been successfully electrostatically bonded to silicon and has survived processing to 900°C without optical degradation. It has a softening point of 1050° C which is 75° C higher than the Corning 1737 glass we used to successfully fabricate the 10.3% and 11.0% devices. The TCE (thermal expansion coefficient) of this glass is more closely matched to silicon at $33.5 \times 10^{-7}/^{\circ}\text{C}$ than the 1737 glass which has a TCE of $37.8 \times 10^{-7}/^{\circ}\text{C}$. This should provide for reduced electrostatic bond induced stress at the glass-silicon interface. Projected maximum processing temperature of this glass (electrostatically bonded to silicon) is approximately 975°C. Figure 9 shows optical transmission data test results of various glasses including the custom compound.

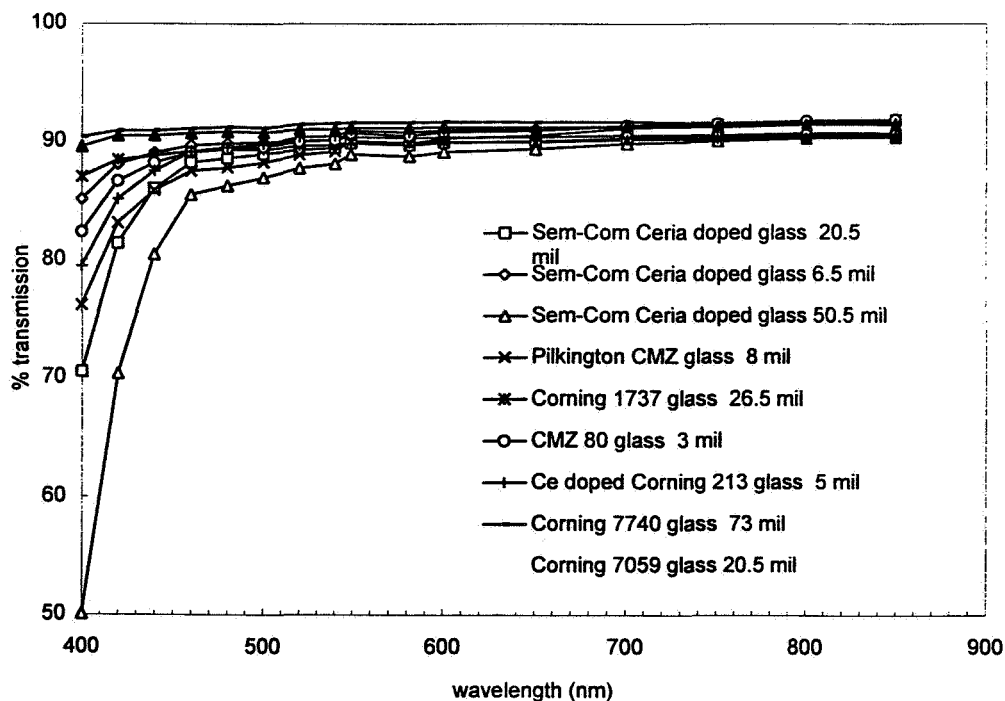


Figure 9. Optical transmission properties of various glasses

The change in output power of MISC device #CZ55 over 100 cycles from -80°C to +130°C was measured. Duration of one complete cycle was approximately seven minutes. I-V measurements were taken at 0 cycles, 25 cycles, 57 cycles, 76 cycles, and 100 cycles. No significant change in output power was found over the duration.

SUMMARY

A wide variety of military, space, and commercial markets can be served by this technology. In order to penetrate these markets with this new class of solar cell it is necessary to demonstrate the feasibility of solar cell array products that will be cost-effective, lightweight, high power, high voltage, and radiation resistant. The specific technical objective of the Phase II program is to fabricate a prototype of a lightweight, high-efficiency, monolithically interconnected solar cell array with the previously defined operating parameters.

The advantages of utilizing this technology are:

- X Higher Performance
 - ✓ High efficiency thin-device structure and light weight result in high specific power
 - ✓ Higher output power and better stability than amorphous or polycrystalline solar arrays
- X Higher Reliability
 - ✓ High reliability interconnections
 - ✓ Radiation hard
- X Higher Design Flexibility
 - ✓ Any size or voltage array can be fabricated cost effectively
 - ✓ High power, large area, cost-effective, array technology
 - ✓ Current and voltage configurable
 - ✓ Cost effective for high voltage in a small area
 - ✓ Arrays are practical for charging battery banks, including applications of voltages of 1 to 500 volts
 - ✓ Per-watt cost is independent of the number of interconnections and the array size
 - ✓ No labor/material cost as associated with cut and tabbed cells less than 100cm²

FUTURE PLANS

A preliminary process outline has been designed for production of large quantities of MISC devices for the terrestrial applications market. Various size wafers can be utilized and these cut to size in the final fabrication step to obtain the desired current/voltage output. This process has been cost analyzed and the initial results are quite favorable. AstroPower will direct market the space power applications. The use of high voltage solar cell arrays has been identified as a critical need for electric propulsion. This solar cell technology can enable electric propulsion for orbit raising missions with a considerable savings in launch cost. Secondly, the use of MISC technology for applications in concentrator solar cell arrays is very interesting due to the lower I^2R losses associated with the high voltage output of the solar cells as compared to high current. Presently AstroPower is preparing to deliver prototype MISC terrestrial and concentrator solar cells for integration into array products by other manufacturers.

REFERENCES

1. Rand, R.B. Hall, and A.M. Barnett, "Light Trapping in Thin Crystalline Silicon Solar Cells", 21st IEEE Photovoltaic Specialist Conference, May 1990 page 263.
2. Rand and P.A. Basore, "Light Trapping Silicon Solar Cells, Experimental Results and Analysis", 22nd IEEE Photovoltaic Specialists Conference, October 1991.
3. Tada, J.R. Carter, B.E. Anspaugh, and R.G. Downing, "Solar Cell Radiation Handbook", JPL Publication 82-69, 1989.
4. Weinberg, D.J. Brinker, C.K. Schwartz, and R.E. Hart, "Progress in Indium Phosphide Solar Cell Research," SPIE Indium Phosphide and Related Materials for Advanced Electronic and Optical Devices Conference, 1989, page 434.
5. Anspaugh, "Solar Cell Radiation Handbook, Addendum 1", 1989.
6. J.R. Woodyard, "Thin Film Cell Development Workshop Report", Proceedings of the Space Photovoltaic Research and Technology Conference, May 1991, page 48-1.
7. Smith and B.T. Cavicchi, "GaAs Solar Cell Circuit Assembly", 19th Photovoltaics Specialists Conference, New Orleans, May, 1987, page 448.

S17
IN-50402

MONOLITHICALLY INTERCONNECTED GAAS SOLAR CELLS: A NEW INTERCONNECTION TECHNOLOGY FOR HIGH VOLTAGE SOLAR CELL OUTPUT

L.C. DiNetta and M.H. Hannon
AstroPower, Inc.
Newark, DE 19716-2000

ABSTRACT

Photovoltaic linear concentrator arrays can benefit from high performance solar cell technologies being developed at AstroPower. Specifically, these are the integration of thin GaAs solar cell and epitaxial lateral overgrowth technologies with the application of monolithically interconnected solar cell (MISC) techniques. This MISC array has several advantages which make it ideal for space concentrator systems. These are high system voltage, reliable low cost monolithically formed interconnections, design flexibility, costs that are independent of array voltage, and low power loss from shorts, opens, and impact damage. This concentrator solar cell will incorporate the benefits of light trapping by growing the device active layers over a low-cost, simple, PECVD deposited silicon/silicon dioxide Bragg reflector. The high voltage-low current output results in minimal I^2R losses, while properly designing the device allows for minimal shading and resistance losses. It is possible to obtain open circuit voltages as high as 67 volts/cm of solar cell length with existing technology. The projected power density for the high performance device is 5 kW/m² for an AM0 efficiency of 26% at 15X. Concentrator solar cell arrays are necessary to meet the power requirements of specific mission platforms and can supply high voltage power for electric propulsion systems.

It is anticipated that the high efficiency, GaAs monolithically interconnected linear concentrator solar cell array will enjoy widespread application for space based solar power needs. Additional applications include remote man-portable or ultra-light unmanned air vehicle (UAV) power supplies where high power per area, high radiation hardness and a high bus voltage or low bus current are important. The monolithic approach has a number of inherent advantages, including reduced cost per interconnect and increased reliability of array connections. There is also a high potential for a large number of consumer products. Dual-use applications can include battery chargers and remote power supplies for consumer electronics products such as portable telephones/beepers, portable radios, CD players, dashboard radar detectors, remote walkway lighting, etc.

INTRODUCTION

This monolithic interconnection process is capable of achieving high bus voltages while significantly reducing the number of ultrasonic welded, tabbed and soldered, or wirebonded array interconnections commonly used for space solar cell array fabrication. The low system current results in minimal I^2R losses, while properly designing the device allows for minimal shading and resistance losses.

A schematic of the device is shown in Figure 1. This device is fabricated on a semi-insulating or surrogate substrate. The epitaxial layers are grown on a Bragg reflector which results in light trapping and also offers additional electrical isolation from the substrate. The areas in between the solar cell elements are separated by either rendering them non-conductive or physically dividing the epitaxial layer into segments. Following this the base layer and emitter of adjoining segments are connected in a series configuration by etching and patterning appropriately and applying a suitable metallization.

In addition to the reduced interconnect costs and increased reliability, another key benefit of this technology is the wide range of specifications that solar cell arrays can be designed to meet. Monolithic interconnection allows the construction costs to be roughly independent of the array size, power or voltage. Therefore, the cost to manufacture solar cell arrays with output powers ranging from tens of milliwatts up to tens of watts and output voltages ranging from 5 to 500 volts will be roughly the same. This compares favorably to conventionally manufactured, commercial concentrator solar cell arrays, where handling of small parts is very

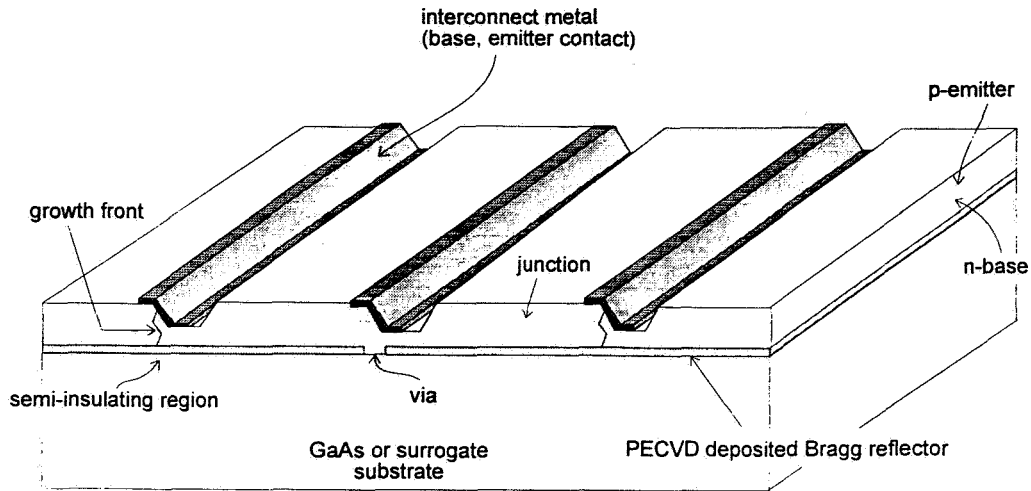


Figure 1. GaAs monolithic array for linear concentrators.

labor intensive and costly. The array can also be configured to provide power at a specified current or voltage by simply changing the metallization mask set. In this way, a wide variety of product specifications can be met using the same fabrication techniques.

Due to the higher voltage attainable by the monolithically interconnected solar cell, the I^2R array losses will be minimized for any bus voltage when compared to conventional GaAs solar cells. Utilizing a higher voltage also results in a weight savings at the array level due to the smaller quantity of high current carrying wire necessary for solar cell interconnection and the reduced dependence on stringing of low voltage devices to achieve the needed bus voltage. This monolithic interconnection technique offers several additional advantages compared to conventional array interconnection technologies for space applications. The reliability of the array is enhanced by reducing the complexity of the interconnections [1], and monolithically interconnected solar cell arrays offer potentially higher yields compared to conventional array manufacturing processes such as welding [2] or soldering. Typical yield reductions in standard array interconnection are the result of breakage due to either mechanical or thermal stress.

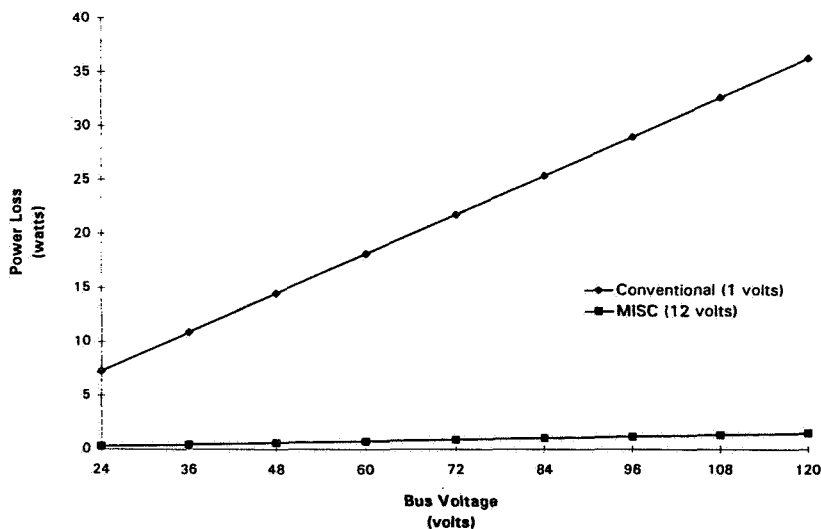


Figure 2. Solar cell voltage effect on power loss.

Another reliability benefit from the high voltage device is the low power loss from shorts, opens, and impact damage at the array level. If the monolithically interconnected solar cells are operated either at the bus voltage or some factor of the bus voltage, loss of a single solar cell within a string will have minimal impact on the array power generation when compared to typical GaAs solar cells. This is shown in Figure 2 using, for instance, a nominal 1.0 volt GaAs solar cell and a 12 volt monolithically interconnected GaAs solar cell. As is shown, the power loss is quite dramatic due to the loss of a string of devices as compared to a single or a few devices when the string of devices becomes disabled.

A monolithic interconnection technique offers several advantages compared to conventional array interconnection technologies. These include:

- The cost of fabricating the array interconnections is reduced and the process can be automated.
- I^2R losses are minimized
- The complexity of the interconnections is reduced thereby enhancing the reliability of the array.
- The interconnection cost is independent of the array size.
- Yields are higher compared to conventional array manufacturing processes such as welding or soldering.

This monolithic interconnection technique offers the potential to significantly reduce the high current levels of concentrator systems without degrading the total system power. The monolithic array will supply power at a lower current and higher voltage because it is configured as a series connected array of small area devices. This type of interconnection cannot be done by any other method simply because of the number and size of the components involved. By reducing the area of array elements, the current is reduced. Reducing the system current has considerable benefit in reducing the power lost to series resistance. For example, an 8 cm² GaAs solar cell at 15-suns delivers on the order of 3.6 A and 1 volt for a power of 3.6 Watts. A similar cell configured as a monolithic array (80 elements at 0.05 x 2 cm²) would deliver the same power at 0.045 A and 80 volts. This is a

considerable reduction of the system current.

The monolithically interconnected array in its simplest form consists of a lateral array of devices connected end to end. Figure 3 shows the projected power as a function of array element width and bus bar width. Using a properly designed prismatic cover, the grid shading can effectively be reduced to zero. Therefore, using coarse, 50 micron grid widths, a power output of over 500 mW/cm² is feasible with the prismatic cover. With an array element or active area width of 0.01 cm, it is possible to achieve 67 volts/cm. An active area width of 0.05 cm enables 18 volts/cm, and an active area width of 0.1 cm results in 10 volts/cm. Higher voltages are feasible using photolithography to reduce the grid width.

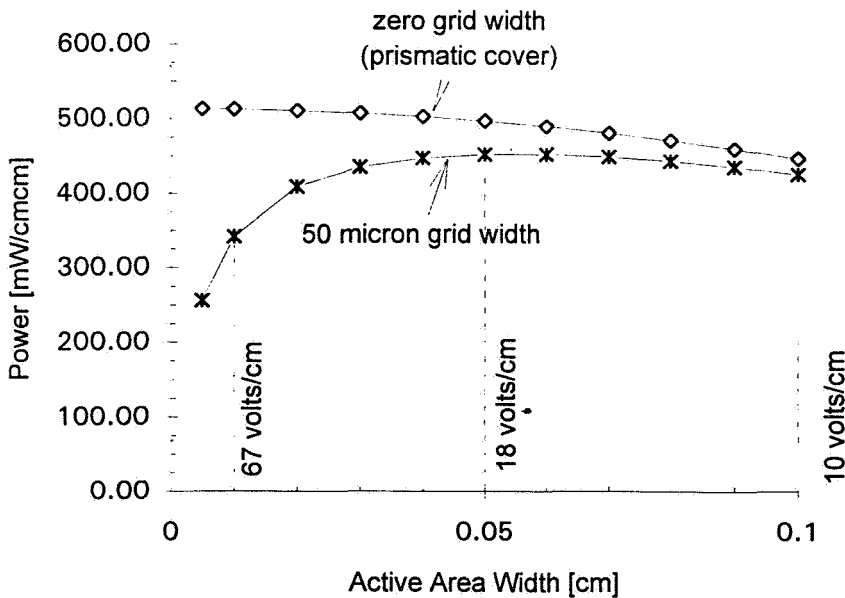


Figure 3. Predicted monolithic array performance. The 0% loss line is an ideal case which includes no shading or series resistance losses (AM0, 15X).

The other cell parameters for this model are: base doping of $3 \times 10^{17}/\text{cm}^3$, base thickness = 1 micron, and emitter sheet resistivity of 18 ohm/ \square .

The monolithically interconnected concentrator solar cell incorporates the light trapping benefits of an ultra-thin GaAs solar cell by laterally overgrowing a PECVD deposited Bragg reflector. This reflector consists of alternating layers of silicon and silicon dioxide deposited by the PECVD process. The silicon/silicon dioxide system offers significant advantages over the use of Bragg reflectors grown by MOCVD or MBE, foremost of which is the low cost. For the concentrator solar cell technology, a non-conducting reflector is desirable for electrical isolation of the substrate and solar cell active layers. The use of lateral overgrowth means the advantages of light trapping are achieved while maintaining a rugged structure supported by a GaAs or surrogate substrate. There is the potential for using low cost substrates such as silicon with a low cost, proprietary, GaAs interlayer. This further enhances the low cost benefits of this technology.

The reflectivity spectrum of a Bragg reflector can be tuned for high reflection depending on the thickness and number of layers. Reflectivity data of a typical silicon/silicon dioxide Bragg reflector is shown in Figure 4.

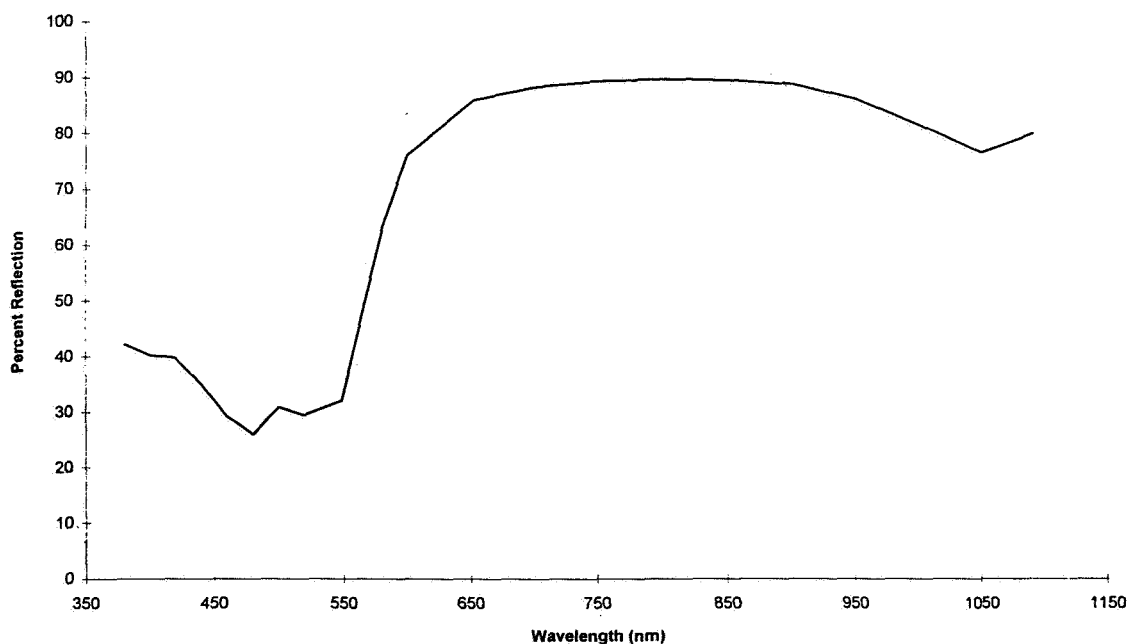


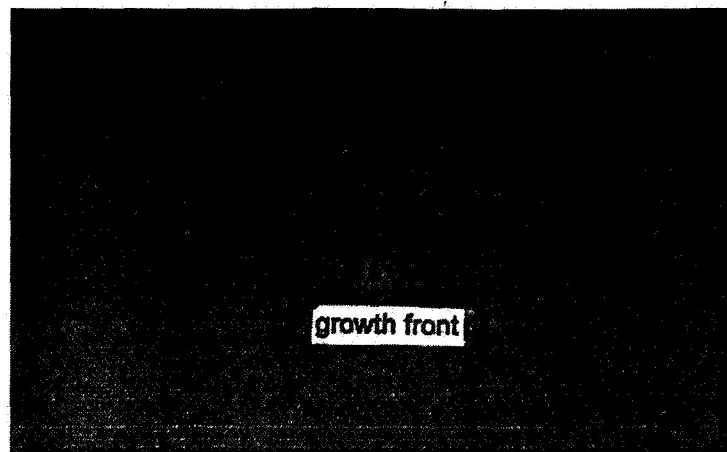
Figure 4. Reflectivity of a two pair silicon/silicon dioxide (55/120/55/120 nm) Bragg reflector on silicon.

To obtain lateral overgrowth, the substrate is masked and patterned using standard photolithography techniques. Openings in the mask (vias) are defined by selective etching to expose the substrate surface. The areas of exposed substrate serve as sites of preferential nucleation; nucleation is limited to the vias, with virtually no deposition on the masking layer. As growth proceeds, crystals nucleated at the vias overgrow the masking layer.

For the monolithically interconnected concentrator device, the interdevice semi-insulating regions can be situated directly over both the growth front and the via openings (see Figure 1). Therefore, the material quality in these regions is not critical. The highest quality material will be in the areas of film laterally overgrown on the Bragg reflector.

AstroPower has extensive experience with the lateral overgrowth of GaAs and AlGaAs over both metals and dielectrics. Figure 5 shows a cross sectional photomicrograph of consecutive AlGaAs layers laterally overgrowing a tungsten mask. The vias were 10 microns wide on 400 micron centers. The overgrowth layer was close to impinging (30 microns between growth fronts) and there was no solvent entrapment or voids. The consecutive layers were uniform and planar. By adjusting the mask spacing and via dimensions, impinging growth layers are feasible and have been demonstrated.

$\text{Al}_{.60}\text{Ga}_{.40}\text{As}$ →
overgrowth layer



AlGaAs DH
LED structure

Figure 5. Cross-section of AlGaAs layers laterally overgrowing a tungsten mask (100X).

SUMMARY

This unique device uses monolithically interconnected elements for linear concentrator arrays. The low system current results in minimal I^2R losses and device modeling enables minimal shading and resistance losses. The technology takes advantage of the benefits of light trapping by incorporating epitaxial lateral overgrowth of a PECVD deposited Bragg reflector. This process is capable of achieving high bus voltages while significantly reducing ultrasonic welded, tabbed and soldered, or wirebonded array interconnections commonly used for space solar cell array fabrication.

REFERENCES

- 1 J.R. WOODYARD, "Thin Film Cell Development Workshop Report", Proceedings of the Space Photovoltaic Research and Technology Conference, May 1991, page 48-1.
- 2 B.S. SMITH AND B.T. CAVICCHI, "GAAs SOLAR CELL CIRCUIT ASSEMBLY", 19TH PHOTOVOLTAICS SPECIALISTS CONFERENCE, NEW ORLEANS, MAY 1987, PAGE 448.

HYDROGEN PASSIVATION OF N⁺P AND P⁺N HETEROEPITAXIAL InP SOLAR CELL STRUCTURES¹

B. Chatterjee, W.C. Davis and S.A. Ringel
Department of Electrical Engineering
The Ohio State University
Columbus, OH 43210

R. Hoffman, Jr.
Essential Research, Inc.
Cleveland, OH 44135

S18
IN-50403

ABSTRACT

Dislocations and related point defect complexes caused by lattice mismatch currently limit the performance of heteroepitaxial InP cells by introducing shunting paths across the active junction and by the formation of deep traps within the base region. We have previously demonstrated that plasma hydrogenation is an effective and stable means to passivate the electrical activity of such defects in specially designed heteroepitaxial InP test structures to probe hydrogen passivation at typical base depths within a cell structure. In this work, we present our results on the hydrogen passivation of actual heteroepitaxial n⁺p and p⁺n InP cell structures grown on GaAs substrates by metalorganic chemical vapor deposition (MOCVD). We have found that a 2 hour exposure to a 13.56 MHz hydrogen plasma at 275 C reduces the deep level concentration in the base regions of both n⁺p and p⁺n heteroepitaxial InP cell structures from as-grown values of $5-7 \times 10^{14} \text{ cm}^{-3}$, down to $3-5 \times 10^{12} \text{ cm}^{-3}$. All dopants were successfully reactivated by a 400 C, 5 minute anneal with no detectable activation of deep levels. I-V analysis indicated a subsequent ~ 100 fold decrease in reverse leakage current at -1 volt reverse bias, and an improved built in voltage for the p⁺n structures. In addition to being passivated, dislocations are also shown to participate in secondary interactions during hydrogenation. We find that the presence of dislocations enhances hydrogen diffusion into the cell structure, and lowers the apparent dissociation energy of Zn-H complexes from 1.19 eV for homoepitaxial Zn-doped InP to 1.12 eV for heteroepitaxial Zn-doped InP. This is explained by additional hydrogen trapping at dislocations subsequent to the reactivation of Zn dopants after hydrogenation.

INTRODUCTION

Electrically active dislocations within InP layers grown on lattice mismatched substrates such as GaAs, Si and Ge currently limit the efficiency of heteroepitaxial InP solar cells (ref. 1). The ~ 8% mismatch in lattice constant for InP/Si, and 4% for both InP/Ge and InP/GaAs, typically result in threading dislocation densities in the range $1-10 \times 10^8 \text{ cm}^{-2}$ within the InP layers, much higher than the theoretically predicted value of 10^5 cm^{-2} necessary to achieve heteroepitaxial cell performance comparable to homoepitaxial InP (refs. 1,2). This fact has prompted the application of many approaches to reduce this high dislocation density and/or the electrical activity of dislocations, including compositionally graded buffer layers, thermally cycled growth and hydrogen passivation (refs. 3,4).

Our earlier work on hydrogen passivation of heteroepitaxial InP test structures grown on GaAs and Ge substrates demonstrated the effectiveness of a post-growth plasma hydrogenation treatment

¹ Work supported by NASA grant no. NAG3-1461.

which reduced the dislocation related deep level concentration from $\sim 6 \times 10^{14} \text{ cm}^{-3}$ to $\sim 3 \times 10^{12} \text{ cm}^{-3}$ in the InP layer (refs. 2,5,6). This passivation was stable up to $\sim 550 \text{ }^\circ\text{C}$, which combined with dopant reactivation occurring at $\sim 400 \text{ }^\circ\text{C}$, opens a $150 \text{ }^\circ\text{C}$ post-passivation processing window for cell completion. The observed deep level passivation was consistent with a 2-3 order of magnitude reduction in reverse leakage current for diodes fabricated within the heteroepitaxial InP test structures. Further detailed analysis showed that hydrogen incorporation fundamentally changes the trapping mechanism of dislocations from the expected extended state behavior, to point-defect-like behavior, significantly reducing the role of dislocations as the dominant feature in the deep level spectra. In fact, the dominant level responsible for reverse biased generation-recombination current switched from a deep dislocation level to a shallow center within the InP bandgap after H-passivation. In this paper we present the first report of deep level passivation by plasma hydrogenation in actual heteroepitaxial InP cell structures grown by low pressure metalorganic chemical vapor deposition (MOCVD). We investigate passivation efficiency in both p^+n and n^+p cell structures. Results of a comparative study of homoepitaxial InP/InP and heteroepitaxial InP/GaAs cell structures with regard to hydrogen diffusion and dopant reactivation kinetics after hydrogenation are discussed to reveal the impact of dislocations on the passivation process.

EXPERIMENTAL

The heteroepitaxial InP on GaAs structures were grown by low pressure MOCVD in a reactor of our own design and construction as previously described [ref. 7]. Precursor species of phosphine, trimethylindium (TMIn), silane and diethylzinc were injected into the hydrogen carrier gas. Reactor chamber pressure was maintained at 150 torr throughout the growth process. A typical InP on GaAs heteroepitaxial growth included a five minute, 620°C anneal in 1.5 torr partial pressure phosphine prior to nucleation of a thin layer of InP at 550°C . The susceptor temperature was then raised to 620°C for the remainder of the growth of the 3-4 μm thick heteroepitaxial layers. A TMIn flow rate of $14.5 \mu\text{mol min}^{-1}$ resulted in a growth rate of 0.61 nm sec^{-1} . Doping of the InP layers was achieved by injection of silane and diethylzinc for n-type and p-type respectively. Figure 1 shows the measured doping profiles of the structures investigated here.

Hydrogenation was performed in a Technics Planar Etch II parallel plate, 13.56 Mhz plasma reactor, using a 30 sccm flow rate of semiconductor grade H_2 , chamber pressure of 750 mTorr, and power density of 0.08 W/cm^2 . Substrate temperatures were varied from 250°C to 275°C . Hydrogen exposure time was varied from 1.5 - 2 hours. Immediately prior to hydrogen exposure, all samples were capped with a thin, hydrogen-permeable, cap layer of SiN_x to prevent InP surface degradation by preferential loss of phosphorous during hydrogenation. Optimum cap thickness was found to be 20 nm for a 2 hour exposure, based on SEM studies of the underlying InP surface as a function of nitride cap thickness. The nitride layer was etched off in dilute HF before metallization. DLTS measurements were performed using a Biorad DL4600 DLTS spectrometer and I-V measurements were done using an HP 4145 semiconductor parameter analyzer. Post hydrogenation dopant reactivation annealing was performed in flowing N_2 at $400 \text{ }^\circ\text{C}$ for 5 minutes. Metallization was performed in an e-beam evaporator using AuGeNi for n-type ohmic contacts and Ag/Zn/Ag for p-type contacts (ref. 8). Test devices were isolated by mesa etching to an active junction area of 0.785 mm^2 .

RESULTS AND DISCUSSION

3.1 Defect passivation in n^+p and p^+n heteroepitaxial InP cell structures

Both n^+p and p^+n cell structures have been used to achieve high efficiency InP homoepitaxial cells to date. For heteroepitaxial cells grown on group IV substrates such as Ge and Si, the p^+n design is preferred due to potential autodoping and the development of back to back diodes for n^+p structures. In view of hydrogen passivation however, both the direction of the built in field of p^+n cells and the strong Zn-H bonding typically observed in p-InP might be expected to impede the in-diffusion of hydrogen into the base region of the heteroepitaxial cell. Hence, hydrogen passivation was performed on cell

structures of both types to compare passivation effectiveness. Figure 2 shows dark I-V plots for the two cell types prior to hydrogen processing (as-grown) and after a 1.5 hour hydrogen exposure plus several post-hydrogenation annealing temperatures. It is seen that the built in voltage improves after hydrogenation for p⁺n but not n⁺p structures, indicating that V_{oc} for the former should be improved. Furthermore, in both cases, hydrogen is seen to significantly improve the reverse leakage current characteristics, shown in table I. The 400 C anneal is required to reactivate the Zn dopants in both cell structures (confirmed by C-V measurements).

Table I. Reverse bias leakage currents for various hydrogenation anneal conditions. Device areas are 0.785 mm².

| $I_{rev} @ -1V$ | n ⁺ p devices | p ⁺ n devices |
|--------------------------|--------------------------|--------------------------|
| As grown | 1.39 mA | 1.11 mA |
| hydrogen + 400 °C anneal | 10.74 μA | 5.21 μA |
| hydrogen + 512 °C anneal | 198 μA | 991 μA |
| hydrogen + 602 °C anneal | 1.25 mA | 1.79 mA |

From this table, we see that leakage currents are reduced by more than 2 orders of magnitude for both cell types after the 400 C dopant reactivation anneal. Only after annealing in excess of 500 C does the leakage current increase toward its original, non-passivated value. What is clear from these results is that neither the direction of the built-in electric field nor preferential trapping of hydrogen in the emitter significantly impedes the desired in-diffusion of hydrogen. However, table I indicates that p⁺n structures exhibited a greater rate of thermal degradation. While the reasons for this are unclear, one possibility might be that Zn is being gettered by threading dislocations as interstitials which are shunting the junction. We have reported in an earlier work using photoluminescence that interstitial Zn is indeed gettered by dislocations in heteroepitaxial InP and we are currently performing SIMS and polaron profiling studies to investigate this possibility in these samples (ref. 9). This suggests that alternative dopants to Zn may be appropriate for heteroepitaxial p⁺n cells.

Figure 3 shows the corresponding DLTS measurements for both the p⁺n and n⁺p structures which confirm that in both cases, hydrogen is passivating deep levels by lowering their concentration by more than 2 orders of magnitude. To our knowledge, this is the first report of successful hydrogen passivation in heteroepitaxial InP cell structures. For the n⁺p structure, the hole trap at 0.69 eV is very close to the peak T1 (comprised of sub-peaks T1A and T1B) that we have reported previously for heteroepitaxial p-InP test structures as related to extended defects resulting from lattice-mismatch (either dislocation cores or point defect clusters) (ref. 2). The dislocation-related hole trap previously labeled T2 in the earlier test structures is not observed in the cell structure until ~ 0.5 μm is removed from the surface. This depth-dependent concentration is reasonable if this level is related to threading dislocations that have nucleated from the InP/GaAs interface. The DLTS spectra of the p⁺n structure indicates passivation of two electron traps in the n-type base having activation energies of 850 meV and 509 meV for the high and low temperature peaks, respectively. This is the first report of deep levels in n-type heteroepitaxial InP and we are currently analyzing the DLTS spectra in detail to determine the relationship of these states with the presence of dislocations and associated defects, and with our results on heteroepitaxial p-type InP.

One concern of the hydrogen passivation process is its stability with respect to moderate temperature exposure and to light exposure. While we are presently investigating the latter, figure 4 demonstrates excellent passivation stability against exposure to a temperature of 80°C. As can be seen, no detectable deep level reactivation was observed for the 24 hour period studied here. Light soaking experiments will be performed on actual cells (i.e. with a grid pattern) that are currently being fabricated.

3.2 Hydrogen diffusion in InP/GaAs and InP/InP cell structures

One of the key issues for hydrogen passivation is the depth of hydrogen diffusion into the cell structures. Our earlier work on specially designed test structures which incorporated a pn junction buried 2 μm below the InP surface demonstrated that hydrogen easily diffuses through the typical base thickness of a heteroepitaxial cell. Here we investigate the impact of dislocations on the hydrogen diffusion process within the n^+p cell structures by monitoring the Zn dopant deactivation using electrochemical C-V profiling for homoepitaxial and heteroepitaxial structures. It has been reported by a number of authors that the dislocations provide 'expressways' for hydrogen to diffuse into the bulk of the samples, with hydrogen also showing a strong preference for these extended defects (ref. 10). We hydrogenated both homoepitaxial and a heteroepitaxial cell structure for 2 hours at 275°C. Figure 5 presents the results of C-V depth profiling of Zn acceptors, before and after hydrogen exposure for the two structures. Both samples show deep passivation depths. However the heteroepitaxial sample shows a deeper and much greater degree of acceptor passivation than its homoepitaxial counterpart. This result confirms that the threading dislocations running from the InP/GaAs interface up to the surface provide a pathway for fast hydrogen diffusion into the base region from the top surface compared with the case where these dislocations are absent. Similar studies were attempted for the n-base regions in the p^-n . However, donor passivation was not observed, consistent with the results of Pearton et al. who have reported that hydrogen is only weakly bonded to Si donors in InP compared to Zn acceptors (ref. 11).

3.3 Acceptor reactivation in n^+p structures

One of the factors which affect hydrogen diffusion is the chemical affinity between the passivating hydrogen species and ionized dopant atoms. In InP, Zn acceptors are known to be strongly passivated by positively charged hydrogen ions, where hydrogen is thought to bond with the neighboring P atom in a bond centered position (ref. 12). It is reasonable to expect that the presence of dislocations in heteroepitaxial material may significantly complicate this process, for at least two reasons. First, dislocations appear to be a major sink for hydrogen. Second, the presence of dislocation strain fields have been shown to getter Zn interstitials, and thereby reduce the substitutional Zn concentration (ref. 9). Zn-H reactivation kinetics for homoepitaxial and heteroepitaxial p-type InP are compared below.

In the absence of an applied electric field, hydrogen-zinc complexes dissociate at temperatures close to 400°C. Such high temperatures are necessary to (1) separate H from Zn, and (2) provide enough energy so that the H species can diffuse away from the Zn ion after reactivation. Zundel et al. (ref. 13) however, have shown that in the presence of a sufficiently strong electric field the dissociation of these zinc-hydrogen complexes follow first-order kinetics since the applied electric field sweeps out the reactivated hydrogen which prevents retrapping inside the depletion region. Following this analysis, we conducted a series of experiments to elucidate this information in heteroepitaxial and homoepitaxial Zn-doped InP using the n^+p cell structure. C-V measurements were made on hydrogenated n^+p structures after systematically annealing under a reverse bias of -8 volts as a function of temperature (70 - 120 °C) and time (5-30 min). Following the analysis of Zundel et al., the inactive carrier concentration, N_i , which is the concentration of carriers removed by passivation, is plotted in figure 6 according to

$$N_i = N_i - N_H \exp(-v_d t)$$

where N_i is the initial carrier concentration of the as grown sample, N_H is carrier concentration at the chosen depth after hydrogenation, v_d is the thermally activated dissociation frequency and t is the time over which the reverse biased annealing (RBA) takes place. The dissociation frequency has a temperature dependence, which is given by

$$v_d = v_0 \exp(-E_D / KT)$$

where E_D is the dissociation energy of the zinc-hydrogen complex. First, the annealing experiments were done for different time periods at a fixed annealing temperature. Then these experiments were repeated

for other temperatures generating figure 7. The slopes of the lines in figure 7 when plotted against the annealing temperatures gives the dissociation energy E_D which is shown in figure 8. Analysis of the homoepitaxial data gives a value of 1.19 eV for E_D , consistent with previous reports by other investigators for zinc acceptors in homoepitaxial InP (ref. 12). However for heteroepitaxial Zn-doped InP, we calculate E_D to be 1.12 eV. To the best of our knowledge this is the first reported values for heteroepitaxial InP and we attribute this lowering to interactions with dislocations in the depletion region.

The local electric and strain fields surrounding the dislocations aid the removal process of hydrogen from the acceptors once hydrogen is thermally liberated, thereby lowering the apparent dissociation energy. DLTS measurements shown in figure 9 support this notion, where additional reduction, or passivation, of the T1 (dislocation-related) level is observed as a function of the RBA process. Since no additional hydrogen is being provided to the InP structure from the ambient, this passivation can only occur by trapping hydrogen that has been liberated from Zn acceptors by the low (70-120 °C) temperature RBA.

4. Conclusions

Hydrogen passivation of n^+ -p and p^+ -n InP heteroepitaxial cell structures grown on GaAs substrates has been demonstrated and investigated. The passivation resulted in a ~ 2 order of magnitude reduction in reverse leakage current at -1 volt, which corresponds to a > 2 order of magnitude reduction in DLTS trap concentration within the base region of each cell structure. No reactivation of deep levels was detected for at least 24 hours due to heating at 80°C in the dark. Fundamental studies of hydrogen diffusion, and Zn reactivation kinetics with regard to the participation of dislocations were performed. It was found that dislocations aid the hydrogen passivation process by providing fast diffusion paths and by lowering the apparent dissociation energy of Zn-H complexes. We are currently processing hydrogen-passivated cells using the procedures presented here, and this will be reported the future.

5. References

1. R.K. Jain and D.J. Flood, "Influence of the Dislocation Density on the Performance of Heteroepitaxial Indium Phosphide Solar Cells," IEEE Trans. Electron. Dev., vol. 40, pp. 128-1934, 1993.
2. B.Chatterjee and S.A. Ringel, "Hydrogen Passivation and its Effects on Carrier Trapping by Dislocations in InP/GaAs Heterostructures, J. Appl. Phys. vol. 77, pp. 3885-3898, 1995.
3. C.J. Keavney, S.M. Vernon, V.E. Haven, S.J. Wojtczuk and M.M. Al-Jassim, "Fabrication of n^+ /p InP Solar Cells on Si Substrates," Appl. Phys. Lett., vol. 54, pp. 1139-1141, 1989.
4. I. Weinberg, C.K. Swartz and D.J. Brinker, "Heteroepitaxial InP Solar Cells on Si and GaAs Substrates," Tech. Digest Int. PVSEC-5, pp. 81-84, 1990.
5. B. Chatterjee, S.A. Ringel, R. Sieg, R. Hoffman and I. Weinberg, "Hydrogen Passivation of Dislocations in InP on GaAs Heterostructures," Appl. Phys. Lett., vol. 65, pp. 1-3, 1994.
6. S.A. Ringel, B. Chatterjee, R.M. Sieg, E.V. Schnetzer and R. Hoffman, Jr., "Material Quality and Dislocation Trapping in Hydrogen Passivated Heteroepitaxial InP/GaAs and InP/Ge Solar Cells," Proc. 1st IEEE WCPEC, pp. 2204-2207, 1994.
7. "High Efficiency InP Solar Cells from Low Toxicity Tertiarybutylphosphine and Trimethylindium by OMVPE", R.W. Hoffman Jr., N.S. Fatemi, D.M. Wilt, P. Jenkins, D.J Brinker and D.A. Scheiman, Proc. 1st IEEE WCPEC p. 1882, 1994.

8. N.S. Fatemi, V.G. Weizer, D.M. Wilt and R.W. Hoffman, "A Simple, Low Resistance Contact System for Shallow Junction p⁺nn⁺ InP Solar Cells That Preserves Emitter Integrity During Sintering," Proc. IEEE WCPEC, pp. 2129-2132, 1994.
9. R.M. Sieg, B. Chatterjee and S.A. Ringel, "Evidence for Enhanced Zinc Interstitial Concentration in Strain-Relaxed Heteroepitaxial Indium Phosphide," Appl. Phys. Lett. vol. 66, pp. 3108-3110, 1995.
10. J.M. Zavada, S.J. Pearton, R.G. Wilson, C.S. Wsu, M. Stavola, F. Ren, J. Lopata, W.C. Dautremont-Smith and S.W. Novak, "Electrical Effects of Atomic Hydrogen Incorporation in GaAs on Si," J. Appl. Phys. vol. 65, pp. 347-353, 1989.
11. W.C. Dautremont-Smith, J. Lopata, S.J. Pearton, L.A. Koszi, M. Stavola and V. Swaminathan, "Hydrogen Passivation of Acceptors in p-InP," J. Appl. Phys. vol. 66, pp. 1993-1996, 1989.
12. S.J. Pearton, W.S. Hobson and C.R. Abernathy, "Dissociation Energies of Acceptor-Hydrogen Complexed in InP," Appl. Phys. Lett. vol. 61, pp. 1588-1590, 1992.
13. T. Zundel and J. Weber, "Dissociation Energies of Shallow-Acceptor-Hydrogen Pairs in Silicon," Phys. Rev. B. vol. 39, pp. 549-552, 1989.

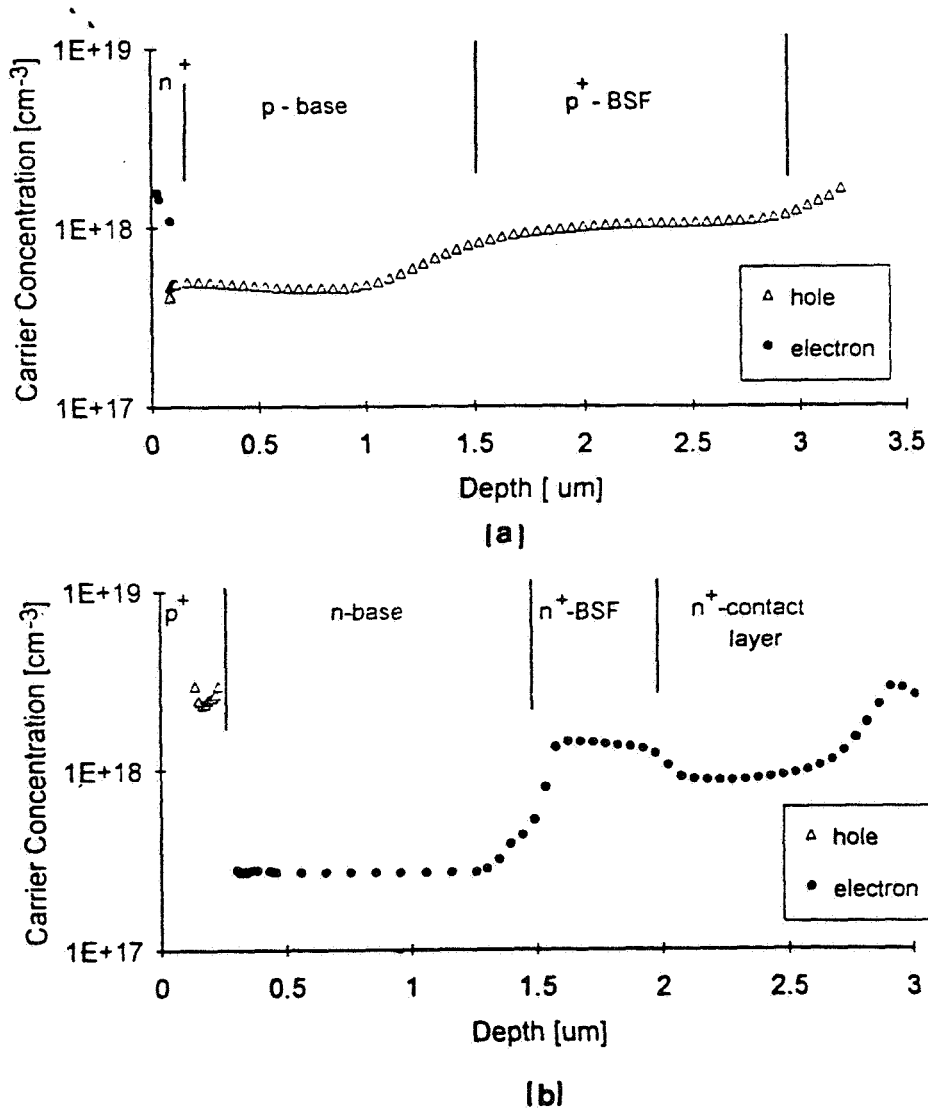


Figure 1. Electrochemical C-V profiles of carrier concentration for (a) n⁺/p/p⁺ and (b) p⁺/n/n⁺/n⁺ cell structures grown on p⁺-GaAs substrates used in this study.

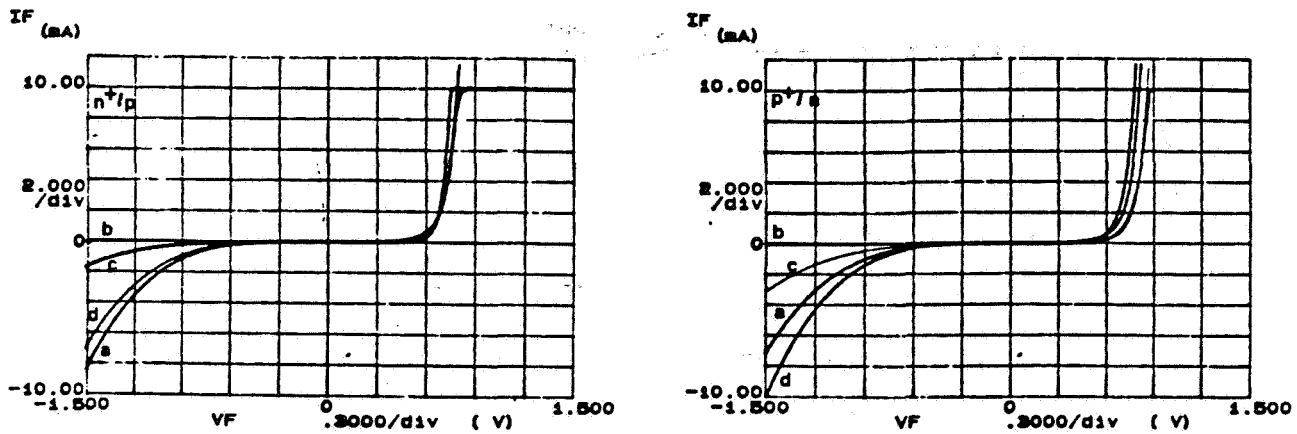


Figure 2. Dark I-V characteristics of (a) n+p and (b) p+n structures. For each case, a-d denote as-grown, 1.5 hr. H-passivation + 400 °C anneal, 1.5 hr. H-passivation + 512 °C anneal, and 1.5 hr. H passivation + 602 °C anneal conditions. All anneals were for 5 minutes.

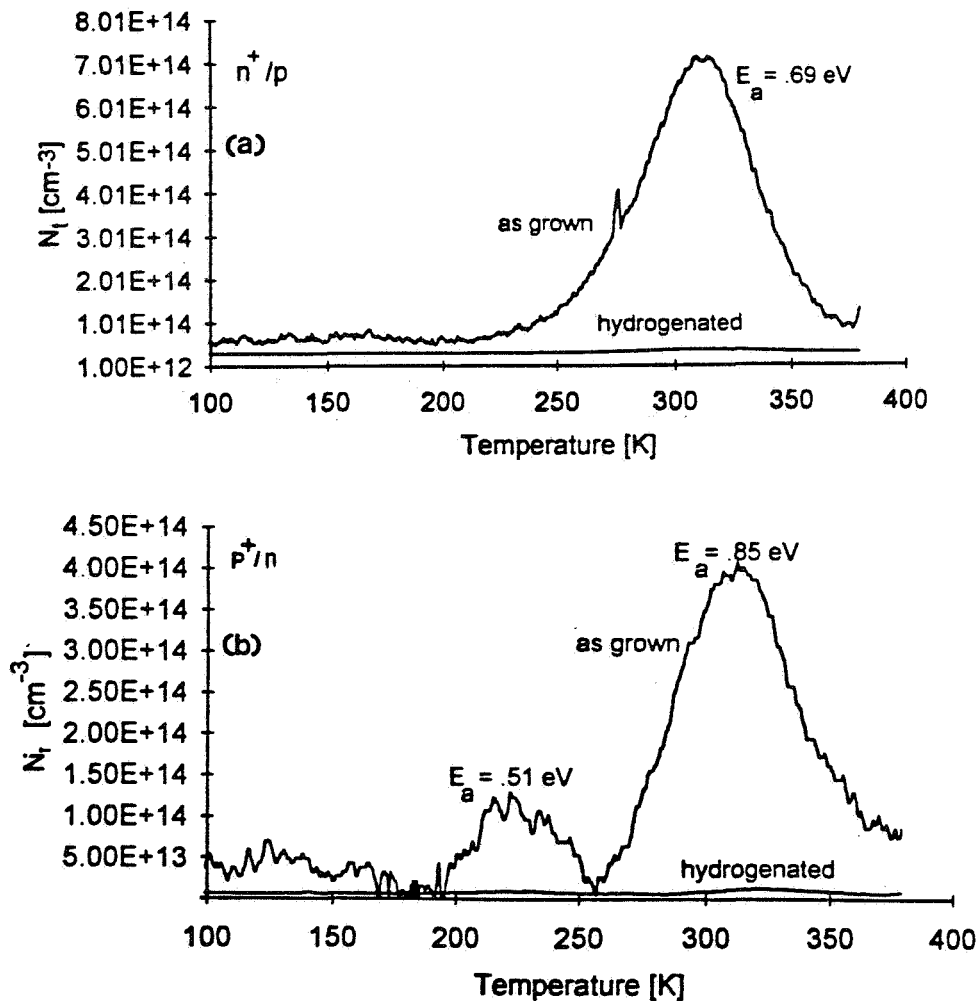


Figure 3. DLTS spectra of for (a) n+p and (b) p+n InP/GaAs device structures in the as-grown state and after a 2 hr. H-passivation exposure plus dopant reactivation anneal.

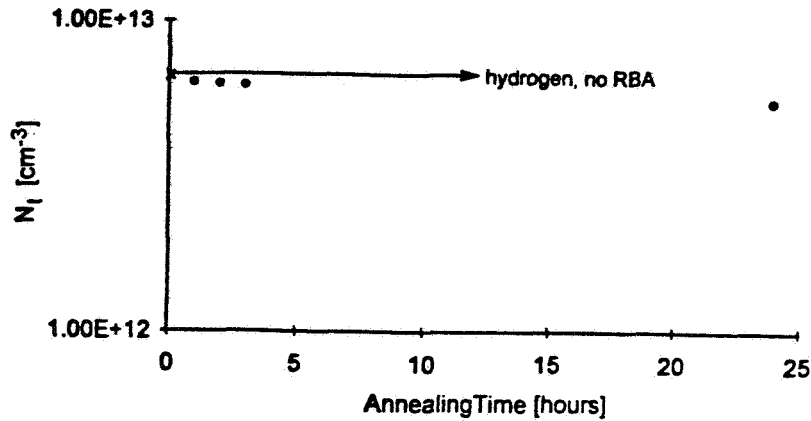


Figure 4. Stability of passivated deep levels against long term annealing in the dark at 80° C as obtained from DLTS peak heights of the annealed samples.

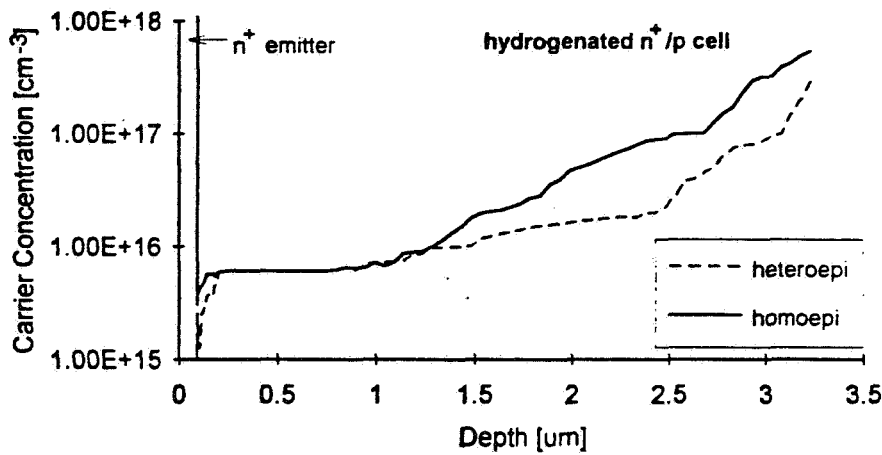


Figure 5. Electrochemical C-V Zn-acceptor profiles comparing passivation depth in heteroepitaxial and homoepitaxial n+/p structures after a 2 hour hydrogen plasma exposure.

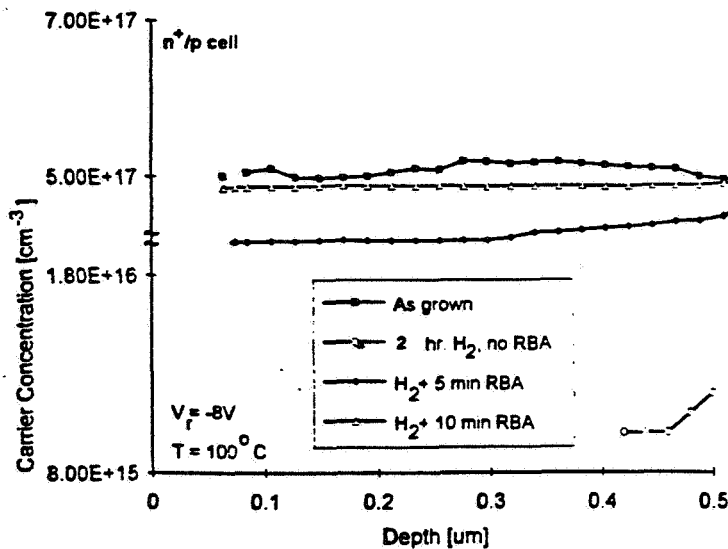


Figure 6. C-V doping profiles of heteroepitaxial n+/p InP/GaAs structures, for as grown and hydrogenated (2 h, 275°C) samples annealed at 100° C under -8V reverse bias for various time periods. The plots were obtained from C-V data.

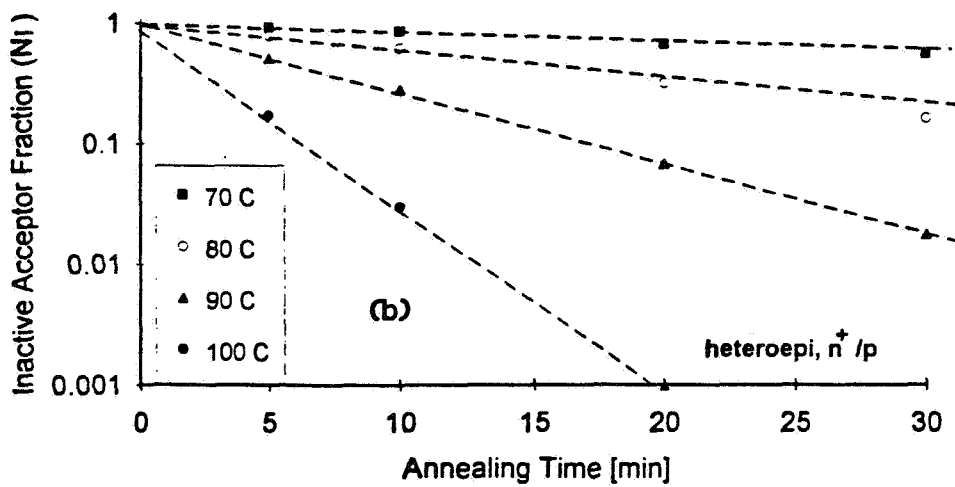
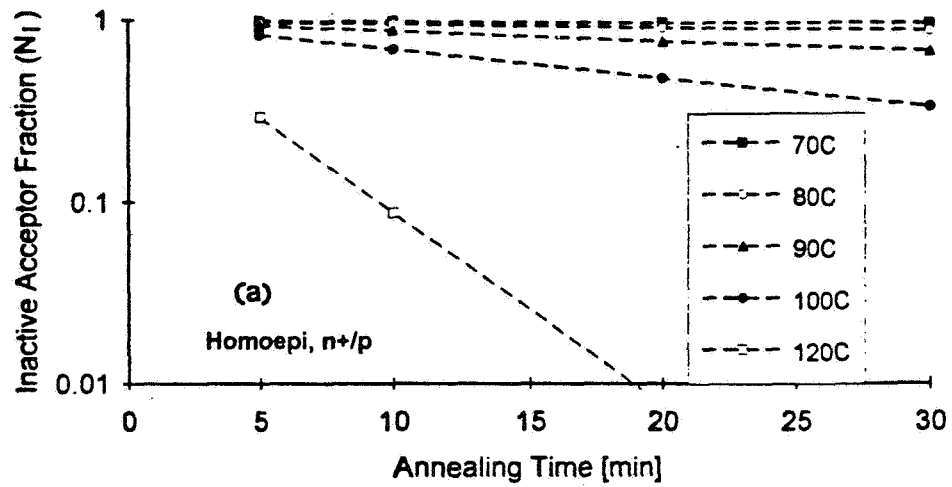


Figure 7. Inactive acceptor fraction versus bias application time at different temperatures in the high field region of hydrogenated n⁺p diodes for (a) homoepitaxial and (b) heteroepitaxial structures.

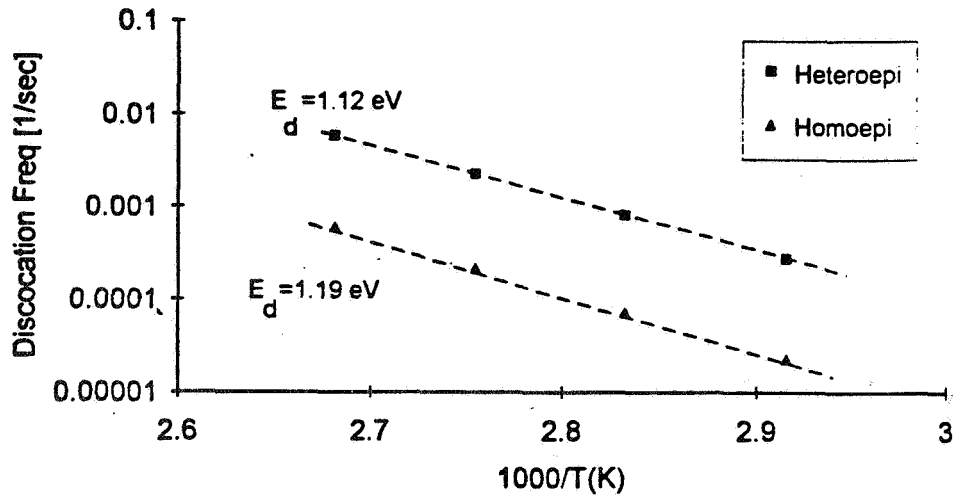


Figure 8. Arrhenius plots of the dissociation frequencies of Zn-H complexes in homoepitaxial and heteroepitaxial n/p devices. The dissociation energies are indicated in the figure.

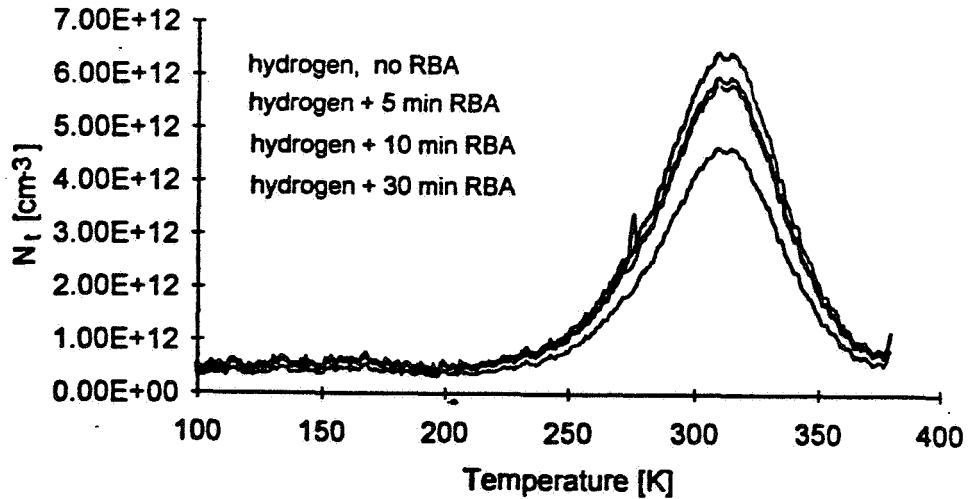


Figure 9. Effect of RBA at 80 °C on the DLTS spectra, showing further passivation of the deep levels after RBA experiments, for heteroepitaxial n/p structures.

THE GROWTH OF LOW BAND-GAP InAs ON (111)B GaAs SUBSTRATES¹

R. E. Welser and L. J. Guido

Yale University

New Haven, Connecticut 06520-8284

S19
IN-50404

Summary

Growth on the (111)B orientation exhibits a number of advantageous properties as compared to the (100) during the early stages of strained-layer epitaxy. In accordance with a developing model of nucleation and growth, we have deposited thin (60 Å - 2500 Å), fully relaxed InAs films on (111)B GaAs substrates. Although thicker InAs films are subject to the formation of twin defects common to epitaxy on the (111)B orientation, appropriate control of the growth parameters can greatly minimize their density. Using this knowledge base, InAs films up to 2 μm in thickness with improved morphology and structural quality have been grown on (111)B GaAs substrates.

Introduction

The use of low band-gap materials is of interest for a number of photovoltaic and optoelectronic applications, such as bottom cells of optimized multijunction solar cell designs [1], long wavelength light sources, detectors, and thermophotovoltaics. However, low band-gap materials are generally mismatched with respect to lattice constant, thermal expansion coefficient, and chemical bonding to the most appropriate commercially available substrates (Si, Ge, and GaAs). For the specific case of III-V semiconductor heteroepitaxy, one must contend with the strain induced by both lattice constant mismatch at the growth temperature and differences in the rates of mechanical deformation during the cool-down cycle. Several experimental techniques have been developed to minimize the impact of these phenomena (i.e., compositional grading, strained-layer superlattices, and high-temperature annealing). However, in highly strained systems such as InAs-on-GaAs, three-dimensional (3-D) island formation and large defect densities ($\geq 10^8 \text{ cm}^{-2}$) tend to limit their applicability. In these particular cases, the surface morphology and defect density must be controlled during the initial stages of nucleation and growth.

¹ This work has been supported by the NASA Graduate Student Researchers Program (NGT-50832) and by the National Science Foundation via the Presidential Faculty Fellowship Program (ECS-9253760).

Thin Film Evolution

At the last SPRAT conference, we reported on a study of the evolution of InAs islands on (100) and (111)B GaAs substrates [2]. Highly strained semiconductor systems like InAs-on-GaAs, with a 7.1% lattice mismatch, grow in the Stranski-Krastanov growth mode in which the deposition of a two-dimensional (2-D) wetting layer is followed by the formation of discrete 3-D islands. The density of the discrete islands is a function of growth parameters, which, for the metalorganic chemical vapor deposition (MOCVD) system used in these investigations, are substrate temperature (T_s), TMIIn flow (f_{TMIIn}), and AsH₃ flow (f_{AsH_3}). Moreover, the density, geometry, and defect structure of the 3-D islands differ between the two orientations.

As the film thickens, the islands coalesce to form a continuous film. The thickness at which this happens is a function of the density (N_i) and the width-to-height ratio (w/h) of the initially discrete 3-D islands (Figure-1). Specifically, a 2-D film forms more quickly with higher N_i and the larger w/h .

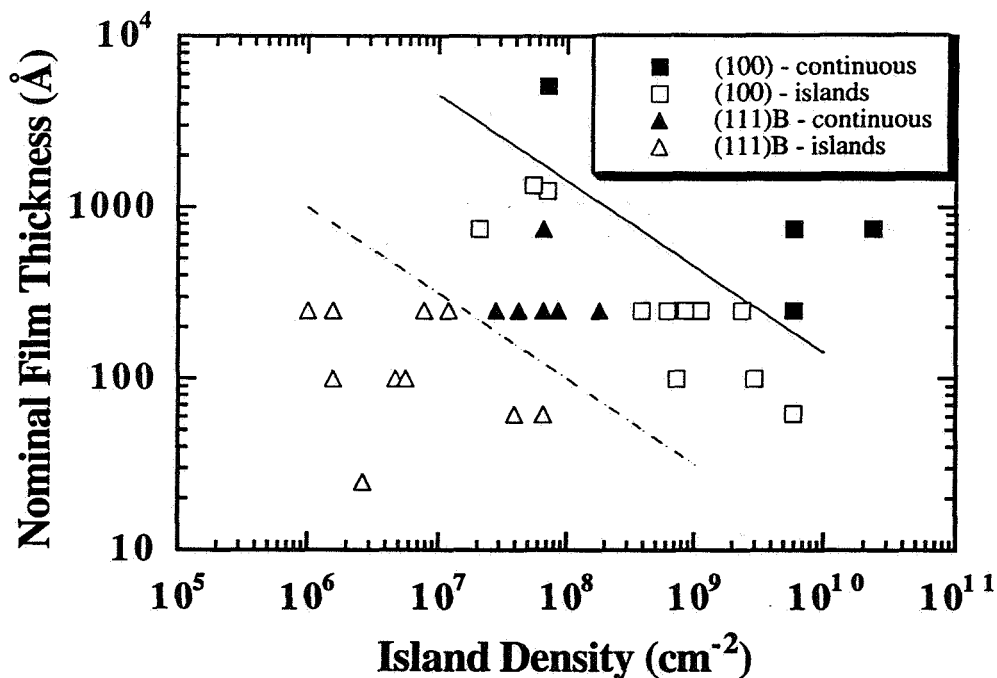


Figure-1 The transition in thin film morphology from discrete 3D islands to a continuous layer as a function of nominal film thickness, island density, and width-to-height ratio. The critical thickness (t_c) at which this transition takes place can be expressed as $t_c = N_i^{-1/2}(w/h)^{-1}$. The solid line assumes a $w/h \sim 7$ for the (100) orientation, while the dashed line takes $w/h \sim 100$, which is more appropriate for the (111)B substrate.

Featureless 250 Å films have been deposited on both substrate orientations by adjusting the growth parameters in such a way as to increase the island density. However, these films differ remarkably in terms of surface roughness and defect density. The improved properties of films on (111)B substrates can be attributed to the lower density, flatter geometry, and fewer threading defects of the initial islands on that orientation. In particular, (111)B films are atomically terraced with at least an order of magnitude reduction in threading dislocation density as compared to films on (100) substrates. While these thin 250 Å films on the (111)B approach the idealized condition for lattice-mismatched films of efficient strain relaxation between the epilayer and the substrate with a minimal number of threading defects, thicker InAs films on the (111)B orientation are subject to the formation of hillocks which quickly degrade the film morphology.

Growth on (111)B Substrates

Even in the simple case of homoepitaxy, hillock formation is a common problem which has been attributed to the formation of twin defects [3,4]. While tilted substrates have typically been employed in the past to reduce hillock density, recent molecular beam epitaxy (MBE) results suggest that nearly featureless films can be deposited on (111)B substrates under a narrow range of growth conditions, even if substrates are on-orientation [5,6]. We have reproduced these results in our MOCVD system (Table I).

Table I : Hillock density as a function of growth parameters for 2500 Å homoepitaxial GaAs films on (111)B substrates.

| T_s (°C) | f_{TEGa} (sccm) | f_{AsH_3} (sccm) | Hillock Density (cm^{-2}) |
|------------|--------------------------|---------------------------|--------------------------------------|
| 525 | 23 | 100 | 5×10^6 |
| 600 | 23 | 100 | 5×10^6 |
| 650 | 23 | 100 | 5×10^3 |
| 700 | 23 | 100 | 50 |
| 600 | 140 | 100 | 1×10^8 |
| 600 | 140 | 500 | 1×10^7 |
| 600 | 23 | 100 | 5×10^6 |
| 600 | 23 | 500 | 1×10^6 |

Although hillock density is particularly sensitive to substrate temperature, it is also found to be a function of all the growth parameters. At a fixed temperature, slower growth rates and a higher As overpressure both tend to reduce the number of twins. By appropriately altering growth conditions, hillock density can be reduced by over six orders of magnitude.

2-Step Approach

With this in mind, we have implemented a 2-step procedure for the growth of thicker InAs films on (111)B GaAs substrates. In the first step, optimized conditions for the deposition of a specular, strain-relaxed 250 Å film of InAs are employed. Next the growth is interrupted, and the conditions altered to approximate those yielding specular, lattice-matched GaAs films. In this way, the hillock density on lattice-mismatched 2500 Å InAs films has been reduced by over an order of magnitude.

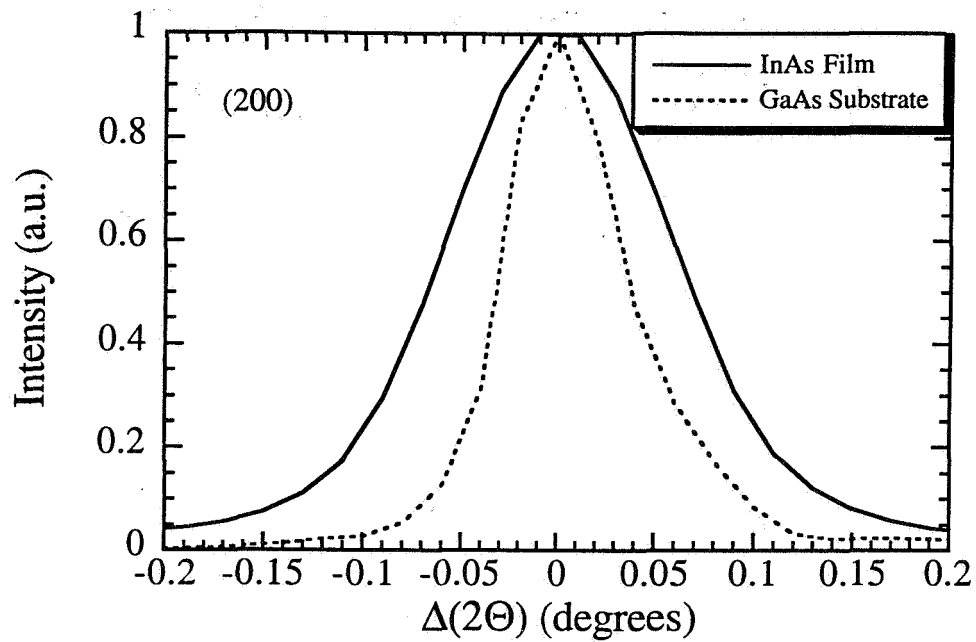
InAs films grown on (111)B GaAs substrates employing this 2-step procedure still exhibit similar improvements in structural properties compared to InAs films on (100) GaAs. Figure-2 shows the x-ray diffraction peaks from 2500 Å InAs films on (100) and (111)B GaAs substrates. In both cases, the separation of the film and substrate peaks suggests that both films are nearly fully relaxed. However, the full width at half maximum (FWHM) of the film peak on the (100) orientation is roughly twice that of the substrate, indicating a substantial degradation in structural quality. On the other hand, the film peak FWHM on the (111)B is nearly the same as that of the substrate, suggesting an improved structural quality. Indeed, cross-sectional TEM of these films indicates at least an order of magnitude lower threading dislocation density in the (111)B film.

Conclusions

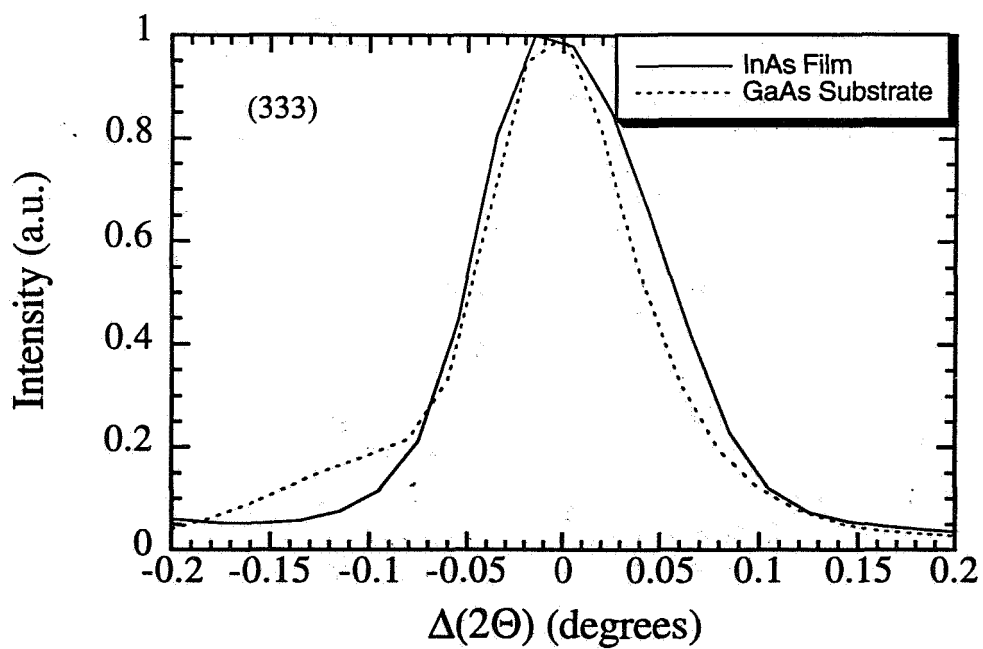
We have produced atomically terraced, fully relaxed InAs films on (111)B GaAs substrates with misfit dislocations largely confined to the epilayer / substrate interface. The advantages of the (111)B orientation stem from the shape of the initial InAs islands, their density (which can be manipulated by adjusting growth conditions), and the nature of their defect structure. Thicker InAs layers on the (111)B are susceptible to growth defects similar to those observed for GaAs homoepitaxy on (111)B substrates. However, by implementing a 2-step growth approach, thicker layers of InAs films with reduced growth defect density have been grown on the (111)B orientation. Thus, the use of (111)B substrates may have the potential to yield high quality, strain-relaxed material for device applications.

References

1. R. E. Welser and L. J. Guido, *Solar Energy Materials and Solar Cells* **36**, 349 (1995).
2. R. E. Welser and L. J. Guido, *Proc. of SPRAT XIII*, Cleveland, OH, June 14-16, 1994, p. 409.
3. A. Y. Cho, *J. Appl. Phys.* **41**, 2780 (1970).
4. K. C. Rajkumar, P. Chen, and A. Madhukar, *J. Appl. Phys.* **69**, 2219 (1991).
5. L. Vina and W. I. Wang, *Appl. Phys. Lett.* **48**, 36 (1986).
6. P. Chen, K. C. Rajkumar, and A. Madhukar, *Appl. Phys. Lett.* **58**, 1771 (1991).



(a)



(b)

Figure-2 X-ray diffraction data from 2500 Å films grown on (a) (100) and (b) (111)B GaAs substrates.

S20 IN-50405

DESIGN OF A THREE-LAYER ANTIREFLECTION COATING FOR HIGH EFFICIENCY INDIUM PHOSPHIDE SOLAR CELLS USING A CHEMICAL OXIDE AS FIRST LAYER

Jacques Moulot
Cleveland State University,
Cleveland, Ohio 44115

Chandra Goradia
Cleveland State University,
Cleveland, Ohio 44115

Mircea Faur
Cleveland State University,
Cleveland, Ohio 44115

Manju Goradia
Cleveland State University,
Cleveland, Ohio 44115

Maria Faur
NASA Lewis Research Center
Cleveland, Ohio 44135

Sheila Bailey
NASA Lewis Research Center
Cleveland, Ohio 44135

ABSTRACT

It is well known that the behavior of III-V compound based solar cells is largely controlled by their surface, since the majority of light generated carriers (63% for GaAs and 79% for InP) are created within 0.2 μm of the illuminated surface of the cell. Consequently, the always observed high surface recombination velocity (SRV) on these cells is a serious limiting factor for their high efficiency performance, especially for those with the p-n junction made by either thermal diffusion or ion implantation. A good surface passivation layer, ideally, a grown oxide as opposed to a deposited one, will cause a significant reduction in the SRV without adding interface problems, thus improving the performance of III-V compound based solar cells. Another significant benefit to the overall performance of the solar cells can be achieved by a substantial reduction of their large surface optical reflection by the use of a well designed antireflection (AR) coating.

In this paper, we demonstrate the effectiveness of using a chemically grown, thermally and chemically stable oxide, not only for surface passivation but also as an integral part of a 3-layer AR coating for thermally diffused p^+n InP solar cells. A phosphorus-rich interfacial oxide, $\text{In}(\text{PO}_3)_3$, is grown at the surface of the p^+ emitter using an etchant based on HNO_3 , $o\text{-H}_3\text{PO}_4$ and H_2O_2 . This oxide has the unique properties of passivating the surface as well as serving as a fairly efficient antireflective layer yielding a measured record high AM0, 25 $^\circ\text{C}$, open-circuit voltage of 890.3 mV on a thermally diffused InP(Cd,S) solar cell. Unlike conventional single layer AR coatings such as ZnS, Sb_2O_3 , SiO or double layer AR coatings such as ZnS/MgF₂ deposited by e-beam or resistive evaporation, this oxide preserves the stoichiometry of the InP surface. We show that it is possible to design a three-layer AR coating for a thermally diffused InP solar cell using the $\text{In}(\text{PO}_3)_3$ grown oxide as the first layer and Al_2O_3 , MgF₂ or ZnS, MgF₂ as the second and third layers respectively, so as to yield an overall theoretical reflectance of less than 2%.

Since chemical oxides are readily grown on III-V semiconductor materials, the technique of using the grown oxide layer to both passivate the surface as well as serve as the first of a multilayer AR coating, should work well for essentially all III-V compound-based solar cells.

INTRODUCTION

Calculations show that the majority of light generated carriers in direct bandgap III-V compound semiconductor based solar cells, are created within 0.2 μm of the illuminated surface of the cell⁽¹⁾. For such materials, surface recombination velocity (SRV) and p/n junction depth

considerations are of critical importance in the design of high efficiency solar cells. Even though published values of SRV on InP and GaAs vary over a wide range, depending on the surface preparation and the techniques used for measurement⁽²⁾, it is estimated that SRV values can be as high as 1.8×10^7 cm/s^(3,4), even for epitaxially grown cells. Therefore, thin emitters and reduced SRV appear to be necessary conditions for the fabrication of high efficiency III-V compound based solar cells. A good surface passivation layer, ideally a grown oxide, will cause a significant reduction of the SRV without adding semiconductor/oxide interface traps and oxide bulk defects which are inherent to deposited oxides, thus improving the overall performance of the III-V compound based solar cell. Yet another obvious but not often properly addressed limitation to high performance of these cells, is their high surface reflection, particularly in the blue region of the solar spectrum.

In this work, we address these two problems with a new optimized three-layer AR coating for the p⁺n InP(Cd,S) thermally diffused solar cell. A chemical oxide grown on the p⁺-doped emitter serves as the first layer of a three-layer AR coating composed of In(PO₃)₃/Al₂O₃/MgF₂. This In(PO₃)₃ oxide, which is described in detail elsewhere⁽³⁾, is primarily designed as a surface passivating layer, and has yielded a record high AM0, 25°C open circuit voltage V_{OC} of 890.3 mV, measured on a thermally diffused p⁺n InP(Cd,S) solar cell⁽⁵⁾. We also investigate a three-layer AR coating composed of In(PO₃)₃/ZnS/MgF₂. Even though, in this paper, we demonstrate the effectiveness of the above described AR coatings on p⁺n InP solar cells, the concept of using a native oxide passivating layer as the first layer of a multilayer AR coating should benefit any III-V compound semiconductor based solar cells, since chemical oxides are readily grown on most III-V semiconductor materials.

EXPERIMENTAL

The 0.8 cm x 0.6 cm p⁺n InP solar cells were fabricated using the closed ampoule technique to diffuse Cd into n-InP:S (N_D-N_A = 3.5×10^{16} to 3.1×10^{17} cm⁻³) with Cd₃P₂ as the diffusion source. Diffusion temperatures were from 560° to 660 °C. The substrates were Czochralski (LEC) grown with EPD of about $5-7 \times 10^4$ cm⁻². Diffusions were performed through chemically grown P-rich oxide cap layers.

Au-Ge was used for the back contact. The Au-Zn (0.18 to 0.3 μm thick) front contact grid was deposited by evaporation and defined using existing photolithography masks, designed for the n/p cell configuration. Because Au based contacts are known to penetrate into InP during sintering at 430 °C, up to depths which are over three times the initial thickness of the evaporated Au-Zn-Au layer, the thickness of the emitter was kept at quite a high value (>3.5 μm) while keeping the thickness of the evaporated contacts below 0.3 μm. After sintering, the thick emitter was thinned down over the uncontacted area using a chemical etch which we call the PNP etch, based on HNO₃, o-H₃PO₄, and H₂O₂, especially developed for this purpose⁽⁶⁾.

The thermal diffusion process just described is inherently a substantially lower cost process as compared to the epitaxial process of junction formation and can potentially be used for large scale batch production of solar cells. To minimize the surface damage which ordinarily always occurs during thermal diffusion, we used a 3 to 5 nm thick In(PO₃)₃-rich oxide cap layer in our diffusion process. In addition, we further improved the quality of our diffused surface by doing a chemical treatment with the PNP etchant after sintering the front contacts of the cell. Simple chemical treatments of InP surfaces using HNO₃ and HF based etchants were found to decrease the SRV to below 5×10^5 cm/s, e.g. 1.7×10^5 for n⁺-InP and 4.7×10^5 cm/s for p⁺-InP, after rinsing the substrates in a HNO₃ (15%) solution⁽⁴⁾.

Using the PNP etch, from low frequency EG-V measurements, we recorded a surface state density minimum (N_{SS}) at the Cd-diffused p⁺-InP/passivating layer interface as low as 2

$\times 10^{10} \text{ cm}^{-2} \text{ eV}^{-1}$ (7). About 40 nm was removed from the surface of a the p^+n InP structure diffused at 660 °C (surface acceptor concentration: $\sim 4 \times 10^{18} \text{ cm}^{-3}$; junction depth: $\sim 3.5 \mu\text{m}$).

The first layer of the designed three-layer AR coating is chemically grown in the process of thinning the emitter using the PNP etchant. A more detailed description of the composition of this oxide is published elsewhere(7). Here, we will simply state that the residual chemical oxide is a two-layered oxide composed of a thick In-rich outer layer and a P-rich layer at the interface with the emitter. This interfacial oxide is rich in $\text{In}(\text{PO}_3)_3$ and has a bandgap of $6.8 \pm 0.2\text{eV}$ (8). Because the dissolution rate is quite reproducible, a controlled thickness of oxide can be grown to serve as the first layer of the designed three-layer AR coating.

The SiO , Sb_2O_3 , MgF_2 and ZnS layers are all deposited by evaporation techniques.

DESIGN OF THE THREE-LAYER AR COATING

The theoretical design of the three-layer AR coating was conducted using standard optical theory based on the matrix description of each layer of a multilayer system. The optical impedance of each layer is assumed known, in order to reduce the number of unknown parameters in the minimization of the reflectance function, and to maintain the problem within the realistic boundaries of commonly used optical materials. The MATLAB algorithm developed to calculate and optimize the parameters of the AR coating is based on work done by Nagendra, and Thutupalli (1988)(9).

For solar cell applications, the design of a good AR coating, contrary to common practice, should not be based merely on reducing the light reflectance but rather maximizing the external quantum efficiency or minimizing the loss of short circuit current due to reflection. This last criterion, expressed in terms of the integrated current loss, defined as the ratio of the integrated short circuit current of the cell to the ideal zero-reflectance integrated short-circuit current, allows one to take into account the incident light spectrum, and eventually the presence of a protective transparent cover glass.

Our experiments have shown that the commonly used double-layer AR coating, ZnS/MgF_2 , deposited on p^+n InP solar cell surface leads to a net decrease of the open circuit voltage (V_{OC}) of the cell by as much as 50 mV due to an increase in SRV(7). For that reason, we recommend a three-layer AR coating with $\text{In}(\text{PO}_3)_3$ passivating oxide as the first layer, followed by either ZnS/MgF_2 or $\text{Al}_2\text{O}_3/\text{MgF}_2$. The $\text{In}(\text{PO}_3)_3/\text{Al}_2\text{O}_3/\text{MgF}_2$ is a new optical system we are proposing for the p^+n InP solar cell. Al_2O_3 is known for its stability, its high dielectric constant, and its radiation tolerance (higher than that of commonly used SiO_2). Also, Al_2O_3 has a closed packed hexagonal crystal structure, closer to that of $\text{In}(\text{PO}_3)_3$. We expect Al_2O_3 to be superior to ZnS . MgF_2 is a generally preferred outer layer which refractive index of 1.37 gives a good optical transition to many protective coverglass/adhesive systems(i.e. fused silica/adhesive 1.46/1.43, microsheet/adhesive 1.53/1.43).

RESULTS AND DISCUSSION

Table 1. and Table 2. give optimum designs of three-layer AR coatings using $\text{In}(\text{PO}_3)_3/\text{ZnS}/\text{MgF}_2$ and $\text{In}(\text{PO}_3)_3/\text{Al}_2\text{O}_3/\text{MgF}_2$ for different thicknesses of the first layer $\text{In}(\text{PO}_3)_3$ and a AMO spectrum ranging from 300 nm to 950 nm. The symbols ICL and IRL represent the Integrated Current Loss, and the Integrated Reflection Loss respectively defined as

$$ICL = 1 - \frac{\int_{\lambda_1}^{\lambda_2} J_{sc,R \neq 0}(\lambda) d\lambda}{\int_{\lambda_1}^{\lambda_2} J_{sc,R=0}(\lambda) d\lambda} \quad \text{and} \quad IRL = \frac{\int_{\lambda_1}^{\lambda_2} R(\lambda) d\lambda}{\int_{\lambda_1}^{\lambda_2} d\lambda}$$

The results suggest that the $\text{In}(\text{PO}_3)_3/\text{Al}_2\text{O}_3/\text{MgF}_2$ coating gives a lower ICL than $\text{In}(\text{PO}_3)_3/\text{ZnS}/\text{MgF}_2$ mainly because of a lower blue reflectance, as shown in Fig. 1.

Considering the first layer of the AR coating, Fig.2 shows that the two-layered oxide ($\sim 750 \text{ \AA}$) reduces the surface reflectance of an InP solar cell from an average 40% (curve a) on a bare surface with no oxide, to about 20% (curve c). In this particular case, after removing the In-rich outer oxide layer, the reflectance of the remaining thin $\text{In}(\text{PO}_3)_3$ oxide (300 \AA) is about 25% (curve b). In Fig. 3, it can be seen that a thick two-layered oxide $\text{In}_2\text{O}_3(\sim 900 \text{ \AA})/\text{In}(\text{PO}_3)_3(\sim 300 \text{ \AA})$ gives a lower overall reflectance than a single layer of SiO (800 \AA thick). Its blue reflectance is lower than either SiO, Sb_2O_3 (750 \AA thick), or a double layer of ZnS/MgF_2 (not shown here). However, Sb_2O_3 has lower mid-spectrum reflectance. Our experiments show that single layers of SiO, Sb_2O_3 as well as a double layer of ZnS/MgF_2 , even though they reduce the surface reflection, also tend to increase the surface recombination velocity on the emitter of a p^+n InP solar cell, leading to a decrease of the open circuit voltage by as much as 50 mV⁽⁷⁾. Although the reflectance of the double-layer chemical oxide is lower than that of SiO, it is still too high for use as the only layer of an efficient AR coating. Furthermore, the In-rich outer oxide layer is unstable and quite electrically conductive, causing a noticeable drop in the shunt resistance R_{sh} and V_{oc} of the cells. It therefore cannot be used, but should rather be removed so that only the P-rich oxide remains for use as the first of a three-layer AR coating.

Curve d) of Fig. 2 shows the calculated reflectance of a three-layer antireflective coating composed of $\text{In}(\text{PO}_3)_3$ (400 \AA), Al_2O_3 (549 \AA), and MgF_2 (712 \AA). It can be seen that the reflectance is reduced to an average of less than 2% when the three-layer coating is used. As, shown in table 1, the actual loss of current density due to reflection loss, will be less than 1%, when one takes into account the spectral response of the InP solar cell.

In Table 3 are presented measured and predicted performance parameters of p^+n (Cd,S) InP solar cells. Rows 1,3 and 4 of the data refer to thick In-rich chemical oxides ($\sim 900 \text{ \AA}$ to 1500 \AA) over an interfacial P-rich oxide ($\sim 300 \text{ \AA}$ to 400 \AA). The parameters in rows 2 and 5 were measured after removing the In-rich oxide from the surface. The increase in V_{oc} and FF are expected as current leakage occurs through the In-rich oxide outside the mesa etched active area. The increase in FF is a consequence of an increase in R_{sh} when the In-rich oxide is removed. After depositing 850 \AA of SiO over the 400 \AA thick P-rich oxide, the increase in J_{sc} is consistent with a decrease in reflectivity. The last row of table 3. gives an experiment-based projection of the performance of the cell in row 6, using the optimum three-layer AR coating designed, the grid coverage of a newly acquired photolithography mask (5%), and an experimentally achievable improved series resistance of about 0.8 \Omega-cm^2 . The projected J_{sc} and V_{oc} values of 37 mA/cm^2 and 894 mV respectively can be obtained based on the quantum efficiency curve of this cell. A fill factor, and efficiency values of 80% and 19.4% respectively can be achieved on such a cell. It should be pointed out that these values are below the experiment-based projections for our state-of-the-art p^+n InP solar cells where in addition to using the designed 3-layer AR coating, reducing the emitter junction depth to less than 0.3 \mu m , the specific contact resistance to less than $10^{-3} \text{ \Omega-cm}$, should make a solar cell of efficiency, $\eta=21.3\%$ achievable⁽⁵⁾.

CONCLUSIONS

The dual problem of surface passivation and antireflection coating design of III-V compound based solar cells have been addressed. We have designed a three-layer optimized AR coating for p⁺n InP solar cell, which brings the average reflectance down from about 40% to less than 2% while at the same time significantly improving the J_{SC} and V_{OC} by passivating the top surface of the emitter. This has been accomplished by using a chemically grown In(PO₃)₃-rich passivating oxide layer as the first layer of a 3-layer AR coating, with Al₂O₃ and MgF₂ as the second and third layers. We believe that the significant front surface passivation is to a large extent responsible for our achieving the record high efficiency V_{OC} of over 890 mV. This concept of using a passivating chemically grown oxide as the first layer of a multilayer AR coating can be beneficial to other III-V compound solar cells as well.

REFERENCES

- (1). M.B. Spitzer, B. Dingle, J. Dingle, and R. Morrison, "A review of Indium Phosphide Space Solar Cell Fabrication Technology", Proceedings of the 21st IEEE Photovoltaic Specialists Conference, 1990, pp. 196-206.
- (2). J.F. Wager and C.W. Wilmsen, Physics and Chemistry of III-V compound Semiconductor Interfaces, edited by Carl W. Wilmsen, Plenum Press, 1985, pp. 165-211.
- (3). M.Faur, M.Faur, P.Jenkins, M.Goradia, S.Bailey, D.Jayne, I.Weinberg and C.Goradia, "Study of Surface Passivation of InP," Surface and Interface Analysis, 15, 745 (1990)
- (4). P.Jenkins, M.Goradia, M.Faur, S.Bailey and M.Faur, "Measurement of Surface Recombination Velocity on Heavily Doped Indium Phosphide," Proc. 21st IEEE PVSC, 1990, p.399.
- (5). M. Faur, M. Faur, D.J. Flood, C. Goradia, D.J. Brinker, M. Goradia, J. Moulot, S. Bailey, N.S. Fatemi, P.P. Jenkins, and D. M. Wilt, "Status of Diffused Junction p⁺n InP Solar Cells for Space Power Applications", First World Conference on Photovoltaic Energy Conversion, December 5-9, 1994, Hawai.
- (6). M.Faur, M.Faur, D.T.Jayne, S.Bailey and M.Goradia, " Etchant for Chemical Thinning of InP and its Applications in the Fabrication of InP Diffused Junction Solar Cells," Surface and Interface Analysis, 21, 110 (1994)
- (7). M.Faur, M.Faur, D.J.Flood, D.J.Brinker, C.Goradia, S.Bailey, I.Weinberg, M.Goradia, D.T.Jayne, J.Moulot and N.Fatemi, "Effective First Layer Antireflecting Coating on InP Solar Cells Grown by Chemical Oxidation," Proc. 6th Int'l IPRM Conf. , 1994, p. 492.
- (8). J.Joseph, Y.Robach, G.Hollinger, P.Ferret and M.Pitval, "The Passivation of InP by In(PO₃)₃ for MISFET Applications," Proc. 1st Int'l Conference on Indium Phosphide and Related Materials IPRM, 1989, p.268.
- (9). C.L. Nagendra and G.K.M. Thutupalli, "Design of Three-layer Antireflection Coatings: A Generalized Approach", Applied Optics, vol. 27, no.11, 1 June 1988, pp. 2320-2332

Table 1: Summary of 3-layer ARC design with $\text{In}(\text{PO}_3)_3/\text{Al}_2\text{O}_3/\text{MgF}_2$

| $d_{\text{In}(\text{PO}_3)_3}$ (Å) | $d_{\text{Al}_2\text{O}_3}$ (Å) | d_{MgF_2} (Å) | J_{sc} (AMO) mA/cm^2 | ICL (%) | IRL (%) |
|---------------------------------------|------------------------------------|---------------------------|--|------------|------------|
| 50 | 647 | 490 | 43.99 | 1.62 | 2.12 |
| 100 | 602 | 510 | 44.00 | 1.60 | 2.09 |
| 150 | 534 | 558 | 44.03 | 1.54 | 2.01 |
| 200 | 460 | 616 | 44.06 | 1.46 | 1.85 |
| 250 | 420 | 641 | 44.11 | 1.37 | 1.73 |
| 300 | 422 | 635 | 44.17 | 1.23 | 1.54 |
| 350 | 425 | 624 | 44.24 | 1.06 | 1.38 |
| 400 | 549 | 712 | 44.43 | 0.64 | 1.03 |
| 450 | 425 | 656 | 44.34 | 0.83 | 1.81 |
| 500 | 500 | 465 | 44.06 | 1.48 | 2.79 |

Table 2: Summary of 3-layer ARC design with $\text{In}(\text{PO}_3)_3/\text{ZnS}/\text{MgF}_2$

| $d_{\text{In}(\text{PO}_3)_3}$ (Å) | d_{ZnS} (Å) | d_{MgF_2} (Å) | J_{sc} (AMO) mA/cm^2 | ICL (%) | IRL (%) |
|---------------------------------------|-------------------------|---------------------------|--|------------|------------|
| 50 | 466 | 899 | 44.29 | 0.95 | 1.30 |
| 100 | 415 | 898 | 44.28 | 0.97 | 1.36 |
| 150 | 363 | 894 | 44.27 | 0.99 | 1.40 |
| 200 | 417 | 767 | 43.08 | 3.66 | 6.13 |
| 250 | 197 | 825 | 43.75 | 2.15 | 2.59 |
| 300 | 239 | 918 | 44.3 | 0.93 | 1.79 |
| 350 | 291 | 773 | 43.88 | 1.88 | 1.89 |
| 400 | 240 | 760 | 43.78 | 2.10 | 2.06 |
| 450 | 178 | 753 | 43.69 | 2.29 | 2.22 |
| 500 | 114 | 752 | 43.64 | 2.41 | 2.33 |

Table 3: AM0, 25°C performances of selected p⁺n InP diffused solar cells measured at NASA LeRC.

| AR Coating | Approx. Emitter Thickness (μm) | Rs (Ω-cm ²) | Jsc (mA/cm ²) | Voc (mV) | FF (%) | η (%) |
|--|--------------------------------|-------------------------|---------------------------|----------|--------|-------|
| In ₂ O ₃ (~1500 Å)/In(PO ₃) ₃ (~400Å) | 0.45 | 3.52 | 26.3 | 887.6 | 69 | 11.98 |
| In(PO ₃) ₃ (~400Å) | 0.45 | 3.24 | 27.5 | 884.6 | 73.7 | 12.95 |
| In ₂ O ₃ (~900 Å)/In(PO ₃) ₃ (~300Å) | 0.4 | 3.35 | 28.2 | 881.7 | 72.6 | 13.2 |
| In ₂ O ₃ (~1100 Å)/In(PO ₃) ₃ (~400Å) | 0.3 | 4.38 | 29.4 | 877.2 | 61.7 | 11.63 |
| In(PO ₃) ₃ (~400Å) | | | 27.6 | 886.6 | 62.8 | 11.25 |
| SiO ₂ (~850Å)/In(PO ₃) ₃ (~400Å) | | | 30.95 | 887.5 | 61.5 | 12.36 |
| * Optimized In(PO ₃) ₃ (400Å)/Al ₂ O ₃ (549Å)/MgF ₂ (712Å) | 0.3 | 0.8 | 37.1 | 894.2 | 80.1 | 19.43 |

Cell area: 0.48 cm²; front coverage: 9.55%; distance between the 0.3μm thick fingers: 620μm. * Experiment-based projected parameters for the cell in row 6.

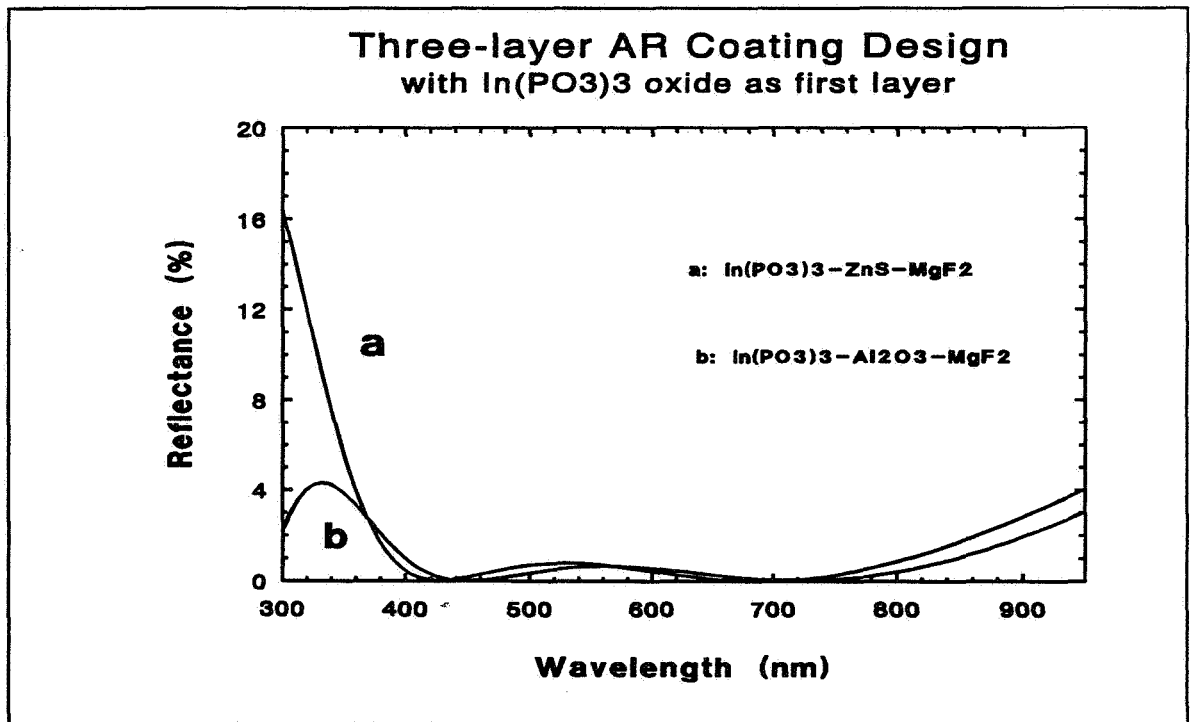


Fig. 1. Reflectance on optimized Three-layer AR coating using: a) In(PO₃)₃/ZnS/MgF₂ b) In(PO₃)₃/Al₂O₃/MgF₂

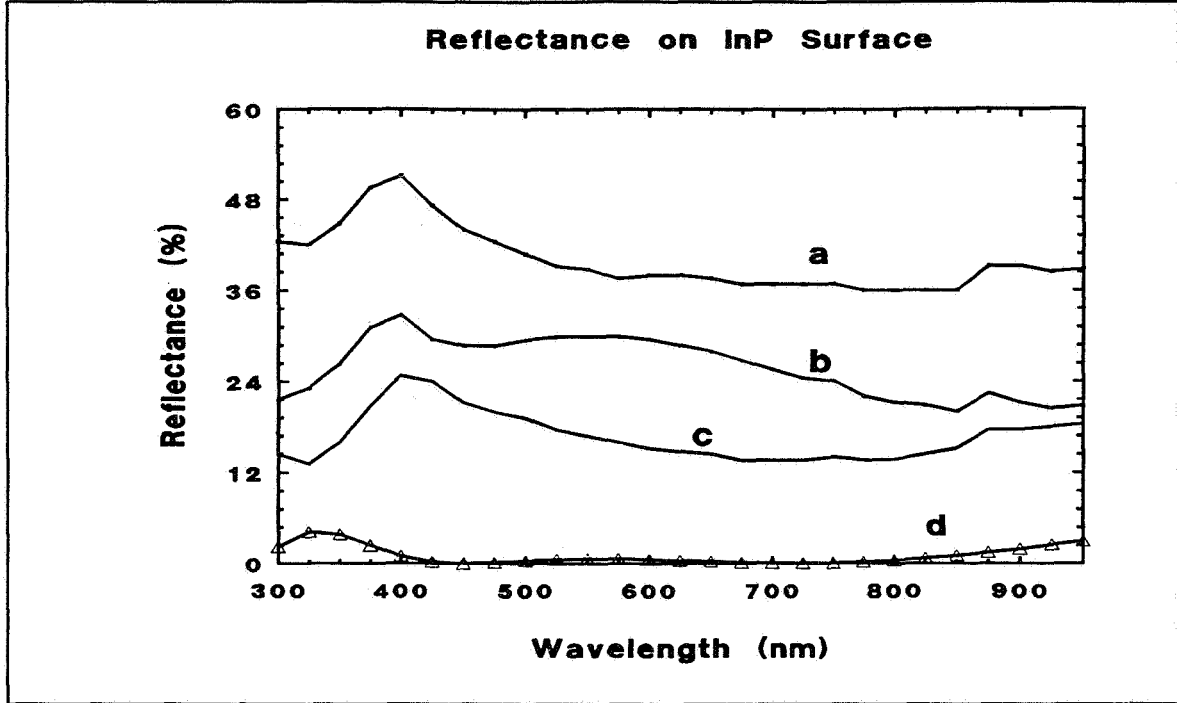


Fig. 2: Surface reflectance vs. wavelength of a) a bare p⁺n InP surface (no oxide), no grid fingers; p⁺n InP solar cells with: b) 10.5% grid coverage, 400 Å thick surface oxide layer; c) 10.5% grid coverage and 750 Å surface oxide; d) a 3-layer AR coating, In(PO₃)₃/Al₂O₃/MgF₂.

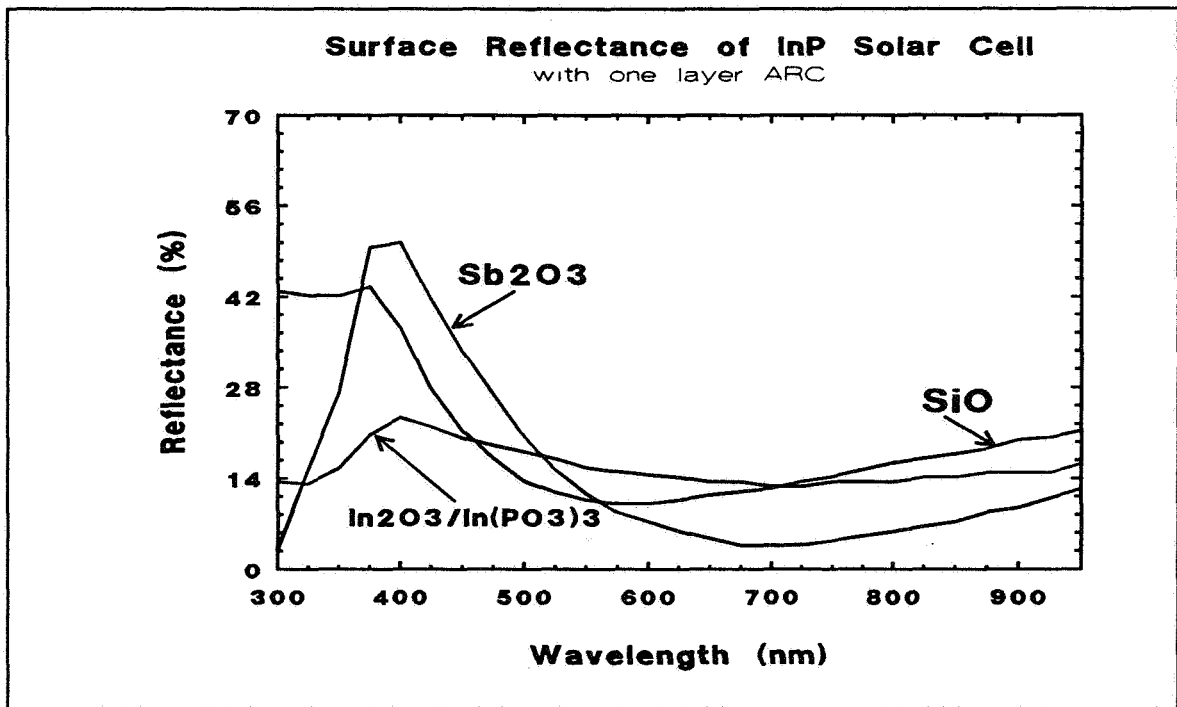


Fig. 3: Surface reflectance vs. wavelength of p⁺n InP solar cells using single layer AR coating of the passivating chemical oxide (In₂O₃/In(PO₃)₃ ~1100/400Å); SiO (800Å); and Sb₂O₃ (750Å).

LIGHTWEIGHT, LIGHT-TRAPPED, THIN GaAs SOLAR CELL FOR SPACECRAFT APPLICATIONS: PROGRESS AND RESULTS UPDATE¹

M.H. Hannon, M.W. Dashiell, L.C. DiNetta, and A.M. Barnett
AstroPower, Inc.
Newark, DE 19716-2000

IN-50400
S21

ABSTRACT

Progress is reported with respect to the development of ultra-lightweight, high performance, thin, light trapped GaAs solar cells for advanced space power systems. Conversion efficiencies of 17.9% (AM0, 1X) have been demonstrated for a 3 μm thick, 1 cm^2 solar cell. This results in a specific power of over 1020 W/kg (with a 3 mil cover glass) and a power density of 240 W/m². Device parameters were 1.015 volts open circuit voltage, 80% fill factor, and a short-circuit current density of 29.54 mA/cm². In addition to silicone bonding, the use of electrostatic bonding to attach the cover glass support to the front surface enables an ultra-thin, all back contact design that survives processing temperatures greater than 750°C. This also results in a 10% reduction of the cell weight for a potential specific power of 1270 W/kg. All back contact, ultra-thin, electrostatically bonded GaAs solar cell prototypes have been fabricated demonstrating an open circuit voltage of 1 volt for a cell base thickness of 1 μm with a 0.5 μm emitter. This technology will result in a revolutionary improvement in survivability, performance, and manufacturability of lightweight GaAs solar cell products for future Earth-orbiting science and space exploration missions. The thin, electrostatically bonded, all back contact GaAs device technology has multiple uses for specialty high performance solar cells and other optoelectronic devices.

INTRODUCTION

A schematic cross-sectional representation of the silicone bonded AstroPower prototype thin GaAs solar cell design is shown in Figure 1. This device is supported by a 3-mil cover glass which has been attached to the front surface with a 1-mil silicone adhesive.

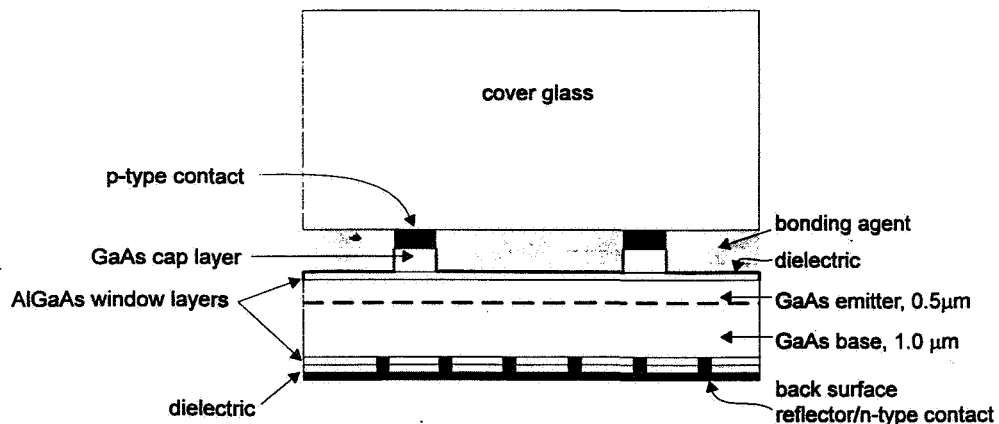


Figure 1. Ultra-thin GaAs solar cell with light trapping.

¹This research was supported in part by the Department of the Air Force and managed by Phillips Laboratory, Space Power and Thermal Management Division under SBIR contract #F29601-93-C-0188.

The improved device design utilizes electrostatic bonding to attach the cover glass support to the front surface, enabling an ultra-thin, all back contact design that eliminates grid shading. The electrostatically bonded, ultra-thin structure survives process temperatures exceeding 750°C. The conceptual design of this unique solar cell is shown in Figure 2. The p-type region is diffused from the back of the device to the emitter.

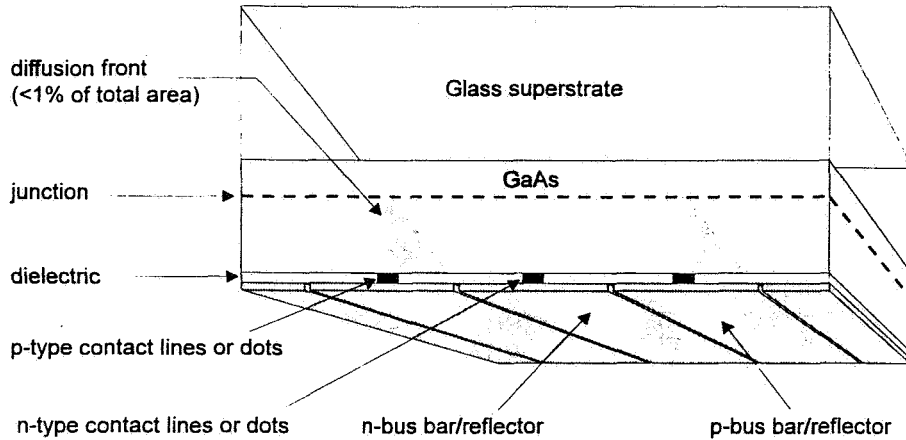


Figure 2. Electrostatically bonded, all back contact, ultra-thin GaAs solar cell.

The benefits of this device technology include the following:

- specific power improvements over state of the art GaAs/Ge devices
- high radiation resistance and lower on-orbit operating temperature
- all back contact design which simplifies electrostatic bonding and eliminates grid shading
- array tabbing does not require wraparound interconnections
- enables cost-effective manufacturing, eliminates adhesive degradation, and provides high structural integrity
- transferable to any epitaxial growth technology and various solar cell materials and designs including tandem solar cells and high voltage concentrator cells
- applicable to integrated logic components, LEDs, LED displays, flat screen display drivers, waveguides, and microwave devices

High Performance Benefits

The ultra-thin, lightweight, light-trapped GaAs solar cell design offers a high specific power in comparison to silicon and GaAs/Ge devices, which is important for space applications (ref. 1). Light trapping increases the effective optical path length with the use of a reflector. The benefits of light trapping in GaAs can be realized by increased optical absorption, collection efficiency and photon recycling (ref. 2). These features lead to increased open circuit voltages and short circuit currents (ref. 3).

Radiation damage is the primary degradation mechanism for GaAs solar cells deployed in space. The ultra-thin, light-trapped GaAs solar cell will have significantly increased EOL efficiencies compared with conventional solar cell structures because of the thin device layers associated with the structure. This design will be less sensitive to changes in bulk diffusion length due to the increased optical path length and decreased recombination volume.

Thermal stability and tolerance to UV degradation are inherent to the thin device structure and electrostatically bonded 3-mil glass superstrate. There is neither a darkening effect such as that which occurs with adhesives after extended exposure to UV light, nor degradation of the bond interface. The maximum power to

weight ratios can be attained since no additional material is used to form the bond and the electrostatic bond will not suffer from degradation upon exposure to high temperatures.

The all back contact technology enables tabbing to the p-type and n-type regions of the device to be easily accomplished from the back of the structure. Placement of the grid pattern for both the n- and p-type contacts on the back of the solar cell eliminates grid shading losses for light entering the front of the device. In contrast to other coplanar contact designs, this technology eliminates the need for micro-machining the solar cell.

The high performance benefits of AstroPower's ultra-lightweight, thin, light trapped GaAs solar cells enable the devices to meet the technology demands for solar cells with increased performance, as required for the space cell industry (ref. 4).

RESULTS AND DISCUSSION

The highest efficiency obtained for an ultra-thin, adhesive bonded, LPE grown device achieved to date at AstroPower is 17.9%. The results of the current-voltage and quantum efficiency measurements are shown in Figures 3 and 4. As can be seen, the open circuit voltage and fill factor are quite high. The quantum efficiency measurement indicates some losses in blue response which can be improved with optimization of the emitter and window layer.

Table I lists the weight contribution of the major material components for this solar cell. Reducing the device thickness to 2 microns, with a 2 micron-thick GaAs contact layer, would reduce the GaAs contribution to 5% of the total cell weight. Also, with the electrostatically bonded, all back contact device, the weight of the adhesive, which is approximately 10% of the total cell weight, would be eliminated. This weight reduction will lead to the highest possible power densities (greater than 1270 W/kg) for these ultra-thin solar cells.

| | |
|--------------------|--------------------------|
| Voc | 1.015V |
| Jsc | 29.54 mA/cm ² |
| Fill Factor | 80.3% |
| Area | 1 cm ² |
| Thickness | 3 μm |
| Specific Power | 1020 W/kg |
| AM0, 1X efficiency | 17.9% |

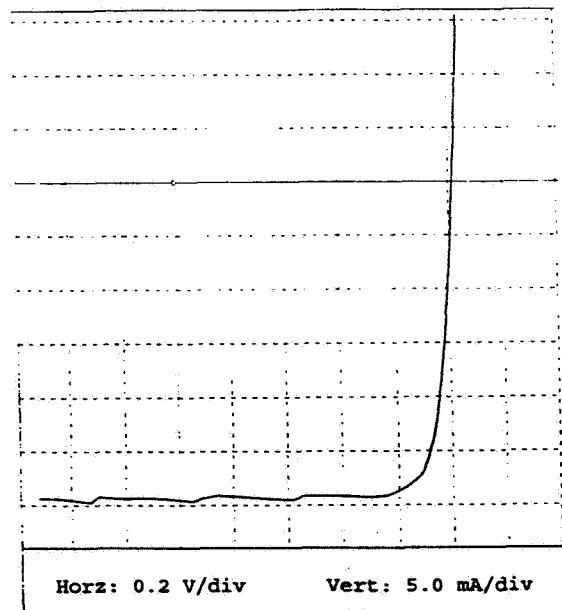


Figure 3. Current voltage measurement for ultra-thin device G13901A.

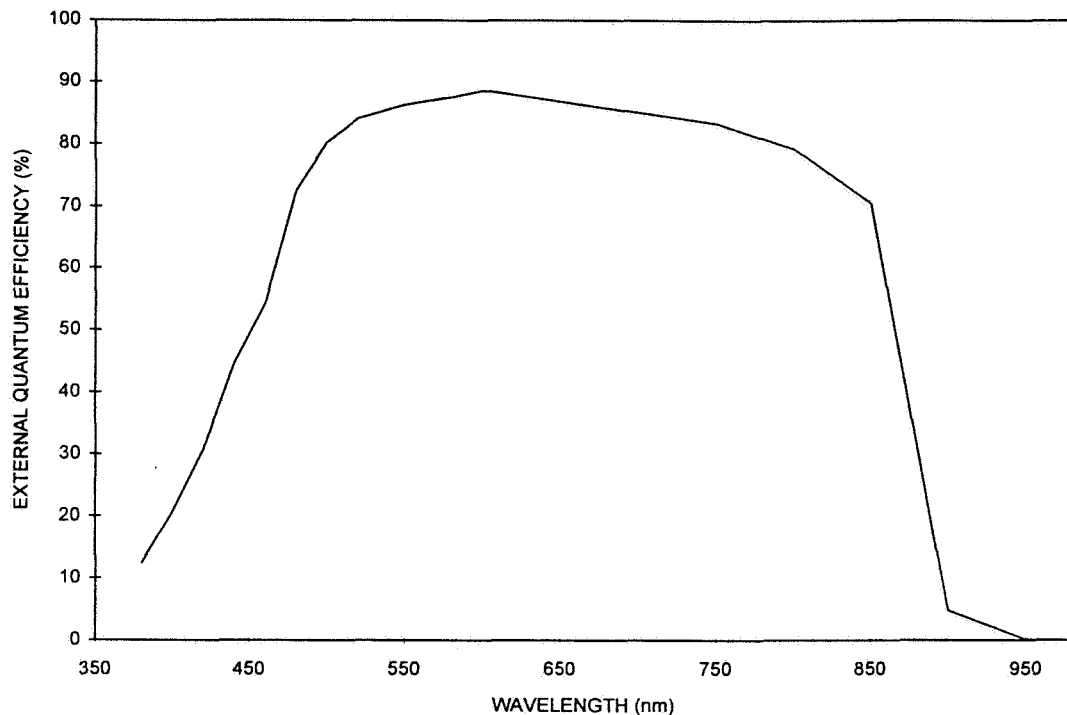


Figure 4. External quantum efficiency measurement for ultra-thin device G13901A.

Table 1. Weight contribution of the major solar cell components for the ultra-thin device (G13901A).

| Material | Density | Total Weight/cm ² | Percentage of Total Cell Weight |
|-----------------------------------|------------------------|------------------------------|---------------------------------|
| Pilkington CMG glass (3-mil) | 2.554g/cm ³ | 19.46mg | 82% |
| Sylgard Silicone Adhesive (1-mil) | 0.9g/cm ³ | 2.29mg | 10% |
| Gallium Arsenide | 5.32g/cm ³ | 1.85mg | 8% |

Typical values for the dark diode reverse saturation current densities for the GaAs solar cells are $3 \times 10^{-19} \text{A/cm}^2$ and $5 \times 10^{-11} \text{A/cm}^2$ for the diffusion and depletion region recombination components respectively. These current densities provide an indication of the junction quality, minority carrier lifetime, and surface passivation for the device. The dark diode current values obtained at AstroPower are among the best reported by a number of researchers for high efficiency GaAs solar cells (refs. 5, 6, and 7), further demonstrating the value of near equilibrium growth processes.

Light-trapping has been demonstrated on the ultra-thin devices. The external quantum efficiency curve illustrated in Figure 5 shows an increase in long wavelength response (between 650 and 870 nm) of the thinned solar cell with a back surface reflector, compared to the same device before the thinning procedure (on the GaAs substrate). The external quantum efficiency of this device was increased by 5.2% at 850 nm with the incorporation of a back surface reflector. The gain in short circuit current density for this solar cell is approximately 0.7 mA/cm^2 . This gain is expected to increase as the active device thickness is decreased to less than 2 microns. The blue response of this device was low due to a non-optimized AlGaAs front surface passivation layer.

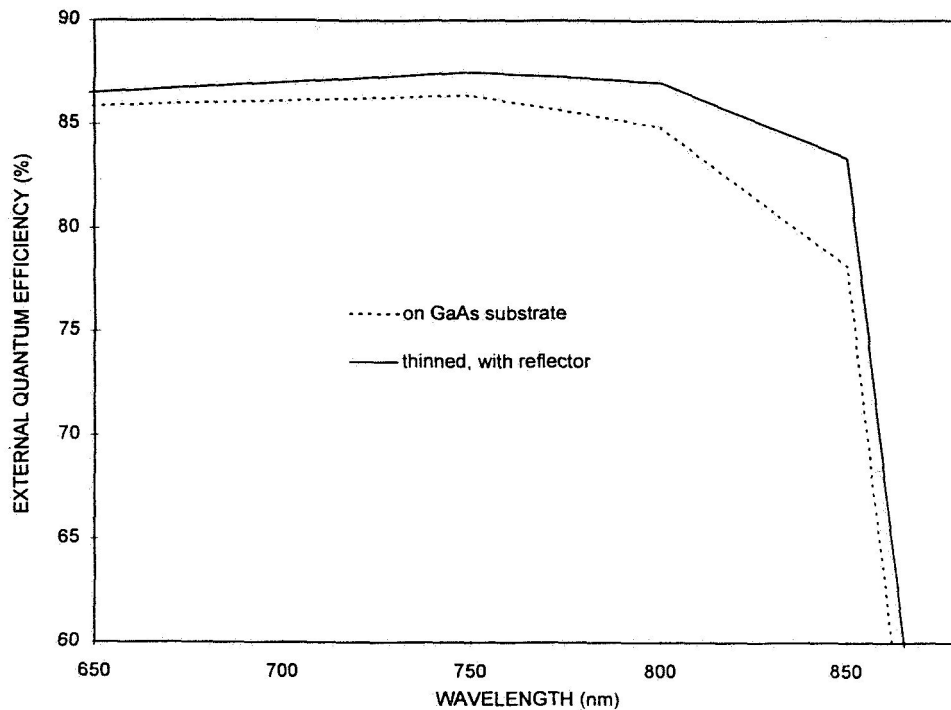


Figure 5. External quantum efficiency of sample G13405B.

Photographs of the ultra-thin, light trapped device are shown in Figure 6. The front surface is shown in Figure 6a and the back surface including the n-type contacts and silver reflector is shown in Figure 6b.

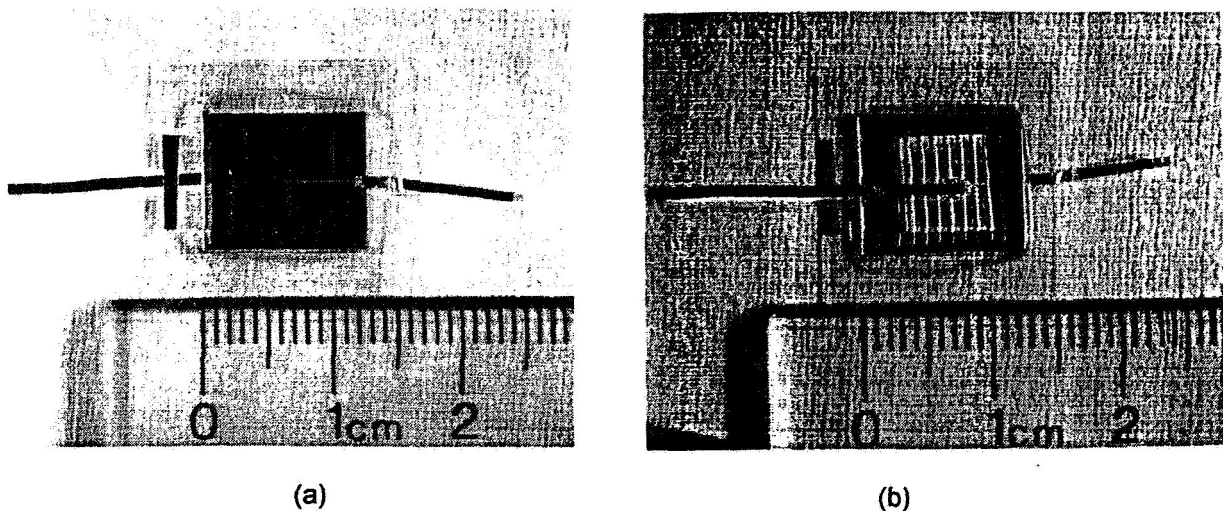


Figure 6. Photograph of the front (a) and back (b) surface of the ultra-thin, light trapped GaAs solar cell.

Fabrication of large area (8 cm^2) devices is underway. A photograph of an 8 cm^2 GaAs solar cell fabricated on the GaAs substrate is shown in Figure 7. Similar devices are being processed as ultra-thin, light trapped solar cells. The results of six 1 cm^2 devices processed from one $2 \times 4 \text{ cm}^2$ LPE growth are shown in Table II. The performance of these devices demonstrates the capability of the material to support large area devices.

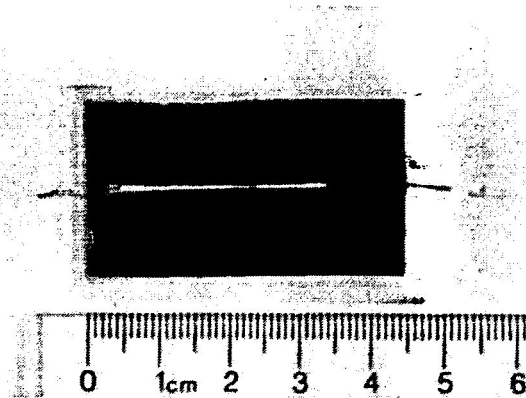


Figure 7. Photograph of a large area (8cm²) GaAs solar cell.

Table II. Current-voltage characteristics of six 1 cm² devices fabricated from one large area (8cm²) LPE growth.

| Cell Number | Voc (V) | Jsc (mA/cm ²) | Fill Factor (%) | Efficiency (AM0, 1X, 25°C) on GaAs substrate (%) | Efficiency (AM0, 1X, 25°C) of Ultra-thin Device (%) |
|-------------|---------|---------------------------|-----------------|--|---|
| G13901A | 1.020 | 29.0 | 78.9 | 17.29 | 17.98 |
| G13901B | 1.015 | 30.0 | 79.3 | 17.89 | 17.56 |
| G13901C | 1.007 | 29.1 | 78.3 | 16.98 | 16.98 |
| G13901D | 1.008 | 30.2 | 73.8 | 16.64 | 13.94 |
| G13901E | 1.011 | 31.0 | 78.4 | 18.20 | 17.30 |
| G13901F | 0.987 | 30.8 | 72.5 | 16.33 | 15.17 |
| Median | 1.010 | 30.1 | 76.4 | 17.14 | 17.14 |

For the all back contact, electrostatically bonded, ultra-thin GaAs solar cells, the p-type emitter is extended to the back of the solar cell by a selective diffusion. The surface area of the diffusion front is less than 1% of the total area of the ultra-thin solar cell. Zinc diffusion profiles were determined by electrochemical CV profiles at BioRad Semiconductor in Mountain View, California. The electrochemical CV profiles for two zinc diffusions into n-type GaAs substrates (Si: 0.89-3.92x10¹⁸/cm³) are shown in Figures 8. Figure 8a shows the results of a 2 hour zinc diffusion at 700°C. The p-region extends at least 1.5 microns into the GaAs substrate and has a high conductivity. The results of a 2 hour zinc diffusion at 750°C are shown in Figure 8b. the p-region extends at least 3 microns into the GaAs substrate and has a high conductivity (50(Ω-cm)⁻¹). These measurements indicate that the resistance of the zinc diffused regions is minimal and the width of the back contact fingers can be reduced to less than 25 microns without hindering the performance of the solar cell.

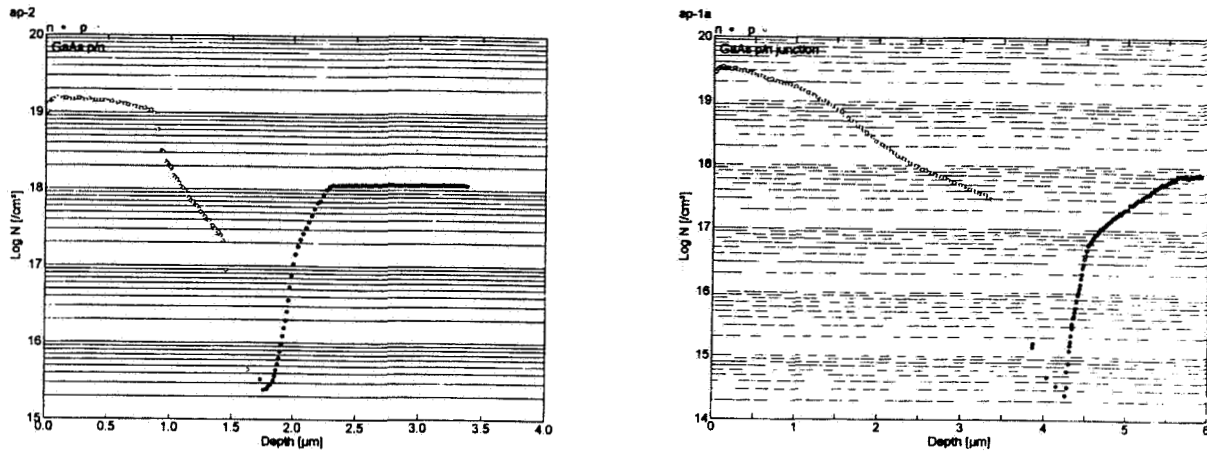


Figure 8. Electrochemical CV profiles for zinc diffusion into a GaAs substrate a) 2 hour zinc diffusion at 700°C and b) 2 hour zinc diffusion at 750°C.

In order to achieve a high efficiency, ultra-thin, all back contact solar cell, a high temperature glass formulation that is CTE matched to GaAs and has a high softening point has been developed. This glass has a softening point of 890°C, and a CTE of $6.0 \times 10^{-6}/K$. The annealing point of this glass is approximately 650°C. Void-free, 6 cm² bonds to LPE GaAs layers on GaAs substrates have been obtained with this high temperature glass.

GaAs solar cell structures electrostatically bonded to this glass survive the substrate removal procedure and subsequent processing steps. Ultra-thin (less than 5 microns) GaAs/glass laminates have been heat cycled to 750°C for two hours and cooled in liquid nitrogen with no degradation of the bond interface. Electrostatic bonding to this high temperature glass formulation enables high temperature device processing to occur after coverslide bonding. Future plans include space qualifying this glass with the appropriate testing laboratory and continuing to work with the glass manufacturer to ensure space survivability of the glass superstrate.

Prototype all back contact devices are presently being processed. To date, open circuit voltages of 1 volt have been demonstrated for a cell base thickness of 1.0 micron with a 0.5 micron emitter. In addition to completing 16 and 25 cm² all back contact solar cells on LPE material, this technology will be demonstrated on MOCVD material over the next few months.

CONCLUSIONS

High performance, lightweight, thin, light trapped GaAs solar cells have been demonstrated. Conversion efficiencies of over 17.9% (AM0, 1X) have been demonstrated resulting in a specific power of 1020 W/kg (with a 3-mil cover glass) and a power density of 240 W/m². The incorporation of light trapping has increased the external quantum efficiency of these solar cells in the long wavelength range. Large area, electrostatically bonded, ultra-thin GaAs solar cell structures have demonstrated survivability to 750°C, with no degradation of the bond interface. Prototype all back contact devices with open circuit voltages of 1 volt have been fabricated. Future plans include completing 4 cm² all back contact, electrostatically bonded, thin, light trapped GaAs solar cells on both LPE and MOCVD material for a potential specific power of 1270 W/kg.

The success of this program can lead to the deployment of high performance, thin GaAs solar cells in the space environment. AstroPower's solar cell design can have a significant impact on the longevity and power generation capabilities of space power supplies. The fabrication technology has multiple uses for specialty high performance solar cells and other optoelectronic devices.

REFERENCES

1. Kelly Gaffney, "Air Force Activities in Space Photovoltaic Power System Technology", Proc. NASA Space Photovoltaic Research and Technology Conference, Cleveland, Ohio (1994).
2. G. Lush and M. Lundstrom, "Thin film approaches for high efficiency III-V cells", Solar Cells, 30 (1991).
3. C.B. Honsberg and A.M. Barnett, "Light Trapping in Thin Film GaAs Solar Cells", Proc. 22nd IEEE Photovoltaic Specialists Conference, Las Vegas, Nevada, (1991).
4. P.A. Iles and F. Ho, "Technology Challenges for Space Solar Cells", Proc. 24th IEEE Photovoltaic Specialists Conference, (1994).
5. L.C. Olsen, G. Dunham, F.W. Addis, D. Huber, and D. Daling, "Electro-optical Characterization of GaAs Solar Cells, Proc. 19th IEEE Photovoltaic Specialists Conference, (1987).
6. P.D. DeMoulin, C.S. Kyuno, M.S. Lundstrom, and M.R. Melloch, "Dark IV Characterization of GaAs p/n Heteroface Cells, Proc. 19th IEEE Photovoltaic Specialists Conference, (1987).
7. S.A. Ringel, A. Rohatgi, and S.P. Tobin, "An Approach Toward 25% Efficient GaAs Heteroface Solar Cells, IEEE Transactions on Electron Devices, vol. 36, No. 7, July 1989.

522-20

50407

125895

10p

LABORATORY INSTRUMENTATION AND TECHNIQUES FOR CHARACTERIZING MULT-JUNCTION SOLAR CELLS FOR SPACE APPLICATIONS

James R. Woodyard
Wayne State University
Detroit, Michigan 48202

ABSTRACT

An integrated system is described which consists of a spectral radiometer and dual-source solar simulator, and personal computer based current-voltage and quantum efficiency equipment. The spectral radiometer is calibrated using a tungsten-halogen standard lamp with a calibration based on NIST scales. The quantum efficiency apparatus includes a photodiode calibrated using NIST scales and a monochromatic probe beam. The apparatus is used to measure the dependence of the absolute external quantum efficiency of solar cells at various forward-bias voltages including the maximum-power point under AM0 light bias. Quantum efficiencies of multi-junction cells were measured with both spectral-light bias and AM0 light bias. Measured spectral irradiances of the dual-source simulator were convoluted with cell quantum efficiencies to calculate cell currents as function of voltage. The calculated currents agree with measured currents at the 1% level.

INTRODUCTION

Multi-junction solar cells are attractive for space applications because they can be designed to convert a larger fraction of AM0 into electrical power than single-junction cells. The performance of multi-junction cells is much more sensitive to the spectral irradiance of the illuminating source than single-junction cells. The design of high efficiency multi-junction cells for space applications requires matching the optoelectronic properties of the junctions to AM0 spectral irradiance. Unlike single-junction cells, it is not possible to determine the quantum efficiency of multi-junction cells using only a monochromatic probe beam. It is necessary to use a light bias because of the series nature of the cell structure. Burdick and Glatfelter (1) reported a measurement technique for multi-junction cells which employs a spectral light-bias technique. While the method is useful for understanding and improving multi-junction solar cells, it does not yield the absolute quantum efficiency under AM0 light-bias. Because of the non-linear nature of multi-junction cells, current-voltage characteristics under AM0 conditions cannot be calculated from measurements under non-AM0 conditions using spectral-correction methods.

The goal of the research is to develop a solar simulator which approximates AM0 spectral irradiance, and laboratory instrumentation and techniques, for use in measuring the quantum efficiency and I-V characteristics of multi-junction solar cells under AM0 power-generating conditions. An integrated system is described which consists of a spectral radiometer and dual-source solar simulator, and personal computer based current-voltage and quantum efficiency equipment. The spectral radiometer is calibrated using a tungsten-halogen standard lamp which has a calibration traceable to National Institute of Science and Technology (NIST) scales. The calibrated spectral radiometer is used to measure the spectral irradiance of the light-bias beam and obtain an integral fit of it in two spectral regions to the World Radiation Laboratory (WRL) AM0 spectral irradiance data. The solar simulator produces a light-bias beam which is used for current-voltage and external absolute quantum efficiency measurements. The quantum efficiency apparatus includes a photodiode calibrated using NIST scales and a monochromatic probe beam. The apparatus is used to measure the absolute external quantum efficiency of triple-junction solar cells at various forward-bias voltages under both spectral-light and AM0 light-bias conditions.

SOLAR SIMULATOR DEVELOPMENT

The spectral irradiance of the solar simulator plays an important role in the characterization of multi-junction solar cells. Characterization techniques such as light I-V and light-biased quantum efficiency measurements require

matching the solar simulator spectral irradiance as close as possible to the AM0 spectrum in order to predict the performance of cells in a space environment with AM0 illuminance.

The spectral irradiance of the solar simulator used in this work was measured with a spectral radiometer constructed and calibrated in our laboratory. The spectral radiometer employs an integrating sphere, order-sorting filters, single-stage monochromator and detector; the detector is a silicon photodiode and temperature stabilized. The instrument is computer interfaced for control purposes, and data acquisition, display and analyses. The spectral radiometer was calibrated with a type FEL 1000 W quartz tungsten-halogen standard lamp traceable to NIST scales; calibrations were carried out using the procedure specified in NBS Special Publication 250-20. The accuracy of measurements in the 350 to 900 nm range is believed to be better than 4%; the precision of consecutive spectral scans is better than 1%.

A model SS1000 solar simulator manufactured by Optical Radiation Corporation (ORC) was used in this work. The light source in the simulator is a xenon high-pressure discharge lamp. The spectral irradiance of the solar simulator, as delivered by ORC, is shown in Figure 1 by the filled circles. The spectral irradiance of the WRL AM0 solar spectrum is shown for comparison purposes in the figure by the solid line. The spectral irradiance of the simulator differs from AM0 in a major way in the 300 to 370 nm and 650 to 1000 nm wavelength ranges. Above 800 nm the spectral irradiance of the solar simulator is dominated by xenon lines. The differences in spectral irradiances of the ORC solar simulator when compared to AM0, while generally not important in characterizing single-junction solar cells, can introduce major errors in light I-V and quantum efficiency measurements of multi-junction cells.

The solar simulator was modified to produce a spectral irradiance in closer agreement with the spectral irradiance of the AM0 solar spectrum using a design reported by Bennett and Podlesny (2). In order to obtain a better match with the AM0 spectral irradiance at wavelengths above 700 nm, a 600 W tungsten-halogen lamp and cold mirror were added to the solar simulator. A diagram illustrating the optics of the modified simulator is shown in Figure 2.

The design includes two elliptical mirrors and a flat cold mirror to focus illumination from the tungsten-halogen and xenon lamps on an optical integrator; the design produces a horizontal light beam which is compatible with the horizontal optics of the spectral radiometer and quantum efficiency apparatus. The cold mirror was custom fabricated to transmit wavelengths greater than 750 nm and reflect shorter wavelengths. The original folding mirror in the simulator was replaced with the cold mirror; it is mounted at forty-five degrees with respect to both the xenon and tungsten-halogen lamps. The cold mirror serves two purposes. It trans-

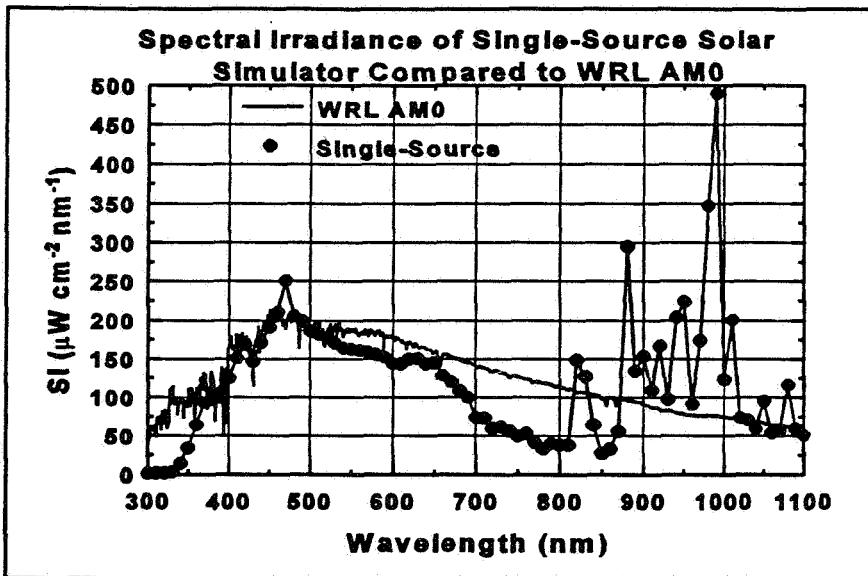


Figure 1: Measured spectral irradiance of single-source solar simulator compared with World Radiation Laboratory AM0 spectral irradiance.

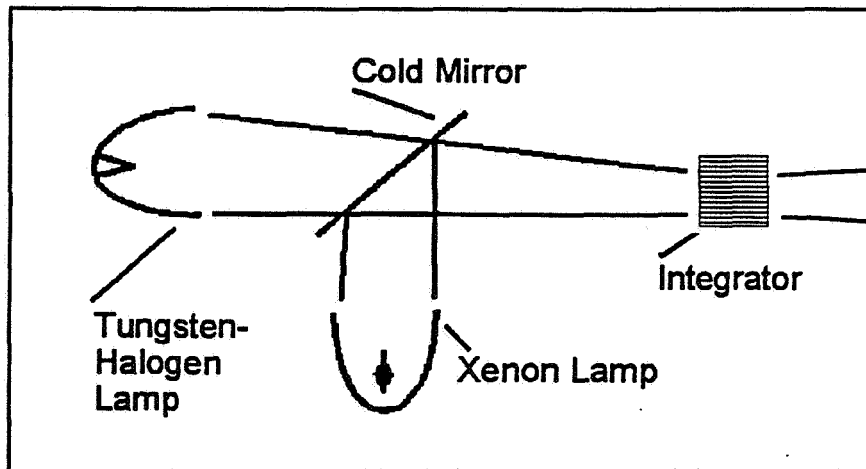


Figure 2: Optics of Dual-Source Simulator

mits the xenon spectrum at wavelengths greater than 750 nm and reflects wavelengths less than 750 nm. The effect of the mirror on the spectral irradiance of the xenon lamp is to attenuate the xenon lines shown in Figure 1. The mirror transmits the spectral irradiance of the tungsten-halogen lamp with wavelengths greater than 750 nm while reflecting wavelengths less than 750 nm.

The optics of the solar simulator, as delivered by ORC, incorporated a second folding mirror, Vicor beam splitter and Pyrex collimating lens. The Vicor beam splitter was used to produce an optical signal for the feed-back circuit which stabilizes the xenon lamp current. The folding mirror and collimating lens produce a vertical beam focussed on a horizontal work surface. The folding mirror and lens were removed to produce a horizontal light beam. The Vicor beam splitter was replaced with a high-quality quartz beam splitter. The modification in the optics also increased the UV throughput of the simulator. Additional air cooling capacity was added in order to dissipate the power produced by the tungsten-halogen lamp. The electronics supplied by ORC with the simulator were used to power and control the xenon lamp. A D.C. power supply regulated at the 0.01 % level was added to the system for powering the tungsten halogen lamp. The stability of the dual-source light beam intensity is at the 0.1 % level.

The spectral irradiance of the dual-source solar simulator was fit to the WRL AM0 spectrum by integrating and comparing the two spectral irradiances in two regions. The simulator and WRL spectral irradiances were integrated in two regions and compared. One region employed wavelength limits of 350 and 750 nm; the other region had limits of 750 and 900 nm. The limits of 350 and 900 nm were selected because the quantum efficiency of the triple-junction solar cells investigated in this work is negligible outside this wavelength range. The wavelength limit of 750 nm was selected because it is the bandpass of the cold mirror. Selection of the two regions in this manner made it possible to obtain integrated spectral irradiance fits in each region almost independently of each other by adjusting the current in the corresponding lamp; most of the spectral irradiance in the 350-750 nm range is due to the xenon lamp while the tungsten-halogen lamp produces most of the spectral irradiance in the 750-900 nm range.

The fit of the solar simulator spectral irradiance to the WRL AM0 spectrum was carried out using a procedure which included calibrating the spectral radiometer; adjusting the currents in the xenon and tungsten lamps; measuring

the simulator spectral irradiance; integrating the measured and WRL AM0 spectral irradiances in the 350 to 750 nm and 750 to 900 nm ranges; calculating the percentage error in the integrated measured and WRL AM0 spectral irradiances in the two wavelength regions; and repeating the process until the error in each of the regions was less than 1%. The spectral irradiance of the dual-source simulator compared to the WRL AM0 spectrum is shown in Figure 3 by the filled circles. Comparison of the spectral irradiances in Figures 1 and 3 shows the dual-source solar simulator produces a spectral irradiance which is in significantly better agreement with the WRL AM0 spectrum. The percentage difference between the integrated spectral irradiance of dual-source simulator compared to WRL AM0 in Figure 3 is +0.06% in the 350 to 750 nm wavelength range and -0.9% in the 750 to 900 nm range.

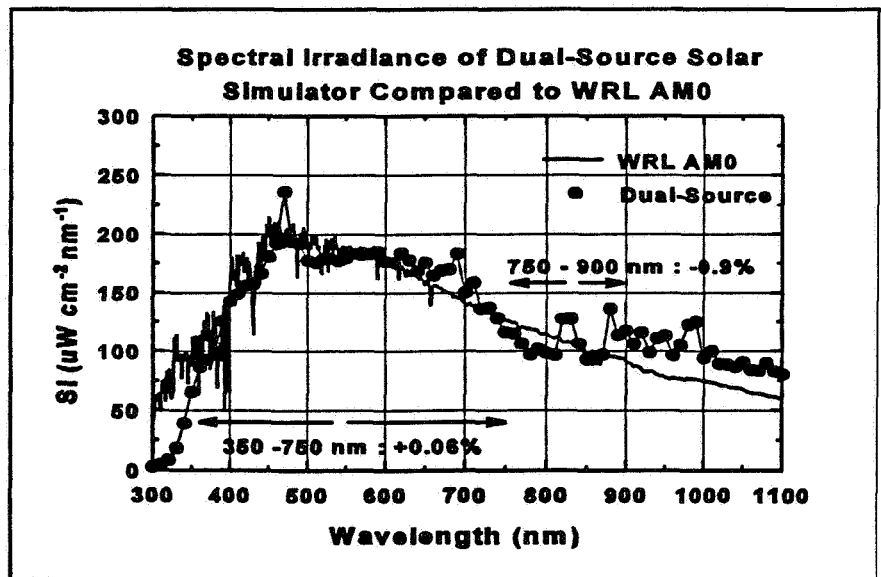


Figure 3: Spectral Irradiance of dual-source solar simulator compared with World Radiation Laboratory AM0 spectral irradiance.

QUANTUM EFFICIENCY SYSTEM DESCRIPTION

The quantum efficiency (QE) system was designed and constructed to carry out measurements under three conditions: dark, spectral-light bias and AM0 light bias. A second personal computer is used to control the QE system, as well as data acquisition, display and analyses. The design permits quantum efficiency measurements with an accuracy better than 2% over the 400 to 1000 nm wavelength range. The probe beam intensity and calibrate

detector response result in reductions in accuracy outside this wavelength range. The major components of the system include two computer-interfaced Scientific Measurement System, Inc. MonoSpec 27 monochromators; two computer-interfaced motorized filter wheels with filters for order sorting and spectral-light bias; UV-grade fused silica lenses and beam splitter; two magnesium fluoride coated Al mirrors; computer interfaced Stanford Research Systems model SR830 DSP lock-in amplifier and chopper; 60 watt quartz-tungsten-halogen (QTH) lamp; and a computer-interfaced Hewlett-Packard model 6038A power supply for the QTH lamp.

The two monochromators were mounted in tandem and used with the QTH lamp to produce a monochromatic probe beam for QE measurements of solar cells. Two monochromators are employed to reduce the stray-light level in the probe beam. Each monochromator has a ruled 1200 grooves/mm grating blazed at 500. The subtractive mode is used for the physical configuration of the monochromators along with 4 mm slit widths to optimize light throughput. The measured resolution of the two monochromators is 20 nm. The monochromators are capable of higher resolution at the expense of probe beam intensity. The monochromator containing the entrance slit and located next to the input optics is referred to as monochromator #1 in the following discussion; the other monochromator contains the exit slit and is referred to as monochromator #2.

Optical components located in front of the entrance slit of monochromator #1 serve to focus an A.C. light beam on the entrance slit and provide order-sorting capability. The optics include a QTH lamp, collimating lens, beam chopper and filter wheel. The beam chopper and filter wheel are mounted next to the entrance slit of the first monochromator. The beam chopper is used in conjunction with the lock-in amplifier to detect the response of the test solar cell to the monochromatic A.C. probe beam. The filter wheel contains four long pass filters. The filters provide order-sorting of the light-beams passing through the monochromators. The filters serve to reject the n th order beams of wavelength λ/n in the QE probe; the higher order beams can introduce large errors in QE measurements.

The optical components at the exit slit of monochromator #2 produce two light beams from the A.C. monochromatic probe beam which passes through the exit slit. The beams are used to measure the absolute external QE of a test solar cell. The configuration of the optical components is shown in Figure 4. The components include a beam splitter, two mirrors, lens, calibrated silicon photodiode, test-cell holder and filter wheel, and miscellaneous optical rails and holders. The components are enclosed in a black light-tight aluminum box.

The monochromatic A.C. probe beam emanating from the exit slit of monochromator #2 is split into two separate light beams by the beam splitter. The light beam reflected from the beam splitter is focussed on the calibrated detector by the lens; the detector is a calibrated silicon photodiode and serves as the reference detector for the QE measurements. The photodiode calibration is traceable to NIST scales and permits determining the absolute number of photons incident on the test cell. The second light beam transmits the beam splitter and is incident on the flat mirror; it is reflected onto the concave mirror which focusses the beam on the test cell. The optics do not permit measurement of the reflected light from the test cell. The QE values measured by the system and reported in this paper are absolute external quantum efficiencies.

A D.C. light beam originating from the solar simulator and passing through the filter wheel shown in Figure 4 is incident on the test cell; it is coincident with the optical axis defined by the test cell and filter wheel. The spectral content of the light beam is determined by the filter wheel. Three positions on the filter wheel are used to hold filters which pass spectra for measuring QE of triple-junction cells under spectral-light bias conditions (1); each filter passes

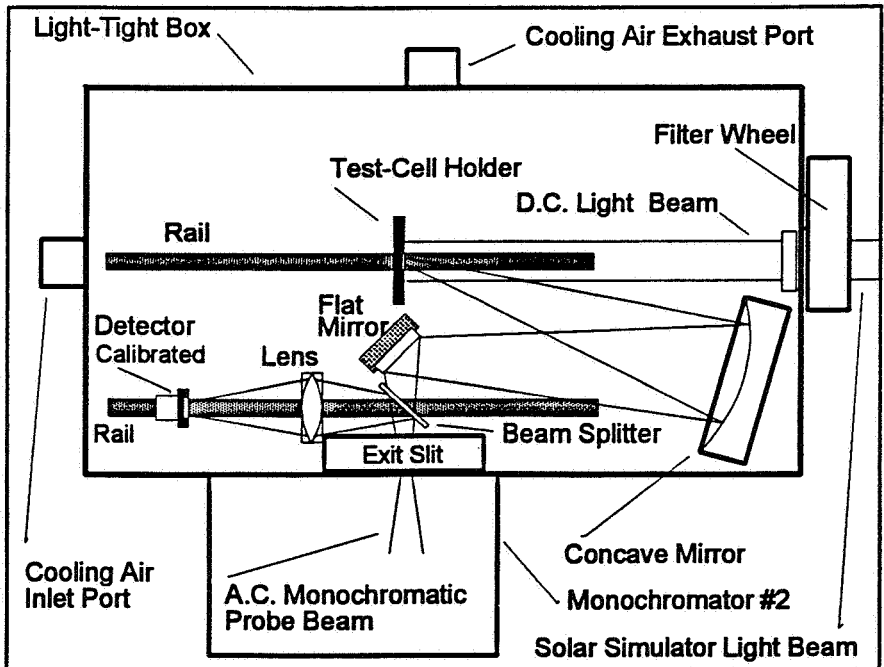


Figure 4: Top view of optical components located at the exit slit of monochromator #2.

a portion of the simulator spectrum for "turning-on" two of the three junctions of a test cell. One position on the filter wheel is open and used for AM0 light-bias measurements; another position contains a black aluminum disk and is used for measuring QE under dark conditions.

Temperature control of solar cells during light-bias measurements is accomplished by directing room temperature air on the back of the cell mounted in the test-cell holder. Figure 4 shows the cooling air inlet port which is mounted opposite the test-cell holder. Air is exhausted through the cooling air exhaust port which is baffled to prevent ambient light from entering the light-tight box. The air flow is set to insure the active junction of the test solar cell is maintained at room temperature; the junction temperature is monitored by measuring the open circuit voltage of the test cell. Temperature probes are included in the system to monitor the ambient air temperature in the light-tight box and the temperature of the test-cell holder.

The system was designed to minimize electrical noise. Electrical connection of the test and reference cells to a multiplexer and lock-in-amplifier are made with BNC cables and connectors. Ground loops are minimized through the use of a single common ground for all the electrical components; all electrical components are also electrostatically shielded. The background current levels are less than $1\text{E-}12$ A and the A.C. monochromatic probe currents of the order of $1\text{E-}6$ A. The wavelength is scanned by stepping both of the monochromators in 20 nm intervals, and measuring and logging ten values of the current at each wavelength. The standard deviation of the ten current values is typically of the order of $1\text{E-}3$ of the average value of the measured current. The calibrated detector and test cell currents are measured sequentially at each wavelength using a multiplexing circuit and lock-in amplifier.

Calibration of the QE system is accomplished following alignment of the optical components and carrying out two scans. One scan is carried out with the calibrated detector in the position shown in Figure 4; a second scan is done with the calibrated detector positioned in place of the test-cell holder. Computer software is used to calculate a calibration vector which is used in subsequent scans to determine the absolute external QE of solar cells mounted in the test-cell holder. The calibration vectors are saved on the hard drive and used to determine the long-term stability of the system. Following a wavelength scan, absolute external QE values are displayed on the computer monitor in graphical form and in tabular form on the printer. The tabular data are also saved on the computer hard drive for archival purposes and subsequent analyses. Computer control of the filter wheels, monochromators, QTH lamp power supply, and lock-in amplifier makes it possible to measure QE over a selected wavelength range in about twenty minutes. The stability of the system for successive scans is at the 0.1% level.

SINGLE-JUNCTION QE RESULTS

The instrumentation was used to measure the absolute external QE of a single-junction a-Si:H alloy solar cell with a superstrate structure (3). The results of the measurements for the cell without light bias at 24 °C under short-circuit conditions are shown in Figure 5 by the open-square symbols. The maximum value in QE is 0.81 and occurs at 590 nm. QE decreases below 400 nm because of absorption in the glass superstrate and top p-doped layer. The reduction in QE above 700 nm is due to the band gap of the intrinsic layer. The details of QE in the 400 to 700 nm range reflect the roles of the doped layers, intrinsic layer thickness and carrier transport. QE was measured at 24 °C using the AM0 light bias shown in Figure 3; the results are shown in Figure 5 by the open triangular symbols. The effect of AM0 light bias on QE is not discernible on the graph. The measurements show that changes in the occupancy of the sub-band-gap states resulting from high carrier injection levels do not

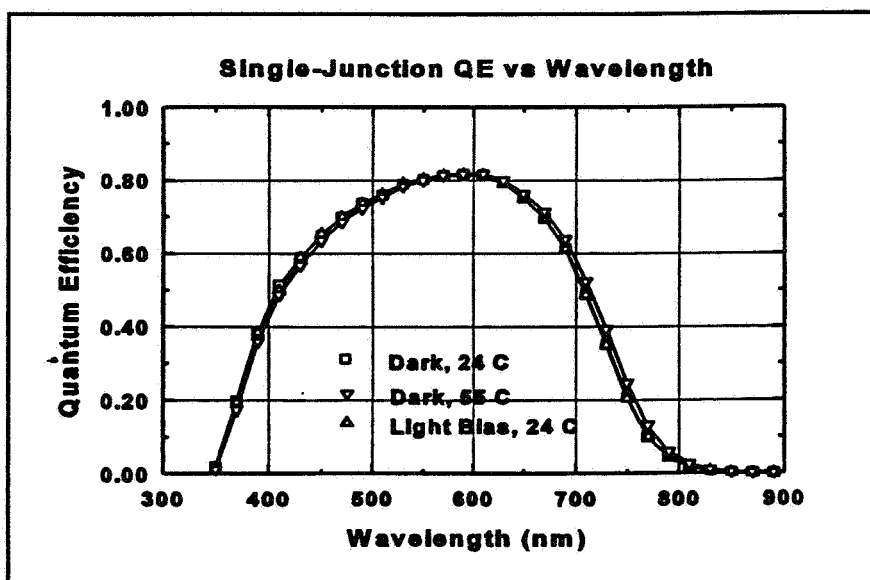


Figure 5: Quantum Efficiency of a single junction a-Si:H alloy solar cell under dark and light-bias conditions at 24 °C, and under dark conditions at 55 °C.

have a major effect on carrier transport and collection in single-junction a-Si:H alloy solar cells. The light-tight box shown in Figure 4 was heated to 55 °C and QE measured under dark conditions. The results of the measurements are shown by the inverted triangular symbols in Figure 5. QE differences of the order of a few percent are discernible and may be attributed to the temperature coefficients of both the test cell and calibrated detector. The 55 °C measurements show the techniques employed are not critically sensitive to room temperature variations of the order of a few degrees.

The effect of forward-bias voltage on QE for a single-junction a-Si:H alloy solar cell was investigated under light-bias conditions at 24 °C. The voltage was stepped in increments of 0.1 V from 0.0 to 0.8 V. The results of the measurements are shown in Figure 6.

The measurements show QE is insensitive to forward bias from 0.0 to 0.5 V. The peak value in QE is 0.8 and occurs at 580 nm. At a forward bias of 0.6 V, approximately the maximum-power point, QE begins to decrease and the peak value shifts to lower wavelengths. Significant decreases occur in QE as the forward bias is increased and approaches the open-circuit voltage. At 0.8 V, the peak in QE is 520 nm and the value is 0.08. An interpretation of the wavelength shift in the peak of QE shown in Figure 6 is as the forward bias voltage is increased, the trapped charge in the intrinsic layer plays an increasing important role in skewing the electric field distribution towards the front of the cell; this in turn shifts the peak in QE to a lower wavelength, and influences carrier transport and decreases carrier collection.

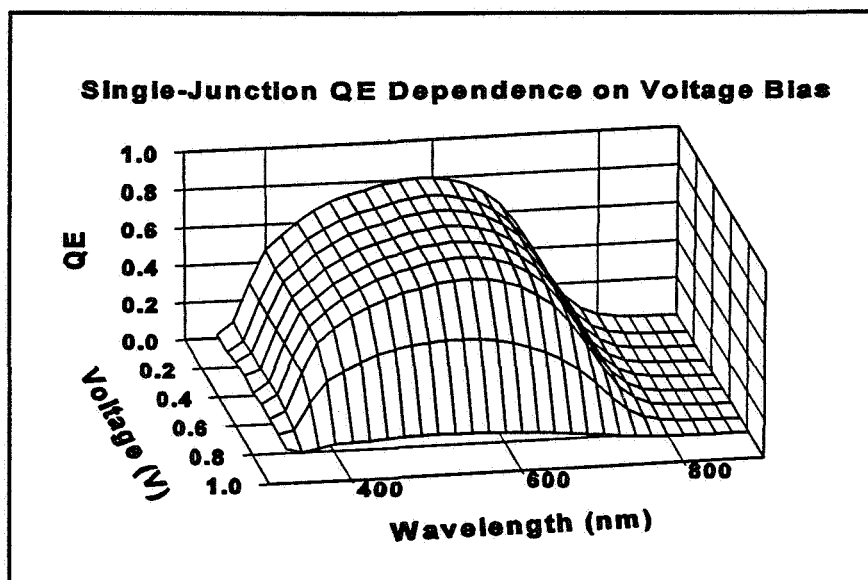


Figure 6: Three dimensional view of the quantum efficiency dependence on forward-bias voltage for a single-junction a-Si:H alloy solar cell.

The instrumentation and measurement methods were evaluated by comparing the short-circuit current measured under AM0 light bias, $I_{sc}(\text{meas})$, with a calculated short-circuit current, $I_{sc}(\text{calc})$. The value of the calculated short-circuit current was obtained by convoluting the measured quantum efficiency values, $QE(\lambda_i)$, shown in Figure 5 with the measured spectral irradiance values, $SI(\lambda_i)$, shown in Figure 3. The convolution was carried out over the 350 to 900 nm wavelength range. The calculated short-circuit current was obtained using the expression:

$$\text{Equation 1} \quad I_{sc}(\text{calc}) = \frac{A}{1239} \sum_i QE(\lambda_i) \times SI(\lambda_i) \times \lambda_i \times \Delta\lambda \quad \left[\frac{\text{Coulombs}}{\text{Joules} \times \text{nm}} \right]$$

where λ_i is the wavelength, $\Delta\lambda$ the monochromator step width and A the cell area. The results of the convolution are shown in Table I. The agreement of $I_{sc}(\text{meas})$ with $I_{sc}(\text{calc})$ is better than 1%. $I_{sc}(\text{meas})$ was measured with a Keithley model 236 source measurement unit recently calibrated with NIST scales referenced to NIST publications #252194 and #251357; $I_{sc}(\text{calc})$ was calculated using measured $QE(\lambda_i)$ and $SI(\lambda_i)$ values traceable to NIST scales, as indicated in the preceding section. The agreement between $I_{sc}(\text{calc})$ and $I_{sc}(\text{meas})$ is believed to result from using good measurement techniques and instrumentation calibrated with scales traceable to NIST. The measurements characterize the behavior of a single-junction a-Si:H cell under forward and light bias. They also demonstrate the validity of the measurement techniques for characterizing single-junction solar cells. These observations also prove useful in understanding the behavior of triple-junction solar cells under various biasing conditions.

Table I

| Cell | $I_{sc}(\text{meas})$ (mA) | $I_{sc}(\text{calc})$ (mA) | $\Delta I_{sc} / I_{sc}$ (%) |
|------|-------------------------------|-------------------------------|---------------------------------|
| X302 | 6.315 | 6.353 | 0.6% |

SPECTRAL-BIAS TRIPLE-JUNCTION QUANTUM EFFICIENCY RESULTS

QE measurements of triple-junction a-Si:H cells under short-circuit conditions were carried out using the spectral light-bias technique (1). The structure of the triple-junction cells has been previously discussed (3). The light bias technique is based on selectively injecting carriers in cell junctions, and "turning-off" and "turning-on" junctions. A junction is referred to as "turned-off" when there is relatively little optical injection of carriers in the junction; it is "turned-on" when there is a relatively large optical injection of carriers. When one junction is "turned-off", and the other two junctions are "turned-on", the "turned-off" junction limits the current in the cell. QE of a junction limiting the cell current can be determined using an A.C. monochromatic light beam, referred to as the probe beam. The carrier injected by the probe beam in the "turned-off" junction increases the photoconductivity and produces an A.C. current which characterizes QE of the junction under the conditions of the measurement. The injection of carriers in the junctions is determined by the spectral irradiance of the D.C. light beam and the optoelectronic properties of each of the three junctions. The spectral irradiance of the D.C. light beam used in the spectral light-bias technique is varied to selectively "turn-on" two of the three junctions in the triple-junction solar cell. The filter wheel contains three filters; each filter has a spectral transmission which filters the AM0 solar simulator beam to produce a spectral irradiance which "turns-on" two of the three junctions. The first filter "turns-on" the middle and bottom junctions, the second filter "turns-on" the top and bottom junctions, and the third filter "turns-on" the top and middle junctions. Thus the first filter makes it possible to measure QE of the top junction, the second filter the QE of the middle junction, and the third filter the QE of the third junction.

The quantum efficiencies measured with the spectral-light bias technique for the top, middle and bottom junctions of an a-Si:H alloy triple-junction solar cell are shown in Figure 7; the values were measured at 24 °C. The top junction is represented by the curve with the closed circles. The peak in QE of the top junction is about 0.54 at 440 nm. QE of the middle junction is shown by the closed squares; it peaks at 600 nm with a value of about 0.53. QE of the third junction is represented by the closed triangles and peaks at 720 nm with a value of about 0.53.

The relative intensity of the A.C. probe and D.C. spectral light-bias was investigated and the results are shown in Figure 8. The intensity of the probe beam is important in obtaining reliable QE values. The probe beam intensity must be much less than the intensities of the three D.C. spectral light-bias beams.

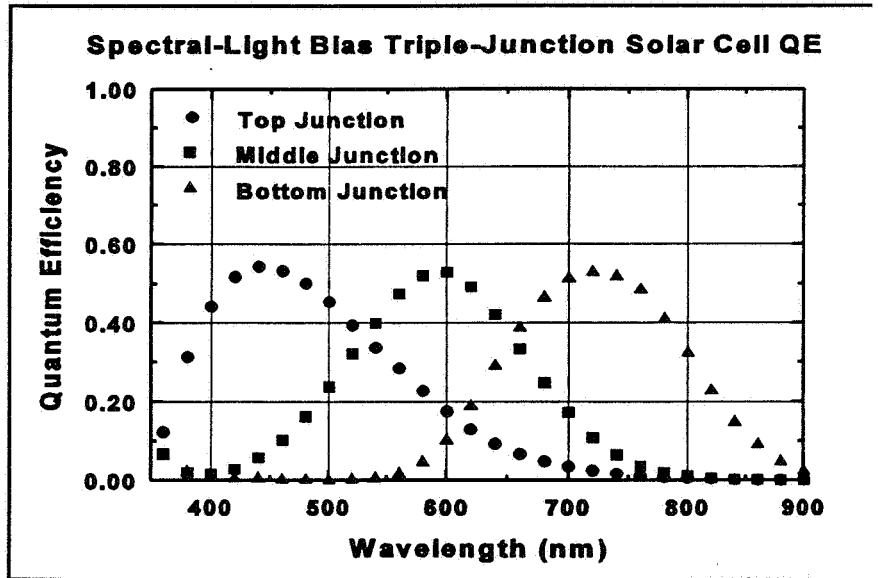


Figure 7: Spectral light-bias quantum efficiencies of the top, middle and bottom junctions for an a-Si:H triple-junction solar cell.

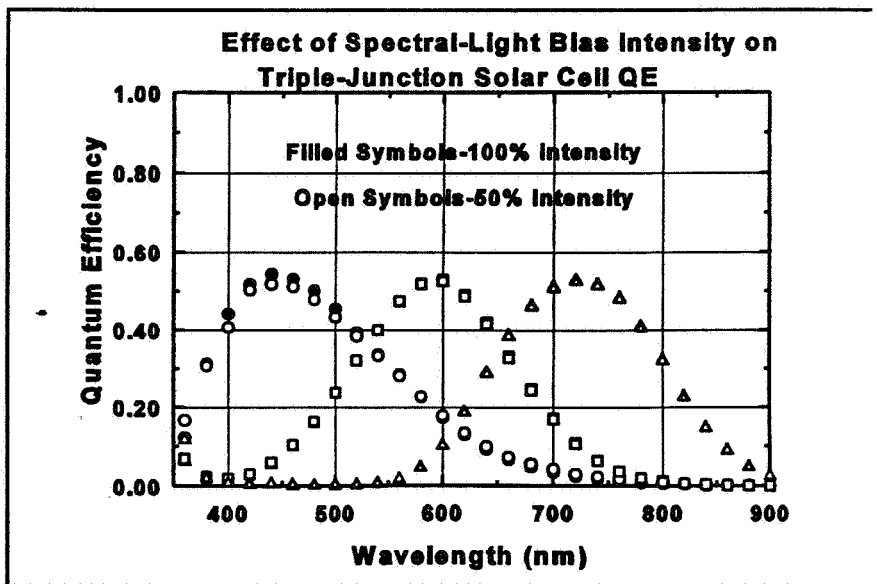


Figure 8: Effect of spectral-light bias intensity on QE for an a-Si:H alloy triple-junction solar cell.

The role of the relative beam intensities was evaluated by measuring QE with an attenuated probe beam and comparing it with QE values obtained with an unattenuated probe beam. The results of measurements with a 50% probe beam attenuation are shown in Figure 8. The symbols used to represent the various junctions are the same as Figure 7. Filled symbols represent QE measurements with the unattenuated probe beam; the QE values measured with the unattenuated beam are referred to as 100% intensity in Figure 8. The open symbols in the figure are plotted over the closed symbols and correspond to QE values measured with the probe beam attenuated 50%. Figure 8 shows QE of the middle and bottom junctions is not influenced by the probe beam intensity; the top junction shows a reduction in measured QE values of the order of a few percent when the probe beam intensity is attenuated by 50%. Hence it may be concluded the QE values obtained with the spectral light-bias technique are not significantly influenced by the probe beam intensities used in these measurements.

The measurements on the triple-junction solar cells show the top junction is effective in absorbing the shorter wavelengths of an AM0 spectrum, while the bottom cell absorbs the longer wavelengths, and the middle cell the intermediate wavelengths. Since the junctions are in series, the photocurrent in each junction is the same under power-generating conditions. The design of a triple-junction cell requires optimal junctions to convert the largest fraction of the AM0 spectrum into electrical energy. If the cell design is not optimal, then one of the junctions may limit the photocurrent, and carrier recombination in the other two junction will result in lower cell efficiency. The structure of the quantum efficiency of a triple-junction cell measured under AM0 D.C. light bias is useful in evaluating the design of the cell. If the measured QE resembles one of the curves in Figure 7, the results will suggest cell performance is limited by the junction which corresponds to the curve.

AM0 LIGHT-BIAS TRIPLE-JUNCTION QUANTUM EFFICIENCY RESULTS

The quantum efficiency of triple-junction a-Si:H alloy solar cells were measured using a D.C. light-bias beam produced by the solar simulator adjusted to produce the spectral irradiance shown in Figure 3. The measurements were carried out with the cells under short-circuit current conditions. The results of measurements are shown in Figure 9. The peak value of QE is at 460 nm with a value of about 0.40. The curve in Figure 9 has approximately the same shape as the curve in Figure 7 for the top-junction of the cell. Figure 7 shows the peak value is 0.54 at 440 nm for the top junction of the cell measured. The results suggest the performance of the triple-junction cell under AM0 light bias is limited by the top junction. QE of three triple-junction cells were measured; the results of the measurements were convoluted with the solar simulator spectral irradiance using Equation 1 in order to obtain a calculated value for the short-circuit current. The results of the calculations are shown in Table II. $I_{sc}(calc)$ is within about 1% of $I_{sc}(meas)$ for the three cells. The calculations confirm the validity of the D.C. light-bias technique for determining QE of triple-junction cells.

The role of forward bias on QE of a triple-junction solar cells under AM0 D.C. light bias was investigated. A cell was maintained at 24 °C and QE measured with forward biases ranging between 0 and 1.82 V. The voltage at the

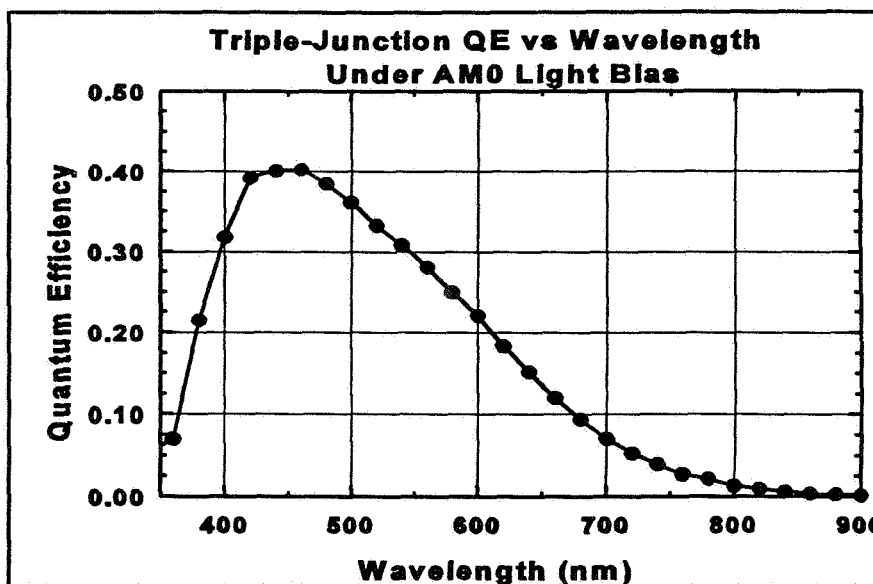


Figure 9: Quantum efficiency of a-Si:H alloy triple-junction solar cell under AM0 light bias.

Table II

| Cell | $I_{sc}(meas)$ (mA) | $I_{sc}(calc)$ (ma) | $\Delta I_{sc}/ I_{sc}$ (%) |
|------|------------------------|------------------------|--------------------------------|
| ST05 | 2.338 | 2.361 | 1.0% |
| ST17 | 2.386 | 2.395 | 0.4% |
| ST38 | 2.253 | 2.279 | 1.1% |

maximum-power point was about 1.7 V and the open-circuit voltage was about 2.2 V. Forward biases of 0, 0.62, 1.02, 1.42, 1.62 and 1.82 V were used. The results of the measurements are shown in Figure 10. Both the wavelength corresponding to the QE peak value and the peak value of QE are strongly influenced by the forward-bias voltage. The peak value of QE decreases from 0.40 to 0.08 as the forward bias increases from 0 to 1.82 V; for the same increases in the forward bias, the wavelength for the peak QE value increases from 460 to 600 nm. The measurements show QE under short-circuit conditions is considerably different than QE measured near the maximum-power point. While the short-circuit measurements suggest the performance of the cell is limited by the top junction, the measurements near the maximum-power point suggest both the top and middle junctions are limiting the operation of the cell.

The response of the triple-junction cell was further tested by qualitatively varying the spectral irradiance of the solar simulator by changing the current in the tungsten-halogen lamp. The lamp current was varied from 5.0 to 2.9 A; 5.0 A is the current which produced the fit to WRL AM0 shown in Figure 3. As the lamp current was decreased, the spectral irradiance beyond 750 nm decreased. Figure 11 shows the behavior of QE. The quantum efficiency with a lamp current of 5.0 A is the same as the values plotted in Figure 9. The QE curve with a lamp current of 2.9 peaks at 720 nm and has a value of 0.47; it is similar to the curve produced by the bottom junction shown in Figure 7. Thus as expected from the changes in the spectral irradiance produced by reducing the current in the tungsten-halogen lamp, the cell current is limited by the top junction when the lamp current is 5.0 A; the current in the bottom junction limits the cell current when the lamp current is 2.9 A.

The investigations of QE measured under AM0 light bias conditions reported in this section are preliminary, however, the results show agreement at the 1% level between measured short-circuit currents and currents calculated from measured cell quantum efficiencies and solar simulator spectral irradiances. Studies need to be done to determine the specifications of both the spectral irradiance and radiance of AM0 solar simulators to be used in the characterization of multi-junction cells. The accuracies will depend, among other things, on the number of junctions in the multi-junction cells and the optoelectronic properties of each of the junctions. The work to determine the

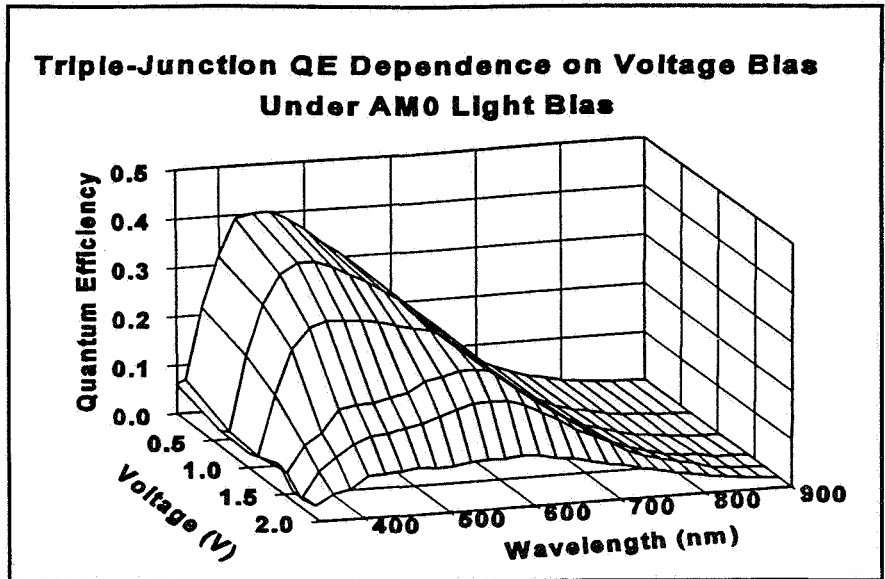


Figure 10: The dependence of the quantum efficiency of a triple-junction a-Si:H alloy solar cell on forward-bias voltage for AM0 light bias.

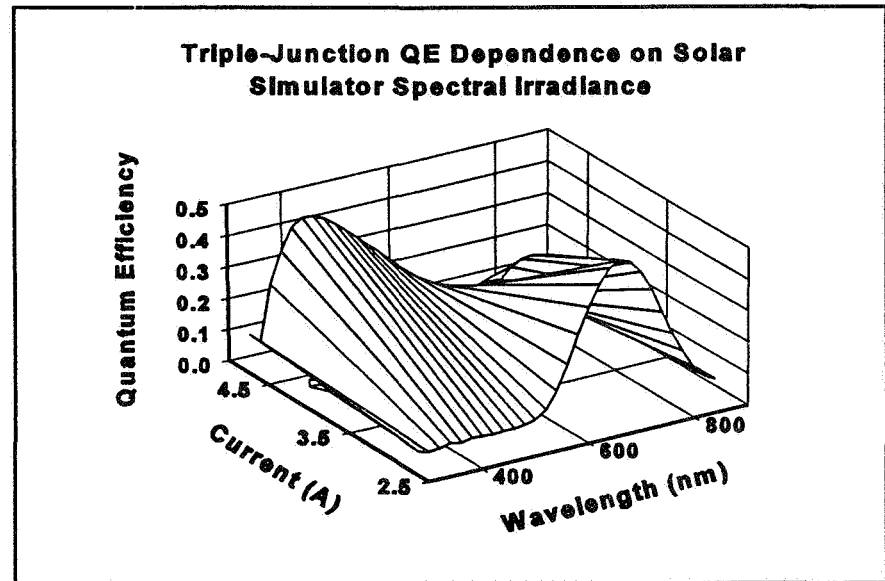


Figure 11: Dependence of triple-junction quantum efficiency on spectral irradiance of solar simulator. The spectral irradiance of the solar simulator was varied by changing the filament current in the tungsten-halide lamp.

specifications for AMO solar simulators can be carried out using small area cells, i.e., cells of the order of 1.0 cm² in area. While device simulation studies are useful for designing cell structures and defining the optoelectronic of each junction, laboratory characterization of cells should be carried out both to facilitate solar cell development and optimize the limited resources available for space testing.

SUMMARY

An integrated system was described which consists of a spectral radiometer and dual-source solar simulator, and personal computer based current-voltage and quantum efficiency equipment. The spectral radiometer was calibrated with a tungsten-halogen standard lamp. The quantum efficiency apparatus employed a calibrated reference detector which was used in measuring the absolute external quantum efficiency of triple-junction a-Si:H ally solar cells. The calibrations of the lamp and photodiode, as well as the source measurement unit used to measure cell currents were based on NIST scales. Quantum efficiencies were measured using both the spectral-light bias and AMO light-bias techniques. Quantum efficiencies measured with the AMO light-bias technique were shown to be dependent on forward-bias voltage and the spectral irradiance of the AMO light-bias beam. Measured spectral irradiances and quantum efficiencies were convoluted to calculate cell short-circuit cell currents. Calculated currents compared with measured short-circuit currents at the 1% level .

REFERENCES

- * Appreciation is expressed to Kenneth R. Lord II, Michael R. Walters and Fazal UrRahman Syed for their contributions to this work.
- 1. Joseph Burdick and Troy Glatfelter, Solar Cells **18** (1986) page 301.
- 2. M. Bennett and R. Podlesny Proceedings of the 21st IEEE Photovoltaic Specialists Conference (1990) page 1438.
- 3. Kenneth R. Lord II, Michael R. Walters and James R. Woodyard, Proceedings of the 23st IEEE Photovoltaic Specialists Conference (1993) page 1448.

523
IN-50408

SOLAR CELL ANGLE OF INCIDENCE CORRECTIONS¹

by

Dale R. Burger and Robert L. Mueller
Jet Propulsion Laboratory, California Institute of Technology
Pasadena, California 91109

The Mars Pathfinder mission has three different solar arrays each of which sees changes in incidence angle during normal operation. When solar array angle of incidence effects was researched little published data was found. The small amount of published data created a need to obtain and evaluate such data. The donation of the needed data, which was taken in the fall of 1994, was a major factor in the preparation of this paper.

BACKGROUND

The Mars Pathfinder cruise phase solar array is body-mounted and will be providing primary spacecraft power at angles from normal to at least 60 degrees off-normal. The lander solar array is also fixed and, due to its location on the surface of Mars, will see a constantly changing incidence angle during a day. The Microver is a mobile experiment on Mars with a solar array as its top surface and thus will also see constant changes in incidence angle both from sun position and vehicle orientation.

A search of the literature for angle of incidence data turned up only a few references (1-4) and no tabular data. Reference 1 lists the following possible causes of off-normal array power loss other than the cosine correction:

- a. "Optical effects relating to the first-surface reflectance of the cover slide;
- b. Optical effects relating to apparent changes in the optical thickness of coatings and filters, thereby causing apparent changes in the spectral transmittance and reflectance values;
- c. Edge effects relating to refraction, scattering and additional light collection by solar cells and covers, especially by thicker covers; and
- d. Shadowing of solar cells by solar cell cover edges, solar cell interconnectors, wires, and other relatively small array components."

Reference 2 mentions as possible causes items a. and b. above while Reference 3 mentions items a., b., and expands upon c. by varying cell-to-cell spacing and cover slide thickness. Reference 3 also adds the following possible power loss cause:

- e. Accelerated UV degradation of adhesive due to edge channelling of UV light.
Reference 4 mentions item a. and adds the following possible causes (which are primarily terrestrial concerns):
- f. Shadowing by particulate soiling; and
- g. Effect of white or black background.

Due to limitations in space and our data we will be discussing only items a., b., and c. in this paper.

¹The work described in this paper was carried out by the Jet propulsion Laboratory, California Institute of technology, under a contract with the National Aeronautics and Space Administration.

DATA COLLECTION

The Large Area Pulsed Solar Simulator (LAPSS) is a research tool at JPL and was used for creating and collecting all of the data in this paper. The LAPSS has been described in detail elsewhere (5) and thus will not be described here. The data used in this paper was contributed by Applied Solar Energy Research, City of Industry, California and is gratefully acknowledged.

CELLS

The 28 cells used in this study were from seven different lots made with standard processes but were considered to be research cells and thus no effort was made to compare any cell performance values except the response of their short circuit current (I_{sc}) to changes in angle of incidence.

Angle of incidence measurements were made on the cells by attaching them to a divider head which was carefully aligned normal to the light beam at 0 angle of incidence.

The Applied Solar Energy Corporation (ASEC) cells were all 4 cm by 4 cm GaAs/Ge with the usual two layer anti-reflection coating on the top surface. Each cell had a CMX coverglass having a cerium oxide ultra-violet absorption capability. The Pilkington specification for CMX coverglass shows a quarter-wavelength anti-reflection coating of MgF_2 on the front surface to maximize transmission at 600 nm.

THEORY

Before data reduction and analysis was attempted, a number of potential angle of incidence dependent effects were examined.

Cosine - The cosine correction is due to the change in effective array collection area due to the projection of the off-normal array surface onto a plane normal to incident sunlight.

Fresnel Reflectivity - Fresnel reflection is due to the interface between two optical media having different indices of refraction. The reflected portion of the incident light is given by:

$$r = \frac{1}{2} \left[\frac{\tan^2(\phi_1 - \phi_2)}{\tan^2(\phi_1 + \phi_2)} + \frac{\sin^2(\phi_1 - \phi_2)}{\sin^2(\phi_1 + \phi_2)} \right] \quad (1)$$

where ϕ_1 is the incident beam angle and the refracted beam angle, ϕ_2 , is:

$$\phi_2 = \arcsin\left(\frac{n_1}{n_2} \sin \phi_1\right) \quad (2)$$

COATINGS AND FILTERS

Coverglass AR Coating - The MgF_2 antireflective coating that is normally used on the front surface of a coverglass is a single layer and thus an increase in the angle of incidence will show little effect from this coating (6). There could be a small shift of the center frequency toward shorter wavelengths which could cause a small decrease in output.

Filters - There were no low absorption filters such as blue-red reflection or infra-red reflection, on the coverglass or the cell front surface therefore optical effects from these filters was not a concern.

EXTREME ANGLE EFFECTS

There is a possibility of trapping light or shadowing a cell when very large incidence angles are encountered. These effects are difficult to quantify but have been reported [3].

LOW INTENSITY EFFECTS

Temperature - A decrease in temperature is normal when the angle of incidence increases for a solar array exposed to constant sunlight. The pulsed light source of the LAPSS (about 3 msec every 5-10 min.) should not create any temperature effects so this factor could be ignored.

Voltage - Lower intensities due to angle of incidence do result in lower cell voltages. This study however only focused upon the short circuit current and thus should not have to correct for this effect.

DATA REDUCTION

The raw data was reduced by use of a JPL BASIC program called REPLOT. This program takes header file information such as temperature, standard cell I_{sc} , and analog-to-digital counts and uses this information to convert and correct the digital count IV data for each separate angle of incidence. This data is shown on Figure 1 as a solid line.

The normal (0 degree angle of incidence) short circuit current (I_{sc}) value was first corrected for the small reflection loss at normal incidence (i.e. 1.7% for index of refraction of 1.3) by dividing the I_{sc} value at normal incidence by one minus the reflection loss. This corrected I_{sc} value was then used to create two other sets of values: a predicted I_{sc} versus angle of incidence using the cosine correction only (shown on Figure 1 as long dashed lines); and a predicted I_{sc} versus angle of incidence using both cosine and Fresnel corrections (shown on Figure 1 as short dashed lines).

While it was known that the front surface was coated with magnesium fluoride (MgF_2), the exact value of the coverglass front surface index of refraction was unknown and coverglass from the same lot was not available for measurement. A published material value of 1.38 was first used in the Fresnel equation (1) but later a better fit between actual and predicted values was found by using an index of refraction of 1.30.

A prediction error was used to normalize the results as well as to determine the validity of using the cosine and Fresnel reflectivity approach. The prediction error was calculated by subtracting the measured data from the predicted value and then dividing by the measured data. The results for 27 of the experimental cells is given in Table I below and shown in Figure 2. One cell was dropped from the study due to loss of one measured value.

Table I - Prediction Errors

| Cell No. | Angle of Incidence | | | | |
|----------|--------------------|----------|----------|----------|----------|
| | 10 | 20 | 30 | 40 | 65 |
| 1 | -0.00063 | +0.00121 | -0.00064 | -0.00290 | -0.00756 |
| 2 | -0.00166 | -0.00495 | -0.00222 | -0.00375 | -0.00742 |
| 3 | -0.00027 | -0.00020 | -0.00033 | -0.00243 | -0.00878 |
| 4 | -0.00299 | -0.00402 | -0.00363 | -0.00565 | -0.01030 |
| 5 | -0.00080 | +0.00027 | -0.00045 | -0.00010 | -0.00796 |
| 6 | -0.00049 | +0.00171 | +0.00084 | +0.00031 | -0.00704 |
| 7 | -0.00363 | -0.00468 | -0.00722 | -0.00927 | -0.01534 |
| 8 | -0.00051 | -0.00323 | -0.00471 | -0.00541 | -0.01001 |
| 9 | +0.00018 | -0.00202 | -0.00168 | -0.00586 | -0.01372 |
| 10 | -0.00055 | -0.00167 | -0.00262 | -0.00151 | -0.00281 |

| | | | | | |
|----|----------|----------|----------|----------|----------|
| 11 | -0.00086 | -0.00517 | -0.00421 | -0.00637 | -0.01178 |
| 12 | -0.00382 | -0.00624 | -0.00921 | -0.01081 | -0.01434 |
| 13 | -0.00141 | -0.00230 | -0.00513 | -0.00631 | -0.01056 |
| 14 | -0.00143 | -0.00411 | -0.00345 | -0.00474 | -0.00813 |
| 15 | -0.00135 | -0.00225 | -0.00267 | -0.00497 | -0.00608 |
| 16 | -0.00261 | -0.00404 | -0.00604 | -0.00930 | -0.01696 |
| 17 | -0.00108 | -0.00043 | -0.00284 | -0.00417 | -0.01113 |
| 18 | -0.00045 | -0.00032 | +0.00059 | -0.00408 | -0.01258 |
| 19 | -0.00151 | -0.00187 | -0.00317 | -0.00440 | -0.01308 |
| 20 | -0.00175 | -0.00376 | -0.00490 | -0.00856 | -0.01828 |
| 21 | -0.00094 | -0.00326 | -0.00582 | -0.00717 | -0.01259 |
| 22 | -0.00456 | -0.00740 | -0.00758 | -0.00742 | -0.00995 |
| 23 | -0.00209 | -0.00287 | -0.00224 | -0.00388 | -0.00935 |
| 24 | -0.00102 | -0.00305 | -0.00206 | -0.00486 | -0.00919 |
| 25 | -0.00217 | -0.00027 | -0.00538 | -0.00782 | -0.01326 |
| 26 | -0.00376 | -0.00661 | -0.00737 | -0.00851 | -0.01402 |
| 27 | -0.00322 | -0.00697 | -0.00717 | -0.00598 | -0.01447 |

Note: the expected random error for lsc values taken with the LAPSS is no greater than +/- 0.003.

STATISTICAL FIT

For small angles of incidence the cells had cosine times Fresnel predicted values which closely matched the measured values. However, it was noted that the error between predicted values and measured values increased with angle of incidence. This trend is seen in Figure 2 and Tables I and II. It can also be noted in Figure 2 that the spread increases with angle of incidence which is expected from the effects of the systematic errors which are discussed below.

Table II

| Ang. of Incidence | 10 | 20 | 30 | 40 | 65 |
|-------------------|---------|---------|---------|---------|---------|
| Mean of Error | -0.0017 | -0.0029 | -0.0038 | -0.0054 | -0.0110 |
| Std. Dev. | 0.0013 | 0.0025 | 0.0027 | 0.0027 | 0.0035 |
| Max. Error | 0.0002 | 0.0017 | 0.0008 | 0.0003 | -0.0028 |
| Min. Error | -0.0046 | -0.0074 | -0.0092 | -0.0108 | -0.0183 |

Also of interest in Figure 2 is that there seemed to be a normal distribution of the errors around the means. This hypothesis was checked using a chi-squared test with 3 degrees of freedom. The results for 10, 20, 30, 40, and 65 degrees were 8.68, 5.475, 1.967, 1.47, and 1.493 respectively. These chi-squared values were found to be acceptable at the 0.05 level when compared with the 0.95 percentile chi-squared value of 7.815 except the measurements at 10 degrees where there were 15 values that fell between the mean and +1 sigma and only 4 between the mean and -1 sigma. The only reason that could be found for the skewed values was the possibility that running all of the tests by rotating the dividing head clockwise as viewed from the top could have introduced some systematic error. After considering the size of the values involved compared to the LAPSS measurement accuracy of +/-0.003 and the sensitivity of the mean to outlying values it was decided not to pursue this

finding.

TREND ANALYSIS

Since the plot in Figure 2 shows a definite trend this trend was plotted as Figure 3 by using the mean values at each angle as a data point. A fourth order regression curve was selected as the best fit and this curve gave a good fit to the plotted data with an R value of 0.99988. No conclusions were drawn from this finding.

Possible explanations for the trend of larger measured data values than predicted values include the following:

- a. Onset of the expected extreme angle improvement;
- b. Improved cell performance due to the MgF_2 AR coating center frequency shift toward shorter wavelengths;
- c. Improved cell performance due to longer optical path length near the cell junction.
- d. Error in the assumed effective index of refraction.

There was no practical way to check on possibilities a., b., and c. Possibility d. however was checked by selecting a "typical" experimental cell (i. e., one which had prediction errors similar to the mean of all of the cells). Cell #13 prediction errors were a reasonable fit to the mean values. Values for an effective index of refraction of n_2 were assumed as 1.25, 1.30, and 1.35 with results as shown in Table III.

Table III

| Index n_2 | Angle of Incidence | | | | |
|----------------|--------------------|----------|----------|----------|----------|
| | 10 | 20 | 30 | 40 | 65 |
| 1.25 | -0.00175 | -0.00260 | -0.00527 | -0.00593 | -0.00223 |
| 1.30 | -0.00141 | -0.00230 | -0.00513 | -0.00631 | -0.01056 |
| 1.35 | -0.00159 | -0.00250 | -0.00548 | -0.00713 | -0.01788 |

Table III shows that the 1.30 effective index of refraction value minimizes the prediction error at the small angles where the error should be small and does have a trend of larger negative errors at larger angles of incidence. The 1.25 effective index of refraction value minimizes the total prediction error but with no trend to the error except a possible positive prediction error at angles above 65 degrees. The 1.35 effective index of refraction value produces prediction errors which are in all cases larger than those of the 1.30 value. Considering the previously reported performance increase at extreme angles of incidence it has been decided to remain with the assumed 1.30 effective index of refraction value. What would have been very useful in this study is measured data beyond 65 degrees which might allow a better resolution of this question.

While an increasing angle of incidence effect was probably seen, extreme angle effects were not conclusively noted since the measurements were only taken to an angle of incidence of 65 degrees. A more detailed search of the region between 80 and 90 degrees is required in order to fully answer this question. Possible additional factors of interest for extreme angle effects are noted in Reference 3 as: cover slide optical properties, cover slide thickness, and inter-cell spacing.

SYSTEMATIC ERRORS

There are three different systematic error causes: large incidence angles; reduced reading size, and assumed index of refraction.

Large Incidence Angles - The cosine function is changing very rapidly at large incidence angles so small angle errors become a problem. Alignment of the cell samples to the light beam was done with care but the source is 36 feet away from the sample and there is no hard-mounted goniometer

to use as a reference. An additional problem would be stray room light and wall reflection which become larger percentage effects as the incidence angle increases. This effect was minimized by turning off the room lights.

Reduced Reading Size - As the incidence angle increases the Isc decreases so small measurement errors in Isc become magnified. Of particular interest is the rounding error since all readings large or small are presented with only two decimal digit accuracy.

Assumed Index of Refraction - As mentioned above, the coverglass front surface index of refraction used for all predicted values was set at 1.30 to obtain the best data fit. This was done early in the analysis by using data from only seven of the ASEC cells. Predicted cosine times Fresnel curves for all cells used this value. A better controlled experiment would measure this value using coverglass from the same lot.

There is some beam decollimation but this effect was measured in Reference 3 and found to be less than 0.5 degrees for a setup similar to the JPL LAPSS. The apparent size of the JPL LAPSS light source is calculated to be 0.56 degrees on the diagonal of the rectangular source area. This compares favorably with the sun's apparent size from Earth which is 0.53 degrees.

RANDOM ERRORS

LAPSS - The best estimate of the LAPSS random measurement error is a maximum of +/- 0.3%.

A/D Count - The data acquisition system used on the LAPSS is typical in that it uses a digitized representation of the analog data which consist of whole counts. Rounding off to the nearest count is then a random error equal to, at most, 1 part in 4096 or roughly 0.024%.

Temperature - Temperature measurements are displayed on the meter to the nearest tenth of a degree so the rounding of this value is a random error equal, at most, to 5 parts in about 2800. Fortunately the Isc sensitivity to this error for gallium arsenide cells is about 0.0175%/degC and 0.0145%/degC for silicon cells so the overall temperature error effect of a 0.05 degree rounding error is small.

Angle - The divider head has 0.1 degree gradations and a backlash of 1.5 gradations. Care was taken to always move in the same direction to minimize backlash so the setting error would be about 0.05 degree or about +/-1.0% in the worst case at 85 degrees angle of incidence. This study only took readings in a counter-clockwise direction as viewed from above.

TOTAL RANDOM ERROR

The LAPSS error can not be included in the total random error since it already contains the other two errors. With that in mind and the fact that the count and temperature errors are independent, the total random error is calculated as the square root of the sum of the squares: 0.000255 or 0.0255%. This total random error is not large enough to invalidate the conclusions made below.

OTHER ERRORS

At least one other error source must be mentioned in this discussion. The tests were run only on single cells which would not necessarily give the same results as tests run on full arrays. Edge effects, reflections, and shadowing effects are all possible confounding errors if the conclusions drawn below are applied to arrays which was the original intent.

CONCLUSIONS

Using the combined cosine and Fresnel corrections gave very good predictions of the measured data. For a typical example see Figure 1.

An empirically derived value of the coverglass front surface index of refraction should be used if possible rather than a published material value.

There is probably an effect from increasing angle of incidence which could not be explained in detail.

REFERENCES

1. Solar Cell Array Design Handbook, Vol. 1, JPL Document #SP 43-38, Vol. 1, Jet Propulsion Laboratory, Pasadena, CA, Oct. 1976, pp 4.2-1 & -2 and 4.8-1 & -2.
2. Ross, R. G., Jr., et. al., "Measured Performance of Silicon Solar Cell Assemblies Designed for Use at High Solar Intensities," JPL Publication #TM 33-473 (N71-23780), March 15, 1971, pp 113-115.
3. Opjorden, R. W., "Solar Cell Optical Design Considerations," Conf. Rec. of 9th IEEE PVSC, Silver Springs, MD, May 2-4, 1972, pp 164-173.
4. Wilson, A. and Ross, R. G., Jr., "Angle-of-Incidence Effects on Module Power and Energy Performance," Progress Report 21, April 1982 to January 1983, and Proc. of 21st PIM, JPL Doc. #5101-222, Jan. 1983, (NTIS, PC A22/MF A01; 1), pp 423-426.
5. Mueller, R. L., "The Large Area Pulsed Solar Simulator (LAPSS)," JPL Publication #93-22, Rev. A, July 15, 1994.
6. Heavens, O. S., "Optical Properties of Thin Solid Films," Butterworths Scientific Publications, London, 1955, pp. 208-215.

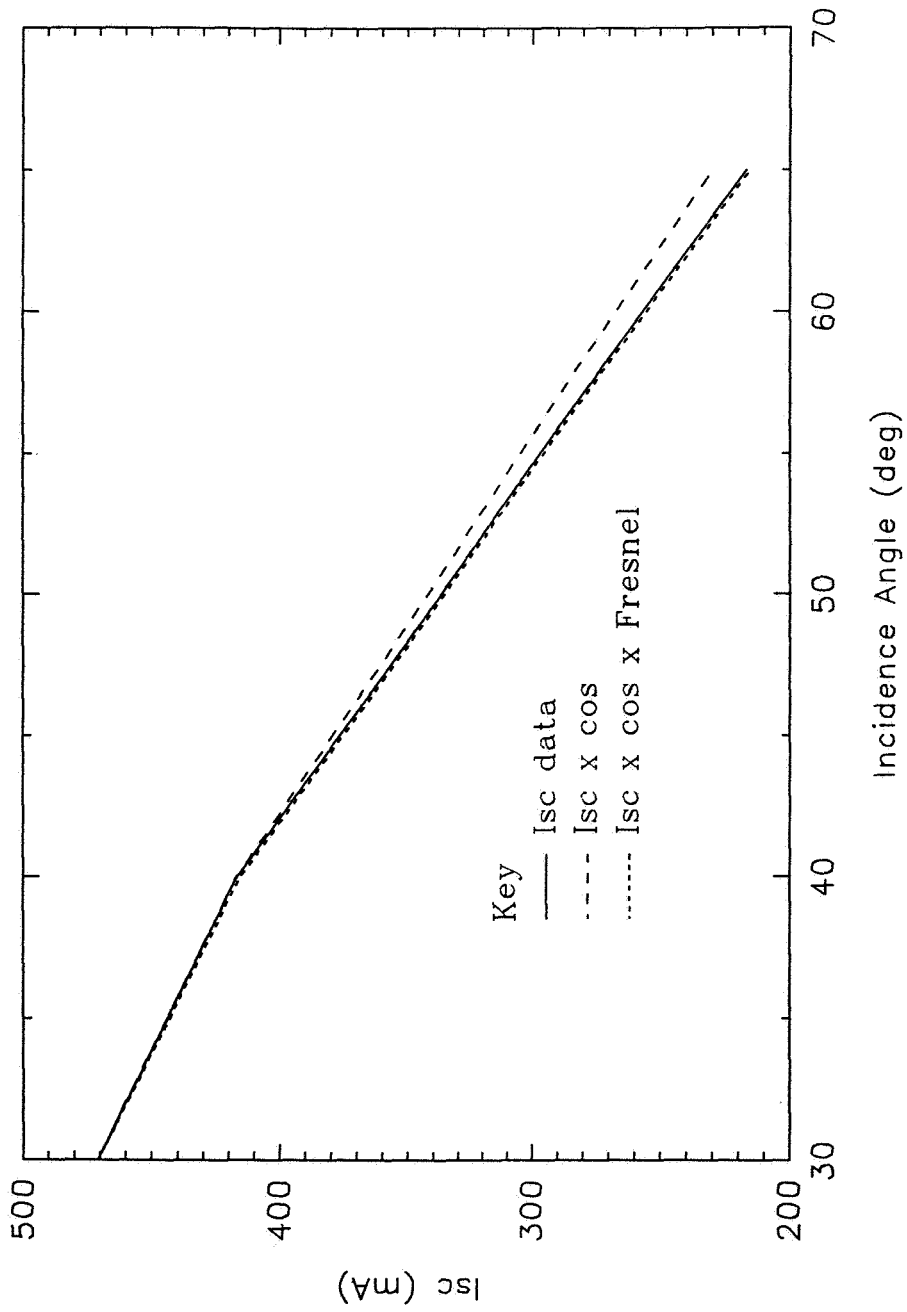


Figure 1 – Comparison Between Predicted and Measured Isc Values

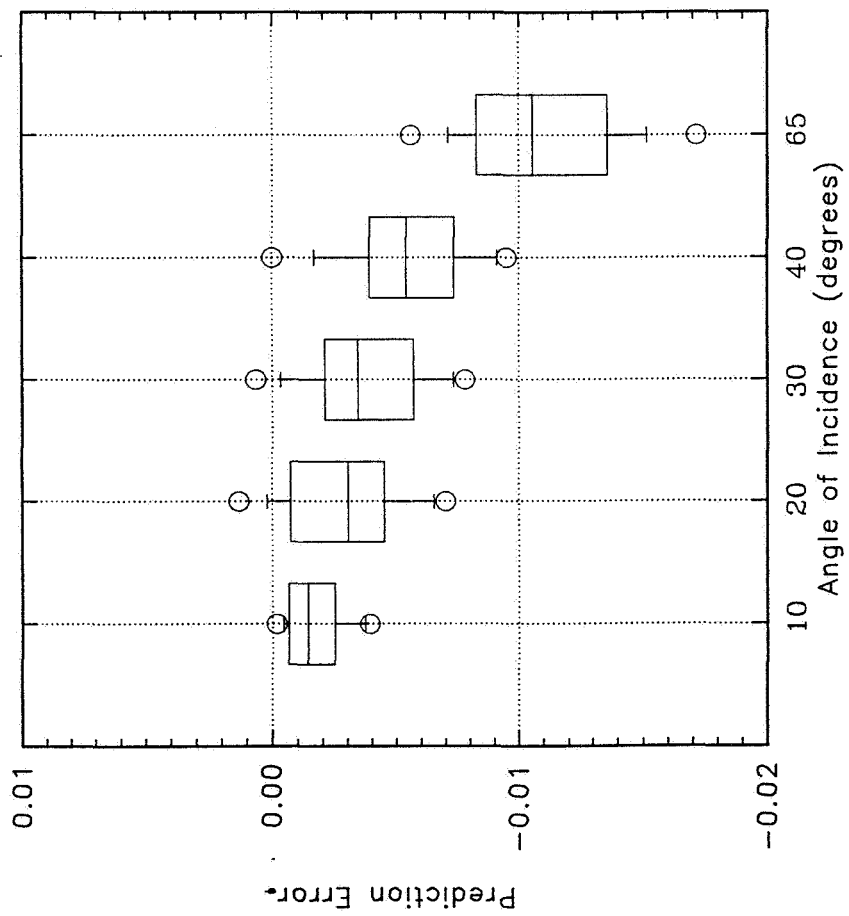


Figure 2 - Prediction Error vs Angle of Incidence

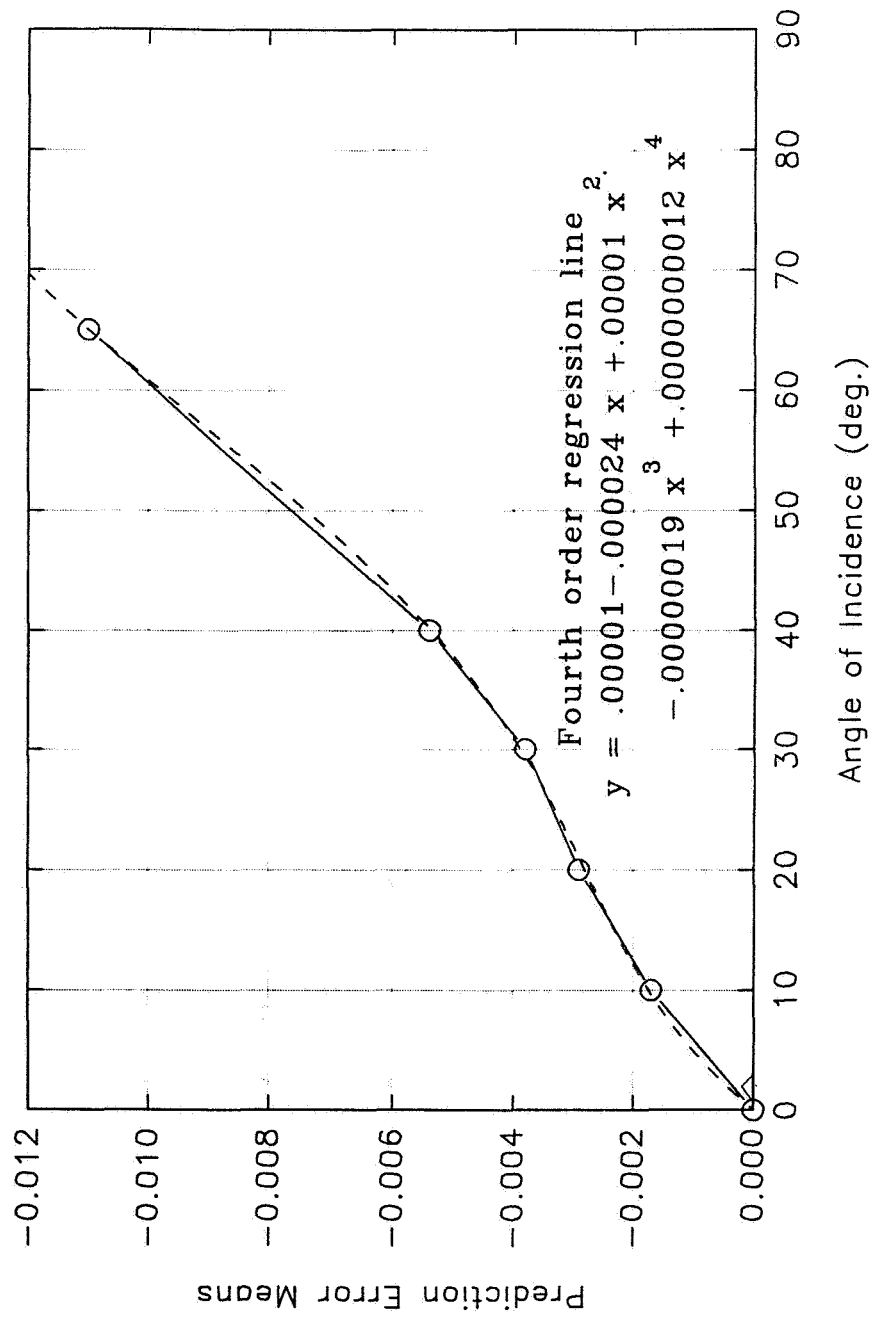


Figure 3 - Fourth Order Fit of Prediction Error Means

LOW INTENSITY LOW TEMPERATURE (LILT) MEASUREMENTS AND COEFFICIENTS ON NEW PHOTOVOLTAIC STRUCTURES

David A. Schelman and Phillip P. Jenkins
NYMA Inc.
Brook Park, Ohio, 44142

S24
IN-50409

David J. Brinker
NASA LeRC
Cleveland, Ohio 44135

Joseph Appelbaum
Tel-Aviv University
Tel-Aviv, Israel, 69978

ABSTRACT

Past NASA missions to Mars, Jupiter and the outer planets were powered by radioisotope thermal generators (RTGs). Although these devices proved to be reliable, their high cost and highly toxic radioactive heat source has made them far less desirable for future planetary missions. This has resulted in a renewed search for alternate energy sources, some of them being photovoltaics (PV) and thermophotovoltaics (TPV). Both of these alternate energy sources convert light/thermal energy directly into electricity. In order to create a viable PV data base for planetary mission planners and cell designers, we have compiled low intensity low temperature (LILT) I-V data on single junction and multi-junction high efficiency solar cells. The cells tested here represent the latest photovoltaic technology. Using this LILT data to calculate Short Circuit Current (I_{sc}), Open Circuit Voltage (V_{oc}), and Fill Factor (FF) as a function of temperature and intensity, an accurate prediction of cell performance under the AM0 spectrum can be determined. When combined with QUantum efficiency at Low Temperature (QULT) data, one can further enhance the data by adding spectral variations to the measurements. This paper presents an overview of LILT measurements and is only intended to be used as a guideline for material selection and performance predictions. As single junction and multi-junction cell technologies emerge, new test data must be collected. Cell materials included are Si, GaAs/Ge, GaInP/GaAs/GaAs, InP, InGaAs/InP, InP/InGaAs/InP, and GaInP. Temperatures range down to as low as -180°C and intensities range from 1 sun down to .02 suns. The coefficients presented in this paper represent experimental results and are intended to provide the user with approximate numbers.

BACKGROUND

With increasing concerns over the safety and cost of RTGs, alternate power sources are being sought. NASA's current stand on this issue is to avoid using nuclear power sources unless there is no feasible alternative. One such alternate source of power is photovoltaics, which are widely used today in both space and terrestrial power systems. Most solar cells are designed to operate at 1 sun intensity (AM0, 136.7 mW/cm^2) and moderate temperatures (20° to 80°C). As space exploratory missions extend beyond earth's orbit, temperature and intensity become a concern. Missions are being proposed for Mars, Jupiter, the outer planets, and beyond the solar system. At these distances, both intensity and array operating temperature drop. Intensity changes inversely as the square of the distance. Temperature calculations are based on intensity and emissivity. The array temperature can be as low as -140°C at 6 astronomical units (A.U.), i.e. Jupiter intensity is 5 mW/cm^2 and -130°C at 5.2 A.U. (1). A plot of Intensity vs distance is shown on the following page, this plot also includes relative array temperatures at various planetary distances.

With early LILT measurements dating back 15-25 years, most of the available data is outdated. Solar cells have become more efficient and more reliable over a range of environmental conditions. Early LILT data was also performed using older techniques with limited temperature and intensity regulation, and less sensitive measuring equipment. Flight hardware costs continue to increase, which decreases their allowable design margins. Updating these measurements is crucial for the recent resurgence in PV for interplanetary missions.

Most temperature effects on solar cell output are understood. As cell temperature drops open circuit voltage V_{oc} will increase linearly, and short circuit current I_{sc} will decrease due to a shift in bandgap (the absorption coefficient

also decreases with temperature). Fill Factor will tend to increase proportionally with voltage but there are many other mechanisms that contribute to its temperature dependence (2). The most important effect is that the dark current I_0 decreases as temperature decreases. The temperature effects on voltage and current can be seen in the following equations (3,4):

$$V_{oc} = \frac{\gamma k T}{q} \left(\frac{I_{sc}}{I_0} + 1 \right) \quad (1)$$

$$I(V) = I_{sc} - I_0 \left[e^{\left(\frac{qV}{\gamma k T} \right)} - 1 \right] \quad (2)$$

$$I_0 \propto T^3 e^{-\frac{E_g}{kT}} \quad (3)$$

where T is temperature, γ is the ideality factor, typically between 1 and 2, k is Boltzman's constant, E_{g0} is the bandgap, and q is the charge on an electron. As temperature decreases, the bandgap of the semiconductor material increases. This decreases the spectrum which can be absorbed and reduces the photocurrent.

Other LILT effects are not well known. Tandem cells in series must be current matched. As the band gap shifts with temperature, the current matching may be lost. As cells drop in temperature and intensity, these changes can be nonlinear. Cells may become shunted and/or carriers and dislocations may be "frozen out". Three common LILT phenomenon that lead to performance degradation include cell shunting, formation of a rear contact Schottky barrier, and the "broken knee" or "flat spot" curve shape (5,6).

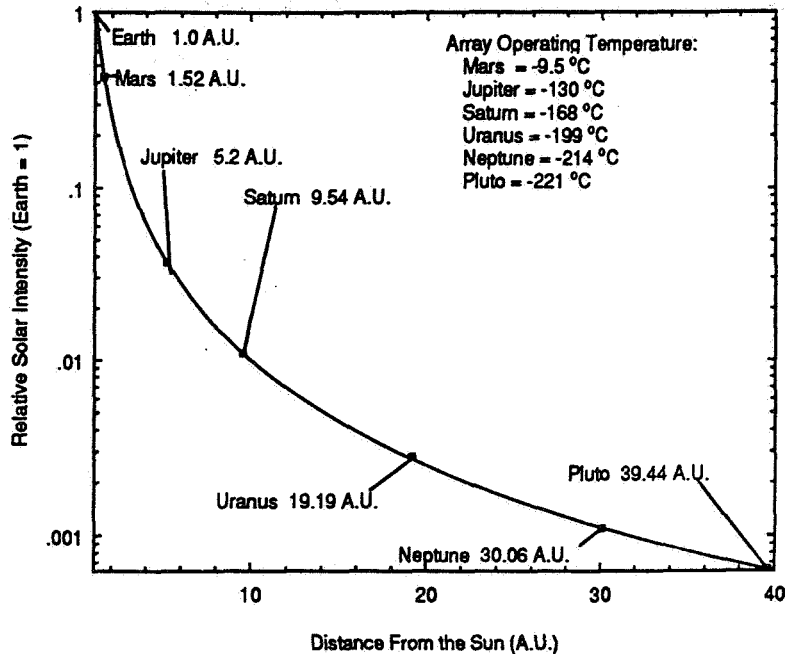


Figure 1: Solar Intensity vs. Distance From the Sun

CELL TYPES

The cells used for this experiment represent a broad range of new cell materials. Only one of the cells tested was obtained from a production run; all other cells were grown in research labs. These materials were grown on substrates which include Si, GaAs, Ge, and InP. The cells are:

- GaInP/GaAs two-terminal monolithic tandem grown on GaAs.
 - GaInP cell on GaAs (inactive)
 - GaAs cell with a GaInP window layer.
- InP/InGaAs two-terminal monolithic tandem grown on InP.
 - InP cell
 - InGaAs cell with a InP window and grown latticed matched on InP
- GaAs/Ge (passive Ge), GaAs grown on Ge.
- Si 2 Ω -cm with BSF. This a production cell.
- InP MOCVD
- .72 eV InGaAs (InP window, InP substrate)
- GaSb (bottom cell of GaAs on GaSb tandem stack)

TEST DESCRIPTION

The test consisted of measuring IV curves of solar cells at varying light intensities and temperature. The

temperatures ranged from 25°C to -185°C. The intensities ranged from 1 sun down to .03 suns, or equivalent distances of 1 to 6 au. I-V curves were run every 25°C at 2.8, 4.7, 11.5, 46, and 136.7 mW/cm² intensities. The information included in this paper is only a summary of the data analysis. Figure 2 shows a diagram of the test setup.

The tests were all conducted at NASA Lewis in the Solar Cell Evaluation Lab. A Spectrolab X-25 solar simulator was used to measure the cells. This simulator provides a close match to the AM0 spectrum but it is not exact. A monitor cell was placed outside the low temperature plate to correct for flicker in the arc lamp light source. All the cells were mounted to a test plate and placed in a closed environment with a quartz window and constant nitrogen purge. Temperature of the test plate was maintained by cooling with liquid nitrogen and heating with resistive heaters. Up to eight cells can be tested simultaneously with this setup. All of the cell measurements and temperatures are computer controlled. Cells were measured with standard 4-wire techniques and contacted using Kelvin probes; no epoxies or solders were used to contact the cell.

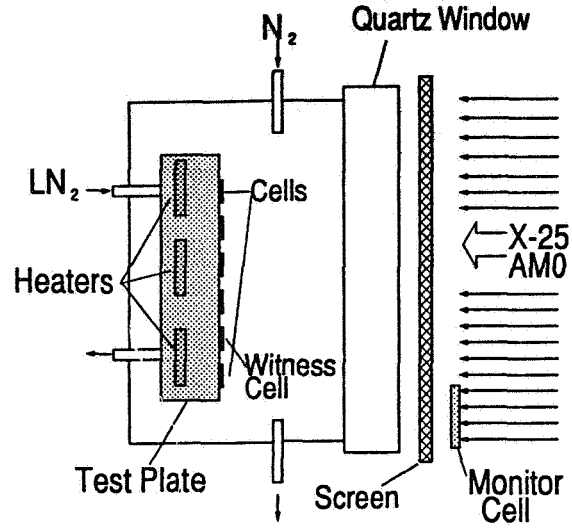


Figure 2 LILT Test Setup

A single thermocouple embedded in the test plate is used for temperature control. Additionally, four witness cells of similar material and thickness as the test cells were mounted to the test plate and used as a temperature reference for the cells. A temperature measurement was made at the beginning and end of each IV curve so that accurate V_{oc} vs T and I_{sc} vs T correlations could be made. Typically, a temperature drift of less than 2° was observed during an IV curve. Each IV curve was performed from V_{oc} to I_{sc} .

Light intensity was set up for 1 sun by adjusting the lamp intensity to match I_{sc} on a calibrated GaAs/Ge cell at the plane of the test cells. Intensity was decreased by using metal screens, which lower the amount of light on the cells without changing the spectrum. The cells were placed far enough behind the screens to avoid 'hot spots' on the individual cells.

LILT DATA

All the test data was used to calculate temperature coefficients for V_{oc} , I_{sc} , and FF. The data analysis is presented by cell type. Any anomalies in the cells are shown in the plots of the data or mentioned in the text. All of the data are normalized to the value at 25°C so that they can be used independently of cell size. Temperature coefficients are presented in Tables I and II on the following pages. All of these cells were optimized for 1 sun or greater intensities.

GaNP/GaAs

The GanP/GaAs cell is a monolithic tandem cell consisting of series connected current matched cells. The cells are series connected using a tunnel junction. This cell had nearly linear temperature/intensity dependence to about -90°C, with peak efficiency at around -50°C. Below -90°C, the cell voltage flattened and then dropped to near room temperature values. A plot of this data at 1 sun is shown in Figure 3. This loss of output below -90°C can be attributed to the eventual current mismatch of the two cells, parasitic losses in the tunnel junction, and additional voltage loss from changes in dark current.

A GanP cell and a GaAs cell with a GanP window layer were measured separately. Data on these two individual cells show that the drop in current is due to limiting by the bottom cell. Both of these cells continue to operate well below -90°C and indicate that the probable loss in tandem performance could be in the tunnel junction.

InP/InGaAs

The InP/InGaAs cell is a monolithic tandem cell consisting of series-connected current matched cells. This cell also had typical temperature/intensity dependence to about -90°C. This cell had a peak efficiency at near -90°C. Below -90°C, the cell voltage becomes nonlinear. A plot of this data is shown in Figure 4. The voltage change does not coincide with the current drop.

Plots of an InP cell and an InGaAs cell with an InP window layer measured separately show typical temperature/intensity dependence over the entire range of measurements. The voltage slope of both cells tends to lessen below -90°C. The current of the InGaAs cell changes very little with temperature. This is due to the shift at both ends of the spectrum. The InP window layer is shifting along with the band edge of the InGaAs cell which, when integrated over an AM0 spectrum, shows little net change in current. This is clearly demonstrated in the QULT measurements (7).

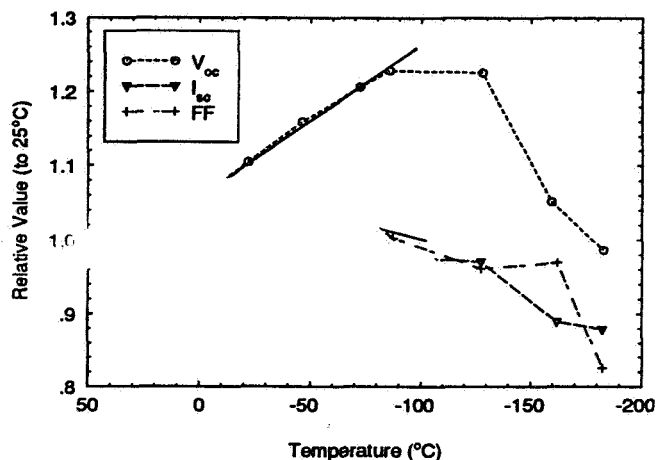


Figure 3 GaInP/GaAs at 1 Sun

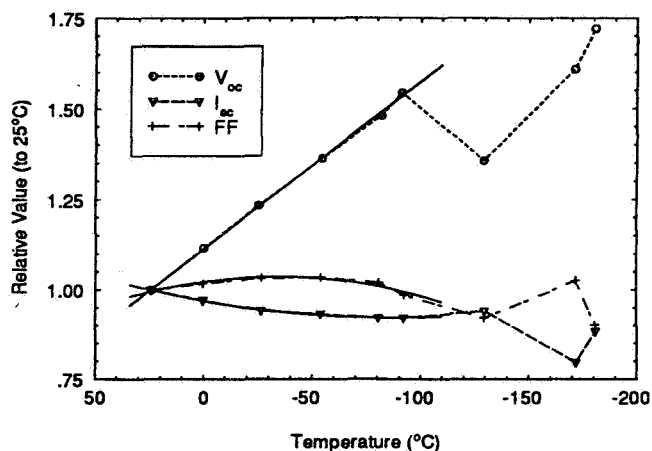


Figure 4 InP/InGaAs at 1 Sun

Si Cells

The Si cell is a 2Ω-cm cell with a BSF. The 1 sun temperature data is shown in Figure 5. Below -100°C the voltage slope is much lower. This cell had typical temperature/intensity dependence over the entire range of measurements. Si efficiency increased by 70% from 25° down to -180°C, where it peaks. This cell tends to operate the best at low temperature due to its shift in bandgap. The bandgap shifts from 1.21 eV up to 1.45 eV, which is the optimum bandgap single-junction cells under AM0.

InP Cell

This InP cell had typical temperature/intensity dependence over the entire range of its measurements. The voltage slope did change at temperatures below -75°C, but the change was not as much as seen on the previous cells. The efficiency on this cell continued to rise over the entire temperature range, increasing by 30% from room temperature down to -180°C.

InGaAs Cell

The InGaAs cell is grown lattice matched (1.42 eV) to InP with an InP window layer. The voltage also exhibits a prominent slope change below -100°C. The two InGaAs cells measured here had slightly different coefficients, which may be a function of their design (two different research labs).

GaAs/Ge and GaAs Cell

The GaAs/Ge cell was cut down from a large area cell and shows severe shunting at low intensities due to the cutting. Full area cells had no shunting problems. This cell also had a slope change in voltage below -75°C. The cell had a Schottky barrier at temperatures below -125°C, seen as a bend in the IV curve near V_{oc} .

Low Intensity measurements were conducted on all cells at every temperature recorded above. The behavior of I_{sc} and V_{oc} followed predicted performance within the ranges of the temperature coefficients presented above.

The short circuit current varied linearly with intensity and the open circuit voltage varied with the linearly logarithm of I_{sc} . The Fill Factor tended to follow V_{oc} . The GaInP/GaAs cell at room temperature and -90°C data follow typical temperature trends. The changes in voltage slope at lower temperatures reflect possible changes in dark current I_0 as voltage is defined in equation 1.

TEMPERATURE CORRECTION

The basis for this paper is to attempt to create a data base for temperature coefficients for a wide variety of current cell structures. Use of these coefficients can be derived from the following equation:

$$\frac{1}{P_{max}} \frac{dP_{max}}{dT} = \frac{1}{I_{sc}} \frac{dI_{sc}}{dT} + \frac{1}{V_{oc}} \frac{dV_{oc}}{dT} + \frac{1}{FF} \frac{dFF}{dT} \quad (4)$$

From the above equation, which is based on the maximum power point, temperature correction can be applied directly. Simpler techniques apply correction to V_{oc} , I_{sc} , and P_{max} (or FF), then use curve fitting to generate the IV curve. This correction works well with normal IV curves, but does not accurately represent larger cells or arrays which contain steps or inconsistencies in the IV curve. The following two equations can be applied on a point by point basis to generate an approximate temperature corrected IV curve.

$$V_{new\ temp} = V_{meas} \left(1 + (\Delta T) \left(\frac{1}{V_{oc}} \frac{dV_{oc}}{dT} + \frac{V_{meas} I_{meas}}{P_{max_{meas}}} \frac{1}{FF} \frac{dFF}{dT} \right) \right) \quad (5)$$

and

$$I_{new\ temp} = I_{meas} \left(1 + (\Delta T) \left(\frac{1}{I_{sc}} \frac{dI_{sc}}{dT} \right) \right) \quad (6)$$

The Fill Factor correction is applied to the voltage equation, but it could be used in the current equation if preferred. Second order equations can be substituted directly for the single coefficients. In all cases, voltage goes up and current goes down as temperature decreases. For use in arrays, series and parallel multipliers must also be used (series cells add in voltage, parallel cells add in current).

CONCLUSION

The data presented in this paper presents a brief overview of the temperature and intensity characteristics of new cell technologies. The temperature coefficients will help create a database for mission planners. This work is a continuation of the QULT and LILT measurements published previously (7,8). A comparison of the results of this paper with those obtained by QULT shows that I_{sc} obtained with temperature-dependent spectral response is in good agreement with I_{sc} dependence measured with an AM0 simulator. It should be noted that temperature coefficients tend to vary among similar cells, and the spectrum of the X-25 simulator does not exactly match the AM0 spectrum (it contains more infrared and less ultraviolet).

The coefficients are indicated for the typical characteristics of cells showing common trends. These common trends are; higher bandgap cells have lower coefficients; voltage increases and current decreases with lowering temperature; V_{oc} is proportional to the log of intensity, current is directly proportional to intensity, and fill factor tends to drift up to a peak and drop down.

Although multi-junction cells offer higher efficiency than single cells, they do present problems if used over a wide range of temperatures. Monolithic tandem cells must be designed to match current over a wide range of

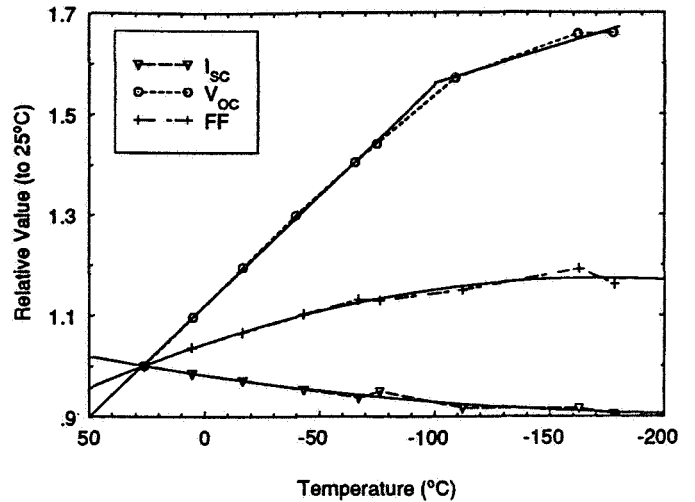


Figure 5 Si at 1 Sun

temperatures, where changes in temperature cause a shift in bandgap. In both tandem cells presented here, the bottom cell current remained relatively flat, this is due to the bandgap shift of both cells, the spectral window to the bottom cell remained constant. Tandem cells measured here worked well together to -90°C and then started to drift nonlinearly.

Most of the cells measured exhibited two slope curves for V_{oc} vs temperature. This characteristic is indicative of a change in the I_0 as well as I_{sc} . Different recombination mechanisms affect different voltage ranges and temperatures, i.e., Hall Schottky Read, tunneling recombination, junction recombination, and surface recombination. The voltage slope at lower temperatures tended to be less than near room temperature. Within the range of temperatures measured for most cells, a peak in fill factor peak could be observed; this required a second order equation for curve fitting.

The plots shown in Figure 6 indicate that the voltage coefficients tend to increase linearly as a function of the log of intensity and that their slope also increase with decreasing bandgap. This trend can be mathematically demonstrated. It can be used to extrapolate temperature coefficients for a wide range of intensities.

The authors would like to graciously thank National Renewable Energy Labs, Applied Solar Energy Corporation, Spire Corporation, Boeing Corporation, and JX Crystals for providing cells which were used for these measurements. The authors intend to continue to add to this data as new requirements and cells become available.

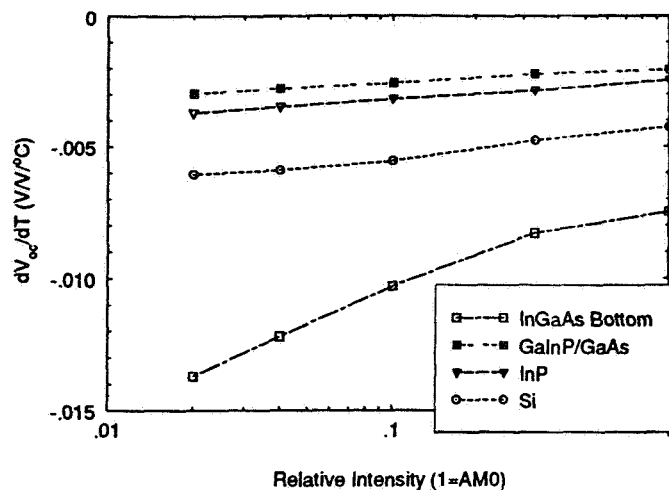


Figure 6 V_{oc} Coefficient vs Log(Intensity) on Cells

REFERENCES

- 1) Ho, J.C., Bartels, F. T. C., and Kirkpatrick, A. R., 1970, "Solar Cell Low Temperature, Low Solar Intensity Operation". Conference record of the 8th IEEE Photovoltaic Specialists Conference, pp. 150-154.
- 2) Hovel, Harold J., "Semiconductors and Semimetals, Volume 11, Solar Cells", Academic Press, 1975, pp 166-180
- 3) Hu, Chenming, and White, Richard M., 1983, "Solar Cells, From Basic to Advanced Systems", McGraw-Hill, pp 57-63
- 4) Yang, Edward S., "Fundamentals of Semiconductor Devices", McGraw Hill Book Company, 1978, pp 103-108.
- 5) Stella, Paul M., Pool, Frederick S., Nicolet, Marc A., and Iles, Peter A., 1994, "PV Technology for Low Intensity, Low Temperature, (LILT) Applications", First World Conference on Photovoltaic Energy Conversion, pp. 2082-2085
- 6) Weizer, V. G., and Broder, J. D., 1982, "On the Cause of the Flat-Spot Phenomenon Observed in Silicon Solar Cells at Low Temperature and Low Intensities", J. Appl. Phys., Vol. 53, No. 8, August 1982, pp. 5926-5930.
- 7) Jenkins, Phillip, Scheiman, David, and Brinker, David, 1994, "Prediction Short Circuit Current of Single Junction and Multi-Junction Solar Cells at low temperature for Planetary Missions", First World Conference on Photovoltaic Energy Conversion, pp. 2012-2015.
- 8) Scheiman, David A., Jenkins, Phillip P., Brinker, David J., 1995, "Low Intensity Low Temperature (LILT) Measurements on New Photovoltaic Structures", 30th IECEC, 95-353, Vol. I, pp.327-332

TABLE I : Temperature Coefficients of Multi-Bandgap Cells and SubCells

| Range(°C) | 1 Sun | .33 Suns | .1 Suns | .04 Suns | .02 Suns |
|--|-------------------------|-------------------------|----------------------------------|-------------------------|-----------------------------------|
| <u>GaInP/GaAs</u> | | | | | |
| dV _{oc} /dT 25°,-100° | -0.00206 | -0.00223 | -0.00257 | -0.00278 | -0.00296 |
| dI _{sc} /dT 25°,-100° | 0.000206 | 7.02E-5T + .00296 | 1.032E-5T + 9.61E-4 | 0.0000883 | -1.09E-5T - 2.97E-4 |
| dFF/dT 25°,-100° | -1.54E-5T - 6.15E-4 | -1.742E-5T - 6.4E-6 | -3.70E-6T - 5.07E-4 | -0.0000359 | -1.33E-5T - 8.84E-4 |
| <u>GaInP</u> | | | | | |
| dV _{oc} /dT 25°,-180° | -0.00201 | -0.00226 | -0.00268 | -0.00325 ⁽¹⁾ | -0.00313 |
| dV _{oc} /dT -100°,-180° | | | | -0.00217 | |
| dI _{sc} /dT 25°,-180° | 0.000915 | 0.00112 | 0.000961 | 0.000755 | 0.00109 |
| dFF/dT 25°,-180° | -6.6E-6T - 8.29E-4 | -7.0E-6T - 8.94E-4 | -7.16E-6T - 9.23E-4 | -7.92E-6T - .00102 | -7.98E-6T - .00106 |
| <u>GaAs Bottom Cell (GaInP window)</u> | | | | | |
| dV _{oc} /dT 25°,-125° | -0.00254 | -0.00257 ⁽¹⁾ | -0.00256 ⁽²⁾ | -0.00263 ⁽²⁾ | -0.00264 |
| dV _{oc} /dT -75°,-180° | -0.00136 ⁽⁶⁾ | -0.00137 ⁽⁶⁾ | -0.00160 | -0.00162 | -0.00168 ⁽⁶⁾ |
| dI _{sc} /dT 25°,-180° | 0.000963 | 0.00125 | 0.00114 | 0.00128 | 0.00114 |
| dFF/dT 25°,-180° | 0.0000958 | 0.0000838 | -0.000272 | -0.000412 | -0.000571 |
| <u>InP/InGaAs</u> | | | | | |
| dV _{oc} /dT 25°,-100° | -0.00462 | -0.00543 | -0.0065 | -0.00745 | -0.00772 |
| dI _{sc} /dT 25°,-100° | 1.276E-5T + .00110 | 0.000504 | 0.000306 | 4.78E-6T + 1.15E-4 | 1.182E-5T + 5.87E-4 |
| dFF/dT 25°,-100° | -2.42E-5T - 8.07E-4 | -1.126E-5T - 5.03E-4 | -4.88E-6T - 3.94E-4 | 4.78E-6T + 1.15E-4 | 1.182E-5T + 5.87E-4 |
| <u>InP</u> | | | | | |
| dV _{oc} /dT 25°,-75° | -0.00246 ⁽⁷⁾ | -0.00285 | -0.00317 | -0.00347 | -0.0037 |
| dV _{oc} /dT -75°,-180° | | -0.00214 | -0.0025 | -0.00258 | -0.00284 |
| dI _{sc} /dT 25°,-180° | 0.000442 | 0.000457 | 0.000351 | 2.66E-6T + 8.60E-4 | -0.000535 |
| dFF/dT 25°,-180° | -5.92E-6T - 8.54E-4 | -7.02E-6T - 8.91E-4 | -9.02E-6T - .0011 ⁽²⁾ | -5.86E-6T - .00123 | -4.42E-6T - .00129 ⁽²⁾ |
| <u>InGaAs Bottom Cell (InP window)</u> | | | | | |
| dV _{oc} /dT 25°,-100° | -0.00748 | -0.0083 | -0.0103 | -0.0122 | -0.0137 |
| dV _{oc} /dT -100°,-180° | | -0.00558 | -0.00733 | -0.00908 | -0.00984 |
| dI _{sc} /dT 25°,-180° | -0.0000603 | 0.000117 | -0.0000253 | -0.000171 | 0.0000456 |
| dFF/dT 25°,-180° | -1.114E-5T - .00226 | -1.1584E-5T - .00265 | -1.72E-5T - .00318 | -2.16E-5T - .00392 | -2.34E-5T - .00426 |

Notes: (1) 25°,-100°C; (2) 25°,-75°C; (3) 25°,-125°C; (4) -75°,-180°C; (5) -100°,-180°C; (6) -125°,-180°C; (7) 25°,-180°C

$$dV_{oc}/dT = (V/V)/^{\circ}C$$

$$dI_{sc}/dT = (A/A)/^{\circ}C$$

$$dFF/dT = (\%/)/^{\circ}C$$

Table II: Temperature Coefficients of Single Junction Cells

| Range(°C) | 1 Sun | .33 Suns | .1 Suns | .04 Suns | .02 Suns |
|--|-------------------------|---------------------|-------------------|-------------------------|---------------------|
| GaAs Concentrator Cell | | | | | |
| dV_{oc}/dT 25°,-125° | -0.00193 | | | | |
| dV_{oc}/dT 10°,-180° | -0.00141 | | | | |
| dI_{sc}/dT 25°,-180° | -1.242E-5T + 1.53E-4 | | | | |
| dFF/dT 25°,-180° | -7.78E-6T - .001 | | | | |
| GaAs/Ge (cut from 6 x 6) | | | | | |
| dV_{oc}/dT 25°,-75° | -0.00205 | -0.00232 | -0.00256 | | |
| dV_{oc}/dT -75°,-180° | -0.000338 | -0.000327 | -0.000364 | | |
| dI_{sc}/dT 25°,-180° | -4.24E-6T + 2.61E-4 | 0.000739 | 0.000654 | | |
| dFF/dT 25°,-180° | -1.492E-5T + 3.13E-4 | 0.000639 | -7.2E-6T + 1.5E-5 | | |
| InP | | | | | |
| dV_{oc}/dT 25°,-75° | -0.00248 | | | | |
| dV_{oc}/dT -75°,-180° | -0.00209 | | | | |
| dI_{sc}/dT 25°,-180° | 0.000436 | | | | |
| dFF/dT 25°,-75° | -0.000642 | | | | |
| Si (2Ω·cm.) | | | | | |
| dV_{oc}/dT 25°,-75° | -0.00425 ⁽¹⁾ | -0.00476 | -0.00553 | -0.00589 ⁽¹⁾ | -0.00605 |
| dV_{oc}/dT -75°,-180° | -0.0140 ⁽⁶⁾ | -0.00189 | -0.00309 | -0.0044 ⁽⁶⁾ | -0.00401 |
| dI_{sc}/dT 25°,-180° | 2.98E-6T + 6.75E-4 | 9.96E-6T + .00144 | 0.000451 | 3.38E-6T + 8.73E-4 | 1.28E-5T + .00108 |
| dFF/dT 25°,-180° | -8.90E-6T - .00152 | -1.176E-5T - .00130 | 8.66E-6T - 9.0E-4 | 9.64E-6T + 9.16E-4 | -1.03E-5T - 9.94E-4 |
| InGaAs (InP window layer, .72 eV) | | | | | |
| dV_{oc}/dT 25°,-100° | -0.00534 | | | | |
| dV_{oc}/dT -100°,-180° | -0.00348 | | | | |
| dI_{sc}/dT 25°,-180° | 3.38E-06T + 2.12E-4 | | | | |
| dFF/dT 25°,-180° | -1.55E-5T - .00138 | | | | |
| GaSb | | | | | |
| dV_{oc}/dT 25°,-75° | -0.00466 | | | | |
| dV_{oc}/dT -75°,-180° | -0.00274 | | | | |
| dI_{sc}/dT 25°,-180° | -3.34E-5T + 2.41E-4 | | | | |
| dFF/dT 25°,-180° | -8.20E-6T - .00225 | | | | |

Notes: (1) 25°,-100°C; (2) 25°,-75°C; (3) 25°,-125°C; (4) -75°,-180°C; (5) -100°,-180°C; (6) -125°,-180°C; (7) 25°,-180°C

$$dV_{oc}/dT = (V/M)/°C$$

$$dI_{sc}/dT = (A/A)/°C$$

$$dFF/dT = (%/%) / °C$$

A SUMMARY OF THE INTERNATIONAL WORKSHOPS ON SPACE SOLAR CELL CALIBRATION AND MEASUREMENT TECHNIQUES

D.J. Brinker, H.B. Curtis and D.J. Flood
NASA Lewis Research Center
Cleveland, Ohio

P. Jenkins and D.A. Scheiman
NYMA Setar, Inc.
Brook Park, Ohio

S25
IN-50410

ABSTRACT

The first two of a planned series of international workshops concerning space solar cell calibration and measurement techniques have been held within the past year. The need for these workshops arose from the increasing complexity of space solar cells coupled with the growing international nature of the market for space cells and arrays. The workshops, jointly sponsored by NASDA, ESA and NASA, have the objective of obtaining international agreement on standardized values for the AM0 spectrum and constant, recommendations for laboratory measurement practices and the establishment of a set of protocols for making interlaboratory comparison measurements. The results of the first two workshops, held in Waikiki, Hawaii, USA in 1994 and Madrid, Spain in 1995, are presented.

INTRODUCTION

The market for both space solar cells and arrays has become more international in recent years. At the same time, space cell design is becoming increasingly complex with a corresponding increase in the difficulty of providing accurate on-orbit performance predictions. Thus the need for the universality of calibration and laboratory measurements was recognized and a series of workshops concerning these issues has been initiated. The workshops, of which two have been held and a third is planned, have been jointly sponsored by the European Space Agency (ESA), the National Space Development Agency of Japan (NASDA) and the National Aeronautics and Space Administration (NASA). The objectives of the workshops include agreement on standardized values of the Air Mass Zero (AM0) solar constant and spectral intensity distribution, recommendations for laboratory measurement practices and establishment of a set of protocols for making interlaboratory comparison measurements. The international intercomparison will include both primary reference standards and laboratory techniques. The workshops were to be held at approximately one year intervals in conjunction with major space photovoltaic conferences in order to maximize attendance.

1st WORKSHOP

The First International Workshop on Space Solar Cell Calibration and Measurement Techniques was organized by the NASA Lewis Research Center. It was held on December 12-13, 1994 in Waikiki, Hawaii, directly following the 1st World Conference on Photovoltaic Energy Conversion. Thirty-four participants from England, France, Germany, Japan, Spain and the United States attended the workshop. Their affiliations are listed in Table I. During an opening plenary session, each of the sponsoring agencies presented their objectives for the workshop. Furthermore, it was decided that smaller working groups would be optimum in light of the diverse topics to be addressed and the short time (two days) allotted for the workshop. The three

Table I - Affiliations of 1st Workshop Participants

| <u>Japan</u> | <u>United States</u> | <u>Europe</u> |
|-----------------------|----------------------|----------------------|
| Adv. Eng Services Co. | Hughes Space & Com. | Deutsche Aerospace |
| Hi-Reliability Comp. | NASA LeRC | DRA |
| ISAS | NREL | EEV Ltd. |
| JQA | Spectrolab | ESA-ESTEC |
| NASDA | USAF/Phillips Lab | ESTI |
| Opto Research Corp. | | Fraunhofer Institute |
| Sharp Corp. | | INTA/Spasolab |
| Wacom R&D Corp. | | |
| M. Wantanabe & Co. | | |

working groups would discuss primary standard solar cells, multijunction devices and laboratory practices. Reports from each of the three groups would be presented at a closing plenary session, with written reports to be prepared and distributed after the close of the workshop.

Primary Standard Solar Cells

The need for accurate laboratory measurement of space cells is increasing as the cells become more complex and mission planners demand ever more precise guarantees of on-orbit performance as the margins in power systems shrink. These laboratory measurements are possible only with the use of primary (or reference) standard cells. Historically, primary standards have been made through the use of high altitude balloons (JPL and CNES), Shuttle experiments (NASA and ESA) and high altitude aircraft (LeRC). The two balloons and the aircraft are the only methods currently utilized. Concerns of primary standard cell users were voiced in the working group and include: the seasonal nature and limited space available on calibration flights, the cost of an independent calibration program prohibits users from generating their own standards, and the aging of standard cells, creating the need for regular re-flight. An indoor (laboratory) method of primary cell calibration was proposed. It is based on the the measurement of the spectral response of the cell and the spectral irradiance of the solar simulator lamp. A number of disadvantages and concerns with this method were identified and a comparison with traditional methods was recommended before any further action could be taken on the proposal. The conclusions and recommendations of the working group were: 1) increased opportunities to create space-based primary standards are needed, 2) a research effort to measure the AM0 spectrum should be advocated, 3) an international standard for the AM0 spectrum and constant needs be chosen and, 4) an international intercomparison of primary standards should be established.

Multijunction Devices

Multijunction solar cells present new problems because of the requirement for current matching of the two or three cells of the devices currently under development. Not only are primary standards of complete devices necessary, but calibrated subcells will most likely be required. Because the different subcells in the multijunction device generally have different radiation-hardness characteristics, care must be taken in differentiating between Beginning of Life (BOL) and End of Life (EOL) performance, with each condition requiring a set of primary standards. Accurate determination of temperature coefficients is also required, with the different subcells having different temperature coefficients. Most single source solar simulators, unless carefully filtered, are inadequate for determination of these coefficients. Precision current-voltage characterization of subcells and full MJ devices will require spectrally tunable solar simulators and subcell standards. The working group presented the following issues and recommendations to the full workshop: 1) determination of how well reference cells must be spectrally matched to test cells to avoid spectral mismatch corrections, 2) optimization of spectral adjustment of simulator for production testing, 3) perform an

uncertainty analysis to allow extrapolation of laboratory measurements to actual space performance and, 4) round robin cross-checking.

Laboratory Practices

It was recommended in that the World Meteorological Organization's (WMO) solar spectrum and constant (136.7 mW/cm²) be adopted as a standard. However, each organization will continue to use its own standards until formal agreement is reached. For intercomparison, a cell temperature of 25 °C will be used. Full area illumination for spectral response/quantum efficiency measurements and total area for efficiency calculations was also recommended. A round robin intercomparison was proposed for current-voltage and spectral response measurements. Each of the three sponsoring agencies will provide cells as follows:

| Cell type | Irradiated | Japan | Europe | United States |
|------------|------------|-------|--------|---------------|
| Silicon | No | X | X | X |
| Silicon | Yes | X | X | X |
| GaAs | No | | X | X |
| GaAs | Yes | | X | X |
| Hi Eff. Si | No | X | | |
| Hi Eff. Si | Yes | X | | |

A solar cell holder compatible with both the JPL and CNES balloons was designed and will be used to mount the cells designated for the intercomparison.

2nd WORKSHOP

The final action of the 1st Workshop was agreement as to the necessity of a second workshop, to be held within the next year. This workshop, organized by the European Space Agency and hosted by the Spanish National Institute of Aerospace Technology (INTA), was held in Madrid on September 12-13, 1995, directly following the Fourth European Space Power Conference. Twenty-five participants from China, England, France, Germany, Japan and the United States attended; the affiliation of these attendees is given in Table II. The three working groups from the 1st Workshop reported their findings at an opening plenary session. The primary objectives of the Workshop were to conclude the discussions begun in the 1st Workshop and to finalize and implement plans for the round robin comparisons. As in the case of the 1st Workshop, smaller working groups were formed. These groups were primary standards, AM0 solar spectrum and constant; laboratory measurement practice; multijunction devices and round robin measurements.

Primary Standards, AM0 Solar Spectrum and Constant

The tentative agreement on the WMO solar spectrum and constant from the 1st Workshop was reaffirmed. Participants in this workshop agreed to survey the "radiometry" communities in their respective countries for recommendations on AM0 spectrum and intensity. A temperature of 25 °C was decided upon for all laboratory current-voltage and spectral response measurements. The calibration of primary standards was discussed, with continued reservations about the indoor methods expressed. It was decided that calibration methods be designated as either "synthetic" (laboratory-based, spectrally corrected) or "space-based" (high altitude balloon or aircraft, Shuttle or similar flight experiment).

Laboratory Measurement Practice

A general agreement was reached on 25 °C as a reference temperature for all round robin measure-

Table II - Affiliations of 2nd Workshop Participants

| | | |
|-----------------------|-------------------------|----------------------|
| <u>Japan</u> | <u>United States</u> | <u>Europe</u> |
| Adv. Eng Services Co. | NASA LeRC | CNES |
| Hi-Reliability Comp. | | Deutsche Aerospace |
| ISAS | | EEV Ltd. |
| JQA | <u>China</u> | ESA-ESTEC |
| NASDA | China Acad. Space Tech. | Fraunhofer Institute |
| Opto Research Corp. | | INTA/Spasolab |
| Sharp Corp. | | |

ments. After a discussion of laboratory practices at the various institutions represented in the working group, it was decided that two areas that would best benefit from a comparison of results would be the determination of temperature coefficients and spectral response characteristics. The cell complement would be the same as that designated during the 1st Workshop, except the cells would not be mounted. The temperature range for temperature coefficient determination would be +20 to +80 °C, all results would be blind until full completion of the testing. ESA, NASDA and NASA LeRC would participate. The same cell set will be used for the spectral response measurements, with test conditions left up to the individual agencies but fully documented. An exchange of test procedures for common laboratory measurements was agreed to by ESA, NASDA and NASA.

Multijunction Devices

Various measurement techniques and equipment are in use for characterizing multijunction solar cells. The strengths and weaknesses of the techniques, as well as any previously unforeseen anomalies, need to be identified. This can best be accomplished through a MJ solar cell measurement investigation. It will not be a comparison of results, but a practical opportunity to assess measurement techniques for real space cells. NASA LeRC will obtain and mount about 10 GaInP/GaAs two junction solar cell. LeRC will test the cells on the Lear aircraft (both Isc and IV measurements) and distribute them to the following possible collaborators:

| | <u>United States</u> | <u>Europe</u> | <u>Japan</u> |
|-----------|----------------------|----------------|--------------|
| Agencies: | LeRC | ESTEC | NASDA |
| | JPL | INTA | ISAS |
| | | CNES | |
| | | DRA | |
| | | ISE (Freiburg) | |

After testing at the various agencies, the cells will be returned to LeRC for reflight on the Lear aircraft. All results will be distributed to all participants.

Round Robin Measurements

A working group devoted to round robin measurements was created at the 2nd Workshop. However, its results mirrored some of those from the working groups previously discussed. They suggested blind round robin of current-voltage and spectral response measurements be conducted and agreed with the MJ working group that a round robin for multijunction cells is premature. A round robin of primary calibration standards would be conducted between the agencies currently calibrating cells, i.e., CNES, JPL and NASA LeRC. Each participant will provide two cells, one silicon and one gallium arsenide, six cell in all. The intercomparison will be conducted fully blind, with all data to be distributed only after the calibrations are complete.

The 2nd Workshop ended with a plenary session at which time the four working groups reported their results. Preliminary written reports from two of the groups were distributed, with a final, complete Workshop Report to be distributed by year's end. A third workshop was decided upon, as a forum for reporting and discussion of the results of the several measurement activities begun at this workshop. The 3rd Workshop will be held in Japan in November, 1996, following the 9th International Photovoltaic Science and Engineering Conference. The workshop will be hosted by NASDA.

CONCLUSION

The first two of a planned series of International Workshops on Space Solar Cell Calibration and Measurement Techniques have been held during the past year with some forty participants from six countries. The need for these workshops arose from the increasing complexity of space solar cells coupled with the growing international nature of the market for space cells and arrays. The objectives of the workshops include agreement on standardized values of the (AM0) solar constant and spectral intensity distribution, recommendations for laboratory measurement practices and establishment of a set of protocols for making interlaboratory comparison measurements. Toward meeting these goals, three round robin measurement activities have been started: 1) primary calibration standards, 2) laboratory current-voltage and spectral response characterization and 3) laboratory temperature coefficient determination. A multijunction cell measurement investigation will also be conducted. The results of these activities will be reported and discussed at a third workshop, to be held in Japan during November of 1996.

Review of Recent Thermophotovoltaic (TPV) Research at Lewis Research Center

Donald L. Chubb, Brian S. Good and David M. Wilt
NASA Lewis Research Center
Cleveland, OH 44135

326
IN-50411

and

Roland A. Lowe, Navid S. Fatemi and Richard H. Hoffman
Essential Research, Inc.
Cleveland, OH

and

David Scheiman
NYMA, Inc.
Brookpark, OH

ABSTRACT

Thermophotovoltaic (TPV) research at NASA Lewis Research Center that began in the late 1980's is reviewed. This work has been concentrated on low bandgap indium gallium arsenide (InGaAs) PV cells and rare earth - yttrium aluminum garnet (YAG) thin film selective emitters, as well as, TPV system studies. An emittance theory has been developed for the thin film emitters. Experimental spectral emittance results for erbium Er-YAG and holmium Ho-YAG show excellent emittance ($\geq .7$) within the emission bands. The .75 eV InGaAs PV cells fabricated at Lewis have excellent quantum efficiency. An efficiency of 13% has been measured for this cell coupled to an Er-YAG selective emitter and a short pass IR filter.

Introduction

Thermophotovoltaic (TPV) energy conversion is not a new concept. It has its origins at MIT in the late 1960's. Early TPV work was confined to the use of silicon Si photovoltaic (PV) cells, which require high temperature ($\geq 2000\text{K}$) emitters to make an efficient system. In recent years, however, two significant advances have occurred that make possible efficient TPV energy conversion at moderate temperatures ($< 2000\text{K}$). The first of these developments is efficient low bandgap photovoltaic (PV) cells such as gallium antimonide (GaSb) and indium gallium arsenide (InGaAs). Efficient selective emitters that have single strong emission bands at photon energies that match the PV cell bandgap energy is the second important development.

Before beginning the review of the TPV research at Lewis a definition of a TPV system is in order. Figure 1 is a schematic of a general TPV system. Any thermal energy source, such as the sun, combustion or a nuclear reaction can be the input energy for the system. However, the thermal energy must be converted to radiant energy that can be efficiently converted to electrical energy by the photovoltaic (PV) cells. Thus the radiant energy must have a photon energy equal to or greater than the PV cell bandgap energy. There are two methods for obtaining the bandgap-matched radiation. Either a selective emitter, which emits most of its

energy in a single bandgap-matched emission band, or a bandpass filter - grey body emitter combination, which results in a single bandgap-matched emission band can be used to obtain efficient TPV conversion. Therefore, there are two basic TPV systems; selective emitter or filter. In this paper we review the research on selective emitters, low bandgap InGaAs PV cells, as well as, TPV systems studies.

$$\eta_{th} \text{ (thermal efficiency)} \quad \times \quad \eta_{Ef} \text{ (emitter-filter efficiency)} \quad \times \quad \eta_{PV} \text{ (PV efficiency)} = \eta_T \text{ (system efficiency)}$$

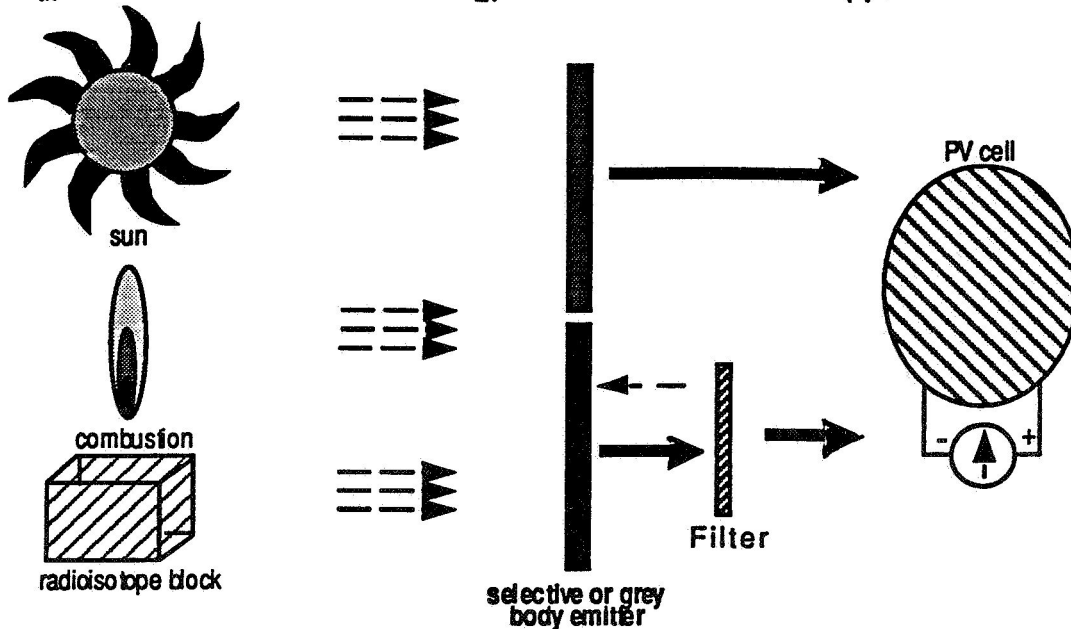


Figure 1 Thermophotovoltaic (TPV) Energy Conversion Concept

Selective Emitters

The ideal selective emitter would have a single emission band with an emittance approaching one within that band and negligible emittance outside the emission band. For the photon energy or wavelength region of interest in TPV (1-3 μ m), an electronic transition of an atom or molecule is required to produce the desired radiation. However, when atoms are compressed to solid state densities the emission is not characterized by narrow line emission as with an isolated atom, but by a continuous emission spectrum.

Most solid state materials behave like a grey body emitter, namely they have nearly constant spectral emittance. The only way to obtain a selective emitter is to find a material that behaves like an isolated atom. At low densities such as with a gas or plasma the emission is like that of an isolated atom. Therefore, the first selective emitter we looked at was a cesium plasma (1). And in fact the emitter efficiency was large (>.7). However, a plasma emitter has two problems. First of all the operation temperature is too high and secondly the low plasma density means the power density in the emission band is low.

Fortunately, there are a group of atoms that at solid state densities behave nearly like isolated atoms. These are the rare earth atoms. For doubly and triply charged ions of these elements in crystals the orbits of the valence 4f electrons, which account for emission and absorption, lie inside the 5s and 5p electron orbits. The 5s and 5p electrons "shield" the 4f valence electrons from the surrounding ions in the crystal. As a result, the rare earth ions in the solid state emit in narrow bands rather than in a continuous grey body manner. For temperatures of interest the rare earths have one strong near-infrared band associated with electron transitions from the lowest energy level to the ground state. The spectra of these rare earth ions in crystals have been extensively studied. Most of this work is summarized in the text of Dieke (2).

The first selective emitter investigation (3) of the rare earths in oxide form showed the strong infrared emission bands. However, emittance outside the emission band was also large so that the emitter efficiency was low. In the late 80's Nelson and Parent (4, 5) reported a large improvement in rare earth oxide emitters. Their emitters are constructed of bundles of small diameter (5-10 μ m) rare earth oxide fibers similar to the construction of the Welsbach mantle used in gas lanterns. The very small characteristic dimension of these

emitters results in low emittance outside the emission band and thus greatly increased efficiency. At the Auburn Space Power Institute fibrous rare earth oxide emitters are being fabricated by a paper making process (6). The fibrous selective emitters are well suited to a combustion driven system where the fibrous mantle surrounds the flame. However, for coupling to other thermal energy sources likely to be used for a space power system, such as nuclear or solar, the fibrous emitter is not so well suited. As just stated, it was the small characteristic dimension that made the fibrous emitters efficient. Another geometry for achieving a small characteristic dimension and also easily coupling to any thermal source is a thin film. A thin film containing a rare earth on a low emittance substrate can be easily attached to any thermal source. In addition, a thin film is more durable than a fibrous geometry. Therefore, we began theoretically and experimentally investigating rare earth containing thin film selective emitters (7, 8). Until now, the most successful thin film emitter is yttrium aluminum garnet (YAG, $Y_3Al_5O_{12}$) doped with rare earths (9). The rare earth doped YAG, where the rare earth ion replaces the yttrium ion, is grown as a single crystal and then cut and polished to the desired thickness. A low emittance, opaque substrate must be placed between the emitter and thermal source to block the grey body emission from the thermal source.

Although YAG can be doped with any of the rare earths most of our research has been confined to Er-YAG and Ho-YAG (9, 10, 11, 12). With emission bands at $\lambda_b = 1.55 \mu m$ and $\lambda_b = 1.95 \mu m$, respectively, they are of most interest for TPV application. The theoretical analysis of the thin film emitter is based on one dimensional radiative transfer theory (8, 13, 14) that includes scattering, as well as, emission and absorption. If scattering is included the theory is quite complicated. However, neglecting scattering allows an analytic solution for the spectral emittance, ϵ_λ (13).

$$\epsilon_\lambda = \frac{(1-\rho_{\lambda 0})}{D_\lambda} \left\{ 2h_- [\epsilon_{\lambda s} + n_\lambda^2(1-\epsilon_{\lambda s})(1-2E_3(K_{\lambda d}))] + n_\lambda^2 \left[h_+ (1-2E_3(K_{\lambda d})) - \mu_m^2 D_\lambda \left(1-2E_3\left(\frac{K_{\lambda d}}{\mu_m}\right) \right) \right] \right\} \quad (1)$$

Where $\epsilon_{\lambda s}$ is the substrate emittance, $\rho_{\lambda 0}$ is the reflectance at the emitter surface, n_λ is emitter material index of refraction, $K_{\lambda d} = \alpha_\lambda d$ is the emitter optical depth where α_λ is the extinction coefficient (= absorption coefficient for no scattering) and d is the emitter thickness. Other quantities appearing in eq. (1) are the following.

$$h_+ = 1 - 4\rho_{\lambda 0}(1-\epsilon_{\lambda s})\mu_m^2 E_3(K_{\lambda d}) E_3\left(\frac{K_{\lambda d}}{\mu_m}\right) \quad (2)$$

$$h_- = E_3(K_{\lambda d}) - \mu_m^2 E_3\left(\frac{K_{\lambda d}}{\mu_m}\right) \quad (3)$$

$$D_\lambda = 1 - 4\rho_{\lambda 0}(1-\epsilon_{\lambda s})E_3^2(K_{\lambda d}) \quad (4)$$

$$\mu_m^2 = 1 - 1/n_\lambda^2 \quad (5)$$

$$E_3(x) = \int_0^1 u e^{-x/u} du \approx \frac{1}{2} e^{-3/2x} \quad \text{Exponential Integral of order 3} \quad (6)$$

As eq. (1) indicates the parameters that determine the spectral emittance are the optical depth, which depends on the extinction coefficient and film thickness, the substrate emittance, emitter material index of refraction, and reflectance at the emitter surface. Refraction at the emitter surface is accounted for by the quantity $\mu_m = \cos \theta_m$, where θ_m is the maximum angle of incidence at the emitter surface for radiation to escape the film ($\sin \theta_m = 1/n_\lambda$ from Snell's Law for refraction).

The dependence of ϵ_λ on $K_{\lambda d}$ is approximately $1 - \exp(-3K_{\lambda d}/2)$ since $E_3(x) \approx 1/2 \exp(-3x/2)$. Equation (1) also shows the importance of substrate emittance. For regions outside the emission band where α_λ and thus $K_{\lambda d}$ is small ($E_3(0) = 1/2$) the emittance will be dominated by the substrate emittance, $\epsilon_{\lambda s}$. Thus it is important to have low substrate emittance to minimize the emission outside the emission band and thus maximize the emitter efficiency. Low $\epsilon_{\lambda s}$ also implies the reflectance ($1 - \epsilon_{\lambda s}$) at the substrate approaches 1 which means that a significant contribution ($1 - \epsilon_{\lambda s}$ term in eq. (1)) to the emission band results from reflection at the substrate. Therefore, low substrate emittance minimizes emission outside the emission band where α_λ is

small and increases emission within the emission band where α_λ is large.

Knowing the spectral emittance, ϵ_λ , the emitter efficiency, η_E , defined as follows, can be determined.

$$\eta_E = \frac{\text{power emitted in emission band}}{\text{total power emitted}} = \frac{\int_{\lambda_u}^{\lambda_l} \epsilon_{\lambda b}(T_E, \lambda) d\lambda}{\int_0^\infty \epsilon_\lambda \epsilon_{\lambda b}(T_E, \lambda) d\lambda} \quad (7)$$

Where $\epsilon_{\lambda b}$ is the black body emissive power and λ_u is the short wavelength limit of the emission band and λ_l is the long wavelength limit of the emission band.

$$\epsilon_{\lambda b}(T_E, \lambda) = \frac{2\pi hc_0^2}{\lambda^5 \left[\exp\left(\frac{hc_0}{\lambda k T_E}\right) - 1 \right]} \quad (8)$$

And h is Planck's constant, c_0 is the vacuum speed of light, k is Boltzmann's constant and T_E is the emitter temperature. We have found (11,12) that the spectral emittance can be split into 4 bands. For the region $0 \leq \lambda \leq \lambda_u$ the spectral emittance is nearly a constant, ϵ_u . Within the emission band ($\lambda_u \leq \lambda \leq \lambda_l$) the emittance shows some variation but can also be approximated as a constant, ϵ_b . For $\lambda_l \leq \lambda \leq \lambda_c$ the emittance is also a constant, ϵ_l , where $\lambda_c = 5 \mu\text{m}$ for YAG. For $\lambda_c \leq \lambda \leq \infty$ the extinction coefficient for YAG is large so that the emittance, $\epsilon_c \rightarrow 1.0$. Therefore, if ϵ_λ is approximated by the four band model just described equation (7) becomes the following.

$$\eta_E = \left[1 + \frac{\epsilon_l}{\epsilon_b} \frac{G(u_c)}{F(u_1, u_u)} + \frac{\epsilon_u}{\epsilon_b} \frac{H(u_u)}{F(u_1, u_u)} + \frac{\epsilon_c}{\epsilon_b} \frac{L(u_c)}{F(u_1, u_u)} \right]^{-1} \quad (9)$$

Where,

$$F(u_1, u_u) = \int_{u_1}^{u_u} \frac{x^3}{e^x - 1} dx \quad u_1 = \frac{hc_0}{\lambda_1 k T_E}, \quad u_u = \frac{hc_0}{\lambda_u k T_E} \quad (10)$$

$$G(u_c) = \int_{u_c}^{u_1} \frac{x^3}{e^x - 1} dx \quad (11)$$

$$H(u_u) = \int_{u_u}^{\infty} \frac{x^3}{e^x - 1} dx \quad (12)$$

$$L(u_c) = \frac{\pi^4}{15} - \int_{u_c}^{\infty} \frac{x^3}{e^x - 1} dx \quad u_c = \frac{hc_0}{\lambda_c k T_E} \quad (13)$$

As equation (9) shows the emitter efficiency depends on the ratio of the emittances outside the emission band ($\epsilon_u, \epsilon_l, \epsilon_c$) to the emittance for the emission band, ϵ_b , as well as, the emitter temperature, T_E , and the emission band location (λ_u & λ_l) and the cutoff wavelength, λ_c . For given values of the emittance ratios and emission band location there is an optimum temperature for maximum efficiency (7). Lowe (11, 12), et al. have experimentally found that the optimum T_E for Ho-YAG with an emission band centered at $\lambda = 1.95 \mu\text{m}$ is approximately 1650K. For Er-YAG, which has an emission band at $\lambda_b = 1.55 \mu\text{m}$ the optimum T_E will be higher. Theoretically (7, 8), it has been found that for the case where $\epsilon_l = \epsilon_u = \epsilon_c$, maximum η_E occurs when $E_b / k T_E \approx 4$, where $E_b = hc_0 / \lambda_b = (hc_0 / 2) (1 / \lambda_u + 1 / \lambda_l)$ is the photon energy at the center of the emission band.

As mentioned earlier, the rare earth oxide fibrous emitter is efficient because of the small dimension of the fibers. In the case of the thin film emitter there will be an optimum thickness for maximum efficiency. This can be seen by considering equation (9). For a given T_E and emission band, the efficiency will be a maximum when the emittance ratios ϵ_l / ϵ_b , ϵ_u / ϵ_b and ϵ_c / ϵ_b are a minimum. As already mentioned in discussing the spectral emittance (eq. (1)), the emittance has nearly an exponential dependence $1 - \exp(-3K_{\lambda}d/2)$ on optical depth, $K_{\lambda}d (= \alpha_{\lambda}d)$. Therefore, for $d = 0$, $\epsilon_{\lambda} = \epsilon_{\lambda b}$ and therefore $\epsilon_l = \epsilon_u = \epsilon_c = \epsilon_b$. As d increases ϵ_b will increase much faster than ϵ_l , ϵ_u and ϵ_c since $\alpha_b \gg \alpha_l$, α_u and $\epsilon_c = \text{constant}$. As a result the emittance ratios will decrease and η_E will increase to a maximum for some optimum d . For d greater than the optimum value the emittance ratios will begin to increase since ϵ_b will be nearly constant at its asymptotic value for $K_{\lambda}d \rightarrow \infty$ while ϵ_l and ϵ_u will be still increasing. Therefore, η_E will start to decrease. Lowe (12), et al. experimentally found the optimum thickness for Er-YAG to be .7 to 1.0 mm. Since this is rather a large dimension for a thin film a more appropriate title should be "thick" film selective emitter rather than thin film selective emitter.

Now consider experimental results for Ho-YAG and Er-YAG selective emitters. The first parameter of interest in evaluating a selective emitter is the extinction coefficient α_{λ} since the spectral emittance depends primarily on α_{λ} (eq. (1)). The extinction coefficient at room temperature was calculated using measured values of the spectral transmittance and reflectance (9). Figure 2 shows the extinction coefficients of Ho (25%) -YAG and Er (40%) -YAG (the percentages refer to the percentage of Ho and Er ions that replace the yttrium ions in the YAG crystal). As can be seen the extinction coefficients within the emission bands are large ($> 10 \text{ cm}^{-1}$) compared to regions outside the emission bands where $\alpha_{\lambda} < 1.0 \text{ cm}^{-1}$. Therefore, we would expect the same result when the spectral emittance within the emission bands are compared to the spectral emittances outside the emission bands.

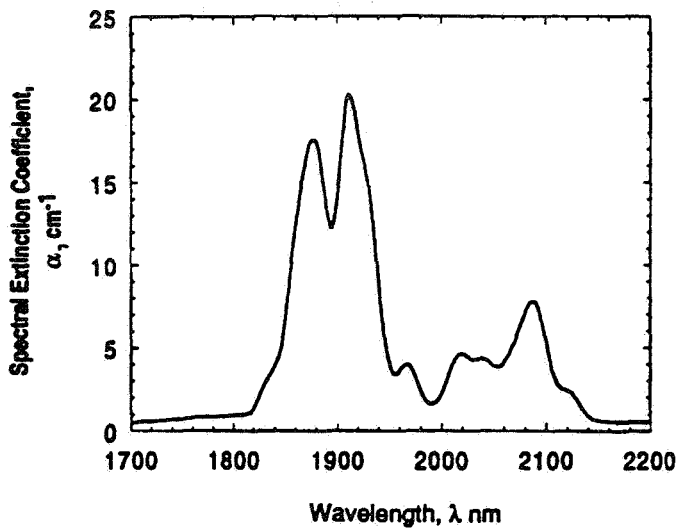


Figure 2(a) Ho (25%) - YAG

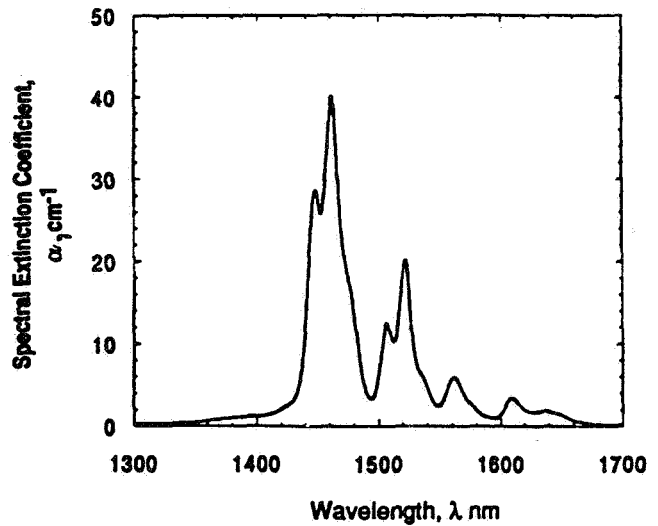


Figure 2(b) Er(40%) - YAG

Figure 2 Extinction Coefficient from Measured Transmission and Reflectance
(a) Ho(25%)-YAG (b) Er(40%)-YAG.

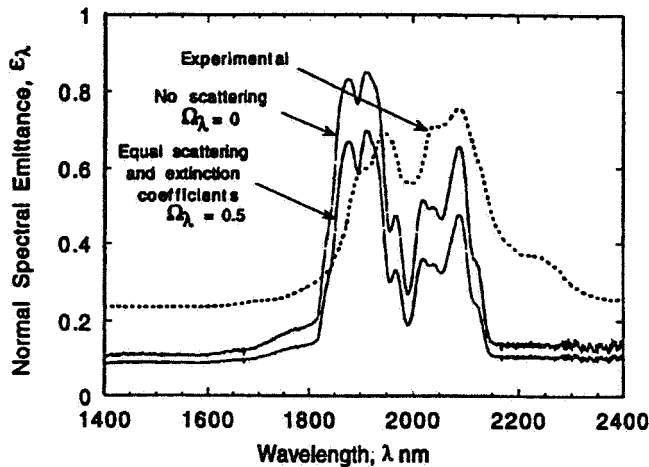


Figure 3 (a) Ho (25%)-YAG

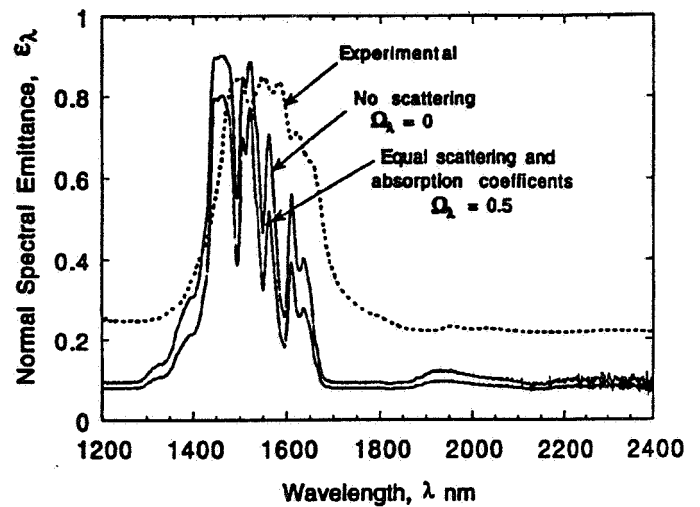


Figure 3(b) Er (40%)-YAG

Figure 3 Theoretical and experimental spectral emittance ϵ_λ with platinum foil substrate. Theoretical calculations assumed constant substrate emittance ($\epsilon_s = .2$) and index of refraction for YAG ($n_f = 1.9$). (a) Ho(25%)-YAG, .65mm thick; front surface temp. = 1380K, back surface temp. = 1616K, average temp. = 1500K. (b) Er(40%)-YAG, 1.04mm thick, front surface temp. = 1398K, back surface temp. = 1606K, average temp. = 1500K.

In Figure 3 the measured spectral emittances at an emitter temperature of 1500K with platinum substrates are compared to the theoretical emittances. The emitter temperature is the average of the front (emitting surface) and back (substrate surface) surface temperatures. The theoretical calculations (8, 14), which include scattering, assumed a constant substrate emittance ($\epsilon_s = .2$) for platinum and a constant index of refraction ($n_f = 1.9$) for the emitter. Also, the theory used the measured, room temperature extinction coefficient and assumed a constant emitter temperature. Since these calculations were performed the theory has been modified to allow a linear temperature variation across the emitter (14). In comparing the theoretical and experimental ϵ_λ results, several features should be noted. First, the emittance in the emission bands is large. Second, results with small scattering ($\Omega_\lambda \leq .5$) agree more closely with the measurements. Third, the measured emittance outside the emission band is considerably higher than the theoretical values. Part of this discrepancy results from experimental error. In wavelength regions of low emittance, background radiation becomes significant so that the measured emittances are larger than the actual values (9, 10). Finally, the theoretical emittance outside the emission band is smaller than the assumed platinum substrate emittance ($\epsilon_s = .2$). This result occurs because part of the substrate emission is totally reflected at the emitter surface due to the refractive limit (μ_m^2 term in h_- term of eq. (1).

To summarize the selective emitter discussion the following points should be emphasized. First of all, the thin film Ho-YAG and Er-YAG selective emitters have large emittances ($\geq .6$) within their emission bands. However, the emittance outside the emission bands is also larger than predicted. For $\lambda > 5\mu\text{m}$ YAG has a large extinction coefficient therefore the emittance for $\lambda > 5\mu\text{m}$ will be large. For $\lambda < 5\mu\text{m}$ the source for most of the emission outside the emission bands is the substrate. Therefore, it is essential that the substrate emittance be small in order to obtain good emitter efficiency. As pointed out earlier, low substrate emittance (high substrate reflectance) increases the emittance within the emission band as well. Currently, we are investigating other host materials for the rare earth ions. Also, other low emittance substrate such as rhodium are being investigated.

INDIUM GALLIUM ARSENIDE PHOTOVOLTAIC CELLS

The TPV need for a low bandgap energy photovoltaic (PV) cell is the main reason the Lewis research program (15,16) on indium gallium arsenide ($\text{In}_x\text{Ga}_{1-x}\text{As}$) PV cells was initiated. $\text{In}_x\text{Ga}_{1-x}\text{As}$ is a direct bandgap semiconductor material that has a bandgap ranging from .35eV to 1.42eV depending on the In/Ga ratio. It is of interest for tandem solar cells (17), as well as for TPV. Besides Lewis, $\text{In}_x\text{Ga}_{1-x}\text{As}$ research is being carried out at several laboratories including NREL (17, 18, 19), Spire Corporation (20), Research Triangle Institute (21) and Rensselaer Polytechnic Institute (22).

$\text{In}_x\text{Ga}_{1-x}\text{As}$ devices were grown on InP substrates by Organo Metallic Vapor Phase Epitaxy (OMVPE) in a horizontal, low pressure reactor designed and constructed at Lewis. Details of the growth method are given in references 15 and 16. Three different bandgap devices have been grown. The first cell grown was $\text{In}_{.53}\text{Ga}_{.47}\text{As}$ with a bandgap energy, $E_g = .75\text{eV}$, and a lattice constant matched to InP. Also, cells with $E_g = .66\text{eV}$ and $.60\text{eV}$, which are not lattice matched to InP, were grown by incorporating step graded buffer layers between the InP substrate and the cell structure. These layers are intended to minimize the density of dislocations in the active device. The device structures are shown in Figure 4.

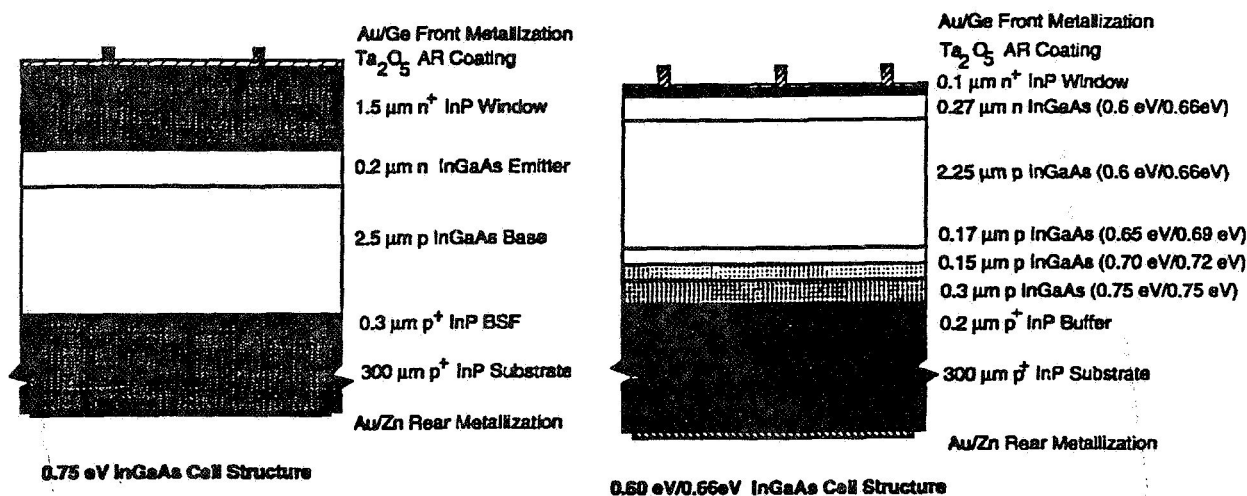


Figure 4 Lattice matched (0.75eV) and mismatched (0.60/0.66eV) InGaAs device structures.

In TPV applications the photon generated current densities will be large ($1\text{-}10\text{a/cm}^2$). Therefore it is critical to reduce series resistance losses as much as possible. For this reason highly doped InP window layers are used to reduce the resistance between the current collecting grid fingers. A balance between the absorption losses of the window layer and the reduction in series resistance means there will be an optimum window thickness. Due to the lattice mismatch only thin window layers can be used on the .66 and .60eV cells. Antireflecting (AR) coatings of tantalum oxide (Ta_2O_5) were applied to reduce reflection in the wavelength regions near the cell bandgaps.

Detailed performance results for the three InGaAs cells are given in references 15 and 16. In this paper we will consider the spectral response and the unilluminated current-voltage relations (dark diode data). In Figure 5 the external quantum efficiency for the cells is shown. As can be seen the lattice matched, .75eV cell attains the largest quantum efficiency ($> 90\%$). The .66 and .60eV cells have lower quantum efficiency and also show a "roll off" for the long wavelengths that the .75eV cell goes not show. Because of the many dislocations in lattice mismatched cells the minority carrier lifetimes will be short. This fact coupled with longer absorption lengths for long wavelength photons accounts for the "roll off" at the long wavelengths. Optimization of base thicknesses, doping levels and the lattice grading structure should improve the long wavelength response.

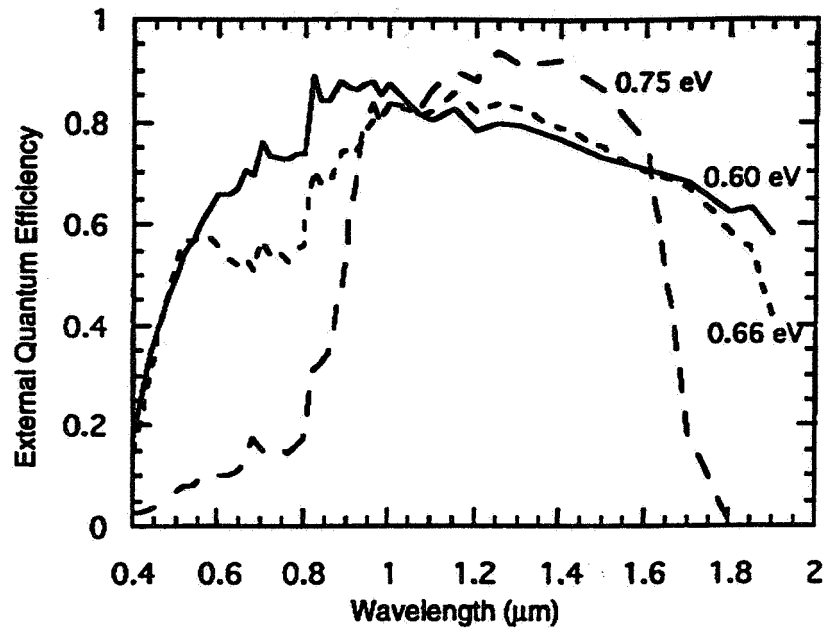


Figure 5 External Quantum Efficiency measurements of InGaAs photovoltaic devices with anti-reflective coatings.

| Bandgap (eV) | A | J01 (A/cm ²) | Rs(Ω) | Rsh (Ω) |
|--------------|------|--------------------------|-------|---------|
| 0.75 | 1.01 | 3.6e-8 | 0.453 | 3.4e3 |
| 0.66 | 0.99 | 6.5e-6 | 0.431 | 2.5e3 |
| 0.60 | 0.96 | 2.2e-5 | 0.387 | 8.0e2 |

Table 1 InGaAs photovoltaic device diode characteristics for three different bandgaps. The second column ("A") is the diode ideality factor, J01 is the reverse saturation current (dark current), Rs is the series resistance and Rsh is the shunt resistance.

In Table I the dark diode data for the three cells is shown. As can be seen the dark saturation current, j_{01} increases considerably in going from the .75eV lattice matched cell to the .66eV and .60eV lattice mismatched cells. There is also a significant decrease in the shunt resistance, R_{sh} , in going from .75eV to .60eV. Also note that the diode ideality factor $A \approx 1$ for each of the cells so that recombination current in the depletion region is negligible. Finally, the series resistance, R_s , shows a small increase in going from the .60eV cell to the .75eV cell.

The large dark saturation currents and "roll off" in quantum efficiency for long wavelengths for the lattice mismatched cells result mainly because of dislocations. Currently, buffer layer design and dislocation passivation techniques are under development to alleviate these problems. In addition a new cell structure that addresses two important TPV issues is being fabricated. First of all, photons reaching the PV cell with energy below the bandgap energy are a loss to the system unless they can be reflected back to the emitter where they are absorbed. Therefore, placing a highly reflecting surface such as gold on the backside of the cell will reflect these low energy photons back to the emitter as long as the substrate does not absorb them. The second issue is the high current density and low voltage associated with low bandgap energy cells necessary for TPV. By using an array of series connected InGaAs cells the total current can be reduced and output voltage increased thus reducing resistive

losses. The cell array structure that uses series connection and also a backside reflector is the monolithically integrated module (MIM) device shown in Figure 6. In this case semi-insulating InP is used as a substrate. The semi-insulating InP is transparent to low energy photons, which are reflected by the gold layer on the cell backside. Reflection data for a 350 μm thick semi-insulating InP wafer with polished surfaces and gold on one side is shown in Figure 7. Also shown is the reflectance of a MIM cell without an AR coating. As can be seen > 80% reflection is achieved for the long wavelength (low energy) photons.

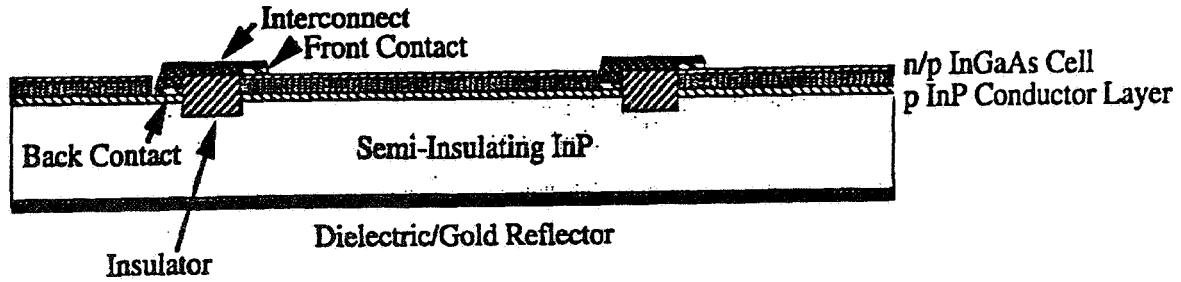


Figure 6 Monolithically Integrated Module (MIM) InGaAs device design.

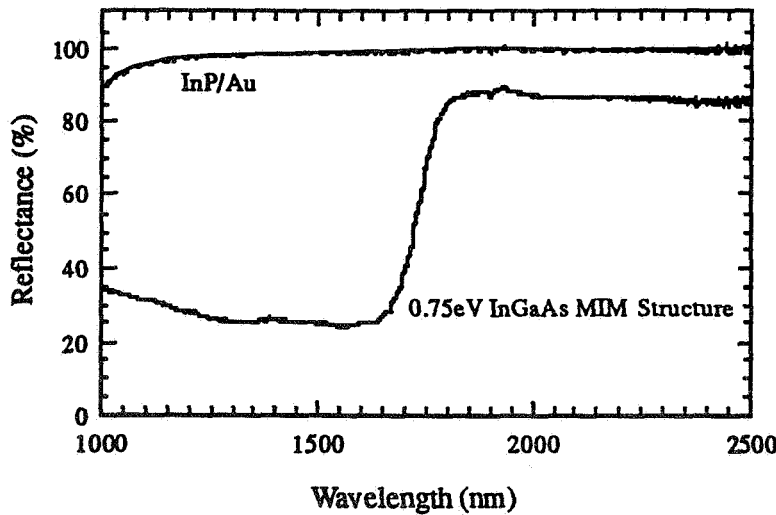


Figure 7 Spectral reflectances of polished 350 μm thick InP wafer with gold backside and $E_g = .75 \text{ eV}$ InGaAs MIM PV cell

To summarize the InGaAs research the following points can be made. Excellent quantum efficiency has been measured for the three InGaAs cells investigated. However, dislocations in the lattice mismatched cells causes a roll-off in the long wavelength quantum efficiency, as well as, reduced minority carrier lifetimes and therefore increased dark saturation currents. The new MIM structure, which is advantageous for TPV applications as discussed above, is now being fabricated.

TPV SYSTEMS STUDIES RESULTS

A computer model for a general TPV system has been developed at Lewis to determine overall TPV system performance (23). The model has been applied specifically to a solar driven thermophotovoltaic (STPV) system (24) in addition to the general case where the thermal source is not specified (23). Details of the model can be found in references 23 and 24. In this paper we present results comparing filter and selective emitter TPV systems obtained using the systems model.

An important assumption of the model is that the wavelength range ($0 \leq \lambda \leq \infty$) is divided into four bands. Within each band the optical properties of each of the components in the system are assumed constant. The boundaries of each of these bands is determined by the emitter properties or the filter properties depending on which system is being considered. As already discussed the rare earth-YAG selective emitters are well characterized by such a four band model. Since we are comparing filter and selective emitter systems the model used for the PV cell is the same for both systems. We assume an ideal PV cell model. That is the cell quantum efficiency is 1.0 and the ideal diode equation applies for the current-voltage relation. We also assume the PV cell bandgap energy, E_g , is matched to the emitter emission band energy or the filter bandpass energy. In other words

$$\lambda_1 = \frac{hc_0}{E_1} = \lambda_g = \frac{hc_0}{E_g} \quad (14)$$

Where as discussed earlier, λ_1 , is the long wavelength cutoff for the emitter emission band or the filter bandpass. We also assume a constant dimensionless bandwidth $\Delta E_b / E_b$ for the emitter emission band or the filter bandpass.

$$\frac{\Delta E_b}{E_b} = (E_u - E_1) / \frac{1}{2} (E_u + E_1) \quad (15)$$

Where E_b is the photon energy at the center of the emitter emission band or the filter bandpass and E_u is the high energy cutoff for the emission band or filter bandpass.

The overall efficiency η_T for a general TPV system is defined as follows.

$$\eta_T = \eta_{th} \eta_{Ef} \eta_{PV} \quad (16)$$

Where the thermal efficiency, η_{th} , emitter-filter efficiency, η_{Ef} , and PV efficiency, η_{PV} , are defined as follows.

$$\eta_{th} = \frac{\text{power input to emitter}}{\text{power input to thermal source}} \quad (17)$$

$$\eta_{Ef} = \frac{\text{input power to PV cells for } \lambda \leq \lambda_g}{\text{power input to emitter}} \quad (18)$$

$$\eta_{PV} = \frac{\text{electrical power output from PV cells}}{\text{input power to PV cells for } \lambda \leq \lambda_g} \quad (19)$$

For comparing selective emitter and filter TPV systems the thermal efficiency, η_{th} , need not be considered assuming it is the same for both systems. Therefore, the systems model is used to calculate η_{Ef} and η_{PV} for a given emitter temperature, T_E , with bandgap energy E_g being the independent variable.

The first thing to note about a TPV system is that for a given emitter temperature there is an optimum PV cell bandgap energy for maximum efficiency and output power density. This is illustrated in Figure 8 where results for a selective emitter system based on the rare earth-YAG emitter at $T_E = 1500K$ are shown. For this case the

assumed emittances for the emitter are $\epsilon_c = .75$, $\epsilon_l = .2$, $\epsilon_b = .75$, $\epsilon_u = .2$ and a dimensionless bandwidth, $\Delta E_b / E_b = .15$. These values are representative of the experimental values obtained for Er-YAG and Ho-YAG (9-12). Reflectance for the PV cell was assumed to be zero for all wavelengths. As can be seen from Figure 8 an optimum bandgap energy occurs because η_{EI} decreases while η_{PV} increases with increasing E_g . Also, E_g for maximum power output is slightly lower than E_g for maximum efficiency. Although not shown in the figure, as T_E increases the optimum values for E_g move to larger values.

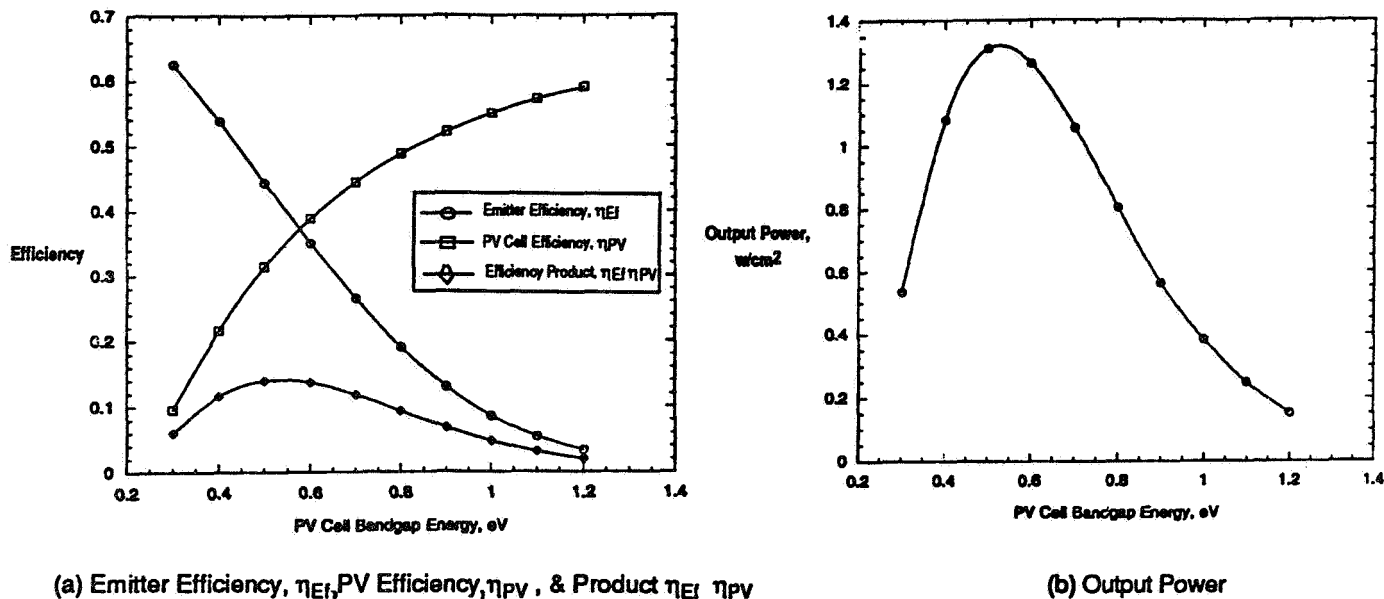


Figure 8 Performance of Rare Earth-YAG selective emitter TPV system at $T_E = 1500K$.

Properties based on experimental data ($\epsilon_l = \epsilon_u = .2$, $\epsilon_b = \epsilon_c = .75$, $\Delta E_b / E_b = .15$).
Ideal PV cell (quantum efficiency = 1.).

Now consider the comparison between the rare earth-YAG selective emitter system and two filter systems. The two filter systems are the resonant-array filter developed by Edtek Corporation (25) and a combination interference-plasma filter being developed by Knolls Atomic Power Lab (26). The resonant array filter (RAF) consists of a reflective metal film (gold) containing precisely aligned (1nm precision) small cross shaped holes. The outstanding feature of this filter is the large reflectance outside the bandpass region ($r_l = r_u = .95$, $r_c = .97$). However, it also has relatively low transmission ($\tau_b = .5$) in the bandpass region ($\lambda_u \leq \lambda \leq \lambda_l$). The dimensionless bandwidth for the RAF is $\Delta E_b / E_b = .4$. With further development it is hoped that a transmission of .8 can be obtained (25). The combination plasma-interference filter (PIF) consists of alternating layers of high and low index of refraction materials with a coating (such as indium tin oxide) on the back side that functions as a cutoff filter (26) (large reflectance for $\lambda > \lambda_c$). The combination filter has good transmission ($\tau_b = .7$) in the bandpass region and large reflectances ($r_u = r_c = .8$, $r_l = .9$) outside that region. The dimensionless bandwidth for the PIF is $\Delta E_b / E_b = .6$. For the RAF and PIF systems we assumed a grey body emitter with an emittance $\epsilon_l = \epsilon_b = \epsilon_l = \epsilon_c = .9$. Also, we assumed the filters were lossless (no absorption) so that $r + \tau = 1$, where r is reflectance and τ is transmission. This is a rather large assumption since the filter receives the entire radiative output of the grey body emitter. Thus a small (<.1) absorptance is a significant loss to the system (7).

As well as low absorptance, a filter TPV system must have large reflectance outside the bandpass region (r_u , r_l , r_c) in order to have high efficiency. Similarly, in a selective emitter system the emittance outside the emission band (ϵ_u , ϵ_l , ϵ_c) must be low compared to the emittance within the emission band, ϵ_b . One method for

compensating for the significant emittance ($\epsilon_i = \epsilon_u = .2$, $\epsilon_c = .75$) outside the emission band is to use a PV cell that has large reflectance outside the emission band and thus reflect this out-of-the emission band radiation back to the emitter. The MIM InGa As cell discussed earlier is just such a PV cell. Therefore, for comparing the selective emitter system and the filter systems we assumed a reflecting PV cell for the out-of-the emission band radiation in the selective emitter system (SER). Since the filter systems have large reflectances outside the bandpass region a reflecting PV cell is not required in those systems. For the PV cell we assumed the following reflectances; $r_u=r_b=.03$, $r_i=r_c=.8$, which should be representative of the MIM InGaAs structure.

In Figure 9, the product of efficiencies, $\eta_{EF} \eta_{PV}$, for the two filter systems (RAF AND PIF) and the rare earth-YAG selective emitter system (SER) are compared at $T_E = 1500K$. As can be seen the RAF system yields the largest efficiency followed closely by the PIF system. Also note that the optimum bandgap energy is largest for the RAF system. There are two reasons why the filter systems have larger efficiency than the selective emitter system. First of all, as discussed earlier, the filters have been assumed to have no absorptance so the calculated efficiency is larger than for a real system. Second, the large reflectances for regions outside the bandpass region in the case of the filters is the main reason for their good efficiency.

A comparison of the output power for the three systems is shown in Figure 10. In this case the PIF system produces significantly more output power than either the RAF or SER systems. The SER system produces slightly more power than the RAF. For a TPV system the output power, P_{EL} , is proportional to the following quantities.

$$P_{EL} \sim \tau_b \epsilon_b \Delta E_b \quad (20)$$

Therefore, it is the large dimensionless bandwidth ($\Delta E_b / E_b = .6$) and large transmission-emittance product in the bandpass region ($\tau_b \epsilon_b = .63$) that accounts for the PIF system having the largest output power. Even though the SER system has a much smaller dimensionless bandwidth ($\Delta E_b / E_b = .15$) than the RAF system ($\Delta E_b / E_b = .4$), the low bandpass transmission-emittance product ($\tau_b \epsilon_b = .45$) for the RAF system results in the RAF system having the lowest output power. Also, note from Figures 9 and 10 that the optimum E_g for maximum power output is smaller than the optimum E_g for maximum efficiency. This result was pointed out earlier in discussing Figure 8.

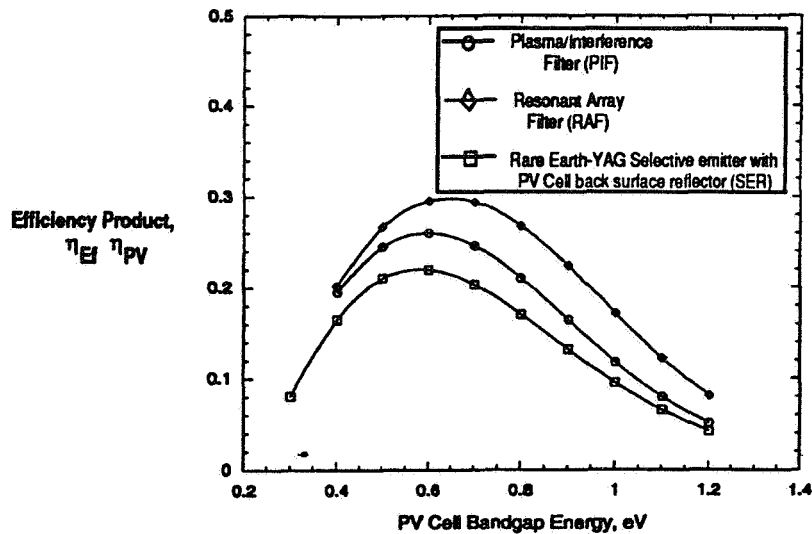


Figure 9 Efficiency comparison of lossless filter and Rare Earth-YAG selective emitter TPV systems at $T_E = 1500K$. Filter properties; PIF ($\epsilon_i = \epsilon_b = \epsilon_c = .9$, $r_i = .9$, $r_u = r_c = .8$, $r_b = .3$, $\tau = 1 - r$, $\Delta E_b / E_b = .6$). RAF ($\epsilon_i = \epsilon_b = \epsilon_u = \epsilon_c = .9$, $r_i = r_u = .95$, $r_c = .97$, $r_b = .5$, $\tau = 1 - r$, $\Delta E_b / E_b = .4$). Selective emitter properties; SER ($\epsilon_i = \epsilon_u = .2$, $\epsilon_b = \epsilon_c = .75$, $r_u = r_b = .03$, $r_i = r_c = .8$, $\Delta E_b / E_b = .15$) Ideal PV cell model used for all cases.

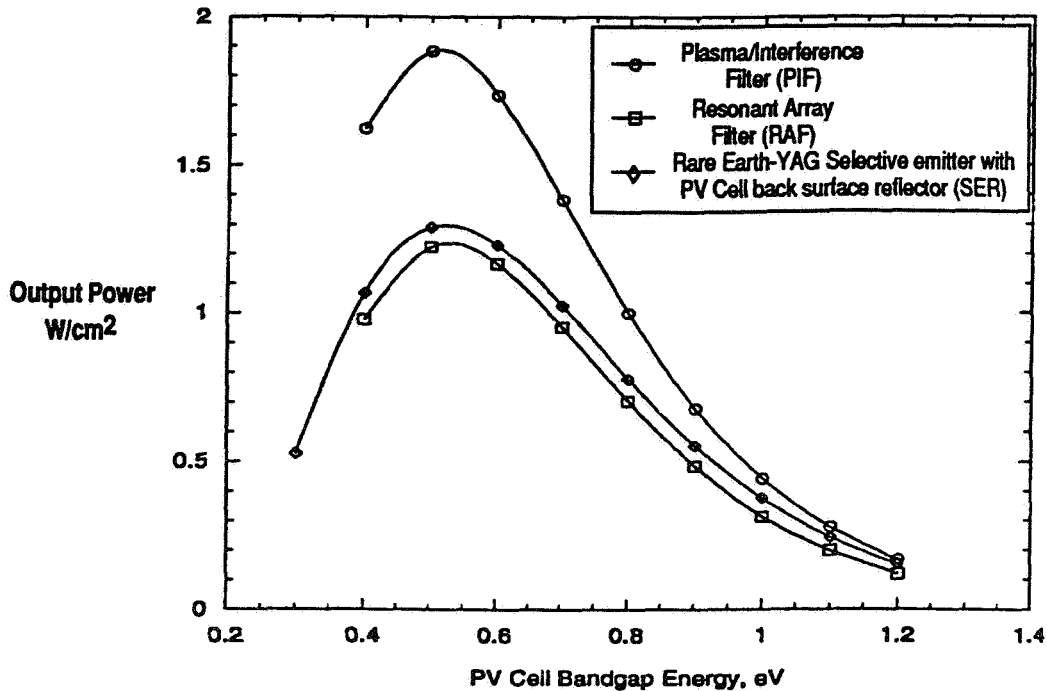


Figure 10 Power output comparison of lossless filter & Rare Earth-YAG selective emitter TPV Systems at $T_E = 1500K$. Same conditions as Figure 9.

Based on the results of Figures 9 and 10 it would appear that the filter systems will perform better than the rare earth-YAG selective emitter system. However, as already mentioned if filter absorptance were included the calculated filter system efficiencies will be reduced. Also, improvements to the selective emitter efficiency can be made by reducing the emittances and increasing the PV cell reflectances in the regions outside the emission band. Improving the filter systems efficiency will be more difficult since they already have large reflectance in the regions outside the bandpass. However, the power output of the RAF system can be improved by increasing the bandpass transmission from its present low value ($\tau_b = .5$). Power output of the SER system can also be increased by increasing the bandwidth (ΔE_b) by doping the YAG emitter with two rare earths with contiguous emission bands such as erbium Er and thulium Tm (10). At the present time there is no clear winner in choosing between filter and selective emitter TPV systems. Two important issues not yet considered, reliability and cost, will probably be the deciding issues in determining whether any TPV system becomes a viable energy converter for space or commercial application.

EXPERIMENTAL InGaAs PV CELL PERFORMANCE COUPLED TO Er-YAG SELECTIVE EMITTER

To complete the review of the Lewis TPV research we will discuss recent experimental results obtained by coupling the rare earth-YAG thin film emitter and $In_xGa_{1-x}As$ PV cells (27). Several combinations of rare earth-YAG and $In_xGa_{1-x}As$ PV cells were investigated (27). However, in this paper only the Er-YAG and $In_{.53}Ga_{.47}As$ ($E_g = .75eV$ ($1.65 \mu m$)) results will be discussed. This is a well matched system since the emission band of Er (Figure 3b) ranges from $\lambda_d \approx 1.4 \mu m$ to $\lambda_l \approx 1.7 \mu m$ and the bandgap energy for $In_{.53}Ga_{.47}As$ is $\lambda_g = 1.65 \mu m$.

A schematic of the experimental apparatus is shown in Figure 11. The Er-YAG emitter is heated on the inside of the door of an atmospheric furnace. Radiation from the emitter is concentrated by a highly reflecting platinum tube on to either a thermopile detector to measure the total radiant power incident on the PV cell or on to the InGaAs PV cell. The measured PV cell efficiency is therefore given by the following expression.

$$\eta'_{PV} = \frac{\text{measured maximum output power}}{\text{measured total radiant input power}} = \frac{P_{EL}}{P_{in}} \quad (21)$$

The maximum output power, P_{EL} , was determined from measured current-voltage curves. It should be pointed out that η'_{PV} given by equation (21) is not the same as η_{PV} given by eq. (19). The radiation in the denominator of eq. (19) includes only photons with energy greater than the bandgap energy ($\lambda \leq \lambda_g$) whereas P_{in} in equation (21) includes all photon energies. As a result, ($\eta_{PV} \geq \eta'_{PV}$).

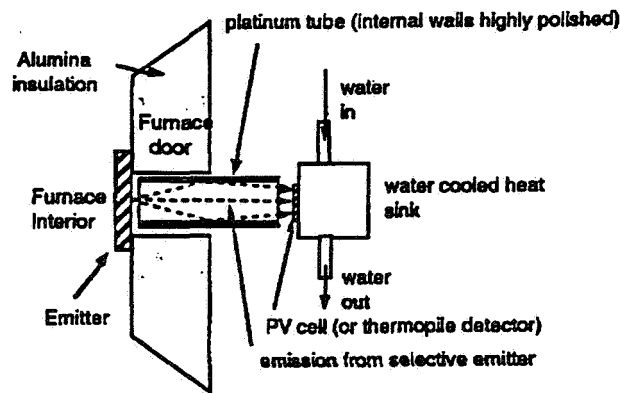


Figure 11 Schematic diagram of test apparatus used to measure PV efficiency.

Properties of the Er-YAG emitter and $\text{In}_{.53}\text{Ga}_{.47}\text{As}$ PV cell used in the experiment have already been described. For these experiments the Er-YAG emitter was .4mm thick with a platinum foil substrate backed with silicon carbide (SiC). SiC has large emittance (= absorptance) so that there is good thermal coupling between the furnace and the emitter. This good thermal coupling reduces the temperature gradient across the emitter. The .75eV InGaAs cell used in the experiment had a thinner (.05-.1 μm) InP window layer than the cell shown in Figure 4 and an area of 1cm².

Two systems were experimentally considered. The first system consisted of the Er-YAG emitter and the $\text{In}_{.53}\text{Ga}_{.47}\text{As}$ PV cell. The second system consisted of the same emitter and cell but added an interference shortpass IR filter between the emitter and PV cell. The filter had a cutoff at $\lambda \approx 1.6\mu\text{m}$. For $\lambda > 1.6\mu\text{m}$ the filter has greater than .9 reflectance. For $\lambda \leq 1.6$ the filter transmission $\approx .7$. Therefore, most all radiation with $\lambda > 1.6\mu\text{m}$ will be reflected back to the emitter when the filter is used. (In that case $\eta'_{PV} \approx \eta_{PV}$).

The I-V curves and cell performance parameters obtained for the two systems operating with $T_E = 1373\text{K}$ are shown in Figure 12. Obviously, the addition of the filter greatly improves η'_{PV} (going from 2.3% to 13.2%). However, the output power ($P_{EL} = J_{SC}V_{OC}FF$) is reduced by a factor of two with the filter because of the filter transmission loss. Use of the MIM cell structure with the back surface gold reflector will give the efficiency improvement possible with the filter but not suffer the reduction in power resulting from the transmission loss.

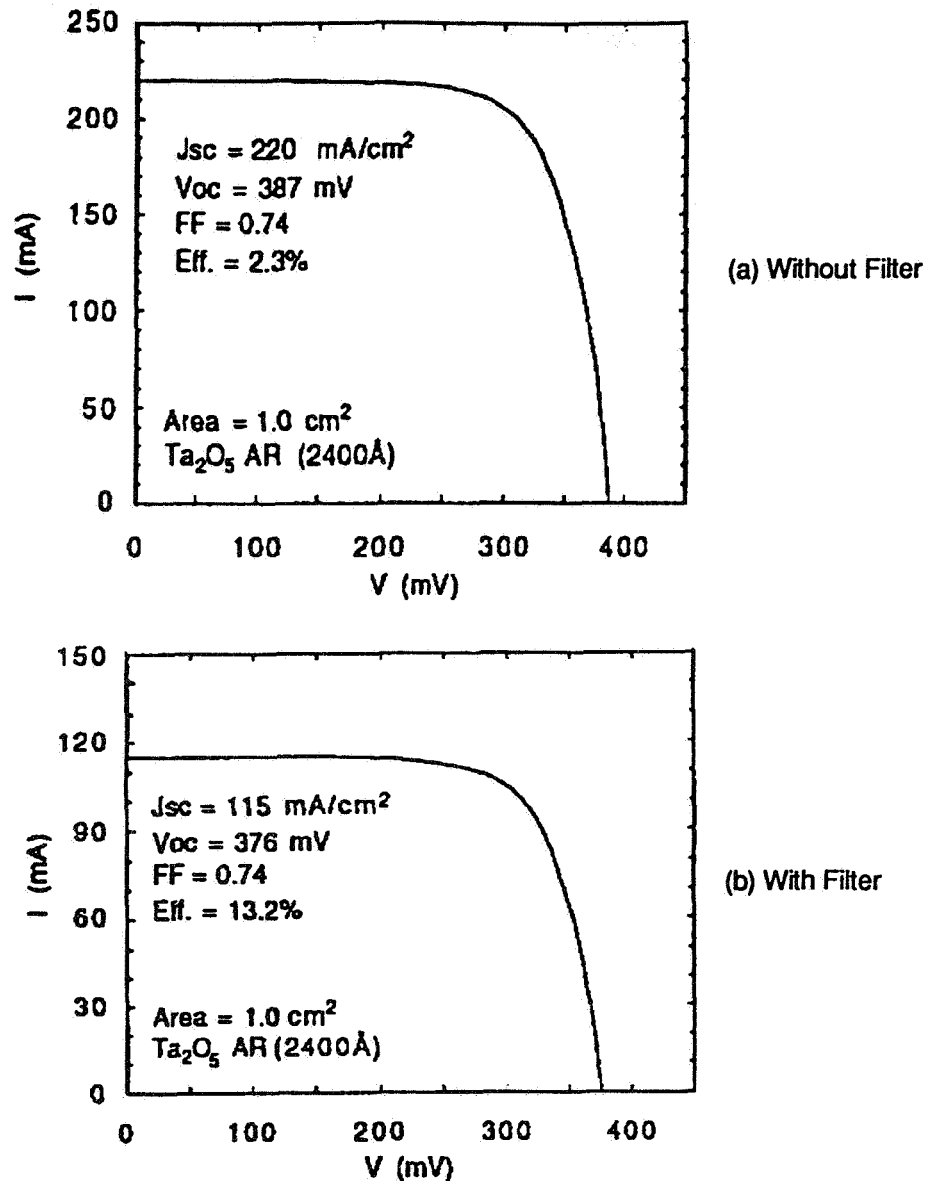


Figure 12 I-V curves for the 0.75 eV InGaAs PV AR coated cell coupled to the Er-YAG selective emitter at $T_E = 1100^\circ \text{C}$ (a) without filter, (b) with filter.

CONCLUSION

Considerable TPV research has been carried out at Lewis beginning in the late 1980's. The work has been concentrated on thin film rare earth-YAG selective emitters and $\text{In}_x\text{Ga}_{1-x}\text{As}$ PV cells, as well as, theoretical and experimental systems studies. Rare earth-YAG selective emitters with excellent emission band emittance ($> .7$) have been produced. However, further research is required to reduce the radiation outside the emission band. This research is directed at looking at new host materials for the rare earths and lower emittance substrates.

The lattice matched .75eV InGaAs PV cells fabricated at Lewis have yielded excellent quantum efficiency. A cell efficiency of 13.2% was measured using an Er-YAG emitter and short pass filter. However, for the lattice mismatched InGaAs cells, dislocations resulting from the lattice mismatch cause reduced quantum efficiency and increased dark saturation current. A new monolithically integrated module (MIM) structure is being fabricated that is better suited for TPV applications.

A TPV systems model developed at Lewis is able to model any possible TPV system. The model has

been used to compare filter and selective emitter TPV systems. However, since filter absorptance losses were not included in the model it is not possible to say which system will yield the larger efficiency. With lossless filters the model predicts that the filter systems will yield the largest efficiency.

REFERENCES

1. R. A. Lowe, C. Goradia, M. Goradia and D. L. Chubb, *J. Appl. Physics*, 68, 5033 (1990).
2. G. H. Dieke, "Spectra and Energy Levels of Rare Earth Ions in Crystals" (Interscience, New York, 1968).
3. G. E. Guazzoni, *Appl. Spectra*. 26, 60 (1972).
4. R. E. Nelson, in *Proceedings of the 32nd International Power Sources Symposium* (Electrochemical Society, Pennington, NJ, 1986) pp 95-101.
5. C. R. Parent and R. E. Nelson, in *Proceedings of the 21st Intersociety Energy Conversion Engineering Conference* (American Chemical Society, Washington, D. C., 1986), Vol. 2, pp 1314-1317.
6. P. L. Adair and M. F. Rose, in *Proceedings of The First NREL Conference on Thermophotovoltaic Generation of Electricity*, (American Institute of Physics Conference Proceedings 321, 1994), pp 245-262.
7. D. L. Chubb, in *Proceedings of the 21st Photovoltaic Specialists Conference* (IEEE, New York, 1990) pp 1326-1342; also NASA TM - 103290, 1990.
8. D. L. Chubb and R. A. Lowe, *J. Appl. Phys.*, 74, 5687 (1993).
9. R. A. Lowe, D. L. Chubb, S. C. Farmer, and B. S. Good, *Appl. Phys. Lett.* 64, 3551 (1994)
10. R. A. Lowe, D. L. Chubb, and B. S. Good, in *Proceedings of The First NREL Conference on Thermophotovoltaic Generation of Electricity*, (American Institute of Physics Conference Proceedings 321, 1994), pp 291-297.
11. R. A. Lowe, D. L. Chubb, and B. S. Good, in *Proceedings of the First World Conference on Photovoltaic Energy Conversion*, (IEEE, 1995).
12. R. A. Lowe, B. S. Good and D. L. Chubb, in *Proceedings of 30th Intersociety Energy Conversion Engineering Conference* (IECEC), (American Society of Mechanical Engineers, 1995), vol. 2, 511-515.
13. D. L. Chubb, R. A. Lowe and B. S. Good, in *Proceedings of The First NREL Conference on Thermophotovoltaic Generation of Electricity*, (American Institute of Physics Conference Proceedings 321, 1994), pp 229-244.
14. B. S. Good, D. L. Chubb and R. A. Lowe, in *Proceedings of The First NREL Conference on Thermophotovoltaic Generation of Electricity*, (American Institute of Physics Conference Proceedings 321, 1994), pp 263-275.
15. D. M. Wilt, N. S. Fatemi, R. W. Hoffman, Jr. et al., *Appl. Phys. Lett.* 64, 2415 (1994).
16. D. M. Wilt, N. S. Fatemi, R. W. Hoffman, Jr. et al., in *Proceedings of The First NREL Conference on Thermophotovoltaic Generation of Electricity* (American Institute of Physics Conference Proceedings 321, 1994), pp 210-220.
17. M. W. Wanlass, J. S. Ward, K. A. Emery and T. J. Coutts, in *Conference Record of the 23rd IEEE Photovoltaic Specialists Conference, 1993*, pp 621-627.

18. J. S. Ward, M. W. Wanlass, X. Wu and T. J. Coutts, in Proceedings of The First NREL Conference on Thermophotovoltaic Generation of Electricity (American Institute of Physics Conference Proceedings 321, 1994), pp 404-411.
19. R. K. Ahrenkiel, T. Wangansteen, M. M. Al-Jasaim, M. Wanlass and T. J. Coutts, in Proceedings of The First NREL Conference on Thermophotovoltaic Generation of Electricity (American Institute of Physics Conference Proceedings 321, 1994), pp 412-424.
20. S. Wojtczuk, E. Gagnon, L. Geoffroy and T. Parodos, in Proceedings of The First NREL Conference on Thermophotovoltaic Generation of Electricity (American Institute of Physics Conference Proceedings 321, 1994), pp 177-187.
21. P. R. Sharps, M. L. Timmons, R. Venkatasubramanian, J. S. Hills, B. O'Quinn, J. A. Hutchby, P. A. Illes and C. L. Chu, in Proceedings of The First NREL Conference on Thermophotovoltaic Generation of Electricity (American Institute of Physics Conference Proceedings 321, 1994), pp 194-201.
22. H. Ehsani, I. Bhat, D. Marcy, G. Nichols, J. Borrego, J. Parrington and R. Gutmann, in Proceedings of The First NREL Conference on Thermophotovoltaic Generation of Electricity (American Institute of Physics Conference Proceedings 321, 1994), pp 188-193.
23. B. S. Good, D. L. Chubb and R. A. Lowe, in Proceedings of The Second NREL Conference on Thermophotovoltaic Generation of Electricity (American Institute of Physics Conference Proceedings 1995).
24. K. W. Stone, E. F. Leingang, R. E. Drubka, D. L. Chubb, B. S. Good and D. M. Wilt, in Proceedings of 30th Intersociety Energy Conversion Engineering Conference (IECEC), (American Society of Mechanical Engineers, 1995), vol. 1, pp 713-718.
25. A. Schock and V. Kumar, in Proceedings of The First NREL Conference on Thermophotovoltaic Generation of Electricity (American Institute of Physics Conference Proceedings 321, 1994), pp 139-152.
26. P. F. Baldasaro, E. J. Brown, D. M. Depoy, B. C. Campbell, and J. R. Parrington, in Proceedings of The First NREL Conference on Thermophotovoltaic Generation of Electricity (American Institute of Physics Conference Proceedings 321, 1994), pp 29-43.
27. N. S. Fatemi, R. H. Hoffman, D. M. Wilt, R. A. Lowe, L. M. Garverick and D. Scheiman, in Proceedings of The Second NREL Conference on Thermophotovoltaic Generation of Electricity (American Institute of Physics Conference Proceedings, 1995).

Thermophotovoltaic Generators Using Selective Metallic Emitters

Lewis M. Fraas, John E. Samaras, James E. Avery
JX Crystals Inc.
Issaquah, WA

and

Richard Ewell
Jet Propulsion Labs

S27
N-504/2

Introduction

In the literature to date on thermophotovoltaic (TPV) generators, two types of infrared emitters have been emphasized : gray body emitters and rare earth oxide selective emitters. The gray body emitter is defined as an emitter with a spectral emissivity independent of wavelength whereas the rare earth oxide selective emitter is idealized as a delta function emitter with a high emissivity at a select wavelength and a near zero emissivity at all other wavelengths. Silicon carbide is an example of a gray body emitter (Ref. 1) and Er-YAG is an example of a selective emitter (Ref. 2). The Welsbach mantle in a common lantern is another example of an oxide selective emitter. Herein, we describe an alternative type of selective emitter, a selective metallic emitter. These metallic emitters are characterized by a spectral emissivity curve wherein the emissivity monotonically increases with shorter infrared wavelengths as is shown in Figure 1. The metal of curve "A", tungsten, typifies this class of selective metallic emitters.

In a thermophotovoltaic generator, a photovoltaic cell typically converts infrared radiation to electricity out to some cut-off wavelength. For example, Gallium Antimonide (GaSb) TPV cells respond out to 1.7 microns (Ref. 3). The problem with gray body emitters is that they emit at all wavelengths. Therefore, a large fraction of the energy emitted will be outside of the response band of the TPV cell. The argument for the selective emitter is that, ideally, all the emitted energy can be in the cells response band. Unfortunately, rare earth oxide emitters are not ideal. In order to suppress the emissivity toward zero away from the select wavelength, the use of thin fibers is necessary. This leads to a fragile emitter typical of a lantern mantle. Even given a thin Er-YAG emitter, the measured emissivity at the select wavelength of 1.5 microns has been reported to be 0.6 while the off wavelength background emissivity falls to only 0.2 at 5 microns. This gives a selectivity ratio of only 3. Another problem with a delta function selective emitter is its low power density at practical temperatures because of its narrow emission bandwidth. The concept of selectivity can be generalized by noting that we simply wish to maximize the ratio of in-cell-band power to out-of-cell-band power. Using this generalized selectivity concept and assuming a GaSb cell covered by a simple dielectric filter, we note that the emissivity selectivity ratio for tungsten is 0.3 (at 1.5 microns) / 0.07 (at 5 microns) = 4.3.

In the following sections, we note that the selective metallic emitters can be valuable in both radioisotope TPV generators in space and in hydrocarbon fired TPV generators here on earth.

Radioisotope TPV Generators

The Boeing Company first proposed to the Jet Propulsion Labs (JPL) the use of GaSb infrared cells for RTPV generators arguing that these RTPV generators could outperform currently used RTGs. Subsequently, JX Crystals licensed the GaSb cell technology from Boeing. JPL advocated the use of a tungsten emitter (Ref. 4) while NASA Lewis advocated the use of a Er-YAG selective emitter for this RTPV application. JX Crystals then obtained a small contract to do a RTPV design trade study with personnel at JPL and NASA Lewis as subcontractors. In the following, we describe the results of this trade study.

At the beginning of our design trade study, JPL had already designed the small RTPV generator shown in Figure 2. It used a single General Purpose Heat Source supplying 250 Watts of thermal power. Our contract goal was to evaluate alternative emitters, infrared filters, and low bandgap cells for use in the baseline design. Our most important finding was the fact that the tungsten emissivity curve is in fact selective.

For safety reasons, the emitter temperature for the radioisotope source is limited to 1375 K. If a gray body operating at 1300 K were to be used, its peak energy wavelength would fall at 2.2 microns which is well beyond the GaSb cell band edge wavelength at 1.7 microns. A gray body emitter model then suggests either the use of cells with longer wavelength response or the need for an ideal filter or, alternatively, the need for delta function selective emitters. However, when the black body emission spectrum is multiplied by the Figure 1 curve "A" emissivity function, the peak power wavelength shifts to 1.7 microns as is shown in the spectrum in Figure 3. Given a simple dielectric filter with the transmission spectrum shown in Figure 4, it becomes apparent that a practical RTPV generator can be fabricated with readily available components. The key components then become GaSb cells, simple dielectric filters, and a tungsten emitter. Undeveloped ternary or quaternary cells are unnecessary. Fragile rare earth oxide emitters are unnecessary. And finally, more exotic IR filters are not needed. The performance projections for this simple RTPV generator are given in the following table.

Table I

| GPHS Temp (Kelvin) | Emitter Temp (Kelvin) | GaSb Cell Temp (Kelvin) | GPHS Supply Power (Watts) | Gross Electric Power (Watts) | Net Electric Power (Watts) | Overall System Efficiency |
|--------------------------|-----------------------------|-------------------------------|------------------------------------|---------------------------------------|----------------------------------|---------------------------------|
| 1324 | 1298 | 273 | 250 | 34.4 | 32.7 | 13.1% |
| 1325 | 1299 | 293 | 250 | 31.9 | 30.3 | 12.1 % |

Hydrocarbon Fired TPV Generators using Catalytic Metallic Emitters

JX Crystals has been independently developing hydrocarbon fired TPV generators for applications here on earth. After the above space contract had terminated, personnel at JX Crystals discovered that the short wavelength bias of the tungsten emitter could be generalized to other metals. The Figure 1 curve "B" metal contains a common oxidizing metal catalyst. We demonstrated the usefulness of this curve "B" metal by fabricating a hydrocarbon fired TPV generator using GaSb cells and a Bunsen burner. Our 2 Watt demonstration unit is shown in Figure 5 operating an AM / FM / tape "boom box". This demonstration unit consists of a propane bottle connected to a Bunsen burner with a coil of the curve "B" metal catalyst immersed in the flame serving as the IR emitter. The 20 GaSb cell circuit shown in Figure 6 is then wrapped

around the IR emitter converting the infrared radiant energy into electric power. An illuminated current vs voltage curve for a GaSb cell circuit in a Bunsen burner unit is shown in Figure 7. The actual operation of Bunsen burner TPV electric generator will be demonstrated at the conference.

Figure 8 shows the measured spectrum from our Bunsen burner over the wavelength range of 1 to 5 microns. Note that the spectra from the blue flame from a Bunsen burner without an emitter inserted shows peaks at 4.5 microns and 2.7 microns. These emissions are associated with CO₂ and H₂O vibrations in the gas phase and fall outside of the cells response range. Then with a catalytic metal emitter immersed in the flame we see in Figure 8 the appearance of a substantial amount of radiated power with a peak falling within the response range for GaSb cells. The emitter temperature in this case was measured to be 1520 C (approximately 1800 K). Figure 8 also shows that the spectrum for the catalytic emitter is indeed suppressed beyond 1.5 microns relative to a gray body emitter with an emissivity of 0.3. This experimental result is consistent with our expectations given the Figure 1 Curve "B" emissivity data. If combustion occurs in the gas phase, the energy must then be coupled to the solid emitter which could be an inefficient process. The advantage for catalytic emitters is that the combustion occurs on the emitter surface and the energy is automatically coupled efficiently to the emitter.

Conclusions

We note that certain metals act as selective IR emitters serving to enhance the power emitted at shorter wavelengths and to suppress the out-of-band power lost at longer wavelengths. This is advantageous for GaSb TPV cells responding out to 1.7 microns. For radioisotope TPV generators for use in space, a tungsten emitter operating at 1300 K shifts the peak power wavelength from 2.2 microns for a gray body emitter to 1.7 microns. For a catalytic emitter operating in a hydrocarbon flame at 1800 K, the peak power wavelength shifts to 1.3 microns.

References

1. Pernisz,U.C., Saha,C.K."Silicon Carbide Emitter and Burner Elements for a TPV Converter," The First NREL Conference on Thermophotovoltaic Generation of Electricity, American Institute of Physics Conference Proceedings 321, pp. 99-105, 1994.
2. Lowe,R.A., Chubb,D.L., Good,B.S.," Radiative Performance of Rare Earth Garnet Thin Film Selective Emitters," The First NREL Conference on Thermophotovoltaic Generation of Electricity, American Institute of Physics Conference Proceedings 321, pp. 291-297, 1994.
3. Fraas,L.M., Ballantyne, R.J., Samaras, J.E., Seal,M.R. " Electric Power Production Using New GaSb Photovoltaic Cells with Extended Infrared Response," The First NREL Conference on Thermophotovoltaic Generation of Electricity, American Institute of Physics Conference Proceedings 321, pp. 44-53, 1994.
4. Ewell,R., Chimielewski,A., Nesbith,W. and Sercel,J. "Thermophotovoltaic Power System Final Report," JPL D-10814, May 1993.

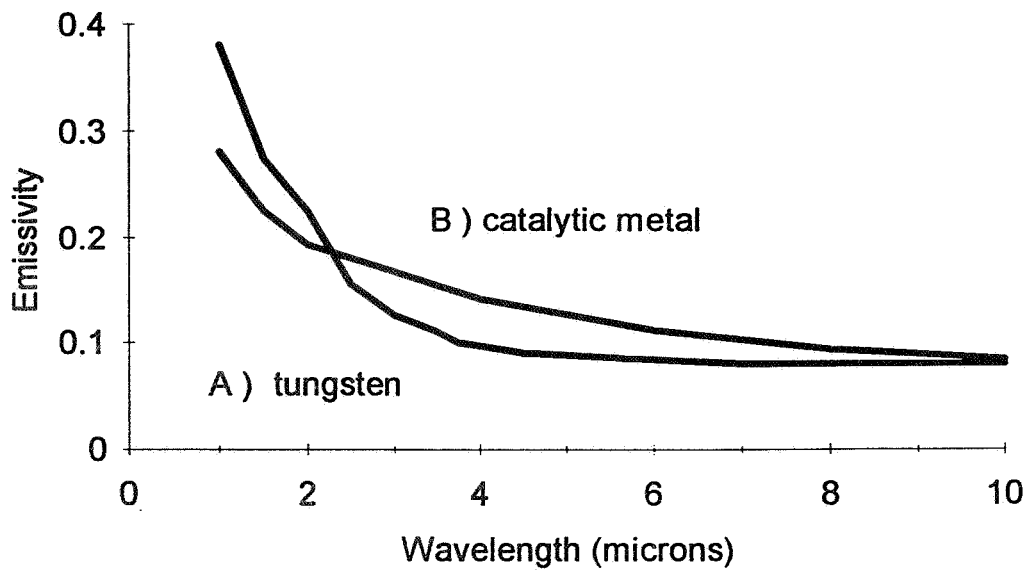


Figure 1. Emissivity of Metal Emitters

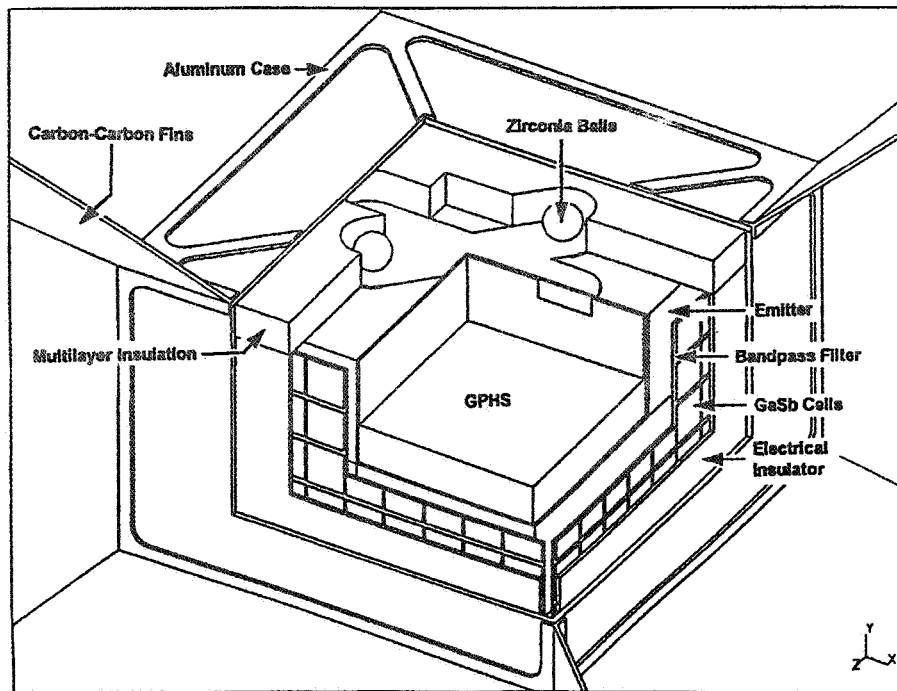


Figure 2. AeroSpace RTPV Generator Design

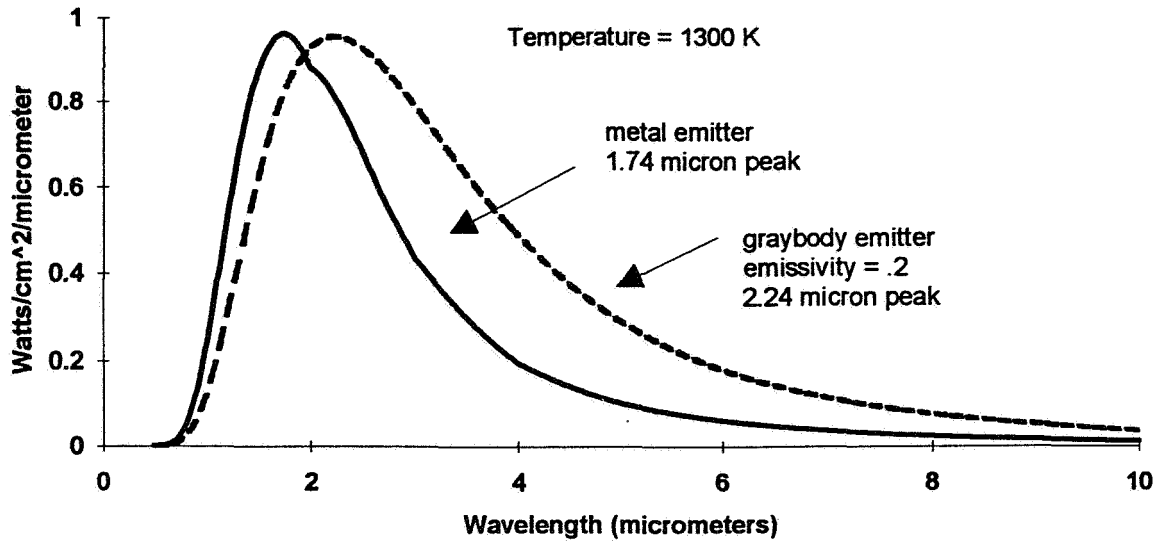


Figure 3. Spectral Emissive Power Shift with Metal Emitter

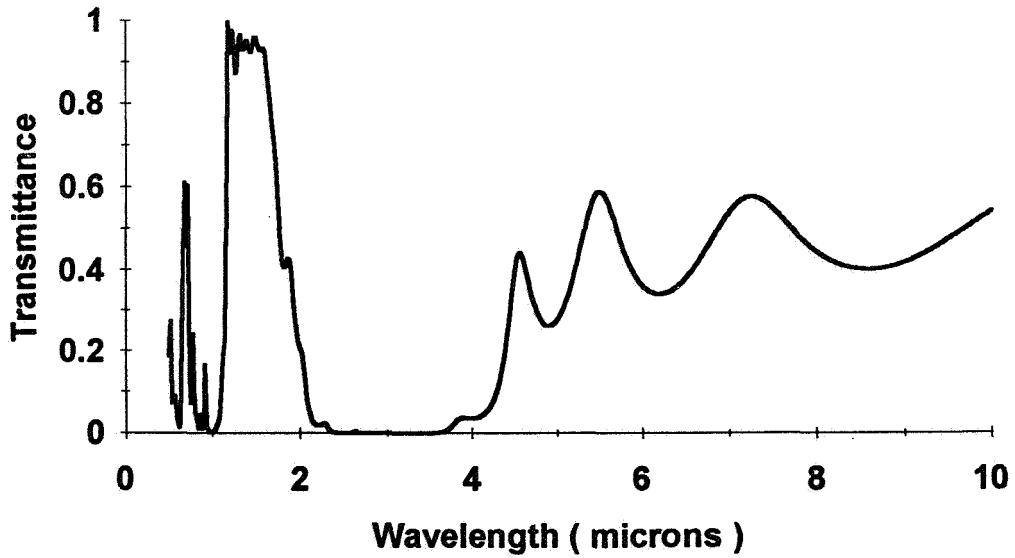


Figure 4. Near Term Dielectric Bandpass Filter

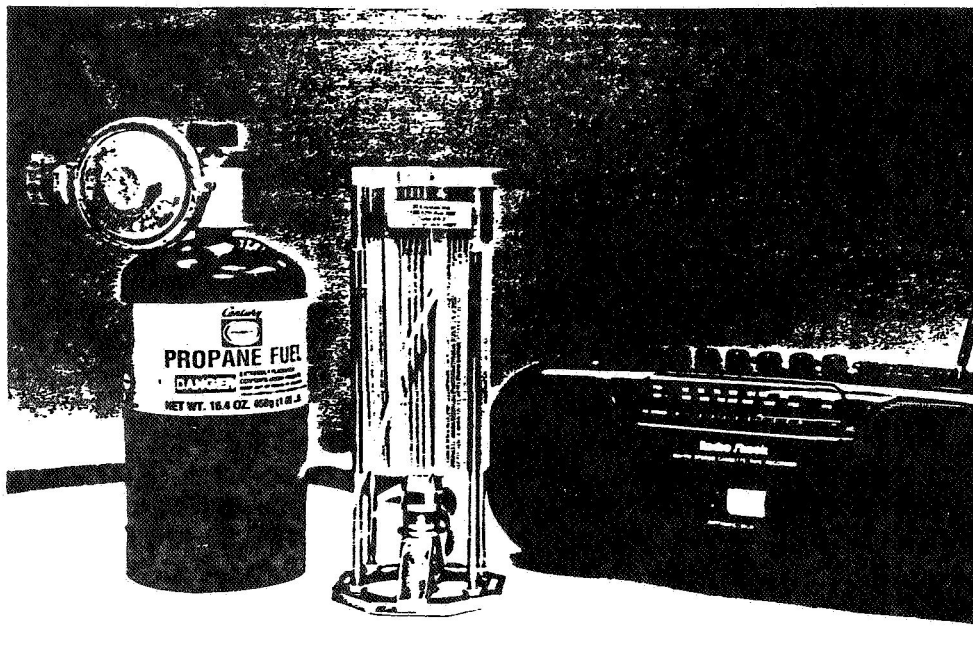


Figure 5. 2 Watt TPV Demonstration

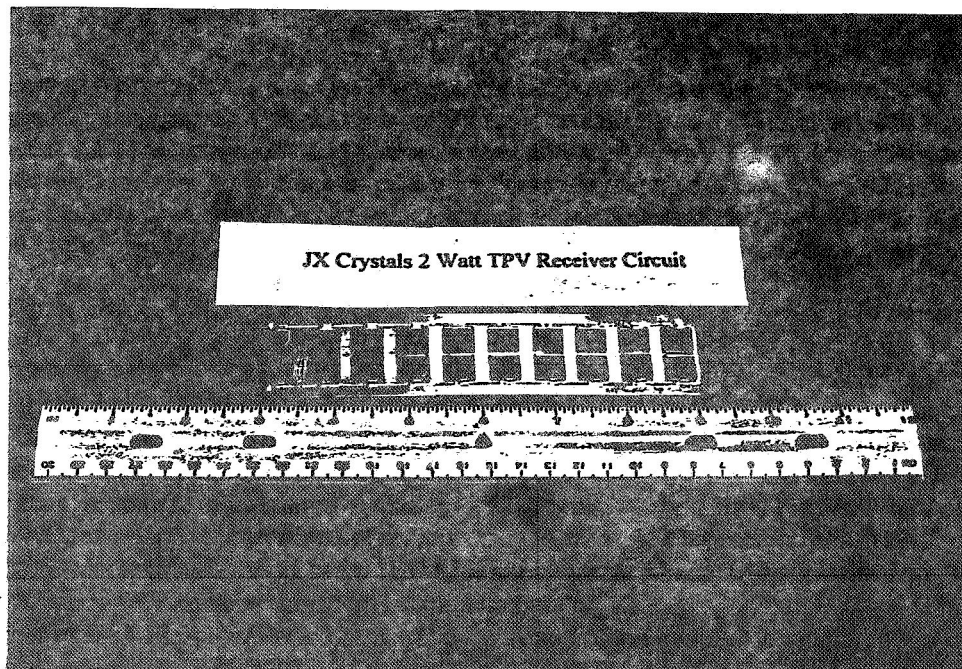


Figure 6. 20 Cell GaSb TPV Receiver Circuit

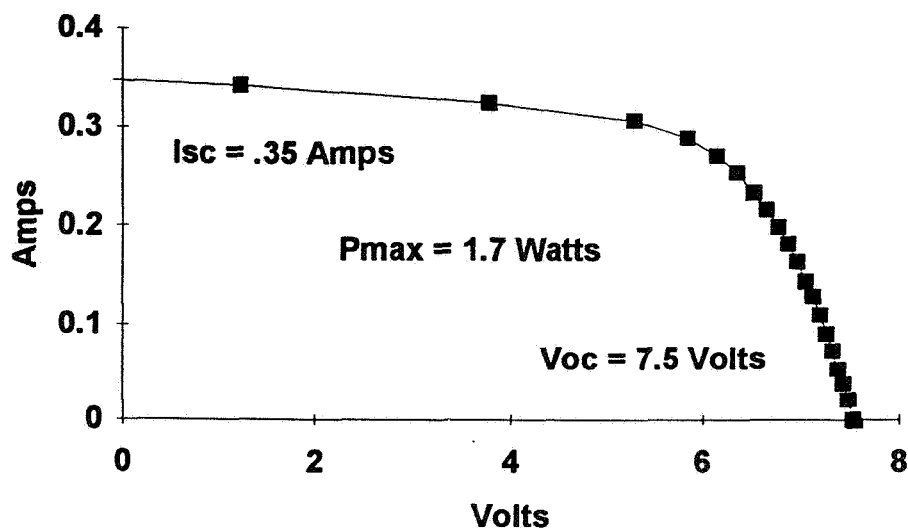


Figure 7. GaSb TPV Circuit with Gas Flame / Metal Mantle Light Source

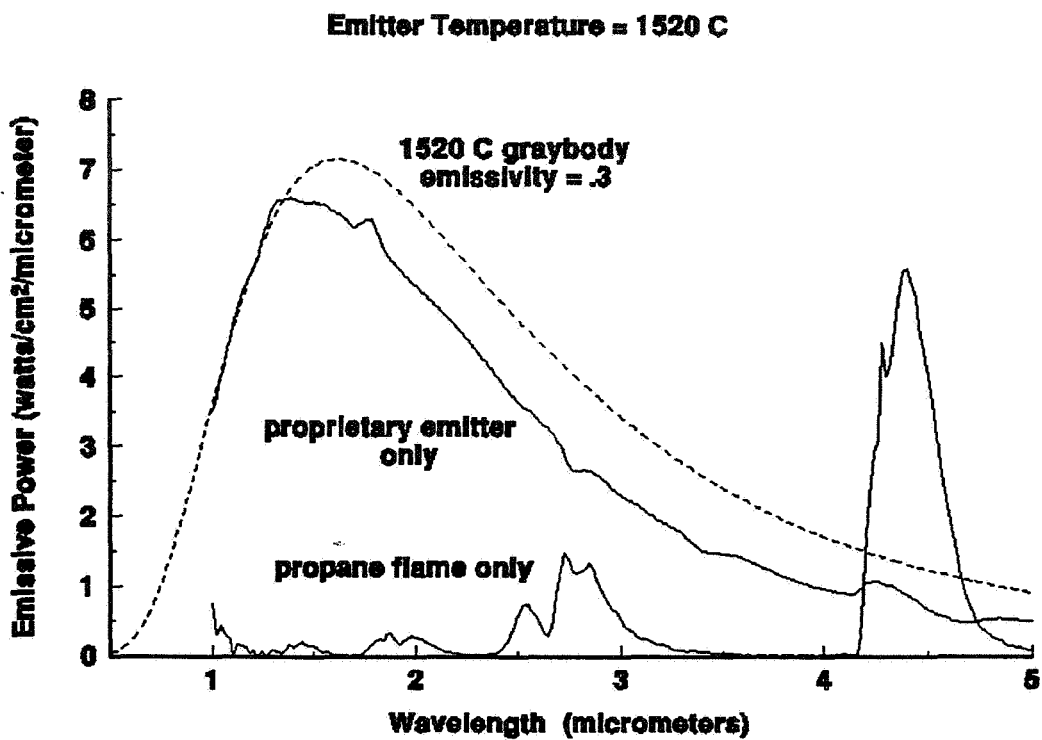


Figure 8. Emissive Power of Proprietary Emitter

828
IN-50413

InGaAsSb/GaSb THERMOPHOTOVOLTAIC CELLS

Z.A. SHELLNBARGER, M.G. MAUK, and L.C. DiNETTA
AstroPower, Inc.
Solar Park, Newark, DE 19716-2000

G.W. CHARACHE
Lockheed/Martin Corp.
P.O. Box 1072, Schenectady, NY 12301-1072

SUMMARY

AstroPower is developing InGaAsSb thermophotovoltaic (TPV) devices. This photovoltaic cell is a two-layer epitaxial InGaAsSb structure formed by liquid-phase epitaxy on a GaSb substrate. The (direct) bandgap of the $\text{In}_{1-x}\text{Ga}_x\text{As}_{1-y}\text{Sb}_y$ alloy is 0.50 to 0.55 eV, depending on its exact alloy composition (x, y); and is closely lattice-matched to the GaSb substrate. The use of the quaternary alloy, as opposed to a ternary alloy — such as, for example, InGaAs/InP — permits low bandgap devices optimized for 1000 to 1500 °C thermal sources with, at the same time, near-exact lattice matching to the GaSb substrate. Lattice-matching is important since even a small degree of lattice mismatch degrades device performance and reliability and increases processing complexity.

Internal quantum efficiencies as high as 95% have been measured at a wavelength of 2 microns. At 1 micron wavelengths, internal quantum efficiencies of 55% have been observed. The open-circuit voltage at currents of 0.3 A/cm² is 0.220 volts and 0.260 V for current densities of 2 A/cm². Fill factors of 56% have been measured at 60 mA/cm². However, as current density increases there is some decrease in fill factor. Our results to date show that the GaSb-based quaternary compounds provide a viable and high performance energy conversion solution for thermophotovoltaic systems operating with 1000 to 1500 °C source temperatures.

1. INTRODUCTION

We report our latest results on InGaAsSb thermophotovoltaic (TPV) cells. TPVs are p - n junction semiconductor devices that convert photons emitted by a heated source directly into electrical power. For TPV systems utilizing thermal radiation from an emitter heated at 1000 to 1500 °C, there is a need for low-bandgap cells with a high spectral response in the range of 1500 to 2500 nm wavelength. This implies a TPV cell with a bandgap of ~0.5 eV. One important potential application is the radioisotope General Purpose Heat Source (GPHS) where 1100 °C blackbody radiation can be used for thermophotovoltaic energy conversion. In this paper we describe high-efficiency TPV devices based on lattice-matched $\text{In}_{0.08}\text{Ga}_{0.92}\text{As}_{0.07}\text{Sb}_{0.93}$ ($E_G = 0.53$ eV) epitaxial layers on GaSb substrates. To our knowledge, this is the first report of the InGaAsSb quaternary alloy applied to TPV devices.

Several theoretical studies have indicated that photovoltaic cells based on the InGaAsSb quaternary alloy are good candidates for TPV applications that require high spectral response in the 1500 to 2500 nm wavelength range. Depending on its alloy composition (x, y), the direct bandgap of the $\text{In}_{1-x}\text{Ga}_x\text{As}_{1-y}\text{Sb}_y$ alloy varies from 0.18 eV (InSb) to 1.43 eV (GaAs). The quaternary alloy can be closely lattice-matched to the GaSb substrate provided the composition is restrained to values such that $y \approx 0.1 + 0.9x$. With this lattice matching condition, the

bandgap of the quaternary alloy ranges from approximately 0.3 to 0.7 eV. However, there is a further limitation due to a wide solid-phase miscibility gap in this quaternary at typical growth temperatures. The miscibility gap evidently precludes bandgaps in the range of 0.35 to 0.5 eV. Therefore, for the spectral range of interest, we assume the lowest attainable bandgap is 0.50 to 0.52 eV. This bandgap range corresponds to an optical absorption edge of 2380 to 2480 nanometers.

It is worth emphasizing that the use of the quaternary alloy, as opposed to a ternary alloy—such as, for example, InGaAs—provides the needed bandgap with, at the same time, near-exact lattice matching to the GaSb substrate. Lattice-matching is important since even a small degree of lattice mismatch degrades device performance and reliability. Although there are epitaxy techniques to partially ameliorate effects associated with lattice mismatch of ternary alloy layers on binary substrates (e.g. defect-filtering superlattices, interrupted growth regimens, etc.), we believe the use of the quaternary alloy to avoid lattice mismatch altogether is a simpler and more effective approach.

The TPV device we are making is a two-layer epitaxial InGaAsSb structure formed by liquid-phase epitaxy on a GaSb substrate at a growth temperature of 515 °C. Liquid-Phase Epitaxy (LPE) is a well-established technology for III-V compound semiconductor devices. A major advantage of LPE for this application is the high material quality, and more specifically, the long minority carrier diffusion lengths, that can be achieved. This results in devices which are equal or superior in performance to those made by other epitaxy processes such as molecular beam epitaxy (MBE) or metal organic chemical vapor deposition (MOCVD). Another major advantage is that LPE is a simple, inexpensive, and safe method for semiconductor device fabrication. Significantly, the LPE process does not require or produce any highly toxic or dangerous substances—in contrast to MOCVD. Also, the epitaxial growth rate with InGaAsSb LPE is ~2 microns/minute which is ten to hundred times faster than MOCVD or MBE. We have successfully scaled up the LPE process for epitaxial growth in a semi-continuous mode on 3-inch diameter wafers. This, combined with the high growth rates, will dramatically improve the manufacturing throughput compared to traditional and more costly epitaxy processes. Our objective is to develop an epitaxial growth technology to produce low-cost, large-area, high efficiency TPV devices.

2. EPITAXIAL GROWTH AND FABRICATION OF InGaAsSb TPV CELLS

InGaAsSb photodiodes, light-emitting diodes, and double heterostructure injection lasers made by liquid-phase epitaxy have been previously reported. We have adapted this technology for the production of InGaAsSb TPV cells.

We use a standard horizontal slideboat technique for the liquid-phase epitaxial growth of the InGaAsSb. The graphite slideboat is situated in a sealed quartz tube placed in a microprocessor-controlled, programmable, three-zone tube furnace. The growth ambient is palladium-diffused hydrogen at atmospheric pressure with a flow rate of 300 ml/min.

The substrates are 500-micron thick, chemically polished (100) oriented, *n*-type GaSb wafers obtained from MCP Wafer Technology, Ltd. (Milton Keynes, UK) or Firebird Semiconductor, Ltd. (Trail, BC, Canada). Substrates are doped to $3\text{-}5 \times 10^{17} \text{ cm}^{-3}$ with tellurium. The substrate resistivity is $9 \times 10^{-3} \Omega\text{-cm}$, and the average etch-pit density is approximately 1000 cm^{-2} .

The growth solutions are indium ($x_{\text{In}}=0.59$), gallium ($x_{\text{Ga}}=0.19$), antimony ($x_{\text{Sb}}=0.21$), and arsenic ($x_{\text{As}}=0.01$). The melts are formulated with 3- to 5-mm shot of high purity (99.9999%) indium, gallium, and antimony metals and arsenic added as undoped InAs polycrystalline material. The total weight of the melt is about 10 g. Prior to growth, the melts are baked out at 700 °C for fifteen hours under flowing hydrogen to de-oxidize the metallic melt components and outgas residual impurities. After bake-out, appropriate dopant impurities are added to each melt. The first melt for the growth of the *n*-type InGaAsSb base layer contains tin or tellurium. The small amount of Te needed to dope the layer (atomic fraction in the melt $\cong 10^{-5}$) is problematic. For reproducible doping, a weighable amount of Te is added as 100 to 200 mg of Te-doped GaSb ($C_{\text{Te}}=10^{19} \text{ cm}^{-3}$). Tin is added to

the melt as 10 to 200 mg of high purity shot. Our preliminary results (Section 3) suggest that high *n*-type doping concentrations can be achieved more readily with tin than with tellurium. However, the relatively high liquid-phase concentration of tin alters the melt composition needed to grow the lattice-matched InGaAsSb quaternary with the desired bandgap. For higher tin doping levels, we will need to re-optimize the melt compositions to include the effects of dilution with additional tin. This will require a phase equilibria analysis and model of a 5-component system (In-Ga-As-Sb-Sn). The second melt for the growth of the *p*-type emitter contains 5 to 100 mg germanium. Presently, we are beginning a more detailed and systematic characterization of impurity segregation and doping in the In-Ga-As-Sb quaternary system with the aim of achieving better control and a greater range of doping concentrations.

The melts are equilibrated for 1 hour at 530 °C and then cooled at a rate of 0.7 °C/min. At 515 °C, the substrate is contacted with the first melt for two minutes to grow a 5-micron thick *n*-type InGaAsSb base layer. Next, the substrate is moved to the second melt for 5 seconds to grow a 0.3-micron thick *p*-type InGaAsSb emitter layer.

Front and back ohmic contacts are formed on the epitaxial InGaAsSb/GaSb structure by standard processing techniques. The back of the substrate is metallized by plating with an 200-nm thick electron-beam evaporated Au:Ge:Au:Ni layer and alloyed at 300 °C. The front contact is a grid of 10-micron wide metallization lines with 100-micron spacing and a single 1-mm wide center busbar. The grid is formed by a photolithography lift-off process with a 200-nm thick electron-beam evaporated Au:Zn:Au metallization. The front grid is thickened to 5 microns by gold electroplating. The front contact is not sintered. The substrate is masked and patterned to define a 1 cm x 1 cm device and isolation etched with a potassium iodide - iodine "gold" etch. Most of our TPV cells are 1 cm x 1 cm in area, although larger cells (2 cm x 2 cm) with comparable performance have also been made. In order to simplify the spectral response analysis, we elected not to apply any anti-reflection coatings to the cells. FIGURE 1 is a top-view photograph of a 1 cm x 1 cm InGaAsSb TPV cell.

3. TPV DESIGN AND OPTIMIZATION

FIGURE 2 shows the TPV device design in cross-section. The fabricated cells have a 0.3 to 0.5 micron thick *p*-type emitter with a Ge concentration of approximately 10^{19} cm^{-3} , as indicated by Secondary Ion Mass Spectroscopy (SIMS). A thicker, more heavily doped *p*-layer will reduce the sheet resistance of the emitter and herefore improve the fill-factor, but will tend to reduce spectral response due to higher free-carrier absorption and ncreased sensitivity to front surface minority carrier recombination.

The base thickness in our cells ranges from 3 to 5 microns with a Te or Sn concentration of about 10^{15} to 10^{18} cm^{-3} , as determined from capacitance-voltage measurements and SIMS. FIGURE 3 shows the SIMS depth profile indicating the abruptness of the *p-n* junction and the depth uniformity of the doping concentrations. There is apparently very little smearing of the doping profile due to diffusion or segregation of dopants. Discrepancies between the Te dopant concentration measured by SIMS (total impurity concentration) and that implied by capacitance-voltage measurements (net donor concentration) indicate that much of the Te is either not ionized or else is compensated. This is a common problem in Te doping of III-V semiconductors, especially in GaSb-based materials, and is probably due to the formation of electrically inactive telluride complexes or compounds in the material. Increasing the Te concentration in the melt showed a "saturation effect" in that the Te doping level did not increase in proportion to the Te concentration in the liquid phase. Our most recent devices incorporate tin as the *n*-type base dopant and have base dopings targeted around 10^{17} cm^{-3} . Modeling indicates that base dopings in this range will yield the optimum open-circuit voltages and short-wavelength quantum efficiencies.

4. TPV DEVICE EVALUATION

We present external and internal spectral response and current-voltage characteristics for 1 cm x 1 cm $p\text{-In}_{0.08}\text{Ga}_{0.92}\text{As}_{0.07}\text{Sb}_{0.93}\text{:Ge} / n\text{-In}_{0.08}\text{Ga}_{0.92}\text{As}_{0.07}\text{Sb}_{0.93}\text{:Te}$ (or Sn) epitaxial cells on an $n\text{-GaSb:Te}$ substrate produced as described above. The *external* spectral response of a typical InGaAsSb TPV cell is shown in FIGURE 4. FIGURE 5 shows the corresponding *internal* spectral response. The lower external spectral response is due to grid shading and reflection of incident light from the uncoated InGaAsSb emitter surface. The grid shading is 18.2%. The absorption edge implied by the spectral response measurements of a number of samples ranged from approximately 2200 to 2250 nm. At a wavelength of 2000 nm, internal quantum efficiencies as high as 95% have been measured, and at a wavelength of 1 micron, internal quantum efficiencies of almost 55% have been observed. The internal quantum efficiency averaged over the spectral region from 1 to 2 microns wavelength is 60%. (It should be noted that for the intended TPV applications, the response of the cell for wavelengths less than 1.5 microns is not important.)

The 1 cm x 1 cm InGaAsSb TPV cells were tested under simulated infrared light using a ZnSe-filtered tungsten source (Carley Lamps, Inc., Torrance, CA) with a spectral emission in the 800 to 3000 nm wavelength range. Under an illumination intensity corresponding to a short-circuit current density of 2 A/cm², open-circuit voltages as high as 0.260 volts have been measured. FIGURE 6 shows the current-voltage characteristics of a 1 cm x 1 cm InGaAsSb TPV cell under an infrared illumination intensity that yields a short-circuit current density of 62.4 mA/cm² and a open-circuit voltage of 0.178 V. The fill-factor is 0.57. To date, the best fill-factors observed are less than 0.6. We believe that one cause of the somewhat low fill-factors is series resistance, which is discussed further in the next section. FIGURE 7 shows open-circuit voltage vs. short-circuit current for varying light intensity. The open-circuit voltage increases logarithmically with illumination intensity and an open-circuit voltage of ~0.250 V is reached for current densities of 1 A/cm². The diode ideality factor in the voltage range of 0.1 to 0.25 V is close to 2, implying that high injection is dominant in this voltage range.

5. CONCLUSION AND DISCUSSION

Our results to date have demonstrated the potential of InGaAsSb TPV devices made by liquid-phase epitaxy. We believe there is still room for substantial efficiency enhancements in these devices by optimization of the doping levels and layer thicknesses. Further improvements might include wide bandgap lattice-matched AlGaAsSb window layers for front surface passivation, and AlGaAsSb back-surface field cladding layers to reduce the reverse saturation current and thereby increase the open-circuit voltage. Highly doped contact layers will provide lower series resistance, as will substrate thinning. Lower series resistance will lead to higher fill factors. Thinning the substrate will also improve heat sinking of the device.

The required performance of a TPV device is dependent on its system application. Spectral control of thermal emitters, the use of selective filters and reflectors, heat transfer, and photon recycling effects need to be included in the device design and system optimization. These considerations are not usually relevant for conventional photovoltaic devices and therefore the design and optimization rules for TPVs will be significantly different than those for solar cells. For example, grid obscuration and reflection are not necessarily losses in TPV systems if photons reflected from the front surface are re-absorbed by the emitter. Our next generation of InGaAsSb TPV devices will incorporate design features to fully exploit photon recycling effects.

REFERENCES

A. ANDASPAEVA, A.N. BARANOV, A. GUSEINOV, A.N. IMENKOV, L.M. LITVAK, G.M. FILARETOVA, and Y.P. YAKOVLEV, "Highly Efficient GaInAsSb Light-Emitting Diodes ($\lambda = 2.2 \mu\text{m}$, $\eta=4\%$, $T = 300\text{K}$)" *Soviet Technical Physics Letters* **14**, 5 (1988) 377-378.

- M. ASTLES, H. HILL, A.J. WILLIAMS, P.J. WRIGHT, and M.L. YOUNG, "Studies of the $\text{Ga}_{1-x}\text{In}_x\text{As}_{1-y}\text{Sb}_y$ Quaternary Alloy System I. Liquid-Phase Epitaxial Growth and Assessment" *J. Electronic Materials* **15**, **1** (1986) 41-49.
- A.N. BARANOV, A.M. LITVAK, K.D. MOISEEV, N.A. CHARYKOV, and V.V. SHERTSNEV. "Melt-Solid Phase Equilibria in the In-Ga-As-Sb and In-As-P-Sb Systems" *Russian J. Physical Chemistry* **64**, **6** (1990) 884-886.
- A.N. BARANOV, V.V. KUZNETSOV, E.R. RUBTSOV, Y.P. YAKOVLEV, and A.A. GUSEINOV, "Kinetics of Crystallization of the $\text{Ga}_x\text{In}_{1-x}\text{As}_y\text{Sb}_{1-y}$ Solid Solutions from the Liquid" *Russian J. Physical Chemistry* **65**, **12** (1991) 1713-1716.
- C. CANEAU, A.K. SRIVASTAVA, A.G. DENTAI, J.L. ZYSKIND, and M.A. POLLACK, "Room-Temperature GaInAsSb/AlGaAsSb DH Injection Lasers at 2.2 μm " *Electronics Letters* **21**, **18** (1985) 815-817.
- J.C. DEWINTER, M.A. POLLACK, A.K. SRIVASTAVA, and J.L. ZYSKIND, "Liquid Phase Epitaxial $\text{Ga}_{1-x}\text{In}_x\text{As}_y\text{Sb}_{1-y}$ Lattice-Matched to (100) GaSb over the 1.17 to 2.33 μm Wavelength Range" *J. Electronic Materials* **14**, **6** (1985) 729-747.
- A.E. DRAKIN, P.G. ELISEEV, B.N. SVERDLOV, A.E. BOCHKAREV, L.M. DOLGINOV, and L.V. DRUZHININA, "InGaSbAs Injection Lasers" *IEEE J. Quantum Electronics* **QE-23**, **6** (1987) 1089-1094.
- A. JOULLIÉ, F. JIA HUA, F. KAROUTA, and H. MANI, "LPE Growth of GaInAsSb/GaSb System: The Importance of the Sign of the Lattice Mismatch" *J. Crystal Growth* **75** (1986) 309-318.
- H. KANO, S. MIYAZAWA, and K. SUGIYAMA, "Liquid-Phase Epitaxy of $\text{Ga}_{1-y}\text{In}_y\text{As}_x\text{Sb}_{1-x}$ Quaternary Alloys on GaSb" *Japanese J. Applied Physics* **18**, **11** (1979) 2183-2184.
- F. KAROUTA, A. MARBEUF, A. JOLLIÉ, and J.H. FAN, "Low Temperature Phase Diagram of the $\text{Ga}_{1-x}\text{In}_x\text{As}_y\text{Sb}_{1-y}$ System" *J. Crystal Growth* **79** (1986) 445-450.
- N. KOBAYASHI, Y. HORIKOSHI, and C. UEMURA, "Liquid-Phase Epitaxial Growth of InGaAsSb/GaSb and InGaAsSb/AlGaAsSb DH Wafers" *Japanese J. Applied Physics* **18**, **11** (1979) 2169-2170.
- J.B. MCNEELY, M.G. MAUK, and L.C. DiNETTA, "An InGaAsSb/GaSb Photovoltaic Cell by Liquid-Phase Epitaxy for Thermophotovoltaic (TPV) Application" *Proc. 1st NREL Conf. on Thermophotovoltaic Generation of Electricity, 1994* T.J. COUTTS and J.P. BENNER, eds., (New York: American Institute Physics, 1995) 221-225.
- K. NAKAJIMA, K. OSAMURA, K. YASUDA, and Y. MURAKAMI, "The Pseudoquaternary Phase Diagram of the Ga-In-As-Sb System" *J. Crystal Growth* **41** (1977) 87-92.
- N. KOBAYASHI and Y. HORIKOSHI, "Pseudoquaternary Phase Diagram Calculation of $\text{In}_{1-x}\text{Ga}_x\text{As}_{1-y}\text{Sb}_y$ Quaternary System" *Japanese J. Applied Physics* **21**, **1** (1982) 201-202.
- K. NAKAJIMA, K. OSAMURA, K. YASUDA, and Y. MURAKAMI, "The Pseudoquaternary Phase Diagram of the Ga-In-As-Sb System" *J. Crystal Growth* **41** (1977) 87-92.
- E. TOURNIÉ, F. PITARD, A. JOULLIÉ, and R. FOURCADE, "High Temperature Liquid Phase Epitaxy of (100) Oriented GaInAsSb Near the Miscibility Gap Boundary" *J. Crystal Growth* **104** (1990) 683-694.
- M.M. WANLASS, J.S. WARD, K.A. EMERY, and T.J. COUTTS, "Ga_xIn_{1-x}As Thermophotovoltaic Converters" *IEEE 1st World Conference on Photovoltaic Energy Conversion* (New York: IEEE Press, 1994) 1685-1691.
- S. WOJTCZUK, E. GAGNON, L. GEOFFROY, and T. PARODOS, "In_xGa_{1-x}As Thermophotovoltaic Cell Performance vs. Bandgap" *Proc. 1st NREL Conf. on Thermophotovoltaic Generation of Electricity, 1994* T.J. COUTTS and J.P. BENNER, eds., (New York: American Institute Physics, 1995) 177-187.

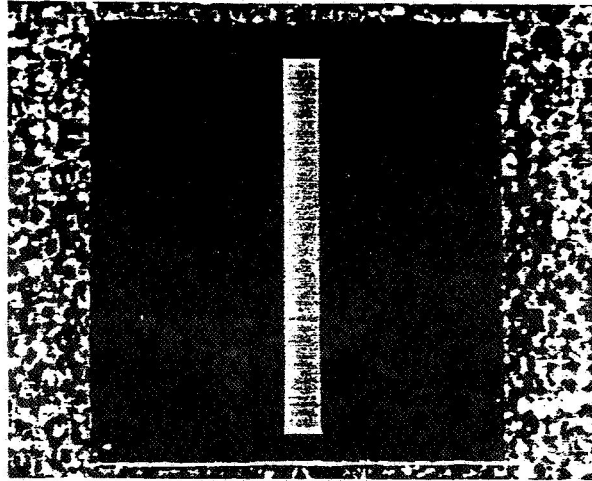


FIGURE 1: Top-view Photograph of a 1 cm x 1 cm InGaAsSb TPV Cell.

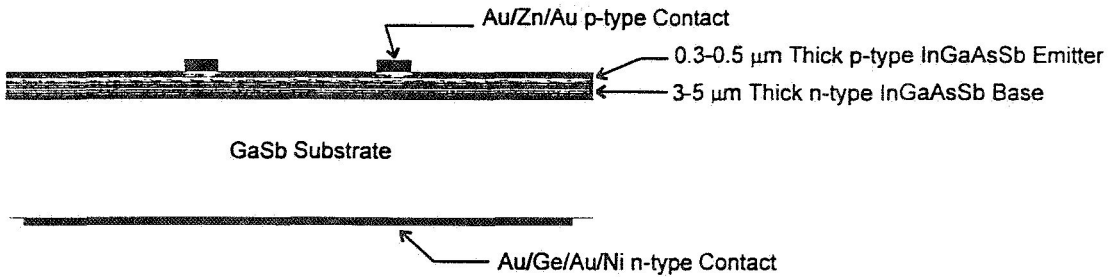


FIGURE 2: InGaAsSb/GaSb *p-n* Junction Thermophotovoltaic Cell Design.

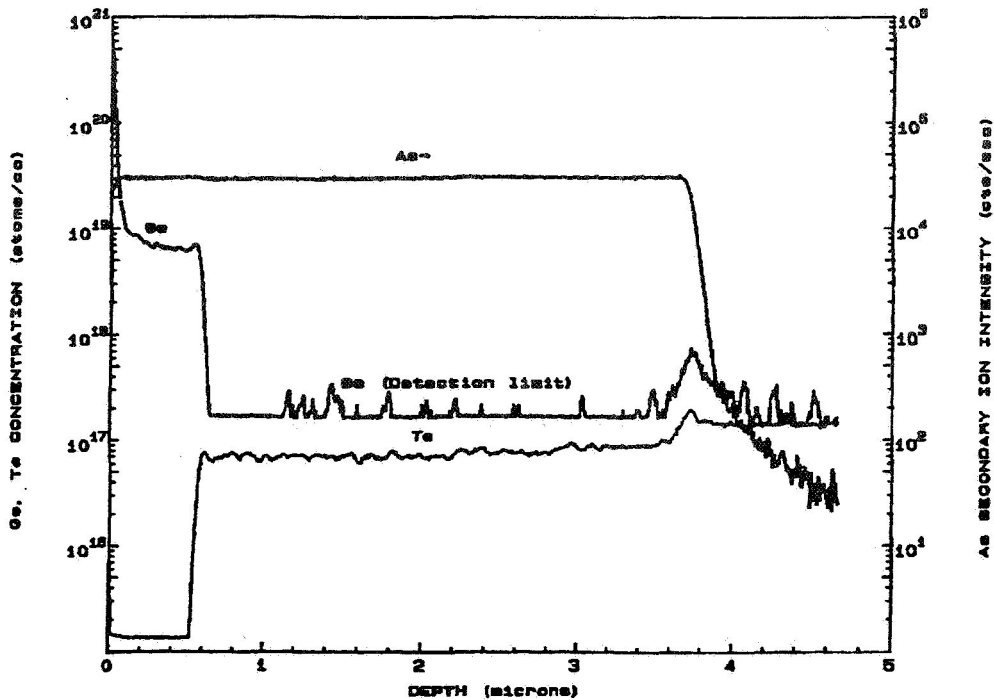


FIGURE 3: SIMS Depth Profile of Doping.

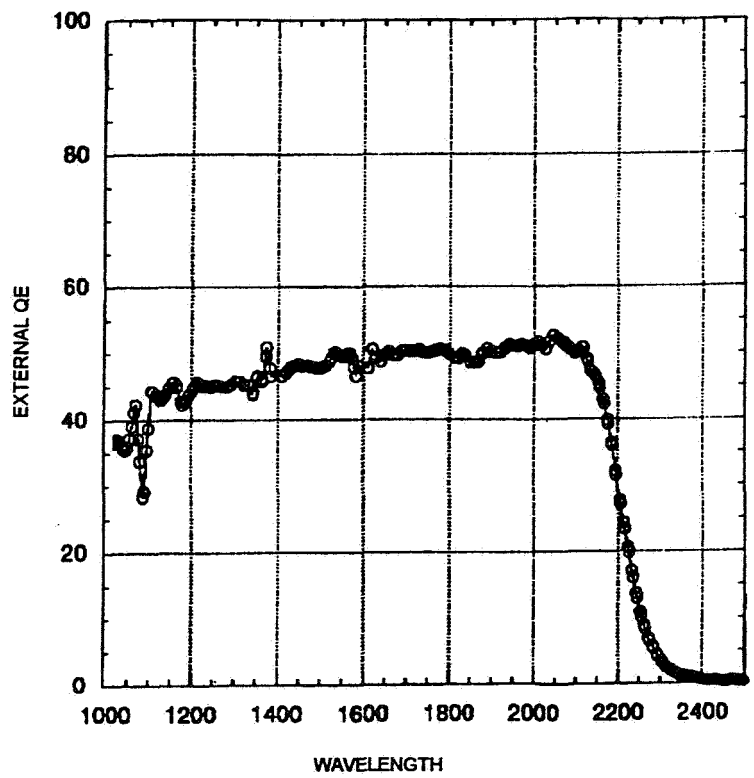


FIGURE 4: External Spectral Response of InGaAsSb/GaSb *p-n* Junction Thermophotovoltaic Cell.

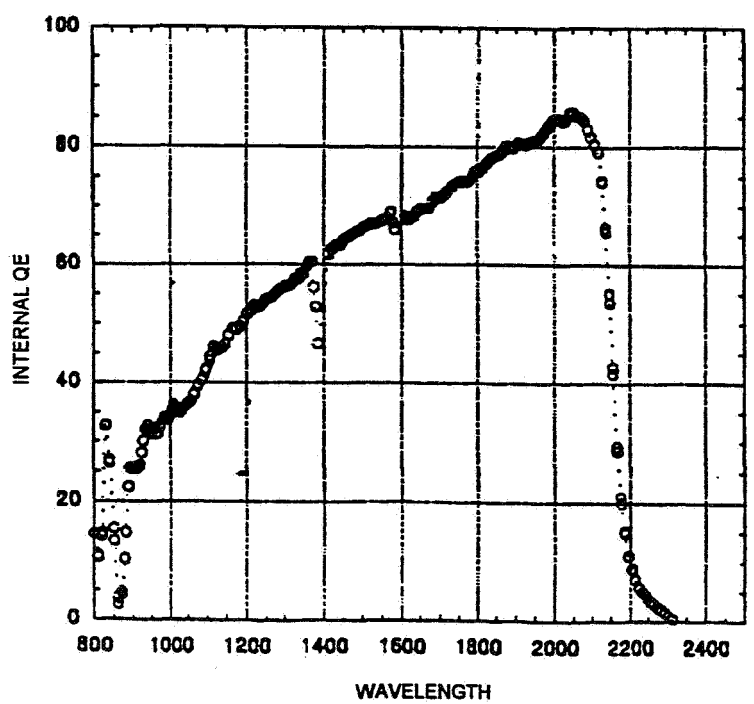


FIGURE 5: Internal Spectral Response of InGaAsSb/GaSb *p-n* Junction Thermophotovoltaic Cell.

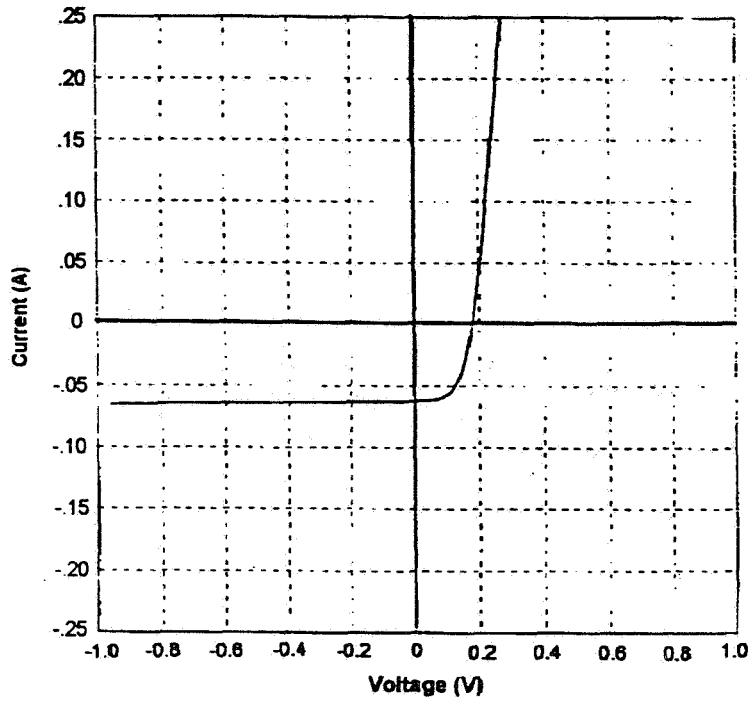


FIGURE 6: Current-Voltage Characteristic of 1 cm x 1 cm InGaAsSb TPV Cell.

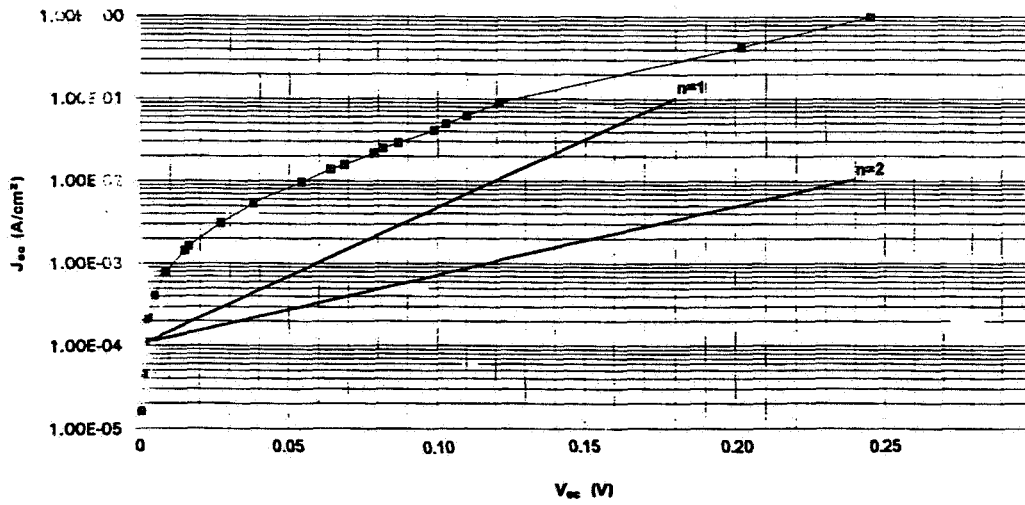


FIGURE 7: Open-Circuit Voltage vs. Short-Circuit Current for InGaAsSb TPV Cell under Varying Illumination Intensity.

MULTIJUNCTION InGaAs THERMOPHOTOVOLTAIC POWER CONVERTER

Steven Wojtczuk
 Spire Corporation
 Bedford, MA 01730-2396

329
 AN-50414

OVERVIEW

The experimental performance of a multijunction monolithic lattice-matched 0.74 eV InGaAs thermophotovoltaic (TPV) power converter under 980C blackbody irradiation is reported. Eight InGaAs PN junctions grown epitaxially on a semi-insulating wafer were monolithically integrated in series to boost the ~ 0.4 V photovoltage per typical InGaAs junction to over 3 volts for the 1 cm² chip. This chip was originally designed and characterized for free-space 1.3 μm laser power beaming¹. The power efficiency of this TPV device is 16% for that part of the blackbody spectrum above the material bandgap. The device is shown to deliver about 1 watt of output power when driven with enough light. This is the first report of such a multijunction TPV device. This is not a traditional tandem cell in which the junctions are stacked vertically. Eight 1mm long by 1 cm wide junctions are **laterally** connected across the device area. This multijunction design has the potential for lower I²R power loss since the smaller PN junction area limits the current to one-eighth that of the equivalent surface area. In essence, the current is traded for voltage to avoid the I²R loss, analogous to the way power utilities avoid I²R loss in high-tension power lines, by transforming the high current, low voltage generated at a power plant into a high voltage at a low current before transmitting the power over great distances. Figure 1 shows the idea behind this device. The present multijunction TPV does not yet work at the 100W/cm² level; the figure is only meant to illustrate the concept.

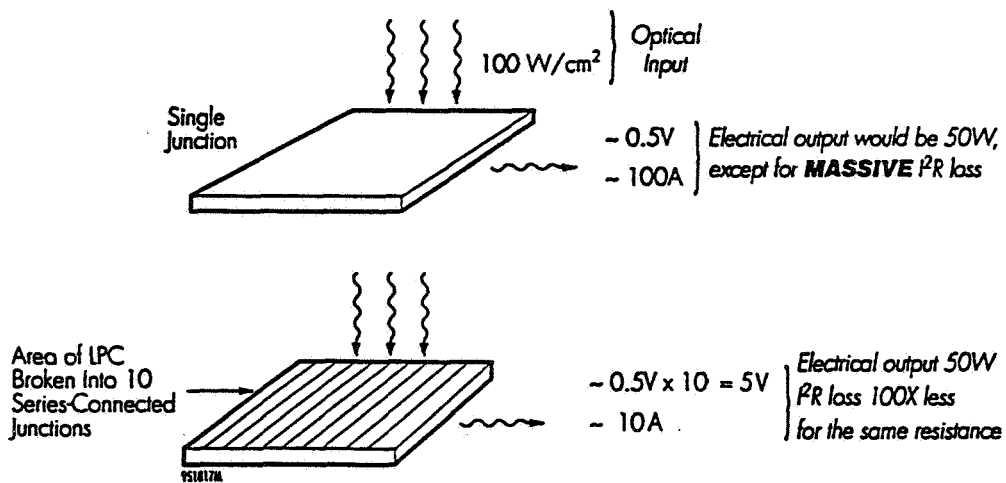


Figure 1 Illustration of how ohmic power loss can be greatly reduced with a multijunction TPV device

DEVICE DESCRIPTION

The epilayer structure and fabrication details were described in the paper¹ discussing 1.3 μm laser power conversion with this device, and are summarized here. Much greater detail, including photographs of the monolithic interconnections between junctions on the chip can be found in the earlier paper. Metal organic chemical vapor deposition was used to epitaxially grow the converter on a semi-insulating InP wafer. The non-conducting wafer is necessary to interconnect the junctions monolithically. This lattice-matched 0.74 eV InGaAs converter used a P-on-N structure to insure that the N InGaAs buried layer (the first layer grown), which does not have the advantage of a metal contact grid to lower its series resistance, is of the lower resistivity N type material. Both N and P InGaAs can be doped to a high level ($> 1e19 /\text{cm}^3$), but the mobility of the N InGaAs is $\sim 25\text{X}$ higher. This layer is made about $3\mu\text{m}$ thick to lower its sheet resistance.

Next a thin, heavily-doped N-InP back surface field/etch stop is grown. This acts as a minority carrier mirror for carriers photogenerated in the device base layer, and aids in the device fabrication (back contact connection) to stop a selective wet etch which etches InGaAs but "stops" at InP. The etch stop property is important since it is possible to overetch the via for the back contact too far into the insulating wafer. The back surface field is much more crucial for TPV than for standard solar cells. In a solar cell, much of the light is at short wavelengths and absorbed in the emitter or space charge region; in a TPV cell most of the light is at long wavelengths and is absorbed in the base region where a low BSF recombination velocity increases the photocurrent noticeably. This base layer, also N-type InGaAs, is more lightly doped than the buried layer (by two orders of magnitude) to increase the diffusion length. Low resistivity is not crucial since the current path is vertical (only $3\mu\text{m}$ long) unlike the buried N-InGaAs where current flows laterally along $1000\mu\text{m}$.

Finally, a heavily doped ($1e19/\text{cm}^3$), thin ($0.3\mu\text{m}$) P-InGaAs emitter layer is grown. A front metal contact grid optimized for the emitter sheet resistance is later evaporated, which compensates for the 250X higher emitter sheet resistance (10X thinner, 25X lower mobility) compared to the buried N-InGaAs. A silicon nitride layer was used to isolate the junction sidewall and prevent interconnect metal from shunting the junction. A finished, packaged device is shown in Figure 2.

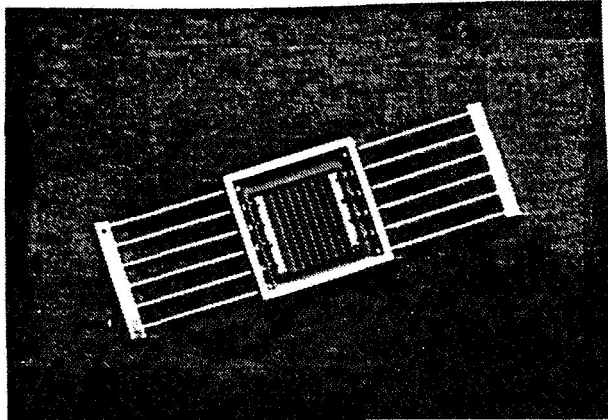


Figure 2 *Packaged eight-junction 0.74eV InGaAs multijunction TPV device. Contact grid too fine too see; thin lines parallel to busbars are the interconnects between the junctions.*

IV CHARACTERISTICS

Figure 3 shows a dark and illuminated I-V curve for the multijunction TPV under a weak (i.e. small area) 980C Infrared Associates blackbody originally made for long wavelength infrared photodiode tests. The 980C temperature was used since this was the highest our calibrated blackbody source would reach. For this 0.74eV bandgap converter, a higher temperature source would have been more desirable. The multijunction short-circuit photocurrent was 6mA (each junction is 0.1cm² so the current density per junction was 60mA/cm²). The open-circuit voltage at this 6 mA level was 2.3V. The I-V fill-factor is ~65%.

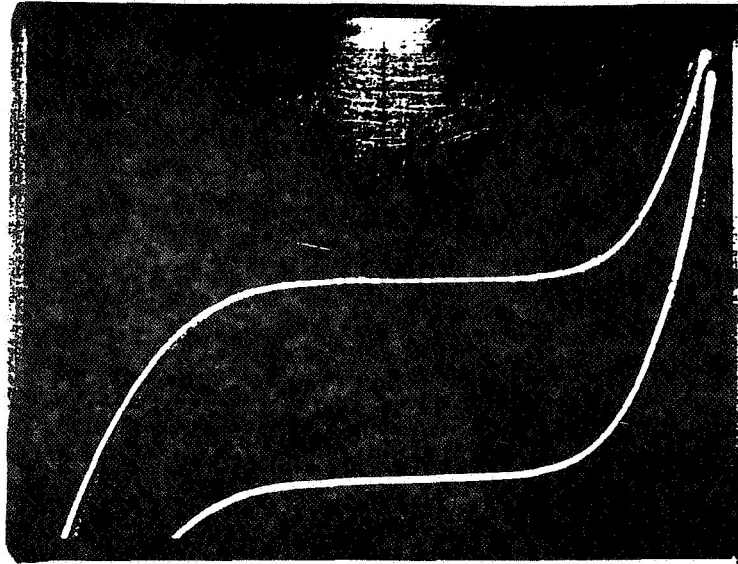


Figure 3 *Dark and illuminated I-V curves for a 0.74eV multijunction TPV converter under weak 980C blackbody irradiation. Vertical scale is 2mA/div and horizontal is 500mV/div.*

In order to calculate efficiency, we need to estimate the usable power falling on the device. The blackbody source aperture had a one-half-inch radius ("R1") situated two-inches ("h") from the TPV device. In order to use an analytical view factor formula for two coaxial circular disks, the rectangular TPV device (1cm by 0.8 cm photoarea) is approximated as a 0.2-inch radius ("R2") circular area (equal to 0.8cm², same as the original photoarea). The view factor "F" for this arrangement is².

$$F = \frac{R2}{R1} (X - \sqrt{X^2 - 1}) \quad \text{where} \quad X = \frac{h^2 + R1^2 + R2^2}{2R1R2}$$

or F is 0.009 (i.e. the TPV receives ~1% of the light emitted by the blackbody). The amount of power from the 980C blackbody above the 0.74eV bandgap (1.65µm cutoff wavelength) is 1.16 W/cm², and the one-inch diameter blackbody aperture has an area of 5.1 cm² so that (5.1x1.16) 5.9 W was emitted at wavelengths the InGaAs multijunction converter could convert. The amount of power incident on the device was then (0.009x5.9) 55mW. The power the device developed was (2.3Vx0.006Ax0.65) 9mW, for a power efficiency of 16%.

Figure 4 shows several I-Vs of the device when driven by a solar simulator to various current levels. A current level of 6mA (corresponding to Figure 3) is shown, along with the IV with illumination driving the device to 50mA (best fill-factor, 70%) and up to the highest photocurrent we could obtain (0.425 amps, fill factor series-resistance limited at 51%). The device delivered $(0.425 \times 3 \times 0.51)$ 0.64 watts at the highest illumination tested.

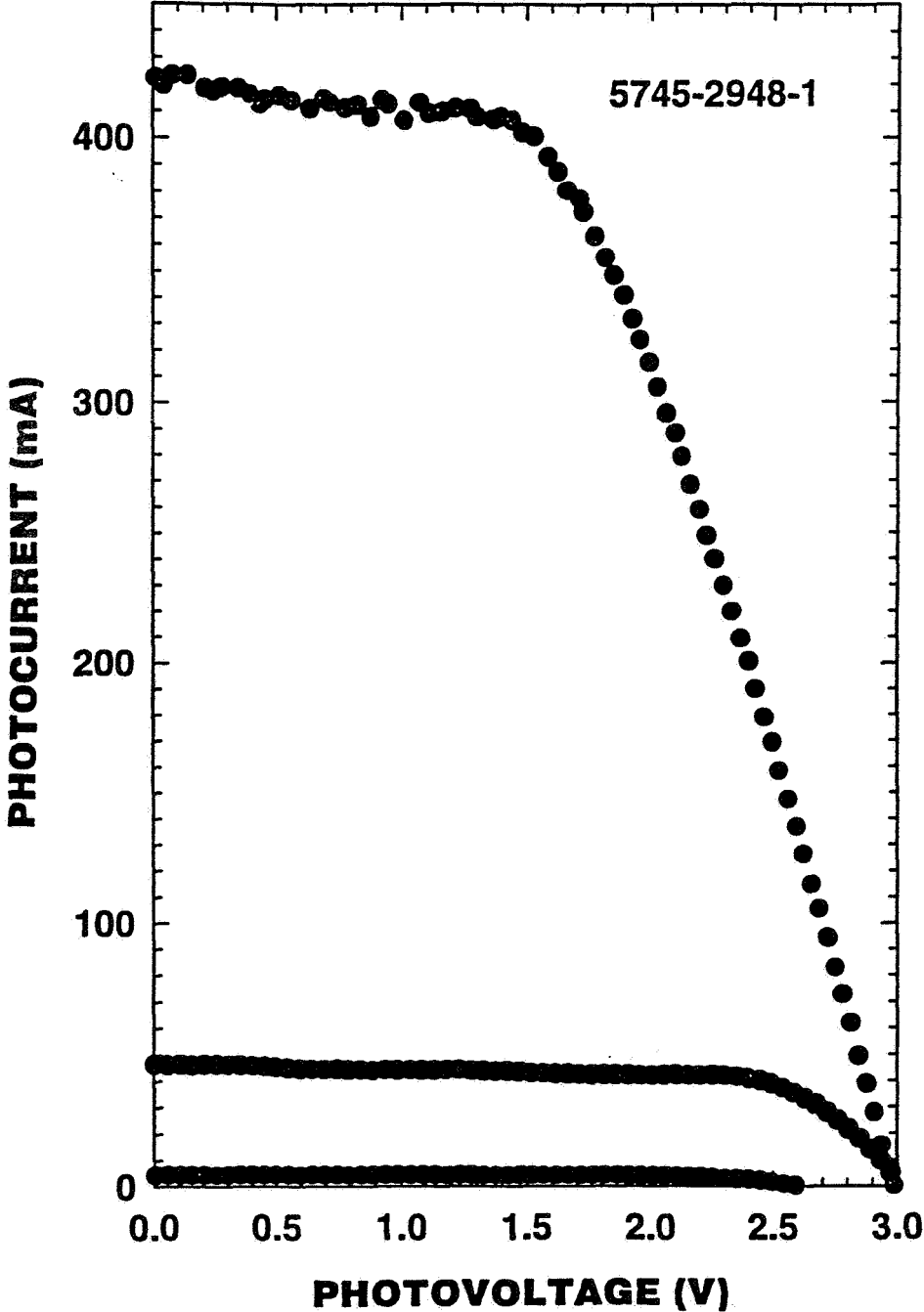


Figure 4 IVs obtained with the multijunction TPV cell at various illuminations with a solar simulator

OHMIC POWER LOSS CALCULATIONS

Figure 4 above shows that this first prototype multijunction TPV technology can deliver about 1 watt, and begins at this level to become limited by ohmic losses. The device can be further improved to lower the ohmic loss. This section outlines the numerical calculations needed to simultaneously minimize:

- I^2R loss in buried N-type InGaAs lateral conduction layer
- I^2R loss in top P-type InGaAs emitter layer (loss lowered by use of metal contact grid)
- shadow loss due to metallic contact grid
- shadow loss due to interconnect

An incident optical power of 100 W/cm^2 was used in the calculations. Figure 5 illustrates one junction of the eight-junction TPV and shows the dimensions and parameters used in the calculation:

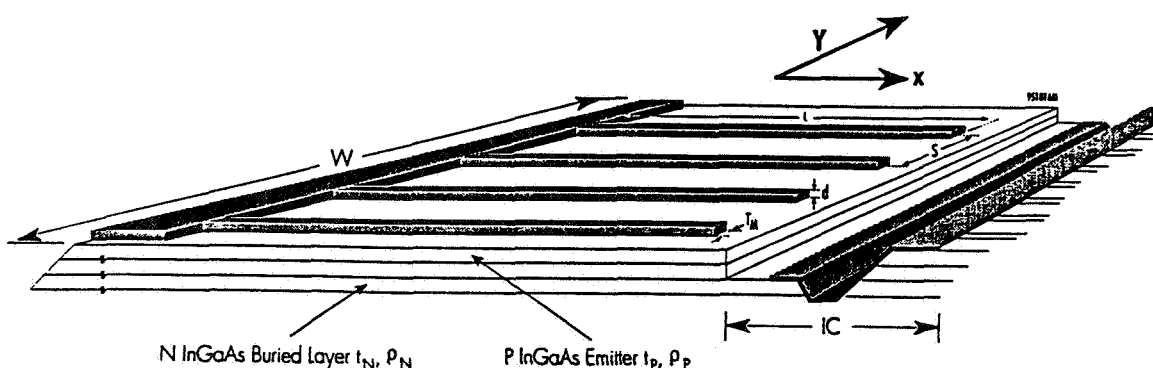


Figure 5 Definition of terms used in calculating loss in one-junction of eight in the TPV.

Loss in buried N⁺ InGaAs - The TPV's are on a semi-insulating InP substrate. The N⁺ buried layer must conduct the photocurrent to the cell edge to be collected by the bottom contact. The total photocurrent $I(X)$ in the layer increases linearly from zero at the edge furthest from the bottom contact, to its maximum value as the end contact is approached:

$$I(X) = \frac{q \eta \phi \lambda}{hc} W X$$

Maximum photocurrent from the incident optical power ϕ (100 W/cm^2), 7.6 A, is at $X = L - IC$, where L is the junction length (1 mm), and "IC" is the interconnect width (100 μm). Here η is the external quantum efficiency (0.8) at an assumed narrow selective emitter peak wavelength λ (1.315 μm), q ($1.602 \times 10^{-19} \text{ C}$), h ($6.626 \times 10^{-34} \text{ J-s}$) and c ($3 \times 10^8 \text{ m/s}$) are constants, and W is the junction width (1 cm) of the multijunction TPV.

The I^2R power loss in the lower N^+ InGaAs layer is then given by:

$$P_{LOSS N} = \int_0^{L-IC} I^2(X) dR = \int_0^{L-IC} I^2(X) \frac{\rho_N dx}{W t_N} = \frac{q^2 \eta^2 \phi^2 \lambda^2 W \rho_N (L-IC)^3}{3 h^2 c^2 t_N}$$

where dR is the incremental resistance, ρ_N is the resistivity ($10^4 \Omega\text{-cm}$) of Spire's N -type InGaAs ($N = 3 \times 10^{19} \text{ cm}^{-3}$, mobility $\sim 2000 \text{ cm}^2/V\text{-s}$), and t_N ($4 \mu\text{m}$) is the thickness of the N InGaAs buried layer. $P_{LOSS N}$ is 0.45W/junction . The available incident optical power on a single junction is:

$$P_{AVA} = \phi W L$$

P_{AVA} is 10W , so that F_N , the ratio of I^2R power loss in the N^+ buried InGaAs layer to the available optical power is 4.5% and is given by:

$$F_N = \frac{P_{LOSS N}}{P_{AVA}} = \frac{q^2 \eta^2 \phi \lambda^2 \rho_N (L-IC)^3}{3 h^2 c^2 t_N L}$$

Loss in upper P^+ InGaAs - The upper P^+ InGaAs emitter is doped ($\sim 3 \times 10^{19} \text{ cm}^{-3}$) similar to the N^+ InGaAs buried layer, but has a $\sim 25\text{X}$ lower hole mobility ($\sim 80 \text{ cm}^2/V\text{-s}$), which would dominate all losses if a top contact grid was not used. Instead of photocurrent flow across the junction width $L - IC$ ($900\mu\text{m}$), with a contact grid the current now only flows across half of the gridline-to-gridline spacing S ($100 \mu\text{m}$), or $50 \mu\text{m}$. This 18X shorter distance than the flow in the N InGaAs buried layer compensates for the 25X lower hole mobility. The photocurrent $I(Y)$ increases from zero at the center of the gap between gridlines to a maximum at a gridline:

$$I(Y) = \frac{q \eta \phi \lambda}{hc} L Y$$

The maximum photocurrent at $Y = S/2$ is 0.042 A . The I^2R power loss, $P_{LOSS P}$, is:

$$P_{LOSS P} = \frac{W}{S} \int_{-S/2}^{S/2} I^2(Y) dR = \frac{W}{S} \int_{-S/2}^{S/2} I^2(Y) \frac{\rho_P dy}{L t_P} = \frac{W q^2 \eta^2 \phi^2 \lambda^2 L \rho_P S^2}{12 h^2 c^2 t_P}$$

where W/S is the number of gridlines per junction, ρ_P is the resistivity ($0.003 \Omega\text{-cm}$) of Spire's P -type InGaAs ($\sim 3 \times 10^{19} \text{ cm}^{-3}$ doping, mobility $\sim 80 \text{ cm}^2/V\text{-s}$), and t_P is the thickness of the InGaAs emitter ($0.3 \mu\text{m}$). The emitter cannot be made much thicker than $0.3 \mu\text{m}$ without the external quantum efficiency η dropping below 80% . $P_{LOSS P}$ is then 0.52 W . F_P , the ratio of I^2R power loss in the emitter sheet resistance to the available

optical power is 5.2% and is given by:

$$F_P = \frac{P_{LOSS P}}{P_{AVA}} = \frac{q^2 \eta^2 \phi \lambda^2 \rho_P S^2}{12 h^2 c^2 t_P}$$

Loss in top contact grid metal - The top contact grid also has I^2R loss. Gold has a resistivity ρ_M of $\sim 3 \times 10^{-6} \Omega\text{-cm}$. The thickness (height) t_M of the evaporated gold is $3 \mu\text{m}$. The width "d" of a gold gridline is $5 \mu\text{m}$. The power loss P_{GRID} , 0.34 W per junction is given by:

$$P_{GRID} = \frac{W}{S} \int_0^{L-IC} I^2(X) dR = \frac{W}{S} \int_0^{L-IC} I^2(X) \frac{\rho_M dx}{d t_M} = \frac{W q^2 \eta^2 \phi^2 \lambda^2 S \rho_M (L-IC)^3}{3 h^2 c^2 d t_M}$$

F_{GRID} , the ratio of I^2R loss in the grid to available optical power is 3.5% and is given by:

$$F_{GRID} = \frac{P_{GRID}}{P_{AVA}} = \frac{q^2 \eta^2 \phi \lambda^2 \rho_M S (L-IC)^3}{3 h^2 c^2 t_M d L}$$

Shadow Loss from Grid and Interconnect - We are now planning to use an interconnect distance "IC" of $100 \mu\text{m}$ out of a total junction width of "L" of $1000 \mu\text{m}$. This means 10% of the total area is "dead" area (i.e. IC/L). In addition, we are now using a top contact grid with gridline width "d" of $5 \mu\text{m}$ on $100 \mu\text{m}$ spacings "S", for an additional shadow loss of 5% (d/S). Total shadow loss (the largest loss mechanism) is 1.5W/junction or 15% and is given by:

$$F_{SHADOW} = \frac{P_{SHADOW}}{P_{AVA}} = \frac{d}{S} + \frac{IC}{L}$$

SUMMARY

We have demonstrated a monolithic eight-junction 0.74eV InGaAs thermophotovoltaic converter with an output power capability of at least 0.64 watts, with voltages up to 3V and currents to 0.425 amps. At this level, the device was series-resistance limited (51% fill factor). At a lower photocurrent level, the best fill-factor was 70%. The device was tested with a sun-simulator and also under a weak, small-area 980C calibrated blackbody source. Under the blackbody, this TPV device exhibited an efficiency of about 16% to the blackbody emission wavelengths above the material bandgap ($1.65 \mu\text{m}$ cutoff wavelength). We discussed the ohmic power losses in the device. We calculated that an upper limit for this device technology may be an efficiency of 27% at power densities up to 100 W/cm^2 . Table I below shows the calculated losses.

Table I Losses in P-on-N multijunction TPV design under 100 W/cm² of 1.3 μm light.

| | Power Loss (W/cm ²) | Power Available (W/cm ²) |
|--|----------------------------------|---------------------------------------|
| Incident Optical Power | | 100 |
| I ² R Loss in N ⁺ Buried Layer | 4.5 | 95.5 |
| I ² R Loss in P ⁺ Emitter | 5.2 | 90.3 |
| I ² R Loss in Metal Contact Grid | 3.4 | 86.9 |
| Shadow Loss due to Grid | 5.0 | 81.9 |
| Shadow Loss due to Interconnect | 10.0 | 71.9 |
| Intrinsic 38% Cell Efficiency (loss due to E _g 0.74eV while V _{oc} ~0.5, QE~0.8, imperfect FF (~0.7) even with no series R) | 44.6 | 27.3 |

REFERENCES

1. S. Wojtczuk, T. Parodos, and G. Walker, "P/N In(Al)GaAs Multijunction Laser Power Converters," *Proc. of XIII SPRAT NASA Conf. Pub. 3278*, 1994, pp. 363-371.
2. M.F Modest, *Radiative Heat Transfer*, McGraw, 1993, pp. 166-173.

GALLIUM PHOSPHIDE ENERGY CONVERTERS

S30
IN-50415

P. E. Sims, L. C. DiNetta, K. Dugan Cavanagh, and M. A. Goetz
AstroPower, Inc.
Newark, DE 19716-2000

SUMMARY

Betavoltaic power supplies based on gallium phosphide can supply long term low-level power with high reliability. Results are presented for GaP devices powered by Ni-63 and tritiated phosphors. Leakage currents as low as 1.2×10^{-17} A/cm² have been measured and the temperature dependence of the reverse saturation current is found to have ideal behavior. A small demonstration system has been assembled that generates and stores enough electricity to light up an LED.

INTRODUCTION

Betavoltaic power generation requires an efficient semiconductor device to convert the beta-generated carriers into useful electric power. AstroPower has developed a gallium phosphide energy converter which is evaluated for two methods of power generation: direct conversion and indirect conversion. Figure 1 shows the indirect conversion concept, which is the most cost effective of the two methods. Figure 2 shows a current-voltage curve for direct conversion using ⁶³Ni as a power source. Figure 3 shows data for an indirect conversion array. For the direct conversion system, the short-circuit current density is 1.9×10^{-8} A/cm². The short-circuit current density for the indirect conversion system is 2.4×10^{-7} A/cm², better than an order of magnitude improvement over the ⁶³Ni fueled device. Improvements in current generation are the key to building betavoltaic power supplies with reasonable cost. Additionally, the utilization of tritium contributes to the safety of the device.

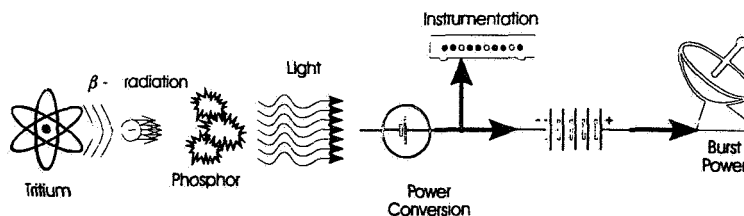


FIGURE 1. Indirect betavoltaic conversion.

RESULTS

Actual two-step tritium-fueled power generation has been accomplished since the last report [1] of a prototype GaP semiconductor betavoltaic converter array. The initial light sources utilized were two custom-made tritium light tubes fabricated by SRB Technologies (Winston-Salem, NC) for \$150. The luminance of these high-pressure tubes was 700μL. Each tube contained 15Ci of tritium and was half silvered to increase the light flux impinging on the array. The short-circuit current of the GaP array illuminated by these two high-pressure tubes was found to be 48nA without any optical containment techniques besides half-silvering the tubes. The effective collection area of this array was 0.2 cm², so the short-circuit current density with this light source was 240 nA/cm². The average open-circuit voltage was 0.997 V/cell. Due to the Federal regulations involving tritium, these lights are still at the factory in North Carolina while the array is in Delaware, so more detailed results other than those presented in Figure 3 are not available.

A second demonstration unit was evaluated using three standard blue tritium markers (Figure 4) as a light source in a reflective enclosure. The luminance of a standard commercial blue marker is approximately 500 μ L and there are no mirrors on the tubes. The best short-circuit current achieved with this configuration was 19nA, which corresponds to 95 nA/cm² current generation (Figure 5) and the single element open-circuit voltage was 0.912 volts. This power supply was found to be capable of charging a commonly available tantalum capacitor so that an LED could be fired about once an hour. Manual triggering was required since the short-circuit current provided by this betavoltaic generator was insufficient to sink into a firing circuit.

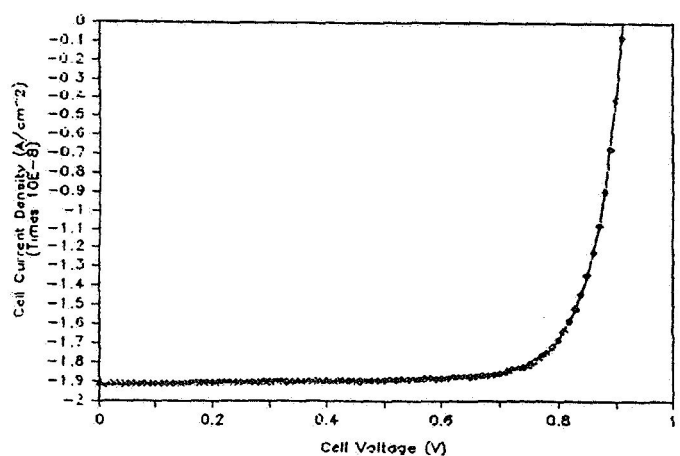


FIGURE 2. GaP betavoltaic device fueled by direct conversion of ⁶³Ni beta-electrons [2].

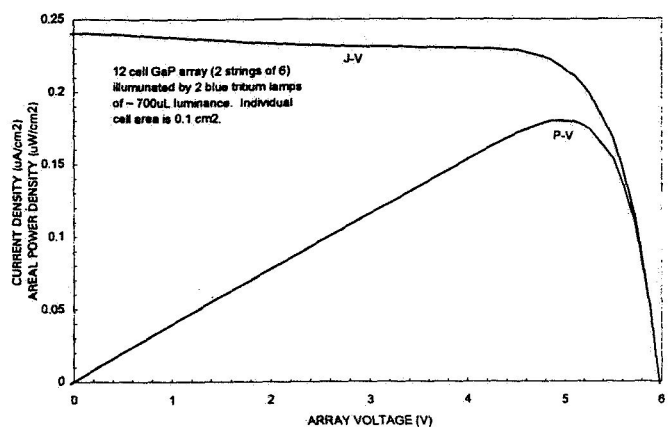


FIGURE 3. GaP betavoltaic array fueled by two custom-made T₂-ZnS:Ag light sources.

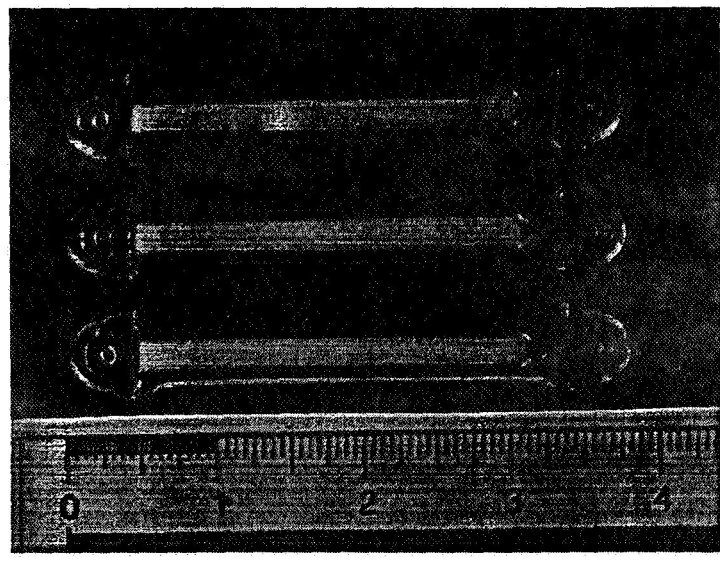


FIGURE 4. Photograph of commercial tritium lamps (scale is in inches).

Table I.
Cell data for array elements illuminated by $\approx 8.24 \mu\text{W}/\text{cm}^2$ ZnS:Ag light (Ref. 1)

| Array Position | Cell | V_{oc} (V) | I_{sc} (nA) | V_{mp} (V) | I_{mp} (nA) | I at 0.8V (nA) | FF | η (%) |
|----------------------------------|------------|--------------|---------------|--------------|---------------|---------------------|-------------|-------------|
| A1 | B114-14-05 | 0.99 | 51 | 0.8 | 45 | 45 | 0.72 | 4.37 |
| A2 | B114-10-05 | 1.03 | 54 | 0.8 | 48 | 48 | 0.69 | 4.66 |
| A3 | B114-10-07 | 0.95 | 52 | 0.8 | 48 | 48 | 0.78 | 4.66 |
| A4 | B114-12-05 | 1.00 | 51 | 0.9 | 44 | 49 | 0.77 | 4.81 |
| A5 | B114-10-04 | 1.03 | 51 | 0.8 | 50 | 50 | 0.76 | 4.86 |
| A6 | B114-14-01 | 1.04 | 53 | 0.8 | 50 | 50 | 0.73 | 4.86 |
| B1 | B114-12-04 | 1.06 | 52 | 0.9 | 46 | 51 | 0.75 | 5.03 |
| B2 | B114-12-02 | 1.01 | 52 | 0.9 | 47 | 52 | 0.80 | 5.14 |
| B3 | B114-12-01 | 1.12 | 53 | 0.9 | 53 | 52 | 0.76 | 5.46 |
| B4 | B114-14-02 | 1.14 | 54 | 1.0 | 50 | 53 | 0.81 | 6.07 |
| B5 | B114-10-01 | 1.08 | 55 | 0.9 | 52 | 54 | 0.79 | 5.68 |
| B6 | B114-10-03 | 1.16 | 55 | 1.0 | 51 | 55 | 0.80 | 6.19 |
| Array | | 6.27 | 145* | 5.25 | 116 | 121 @* 4.8 V | 0.56 | 5.52 |
| Improved high-current GaP device | B115-02-01 | 1.19 | 106 | 0.9 | 100 | 104 | 0.71 | 10.93 |
| Improved high-current GaP device | B115-05-02 | 1.11 | 111 | 0.9 | 108 | 109 | 0.79 | 11.8 |
| 1 cm ² | GaAs cell | 0.24 | 251 | 0.2 | 159 | | 0.52 | 3.86 |

* Current boost is due to the elimination of probe shading after array fabrication.

Table II.
Leakage currents of GaP devices

| Device | V_{oc} (Volts) | I_{sc} (nA) | J_{02} (A/cm ²) |
|------------|------------------|---------------|-------------------------------|
| B126-07-06 | 1.302 | 252 | 1.2×10^{-17} |
| B123-15-17 | 1.288 | 234 | 1.5×10^{-17} |
| B123-06-15 | 1.272 | 300 | 2.6×10^{-17} |
| B126-04-19 | 1.281 | 373 | 2.7×10^{-17} |
| B123-14-22 | 1.276 | 344 | 2.8×10^{-17} |
| B123-05-16 | 1.266 | 343 | 3.4×10^{-17} |
| B124-01-09 | 1.230 | 273 | 5.4×10^{-17} |
| B126-05-02 | 1.212 | 259 | 7.2×10^{-17} |
| B124-05-14 | 1.153 | 207 | 1.8×10^{-16} |
| B123-03-23 | 1.154 | 320 | 2.7×10^{-16} |

Figures 7, 8, and 9 display measured values for the dark current, quantum efficiency, and shunt resistance of a GaP device. These results are displayed as a function of temperature. We have found that GaP behaves very ideally up to about 300°C and can perform for a short duration to about 400°C. The high values of shunt resistance which have been achieved are particularly critical for this application.

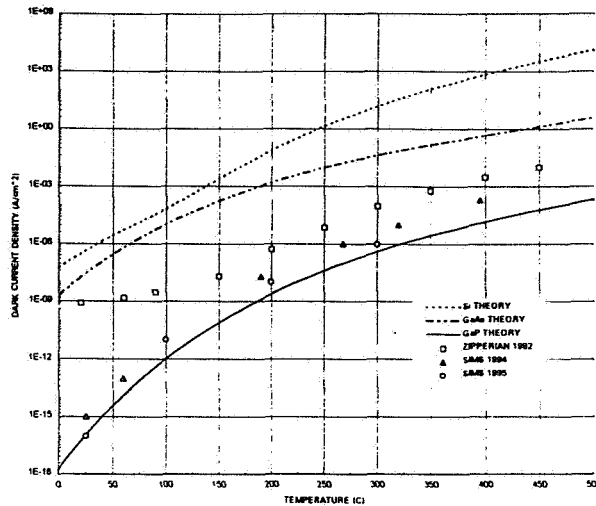


Figure 7. Temperature dependent leakage current of GaP p/n junction diodes [3].

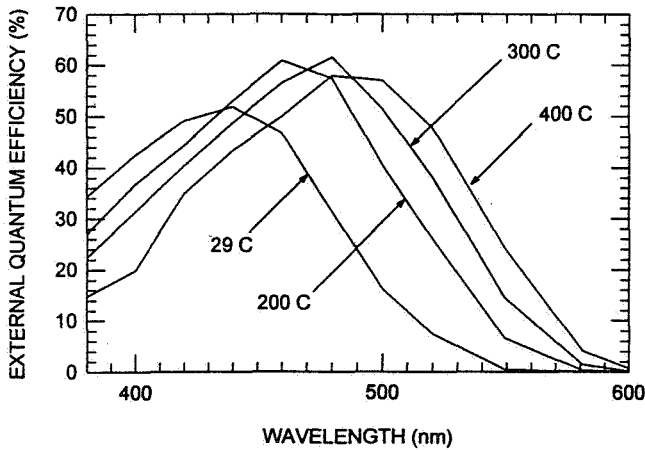


Figure 7. Temperature dependent external quantum efficiency of a GaP photodiode (no AR) [3].

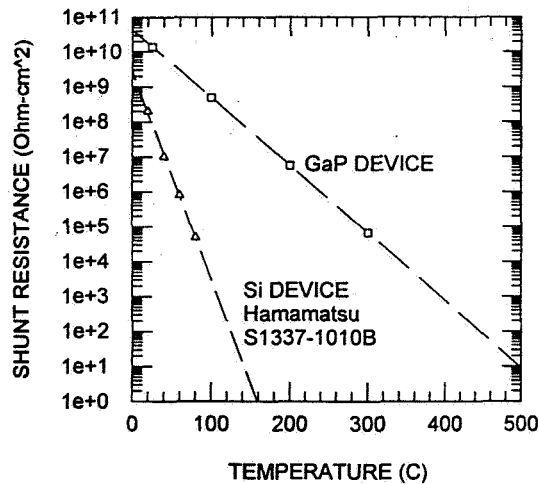


Figure 10. Estimated shunt resistance of a GaP device at different temperatures compared to a commercially available silicon device [3].

The experimentally determined power density for a direct conversion ^{63}Ni fueled system is $1.35 \times 10^{-8} \text{ W/cm}^2$, while the indirect conversion system power density was measured as $1.9 \times 10^{-7} \text{ W/cm}^2$. The significantly higher power available by the indirect conversion of beta radiation to electricity coupled with the safety of the tritium light source as opposed to ^{63}Ni , is desirable for this application. Also of interest is that by using an indirect conversion method, even with a low level beta emitter such as tritium, more power can be generated than with a high beta flux using direct conversion methods.

At the present time, work is ongoing in using tritium light sources to develop safe, high output light sources for a variety of applications. AstroPower is collaborating with Encapsulite, Inc. (Maplewood, NJ) to develop prototype betavoltaic generators using GaP-based devices and microsphere illumination technology. The microsphere concept, which is the high pressure encapsulation of tritium and phosphors in small (<1mm dia.) spheres, holds promise for the achievement of significantly brighter light sources. Encapsulite Inc. believes that luminance's of 1 to 10 FtL are possible using this approach (1FtL \approx 753 μ L). These light sources will enhance the power generating ability of the betavoltaic power conversion system by greatly increasing the incident light flux. The output of the betavoltaic generator is expected to be very stable since there are no semiconductor degradation mechanisms while the output of the generator assembly is expected to be predictable due to the well known decay statistics of the beta emitter. Useful generator lifetimes of 20-years are expected using tritium as a fuel.

CONCLUSIONS

Betavoltaic power generation using GaP devices and tritium powered light sources is technically feasible. A "realistic" power supply is proposed as having a V_{mp} of 5 V and an I_{sc} of 20 μ A, which would require a converter area of approximately 140 cm^2 using a projected current generation density of 720 nA/ cm^2 . A much smaller device area is possible if the microsphere concept is as bright as expected. This configuration would find use in long-term space missions as a housekeeping power supply. This device could both store power for periodic burst transmissions and command/control receptions. It is also possible that this type of device could switch on a more powerful power source as the spacecraft reaches a vicinity where data acquisition activities are planned.

References

- [1] P.E. Sims, L.C. DiNetta, and A.M. Barnett, "High Efficiency GaP Power Conversion for Betavoltaic Applications", Proceedings of the XIII SPRAT Conference, June 1994.
- [2] G.H. Negely, "Gallium Phosphide Converters Optimized for use in Beta-Cells", Final Report for Contract # 09-2988, Sandia National Laboratories, Sept., 1990.
- [3] P.E. Sims, L.C. DiNetta, M.A. Goetz, and J.B. McNeely, "Embedded High-Temperature Optical Transducer for Real Time Combustion Control", Workshop on High Temperature Power Electronics for Vehicles, Fort Monmouth, NJ, April 1995.

CHARACTERIZATION TESTING OF MEASAT GaAs/Ge SOLAR CELL ASSEMBLIES

Mike R. Brown
Curtis A. Garcia
George S. Goodelle
Joseph S. Powe
Joel A. Schwartz

S51
N-30410

Hughes Space and Communications Company
Spacecraft Integration and Structures Business Unit
El Segundo, California 90245

Abstract

The first commercial communications satellite with gallium-arsenide on germanium (GaAs/Ge) solar arrays is scheduled for launch in December 1995. The spacecraft, named MEASAT, was built by Hughes Space and Communications Company. The solar cell assemblies consisted of large area GaAs/Ge cells supplied by Spectrolab Inc. with infrared reflecting (IRR) coverglass supplied by Pilkington Space Technology. A comprehensive characterization program was performed on the GaAs/Ge solar cell assemblies used on the MEASAT array. This program served two functions; first to establish the database needed to accurately predict on-orbit performance under a variety of conditions; and second, to demonstrate the ability of the solar cell assemblies to withstand all mission environments while still providing the required power at end-of-life. Characterization testing included measurement of electrical performance parameters as a function of radiation exposure, temperature, and angle of incident light; reverse bias stability; optical and thermal properties; mechanical strength tests, panel fabrication, humidity and thermal cycling environmental tests. The results provided a complete database enabling the design of the MEASAT solar array, and demonstrated that the GaAs/Ge cells meet the spacecraft requirements at end-of-life.

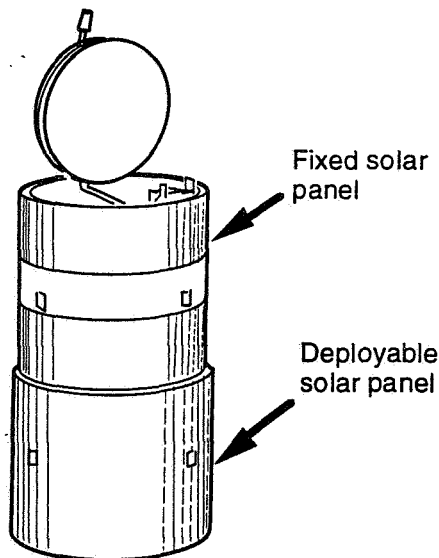


Figure 1. MEASAT HS-376 Spacecraft

Introduction

For roughly thirty years since the advent of satellite communications, spacecraft power generation has been dominated by the use of silicon solar cells. In recent years, the spacecraft industry has experienced a dramatic transition with the introduction of higher efficiency devices, primarily gallium-arsenide solar cells grown on germanium substrates [1]. In the commercial satellite industry, the use of GaAs/Ge (gallium-arsenide on germanium) solar cells was impeded by the high cost of these devices. However, progress in GaAs/Ge manufacturing technology, as well as the demand for higher power spacecraft has now made the use of GaAs/Ge solar cells on commercial spacecraft both feasible and desirable. The first commercial satellite to use GaAs/Ge cells is the MEASAT spacecraft (shown in Figure 1), built by Hughes Space

and Communications Company (HSC). The solar panels were built by Spectrolab Inc. and delivered to HSC in October of 1995; the spacecraft is currently scheduled for launch in December of 1995.

The MEASAT spacecraft, illustrated in Figure 1, is a Hughes HS-376 model spin-stabilized spacecraft. The HS-376 product line began in 1979 and continues in production to this day. The MEASAT program includes two spacecraft. The solar array consists of two cylindrical solar panels as shown in Figure 1. The introduction of GaAs/Ge solar cells on this spacecraft significantly increased the power generation capability of the solar panel. As a result, GaAs/Ge solar cell technology has made a major contribution to the longevity of this product line.

A comprehensive test program was performed by HSC to characterize the on-orbit performance of the solar cell assemblies used on the MEASAT solar panels. This program served two functions; first, to establish the database needed to accurately predict on-orbit performance; and second, to demonstrate the ability of the solar cell assemblies to withstand all mission environments while still meeting end-of-life requirements. The test program and the resulting database are described herein. A summary of the results is shown in Table I. The results provided a complete database enabling the design of the MEASAT solar array, and showed that the GaAs/Ge solar cell assemblies meet the spacecraft requirements at end-of-life.

Test Articles

The solar cell assemblies used on MEASAT consisted of GaAs/Ge solar cells with silver interconnects and coverglass installed. These assemblies are also referred to as CICs (cell-interconnect-coverglass assemblies). These assemblies were manufactured by Spectrolab, Inc.. The interconnects consisted of 25 μm silver mesh. Interconnects were installed by welding to the front ohmic contact of the solar cell. Coverglass was bonded to the solar cells using Dow Corning 93-500 adhesive.

Several coverglass configurations were tested during the characterization test program. These included CMG coverglass [2] supplied by Pilkington Space Technology and Corning 0213 coverglass [3] supplied by Optical Coating Laboratories Inc.. The coverglass types used in the test program are listed in Table II. For the MEASAT flight panels, 150 μm thick CMG/IRR was chosen. This coverglass has an anti-reflective (AR) front surface coating and an infrared reflective (IRR) back surface coating [4].

A total of 470 large area cells and 35 small area cells were used in the characterization test program. Small area cells were used exclusively for ultraviolet radiation, proton radiation, spectral response and temperature profile tests. All other tests were performed with large area cells and assemblies. The large area cells included 100 bare cells (i.e. cells without covers) and 370 assemblies. Large area bare cells had dimensions 3.447 cm x 6.888 cm; the assemblies consisted of bare cells with these same dimensions and covers which were slightly oversized (3.459 cm x 6.904 cm). All large area cells had an average thickness of 135 μm . The small area cells included 20 bare cells and 15 assemblies. Cell dimensions were 2 cm x 2 cm; the small area cell thickness was 175 μm .

Table II. Coverglass Types

| Type | Description | Thickness | Manufacturer | Quantity Of CICs |
|-------------|--|-------------------|---------------------|-------------------------|
| CMG/AR | CMG glass with anti-reflective front surface coating | 80 μm | PST | 100 |
| 0213/AR | Corning 0213 glass with anti-reflective front surface coating | 80 μm | OCLI | 75 |
| CMG/IRR | CMG glass with anti-reflective front surface and infrared reflecting back surface coatings | 80 μm | PST | 60 |
| CMG/IRR | CMG glass with anti-reflective front surface and infrared reflecting back surface coatings | 150 μm | PST | 150 |

Table I. MEASAT Solar Cell Assembly Characterization Tests

| TEST | RANGE/DURATION | RESULT |
|--|--|---|
| Electrical Characterization | | |
| Electrical output | 28 deg C; full I-V curve at AM0 intensity | Characterized performance |
| Covering gain/loss | Measure change in I _{sc} when placing covers on cells at 28 deg C | $\Delta I_{sc}/I_{sc} = -1.1\%$ with CMG/IRR coverglass |
| Angle of incidence | Full I-V curves every 10° from 0° to 80° and at 85° | Characterized performance. EOL deviation from cosine factor = 0.965 with CMG/IRR coverglass |
| Temperature profile | Full I-V curves at -150, -100, -50, 0, 28, 50, 100 and 150 deg C | Characterized performance |
| Spectral response | Measure I _{sc} at wavelengths from 300 to 1000 nm. | Characterized response |
| Reverse bias | Full I-V curves before and after reverse bias at maximum expected voltage | Characterized performance; established screening procedure. |
| Radiation Tests | | |
| Electron radiation | Irradiation with 1 MeV electrons at 4 fluences from 0 to 10 ¹⁵ e/cm ² | Characterized performance (see Figure 6) |
| Proton radiation | Irradiation with 9 MeV protons at 3.33•10 ¹¹ and 5.43•10 ¹¹ p/cm ² | Degradation less than JPL model prediction |
| Ultraviolet radiation | 3100 sun-hours | Degradation less than 1% |
| Reverse bias after radiation | Reverse bias at maximum voltage after 1 MeV electron irradiation at 2.5•10 ¹⁴ e/cm ² | Passed |
| Radiometric Properties | | |
| Emissivity | Determine from reflectance measurements at wavelengths between 4.8 and 26.2 μm. | Average normal emissivity = 0.84 |
| Solar absorptance | Integrated absorptance from measurements at wavelengths between 0.25 to 2.5 μm. | Average normal absorptance = 0.77 with CMG/IRR coverglass |
| Off-angle solar absorptance | Measure solar absorptance at angles of incidence from 0 to 71°. | Cosine weighted average over all angles = 0.72 with CMG/IRR coverglass |
| Mechanical Tests | | |
| Humidity | 30 days at 95% relative humidity and 45 deg C | Passed |
| Contact integrity | 150 gram pull strength required | Passed |
| Bending test | Determine minimum bending radius; ≤ 38 cm required | Passed at 18 cm |
| Thermal cycling (two 30 cm x 30 cm panels) | Interconnected cells mounted on curved panel; 1600 cycles from -150 to 60 deg C | Passed |
| Thermal cycling (76 cm x 76 cm panel) | Interconnected cells mounted on curved panel; 1200 cycles from -150 to 60 deg C | Passed |
| Reverse bias after thermal cycling | Reverse bias at maximum voltage after 1600 cycles from -150 to 60 deg C | Passed |

For thermal cycling tests, solar cell assemblies were welded into strings, and bonded onto solar panel coupons. The first coupon had dimensions 30 cm x 30 cm, and contained 20 solar cell assemblies with 80 μm thick CMG/IRR covers. The second coupon had dimensions 30 cm x 30 cm and contained a total of 12 solar cell assemblies; four cells had 150 μm thick CMG/IRR covers, and the remainder had 80 μm thick AR coated covers (CMG and Corning 0213). Two of the cells on the second coupon with 80 μm thick covers were damaged during coupon assembly. These cells would normally be replaced on a flight panel; hence, they were not included in subsequent testing. The final coupon had dimensions 76 cm x 76 cm and contained 200 solar cell assemblies; of these, 124 had 150 μm thick CMG/IRR covers and the remainder had 80 μm thick AR coated covers (CMG and Corning 0213).

Electrical Characterization Tests

Electrical performance tests were performed at HSC using a Spectrolab X-25 solar simulator, set to AM0 using appropriate balloon flown standard cells. Cell temperature was kept at 28 deg C using a water cooled test fixture. The average electrical output at AM0 and 28 deg C is shown in Table III for each configuration tested.

Table III. Electrical Performance Results

| Coverglass Type | Dimensions (cm) | V _{oc} (mV) | I _{sc} (mA) | P _{max} (mW/cm ²) | Efficiency |
|-----------------|-----------------|----------------------|----------------------|--|------------|
| None | 3.447 x 6.888 | 1029 | 709 | 595 | 18.5%* |
| CMG/IRR | 3.459 x 6.904 | 1018 | 720 | 580 | 18.0%** |
| AR coated | 3.459 x 6.904 | 1026 | 730 | 603 | 18.7%** |

* Based on nominal bare cell dimensions (shown in Table) and a solar constant of 135.3 mW/cm².

** Based on nominal coverglass dimensions (shown in Table) and a solar constant of 135.3 mW/cm².

Covering gain tests were performed by measuring the change in short-circuit current (I_{sc}) obtained when placing a coverglass on a cell, and keeping the cell temperature at 28 deg C. To accomplish this, amyl alcohol (with an index of refraction closely matching that of the adhesive) was used instead of adhesive in between the coverglass and the cell. This method allowed a comparison of the covering gain for different covers on the same solar cell. In addition, by testing the same coverglass on different cells, the effects of variability in cell characteristics were established (they were much smaller than the differences due to the type of coverglass coating).

The covering gain results are summarized in Table IV. As shown in the table, the covering gain for cells with IRR covers was negative, indicating a loss. It should be noted, however, that this test only measures changes in short-circuit current at a constant temperature. As shown below, the IRR covers also provide a lower value of solar absorptance, which reduces the temperature and increases the cell voltage on orbit. For the MEASAT spacecraft, shown in Figure 1, the lower solar absorptance also reduces the total heat input to the spacecraft. The IRR covers were chosen for flight on the basis of all these considerations.

Table IV. Covering Gain Results

| Coverglass Type | Coverglass thickness | # covers tested | # cells tested | Average covering gain |
|-----------------|----------------------|-----------------|----------------|-----------------------|
| CMG/IRR | 150 μm | 21 | 5 | -1.1% |
| CMG/IRR | 80 μm | 6 | 5 | -0.9% |
| CMG/AR | 80 μm | 6 | 4 | 2.1% |

Measurements of electrical output versus angle of incident light were performed at JPL (with the assistance of Bob Mueller) using a Spectrolab large area pulsed xenon solar simulator (LAPSS). I-V curves were taken at angles of incidence ranging from normal incidence to 85°. To summarize the results in a form which is applicable to spinning spacecraft, a loss factor was calculated which represents how the output deviates from the simple cosine loss rule. This factor, known as the deviation from cosine factor, is defined as follows:

$$F(I_{mp}) = \frac{\int I_{mp}(\theta) \cdot d\theta}{I_{mp}(\theta=0) \int (\cos\theta) \cdot d\theta}$$

where $F(I_{mp})$ = deviation from cosine factor for I_{mp}
 I_{mp} = current at maximum power measured at angle of incidence θ

and the integral is taken over the range of angles from -90° to +90°. For most silicon solar cells, the deviation from cosine factor is roughly 0.97 (representing a 3% loss) [5]. The results of this testing showed a deviation from cosine of 0.954 for unirradiated GaAs/Ge cells with IRR covers; for irradiated GaAs/Ge cells with IRR covers, the deviation from cosine was 0.965 (cells were irradiated at $2.5 \cdot 10^{14}$ e/cm² with 1 MeV electrons). GaAs/Ge cells with IRR covers are expected to have a slightly lower factor because the infrared reflecting band moves toward the visible wavelengths at high angles of incidence.

Temperature profile tests included measurements of full I-V curves with solar cells at temperatures from -150 deg C to +150 deg C. Bare 2 cm x 2 cm cells were used for this test. Cells were irradiated with 1 MeV electrons at fluences of 0, 10^{14} , $5 \cdot 10^{14}$ and 10^{15} e/cm². Two cells of each fluence were tested. The results are shown in Figures 2 through 4. As shown in the figure, these cells exhibit the characteristic decrease in voltage and increase in current, with increasing temperature, over most of the temperature range.

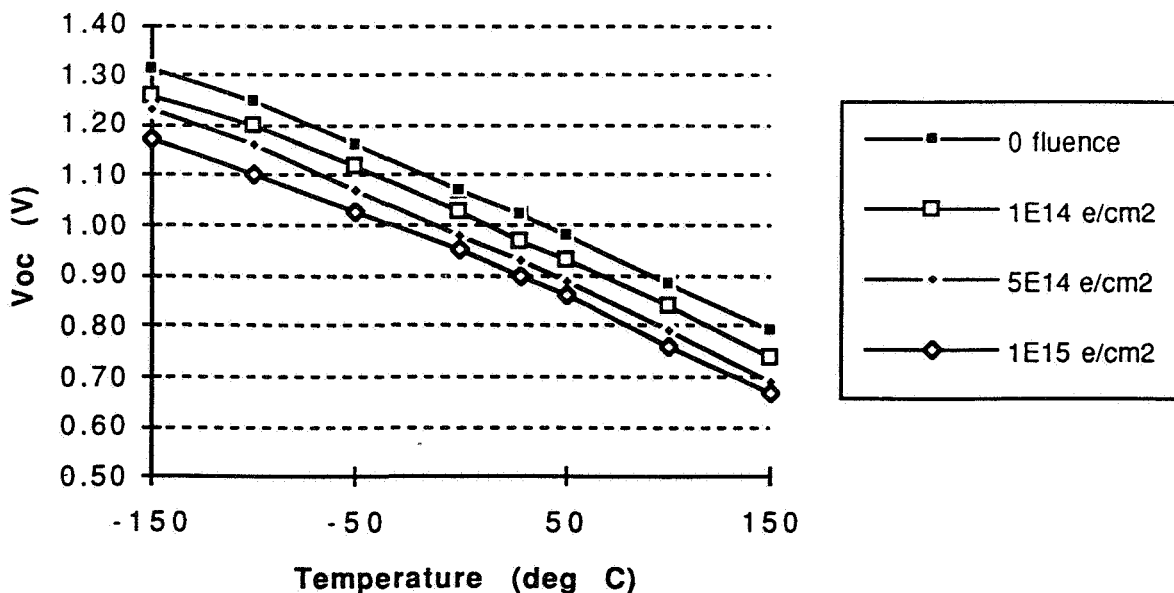


Figure 2. Open-Circuit Voltage Versus Temperature

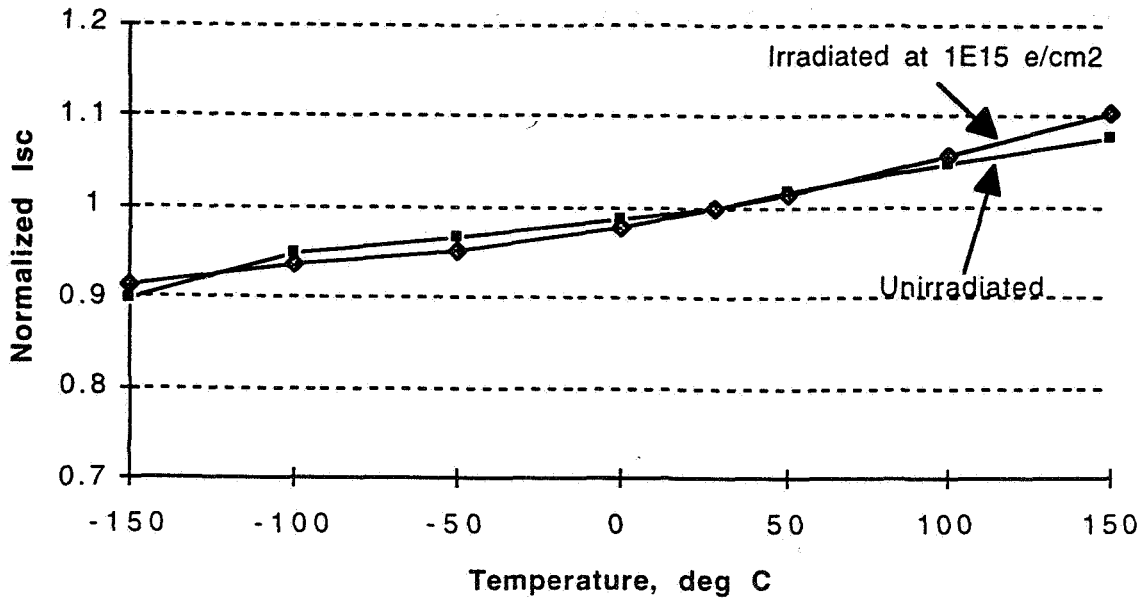


Figure 3. Normalized Short-Circuit Current Versus Temperature

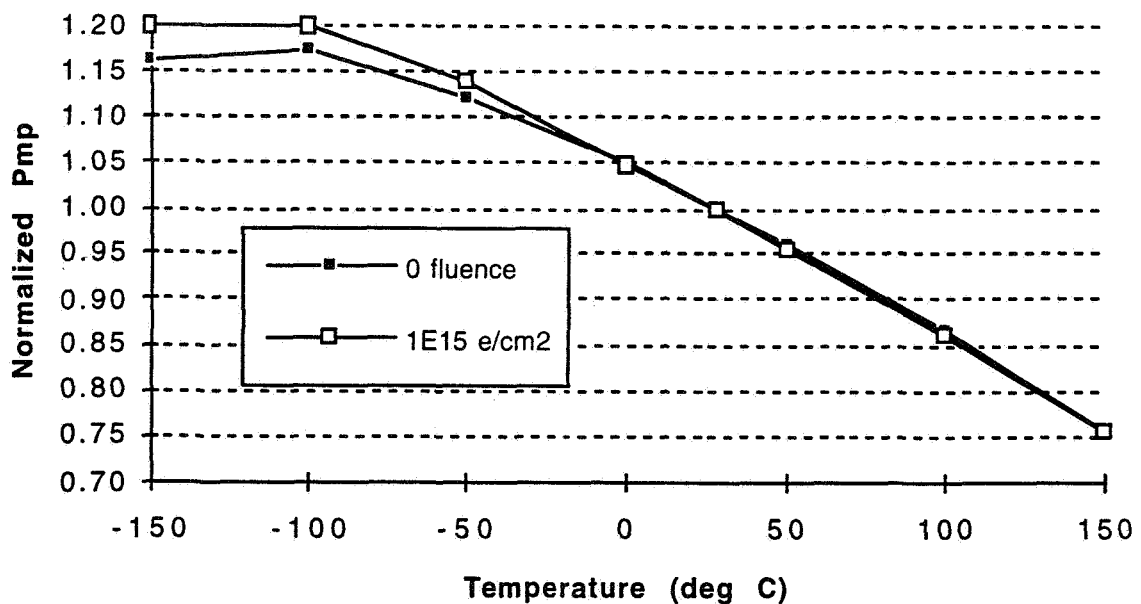


Figure 4. Normalized Maximum Power Versus Temperature

Spectral response results are shown in Figure 5. Spectral response was also measured on 2 cm x 2 cm bare cells. These results show that, like silicon cells, the GaAs/Ge solar cell response is more sensitive to radiation degradation at longer wavelengths. This change in spectral response is probably responsible for the difference observed between the deviation from cosine factors for irradiated and unirradiated cells. The irradiated cells are more dependent on light at blue wavelengths and less dependent on light at red wavelengths. As a result, the irradiated cells are less affected by the movement of the infrared reflecting filter to shorter wavelengths at high angles of incidence.

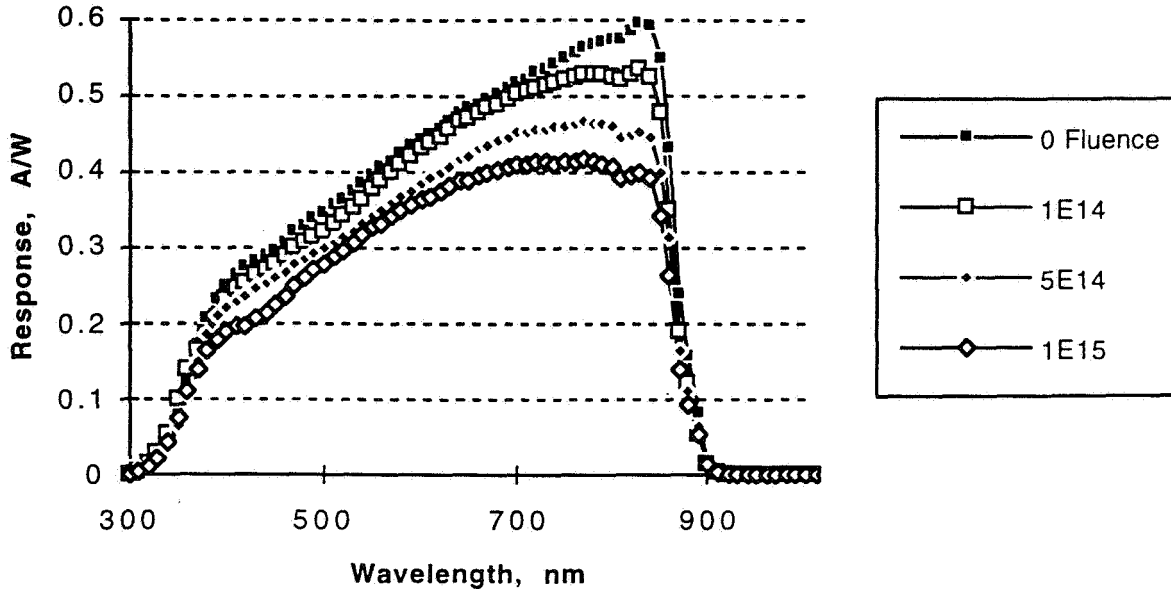


Figure 5. Solar Cell Spectral Response

Reverse bias testing was performed on 370 solar cell assemblies. The procedure used was similar to the screening procedure discussed in reference 6. However, the MEASAT requirements were slightly less severe than those in the reference because the power system design restricted the maximum voltage which a solar cell could reach in the reverse bias condition. The current at this voltage was generally less than full I_{sc} . Hence, each cell was subjected to reverse bias for one minute at the highest reverse bias voltage possible on the MEASAT solar array (5.5 V). Electrical output was measured before and after reverse bias using the X-25 solar simulator. Cells which exhibited a measurable decrease in maximum power were considered failed. This established a procedure for screening of MEASAT flight cells; only cells which passed this test were accepted for flight.

Further testing was performed to determine whether cells which passed the screening process once would pass again after exposure to environmental testing. Environmental testing included exposure to long duration reverse bias, multiple reverse bias exposures, radiation and thermal cycling. Long duration exposure was performed on 25 cells up to 30 minutes. Multiple exposures were performed on 50 cells up to five exposures. Radiation was performed on 7 cells with 1 MeV electrons at a fluence of $2.5 \cdot 10^{14}$ e/cm². Thermal cycling was performed on coupon #2 and consisted of 1600 cycles on from -150 deg C to 60 deg C. The results showed that each cell which passed the screening test before exposure to the environment also passed the screening test after exposure.

Radiation Test Results

Radiation testing included electron, proton and ultraviolet exposure. Electron radiation was performed at the JPL Dynamitron Laboratory. Large area bare solar cells were irradiated with 1 MeV electrons at fluences of 0, 10^{14} , $5 \cdot 10^{14}$, and 10^{15} e/cm². At each fluence, 8 GaAs/Ge cells and 6 silicon control cells were irradiated. The silicon controls served mainly to verify the radiation fluence. The results are summarized in Figure 6. Regression plots for the normalized degradation of each operating parameter are shown in the figure. For maximum power the normalized degradation factor at 10^{15} e/cm² was 0.765. This value is slightly less severe than the value of 0.74 reported in the Solar Cell Radiation Handbook [7].

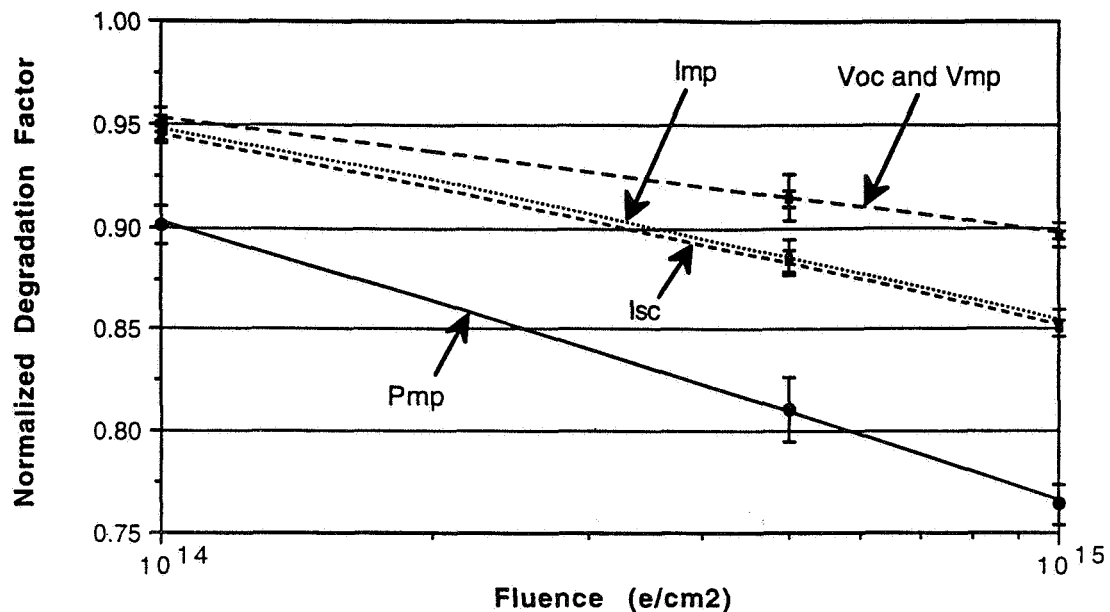


Figure 6. Radiation Degradation With 1 MeV Electrons

Proton radiation was performed at the Caltech Van de Graff accelerator. Small area bare solar cells were irradiated with 9 MeV protons at fluences of $3.33 \cdot 10^{11}$, and $5.43 \cdot 10^{11}$ p/cm². Four GaAs/Ge cells and two silicon controls were irradiated at each fluence. The predicted degradation factor for maximum power was calculated using the proton relative damage coefficients [8], the equivalence factor for conversion from 10 MeV protons to 1 MeV electrons [8] and the electron degradation curve shown in Figure 6. The predicted degradation factors were 0.83 and 0.80 for the two fluences tested; the measured values were 0.86 and 0.81 for the two fluences respectively. In each case, the measured degradation was slightly less severe than the predicted values. To complete the database for the MEASAT program, these results were augmented by additional proton radiation data provided by Spectrolab Inc..

Ultraviolet exposure was performed by James Chow et. al. at Hughes Aircraft Company Electro-Optical Systems Segment. Electrical performance of solar cells during this test was measured using the LAPSS at JPL with the assistance of Bob Mueller. Ultraviolet exposure and performance testing were both performed with the cells under vacuum at 10^{-5} torr. GaAs/Ge test samples included 4 cells with CMG/AR covers, 4 cells with CMG/IRR covers and 4 cells with AR coated Corning 0213 covers. Control samples included 4 silicon cells with fused silica covers and 4 silicon cells with removable fused silica covers, and no coatings or adhesive. Test methods for the UV exposure test are described in reference 9. All cells were exposed to 3100 sun-hours of equivalent UV between the wavelengths of 200 and 400 nm. Electrical output was measured after 0, 400, 1200, 2900 and 3100 hours. Based on the data, it was concluded that UV effects saturated within 1200 hours of exposure. The results are summarized in Table V. All GaAs/Ge solar cell assemblies showed a net degradation of less than 1%.

Radiometric Properties

Normal emissivity was measured using Gier-Dunkle DB-100 infrared spectrophotometer. Solar absorptance was measured using a Lambda 9 spectrophotometer with an integrating sphere. Solar absorptance measurements were performed by James Chow and Lillian Hunter in Hughes Aircraft Company Electro-Optical Systems Segment. The results for normal emissivity solar absorptance are summarized in Table VI.

Table V. Ultraviolet Exposure Results (3100 UV hours)

| | GaAs/Ge cells with CMG/AR covers | GaAs/Ge cells with CMG/IRR covers | GaAs/Ge cells with AR coated Corning 0213 covers |
|---|----------------------------------|-----------------------------------|--|
| Average loss in Isc, raw data | 1.4% | 1.6% | 1.5% |
| Measured system effects | 0.9% | 0.9% | 0.9% |
| Net loss in Isc (raw data less systems effects) | 0.5% | 0.7% | 0.6% |

Table VI. Normal Radiometric Properties

| | GaAs/Ge cells with CMG/AR covers | GaAs/Ge cells with CMG/IRR covers | GaAs/Ge cells with AR coated Corning 0213 covers |
|--------------------------|----------------------------------|-----------------------------------|--|
| Normal emissivity | 0.84 | 0.84 | 0.84 |
| Normal solar absorptance | 0.90 | 0.77 | 0.90 |

Solar absorptance was also measured as a function of the angle of incident light for GaAs/Ge cells with CMG/IRR covers. Measurements at off-normal angles were made using the double bounce technique developed by Andrew Meulenber of Comsat Laboratories. This method uses a pair of solar cells placed within the integrating sphere such that the incoming light is reflected from one cell to the next. Six samples were measured at angles up to 71°. To determine the effective solar absorptance with CMG/IRR covers on a spinning spacecraft, the cosine weighted average absorptance was calculated as follows:

$$\text{Effective solar absorptance} = \frac{\int \alpha(\theta) \cos \theta \, d\theta}{\int \cos \theta \, d\theta}$$

where α = solar absorptance and θ = angle of incidence. To estimate the error inherent in this calculation, the data was fit with several different fitting functions. The final result was an effective solar absorptance of 0.72 ± 0.02 .

Mechanical Tests

Mechanical tests included humidity exposure, contact integrity tests, bending strength and thermal cycling. Humidity exposure consisted of 30 days at 95% relative humidity and 45 deg C. A total of 4 bare cells and 8 assemblies with assorted covers were tested. The maximum allowed degradation in Pmax was 2%. The bare cells passed with an average degradation of 1.0%; the assemblies passed with an average degradation of 1.6%. No difference was observed in the performance of different coverglass types.

Contact integrity tests included front and back tape peel tests, interconnect pull strength, and back contact pull strength. Each test was performed on both bare cells and assemblies. Tape peel testing revealed no evidence of contact or coating delamination. The required pull strength was 150 grams minimum. All cells and assemblies passed.

Bending strength was measured by subjecting assemblies to bending around a cylinder of known radius [5]. Cylinders of decreasing radii were used until visual inspection showed breakage of the coverglass or solar cell. A bending radius of 38 cm or less with no breakage was required. Four assemblies with 80 μm thick covers and four cells with 150 μm thick covers were tested. Cracking was first observed at a bending radius of 18 cm for assemblies with 150 μm thick covers, and at 15 cm for assemblies with 80 μm thick covers.

Thermal cycling was performed on the 3 solar panel coupons described above. Coupons #1 and #2 underwent 1600 cycles from -150 deg C to +60 deg C. Coupon #3 underwent 1200 cycles from -150 deg C to +60 deg C. Electrical output was measured before and after thermal cycling. Measurements were taken at Spectrolab Inc. with the help of Robert Dally using a large area pulsed xenon solar simulator (LAPSS). The maximum allowable degradation due to thermal cycling was 2% in Pmax. Coupon #1 passed with an average measured degradation of 0.9%. Coupon #2 passed with a measured increase in average power of 0.1% (consistent with no change). Finally, coupon #3 passed with no change (0.0%) measured in average power output.

Summary

The solar panels used on the MEASAT spacecraft represent the first GaAs/Ge solar panels on a commercial communications satellite. The solar cell assemblies installed on these panels have been fully qualified and characterized by the test program outlined above. The database generated by this test program can be used to accurately predict the electrical performance of the MEASAT solar array throughout the mission lifetime. In addition, the test results have demonstrated the ability of the solar cell assemblies to successfully withstand all mission environments.

References

- [1] P.A. Iles and F. Ho, Technology Challenges For Space Solar Cells, 1994 IEEE First World Conference On Photovoltaic Energy Conversion Vol. II, IEEE, p. 1957, 1994.
- [2] C.A. Kitchen, A.A. Dollery, K. Mullaney, K. Bogus, Teflon Bonding Of Solar Cell Assemblies Using Pilkington CMZ & CMG Coverglasses - Now A Production Process, 1994 IEEE First World Conference On Photovoltaic Energy Conversion Vol. II, IEEE, p. 2058, 1994.
- [3] Qualification Test Results For Blue-Red Reflecting Solar Cell Covers And Other New Products For The Solar Power Market, P. Beauchamp, B. McLean, M. Larro, 1994 IEEE First World Conference On Photovoltaic Energy Conversion Vol. II, IEEE, p. 2064, 1994.
- [4] Infra Red Reflective Coverglasses: The Next Generation, K. Mullaney, G.M. Jones, C.A. Kitchen, D.P. Jones, IEEE 22nd Photovoltaic Specialists Conference, IEEE, 1991, p. 1593, 1991.
- [5] J.S. Fodor, S.W. Gelb, L.J. Goldhammer, G.S. Goodelle, A.L. Judson, Characterization Testing Of Large Area Solar Cell Assemblies, Proceeding Of The 19th IEEE Photovoltaics Specialists Conference, IEEE, 1987
- [6] L.A. Rosenberg and S.H. Gasner, Reverse-Bias Screening Of Large-Area GaAs/Ge Solar Cells At Low And High Temperature, IEEE 22nd Photovoltaic Specialists Conference, 1993, p.1421.
- [7] B.E. Anspaugh, Solar Cell Radiation Handbook Addendum 1: 1982-1988, JPL Publication 82-69 Addendum 1, Jet Propulsion Laboratory, p. 37, 1989.
- [8] B.E. Anspaugh, Proton and Electron Damage Coefficients For GaAs/Ge Solar Cells, IEEE 22nd Photovoltaic Specialists Conference, 1993, p.1593.
- [9] G.S. Goodelle, G.R. Brooks, J.R. Mosher, High Vacuum UV Test Of Improved Efficiency Solar Cells, IEEE 11th Photovoltaic Specialists Conference, IEEE, 1975, p.184-9.

532
IN-50417

ADVANCED SOLAR PANEL DESIGNS¹

E. L. Ralph and E. B. Linder
Applied Solar Energy Corporation
City of Industry, CA

Solar panel designs that utilize new high-efficiency solar cells and lightweight rigid panel technologies are described. The resulting designs increase the specific power (W/kg) achievable in the near-term and are well suited to meet the demands of higher performance small satellites (smallsats).

Advanced solar panel designs have been developed and demonstrated on two NASA SBIR contracts at Applied Solar. The first used 19% efficient, large area (5.5 cm x 6.5 cm) GaAs/Ge solar cells with a lightweight rigid graphite epoxy isogrid substrate configuration. A 1,445 cm² coupon was fabricated and tested to demonstrate 60 W/kg with a high potential of achieving 80 W/kg.

The second panel design used new 22% efficiency, dual-junction GaInP₂/GaAs/Ge solar cells combined with a lightweight aluminum core/graphite fiber mesh facesheet substrate. A 1,445 cm² coupon was fabricated and tested to demonstrate 105 W/kg with the potential of achieving 115 W/kg.

1.0 INTRODUCTION

This paper will address the construction details for the GaAs/isogrid and dual-junction GaAs/carbon mesh panel configurations. These are ultimately sized to provide 75 Watts and 119 Watts respectively for smallsats or may be used as modular building blocks for larger systems. A detailed weight estimate for each design is provided in Table 1.0-1.

GaAs/isogrid and dual-junction GaAs/carbon mesh coupons have been fabricated and tested to successfully demonstrate critical performance parameters and results are also provided here.

2.0 GaAs ISOGRID SOLAR PANEL ASSEMBLY

The ultimate technical objective is to develop and demonstrate standardized GaAs composite isogrid solar arrays that provide ~80 Watts per kilogram (W/kg) specific power and can be built for one-third current costs within a 3 month turnaround from order to delivery. The design will produce a 75 Watt array power output at Beginning of Life (BOL) using a modular configuration that is ideally suited for small satellites (smallsats) for remote sensing, communication and experimental applications. This is significantly less time and money required to build solar arrays using current practice and is an extremely attractive solution for smallsat developers seeking the best performance value. Hardware and manufacturing processes developed during this program will be intended for production use at a rate of two to three solar array shipsets per month, enabling a long term moderately sized annual product line.

A preliminary design concept of a GaAs composite isogrid solar array was developed for potential future production. This 75 Watt BOL, 0.94 kilogram solar array is ideally sized for smallsat developers and features adaptable voltage output and mounting locations for interface flexibility. Figure 2.0-1 shows the baseline array which includes large GaAs solar cells on a composite isogrid panel substrate, routing wiring and an attachment hinge for spacecraft interface. The routing wiring may be integral to the panel facesheet which is used to isolate

¹ The primary basis of the work discussed was two NASA MSFC SBIR Phase I contracts; NAS8-4057 advanced lightweight high performance isogrid solar array, and NAS8-4056 multijunction GaInP/GaAs/Ge solar cells on carbon mesh substrate.

the solar cells from the substrate. Integral wiring reduces array assembly labor for reduced cost and schedule and improves reliability. The "wires" are actually metal strips sandwiched in the polyimide facesheet structure and are pre-printed by design. Array voltage is designed for either 35 or 70 Volts by selection of appropriate tap points on the output connector. Four arrays can readily be used by a single spacecraft to provide 300 Watts total power. The conveniently located hinge design will be both lightweight and reliable and may be detached for user flexibility. The panel will be reinforced along the hinge mounting bar to support other attachment designs if needed. The array will meet or exceed performance and manufacturing objectives because it uses:

- ◇ large area (36 cm²) GaAs solar cells drawn from ongoing high volume production for ready availability and low cost
- ◇ lightweight composite isogrid technology that is rapidly fabricated with reusable tooling
- ◇ a standardized, modular design that meets user requirements
- ◇ a production ready configuration that has no non-recurring engineering cost

A proof-of-concept GaAs composite isogrid array coupon was successfully developed and demonstrated as an initial project milestone and is shown in Figure 2.0-2. As shown, there are 30 solar cell assemblies on the panel which are identical to current Applied Solar high-volume production cells. Measured results show 18.09% panel efficiency at 28 °C, Air Mass Zero (AM0) which is near the 19% program goal. The best cell on the coupon measures 18.99% efficiency. The panel substrate was manufactured by the Structures and Controls Division of the Air Force Phillips Laboratory. The coupon successfully passed thermal cycling tests and was also examined both visually and after X-ray without notable defects. Total coupon specific power is about 60 W/kg which is approaching the 80 W/kg target. The total coupon manufacturing and test cycle time was under 35 calendar days which met project objectives.

By successfully developing and demonstrating a working GaAs composite isogrid solar array coupon, this project has shown that notable performance and producibility improvements can be gained and forwarded to the smallsat developer who needs low-cost and high-performance solar arrays. Based on these benefits, it is concluded that GaAs composite isogrid solar arrays, as demonstrated here, is an important new capability, and should be qualified and brought into commercialization as soon as possible.

2.1 GaAs SOLAR CELLS

In recent years, GaAs solar cells have displaced silicon as the technology of choice for space systems. GaAs solar cells fabricated on producible germanium substrates offer improved conversion efficiency (>18.5%) at a competitive price. Applied Solar began developing GaAs technology in 1981 and initiated production in 1984. Presently, Applied Solar is continuously producing GaAs solar cells from an existing facility with over 125 kW annual capacity.

Applied Solar will deliver over 170,000 5.5 cm x 6.5 cm solar cells by 1997 for a single contract. The active layers are grown on a 140 mm thick germanium substrate using Metal Organic Chemical Vapor Deposition (MOCVD) and the total finished cell thickness is approximately 160 mm. Cells are normally covered with a coverglass which provides protection and optical filtering. The baseline uses a 100 mm thick ceria doped borosilicate glass. The cell structure is a P-on-N GaAs design on the N-doped germanium substrate which has demonstrated good performance results with a producible manufacturing process. This is a two terminal device; interconnect is made to the back surface metal contact and to a front metal contact which collects current from gridlines that are distributed across the face of the cell.

To date, 50,000 large GaAs solar cells have been produced with 18.5% average conversion efficiency as shown in Figure 2.1-1. 19% is the mode and efficiencies in excess of 19% are achievable by selecting high-end cells from the population. Current large cell production rates are between 3,000 and 6,000 cells per month, and at ~0.9 Watts output per cell, this translates to about 60 kiloWatts per year for this single program.

2.2 ISOGRID PANEL SUBSTRATES

Isogrids are lightweight shell structures stiffened by triangular stiffening ribs integrally co-cured or bonded to the shell. Carbon fiber/polymer composite isogrid structures are preferred to conventional metallic designs as they offer relatively high strength and stiffness to weight ratios, flexibility in design, custom tailoring of desired materials properties, and the ability to perform in diverse environments. Additionally, metal structures require long manufacturing lead times compared to composites which can use advanced fabrication techniques including automated processing.

Composite isogrid technology was originally developed in the 1970's and the Phillips Laboratory initiated research in 1990. Several promising application areas were identified including aircraft and naval vessel structures, terrestrial applications such as infrastructure (bridges) and automotive and space structures including launch vehicles and spacecraft/solar panels. The composite isogrid solar panel design concept shown in Figure 2.2-1 has several performance advantages compared to the traditional aluminum honeycomb structure with aluminum or graphite/epoxy skins. These include at least a 15% weight reduction and improved thermal protection which reduces solar cell operating temperature by 20-30% and translates into a smaller array area needed to meet power requirements. These size reductions combine with improved manufacturing processes to result in lower panel cost. Composite isogrid specific weight as a function of panel size is shown in Figure 2.2-2.

3.0 GaInP₂/GaAs/Ge On CARBON MESH PANEL ASSEMBLY

The preliminary multijunction (MJ) carbon mesh panel for the smallsat mission is shown in Figure 3.0-1. In this case, we utilize 22% efficient GaInP₂/GaAs/Ge solar cells. Using the maximum power voltage of 2.093 V/cell for the MJ, results in a 17 cell series string to meet 34 V bus voltage. Using a cell size of 5.0 cm x 4.9 cm, the layout on the panel is 17 series x 10 parallel. The layout sketch shows two circuit segments -17S x 5P wired in parallel which provides 119 W at 34 V (AM0 28°C). This represents a 67% increase in power output BOL (28°C) for the same size panels, thus demonstrating the significant improvement available using the advanced technology being developed.

The demonstration panel coupon is 38.1 cm x 38.1 cm in size with one circuit consisting of 30 series connected GaAs/Ge solar cells (5.5 cm x 6.5 cm) and a second circuit consisting of 16 series connected MJ solar cells (2 cm x 4 cm). It was successfully fabricated and tested and is shown in Figure 3.0-2. CMX coverglass, 0.010 cm (4 mil) thick with an A/R coating on the top surface, was selected for the MJ cells. The coverglass covers 100% of the solar cell. The standard Applied Solar interconnect made from 25 μm silver-plated Invar was selected. The interconnect has an out-of-plane stress relief loop and there are two interconnects soldered to each MJ cell and three interconnects on each large area GaAs/Ge cell.

The panel substrate is an advanced lightweight design fabricated by Ketema Corporation. It uses a one half inch thick aluminum honeycomb core with high strength lightweight 0.005 inch thick T300/934 graphite cloth/epoxy resin facesheets. A 0.002 inch thick layer of Kapton is co-cured to one facesheet as a dielectric layer. The weight of the 38.1 cm x 38.1 cm panel substrate is 138 grams for a specific weight of 0.9 kg/m² (0.19 lb/ft²).

The 16 MJ cells plus the 30 large area GaAs/Ge cells represent a total of 128 cm² and 1072.5 cm². Average output of the MJ cells was measured and this represents a 33.3 Watt coupon power output capability. Using the actual measured weight of the coupon, one then gets a demonstrated specific power value of 105 W/kg (9.5 kg/kW) and a value of 230 W/m² based on the total coupon area. The packing factor on this small demonstration coupon was only 83% so this is really not representative of a larger panel which typically is 90-95%.

3.1 Multijunction Solar Cells

This solar cell is a 22% efficient, two-junction device, built in a tandem configuration with only two contacts. The active layers are deposited in series by MOCVD on a germanium wafer with a grid contact on top and a full cell contact on the bottom. Therefore, from an external appearance standpoint, it looks identical to the conventional GaAs/Ge or even Silicon solar cells. The two junctions are fabricated within two different semiconductor materials with bandgaps selected to provide sunlight absorption over a wide wavelength range and optimize

collection efficiency for each bandgap. Electrical data of a solar cell used in the panel coupon are shown in Figure 3.1-1. Germanium wafers are used as the substrate for the MOCVD deposition for cost reasons as in the GaAs/Ge solar cell case. This cell is just completing qualification testing this year. It will become available in production quantities in 1996. The early production runs will start out with 2 cm x 4 cm by 200 μ m thickness size cells but with time will increase in size and become thinner, the same as GaAs/Ge type cells did for economic reasons. For this project the 2 cm x 4 cm size cell was selected because of its early availability.

4.0 Benefits and Conclusions

Spacecraft designers often have different reasons for using an advanced solar cell array technology. Overall system cost is usually a strong driving factor; however, there are those cases where the advanced technology is enabling and the cost becomes secondary. In any case, the advanced technologies demonstrated here provide another step function advancement in solar array performance. The higher efficiency and lighter weight panels at both 80 and 115 w/kg are significantly better than any existing technology presently being used on spacecraft. Because of the high efficiency, the array area becomes smaller thus providing cost savings, since attitude control fuel and drag recovery fuel is saved, and allow better stowage for launch. In addition the "standardized" isogrid panel offers an attractive low cost short schedule solution to smallsat requirements.

Cost projections in the trade studies have shown that the multijunction solar cell cost be slightly higher (15-20%) than the GaAs/Ge cells presently used; however, at the array level, costs will be about 5% less due to the fewer number of cells needed on an array to achieve the same power level. At the overall system level, considering the value of the reduced weight, the cost benefits become very large and can represent cost savings equal to the total cost of the array.

Before satellite designers utilize new advanced technology concepts such as those demonstrated in this program, they need to be convinced that the performance properties are there and that the product is reliable. This usually means that a large enough solar panel be built and environmentally tested to verify the design and provide confidence. The design concepts presented here would be an excellent starting point. We have been in contact with various potential users of this advanced users of there advanced technologies and there is genuine interest in seeing them come into commercialization.

Table 1.0-1 Detailed weight estimates for each design approach

| Performance Summary | Phase II Isogrid Array | Phase II MJ/Mesh Array |
|---|------------------------|-----------------------------|
| cell material | gallium arsenide | GaInP ₂ /GaAs/Ge |
| cell size | 5.5 cm x 6.5 cm | 5.0 cm x 4.9 cm |
| number of cells on panel | 86 | 170 |
| panel size | 64 cm x 55 cm | 50.8 cm x 88.9 cm |
| panel power | 75.1 W | 119 W |
| array weight | .94 kg | 1.04 kg |
| array specific power | 80 W/kg | 115 W/kg |
| Solar Cell Assy Characteristics | | |
| cell material | gallium arsenide | GaInP ₂ /GaAs/Ge |
| cell size | 5.5 cm x 6.5 cm | 5.0 cm x 4.9 cm |
| cell thickness (μm) | 139.7 | 139.7 |
| coverglass thickness (μm) | 100 | 100 |
| % efficiency (28 °C, AM0) | 19% | 22% |
| maximum voltage (V) | 0.86 | 2.03 |
| maximum current (A) | 1.069 | 0.359 |
| maximum power (W) | 0.919 | 0.729 |
| cell weight (gms) | 3.13 | 2.15 |
| Circuit Characteristics | | |
| cells per series string | 43 | 17 |
| strings in parallel | 2 | 10 |
| assembly loss (%) | 4% | 4% |
| diode voltage loss (V) | 0.36 | 0.00 |
| panel output voltage (V) | 35.14 | 33.13 |
| panel output current (A) | 2.14 | 3.59 |
| panel output power (W) | 75.13 | 118.94 |
| Panel Substrate Characteristics | | |
| structure material | graphite epoxy isogrid | Al honeycomb |
| structure thickness | 0.863 cm | 1.27 cm |
| skin (faceplate) material | graphite epoxy plane | graphite epoxy mesh |
| skin thickness | 508 μm | 127 μm |
| weight density (bare) | 1.3 kg/m ² | 0.9 kg/m ² |
| panel area | 64 cm x 55 cm | 50.8 cm x 88.9 cm |
| Panel Mass Analysis (all units in grams) | | |
| <i>Add-On Hardware:</i> | | |
| solar cell | 269.18 | 365.5 |
| CMX coverglass | 71.19 | 95.8 |
| coverglass adhesive | 21.23 | 28.56 |
| circuit interconnects | 12.9 | 17.0 |
| cell adhesive | 27.49 | 37.24 |
| end terminations | 0.8 | 1.6 |
| wire, 26 AWG | 4.57 | 9.14 |
| terminal board | 9.0 | 9.0 |
| spot bonds | 1.2 | 2.4 |
| <i>Insulated Panel Substrate</i> | 457.6 | 406.45 |
| <i>Hinge</i> | 35.0 | 35.0 |
| <i>Growth margin</i> | 30.0 | 30.0 |
| Total Estimated Mass | 940.15 | 1,037.68 |

Figure 2.0-1 The baseline GaAs composite isogrid solar array provides 75 Watts and weighs less than 1 kilogram.

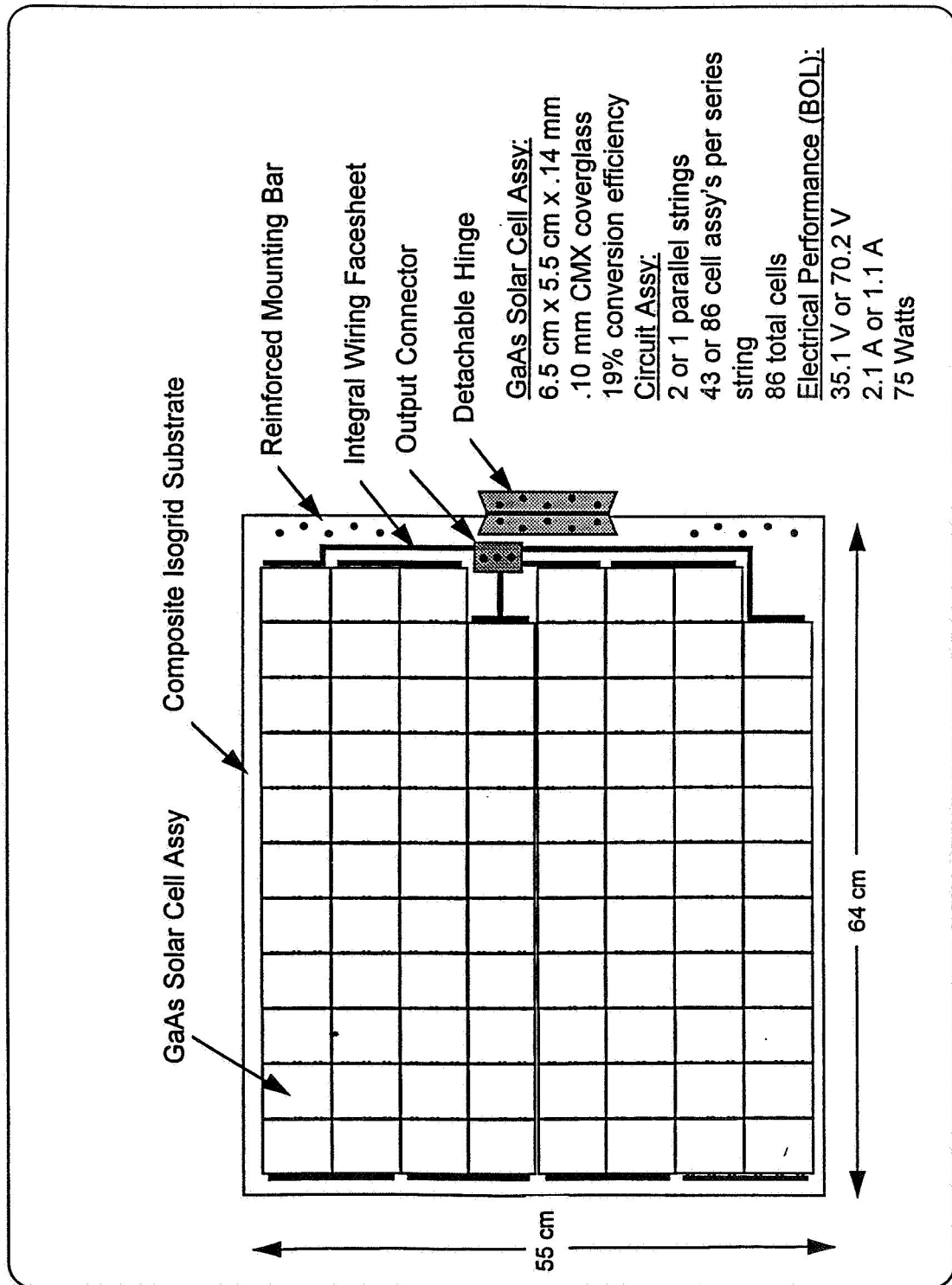


Figure 2.0-2 Proof-Of-Concept GaAs composite isogrid panel coupon measures 38.1 cm on a side

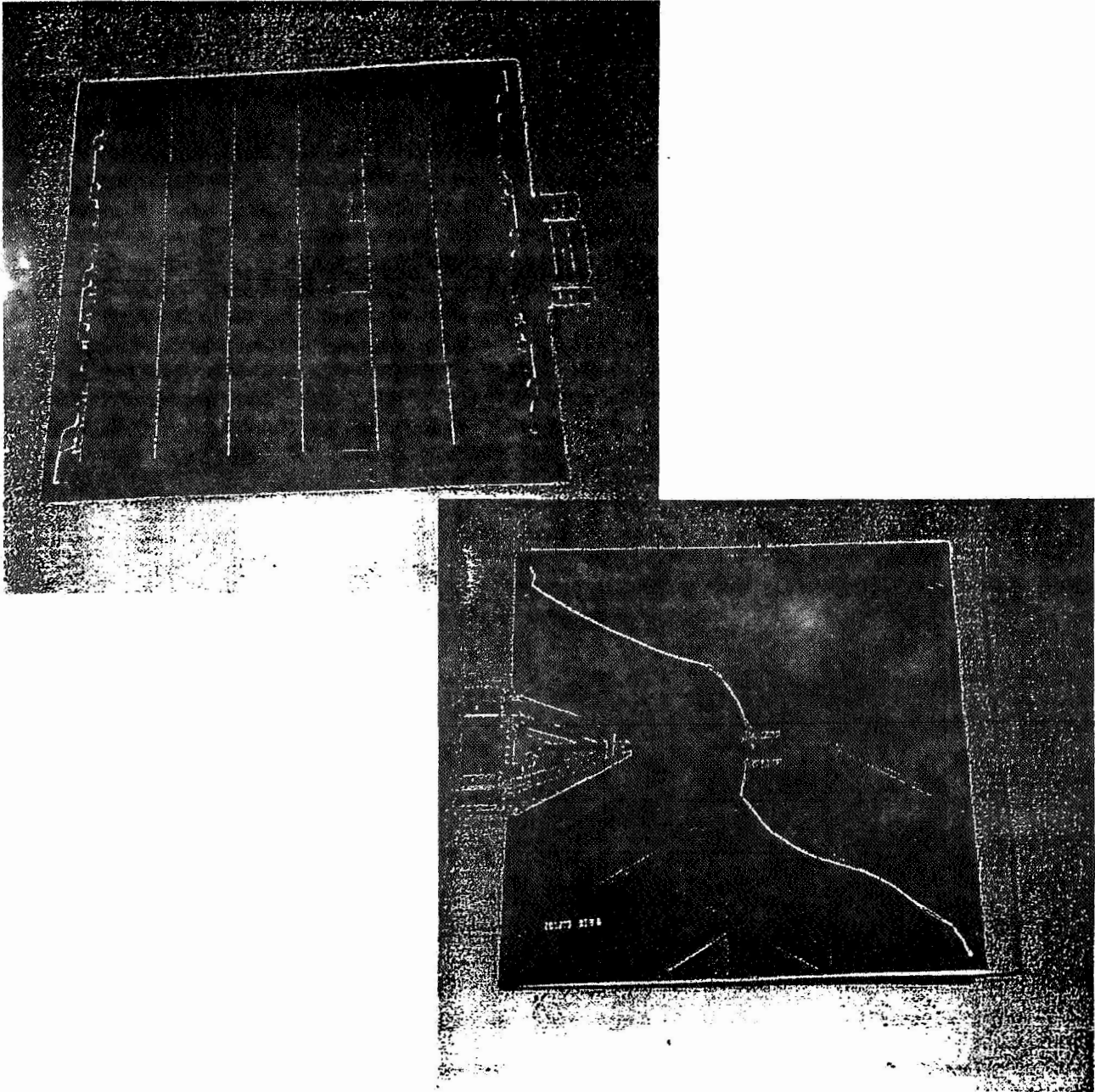


Figure 2.1-1 19% conversion efficiency solar cells are the most frequently produced by current production.

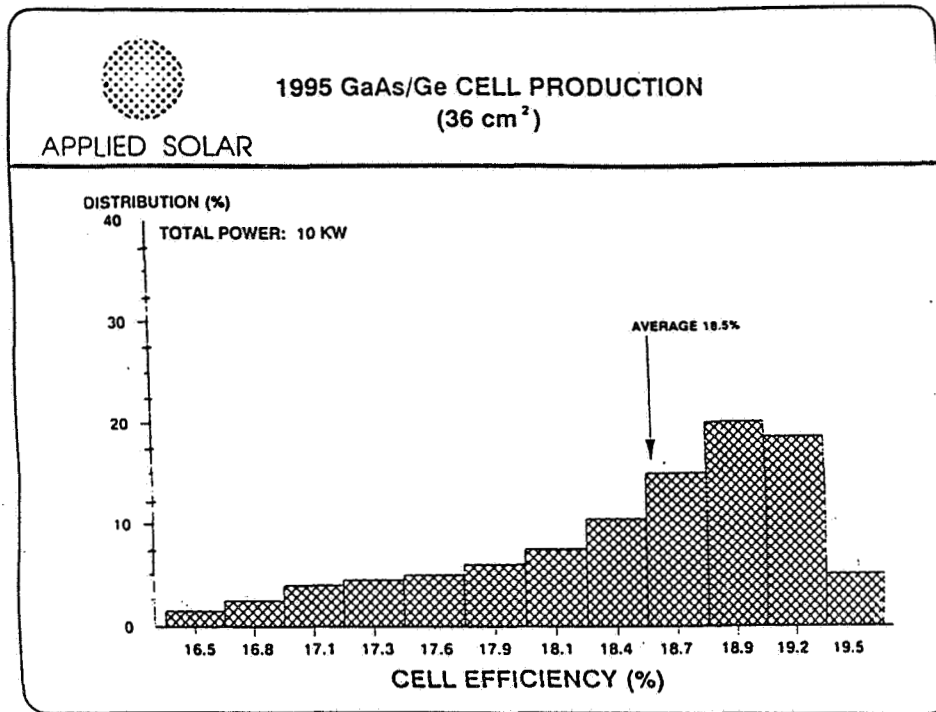


Figure 2.2-1 Composite isogrid array technology uses a low-density triangular structure for high strength and stiffness to weight ratios.

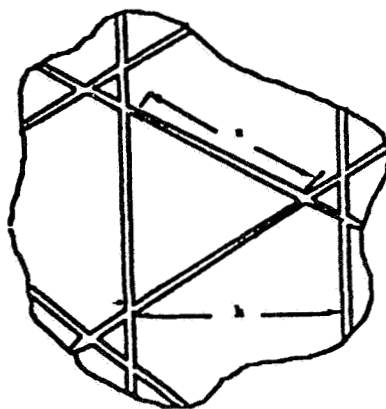


Figure 2.2-2 Panels with edge lengths greater than 50 cm derive the most benefit from composite isogrid technology

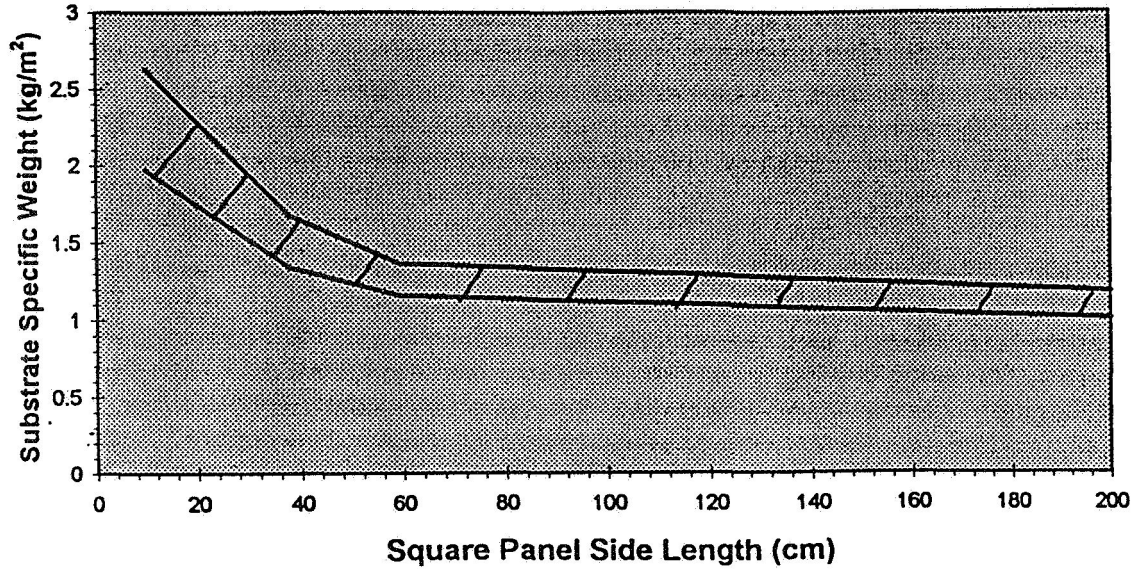
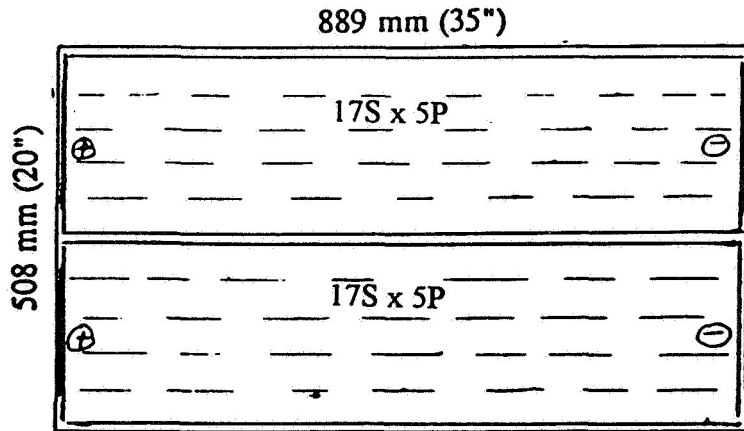


Figure 3.0-1 Multijunction carbon mesh panel provides 115 W/kg



Multijunction Cell Panel

Cell: GaInP₂/GaAs/Ge 2J 22%, 5.5 mil
 5.0 cm x 4.9 cm, 6 mil CMG cover

Panel: 17S x 10P, 170 cells/panel, 119 W at 34 V (AMO 28°C)

Figure 3.0-2 Proof-of-concept 2J-GaAs carbon mesh panel coupon measures 38.1 cm on a side

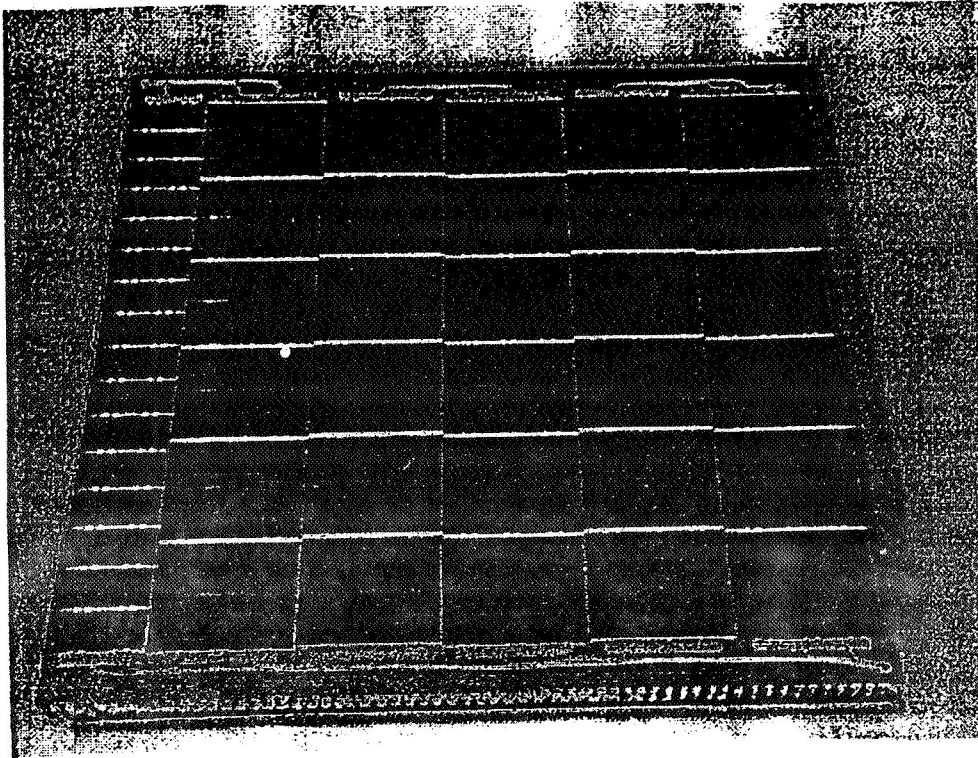
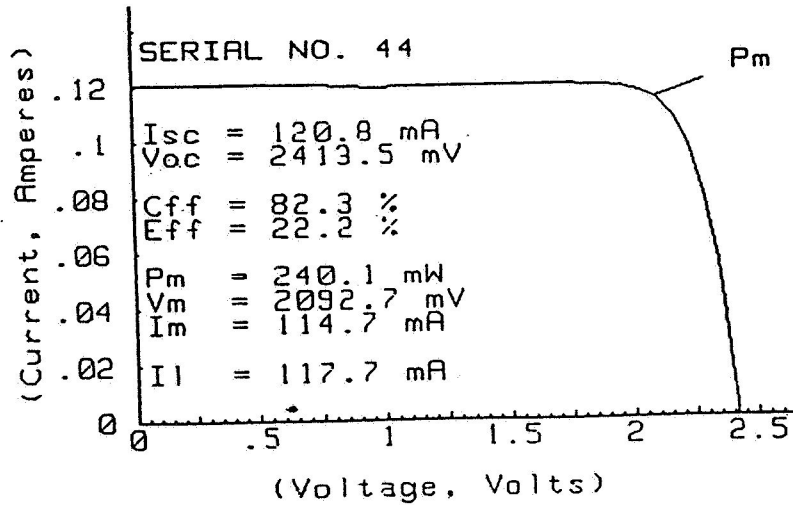


Figure 3.1-1 A 22.2% (Best) 2 cm x 4 cm 2J-GaAs solar cell used on the demonstration coupon



Space Qualification of UV and IR Reflecting Coverslides for GaAs Solar Cells¹

Andrew Meulenberg (301-926-3609)
Consultant
Gaithersburg, MD 20855

S33
IN-50418

ABSTRACT

As part of the space qualification effort for blue-red reflecting coverslides designed for use with GaAs solar cells, the first long-term (3000 hours) UV testing of unirradiated and 1 MeV electron-irradiated GaAs solar cells, with 4 types of multilayer-coated coverslides to reduce operating temperature, has produced some unexpected results. Important conclusions from this study, which includes two parallel tests, are:

- All of the GaAs solar cells with multilayer-coated coverslides display UV degradation. The laboratory data, extrapolated to 10 years in orbit, point to a significant loss mechanism from a combination of absorption and a reduction in optical match in such coatings from this portion of the space environment.
- The effects of contamination in a vacuum system, on the measured degradation in solar-cell short-circuit current during a UV test, depend upon the type of coverslide coatings present on the coverslide surfaces. This has implications for both coated coverslides and optical solar reflectors (OSRs) in space.
- Because of the observed trends in this test and uncertainties in the extrapolation of data for multilayer-coated coverslides, the use of any multilayer-coated coverslides for extended missions (>1 year) cannot be recommended without prior flight testing.

NOTATION

Coverslide Coatings:

| | | |
|-----|---|---|
| ARR | = | antireflecting |
| IRR | = | infrared (IR) reflecting |
| UVR | = | ultraviolet (UV) reflecting |
| BRR | = | blue-red reflecting (UVR on front; IRR on back) |
| DSR | = | double-sided coated coverslides (coating contains both UVR and IRR in the same narrow-band-pass multilayer coating) |
| SSR | = | single-sided coated coverslides (coating contains both UVR and IRR in the same narrow-band-pass multilayer coating) |

INTRODUCTION

Five types of coverslide coatings, designed for GaAs solar cells, have been tested as part of a NASA-sponsored, space-flight qualification for Blue-Red-Reflecting (BRR), multi-layer-coated, coverslides. Covered cells have been tested for degradation from the thermal, solar UV, and radiation environments representative of near-earth orbits. In addition, humidity tests were performed to determine the sensitivity of the multilayer

¹ This paper is based on work performed at COMSAT Laboratories under contract from Goddard Space Flight Center. The final analysis and paper presented here was funded by Hi^x Consultants.

coatings to pre-launch conditions. Coverslides and solar cells were characterized at each step of the test to identify the variation within the components and the reasons for changes observed with each step.

The major concern about any of these coverslides is how will they perform at end-of-mission. Electron irradiation, which alters the spectral response of the solar cells, and UV exposure, which degrades the optical coatings, are the tests most likely to alter the relative merits of the coverslide coatings. The electron results are discussed elsewhere in this proceedings (1) and will only be alluded to here where necessary for completeness. The primary emphasis in this paper is the UV degradation studies and their implications.

A number of unusual results were obtained from this series of tests on coated coverslides for GaAs solar cells. Since such accurate measurements of degradation from extended UV exposure to GaAs solar cells had not been made before, several variations were introduced into the testing to avoid the pitfall of making judgments based on incomplete data. These variations included the UV exposure of both irradiated and unirradiated cells, since silicon solar cells show a further decrease in electrical output when subjected to long-term UV exposure (>1000 hours) after electron irradiation (2). To further extend the effective UV exposure (or accelerate the UV degradation rate), a number of the coverslides were inverted when mounted on the solar cells (to expose the critical multilayer coatings to full UV without the filtering provided by the coverslide which has built-in UV absorption characteristics). The effects of these variations will be described with the data from the tests.

COVERSLIDE AND SOLAR CELL CHARACTERISTICS

The coverslides differ in the manufacturer of the ceria-doped microsheet material (Pilkington CMG and Dow-Corning 0213) and in the types and manufacturer of coatings used. Variations in the results could not be attributed to the coverslide material.

INTELSAT-6 silicon solar cells (designated as I-6) provided a basis for comparison with previous UV degradation studies. These are covered cells of a type that have provided reliable and reproducible UV degradation data over many years. Their coverslides are ceria-doped microsheet (CMS) and are coated with a single-layer AR coating. The cells are coated with a titanium-oxide (TiO_x) AR coating. These cells are more responsive to UV light in the solar spectrum than are GaAs cells and therefore are more sensitive to any UV degradation of the coverslide assembly and/or contamination.

As a baseline for comparison with the multilayer-coated coverslides, standard CMG coverslides, with only an antireflective (AR) coating on the "out" side (designated as ARR coverslides), were included. The next level of complexity is provided by the addition of infrared-reflecting coatings on the backside ("in" side) of AR-coated coverslides. This combination is designated as IRR coverslides.

Three types of multilayer-coated, blue-red reflecting, coverslides (designed for GaAs solar cells) were studied. The simplest of the three replaced the AR frontside coating of an IRR coverslide with a UV reflecting (UVR) coating that compensated for the UV absorption of the ceria-doped microsheet. The UV-reflection edge of the coating roughly matched the UV-absorption edge of the coverslide (~50% at 350 nm). This combination, designated BRR, minimized the loss in solar-cell short-circuit current (I_{sc}) while still providing a significant reduction in solar absorption of the non-useful wavelengths.

The second type of blue-red-rejecting coverslide has a combined UV/IR-reflecting coating deposited only on the front side. This single-side reflector (SSR) has a narrower bandpass than does the BRR coverslide and therefore a lower I_{sc} ; but, it rejects more unusable light. The last type coverslide has identical multilayer UV/IR-reflecting coatings on both sides of the coverslide. This double-sided reflector (DSR) has a somewhat narrower bandpass than does the SSR coverslide, but it rejects more UV and IR light. Unfortunately, it also rejects more usable light in the bandpass region. The absorption and optical mismatch (of the DSR coatings with the adhesive) limits the advantage provided by the greater rejection of both UV and infrared light relative to that of the SSR coverslides. Therefore, even though the SSR coverslides cannot reject as much useless light as the DSR coverslides, they are a better compromise between good cell efficiency and low operating temperature

Figure 1 displays the spectral reflection for the ARR, BRR, and DSR covered solar cells, to indicate the range and nature of the coatings described above. The thermal advantage of the blue-red-reflecting coverslides is significant. Assuming a deployed array and relative to the ARR coverslide, the reduction in cell temperatures for production GaAs cells with BRR and DSR coverslides would be 17°C and 40°C respectively.

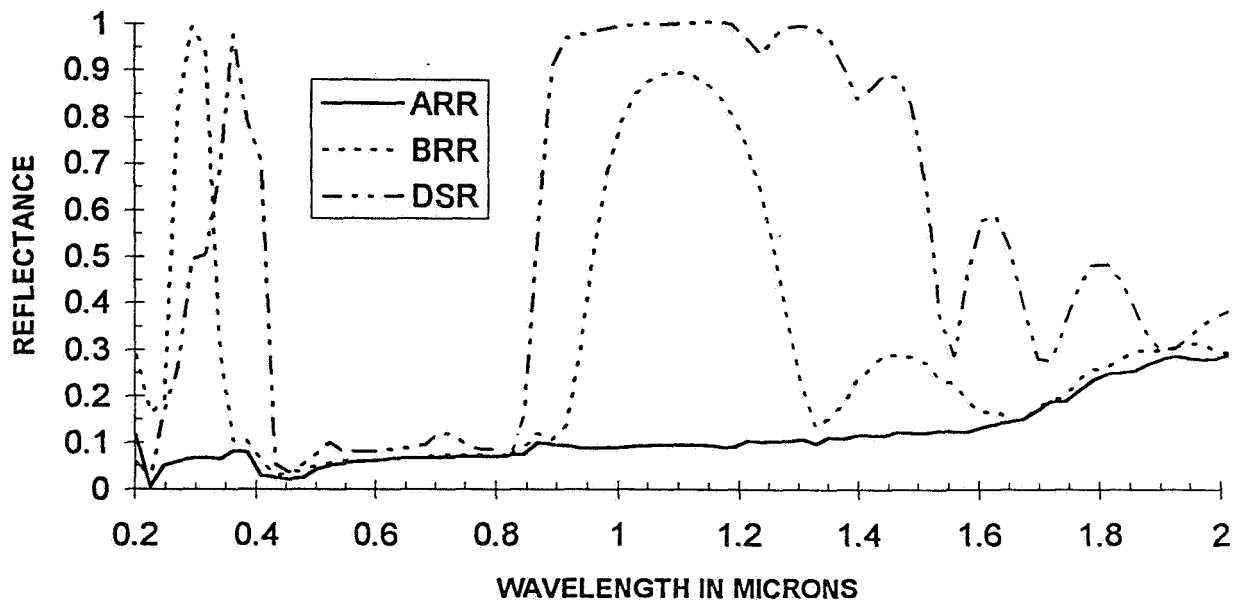


Figure 1. Spectral Reflection of Near-Normally Incident Light From GaAs Solar Cells with Three Different Coverslide Types.

Table I compares the average change in I_{sc} when GaAs solar cells are covered with the 5 coverslide coating types of this test. These covering factors are somewhat higher than the results of a previous test, but the difference is attributed to the solar cells (and perhaps to the fact that, in setting the solar simulator intensity, no GaAs control cells were included to normalize the silicon primary standard cell to the GaAs test cells). Variations in the solar cell AR coatings were recorded, based on color tint prior to covering, and differences in covering factor were observed for the different tints. The cells were sorted and selected to provide each coverslide type with a range of cell tints.

Table I. Percent Change in I_{sc} from Covering of GaAs Cells

| Coverslide | ARR | SSR | BRR | IRR | DSR |
|------------|-----|-----|-----|-----|------|
| % Change | 4.5 | 2.4 | 2.8 | 2.3 | -4.8 |

The difference between the ARR and other coated coverslides is ~2% except for the DSR coverslide which has a too narrowly defined bandpass filter and furthermore has absorption and reflection of light in the usable wavelength region. It is clear that some penalty is paid for the attempt to reduce the infrared light that will heat the cells without providing any electrical energy. The SSR cell covering values are very good, considering the amount of UV and IR that they reflect. The IRR results are disappointing in that their IR reflection is similar to that of the BRR coverslides, but they have no UV reflectors on the front surface.

For reasons described in the Introduction, a set of the coverslides were mounted upside down on the GaAs solar cells. Cells with these inverted coverslides are compared in Table II and can be compared with the correctly mounted coverslides described above (Table I). The effects of optical mismatching are clear and these data are important in understanding the effects of system contamination and UV degradation.

Table II. Percent Change in Isc from "Inverted" Covering of GaAs Cells

| | | | | | |
|------------------------|------------|------------|------------|-------------|-------------|
| Coverslide % Change | ARR 1.5 | SSR 2.1 | BRR 2.0 | IRR -0.8 | DSR -5.0 |
|------------------------|------------|------------|------------|-------------|-------------|

UV DEGRADATION

UV degradation of the various coverslides was determined with two vacuum systems - in parallel, 3000-hour tests to explore several variables. The variables included: coating type and manufacturer; pre-UV exposure to 1 MeV electron irradiation; and, coverslide inversion to determine UV-induced changes in refractive index within the coatings.

Since contamination is an ever-present threat to long-term UV tests, two techniques are used to determine, define, and quantify this contribution to the results. The use of multiple control cells inside the vacuum system, but not exposed to the UV source is the principal technique. Not only do these cells provide a basis for removing systematic variations in the solar simulator, the type of sunshield used gives information on the loss in cell Isc resulting from any contamination. An "external" light shield is placed over part of the large fused-silica window of the vacuum system. This external shield prevents the UV light source from illuminating that portion of the window over a number of the control cells and the control cells underneath the shield. It is removed for electrical measurements with the X-25L solar simulator. An "internal" shield (available on Test 1 only) allows the UV to darken any contamination on the window, but not on the cells. The internal shield is inside the vacuum chamber to cover the control cells not protected by the external shield; but, it cannot protect the chamber window. It is mounted on a vacuum rotary feedthru and swung aside for electrical measurements of the control cells. The internal shield thus provides a long-term measurement of contamination buildup and the rate and extent of UV degradation due to contamination on the window.

The second technique, to quantify contamination in the system, involves the use of a "cleanup" procedure that measures the effect on Isc of cleaning the window and cells individually. This cleanup procedure and results are detailed in Appendix A.

A statistical variation of 0.3% is expected for short term fluctuations in the X-25L and for the measurement system employed in this test. The average, rather than the individual cell values, of the control cells falls within this range, thus indicating longer-term drifts in the solar simulator output intensity or spectrum. Normalization of the test-cell data with respect to the control-cell average will remove this latter effect and multiplicity of cells in each test-cell type and of measurements reduces the short-term statistical variations. The ability of the externally-shielded control cells to remain at the 100% level indicated that, despite the obvious contamination to the window (and the cells) in Test 1, if no UV exposure is experienced, no darkening results.

Test 1 Results

Figure 2 plots the UV degradation results for unirradiated solar cells from Test 1. The figure includes all corrections for the contamination found in Test 1. Assuming that the window contamination is truly represented by the loss in Isc of the internally-shielded ARR cell, we made a linear degradation fit to the data for this cell. This "window-contamination" curve indicates ~4% degradation at 3000 hours. A 0% recovery in Isc, observed in cleaning certain cells at the conclusion of the test(Appendix A), was unique to the UVR-covered cells. In this case, losses from UV darkening of the contamination are compensated by the improved transmission over the usable wavelength range with the addition of contamination between the UVR coating and vacuum. This improvement, which may be provided by the low refractive index of organic contaminant deposited on top of the UVR coating, does not appear with the AR coated coverslides. The correction used for the UVR-coated coverslides (DSR, SSR and BRR) is based on the cleanup data and is slightly more than one half (0.6 times) that for the AR-coated coverslides.

In a study of the normalized averages of the test cells from Test 1 with the proposed contamination contribution removed, validity of the measurement, normalization, and contamination-correction procedures is

indicated by the data of the ARR and I-6 cells. The average of the 4 ARR cells at each measurement point in Figure 2 falls within 0.4% of the 99.8% line (0.998 ± 0.004). If we consider the 3σ value to be $\sim 0.45\%$, then $\sigma_4 \sim 0.15\%$ which is $1/2$ or $1/\sqrt{n}$ of the single-cell statistical variation ($\sigma_1 \sim 0.3\%$), where n is the number of cells in the set. This standard deviation is just what would be expected for the size of the set tested. Fitting the AR covered cell data to a linear degradation curve would bring the standard deviation to $\sigma = \pm 0.2\%$ (± 0.002).

The standard specification for UV tests of silicon cells is that they must display less than 2% degradation after 1000 hours of UV exposure. If no correction for contamination were made, the raw data in this test would clearly fail that requirement. Comparison of the contamination-corrected I-6 cells in Figure 2, with earlier measurements (2), indicates a consistency with their $\sim 2.5\%$ degradation at 3000 UVSH. The I-6 cell data, extrapolated to over 10 years exposure in space (to indicate the expected contribution to array current loss from this mechanism), is consistent with the 4-6% extrapolated degradation observed in many other extended UV tests on this cell type (e.g., References 2 and 3).

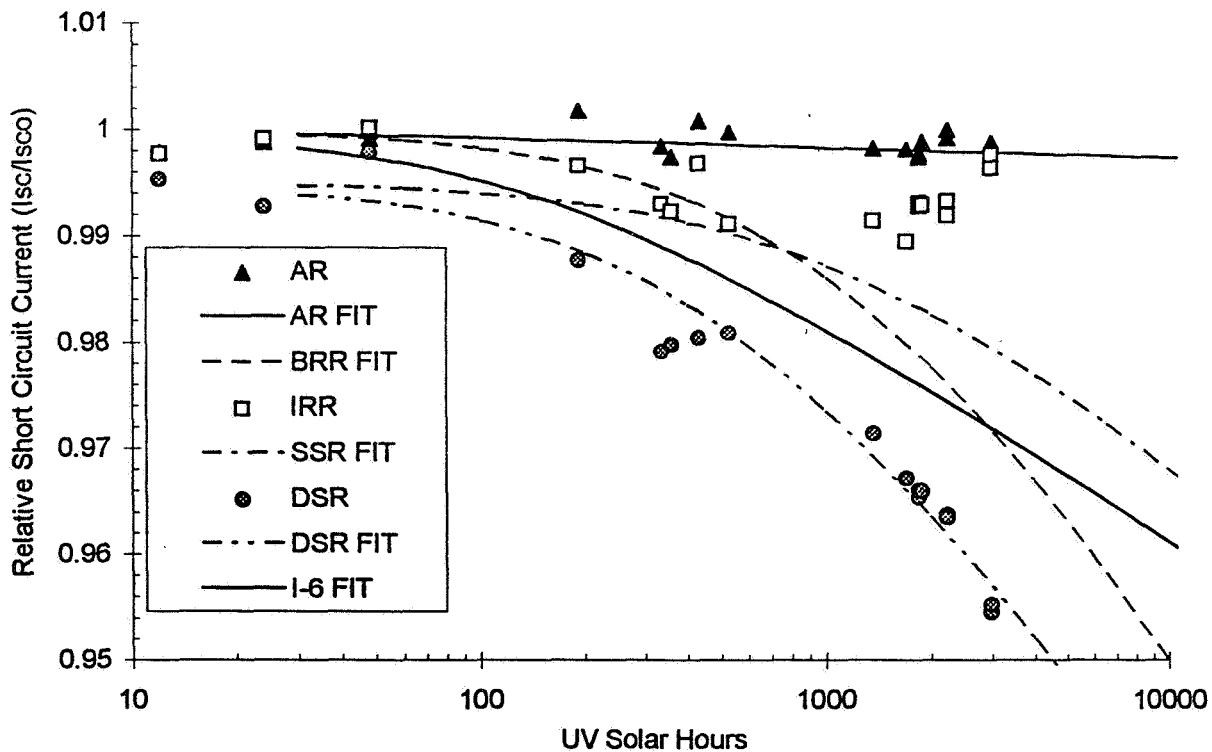


Figure 2. UV Degradation (Test 1) of Isc for GaAs Solar Cells With Various Coverslide Types

The DSR covered cells show the most rapid and greatest UV degradation of the GaAs cells despite their lowest spectral response to UV illumination. Both the SSR and the DSR covered cells displayed a quick drop in Isc of $\sim 0.5\%$ during the early hours of the test. Total degradation of the SSR covered cells (beyond 1000 UVSH) is about one half that of the DSR covered cells, as could be expected for coverslides with UV-sensitive multilayer coatings only on one side rather than two. Extrapolation to 10 years in space indicates about 5% degradation to the SSR coverslides from UV, which is comparable to that expected for silicon cells, but more than the improvement possible from cooler operation with these coatings. Again, extrapolation with multilayer coatings must be suspect.

The BRR cells display the least degradation in Isc of all the multilayer covered cells - - - for the first 1000 UVSH. However, beyond that exposure time the rate increases rapidly and, by the end of the test, their degradation is exceeded only by that of the DSR cells. If normal extrapolation of the data were made to 10 years

exposure, the degradation in Isc would exceed 10%. While such losses seem unlikely, the data gives great concern about use of these coatings in space.

Cells covered with the IRR coverslides show an apparent recovery in Isc with UV and vacuum exposure (~1% after 1000 UVSH). This may be associated with the decrease in Isc observed in these cells before 1000 UVSH, or it may be an independent effect. An early change in refractive index of one layer, which caused a mismatch in the optical coupling, could be matched by a slower change in refractive index of a second layer, which brought back the good coupling and/or increased the transmission through the coverslide. As indicated in Appendix A, a reduction in the contamination correction for the AR coated coverslides would bring the IRR, ARR and I-6 data points down beyond 1000 UVSH. This could be as much as 1% at 3000 UVSH, which would indicate a saturation of the IRR UV degradation beyond 1000 UVSH, rather than a recovery. However, it would also indicate a higher degradation in the ARR and I-6 cells. As mentioned before, the I-6 cells should be more sensitive to degradation from contamination than the GaAs cells; therefore, the contamination correction for these cells should be greater than that for the ARR cells. Such a scenario is self consistent and simplifies the conclusions. It also indicates that the contamination has contributed a systematic error of $\pm 0.5\%$.

The results of the BRR cells provides a warning that a change in refractive index, which may have moderated apparent UV degradation in Isc for hundreds of UVSH, could continue, but to the detriment of these cells. The selection of materials and, probably, the processing of the multilayer coatings could affect the timing and extent of the shifts in UV induced shifts observed in the IRR and BRR coverslides. Furthermore, such changes, observed in all of the multilayer coatings, could have a significant impact on their UV and IR rejection capabilities.

Test 2 Results

The main points of Test 2 are illustrated in Figure 3 with data that includes the final corrections mentioned in the appendix. Most of the cells in this test had their coverslides reversed (indicated in the figure by -r) to determine the effects of filtering the UV light through the coverslide (the DSR coverslides did not change with inversion); therefore, relative values, not absolute values of change are to be considered in the analysis of this figure.

A 1% correction has been made in the initial data points (<1 hr) for the rapid darkening and saturation of that part of the window illuminated by the UV source, and the data are represented by curves, rather than by data points, to remove some clutter. The ARR cell, with coverslide reversed, shows no UV degradation. In this test, the DSR cell shows a higher initial drop than does the SSR cell with the multilayer coating inside. This confirms the Test 1 results that indicate the combined UV/IRR coating clearly has a layer sensitive to UV. The Test 2 DSR results agree with the Test 1 results (within the 0.5% offset from lower degradation in the initial Test 1 data points), thus supporting the choice of contamination correction made in Test 1 for UVR coated coverslides. The lower initial degradation of DSR and SSR Isc in test 1 could be a result of contamination-enhanced optical coupling before UV darkening became significant.

The IRR cell, which showed no initial drop in Isc with the multilayer coating properly placed under the coverslide in Test 1, now displays a 0.5% drop in the first few hours when the coating is exposed directly to the UV. The IRR covered cell, with inverted coverslide, also shows a significantly higher extended UV degradation than the cells with correctly oriented IRR coverslides in Test 1, Figure 2 (~2% vs. 0 - 1% at 3000 UVSH). If this result is a consequence of the unfiltered UV exposure to the multilayer coating, then the implication is that these layers are more sensitive to energetic radiation (UV with $\lambda < 0.35 \mu\text{m}$ or 1 MeV electrons) than to the lower energy UV that passes through the CMG coverslide. This sensitivity to energetic radiation could explain the higher loss in Isc of the IRR covered cells from the electron irradiation than that observed for the GaAs cells covered with other coverslides in the same test[?]. There is also a hint that electron irradiation predisposes the IRR multilayer coating to subsequent UV degradation.

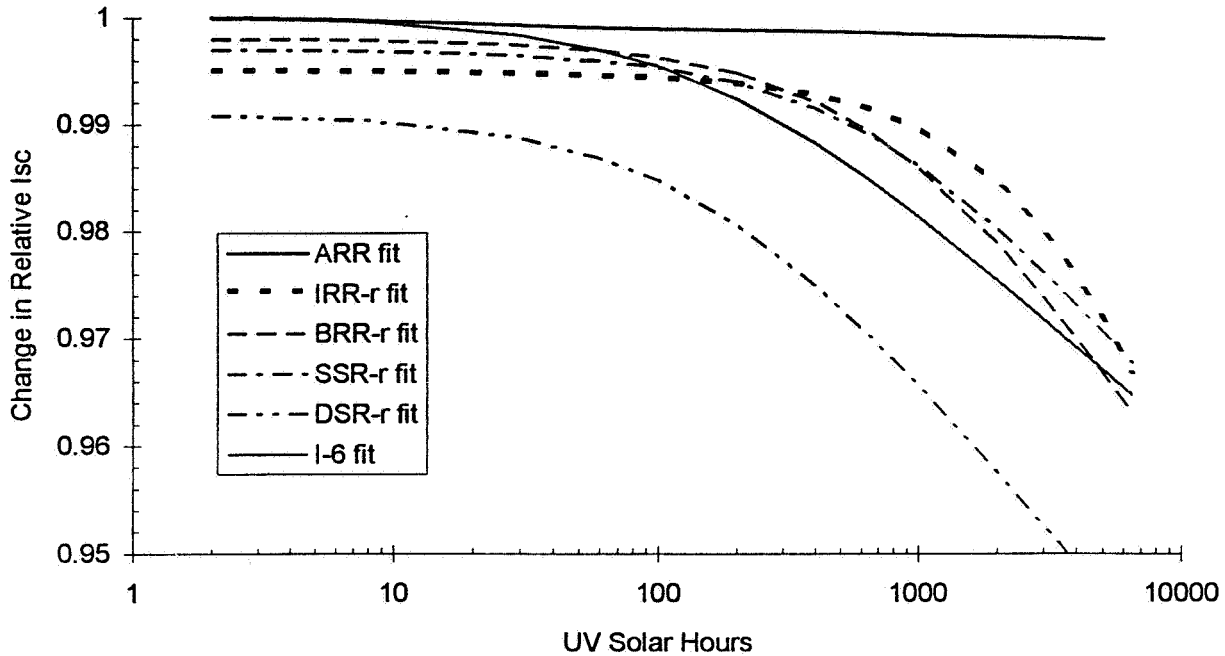


Figure 3. UV Degradation of Reverse-Covered GaAs Solar Cells in Test 2.

The I-6 silicon cell results from Test 2 are included in Figure 3 for comparison with those data in Test 1 and to provide a visual baseline for the GaAs cell results. The curve to fit the Test 2 data is identical to that used to fit the Test 1 I-6 data. This again indicates that the contamination correction for AR coated coverslides made in Test 1 is appropriate.

HUMIDITY AND THERMAL STRESS RESULTS

In addition to the radiation environment testing (electron and UV) performed on the coated coverslides, other standard tests were performed in the space qualification testing of these coverslides. Thermal-cycling tests were of particular concern on the DSR and SSR coverslides since their multilayer coatings introduced sufficient stress in the single-sided coverslides that they bowed; furthermore, slight edge fractures were observed in some of earlier DSR coatings on thicker coverslides.

The cells were heated to 60°C with a flood lamp and then lowered over a liquid nitrogen bath to bring them to -150°C. After this worst-case procedure (to slowly take the coverslide adhesive through the glass point), the cells were dipped in the LN₂ for a slight thermal shock. The cycle was completed with a recovery to 60°C under the flood lamp. The operation took place in a sealed environment to prevent condensation on the cold cells. No visual effects or changes in Isc were observed from this test. No sign of bubbles, blisters, delaminations, or color changes associated with distress in, or caused by, multilayer coatings appeared. Several cells had losses in cell fill factor, which indicated that contacts and/or cell junctions were stressed by the severity of the test. However, no pattern of coverslide type was associated with the losses and such changes are not generally related to coverslides.

The humidity test, which is performed primarily to detect contact corrosion effects, was expected to have no effect on the coverslides or only an effect on the DSR and SSR coverslides which have the multilayer coatings on the outside of the coverslide. Both electrical and reflectance measurements were made on the

covered cells before and after a 1000 hour test with 90% humidity at 50°C. No statistically significant change in the cell Isc was measured. However, the reflectance measurements were quite revealing.

Exterior coatings did change under extended exposure to humidity. The changes are consistent with an increase in refractive index of one or more layers. The changes were smallest for the antireflective and UV reflective coatings of the ARR and BRR coverslides. While the changes in the blue-red-reflecting outer layers of the SSR coverslide were somewhat larger, losses were balanced by gains. The IRR coverslides, with their "buried" multilayer coating, displayed the largest changes in reflectance. Despite a predicted loss in Isc of ~1%, based on the reflectance data, no such loss was measured. The only explanation is that the humidity test changed not just the refractive index of one or more layers of the buried reflector, it reduced their absorption.

DISCUSSION

While variations exist in the individual cells and coverslides of this program and the sample size is small, detailed analysis of the components and combined structures has allowed an understanding of the loss mechanisms to be expected from the space environmental effects. There are several things to consider in the evaluation of coated coverslides.

- Multilayer-coated coverslides do not provide as high a covering factor as AR coated coverslides. The Isc improvement in covering of cells is 1.5 to 3% for multilayer coverslide coatings, if they are good (i.e., low reflection and absorption in the usable wavelength region) and if the cell AR coating is appropriately matched for the coverslide adhesive. The improvement for coverslides with AR-coatings-only is in the 3.5 to 4.5% range for similar conditions.
- Multilayer coatings may be degraded by either particulate (electrons and protons) or UV radiation. Since the coatings consist of different materials with different refractive indices, an individual layer may change with either or both radiation types. The presence of particulate damage in a layer may increase its sensitivity to UV damage. Since multiple layers of widely varying refractive indices are desired for these coatings, the task of finding materials that are insensitive to radiation or that respond in such a manner as to maintain their proper relationship is more difficult than that for a single layer.
- This interdependence of the coating effectiveness on the different layers means that exposure to damaging radiation can cause either improvements or degradation in the transmission of useful light. Furthermore, the dominance of either effect can change with time. Absorption effects are always deleterious and therefore predictable; refractive index changes are neither. Thus, extrapolation of experimental UV degradation data for multilayer-coated coverslides and cells becomes much less certain, if not impossible.
- Thermal improvements in solar-array power performance from multilayer coverslides can vary from 3 to 8% depending on the nature of the reflectors and the extent of light rejection. Subtracting the difference in covering factors from the thermal gain significantly reduces the beginning-of-life improvement. Thus, a 1 - 4% net improvement in beginning-of-life array performance is a more reasonable estimate for the coatings being tested.
- The UV-plus-electron degradation of GaAs cells with multilayer-coated coverslides appears, from this study, to be on the order of 2-4% for one year in space and 3-9% for 10 years (87600 hours) in space (compared to the 1-4% net improvement B-O-L from above). This means that after one year in a space radiation environment, the multilayer coated coverslides may not have any advantage over a simple AR-coated coverslide. The uncertainty in the extrapolation to 10 years is greater than the improvement possible with the multilayer coatings. However, beyond one year, the potential for serious losses relative to AR-coated coverslides is high. The thermal improvement is somewhat less for the IRR coatings; but, the uncertainty in extrapolating data appears as large as that for the other multilayer-coated coverslides and variations within the individual coverslides and cells of a small dataset in this test are too large to predict any net benefits for this coating for extended missions, even in a radiation-free environment.
- The cost of the coatings is not inconsequential. Nevertheless, the savings from use of these coatings for short missions that are power and/or array-size limited could be considerable.

Conclusion: Because of the observed trends and the uncertainty in extrapolation of data, the ability of multilayer-coated coverslides to benefit extended missions (>1 year) is doubtful. The cost of reducing the level of uncertainty must be weighed against the potential benefits for a particular application.

Of the five coverslide types studied in this program, the IRR coated coverslides provided the most surprising results. The measured sensitivity of these IRR multilayer coatings to specific outside influences explains a number of observations made during this report:

- The IRR coverslides initially displayed greater absorption than expected.
- The solar-cell-covering factor was lower than that for the comparable BRR and SSR coverslides
- Degradation in Isc from electron irradiation was higher for the IRR covered cells than for any others
- The degradation of correctly-mounted IRR coverslides on unirradiated GaAs cells displayed unusual behavior with UV exposure over time. No consistent trend was observed, although the overall losses in Isc from UV were small (<1%). UV degradation of a cell with "inverted" IRR coverslide was more consistent (nearly linear with exposure) and on the order of 2% after 3000 UVSH.
- While the other multilayer coatings displayed minimal changes from extended exposure to humidity and heat, the IRR coatings showed major changes in reflectance and, probably, in transmittance.

Conclusion: Whether the humidity and energetic-radiation (1 MeV electrons and UV < 350 nm) sensitivity of the IRR coated coverslides is characteristic of the materials used, or of the batch of coverslides that we received, we cannot tell. Furthermore, the observations are from a limited database (single cells in some cases). Nevertheless, an internally consistent picture has evolved from a data set that initially engendered significantly less confidence than that provided from the other coverslide sets in the test.

REFERENCES

1. A. Meulenber, "Photo-Recovery of Electron-Irradiated GaAs Solar Cells," Proceedings of the 14th Space Photovoltaic Research and Technology Conference, NASA /LeRC, Cleveland, OH, October 24-26, 1995
2. A. Meulenber, "UV Testing of INTELSAT VII, VIIa, and VIII Solar Cells," Proceedings of the 13th Space Photovoltaic Research and Technology Conference, NASA /LeRC, Cleveland, OH, June 14-16, 1994
3. A. Meulenber, "UV Testing of Solar Cells; Effects of Anti-Reflective Coating, Prior Irradiation, and UV Source," Proceedings of the 12th Space Photovoltaic Research and Technology Conference, NASA /LeRC, Cleveland, OH, 1992

APPENDIX A: CLEAN-UP PROCEDURES AND RESULTS

Test 1

The Post-UV Clean-up Procedure is critical to understanding the source and effects of any contamination that might interfere with correct interpretation of the test results. The first step after the UV exposure is terminated is to measure the cells several times over the next few days to determine the existence any light effects such as UV "bleaching" of the coverslides, adhesives, coatings, or contamination. If none of these effects occur, the repeated measurements provide a good statistical base for this endpoint of the UV test and for the beginning of the cleanup procedure. A backfill with dry nitrogen provides a basis for any purely vacuum effects. Exposure to air provides information on the effects of oxygen and humidity on the measured degradation. Removal of the window for cleaning provides the first measurements of the cells, without window, since before vacuum. The clean window is replaced to measure the effects of cleaning contamination from its inner surface. The window is removed again and the cells are cleaned. A comparison with the prior readings without window gives a measure of the cell surface contamination. Final measurement of the cleaned cells, behind a cleaned window, gives a true measure of the effects of contamination.

Figure A-1 shows the effects of the cleanup procedure on the Test 1 solar cell short-circuit currents. These data are normalized relative measurements [i.e., $(I/I_0) / (I_S/I_{S0})$] with the initial values measured at the beginning of the UV test with the cells at 40°C and under vacuum. Within the statistics ($\sigma_1 \sim 0.003$), there is no recovery from exposure to nitrogen, air, or normal humidity (measurements 1 through 7). Comparison of measurements 10 and 11 (with a clean window) to measurements 1-7 in Figure A-1, indicates a recovery of 0.025 - 0.03 (2.5 - 3%) from cleaning the window alone. Comparison of measurements 8 and 9 (contaminated cells) with 12 - 17 (cleaned cells) indicates a somewhat smaller effect ($2 \pm 0.5\%$) from cleaning the cells for 3 out of the 6 coverslide types.

Three coverslide types show no effect of the cleaning procedure. (Remember that all cells in both figures are in the same test chamber and randomly arranged.) The difference between the coverslide coatings is the only possibility. The coverslide types that do not change with cell cleaning in Figure A-1 have UV reflecting coatings and those types without UVR coatings do change. The explanation must be that contamination on the coverslide UVR coating provides an improved optical match, which increases the light transmission into the coverslide. Removal of the contamination reduces absorption losses, but increases the reflection by roughly the same amount. Contamination on the vacuum chamber window does not seem to alter the optical coupling through the window into the cell assemblies. Although such an effect could explain the difference between changes from cleaning the window and cleaning the AR coated cells, only the difference in optical coupling resulting from UV damage would appear in Figure A-1 since the data are normalized against control cells which are not exposed to UV illumination.

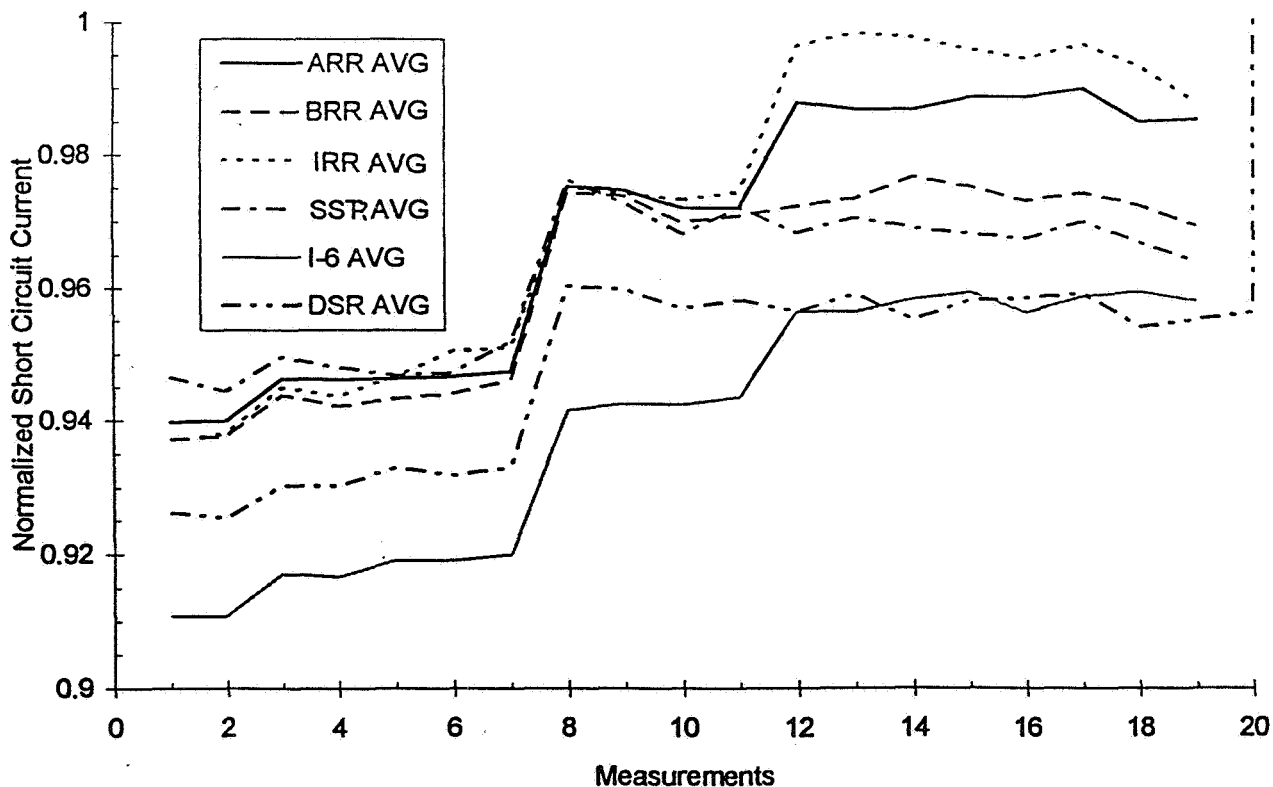


Figure A-1 Change in Normalized Isc for Test 1 Cells during Post-UV Exposure to Dry Nitrogen (3), Air (5), and Window (8) and Cell (12) Cleaning Procedures

The Test 1 results (from the cleanup procedure) indicate that the I-6 and DSR covered cells experienced ~4% degradation of Isc from UV; the SSR and BRR covered cells degraded by, ~3% the ARR covered cells degraded by ~1%, and the IRR covered cells degraded by 0.3 - 1%. If the 0.5% recovery (seen in points 1 through 7) is in the coverslides, not the contamination, then the above values would be increased by this amount.

If the control cell values are low by 1%, then all of the above values would be reduced by 1% and the results would better fit the corrected data in Figure 2. Conversely, if the contamination correction factor for the AR coated coverslides were reduced (e.g., by 1% at 3000 UVSH), the ARR, IRR, and I-6 degradation in I_{sc} in Figure 2 would be increased by 1% at 3000 UVSH and agreement with Figure A-2 would be complete, except for the BRR cells. This only disagreement is then resolved by noting a different annealing rate for the BRR and SSR cells in Figure A-2.

Test 2

The Test 2 cleanup analysis, based on Figure A-2, is similar to that for Test 1, but the results are quite different. Comparison of the cells before and after cleaning the window (measurements 1-5 vs. 9 and 10) shows a bigger effect on the control cells (~0.5% increase in I_{sc}) of cleaning the window than on the test cells. Therefore there is no contamination in Test 2.

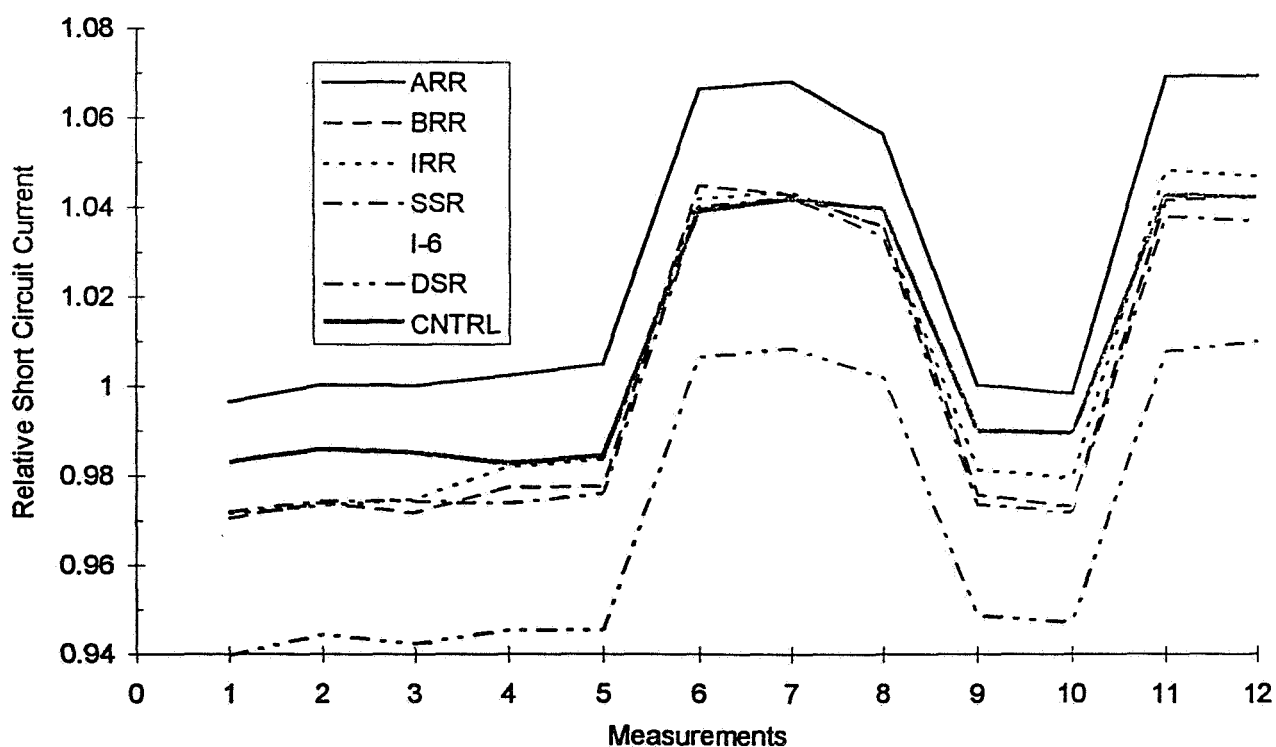


Figure A-2 Change in Relative I_{sc} for Test 2 Cells during Post-UV Exposure to Dry Nitrogen (2), Air (4), and Window (6) and Cell (11) Cleaning Procedures

A second point of interest is the fact that the test cells display a greater than 6% effect of removing or adding the window to the system. Why is this greater than the 5% observed in Test 1 or even than that observed in the control cell data for Test 2? The explanation has to do with the quality of the fused-silica windows. If the window darkens somewhat and saturates quickly (with exposure to UV) and then recovers slowly (with time in the dark and air after the UV test is over) then the above effect is explained. Furthermore, the 1% drop in normalized I_{sc} (test cell data relative to the control cell data) seen at the beginning of Test 2 in the raw data (not shown) would be explained and is now correctable. The slow recovery with time fits the data of Figure A-2, which indicates that no recovery in the test-cell data has occurred during the day of the cleanup procedure.

ONE YEAR OF FLIGHT DATA FROM THE PASP PLUS EXPERIMENT

Henry Curtis
NASA Lewis Research Center
Cleveland Ohio

Dean Marvin
Aerospace Corp.
Albuquerque NM

534
IN-50419

ABSTRACT

Results from the first year of operation of the PASP Plus flight experiment are given. The experiment consists of sixteen individual solar cell modules on twelve different panels. Both planar and concentrator technologies are represented as well as several different cell types. The orbit is 363x2552 km at an inclination of 70 degrees. There are two main purposes of PASP Plus, 1) to determine the interactions between the space plasma and solar arrays biased to plus or minus 500 volts, and 2) to determine the long term radiation performance of a wide variety of solar cell types.

INTRODUCTION

The PASP Plus (Photovoltaic Array Space Power Plus diagnostics) experiment is a photovoltaic flight experiment flying on the Air Force satellite APEX (Advanced Photovoltaic and Electronics Experiment). The satellite was launched on a Pegasus vehicle on Aug. 3, 1994. APEX is in an elliptical orbit with an initial apogee of 2552 km and a perigee of 363 km. The inclination is 70 degrees. This orbit puts the spacecraft in a wide variety of plasma environments and is high enough so the spacecraft receives a significant radiation dose.

The two main purposes of PASP Plus are to determine the interactions between high voltage arrays and the space plasma, and to determine the radiation degradation characteristics of a wide variety of solar cell types. Several of the individual modules are biased at various times at voltages up to plus or minus 500 volts. Arcing rates and leakage currents are monitored during biasing. Radiation damage characteristics are determined by continuous monitoring of I-V data for all the solar modules.

The purpose of this paper is to present the results of the first year of photovoltaic data for the PASP Plus experiment. Cell performance and module thermal performance will be discussed. Comparisons will be made with predicted (AE8 & AP8) cell degradation. On Aug. 11, 1995, after 373 days of operation, the experiment ceased to operate. In all probability, there will be no data beyond the 373 days.

PASP PLUS DESCRIPTION

The PASP Plus experiment consists of twelve photovoltaic panels containing a total of sixteen separate cell modules. Two of the modules are concentrators while the rest are planar. Table I lists the different solar cell modules. There are several different cell types on PASP Plus including silicon, GaAs, InP, amorphous silicon, AlGaAs/GaAs, GaAs/CIS, and GaAs/GaSb.

As noted in Table I, not all of the modules are biased. Ten of the individual modules are biased as part of the plasma interactions experiment. There are three panels with more than one individual module. Module #'s 0, 1, and 2 are all 2x4 cm silicon cell modules on the same panel, while numbers 4 and 6 are GaAs modules on the same panel. The other panel with two modules is the GaAs/CIS panel with two (12 and 13) mechanically stacked modules. Eight of the modules are on a deployed spacecraft panel (0 thru 7), while the other eight

modules are on the top payload shelf of the APEX spacecraft. Both the deployed panel and the payload shelf are pointed toward the sun.

Table I PASP Plus Individual Cell Modules

| <u>PASP + #</u> | <u>Cell Type</u> | <u>Array Type</u> | <u>Bias</u> | <u>Cells</u> | <u>Cover</u> |
|-----------------|---------------------|-------------------|-------------|--------------|--------------|
| 0 | Silicon 2x4 cm | Planar | No | 20 | 6 mils |
| 1 | Silicon 2x4 cm | Planar | Yes | 20 | 6 |
| 2 | Silicon 2x4 cm | Planar | Yes | 60 | 6 |
| 3 | Silicon 8x8 cm | Space Station | Yes | 4 | 5 |
| 5 | Silicon 2.6x5 cm | APSA | Yes | 12 | 2.5 |
| 4 | GaAs 4x4 cm | Planar | Yes | 20 | 6 |
| 6 | GaAs 4x4 cm | Planar | Yes | 12 | 6 |
| 8 | GaAs 4x4 cm WT | Planar | Yes | 4 | 6 |
| 11 | GaAs 4x4 cm | Planar | Yes | 8 | 6 |
| 9 | Amorphous Si 4x4 cm | Planar | No | 1 | 20 |
| 10 | InP 2x2 cm | Planar | No | 10 | 6 |
| 7 | AlGaAs/GaAs | Planar | No | 20 | 24 |
| 12 | GaAs/CIS 2x2 cm | Planar | No | 9 | 2 |
| 13 | GaAs/CIS 2x4 cm | Planar | No | 3 | 2 |
| 14 | GaAs concentrator | Cassegrainian | Yes | 8 | |
| 15 | GaAs/GaSb | Mini-Dome Conc. | Yes | 12 | |

Two of the modules are samples of flexible arrays, Space Station and APSA. Both of these modules are mounted on the deployed panel over a corresponding opening in the panel. This allows these two modules to operate not only with the top surface of the array exposed to the environment, but with the back side also open to space. The APSA module is designed to operate in a GEO orbit, hence a thin layer of germanium was applied to the thin film substrate of the module for atomic oxygen protection. The Space Station module is already designed for LEO operations and the atomic oxygen environment.

In addition to the photovoltaic modules, PASP Plus has several diagnostic instruments onboard to measure the environment through which the spacecraft is flying. Other instruments are used to determine the interactions between the plasma and the biased modules. A Langmuir probe is used to measure the space plasma properties; a dosimeter measures the radiation environment in several energy bands; and a set of quartz crystal micro-balances and calorimeters are used to determine the contamination effects. A transient pulse monitor, an electrostatic analyzer and an electron emitter are used in the plasma interaction portions of the experiment.

RESULTS

Three hours after the launch of the APEX satellite, the PASP Plus experiment was turned on. The experiment is programmed to take one I-V curve every 30 seconds. Hence after eight minutes, all 16 modules have been sampled. The process then repeats itself. This could lead to 1.05 million I-V curves per year if the controller was operational at all times. However there were periods of non-operation for the PASP Plus experiment. There was one very long period from Nov. 4, 1994 to Jan. 14, 1994 (70.8 days) where the controller was turned on only a few times for about 15 minutes. The spacecraft was having problems with the battery charging circuits and all loads were turned off. There were eight other smaller down periods ranging from one to 5 days. Total down time for all periods longer than one day was about 91 days.

All the performance data presented in this paper has been corrected for the variations in the Earth-Sun distance (I_{sc} & P_{max}) and corrected to the average temperature of the first month of I-V data. Temperature coefficients were obtained from ground tests of the PASP Plus experiment in the Boeing Test Chamber in Kent Washington. It was decided to use ground measurements of the temperature coefficients because of the 5-6% variations in flight values of I_{sc} and P_{max} due to albedo effects. (Ref. 1). Figure 1 shows the temperatures for each of the panels that the data were corrected to. For most of the module performance data that follows, I-V curves were taken from data files at approximately two hour intervals. Hence about 12 I-V curves for each day for each module are included. This is stretched a bit for the times when the PASP Plus experiment is off and for times when eclipses occurred. In an effort to smooth out the albedo effects, data are averaged for 25 consecutive points which leads to a data point on the plots about every two days. For most of the data charts that follow, there are 98 points plotted representing over 2400 I-V curves.

The orbit of PASP Plus leads to 4576 revolutions during the first year of flight. Of these, 3537 involved eclipses while 1039 were all sun revolutions. Slightly more than 80% of the first year was spent in sunlight. Since the apogee (2550 km) touches the radiation belts, we have a significant radiation dose. Calculations using AE8 and AP8 indicate an equivalent fluence of $9.7E14$ 1 MeV electrons for a silicon cell with 6 mil covers and 60 mil back shielding. This is for one year and is dominated by protons.

Figure 2 shows normalized P_{max} for three different modules, silicon, GaAs, and InP. They all have six mil coverglasses and thick back shielding. This leads to a direct comparison of the three cell types in a proton dominated orbit. Note the significant differences between the three cell types. InP has degraded to about 92% of its original value while GaAs and silicon have dropped to 87% and 82% respectively. This indicates a distinct trend for InP to be a cell for use in high radiation orbits. How high a radiation orbit? If the data from figure 2 is plotted on a cell efficiency basis where silicon starts at 14%, GaAs at 18.5% and InP at 17.5%, the crossover between GaAs and InP occurs between 6 and 12 months. Hence for missions with radiation doses larger than about one year of the PASP Plus orbit, InP becomes more attractive.

The data in figure show a variation which is due to sunlight reflected off the Earth onto the solar modules. The best way to eliminate this albedo effect is just to plot data when the satellite has no view of the Earth. Hanscom AFB has supplied CD-ROMs with PASP Plus data along with orbital parameters and Sun and spacecraft position vectors. This allows us to chose data as a function of how much of the Earth is viewed. Figure 3 shows P_{max} for Module 0 (Silicon) for albedo free (clear view) data only. Note that the variation are gone and that clear view data is only available during part of the mission due to the orbit. Data with albedo for the same module is plotted in figure 4. Here, all the data is when the satellite is between 40 and 50 degrees out of a clear view position. Note that the variations of about 6% are clearly evident and comparison of figures 3 and 4 show that the albedo free data is at the lower edge of the data with albedo.

The clear view data obviously better represents the actual performance of the module however there is no early data. The first clear view data point is at 26 days into the mission. This makes it difficult to obtain an accurate initial flight value. However we do have a predicted curve based on the actual orbital parameters, AE8 and AP8, and the known relative damage coefficients. Therefore fitting the predicted curve onto the clear view data should give us an accurate initial value. Figure 5 shows some problems in this approach. Here we have plotted the clear view data with two "predicted" curves. The lower curve is based on the AE8 and AP8 models. It dramatically overstates the degradation. The upper curve, labeled "half", is the AE8/AP8 curve with the degradation cut in half. This is not mathematically correct but it does indicate the magnitude of the difference. For all cases where good damage coefficients are available, a similar pattern occurs. AE8 and AP8 overstate the degradation by about a factor of two. At the time of this conference, this problem is under active investigation.

For the remainder of this paper we will use the data with the albedo effects included. Data with albedo effects are available for the entire mission (clear view data for the entire mission will be available in the future). Figure 6 shows P_{max} for the two flexible array modules, Space Station and APSA. As noted before both of these modules are open on the back to the space environment. After one year there is significant degradation in both modules with the thin cell silicon (2.5 mils) APSA module degrading somewhat less than the thick cell silicon (8

mils) Space Station module. Even though Space Station has somewhat more shielding, the inherent radiation hardness of the thin cells is evident. It must be noted that both of these arrays are designed for operation in orbits with much less radiation.

The I-V parameters for the Mini-Dome concentrator module are shown in Figure 7. The degradation in Pmax is only about 7% for the entire year, showing the effects of the shielding of the concentrator. The drop in Isc is only 4% for a module which should be very sensitive to contamination. This, as well as data from contamination monitors indicates a negligible amount of contamination. The concentrator only sees incoming radiation within a small cone hence there are no albedo effects for this module. Figure 8 shows the off-pointing performance of the Mini-Dome concentrator. Usually the spacecraft was pointed towards the sun so well that off-pointing data was difficult to obtain. There were enough available instances to generate the data in figure 8. The module retained 90% of its current out to about 3.5 degrees off normal. This agrees quite well with a predicted value of 4 degrees.

Data for the amorphous silicon module are shown in Figure 9. There is a significant drop in Pmax caused to a large part by a drop in fill factor. Isc and Voc are each down a little over 11%. Much of the degradation is explained by the Stabler-Wronski effect but since this is a triple junction amorphous silicon cell, there may be some current mismatch effects. The cell had a 20 mil cover so radiation damage should be small. In figure 10, the data for the mechanically stacked GaAs/CIS module are shown. The drop in Pmax is about 8% with very little change in fill factor. This is a low degradation for such a thin cover (2 mils). The very thin GaAs cell (CLEFT) and the mechanically stacked configuration should both help reduce degradation.

During the course of the PASP Plus mission, temperatures were obtained on a continuous basis. Figure 11 shows the temperature for the panel with the three silicon modules. Each of the four dates is during a no eclipse period. Note the general increase in module temperature for the first few months. This occurred for all modules. After 5-6 months the temperatures stabilized. We attribute this increase to a darkening of the Z-93 thermal control paint on the PASP Plus Deployed panel and payload shelf where the modules were mounted. This is confirmed by the steady temperatures with time on the APEX solar panels which had no Z-93 paint.

CONCLUDING REMARKS

The PASP Plus flight experiment has completed over one year (373 days) of successful operation. Several items of interest are evident in the data.

- 1) AP8 and AE8 are overestimating the amount of damage the PASP Plus modules are receiving. The elliptical orbit is proton dominated and scrapes the bottom of the radiation belts. Further work is ongoing in this area.
- 2) InP cells have a much better radiation resistance than GaAs or silicon cells in a proton dominated orbit.
- 3) The APSA module is flying with some cracked covers and cells and is performing quite well.
- 4) The modules exhibited about a ten degree temperature rise during the first few months of the mission due to darkening of the Z-93 thermal control paint.
- 5) The Mini-dome concentrator module performed very well with minimal radiation degradation and an as expected off-pointing performance.

REFERENCE

- 1) H. Curtis, M. Piszczor, P. Severance, D. Guidice, & D. Olson, Early Results from the PASP Plus Flight Experiment, First World Conference on Photovoltaic Energy Conversion, Dec. 1994, pages 2169-2172.

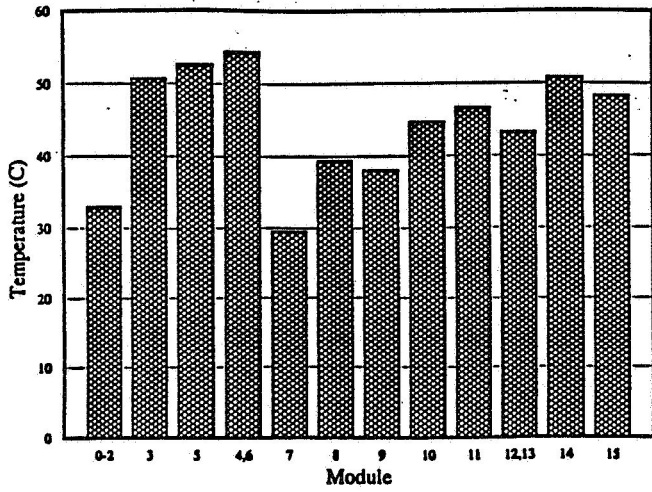


Figure 1. Temperatures for each panel during first month of operation.

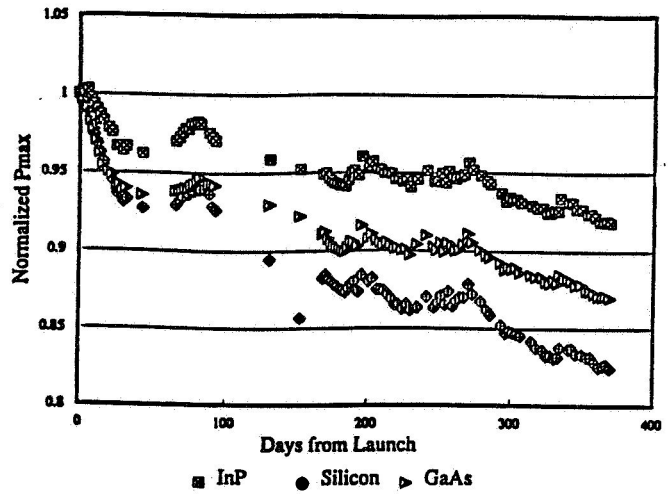


Figure 2. Normalized Pmax for InP, GaAs, & Si, 6 mil covers—thick backs.

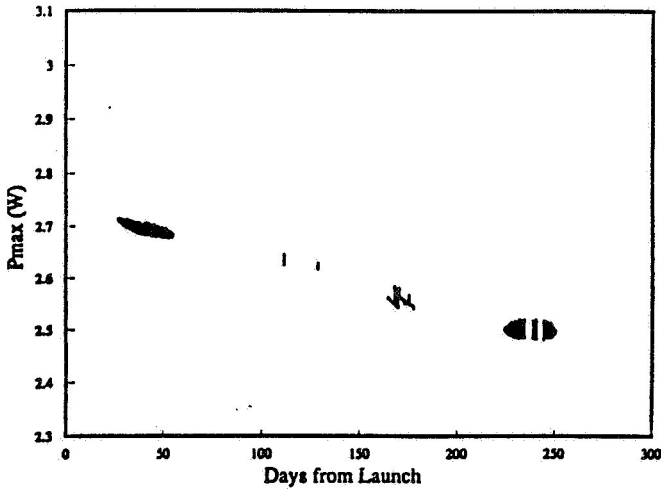


Figure 3. Pmax (clear view) for silicon module #0.

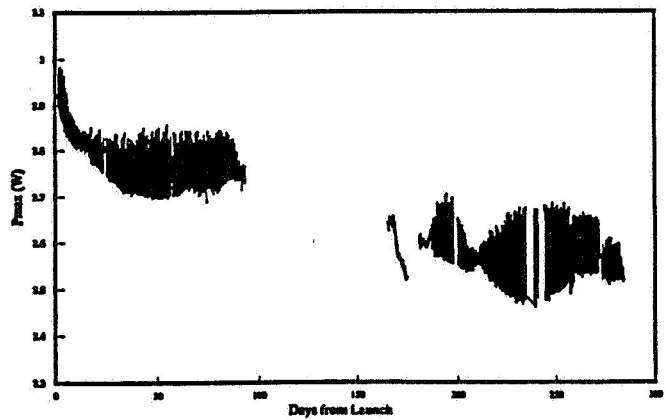


Figure 4. Pmax for silicon module #0, (40-50 degree view).

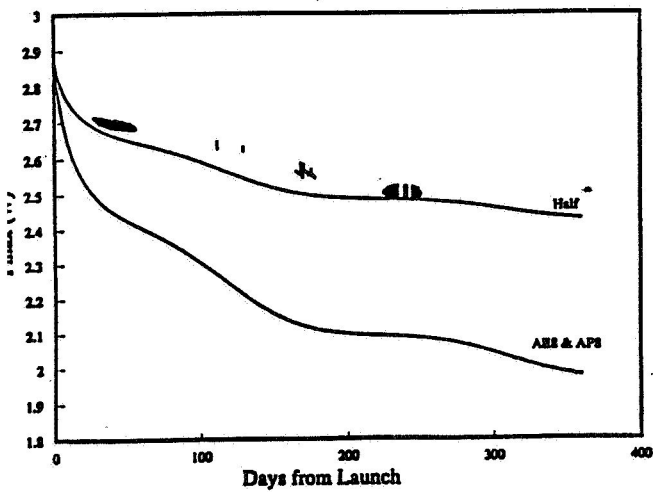


Figure 5. Pmax (clear view) for silicon module #0 with predicted curves.

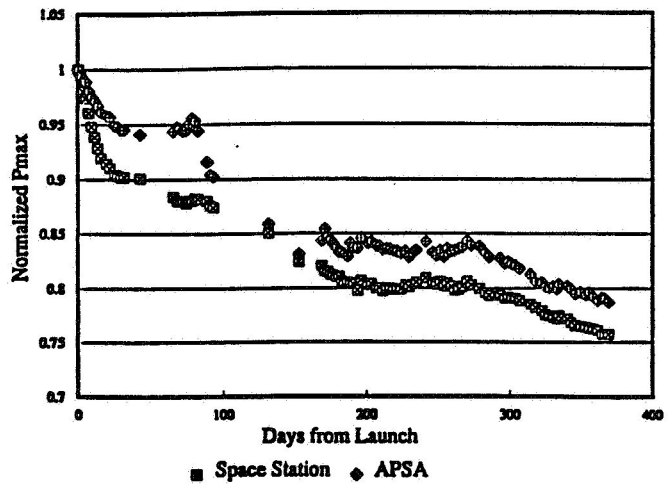


Figure 6. Normalized Pmax for flexible modules.

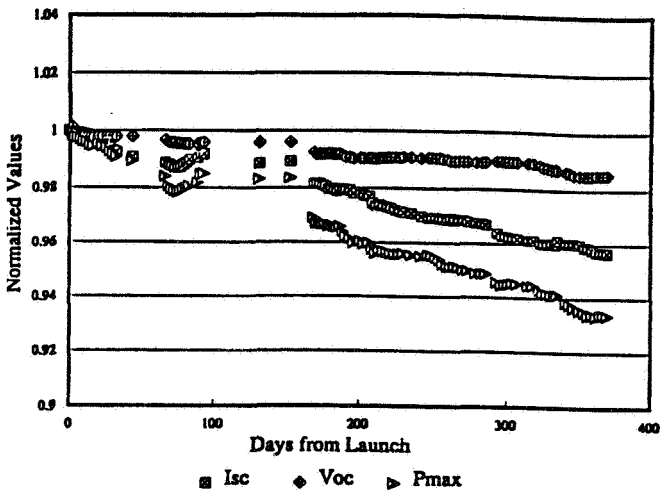


Figure 7. Normalized I-V parameters for Mini-Dome concentrator module.

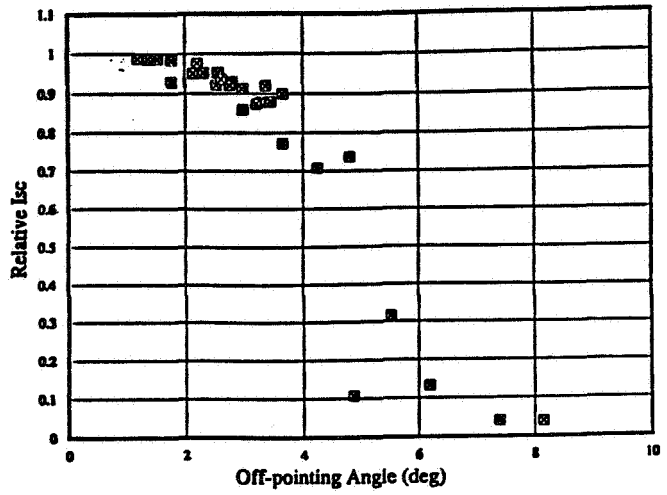


Figure 8. Off-pointing performance of Mini-Dome concentrator module.

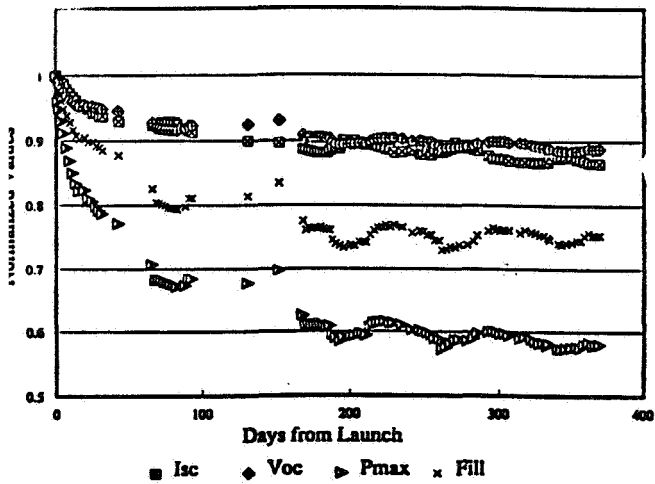


Figure 9. Normalized I-V parameters for amorphous silicon module.

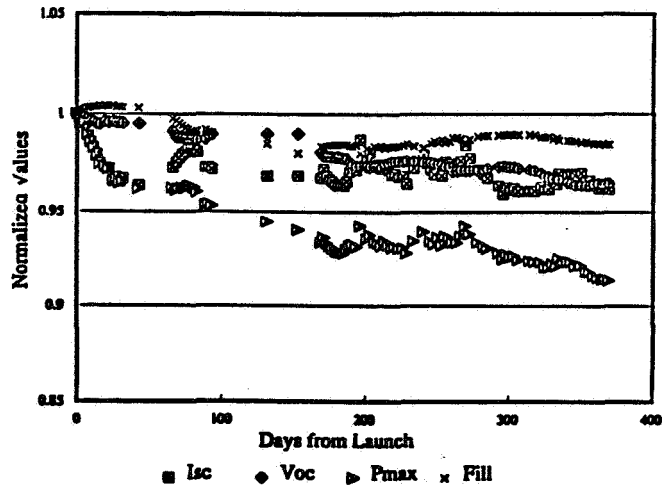


Figure 10. Normalized I-V parameters of GaAs/CIS module.

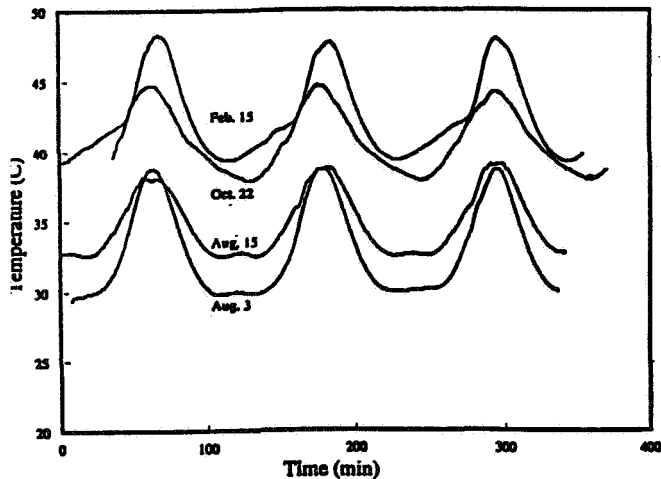


Figure 11. Temperature of silicon panel during several non-eclipse periods.

535-44

50420

125908

12P

PARASITIC CURRENT COLLECTION BY PASP PLUS SOLAR ARRAYS *

V. A. Davis and B. M. Gardner
S-Cubed Division of Maxwell Laboratories
San Diego, California 92121

D. A. Guidice and P. S. Severance
Phillips Lab, Hanscom AFB, MA 01731

SUMMARY

Solar cells at potentials positive with respect to a surrounding plasma collect electrons. Current is collected by the exposed high voltage surfaces: the interconnects and the sides of the solar cells. This current is a drain on the array power that can be significant for high-power arrays. In addition, this current influences the current balance that determines the floating potential of the spacecraft. One of the objectives of the Air Force (PL/GPS) PASP Plus (Photovoltaic Array Space Power Plus Diagnostics) experiment is an improved understanding of parasitic current collection. We have done computer modeling of parasitic current collection and have examined current collection flight data from the first year of operations.

BACKGROUND

Solar arrays provide power for nearly all space systems. Traditionally, solar arrays have operated in the 30 V range to avoid complex interactions with the plasma environment. As space systems become more ambitious, more power, therefore higher voltages, is needed.

The exposed metal and semiconductor surfaces of spacecraft collect ions and electrons from the space plasma. The potential of the spacecraft adjusts until the net current is zero. As each solar cell is at a different potential, some cells collect ions and some collect electrons. For a conventional spacecraft design, the negative side of each array is grounded to the spacecraft chassis. Therefore, the spacecraft body floats negative with respect to the plasma. Figure 1 shows the various currents that contribute to the net current to a spacecraft.

As electrons are faster than ions at the same temperature, spacecraft ground is usually slightly negative. However, it may be necessary to keep the spacecraft body near zero potential with respect to the plasma. For example, an instrument to measure the low energy plasma environment may need to be near plasma ground. Anodization arcing and negative potential arcing are potentially disruptive at potentials greater than 50 to 100 V negative with respect to the plasma (refs. 1 and 2). In these cases active control is used.

At high positive potentials, typically over 200 V, the current rapidly rises due to a phenomena called snapover. Snapover was first observed at NASA/LeRC (refs. 3, 4 and 5). Snapover can occur whenever there is a biased surface adjoining an insulating surface and the bias is above the first crossover of the secondary yield curve of the insulating surface. (refs. 6 and 7) This occurs when the cell potential is above the first crossover for the coverglass or the array support structure.

PASP Plus is the principal experiment integrated onto the Advanced Photovoltaic and Electronics Experiments (APEX) satellite bus (ref. 8). The experiment tested twelve different solar array designs. Parasitic current collection was measured for eight of the designs under various operational and environment conditions. Here we focus on the six flat designs, as the concentrators have minimal current collection as the high potential surfaces are not exposed to the plasma. The arrays considered are listed in Table 1.

* This work is supported by the Air Force Materiel Command.

Table I

| Array Number | Array Type | Number of Cells | Cell Size |
|--------------|---|-----------------|-----------------|
| 1 | Standard Silicon Module with mesh interconnects | 20 | 2 cm x 4 cm |
| 2 | Standard Silicon Module with mesh interconnects | 60 | 2 cm x 4 cm |
| 3 | Space Station with wrap through interconnects | 4 | 8 cm x 8 cm |
| 4 | Thin GaAs/Ge with wire interconnects | 20 | 4 cm x 4 cm |
| 5 | APSA with germanium coating | 12 | 2.6 cm x 5.1 cm |
| 6 | Thin GaAs/Ge with wire interconnects | 12 | 4 cm x 4 cm |
| 8 | Thick GaAs/Ge with wrap through interconnects | 4 | 4 cm x 4 cm |
| 11 | Thick GaAs/Ge with wire interconnects | 8 | 4 cm x 4 cm |

CALCULATIONS

The computation of the current collected by a specific solar array can become intractable. The gap size is of the order of tens of mils while the solar cells are a few centimeters and the entire array can be meters. Each solar cell is at a slightly different potential. The current depends on the geometry of the gap, the geometry of the entire array, the spacecraft, and the plasma conditions.

We are interested in improving our understanding of which aspects of the problem are most important and developing a tool or at least an algorithm to assist spacecraft designers. Our approach was to look in detail at current collection at a single cell gap. Using the computer we can vary each parameter independently. We then developed a formula that estimates the current collected by a single gap. We then incorporated the formula into a tool that adds up the current from all the gaps to give the current collected by an array. Information on the array geometry and how it influences the current are included in the tool.

We did two-dimensional calculations for the various geometries flown. The calculations span the space of plasma conditions, applied potential, and material parameters. We used the calculations and early flight data to develop an analytic formula for the dependence of the current on the primary problem variables. The calculational technique is discussed in a paper presented at the previous SPRAT conference (ref. 9).

The form chosen for the analytic fit appears odd at first glance.

$$\text{Sheath Area} = a A(\text{geom.}) \frac{\phi^{0.35}}{\eta^{0.65}} (\phi \eta)^b \exp\left(\frac{c}{\eta} - \frac{d}{\eta \lambda}\right)$$

The parameters are

$$\phi = \frac{\text{potential with respect to the plasma}}{\text{plasma temperature}}$$

$$\eta = \frac{\text{first cross over}}{\text{potential with respect to the plasma}}$$

$$\lambda = \frac{\text{debye length}}{\text{cell thickness}}$$

The ϕ/η factor is proportional to the potential. The ϕ/η factor modifies the dependence on the temperature and first cross over. The exponential growth with the potential is accounted for by the exponent. The form of the exponent allows for the increase of sheath area with debye length and a decrease in sensitivity to debye length at larger sheath distances. The a, b, c, and d values were adjusted to fit the calculations. A is a function of the array geometry.

The analytic formula was incorporated into the EPSAT computer code (refs. 10 and 11).

FLIGHT DATA

We examined the measured collected current as a function of the applied bias and plasma density for the first nine months of PASP Plus data collection. We focused on measurements made in the ram and with the emitter off. We expect that the wake measurements depend on the attitude of APEX. Generally, when the emitter is on, the APEX floating potential is positive and an algorithm for the determination of the plasma density is needed. To avoid these complications, we confined our early examinations to ram, emitter off measurements.

Leakage current is measured as part of a 30 second sequence of measurements. During each 30 second sequence there are two Langmuir probe sweeps (one up and one down) with the applied bias at zero, and then 23 measurements of the leakage current with the applied bias at a constant. For each 30 second sequence, we used the 22nd current measurement and the plasma density and temperature from the following Langmuir probe sweep. We divided current by the plasma thermal current to compute a collecting area for each measurement.

$$\text{Collecting Area (m}^{-2}\text{)} = \frac{\text{Leakage Current (A)}}{2.68 \times 10^{-14} \text{ Density (m}^{-3}\text{)} \sqrt{\text{Temperature (eV)}}$$

In order to plot the leakage current, we binned and then averaged the data obtained over the nine months. Lower density measurements are excluded because photoemission may play a role. As the plasma conditions and applied bias are correlated with the time on orbit, attitude, and location within the orbit, unknown and unaccounted for systematic factors may influence these measurements.

Several features of interest are clear on inspection of Figure 2.

Overall, the collecting area rises about two orders of magnitude as the applied bias rises one order of magnitude. This is typical of leakage current when snapover plays a role in the current collection process (refs. 12-14). Arrays #1 and #2, the conventional interconnect design, do not rise as quickly, particularly at the high bias end. Also, the current collection curve for array #5, APSA, is different from all of the other arrays.

In general the collected current is several times the array area. Table 2 gives the array and panel areas for the various test solar arrays.

Table II Array and Panel Areas.

| Array | Array Area (m ⁻³) | Panel Area (m ⁻³) |
|-------|-------------------------------|-------------------------------|
| # 1 | 0.016 | 0.129 |
| # 2 | 0.048 | 0.129 |
| # 3 | 0.026 | 0.078 |
| # 4 | 0.032 | 0.129 |
| # 5 | 0.015 | 0.059 |
| # 6 | 0.019 | 0.129 |
| # 8 | 0.0064 | 0.029 |
| # 11 | 0.013 | 0.029 |

There is a minimum collecting area for each plasma density that is the same for all of the arrays. The smallest measured PASP Plus leakage current value is 0.2 μA . This means that the collecting area levels off at $5 \times 10^{-3} \text{ m}^{-2}$ for a plasma density of 3×10^9 and at $5 \times 10^{-4} \text{ m}^{-2}$ for a plasma density of 3×10^{10} . Collecting areas near and below this value are not physically meaningful.

The collecting area does not depend strongly on the plasma density. The collecting area is larger for lower densities (longer debye lengths). The dependence on density is stronger for lower densities.

And finally, there is a large amount of scatter in the graphs. When the several measurements in the same bin are compared, variations of a factor of ten are common.

DISCUSSION AND COMPARISON WITH CALCULATION

In order to compare the measurements with the model described above, it is first necessary to account for the APEX floating potential. The arrays are biased with respect to the APEX chassis. The amount of current they collect depends on the potential with respect to the ambient plasma. Like any spacecraft, there are several sources of current to APEX that must balance. We used the EPSAT (refs. 10 and 11) computer program to model the various components of the current and compute the floating potential.

The electron current collected by solar cells of the power solar arrays that are at positive potential with respect to the plasma is computed using the above model. The ion current collected by the solar cells is assumed to be negligible. The Z-93 paint on the surfaces of the panels is taken to have a conductivity divided by thickness of $10^{-6} \text{ mho m}^{-2}$. The body of APEX is taken to collect ions from a sheath in the same manner as a 0.45 m radius sphere in a flowing plasma. The photoelectron current emitted is taken to be constant at $2 \times 10^{-5} \text{ A m}^{-2}$ when APEX is not in eclipse. And the electron current collected by the test array is modeled as above.

The floating potential of APEX is near zero when the current collected by the test array is less than the ram ion current collected by the spacecraft body. A 0.45 m radius sphere moving at 7700 m s^{-1} in a 10^{10} m^{-3} plasma collects about 0.13 mA. This is the same as the electron thermal current for a 10^{10} m^{-3} , 0.1 eV plasma to a 1.5 m^2 object. The floating potential of APEX shifts when the collecting area exceeds 1.5 m^2 . Therefore the collecting area versus applied bias curve flattens out at 1.5 m^2 .

The flight measurements were taken over a period of months under a variety of conditions. Plasma constituents, plasma temperature, and sunlight/eclipse condition all influence the current to the test arrays. All of these effects are included in the EPSAT computer code. In addition, EPSAT has an orbit propagator (ORB) and a plasma density and temperature model (IRI-86 with an extension to higher altitudes).

For each array, except #5, for each applied bias value, we computed the collected current, plasma density, and plasma temperature at 287 times during the 9 months covered by the flight data. Keeping only the points for which the arrays face the ram direction and APEX is below 1500 km, we computed the collecting area in the same manner as for the flight data, binned the results by density, and averaged. Figure 3 shows the results.

A few general observations can be made regarding the comparison of the calculational results and the flight results. At present the model has less density dependence than observed during flight. The computed current at the higher potentials grows faster than observed. The parameters used for arrays #4 and #6 give current values that are too low and the parameters used for arrays #8 and #11 give current values that are too high.

The current collection characteristic of array #5, APSA, is different from all of the other arrays. We believe that this is because it is coated with a layer of Germanium, which is a semi-conductor. Current is conducted through the Germanium coating even in the absence of plasma. This parasitic current is linear with the applied bias with a resistance of approximately 3 MΩ. Current is also collected from the plasma. This current is comparable to the current collected by an array with a low first cross over potential. Figure 4 shows the effective circuit. Current is collected across the entire surface of the array.

The measured current I_o is given by the following:

$$I_o = f I_p + \frac{\phi_{bias}}{R}$$

The fraction f is used to account for the fact that electrons are collected by the entire surface and not just at the array potential. When we subtract the parasitic current collected from the measured current, we get the collecting area curves shown in Figure 5. The figure compares the experimental results with the results of calculations that treat the array as a constant potential surface on a grounded spacecraft. The calculations were done using the NASCAP/LEO code (ref. 15).

The adjusted flight data values are higher than the calculations. A lower resistance value might provide a better match. Otherwise the calculations substantiate the conclusion that the measured current is the sum of the collected current and the conducted current.

CONCLUSIONS

We examined the current collected as a function of the various parameters for the six non-concentrator designs. The results are similar to those obtained in previous experiments and predicted by the calculations.

We are using the flight data to improve and validate the analytic formula developed. The formula can be used to quantify the parasitic current collected. Anticipating the parasitic current value allows the spacecraft designer to include this interaction when developing the design.

REFERENCES

1. Vaughn, J.A., et al.: Extrapolation of Electrical Breakdown Currents from the Laboratory to Space Station. AIAA 92-0822, AIAA 30th Aerospace Sciences Meeting, Reno, Nevada, 1992.
2. Ferguson, D.C.: The Voltage Threshold for Arcing for Solar Cells in LEO - Flight and Ground Test Results. NASA TM 87259, 1986.

3. Purvis, C.K.; Stevens, N.J.; and Berkopec, F.D.: Interaction of Large High Power Systems with Operational Orbit Charged-Particle Environments. NASA TM X-73867, 1977.
4. Stevens, J.N.: Interactions Between Spacecraft and the Charged-Particle Environment. Spacecraft Charging Technology - 1978, NASA Conference Publication 2071, AFGL-TR-79-0082, 1978, pp. 268-294.
5. Kennerud, K.L.: High Voltage Solar Array Experiments, NASA Rep. CR-121280, 1974.
6. Chaky, R.C.; Nonnast, J.H.; and Enoch J.: Numerical Simulation of Sheath Structure and Current-Voltage Characteristics of a Conductor-dielectric Disk in a Plasma. J. Appl. Phys., vol. 52, 1981, pp. 7092-7098.
7. Katz, I.; and Mandell, M.J.: Differential Charging of High-Voltage Spacecraft: The Equilibrium Potential of Insulated Surfaces. J. Geophys. Res., vol. 87, 1982, pp. 4533-4541.
8. Guidice, D.A.: High Voltage Space-Plasma Interactions Measured on the PASP Plus Test Arrays, this proceedings, 1995.
9. Davis, V.A.; and Gardner, B.M.: Parasitic Current Collection by Solar Arrays in LEO, NASA Conference Publication 3278, 1994, pp. 227-235
10. Kuharski, R.A.; Jongeward, G.A.; Wilcox, K.G.; and Rankin, T.V.: High Voltage Interactions of a Sounding Rocket with the Ambient and System-Generated Environments. IEEE Transactions on Nuclear Science, vol. 37, 1990, pp.2128-2133.
11. Gardner, B.M.; Jongeward, G.A.; Kuharski, R.A.; Wilcox, K.G.; and Rankin, T.V.: The Environmental Workbench: A Design Tool for the International Space Station. AIAA 95-0599, AIAA 33rd Aerospace Sciences Meeting, Reno, Nevada, 1995.
12. Grier, N.T.; and Stevens, N.J.: Plasma Interaction Experiment (PIX) Flight Results. Spacecraft Charging Technology - 1978, NASA Conference Publication 2071, AFGL-TR-79-0082, 1979, pp. 295-314.
13. Grier, N.T.: Plasma Interaction Experiment II (PIX II): Laboratory and Flight Results. Spacecraft Environmental Interactions Technology, 1983 , NASA Conference Publication 2359, AFGL-TR-85-0018, 1985, pp. 333-347.
14. Ferguson, D.C.: RAM/WAKE Effects on Plasma Current Collection of the PIX II Langmuir Probe. Spacecraft Environmental Interactions Technology, 1983, NASA Conference Publication 2359, AFGL-TR-85-0018, 1985, pp. 349-357.
15. Mandell, M.J.; and Davis, V.A.: User's Guide to NASCAP/LEO. LEW-15641, SSS-R-85-7300-R2, 1990. (Available as LEW-15641 from COSMIC, U of Georgia.)

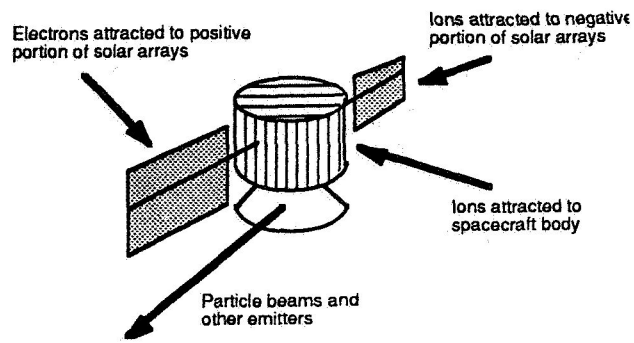
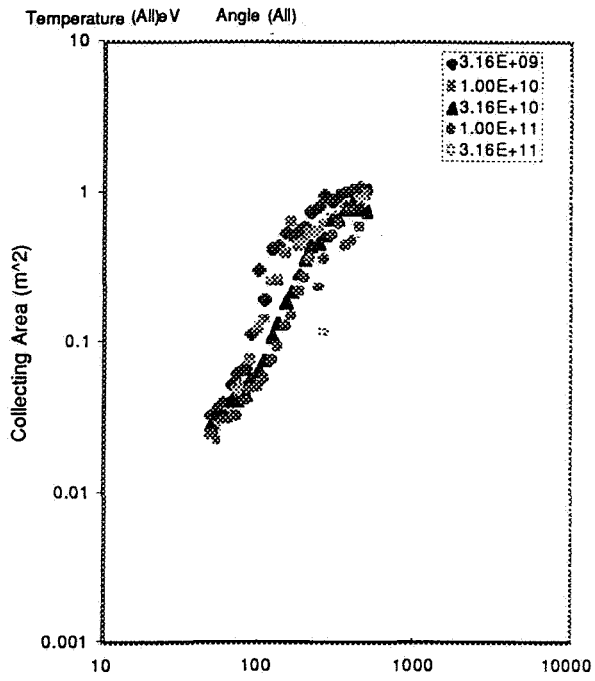
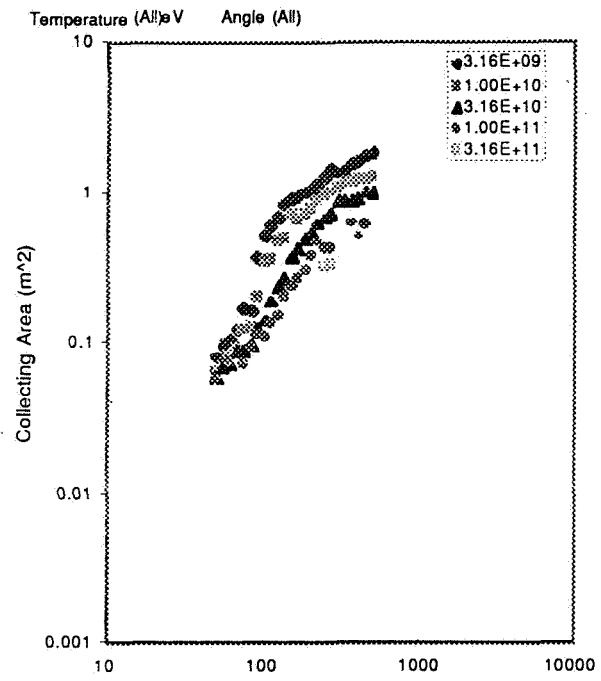


Figure 1.—At the spacecraft floating potential the net current is zero. This current has several components.

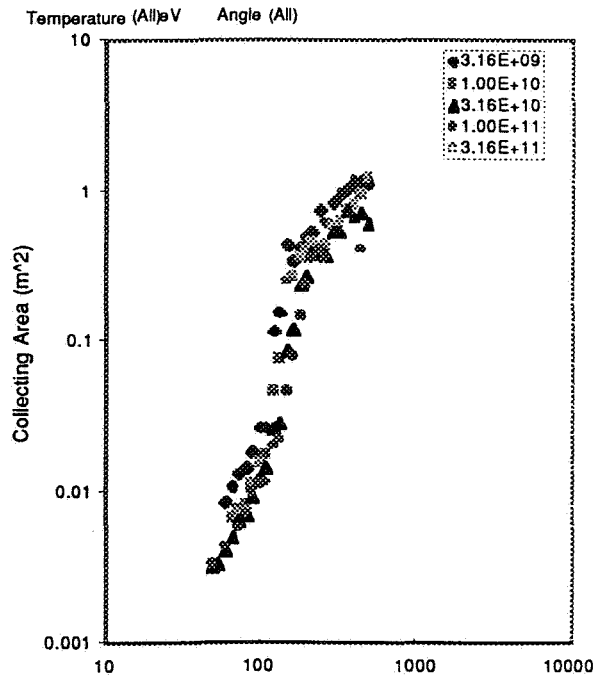
PASP Plus Array #1, Ram, Emitter Off, Day 94215 to 95134



PASP Plus Array #2, Ram, Emitter Off, Day 94215 to 95134



PASP Plus Array #4, Ram, Emitter Off, Day 94215 to 95134



PASP Plus Array #6, Ram, Emitter Off, Day 94215 to 95134

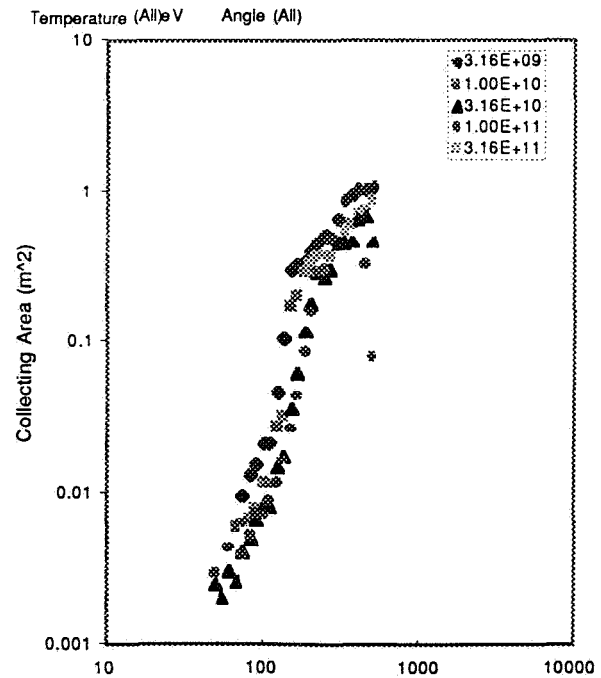
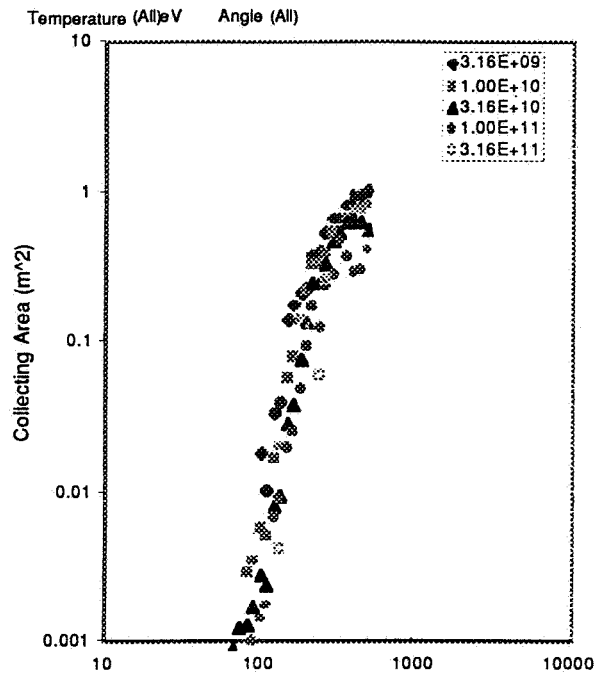
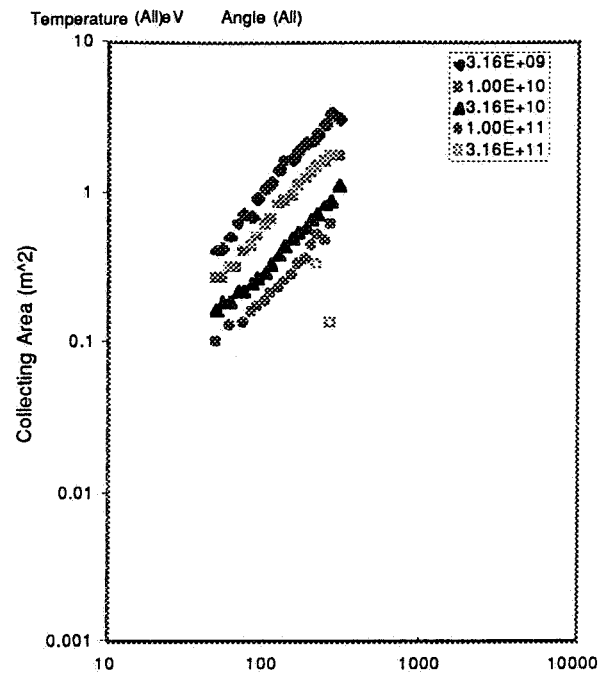


Figure 2.—Experimental collecting area versus applied bias curves.

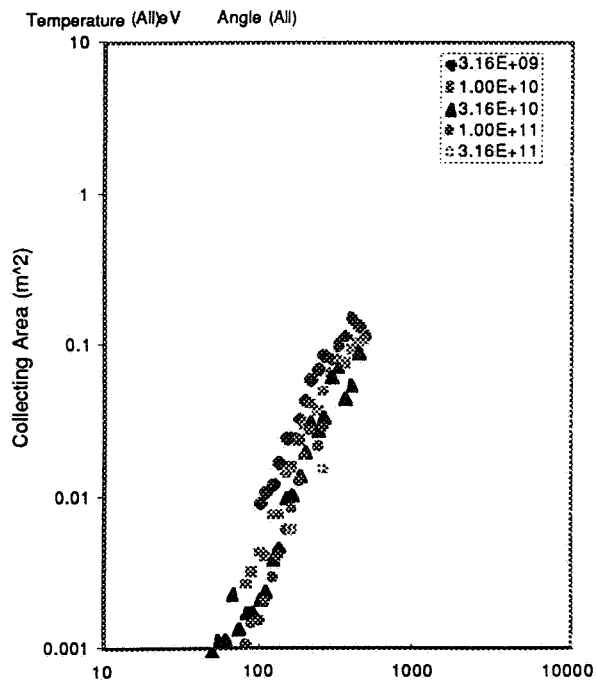
PASP Plus Array #3, Ram, Emitter Off, Day 94215 to 95134



PASP Plus Array #5, Ram, Emitter Off, Day 94215 to 95134



PASP Plus Array #8, Ram, Emitter Off, Day 94215 to 95136



PASP Plus Array #11, Ram, Emitter Off, Day 94215 to 95134

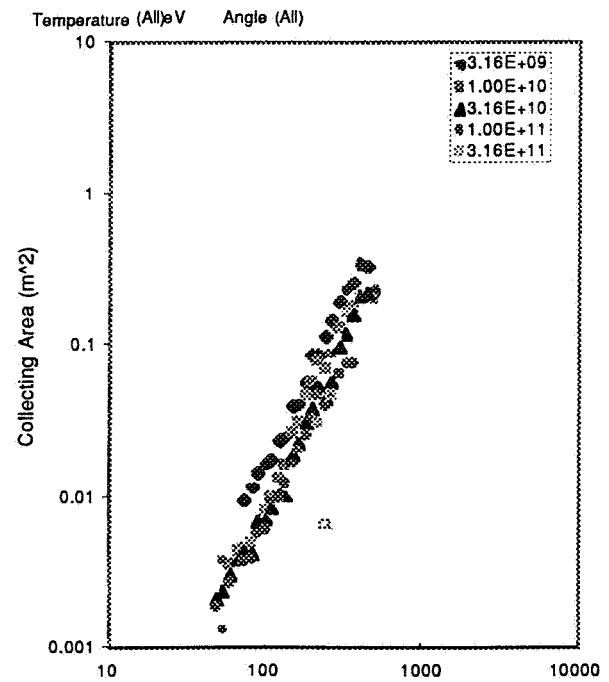
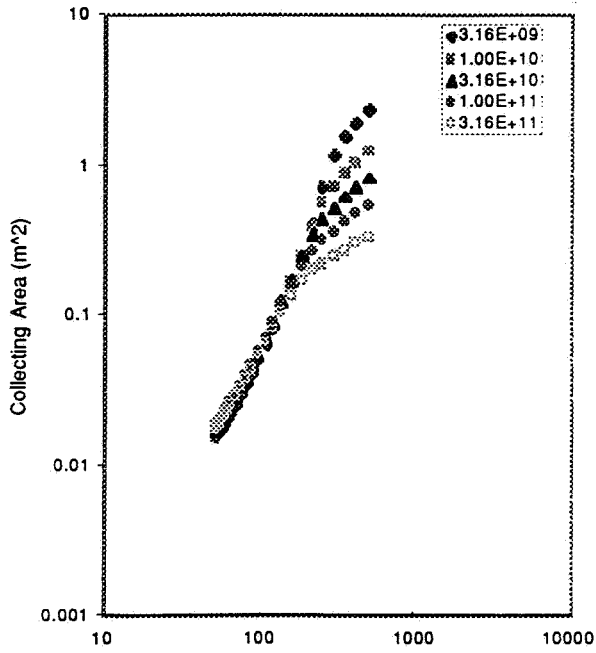
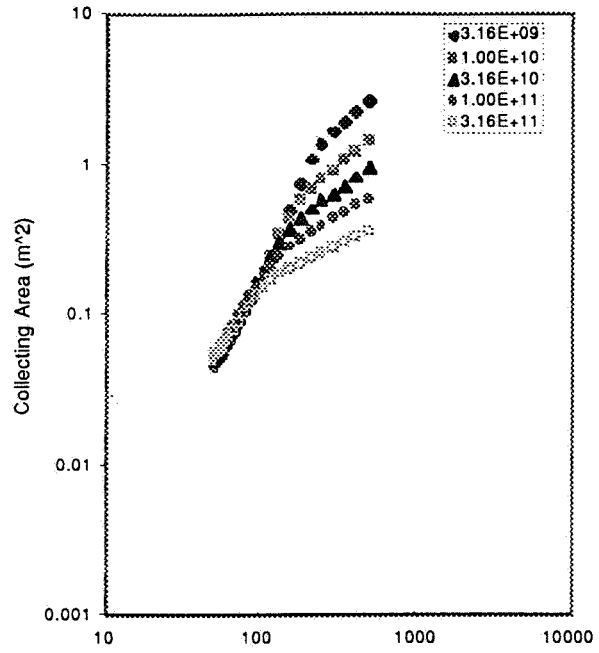


Figure 2.—Experimental collecting area versus applied bias curves.

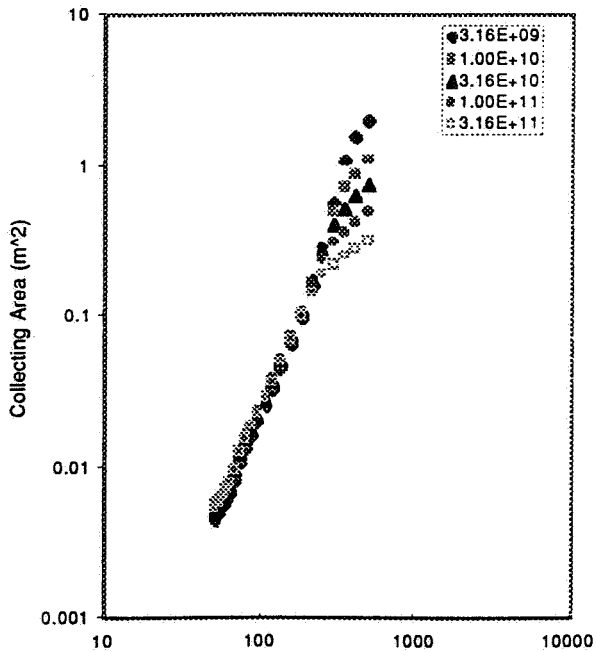
PASP Plus Array #1, EPSAT



PASP Plus Array #2, EPSAT



PASP Plus Array #4, EPSAT



PASP Plus Array #6, EPSAT

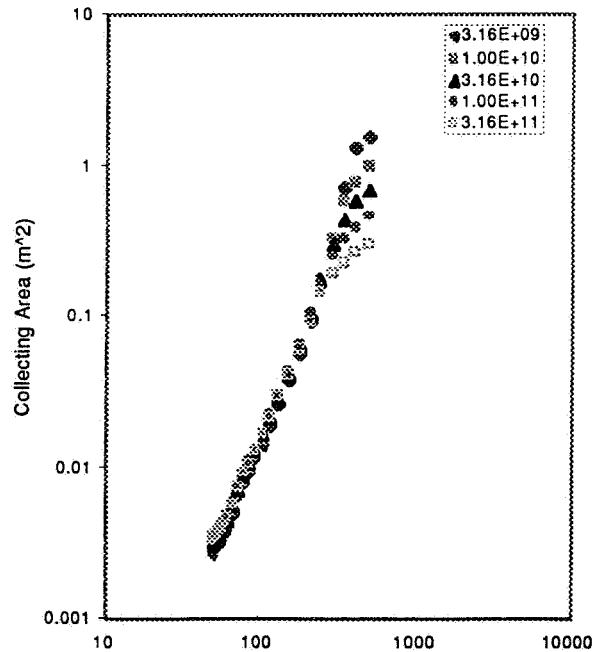
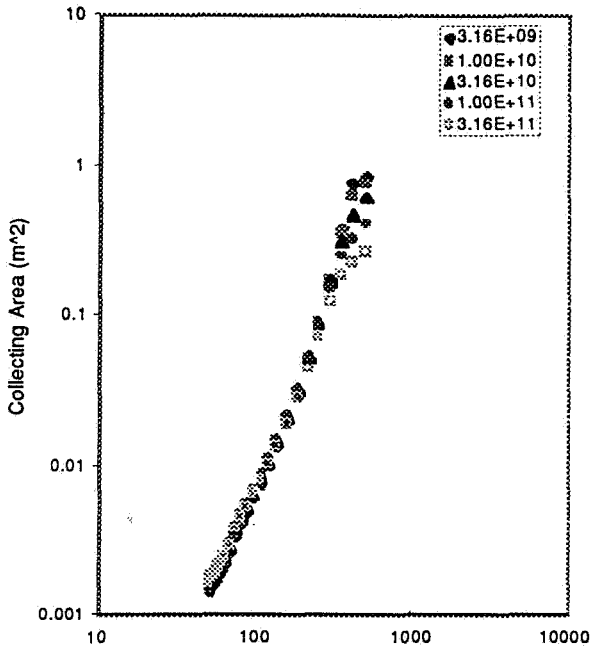
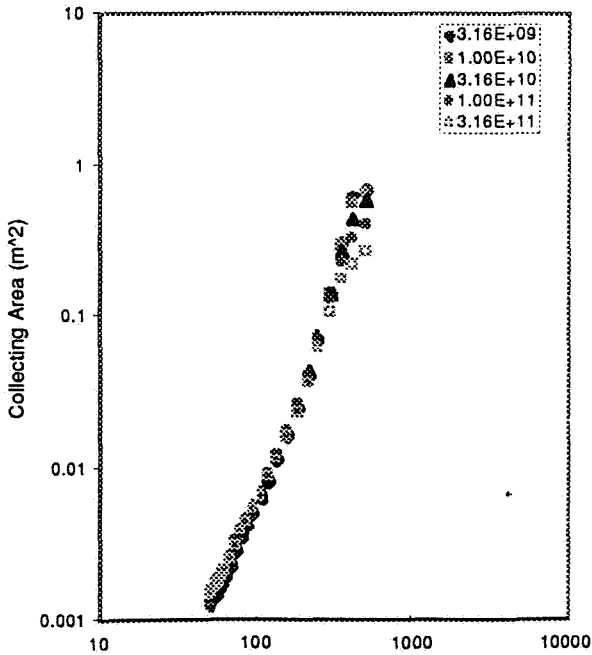


Figure 3.—Computed collecting area versus applied bias curves.

PASP Plus Array #3, EPSAT



PASP Plus Array #8, EPSAT



PASP Plus Array #11, EPSAT

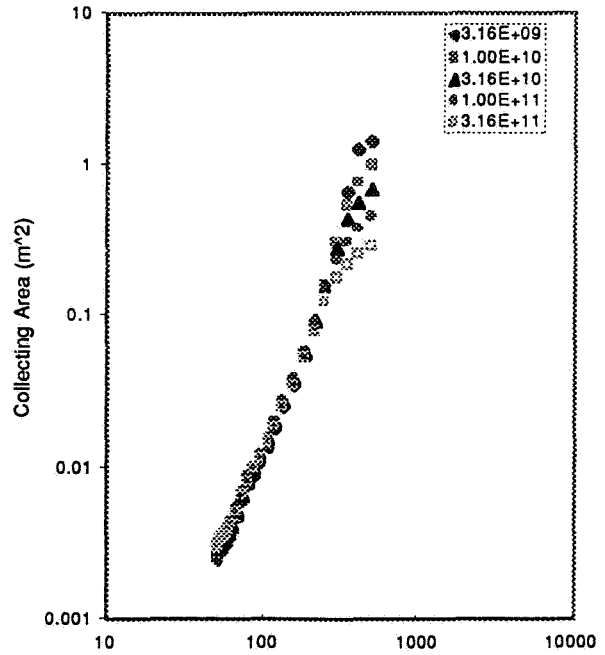


Figure 3.—Computed collecting area versus applied bias curves.

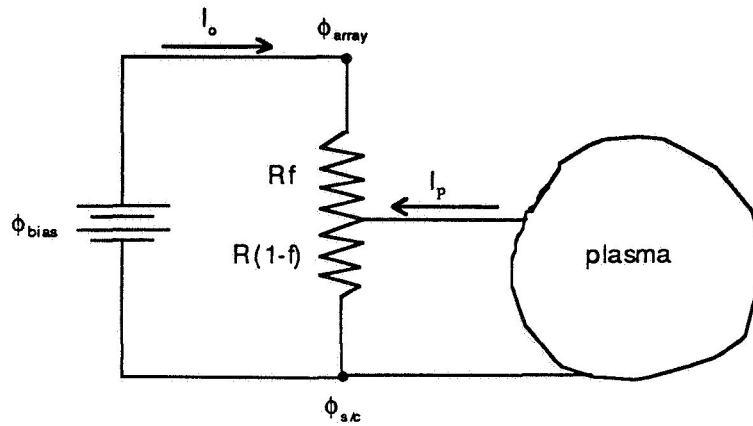


Figure 4.—Effective circuit for collection of current by array 5.

PASP Plus Array #5, Ram, Emitter Off, Day 94215 to 95134

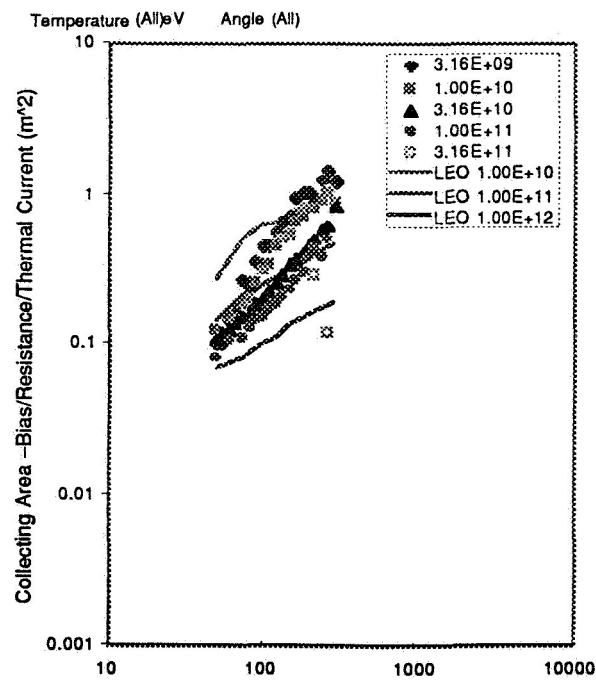


Figure 5.—Array 5 experimental collecting area connected for current through Germanium coating compared with NASCAP/LEO calculations.

HIGH VOLTAGE SPACE-PLASMA INTERACTIONS MEASURED ON THE PASP PLUS TEST ARRAYS

D.A. Guidice
Phillips Laboratory, Geophysics Directorate
Hanscom AFB, MA 01731

S36
IN-50421

INTRODUCTION

Space systems of the late 1990s and beyond will require more efficient space-power sources. In providing electrical power for these new systems, consideration must be given to operating photovoltaic subsystems at higher voltage levels to minimize I^2R losses and/or reduce cable weight. New solar-cell materials are being developed for higher efficiency and less susceptibility to space radiation. Before using these new technologies on operational spacecraft, various environmental interactions questions must be answered by investigations in the actual space environment. The Photovoltaic Array Space Power Plus Diagnostics (PASP Plus) experiment was developed and flown for this purpose. In early 1990, the Air Force's Space Test Program (STP) offered PASP Plus a flight on a satellite put into orbit by a Pegasus launch vehicle. PASP Plus was to be part of the APEX (Advanced Photovoltaic and Electronics EXperiments) mission, set up to fly it and two small "radiation effects on electronics" experiments, CRUX/CREDO and FERRO (1). To make PASP Plus suitable for APEX, a controller with increased functional capability and reduced weight was developed by Amptek, Inc. With the help of NASA Lewis personnel, twelve test arrays were mounted to the payload shelf and one of the deployed panels of the APEX satellite. Diagnostics sensors were incorporated into the experiment. PASP Plus successfully completed all functional and environmental testing, including "one sun simulated" thermal-vacuum tests at the Boeing facility at Kent, WA to give us preflight "array performance vs. temperature" characteristics for later comparison with flight data (2). The experiment was delivered to Orbital Sciences Corp. (OSC) for integration into APEX in July 1992.

The APEX satellite was launched by a standard Pegasus rocket released from a NASA B-52 aircraft (based at Edwards AFB) on 3 August 1994 within the Western Test Range off the coast of California. The release from the B-52, the three stages of rocket firing, the satellite's lock-on to the sun, and the extension of its four deployable panels all occurred without problems. A 70°-inclination, 363 km × 2550 km orbit was achieved, satisfying PASP Plus's data-collecting requirements.

The objectives of the PASP Plus experiment were:

- a. To measure the plasma "leakage" current for different kinds of arrays subjected to positive biasing levels up to +500 V.
- b. To measure the arcing parameters for different kinds of arrays subjected to negative biasing levels up to -500 V.
- c. To measure the long-term deterioration in the power output of arrays using different solar-cell materials when exposed to space radiation.

In all cases, the concept was to establish cause-and-effect relationships between array interactions and environmental conditions. This paper will discuss some of the positive and negative biasing results; another paper at this conference will discuss the space radiation-induced deterioration aspects of the experiment.

PASP PLUS INSTRUMENTATION

The PASP Plus instrumentation consisted of four kinds of equipment:

- a. a set of test arrays, some of which are divided into biased and unbiased modules.
- b. experiment-control instrumentation capable of creating *array* or *spacecraft* conditions under which measurable environmental interactions will occur.
- c. interactions-measuring instrumentation that will quantify what happens when the ambient or created conditions impact the performance of the test arrays.
- d. diagnostic sensors to measure the environmental conditions affecting array performance.

Solar Arrays

To maximize the scope of the investigation, a variety of conventional and advanced-concept solar arrays were included in the array complement. As shown in Table I, twelve different solar arrays were investigated on PASP Plus. Other than Array 0,1,2 (basic silicon, which serves as a standard), array selection were based on the array's availability (at no cost to the experiment) and its possible use on future DoD or NASA space missions.

Table I. PASP Plus Solar Arrays

| <u>Module No.</u> | <u>Cell / Array Type</u> | <u>Number of Cells</u> | <u>Cell Size (cm x cm)</u> | <u>Array Developer</u> |
|-------------------|--------------------------|------------------------|----------------------------|------------------------|
| <u>0,1,2</u> | Si (Std) 8 mil | 20,20,60 | 2 x 4 | RCA / WL |
| <u>3</u> | Si 8 mil wtc [Space Sta] | 4 | 8 x 8 | Lockheed |
| <u>5</u> | Si 2 mil [APSA] | 14 | 2.6 x 5.1 | TRW |
| <u>9</u> | Amorphous Si | 2 | 4 x 4 | TRW/JPL |
| <u>4,6</u> | GaAs/Ge 3½ mil | 20,12 | 4 x 4 | ASEC |
| <u>8</u> | GaAs/Ge 7 mil, wtc | 4 | 4 x 4 | Spectrolab |
| <u>11</u> | GaAs/Ge 7 mil | 8 | 4 x 4 | Spectrolab |
| <u>7</u> | AlGaAs/GaAs | 20 | 2 x 2 | VS Corp. |
| <u>10</u> | InP 12 mil | 10 | 2 x 2 | Spire/NRL |
| <u>12,13</u> | GaAs/CuInSe ₂ | 12,3 | 2 x 2, 2 x 4 | Boeing |
| <u>14</u> | GaAs Mini-Cass | 8 | Concentrator | TRW |
| <u>15</u> | GaAs/GaSb Mini-Dome | 12 | Concentrator | Boeing |

wtc = wrap-through connectors

underlined module = biased

A brief description of the solar arrays is given in Ref. 3. A more detailed description, including cell and array mechanical configurations and color photographs was given in a report by Adams (4).

Control & Diagnostic Instrumentation

The PASP Plus controller carries out all the functions needed to obtain array I-V curves, to apply the biases to the arrays, and to process the data from the interactions-measuring and diagnostic sensors (except the dosimeter) and send the data to the satellite (for real-time or data-dump transmittal back to a ground station). The dosimeter has its own separate interface (power, commands, data) with the satellite. PASP Plus has a suite of diagnostic sensors that include the following:

Sun Sensor: To measure the alignment of the test arrays to the incident solar energy, especially important for the concentrator arrays.

Langmuir Probe (LP): To measure low-energy plasma parameters (density and temperature).

Transient Pulse Monitor (TPM): To detect and characterize the arc-discharges that occur during the negative-voltage biasing of the test arrays.

Electrostatic Analyzer (ESA): To measure 30 eV to 30 keV electron and ion spectra, detect the passage of APEX through an auroral region, and show the vehicle negative potential when a test array is biased to high positive values.

Contamination Monitors: To measure the amount and/or effect of contaminants deposited on array surfaces. Sensors include both quartz crystal microbalances and calorimeters.

Dosimeter: To measure the high-energy particle radiation flux and dose (from ions and electrons) that leads to deterioration in solar-array power output.

APEX SATELLITE

The APEX satellite, shown in Figure 1, is in the form of a hexagonal cylinder 152 cm in height and 96 cm across (112 cm corner to corner). On the top "Payload Shelf" we have seven of the PASP Plus test arrays and some small sensors. Extending up from the Payload Shelf are two 61-cm booms, one holding the Langmuir Probe sensor head and the other holding the APEX magnetometer (used to maintain orientation when the satellite is in eclipse). Beneath the Payload Shelf, we have the Avionics Shelf containing the electronic boxes for the PASP Plus instruments and the other APEX experiments, CRUX/CREDO and FERRO. Attached to the top of four of the hexagon's sides are the four deployed panels, each 152 cm wide by 56 cm long. Three of the panels contain the silicon arrays providing power to the spacecraft; the other "Deployed Payload Panel" contains the remaining five test arrays and a few small sensors (3). The PASP Plus test arrays and instrumentation on the Payload Shelf and Deployed Payload Panel are shown in Figure 2. The APEX satellite is three-axis stabilized and oriented so the PASP Plus test arrays will be sun-pointing to within ± 0.5 degrees (needed for operation of the concentrator arrays).

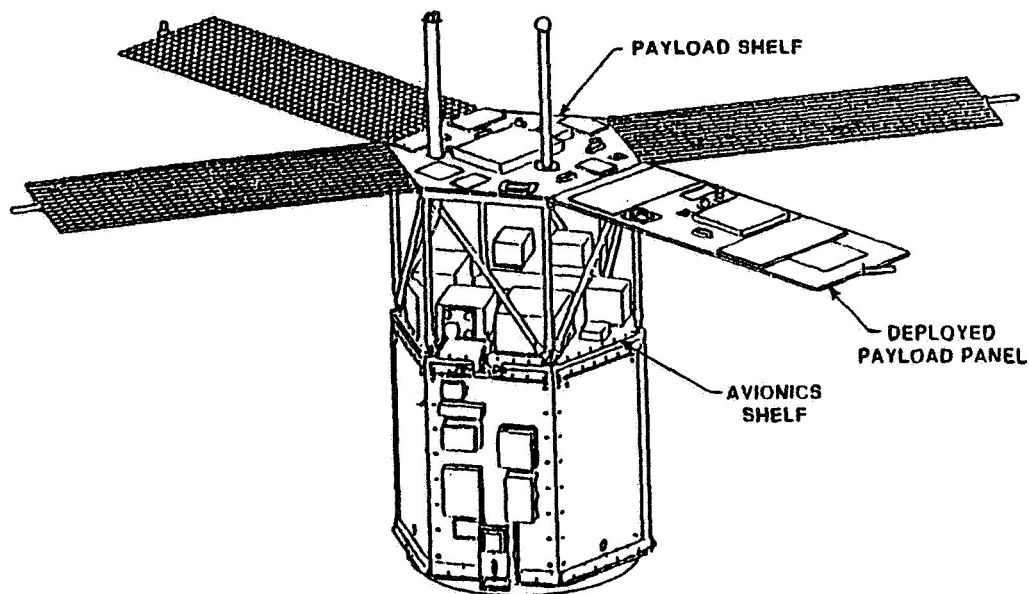
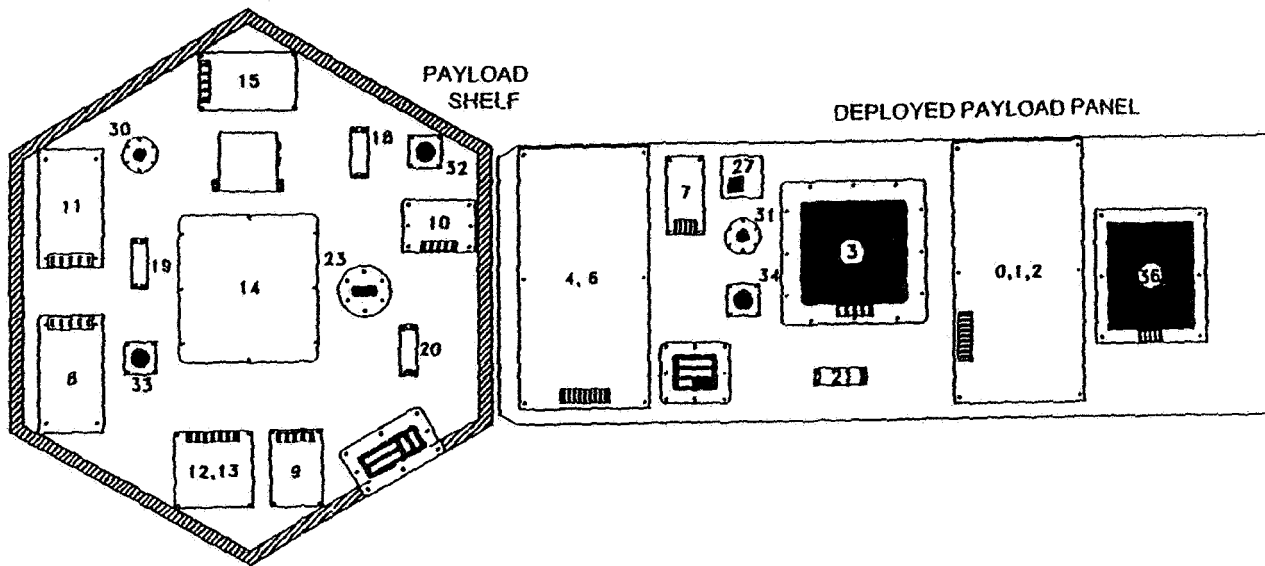


Fig. 1. Advanced Photovoltaic and Electronics Experiments (APEX) Satellite.



| <u>ITEM NO.</u> | <u>INSTRUMENT</u> | <u>ITEM NO.</u> | <u>PASP TEST ARRAY</u> |
|-----------------|------------------------------|-----------------|------------------------------|
| 18,19,20,21 | TPM E-field Sensors | 0,1,2 | Si Standard |
| 23 | LP Boom & Sensor | 3 | Si Wrap-Thru (Space Sta) |
| 27 | PASP Sun Sensor | 4,6 | GaAs on Ge, 3.5 mil |
| 30,31 | Quartz Crystal Microbalances | 7 | AlGaAs/GaAs |
| 32, 33, 34 | Calorimeters | 8 | GaAs on Ge, 7 mil, Wrap-Thru |
| | | 9 | Amorphous Si |
| | | 10 | InP |
| | | 11 | GaAs on Ge, 7 mil |
| | | 12,13 | GaAs/CuInSe ₂ |
| | | 14 | GaAs Mini-Cassegrainian |
| | | 15 | GaAs/GaSb Mini-Dome |
| | | 36(5) | Thin Si(2mil), APSA |

Fig. 2. PASP Plus Instrument and Test Array Layout .

DATA GATHERING

The PASP Plus team undertook experiment *commanding and quick-look* data evaluation (using our on-site GSE) at the Satellite Control Facility at Onizuka AFB, CA. After turn-on and checkout of the PASP Plus instruments and some initial *I-V* curve taking, we began biasing of the arrays on 7 August 1994. Data gathering involving the positive and negative biasing of the PASP Plus test arrays took place at various times over the period from 7 Aug 94 to 1 Jul 95, with several long gaps due to APEX subsystem problems. PASP Plus biasing was halted by an APEX Battery Control Regulator problem on 4 Nov 95. After a thorough study, a software-patch fix was developed and tested by OSC and sent up to the satellite; PASP Plus operation was started again on 15 Jan 95. In the spring of 1995, problems with other satellite subsystems and the time needed to find the appropriate fixes and PASP Plus operating-time limitations caused biasing operations to be halted from 17 May to 1 Jul 95. Finally, on 12 Aug 95 a PASP Plus controller hardware problem resulted in the end of all biasing operations. Table II shows the data gathering periods for positive biasing, summarizing the voltage and plasma density ranges and the environmental and operating conditions encountered. Table III does the same for the negative biasing periods.

Table II. Data Gathering Periods for Positive Biasing

| <u>Biasing Period</u> | <u>Voltage Range</u> | <u>Plasma Den (cm⁻³)</u> | <u>Environment and Operations Comments</u> |
|---------------------------------|----------------------|--|--|
| 7 Aug – 18 Aug 94 | +75 V to +500 V | $6 \times 10^3 \rightarrow 1 \times 10^5$ (2×10^5 rare) | Bias ± 20 min around perigee. Ram angle at perigee $\leq 90^\circ$ until 15 Aug. No eclipse over 7–17 Aug. All biasing in sunlight. Emitter on 1/3 of orbits after 11 Aug. |
| 10 Oct – 16 Oct 94 | +100 V to +300 V | $6 \times 10^2 \rightarrow 2 \times 10^5$ | Biasing around perigee. Ram angle at perigee $\geq 90^\circ$ and no eclipse for whole period. Emitter on about 1/3 of orbits. |
| 24 Oct – 30 Oct 94 ^a | +100 V to +320 V | $4 \times 10^2 \rightarrow 2 \times 10^5$ | Biasing around the orbit. Ram angle at perigee $71^\circ \rightarrow 59^\circ$ for 24-30 Oct. No eclipse until >28 Oct. Emitter not on. |
| 15 Jan – 17 Jan 95 | +75 V to +220 V | $2 \times 10^3 \rightarrow 6 \times 10^5$ | Biasing only in sunlight. Controller off for altitudes >1200 km. Ram angle at perigee $106^\circ \rightarrow 97^\circ$. Emitter not on. |
| 12 Feb – 2 Mar 95 | +50 V to +220 V | $4 \times 10^2 \rightarrow 3 \times 10^5$ | Biasing 40 min before to 30 min after perigee, but off for alt >1200 km when near SAA. No eclipse throughout period. Ram angle at perigee $64^\circ \rightarrow 96^\circ$. Emitter not on. |
| 27 Apr – 16 May 95 | +50 V to +430 V | $4 \times 10^2 \rightarrow 8 \times 10^4$ (1×10^5 rare) | Biasing around orbit, but off for altitudes >1200 km when near SAA. Ram angle at perigee $105^\circ \rightarrow 74^\circ$. Emitter not on. APEX problems! No biasing 17 May – 1 Jul. |
| 31 Jul – 11 Aug 95 | +50 V to +490 V | $2 \times 10^2 \rightarrow 3 \times 10^5$ | Biasing around orbit, but off for altitudes >1200 km when near SAA. Ram angle at perigee $78^\circ \rightarrow 51^\circ$. Emitter not on. PASP+ controller problem 12 Aug! No more biasing. |

Table III. Data Gathering Periods for Negative Biasing

| <u>Biasing Period</u> | <u>Voltage Range</u> | <u>Plasma Den. (cm⁻³)</u> | <u>Environment and Operations Comments</u> |
|--|--------------------------------------|---|--|
| 22 Aug – 3 Sep 94 | -75 V to -450 V | $\leq 6 \times 10^2 \rightarrow 6 \times 10^5$ | No biasing in eclipse after 26 Aug. Higher negative voltages (-220V to -450V) only in sunlight. Unfavorable ram angles at perigee (111°→135°). TPM thresholds set at 0. |
| 17 Oct – 22 Oct 94 | -160 V to -400 V | $\leq 6 \times 10^2 \rightarrow 4 \times 10^5$ | No eclipse period in orbits. Ram angle at perigee is $\leq 90^\circ$ over 17–23 Oct (88°→73°). Arrays #2 and #1 are limited to -380V. TPM thresholds set at 0. |
| 31 Oct – 4 Nov 94 | -160 V to -370 V | $6 \times 10^2 \rightarrow 2 \times 10^5$ | Eclipses return on 29 Oct. Ram angle at perigee 57°→53° in period. Arrays #2 and #1 limited to -300V (orbits include eclipse). TPM threshold at 0. APEX problem 4 Nov! |
| 18 Jan – 11 Feb 95 | -280 V to -460 V | $6 \times 10^3 \rightarrow 6 \times 10^5$ (some higher over 18–20 Jan) | Biasing only <1200 km. For APEX safety, all Controller ops in sunlight until 4/5 Feb, then 10 min at end of eclipse. No significant eclipse meas. Ram angle at perigee 95°→64°. TPM threshold at 0 until 1 Feb, then set at 1. |
| 3 Mar – 26 Mar 95 30 Mar – 1 Apr 95 | -240 V to -430 V -240 V to -300 V | $6 \times 10^3 \rightarrow 8 \times 10^4$ | Bias 12 min before to 42 min after perigee; this includes all of eclipse. Ram angle is $\leq 90^\circ$ only past middle of eclipse. Ram angle at perigee 98°→176°. TPM threshold set at 1. |
| 13 Apr – 18 Apr 95 | -240 V to -370 V | $6 \times 10^3 \rightarrow 3 \times 10^5$ | Bias 20 min before to 40 min after perigee; this includes all of eclipse. Ram angle is $\leq 90^\circ$ only past middle of eclipse. Ram angle at perigee 143°→127°. TPM threshold set at 1. |
| 1 Jul – 18 Jul 95 | -300 V to -460 V | $2 \times 10^2 \rightarrow 4 \times 10^5$ | Biasing around orbit, but off for altitude >1200 km when near SAA. Ram angle is $\leq 90^\circ$ only past middle of eclipse. Ram angle at perigee 135°→109°. TPM threshold set at 1. |
| 19 Jul – 30 Jul 95 | -450 V to -500 V | $2 \times 10^2 \rightarrow 3 \times 10^5$ | Biasing around orbit, but off for altitude >1200 km when near SAA. Ram angle is $\leq 90^\circ$ only past middle of eclipse. Ram angle at perigee is 109°→80°. TPM threshold set at 1. |

NEGATIVE BIASING

The arc rates for the ten negatively biased test arrays were measured by the PASP Plus TPM on APEX. These arc rates have been compared to computer-generated simulations using a semi-analytic arc-rate code developed by M.I.T. (7,8) for the experiment's conventional planar arrays. The simulations were carried out using the measured "arc-rate determining" parameters (bias voltage, ion flux [from plasma density and ram angle], array temperature, etc.) measured aboard APEX during negative biasing operations. Measured and simulated arc-rate results were compared to examine cause-and-effect relationships. Some of the PASP Plus flight results are described and interpreted below.

The measured arc rate for the biased arrays showed a strong dependency on the fabrication and mechanical configuration (i.e., metal interconnect and cell side-edge exposure to the space plasma). The standard silicon array (Modules #1 and #2) showed substantial arcing over a wide range of voltages (>160 V), plasma densities (>10⁹ m⁻³ in ram) and temperatures (in sun and eclipse). This is to be expected since Array 0,1,2 is of old construction (exposed rough-surface interconnects). According to theory (7), if the interconnects have many field-emission sites (microscopically jagged regions with high electric-field enhancement factors), charging processes caused by enhanced-field electron emission can be initiated, leading to collisional ionization of neutral gas desorbed from the cell's coverglass, eventually resulting in an arc discharge. PASP Plus measurements also show that arrays having their interconnects and/or cell side edges shielded from the space plasma have lower arcing rates. The concentrator arrays appear to have almost no arcs, and the arrays with wrap-through connectors have less arcs than would be expected based on other factors. It was also found that for arrays where matched comparisons (modules with the same cell types and array configuration) could be made [i.e., Module #2 with #1; Module #4 with #6], all other factors being equal, arc rate appears to be proportional to module area.

While the old standard silicon array exhibited much higher arc rates than the others, the arc rate of all the arrays showed a strong dependence on bias voltage. See Figure 4 for Module #2. Arcing onset (threshold) voltages were found to be generally in the -100 V to -300 V range; see Table IV below. For the conventional planar arrays, there is general agreement between the PASP Plus results and the computer-generated simulations.

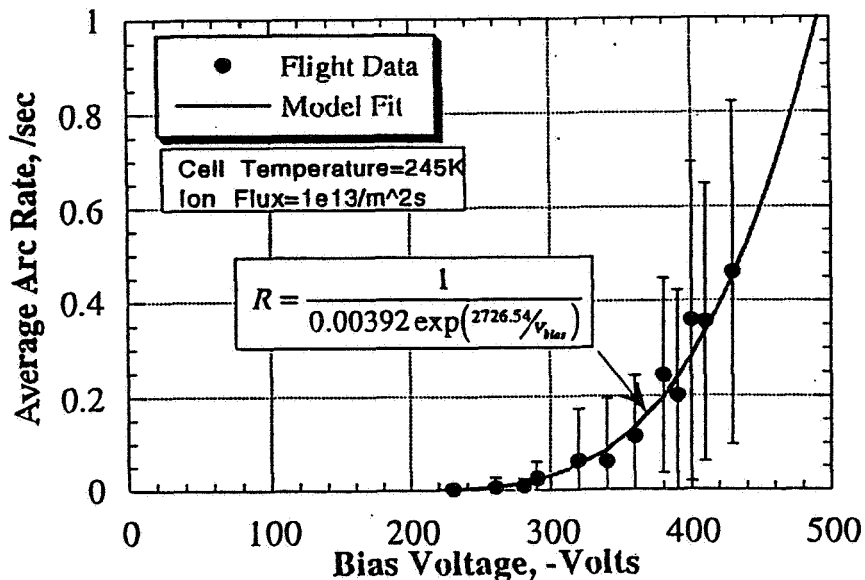


Fig. 4. Average Arc Rate versus Bias Voltage for the Standard Silicon Array, Module #2.

Table IV. Arcing Onset Voltages for the Biased PASP Plus Planar Arrays; Experimental Measurements and Computer-Generated Simulations

| PASP Plus Planar Test Array | In-Space Measured Onset Voltage | Computer-Simulated Onset Voltage |
|--|---------------------------------|----------------------------------|
| 1,2 Silicon (Old Standard) | -160 V | -160 V |
| 3 Silicon (Space Station) with Wrap-Through Connectors | -160 V | Not Derived |
| 5 Thin Silicon (APSA) | -75 V to -125 V | -100 V |
| 4,6 3.5-mil GaAs on Ge | -125 V | -120 V |
| 8 7-mil GaAs on Ge with Wrap-Through Connectors | -260 V to -300 V | Not Derived |
| 11 7-mil GaAs on Ge with conventional interconnects | -180 V | -180 V |

Ion flux ($F_{ion} = n_{ion} v_{ion} \cos\theta_{ram}$) was also found to be an important factor governing arc rate. Access of the plasma's positive ions to the interactions volume between an array's solar cells is necessary for the proper sequence of interactions (leading to arcing) to occur. In general, this requires that the array not be in wake, in most cases this means $\theta_{ram} = \pm 90^\circ$. However, for modules prone to arc (#1 and #2) it was observed that at high negative biases especially in eclipse (cold is another arc enhancing factor) arcing occurred for the module near the edge of the deployed panel (Module #2) for ram angles up to nearly 120° while Module #1 in the center of the panel would not arc until θ_{ram} was $\leq 105^\circ$ (few arcs beyond 90°).

PASP Plus also found that arcing is more prevalent under cold array conditions, especially at the ends of eclipse periods. According to the M.I.T. developed theory (7), one would expect *cold* array temperatures to favor arcing: greater desorption of the neutral gas and its staying in the localized area (having less energy) under cold conditions. An example of the difference in arc rate between high (sunlit) and low (eclipse) array temperatures [+38C and -42C] for Module #2 is presented in Figure 5. The experiment data points are shown as filled circles and the simulation-generated points as open squares. For thin arrays such as the APSA array (#5), temperature is an important arcing factor. Arcing for Array #5, which was not allowed to be biased beyond -300 V, was confined almost exclusively to eclipse periods where its temperature could reach -70C due to its double-sided exposure, very low mass, and thermal isolation.

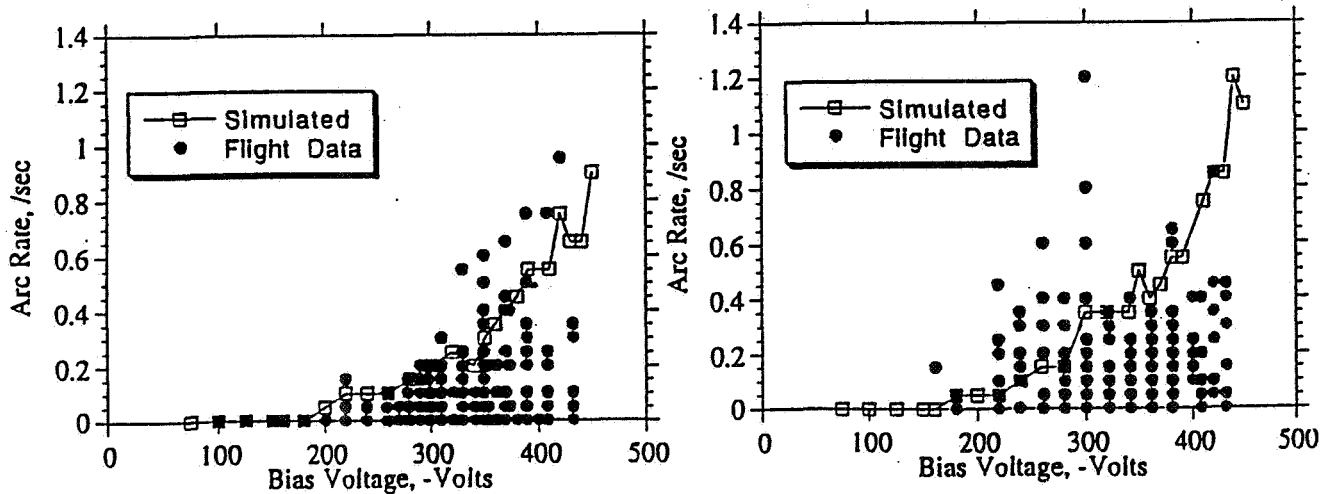


Fig. 5. PASP-Plus Measured and Computer Simulated Arc Rates for Module #2 (Standard Si Array) vs. Bias Voltage at Array Temperatures of +38C [left] in Sunlight and -42C [right] in Eclipse.

CONCLUSIONS

In spite of launch delays and on-orbit satellite problems, the PASP Plus experiment has provided to the space-power community outstanding data for the examination of plasma effects on high-voltage operation and radiation damage effects on array power output. By the summer of 1995, PASP Plus collected an order of magnitude more data about environmental interactions on solar arrays than all previous space-borne photovoltaic experiments combined. Organizations such as the Phillips Laboratory, NASA Lewis Research Center, Massachusetts Institute of Technology, and S-Cubed Division of Maxwell Laboratories are investigating various aspects of space-environment effects on photovoltaic systems based on the most extensive on-orbit data base ever acquired for this purpose.

REFERENCES

- (1) Guidice, D.A., "PASP Plus: An Experiment To Measure Space-Environment Effects on Photovoltaic Power Subsystems," *Fifth Annual Workshop on Space Operations, Applications and Research (SOAR '91)*, NASA Conf. Publ. 3127, pp. 662-668, Feb. 1992.
- (2) Curtis, H., Guidice, D., Severance, P., and Piszczor, M., "Results of Thermal Vacuum Tests for the PASP Plus Flight Modules," *Proc. of XII Space Photovoltaic Research and Technology Conference*, NASA Conf. Publ. 3210, pp. 289-297, May 1993.
- (3) Guidice, D., Severance, P., Curtis, H., and Piszczor, M., "Investigation of Space-Environment Effects on Photovoltaic Technologies by the PASP Plus Experiment", AIAA 95-0371, 33rd Aerospace Sciences Meeting, 9-12 Jan 95.
- (4) Adams, S.F., "Photovoltaic Array Space Power Plus Diagnostics Flight Experiment: Pre-Flight Description of Experimental Photovoltaic Modules", WL-TR-92-2080, Wright Laboratory, Oct. 1992.
- (5) Davis, V.A., "Parasitic Current Collection by Solar Arrays in LEO", 1995 Space Power Workshop, Phillips Lab., 18-20 Apr 95.
- (6) Ferguson, D.C., "Current Collection of Space Station Solar Arrays — Differences between PASP Plus and SAMPIE", 1995 Space Power Workshop, Phillips Lab., 18-20 Apr 95.
- (7) Cho, M., and Hastings, D.E., "Dielectric Charging Processes and Arcing Rates of High-Voltage Solar Arrays," *J. Spacecraft & Rockets*, Vol. 28, pp. 698-706, 1991.
- (8) Soldi, J.D., "Arc Rate Predictions and Flight Data Analysis for the Photovoltaic Array Space Power Plus Diagnostics (PASP Plus) Experiment", M.S. Thesis, M.I.T., 1995.

PRELIMINARY CHAOTIC MODEL OF SNAPOVER ON HIGH VOLTAGE SOLAR CELLS

Willie R. Mackey
NASA Lewis Center
Cleveland, Ohio

SST
IN-50422

High voltage power systems in space will interact with the space plasma in a variety of ways. One of these, Snapover, is characterized by a sudden enlargement of the electron current collection area across normally insulating surfaces. A power drain on solar array power systems will result from this enhanced current collection. Optical observations of the snapover phenomena in the laboratory indicate a functional relation between bias potential and surface glow area. This paper shall explore the potential benefits of modeling the relation between current and bias potential as an aspect of bifurcation analysis in chaos theory. Successful characterizations of snapover as a chaotic phenomenon may provide a means of snapover prevention and control through chaotic synchronization.

Introduction:

Nonlinear physical systems that exhibit unstable behavior have recently been reexamined for the existence of chaotic behavior. (ref. 1) Chaotic behavior has been observed in laboratory plasmas (ref. 11-14). Chaotic behavior in plasma has been observed within ion sheaths due to DC currents in double plasma devices. Recently, an application of chaos theory as a control variable in nonlinear systems has received considerable attention (ref. 2-10). Spacecraft plasma interactions are primarily nonlinear and therefore may provide opportunities for chaotic analysis. Due to the remote nature of space studies, chaotic time series signal analysis may provide a significant means of spacecraft system control and diagnosis.

We begin the modeling process from spacecraft-plasma interactions empirical equations. Utilizing the "basis space" (ref. 1) of model chaotic systems to acquire analytic differential equations. This in turn can lead to predictions of experimentally observable by parameter variation which alters the phase space structure. Direct correlation of the model chaotic system with empirical equations may improve the validity of fitted models.

Bifurcation analysis:

Bifurcation analysis is concerned with how steady state solutions of a nonlinear system change their qualitative character as a parameter changes. The onset of instability of a solution usually occurs at the same critical parameter value as the bifurcation. If a sequence of bifurcations occurs as the parameter is varied then chaotic behavior can be initiated.

Bifurcation analysis consists of the following procedures. Let's consider a first order differential equation.

$$\frac{dx}{dt} = B(\alpha, x) \quad (1)$$

Steady state solutions such that $\mathbf{x}(t) = \mathbf{X}$ for all t exist if

Snapover:

Solar arrays consist of strips of solar cells with metallic interconnects between them. The power requirements of large space systems will require high voltages to operate economically. This is due to the necessity to minimize the mass of space hardware. High voltage arrays exposed to the space plasma essentially acts as biased probes attracting and repelling charged particles (ref. 21).

Snapover is a sudden enhancement of current collected from an ambient plasma attributed to secondary electron production from insulator surfaces (ref. 23-26). Exposed solar array interconnects collect electrons from the ambient plasma. Below a critical voltage, the bias voltage is located over the interconnect regions and the surface potential of adjacent insulator materials is essentially zero. Above the critical voltage there is a dramatic increase in current collection and the surface potential approaches that of a conducting plane (Fig. 2)

Figure 3 represent experimental data for a solar array section biased positive with respect to the plasma. For voltages greater than 100-150 volts, the electron current collected by the array increases dramatically. Even though the solar array surface is a dielectric, the surface becomes highly positive and collect current. The plasma sheath grows over the dielectric surfaces for positive potentials. The exposed interconnects or pinholes accelerates electrons which strikes the dielectric. Low energy secondary electrons are released which are collected by the exposed metal. This leave the dielectric cover glass positive, allowing the plasma sheath to grow over the solar cells. The solar array therefore collects as a conductor. This current which flows through the plasma is not available to the spacecraft and therefore represents a power loss to the array. Comparison of current collection between a metallic disks and a disc on "Kapton" insulation confirms that the insulator is involve with the current enhancement (ref. 18). Typically one would expect the insulation to be at floating potential and therefore of a negative "floating" potential which would repel electron resulting in a lower current collection than a plain conducting metallic disk (ref. 17).

Recently Ferguson (ref. 29) and Stillwell (ref. 28) noted optical observation which may clarify the parameter space of the snapover events. The optical data indicates that the snapover moves over the surfaces in response to changes in surface potential due to secondary electron productions.

Snapover is observed also in pinhole current collections (ref. 26). The primary difference being that the field distribution must expand through the pinhole emphasizing the normal distribution of the electric field. Still the controlling factor in current collection is the superposition of the field above the insulation and the exposed conducting surface.

Stevens et al (ref. 20-22), (Fig. 3) developed empirical relations for current collection above and below the snapover voltage of 100 volt for the experiment. Surface voltages traces indicated that below bias voltages of 100 volts dielectric cover glass were slightly negative in potential in order to maintain current balance. Above 100 volts the cover slide potential changed to a value about 50 less than the bias voltage. Expressed as a single formula:

$$I_c = A_i \sqrt{\left(1 + \frac{V}{\epsilon_e}\right)} + A_p \left[1 + \frac{V-100}{\epsilon_e}\right] \quad (8)$$

Where I_c is the current collected, A_i is the total interconnect area, A_p is the solar panel surface area and V is the bias voltage.

Let $V^{1/2} = \phi$ then equ. 8 can be written;

$$B(\alpha, X) = 0 \quad (2)$$

For each value of α ; equilibrium points are determined.

A bifurcation diagram is the plot of all curves $x = X(\alpha)$ in the (α, x) plane (Fig. 1). Stability of the equilibrium point X can be ascertain by considering the behavior of the solution to small perturbations. Performing a Taylor series about a small perturbation and neglecting higher order terms we find that stability to first order will be determine by the growth or decay of;

$$\exp\left[\left(\frac{dB(\alpha, X)}{dx}\right)t\right] = e^{st} \quad (6)$$

If $s < 0$ then all small perturbation vanishes as t increases. If $s > 0$, then X is unstable since small perturbations grow.

Bifurcation analysis examines the evolution of all equilibrium or steady state solutions of by considering the sign of $\nabla B(\alpha, X)$. A basic approach is:

- Identify dissipative phenomena.
- Construct dynamical equations in standard form.
- Characterize equilibrium motion - fixed bifurcation points.
- Characterize oscillatory motion - Hopf bifurcation points.
- Perform parametric studies of the bifurcation points.
- Construct a global portrayal of dynamical behavior by continuation.
- Compare to test data.

Refinement of the model equations and phase space can be achieved by continuation. Laboratory and space experiments only supply limited data points as a scalar time series in terms of a few independent coordinates. Continuation methods will allow generation of an extensive phase space from a few points in phase space. Identification of bifurcations from continuation generated phase spaces can enhance the precision of engineering guidelines in terms of experimental parameters (ref. 10).

Space environment interactions offers many areas for bifurcation analysis such as transition to saturation current as a function of potential, sheath formation as a function of potential, double layer formation, snapover as potential jumps from one equilibrium solution to another. In the spacecraft environment we have the following equilibria and oscillatory regions.

Equilibria: The fundamental physical process for all spacecraft charging is that of current balance, all currents must sum to zero. Key parameters in this process can be the spacecraft potential, orbit, active sources, surface material properties, sheath widths, solar cycle activities, plasma frequency, temperature, size, length effective area.

Oscillations and Transients: Spacecraft power systems will experience arcs, discharge phenomena, currents, plasma waves, switching and orbit eclipse. These effects correspond to periodic solutions to the dynamical equations and therefore limit cycles bifurcation points.

Below we formulate empirical equations for snapover into standard forms for bifurcation analysis.

$$I_c = \mu + \beta\phi + \alpha\phi^2$$

Equ. 13 is in the form of bifurcation equation such as the saddle node (Fig 1). Bifurcation diagrams indicates the points where an equilibrium solution can occur.

Experimental examination of sheath structure around pinholes was performed by Gabriel et al. The potential structure was described by a semiempirical formula (ref. 26).

$$\phi(r, z) = \frac{2\phi_0}{\pi} \arctan\left[\frac{a}{z} \exp\left(-\frac{z}{\alpha}\right)\right] \exp\left(-\frac{r^2}{\lambda^2}\right) \quad (14)$$

ϕ_0 is the potential applied to the exposed electrode in the pinhole, α and λ are empirical parameters.

The energy that electron are accelerated to the surface is determined by $\phi(r, 0)$. The electric field is dominated by the x component. Carruth (ref. 25) use this field in a multiple slit model to determine where the field is zero and reverse signs. This determines which exposed conducting surface will collect electrons. The dominance of the horizontal component provides the basis for transforming the experimental potential into a form suitable for a bifurcation analysis. This field distribution and its consequential derivatives can be transformed into a current potential equation similiar in form to the fold cusp bifurcations. Taking the time derivative of Poisson equations upon equ. 14, we acquire the following form.

$$v = f(\phi)x + g(\phi)x^2 \quad (19)$$

v is the horizontal velocity components of the collection current. x is the distance from the pinhole to the leading edge of the snapover current. By performing a bifurcation analysis of this equation one can determine the range of values for $f(\phi)$, $g(\phi)$ which satisfied the experimental data.

EWB a space environment interactions simulation software (ref. 6) models snapover by requiring current balance between the incident electron current and the divergence of the current carried by the secondary electron layer. The model assumes that secondary electron emission facilitates the spread of high voltage from the conductor onto the insulating surface.

$$\mathbf{E} \cdot \mathbf{n} = [\langle \epsilon \rangle Y \nabla \cdot \mathbf{E}_1]^{1/2} \quad (21)$$

The secondary layer current is proportional to the incident electron current and a strong function of the normal electric field at the surface. Where Y is the secondary electron yield and $\langle \epsilon \rangle$ is the mean secondary electron energy. A core of the charge balance simulation scheme of EWB is an empirical based relation between the charge density distribution and the surface potential.

$$\rho = F(\phi) = \sum F_n \phi^n \quad (23)$$

Given equ. 16, the simulation model therefore can be transform into a bifurcation form.

$$\frac{d\rho}{dt} = \sum F_n(\alpha, \beta) \phi^n \quad (24)$$

where α , β are experimental parameters containing with the "physics" of the model.

Chaotic Synchronization :

The existence of bifurcation points in spacecraft plasma dynamical equations coupled with the modeling of nonperiodic and chaotic phenomena as a sequence of bifurcations will allow the use of chaotic synchronization as an engineering control tool (ref. 2). The control idea is to monitor the system until it come close to a fixed bifurcation point and then change the parameter value until the system lies in the stable solution of the bifurcation region (ref. 5-8). Ott et. al., (ref. 9) developed a method where control can be applied to systems where the dynamical equations are not known. The method is to change a chaotic system into a periodic system by means of a weak time dependent perturbations to an accessible parameter. Carroll et. al., (ref. 8) have driven a subsystem of a chaotic system with the signal from a similar system to synchronization. Brown et. al., (ref. 2) have demonstrated the possibility of synchronizing a fitted model to a time series obtained via experimental observation. This method allows the generation of an ordinary differential equation that models the dynamics of the system that produces the time series. Sprout (ref. 1) has outline 19 standard dynamical equation which demonstrate chaotic behavior. Judd and Mees (ref. 10) has examine the problem of how to choose the best model from within a class of models to fit data. The best model captures the essential dynamics of the time series without over fitting - including in the model aspects of the time series that should be attributed to noise. Such a scheme potentially allows extensive remote diagnostics from a variety of physical parameter from a single time series measurement such as plasma collection current.

Time series measurements forms the basis of the control methods (ref. 3). Experimental measurements are gathered in the form of time series with a prescribed sampling interval or rate. Plasma currents are usually measured by Langmuir probes and thus provide a source of time series data. Synchronization of Langmuir time series data with a class of fitted models accords a non trivial test of the validity of the models.

Nondestructive testing via synchronization will afford the spacecraft design community a valuable tool to spacecraft control. A possible scenario is adapted from Brown et. al., (ref. 2). A new spacecraft with a projected operational life is placed in orbit. Prior to placement the spacecraft and its subsystems is driven by a calibrated external driving signal (plasma chamber?) and a time series is recorded. A model of the dynamics is constructed from part of the time series and the synchronization deviation level between the model and the rest of the time series is recorded. Once in orbit we received time series data from the spacecraft and its systems. We attempt to synchronize this orbital time series with the pre flight constructed model. Due to its orbital interactions, there will be changes in the synchronization deviation level due to the orbital and plasma dynamics. By examining and monitoring the changes in deviation we have information on spacecraft systems dynamics from the synchronization physical model. Given the noise invariance of our model we can be assured that our deviations are spacecraft induced and not statistical in nature.

Noise is a feature of Langmuir probe data and it is probable that certain featured of Langmuir noise has a chaotic time signature. This would provide another region for synchronization possibilities - use of noise as a stabilizing control signal via chaotic synchronization. Brown et. al (ref. 2, 3) indicates that synchronization can be maintain with high noise levels.

Conclusion.

Utilizing the results of chaotic synchronization, snapover may be controllable since its empirical based model are amendable to a bifurcation analysis. Bifurcation analysis examines the behavior of solutions to parametric equations at bifurcations points. At bifurcation points a qualitative change in the structure of the equilibrium solutions phase space. Changing one or more parameter might lead to instabilities. Several scheme for instabilities and chaos have been proposed as a series of bifurcations as a parameter is varied. Future work would entail time series analysis of snapover data fluctuations. Transition to chaotic behavior and instabilities can then be simply modeled as a sequence of bifurcations acquired from parametric analysis of the dynamical ions and synchronization methods as a means of system control could be applied.

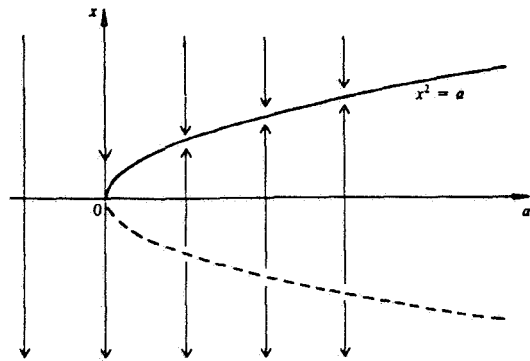


Fig. 1 Bifurcation diagram

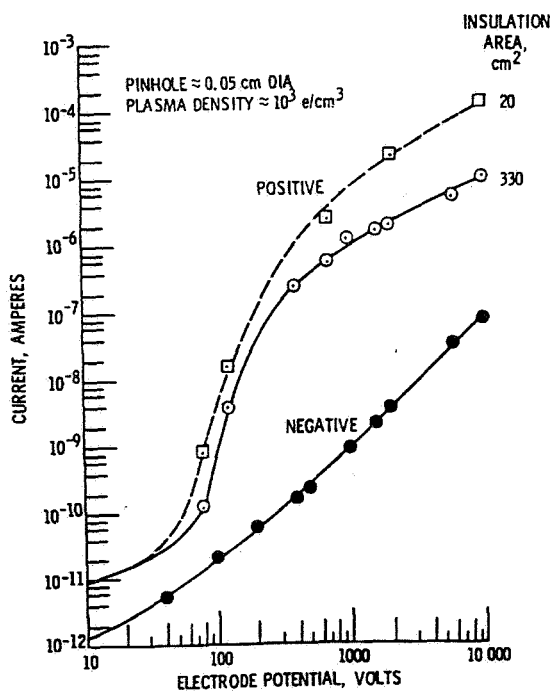


Fig. 2 Snapover ref. 16

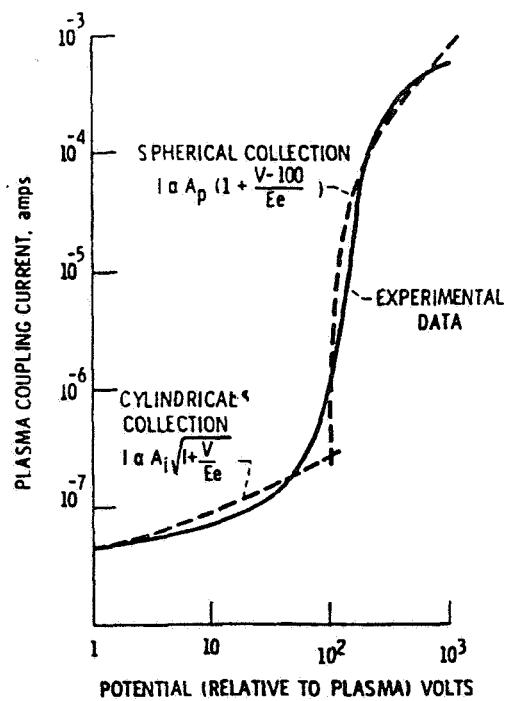


Fig. 3 Fitted model ref. 22

REFERENCES:

- 1) J. Sproott, *Some Simple Chaotic Flow*, PR-B, Vol. 50, No. 2, Aug. 1994, p. R647.
- 2) R. Brown et. al., *Modeling and Synchronizing Chaotic Systems From Experimental Data*, Physics Lett. A, Vol. 194, Oct. 1994, p. 71.
- 3) R. Brown and N. Rulkov, *Synchronization of Chaotic Systems*, Institute Nonlinear Science, Univ. California, San Diego, 1994.
- 4) U. Dressler and G. Nitsche, *Controlling Chaos Using Time Delay Coordinates*, PRL, Vol. 68, No. 1, Jan. 1992, p. 1.
- 5) M. Vieira et. al., *Synchronization of Regular and Chaotic Systems*, PR-A, Vol. 46, No. 12, Dec. 1992, p. R7359.
- 6) L. Pecora and T. Carroll, *Synchronization in Chaotic Systems*, PRL v.64, No. 8, pp.821, Feb. 1990.
- 7) L. Pecora and T. Carroll, *Driving Systems with Chaotic Signals*, PR-A, v.44, No. 4, pp 2374, Aug. 1991.
- 8) T. Carroll and L. Percora, *Synchronizing Chaotic Circuits*, IEEE Trans. Circuits and Systems, Vol. 38, No. 4, April 1991, p. 453.
- 9) E. Ott et. al., *Phys. Rev. Lett.* Vol 64, 1990, p. 1196.
- 10) K. Judd and A. Mees, *On Selecting Models for Nonlinear Time Series*, Univ. of Australia, Research Report, Dept. of Mathematic, Nov. 1994.
- 11) A. Komori et. al., *Bifurcation and Chaos in a Current Carrying Ion Sheath*, Phys. Fluids B, vol. 4, No. 11, Nov. 1992, p. 3573.
- 12) M. Kono et. al., *Cascading Bifurcations to Chaos in a Current Carrying Ion Sheath*, Jour. Phy. Soc. of Japan, Vol. 61, No. 2, Feb. 1992, p. 407.
- 13) P. Cheung nad A. Wong, *Chaotic behavior anh Period Doubling in Plasma*, PRL, Vol. 59, No. 5, Aug. 1987, p. 551.
- 14) T. Braun et. al., *Observation of Deterministic Chaos in Electrical Discharges in Gases*, PRL, Vol. 59, No. 6, Aug. 1987, p. 613.
- 15) C. Purvis, et al, *Interaction of Large, High Power Systems with Operational Orbit Charged Particle Environments*, NASA TM-73867.
- 16) S. Domitz and N. Grier, *The Interaction of Spacecraft High Voltage Power Systems with the Space Plasma Environment*, NASA TMX-71554.
- 17) N. Grier and S. Domitz, *Current From A Dilute Plasma Measured Through Holes In Insulators*, NASA TN D-8111, Dec. 1975.
- 18) N. Grier and D. McKinzie, *Current Drainage To A High Voltage Probe In A Dilute Plasma*, NASA TM X-67890, Jan. 1972

- 19) G. B. H. Hillard, *Plasma Current Collection of Z-93 Thermal Paints*, J. Spacecraft, Vol. 30, No. 6, p.767.
- 20) N. Steven, et. al, *Investigation of High Voltage Spacecraft System Interactions with Plasma Environments*, AIAA paper 78-672, 4/25-27/78.
- 21) N. Steven, et. al, *Large Space System - Charged Particle Environment Interaction Technology*, AIAA 79-0913.
- 22) N. Stevens, *Review of Bias Solar Array-Plasma Interaction Studies*, NASA TM 82693, 1981.
- 23) M. Mandell and I. Katz, *High Voltage Plasma Interactions Calculations Using NASCAP/LEO*, AIAA paper 90-0725, 1/8-11/90.
- 24) M. Carruth and C. Purvis, *Space Test Program of High Voltage Solar Array/Space Plasam Interactions*
- 25) M. Carruth, *Plasma Collection Through Biased Slits in a Dielectric*, J. Spacecraft, Vol. 24, No. 1, Jan-Feb. 1987, p. 79.
- 26) S. Gabriel, et. al., *Experimental Measurement of the Plasma Sheath Around Pinhole Defects in a Simulated High Voltage Solar Array*, AIAA 83-0311, 1983.
- 27) H. Thiemann, *Particle in Cell Simulation of Sheath Formation Around Biased Interconnectors in a LEO Plasma*, J. Spacecraft, Vol. 27, No. 5, Sept-Oct. 1990.
- 28) R. Stillwell et al, *Current Collection from the Space Plasma Through Defects in Solar Array Insulation*, J. Spacecraft, Vol. 22, No. 6, Nov. 1985, p. 631.
- 29) D. Ferguson et al, *Visualizing Plasma Electric Fields*, NASA Lewis DDF Report, 1995.

538-20

50423

125911

9 P

A LINEAR REFRACTIVE PHOTOVOLTAIC CONCENTRATOR SOLAR ARRAY FLIGHT EXPERIMENT

P. Alan Jones and David M. Murphy
AEC-Able Engineering Co., Inc.
Goleta, California 93117

ABSTRACT

Concentrator arrays deliver a number of generic benefits for space including high array efficiency, low cell area cost savings, protection from radiation effects, and minimized plasma interactions. The line-focus concentrator concept delivers two added advantages: 1. low-cost mass production of the lens material and, 2. relaxation of precise array tracking requirements to only a single axis. New array designs emphasize light weight, high stiffness, stow-ability and ease of manufacture and assembly. The linear refractive concentrator can be designed to provide an essentially flat response over a wide range of longitudinal pointing errors for satellites having only single-axis tracking capability. In this paper we address the current status of the SCARLET linear concentrator program with special emphasis on hardware development of an array-level linear refractive concentrator flight experiment.

INTRODUCTION

High performance, light concentrating solar arrays offer spacecraft users well documented cost and performance benefits. The SCARLET (Solar Concentrator Array with Refractive Linear Element Technology) is the first practical concentrator array that can realistically provide such benefits. An aggressive, 6-month development and flight validation program, sponsored by the Ballistic Missile Defense Organization (BMDO) and NASA Lewis Research Center, will quantify and verify these benefits with in-orbit performance measurements. Given the current economic climate, Return On Investment (ROI) is of primary importance to both commercial and government spacecraft users. The cost and performance benefits to be accrued from the use of SCARLET technology directly contribute to enhanced ROI. In this paper we introduce the basic SCARLET technology, examine its benefits to users, and describe the first-generation flight hardware.

System Benefits

Simply stated, concentrator technology allows arrays to have much lower cell area for a given power level. For instance, a concentrator array with a 15:1 geometric concentration ratio requires about 7% the active solar cell area of a traditional planar array. This equates to a direct 93% reduction in solar cell material costs which is the largest component of total array costs. Further indirect cost benefits accrue from the reduced active cell area. These generic cost benefits will of course favorably impact all mission types.

The main technical barrier to employing satellites in high radiation missions is degradation of cell energy conversion efficiency due to electron and proton impingement. In a planar array, compensating for cell degradation requires the use of larger, more costly arrays due to excessive cell usage. Alternately, system costs are driven up by thick (costly and heavy) radiation protection over the entire cell area, frontside and backside. In such missions the SCARLET array will provide significant mass savings because only 7% of the array requires mass shielding. This mass savings can technically and financially enable certain missions such as medium earth orbit (MEO) communication constellations or a geosynchronous mission employing spiral-out electric propulsion orbit raising. The economic benefits of both of these mission scenarios are well documented.

Additionally, since only 7% of the total area need be populated, high-efficiency multijunction cells can be more economically employed to field a reduced area array to limit aerodynamic drag and/or relax attitude control system requirements. The mission benefits of reduced area arrays have also been well documented (reference 1).

The SCARLET technology mitigates the debilitating effects of interplanetary distances on solar cell efficiency. These LILT (Low Intensity, Low Temperature) effects increase the size and hence cost of a solar array for a multi-AU (Mars and beyond) spacecraft. Although LILT effects can be minimized by cell design, concentrator technology offers a less expensive way of addressing the issue. For instance, at 4 AU the sunlight intensity is approximately 1/16th of that at 1 AU. A 15:1 SCARLET array would bring the sunlight intensity delivered at the solar cell back to that of the 1 AU range. The cell will then operate at near 1 AU efficiency and will not suffer the full LILT efficiency degradation. The combination of concentrator arrays and LILT-capable cells may enable deep interplanetary missions.

BACKGROUND

The application of concentrator arrays has historically been limited by their waning power response to off-pointed solar vectors. From a risk point of view, the reliance on such tight pointing accuracies is unacceptable. The SCARLET array technology utilizes *pointing error tolerant* refractive Fresnel optics to achieve a 15:1 concentration of the incoming sunlight onto photovoltaic solar cells.

The choice of refractive versus reflective optics is driven by the greater slope error tolerance of refractive focusing. For reflective optics the high surface smoothness required to prevent scattering losses is costly to manufacture and difficult to protect from on-orbit environmental effects. In addition, the tolerance to shape error of the arched Fresnel lens is 300 times greater than the reflective concentrator, which has been shown to be prone to performance losses due to thermal distortions.

The SCARLET design, utilizing the innate error tolerance of the Fresnel optics, is the first practical concentrator solar array because it accommodates the combination of manufacturing tolerances, thermal distortions, and jitter as well as the inevitable off-angle errors due to positioning knowledge and command errors.

PASP+ Experiment

The SCARLET flight validation experiment draws directly from the flight experience and success of the Photovoltaic Array Space Power Plus Diagnostics (PASP+) experiment which flew on the US Air Force sponsored Advanced Photovoltaic and Electronics Experiment (APEX) spacecraft. The concentrator portion of the PASP+ experiment is well described by Piszczor, 1991 (reference 2). The PASP+ concentrator module, manufactured by Boeing (Figure 1), consists of 12 spot-focus, mini-dome Fresnel lenses with GaAs/GaSb mechanically stacked tandem cells. The primary optics are protected from the AO, UV environments anticipated in the APEX orbit (350 km by 1850 km, 70° inclination) by multi-layer optical coatings on the silicone lenses. The technology's tolerance to high radiation fluences and the space plasma environment was also verified. Marvin, 1995, (reference 3) reported very good experimental results for the concentrator module. Total power degradation is about 5% for 300 days of elapsed mission duration. This degradation is considered nominal and indicates the absence of any anomalous environmental degradation mechanisms.

SCARLET/COMET FLIGHT EXPERIMENT

The SCARLET/COMET flight validation program was awarded to the team of AEC-ABLE Engineering Company, Spectrolab, and Entech. Work was initiated in January of 1995 and the first-generation wing was to fly on NASA's COMET spacecraft in July 1995 (Figure 2). The launch of the mission, renamed METEOR, has endured delays throughout the summer. The flight is currently scheduled for late October.

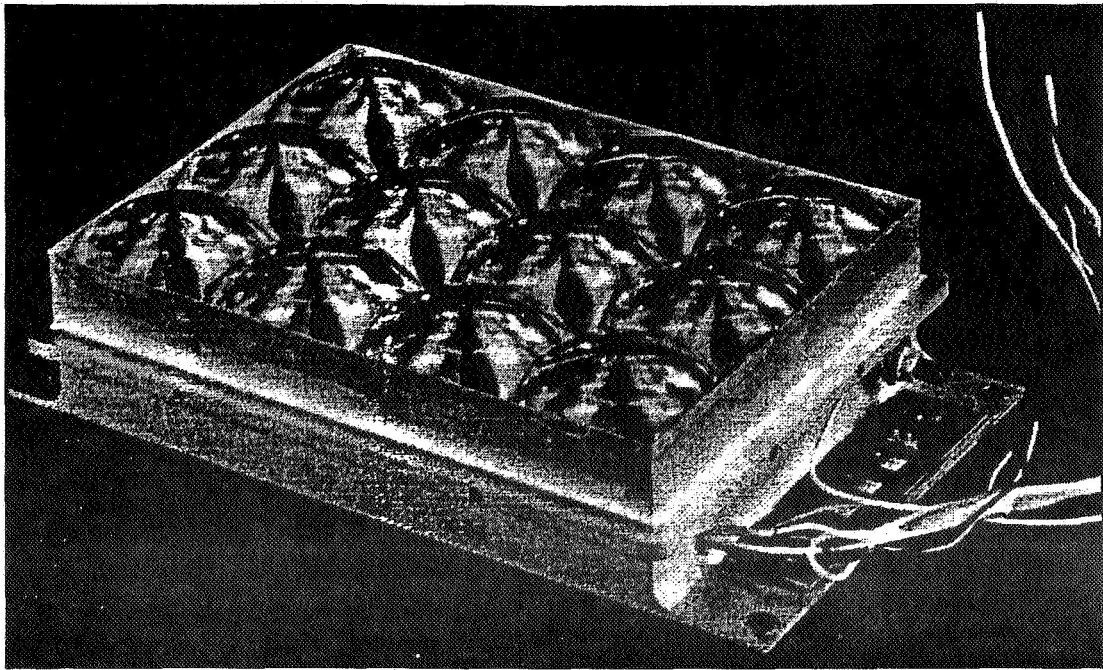


FIGURE 1. PASP+ CONCENTRATOR EXPERIMENT MODULE

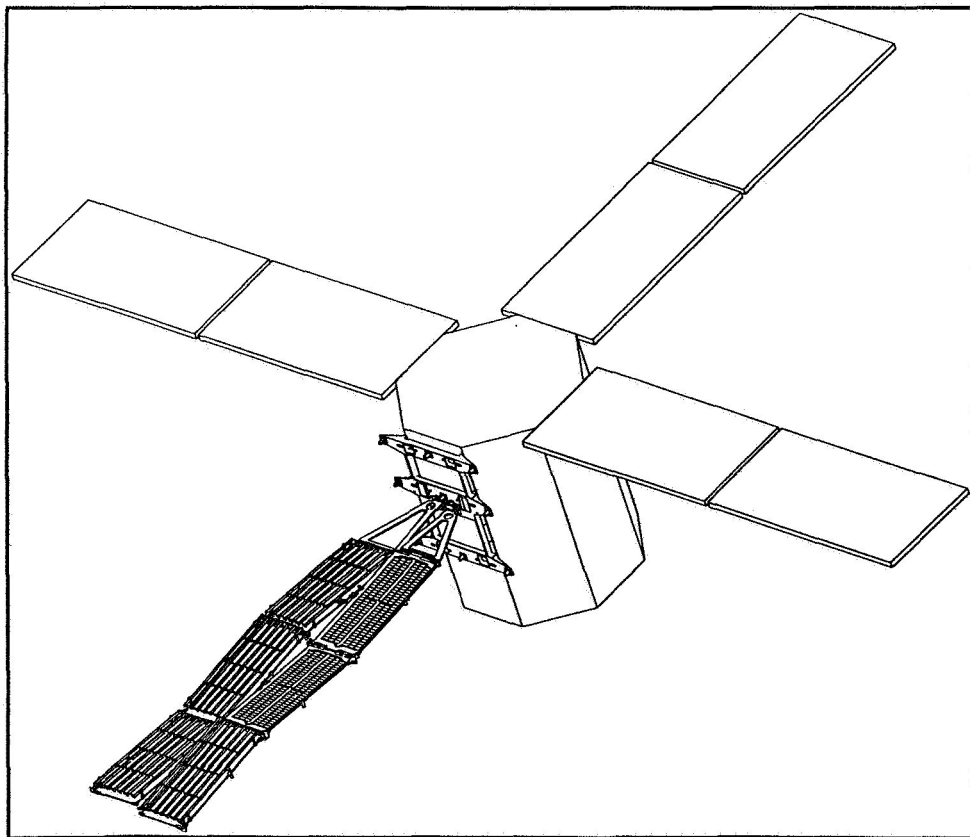


FIGURE 2. COMET/METEOR SPACECRAFT

The flight experiment is a six panel ABLE PUMA deployable array structure populated with Spectrolab GaAs/Ge concentrator solar cells under Entech linear Fresnel primary and compound parabolic concentrator (CPC) secondary optics (Figure 3). This wing will replace one of the four existing silicon cell planar wings. The COMET spacecraft will fly in a nadir orientation most of the time and will orient the spacecraft into a sun pointing, solar-inertial orientation for data acquisition from the array experiment. The wing is composed of four concentrator panels and two silicon cell planar panels. The two planar panels are required to maintain energy balance when the spacecraft is in the nadir mode as all the wings are non-gimbaled.

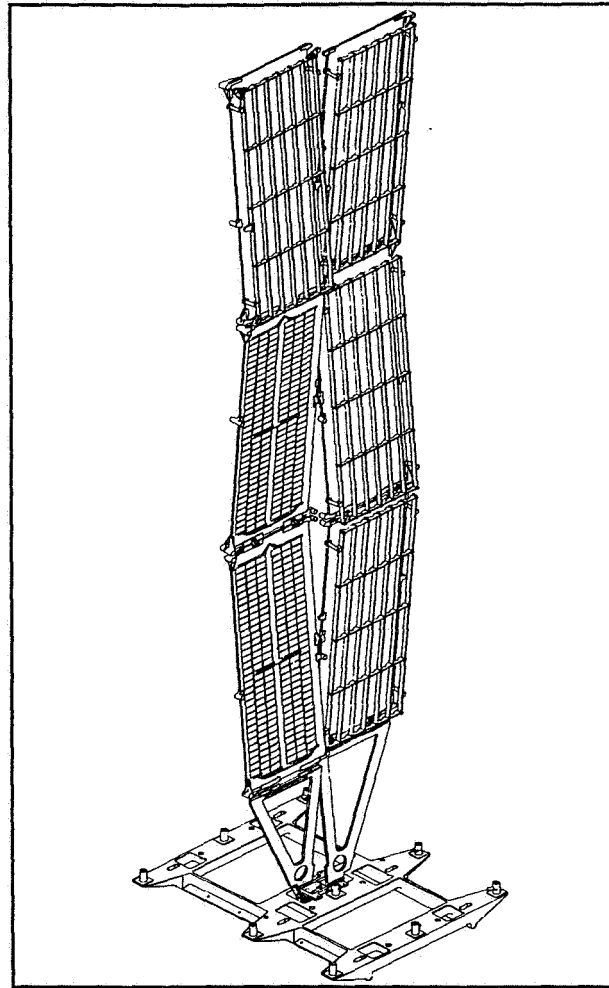


FIGURE 3. SCARLET/METEOR FLIGHT DEMONSTRATION WING

Optics System

The Fresnel primary lens uses a symmetrical refraction arched lens approach. This patented lens provides high optical efficiency (by minimizing reflection losses), outstanding focusing properties, and unequaled tolerance for manufacturing and operational inaccuracies. This remarkable tolerance for shape errors eliminates potential problems due to deflections, distortions, or thermal expansion/contraction effects, which have plagued other types of photovoltaic concentrator systems (especially parabolic trough reflector systems). A ray trace drawing for the baseline optics configuration at the specified off-pointing tolerance of 2° is shown in Figure 4. Note the secondary concentrator at the focus of the Fresnel lens primary concentrator. The secondary reflects rays internally by total internal reflection (TIR), and thus requires no metallic reflector surface.

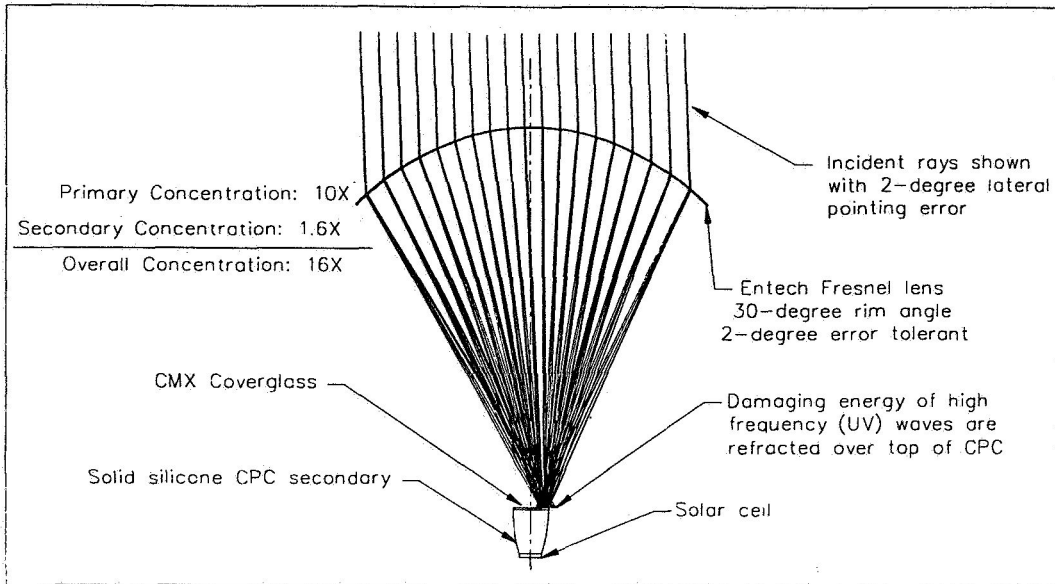


FIGURE 4. SCARLET OPTICS LIGHT RAY TRACE

The linear Fresnel system has a different tolerance to sun vector off-pointing in each of the two principal axes. Tolerance to errors about the longitudinal axis is greater than the tolerance to errors about the lateral axis as shown in Figure 5. This feature can be employed to provide optics for missions planning only a one-axis array tracking mechanism. Longitudinal sun pointing errors of up to 23.5° can easily be accommodated. The data for the particular lens design plotted in Figure 5 shows a 0.5% loss at a 10° longitudinal pointing error and a 10% loss at a 2° lateral pointing error. In practice the desired lateral and longitudinal tracking tolerances are traded against overall light concentration ratio in the system design process.

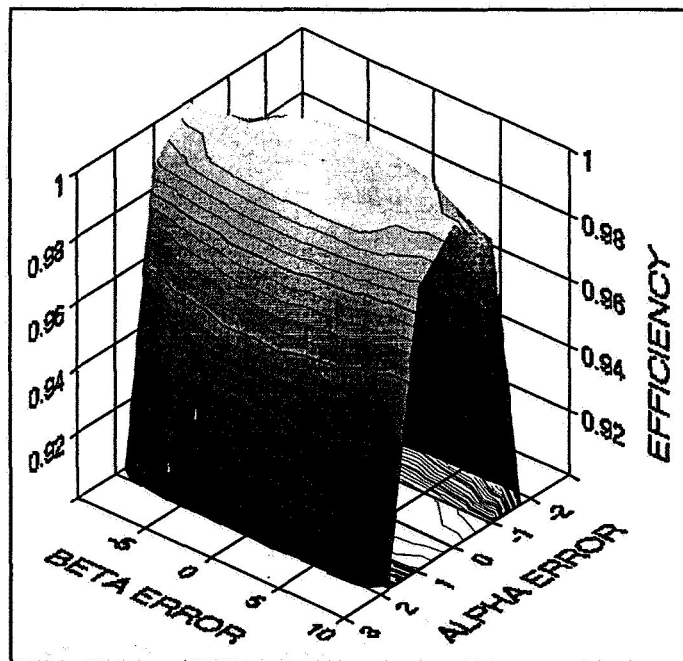


FIGURE 5. OPTICAL OFF-POINTING EFFICIENCY

Module Design

The current SCARLET/METEOR module design is based on GaAs/Ge concentrator cells. Each panel has six strings, each of which are made up of four 12-cell module subassemblies (Figure 6). The concentrator cells, measuring 0.140 inch by 0.600 inch, are attached to the module in a series interconnection made with a Kapton flex circuit. Three bypass diodes on each module are attached to the circuit with surface mount techniques. One blocking diode per string is similarly attached to the first of the four modules in a string.

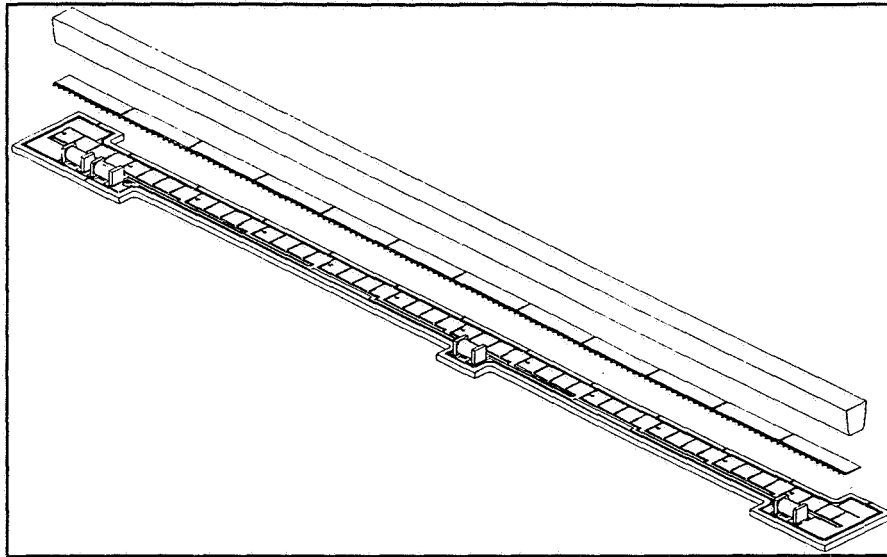


FIGURE 6. SCARLET MODULE DESIGN

The design is oriented for cost-effective mass production techniques. The CPC secondary optics are molded as a single piece so that only a single secondary bond operation is performed instead of twelve bond operations. And the cell placement and attachment is amenable to standard pick and place electronic assembly operations. The cell interconnection to the circuit is accomplished with an automated sonic wire bonding step. Figure 7 shows a close-up photo of two flight modules mounted onto the substrate. The cells can be seen through the CPC optics.

Deployable Optics

A critical feature of the SCARLET design is the achieved reduction in the required stowage volume. Concentrator optics require a finite focal length that historically has defined the array's required stowed thickness and, hence, volume. These volumes are typically too large for most missions. The SCARLET system utilizes a deployable optics system to maintain a small stowage volume. Two patent-pending approaches for lens deployment have been defined.

One utilizes a system of lenticular springs to deploy the Fresnel lenses. The other uses a precision linkage system to articulate the lenses into position. The former design is implemented in the SCARLET/METEOR flight experiment hardware. SCARLET's tight stowage volume is shown in Figure 8. One of the flight panels is shown in Figure 9 with its primary optics deployed above the populated substrate panel.

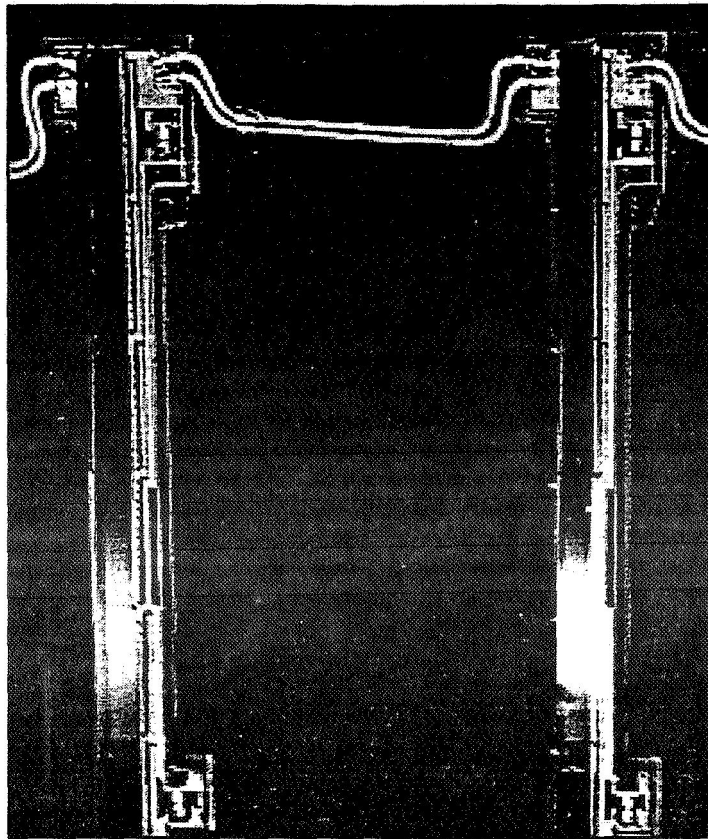


FIGURE 7. SCARLET MODULES

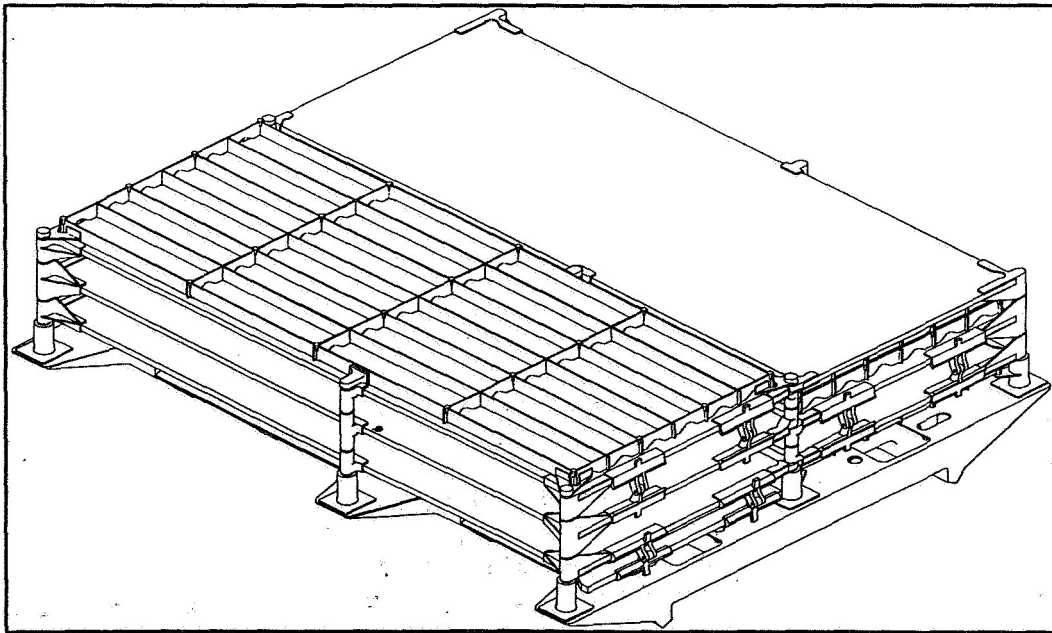


FIGURE 8. STOWED SCARLET WING

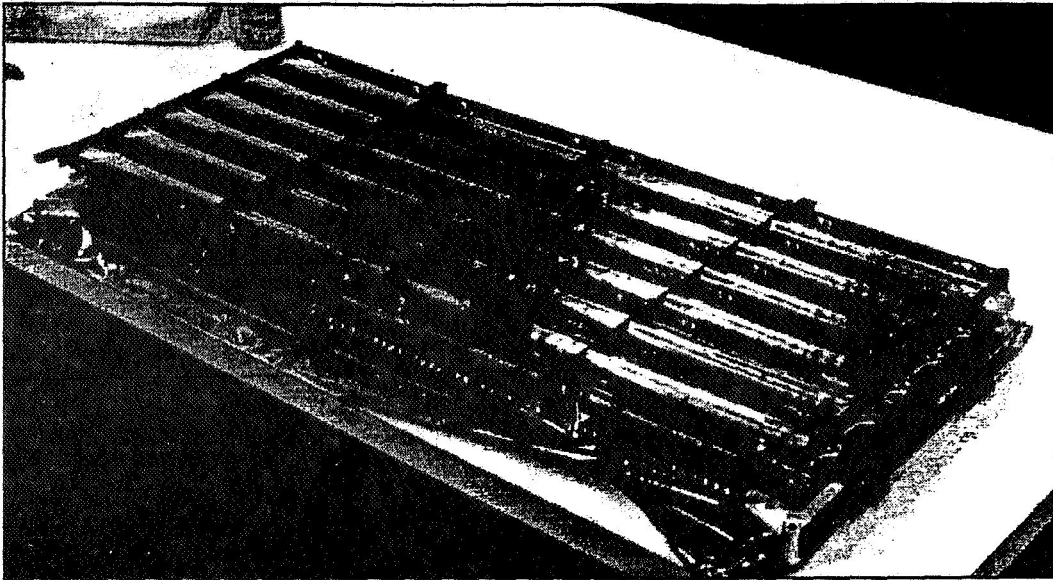


FIGURE 9. SCARLET PANEL WITH DEPLOYED OPTICS

PERFORMANCE

Various design and analytical trade studies were performed to assess the near-term performance of the SCARLET technology as it evolves from the current no-frills, schedule-driven experiment design towards application as a primary power source on a flight program. The results, which incorporate thermal, optical, and radiation analyses, are in keeping with the technology assessments put forward by Caveny, 1994, (reference 4) and Piszczor, 1994 (reference 5) which anticipate EOL specific powers in the 70 W/kg to 100 W/kg range. Figure 10 depicts the near-term EOL specific power trends for SCARLET concentrator technology for three solar cell assumptions. Analyses of subsequent development indicates EOL performance approaching 115 W/kg for a high radiation environment (also shown in Figure 10).

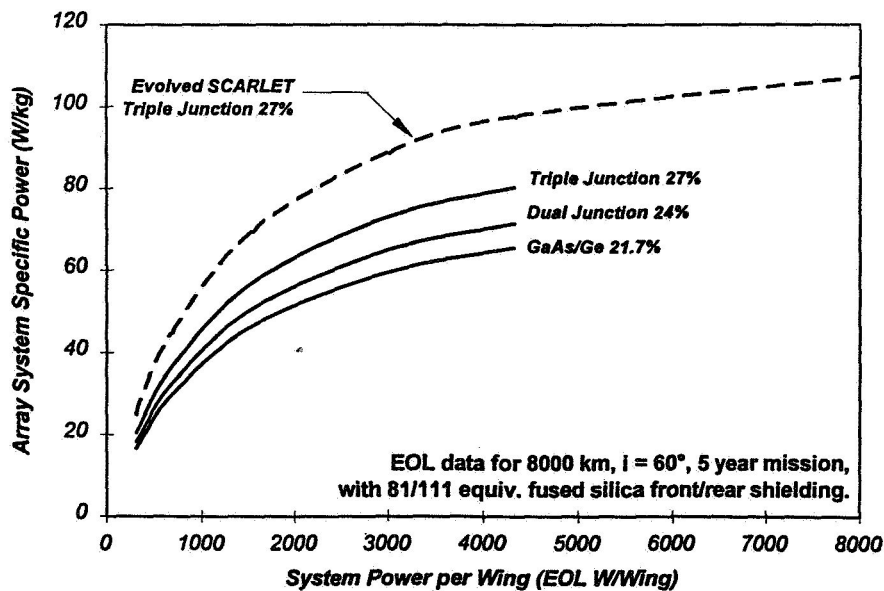


FIGURE 10. SCARLET SPECIFIC POWER PERFORMANCE

CONCLUSION

The SCARLET concentrator technology offers unique capabilities to both commercial and government spacecraft users. These include solar array cost reduction, especially when new, high-performance multijunction cells are employed; mass reduction over traditional planar arrays, especially in high radiation missions such as MEO missions and electric powered LEO to GEO orbit raising; and potentially reduced drag area. SCARLET has near-term applicability as it is significantly far along the development curve as a result of the planned Fall 1995 flight validation aboard the NASA METEOR spacecraft.

REFERENCES

1. Ralph, E.L., "Solar Cell Array Comparisons", Space Power Workshop, Albuquerque, N.M., 1994
2. Piszczor, M.F., Brinker, D.J., Flood, D.J., Avery, J.M., Fraas, L.M., Fairbanks, E.S., Yerkes, J.W., and O'Neill, M.J., "A High Performance Photovoltaic Concentrator Array: The Mini-Dome Fresnel Lens Concentrator with 30% Efficient GaAs/GaSb Tandem Cells", Proceedings of the 22nd IEEE Photovoltaic Specialists Conference, 1991, pp. 1485-1490
3. Marvin, D., "PASP+ Flight Experiment Results", Space Power Workshop, Albuquerque, N.M., 1994
4. Caveny, L.H., and Allen, D.M., "BMDO Photovoltaics Program Overview", Proceedings of the XIII Space Photovoltaic Research and Technology Conference, 1994, pp. 13-21
5. Piszczor, M.L., O'Neill, M.J., and Fraas, L.M., "An Update on the Development of a Line-Focus Refractive Concentrator Array", Proceedings of the XIII Space Photovoltaic Research and Technology Conference, 1994, pp. 313-322

Development of a Solar-cell Dust Opacity Measurement Instrument for Mars Pathfinder

Geoffrey A. Landis
Ohio Aerospace Institute
and

Phillip P. Jenkins
NYMA, Inc.

NASA Lewis Research Center, mailstop 302-1
21000 Brookpark Rd., Cleveland, OH 44135

539
IN-50424

ABSTRACT

The atmosphere of Mars has a considerable load of suspended dust. Over time, this dust is deposited out of the atmosphere. The mechanism and the temporal and geographical variation of this deposition are not well characterized. Measurements of settling rates and dust properties are of considerable scientific interest. Atmospheric dust affects the atmospheric solar absorption and thus the heat balance of Mars, as well as serving as nucleation sites for water and CO₂ frost. Knowledge of dust properties is of critical interest to design and prediction of the lifetime and power output of solar arrays, and also to design of mechanical mechanisms and radiators.

An instrument has been designed and fabricated to measure the dust accumulation during the course of the Mars Pathfinder rover mission. The solar-cell coverglass transmission experiment will measure the change in optical opacity of a transparent coverglass as dust settles on the surface, and a quartz crystal monitor will measure the mass deposited.

Background

The atmosphere of Mars contains a significant load of suspended dust. This is quite visible in the Viking lander photographs by the light color of the sky. The amount atmospheric dust varies with season and with the presence of local and global dust storms, but never drops entirely to zero.

Dust suspended in the atmosphere of Mars is a significant driver of the climate and meteorology of Mars. Absorption of sunlight by dust particles is the primary driver of the thermal properties of the atmosphere [1]. To quote from a review by Zurek *et al* [2]: "The effect of suspended dust on the atmosphere are: (1) dust is an effective absorber of the incoming solar radiation and both absorbs and emits thermal radiation; (2) the amount and possibly the optical properties of suspended dust are highly variable in space and time; and (3) dust hazes can persist for very long periods."

Information on dust deposition rate and properties is of critical use for future mission design [3,4,5,6]. Knowledge of how much dust deposits on solar arrays, the intensity and spectral range of sunlight at the surface of Mars, and the size and shape of particles will be crucial elements for designing missions that will operate on solar power for periods of several years and will have moving parts which will be subject to degradation by dust.

Other than the basic parameters of light scattering, however, the properties of the atmospheric dust are almost completely unknown. The size of the particles is known only roughly (and with considerable disagreement between models); the size distribution and the particle shapes are almost completely unknown. While we do know that dust does settle out of the atmosphere, the mechanism, rates, and geographic variability of dust settling out of the atmosphere are a matter of controversy. Any mission to study the climate of Mars will remain incomplete unless a serious attempt is made to answer fundamental questions about atmospheric dust.

A first attempt to quantitatively measure dust deposition on the surface of Mars will be our experiments flown on the Mars Pathfinder, which will measure the mass and optical opacity of dust settling onto the rover solar array [3,4].

Dust Properties

Settling properties of Mars dust are discussed in earlier papers [5,6]. There are two different models of the size and scattering properties of Mars dust. The conventional model is by Toon *et al* [8], as modified by Pollack *et al.* [9], using sunlight scattering measured from the surface by Viking.

A revised model by Clancy and Lee [10] is based on infrared reflectivity measurements taken from orbit by Viking. The Clancy and Lee model suggests that the dust is composed of much smaller particles than the Pollack model indicates, and that the particles are less absorbing and more reflective. The Pollack *et al.* analysis suggests a cross-section weighted mean radius of 2.75 μm ; Clancy and Lee analysis 0.4 μm or less. The cross-section weighted radius of 1.5 μm estimated by Pang and Ajello [11] is almost halfway between that of the two other models.

Both values are consistent with estimates of the grain size of the surface drift material at the Viking lander sites [12].

The fact that the particle size differs by nearly an order of magnitude is an indication of the difficulty of deducing particle size from optical scattering data. The degree of apparent detail in these models completely obscures how much is unknown. For example, the gamma distribution of particle sizes assumed is an ad-hoc distribution function; the actual distribution of sizes is likely to be different. The light scattering properties are significantly determined by the size and distribution of particle shapes. It is known from the scattering that the particle shapes cannot be spherical, but the actual shapes are impossible to determine from scattering data. Scattering of light from non-spherical particles is very difficult to model, and if a variety of different particle sizes exists, the number of free parameters to model makes it nearly impossible to derive particle information from scattering data. Some researchers suggest that atmospheric dust will not be present as individual particles at all, but as fractal agglomerates with considerable interior void fraction. It is unknown whether the particles are homogeneous or heterogeneous in composition; for simplicity, homogeneous particles have been assumed in modeling, but this is a questionable assumption.

The mechanism and geographical variability of dust settling is likewise unknown. Dust is likely to deposit out of the atmosphere by gravitational settling, by vertical eddy mixing, and by serving as nuclei for ice crystal formation. Alternative mechanisms such as electrostatic precipitation and aggregation by electrostatic bonding may also play a role [13]. It might logically be suggested that during low-opacity times the suspended dust will be smaller in grain size than the average. However, the Mariner 9 measurements tended to indicate that the size distribution during the major storms seems to be essentially constant during the decay [8].

Table 1 [from ref. 5] shows the amount of degradation in solar array performance due to dust obscuration calculated for best and worst case of a 30 day and 2 year mission. Clearly, there is significant variation between cases. Better information on deposition rate is required if solar array performance is to be accurately predicted.

Table 1

Total obscuration of solar array for the Pathfinder (30 day) and network (2 yr) missions

| <u>Case:</u> | <u>obscuration (30 day mission)</u> | <u>obscuration (2 yr mission)</u> |
|--------------|---|---------------------------------------|
| Baseline | 6.6% | 77% |
| Best | 0.5% | 22% |
| Worst | 52.2% | 89% |

Pathfinder Solar-Cell Experiment

Two sensors, comprising the "Materials Adherence Experiment (MAE)," will be flown to Mars on the Pathfinder spacecraft in 1996. The Pathfinder spacecraft, built by the Jet Propulsion Laboratory (JPL), is to be launched in December 1996, and will land on Mars on July 4, 1997. The mission includes both a stationary lander and a small solar-powered rover, named "Sojourner." The MAE instrument is located on the rover. It consists of a Solar Cell experiment (MAE-SC) and a Quartz Crystal Monitor. These have been built, qualified for flight, and delivered to JPL for integration onto the spacecraft. Figure 1 shows the location of the MAE on the Sojourner rover. The actual experiment takes up a footprint of 41 mm by 37.5 mm, including area for a JPL reference solar cell unrelated to the experiment.

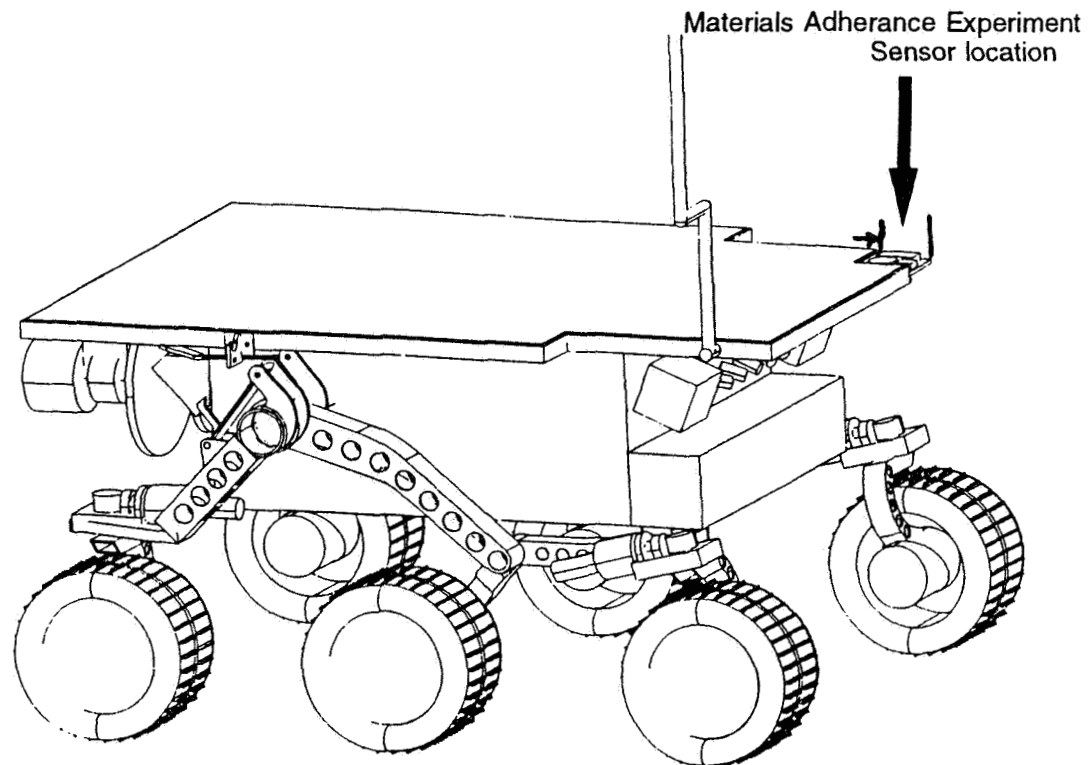


Figure 1 The MAE solar-cell and QCM experiments on the "Sojourner" Mars Pathfinder Microrover

The Solar Cell Experiment consists of a horizontal transparent plate onto which atmospheric dust will settle. This plate normally covers a small GaAs solar cell. A shape-memory alloy ("nitinol") actuator temporarily moves the plate away from the photosensor, to allow a measure of solar intensity without the intervening dust settling plate; then the measurement is repeated through the dust plate, giving a measurement of the solar intensity viewed through the dust collecting plate. The difference between these two measurements monitors the change in opacity due to the dust settled on the plate.

The Solar Cell experiment has the only moving part in the instrument, the actuator which moves the transparent plate away from the sensor. For simplicity and reliability, we designed a novel rotating actuator based on the shape-memory alloy nitinol to do this job. The actuator has only a single moving part. The design and testing of this actuator is described in detail in the paper "A Rotating Arm Using Shape-memory Alloy" [7]. The rotary action is shown (drawn to scale) in Figure 2.

The MAE/SC has been through qualification testing for the Pathfinder flight with no failures.

In addition to the solar cell experiment, the Pathfinder rover will also fly a miniature quartz crystal monitor [3]. The QCM makes an independent measurement of the dust mass, allowing the results from the solar cell experiment to be interpreted in terms of obscuration as a function of dust mass. The quartz crystal monitor is a vibrating quartz wafer about the size of a dime. The surface of the quartz wafer is horizontal and exposed to the sky. As dust settles on the crystal, the frequency of vibration decreases. This serves as a measure of the mass deposited as a function of time. QCM sensors similar to this one have a spaceflight heritage for contamination monitors.

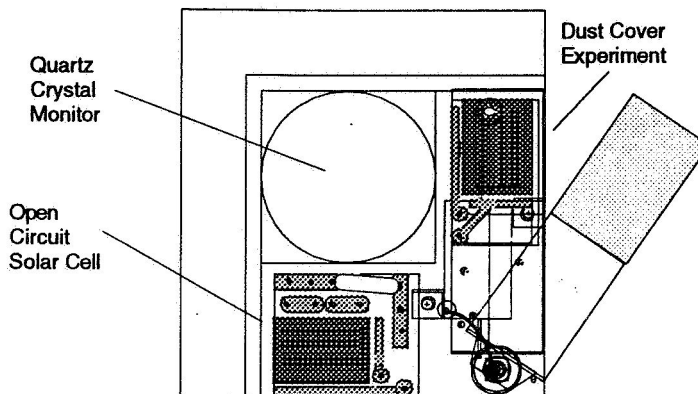


Figure 2: Schematic of the Materials Adherence experiment on the Mars Pathfinder, showing the location on the watchplate of the quartz crystal monitor, the dust cover experiment with nitinol-actuated coverglass (shown in the "open" position), and the open-circuit voltage solar cell.

CADO Instrument Package

An advanced version of this instrument package, named "CADO" ("Characteristics of Atmospheric Dust Observation"), is being developed for flight on a future mission, to obtain detailed information on properties of settled dust. CADO is designed to monitor the rate of deposition of dust on a horizontal surface on Mars, to directly observe the particle sizes and shapes, and to measure the solar insolation at the surface in four spectral ranges.

The CADO instrument set consists of three sensors.

1. *Quartz Crystal Monitor.*
2. *Optical Opacity and Solar Insolation Monitor*, an advanced version of the Pathfinder "Solar Cell experiment".
3. *CCD Microscope.*

The first two sensors on the CADO instrument have direct heritage from the Pathfinder instrumentation, upgraded to make them both smaller and more capable. The third sensor of the set, the CCD microscope, has not previously been flown. The CCD microscope has been successfully developed through the breadboard stage under NASA Lewis discretionary funding. This project has just completed its second year.

The CADO instrument set is described in more detail elsewhere [3].

Sensitivity

It is important that the sensitivity of the proposed instruments is sufficient to actually measure the expected properties of dust. For a baseline calculation, a typical optical depth of the atmosphere is $\tau=1.0$ is assumed, and the particles are assumed to settle out of the atmosphere with an exponential decay time of 100 days. Assuming parameters of the Pollack model, this yields a coverage of 0.36% per day [5,6], and an obscuration of 0.22% per day. Thus, a single day's coverage will be measurable with

the Optical Obscuration Sensor as long as the A/D conversion is 9 bits or more. Ten days coverage will be detectable with 8 bits of A/D accuracy. The A/D for the sensor is a 12 bit A/D (11 bits usable), and therefore it is reasonable to expect that the dust obscuration will be visible.

The mass-weighted average particle radius is 3.9 microns. If the average particle density is 2.5 grams/cm³, the mass deposition rate is 4.7 micrograms per cm² per day. Since the QCM sensitivity is in the 10 nG range, sensitivity is no difficulty.

At a cross-section weighted average particle size of 2.75 micron, the particle number density to be expected corresponds to 1.5·10⁴ particles/cm² per day. If the magnification chosen for the microscope is 20x, this will result in 3 particles being imaged per day. This is sufficient to accumulate good statistics on particle size over an extended mission.

References

1. J.B. Pollack, "Properties of Dust in the Martian Atmosphere and Its Effect on Temperature Structure," Chapter III, *Adv. Space Res., Vol. 2, COSPAR*, 45-56 (1982).
2. R.W. Zurek, J.R. Barnes, R.M. Haberle, J.B. Pollack, J.E. Tillman and C.B. Leovy, "Dynamics of the Atmosphere of Mars," Chapter 26, *Mars*, University of Arizona Press, Tucson, 1992, 835-933.
3. G. Landis, P. Jenkins, J. Flatico, L. Oberle, M. Krasowski and S. Stevenson, "Development of a Mars Dust Characterization Instrument," presented as paper IAF-95-U.4.09, *46th International Astronautics Federation Congress*, Oslo Norway, 2-6 Oct. 1995, and at the Intermarsnet workshop, Capri, Italy, 29 Sept. 1995.
4. G. Landis, "Instrumentation for Measurement of Dust Deposition on Solar Arrays on Mars," presented at Case for Mars V, Boulder CO, 26-29 May 1993
5. G. Landis, "Dust-Induced Degradation of Solar Arrays on Mars," *Proceedings of the 1st World Photovoltaic Energy Conversion Conference*, Hawaii, Dec. 5-9 1994, 2030-2033.
6. G. Landis, "Dust Obscuration of Mars Photovoltaic Arrays," Paper IAF-94-380, 45th International Astronautical Federation Congress, Jerusalem, Oct. 9-14 1994.
7. P. Jenkins and G. Landis, "A Rotating Arm Using Shape-memory Alloy," presented at Space Mechanisms Conference, NASA Johnson Space Center, Houston, TX, 17-19 May 1995.
8. O.B. Toon, J.B. Pollack, and C. Sagan, "Physical Properties of the Particles Composing the Martian Dust Storm of 1971-1972," *Icarus*, Vol. 30, 663-696 (1977).
9. J.B. Pollack, D.S. Colburn, F.M. Flassar, R. Kahn, C.E. Carlston, and D. Pidek, *J. Geophysical Research*, Vol. 84 No. B6, 1979, p. 2929-2945.
10. R.T. Clancy and S.W. Lee, "A New Look at Dust and Clouds in the Mars Atmosphere," *Icarus*, Vol. 93, 135-158, 1991.
11. R.A. Kahn, T.Z. Martin and R.W. Zurek, "The Martian Dust Cycle", *Mars*, University of Arizona Press, Tucson, 1992.
12. H.J. Moore, R.E. Hutton, G.D. Clow, and C.R. Spitzer, *Physical Properties of the Surface Materials at the Viking Landing Sites on Mars*, U.S. Geological Survey Professional Paper 1389, pp. 117 and 130 (1987).
13. R. Greeley, N. Lancaster, S. Lee and P. Thomas, "Martian Aeolian Processes, Sediments, and Features," Chapter 22, *Mars*, University of Arizona Press, Tucson, 1992, 730-766.
14. J. Appelbaum, G. Landis and I. Sherman, "Solar Energy on Mars: Stationary Collectors," *Journal of Propulsion and Power*, Vol. 11 No. 3, 554-561 (1995).
15. J. Appelbaum, G. Landis and I. Sherman, "Sunlight on Mars: Update 1991," *Solar Energy*, Vol. 50 No. 1, 35-51 (1993).
16. R.B. Singer, AGU paper 2B1214, "Minerology of High-Albedo Soils and Dust on Mars," *J. Geophysical Research*, 10,159-10,168 (1982).
17. E.A. Guinness, R.E. Arvidson, M.A. Dale-Bannister, R.B. Singer and E.A. Brukenthal. "On the Spectral Reflectance Properties of Materials Exposed at the Viking Landing Sites," *Proc. 17th Lunar and Planetary Science Conf., Part 2, JGR Vol. 92, No. B8, E575-E587* (1987).

*Information on Mars Pathfinder probe can be found at the Mars Pathfinder home-page, <http://mpfww.jp.nasa.gov/>

540-44
50425
125913
2p

Multijunction Cell Workshop

Sarah Kurtz
NREL
Golden CO

Henry Curtis
NASA/Lewis
Cleveland OH

The multijunction cell workshop met on Tuesday afternoon with over 30 attendees from a wide variety of companies and labs. Several topics were discussed, with the most discussion on the following items.

- 1) What needs to be done to fly GaInP/GaAs cells in the ENTECH linear concentrator for SCARLET II?
- 2) Wrap-through or wrap-around contacts -- are they available, why are they useful, and why they are not used more.
- 3) Directions to consider, including use of superlattices, 3 or 4 junctions, stacked cells, etc.
- 4) Measurements -- does every cell need to be tested under both red and blue illumination?

(note to make sure they get a stack of power for ASEC)
The MANTECH program started in September will allow both ASEC and Spectrolab to establish a large scale production capability for the GaInP/GaAs/Ge cells.

The New Millennium program has chosen to use multijunction concentrator cells in a 2 kW array. They are expecting to use GaInP/GaAs, but have many questions regarding moving this technology from planar to the concentrator configuration:

-Making smaller cells will improve yield in the short term, but in the long run this will not be a major issue.

-The existing cell designs will not need any significant modification for low concentration (10X). Small refinements include:

- The grids need to be redesigned,
- The emitter may be slightly more doped,
- The thickness of the top cell may need to be adjusted for the optically changed spectrum,
- The distance from the lens to the cell needs to be optimized.

There was concern about the rigidity of the support structure being adequate for concentrators. In the linear direction, off pointing of 10 to 15 degrees can be tolerated. In the other direction the structure must support off pointing less than two degrees.

It was pointed out that concentrators pose a serious risk since a tumbling satellite will get no power from a concentrator system yet will get some power from a planar system. There are instances where spacecraft have lost their attitude control system for a period of time. A hybrid of planar and concentrator systems gives better assurance in such cases.

Lockheed Martin is interested in using wrap-through contacts on the GaInP/GaAs on Ge cells. By using the wrap-through contacts they were able to automate the flexible array assembly process for Si cells. For the Ge based cells the potential gain may be even greater.

Spectrolab is patenting a wrap-through process that will work for the GaInP/GaAs and GaAs cells on Ge. They have demonstrated their design on small volumes, but have not scaled it up. Similarly, ASEC has a wrap-

through process for the III-V cells but have not found any customers. They investigated both organic and inorganic-based concepts but only the inorganic concept uses space qualified materials. Their yield must be improved to make this a good manufacturing process. The wrap-through process does add some cost at the cell level, but it's not clear how this will compare to the savings at the array level.

A number of potential directions for space cells were discussed. At the moment, everyone sees things headed toward the GaInP/GaAs/Ge cell. However as production levels increase along with order volume, the economics and marketing philosophies may change somewhat. Sometimes the most important criteria is W/kg and sometimes W/m² is more important. Although the customers may be asking for lower cell prices, when the total systems costs are considered higher solar cell efficiencies usually justify higher cell costs.

The GaInP/GaAs/Ge and Inp/GaInAs systems are both lattice matches, so they don't need to use superlattice or graded layer schemes. However, a number of uses for superlattices or graded layers were identified: 1. Growth of InP on Ge or Si (Ge is easier than Si because of the thermal expansion differences). 2. Growth of GaInP/GaAs on Si. 3. Superlattices can give radiation resistance if they make multiple junctions, reducing the distance any minority carrier might need to travel before being collected. 4. Bragg reflectors. 5. Superlattices or graded layers are beneficial to any lattice-mismatched material system.

The question was raised as to whether we really want to increase the number of junctions or, after two junctions, the added efficiency is not worth the extra cost of generating the third (or fourth) junction. For the case of GaInP/GaAs/Ge with an active Ge junction vs. inactive junction, it is actually easier to grow it with an active Ge junction; no added cost is incurred by the third junction but the efficiency can be increased by up to 2.3% (absolute). Clearly, in this case, one more junction is an advantage. Other systems may or may not show such an advantage when another junction is added. The value of the lowest junction is especially questionable as the cell temperature is increased. However the low band gap cells have the strongest performance for outer planet missions. Al containing materials should not necessarily be ruled out.

Stacked cells were generally considered acceptable as long as they could be connected in a two-terminal configuration. A suggestion was made to push some array integration onto the cell vendors.) The stacked cells have some advantages including being able to be separately tested before being connected and may have more radiation resistance.

The weight of the cells can potentially be reduced by removing the substrate. Three methods for doing this include CLEFT, lift-off using an AIAs release layer, and sacrifice of substrates (Ge). CLEFT has the disadvantage of needing to repolish the wafer after each use while the AIAs lift off only works on small cells (one dimension must be less than or equal to 1 cm). RTI found sacrifice of a cheap Ge substrate to be cheaper than the CLEFT method. Once the substrate is removed, the device must be mounted on another material. Mounting directly on a coverslip will not work if a metal grid is included. There was a lot of skepticism about the reliability of these devices after being mounted to another material. Will they survive the pull strength and thermal cycling tests?

The question of how to test multijunction arrays was discussed (and will be addressed in the next day's workshop). Being able to control the spectrum (relative amounts of red and blue light) is more important than being able to mimic the exact AM0 spectrum. The needs for cell testing and array testing may be different. There were contradictory opinions about whether one measurement can adequately characterize a two junction device. ASEC tests every cell for both bottom and top cell performance. Spectrolab is developing statistics so that only some fraction of the cells will need to have both junctions tested. The question of how to calibrate reference cells was left for discussion at the following workshop.

541-44
50426
125914
3P

**Report on Workshop
on
Radiation Damage**

Geoffrey P. Summers
Naval Research Laboratory and
University of Maryland Baltimore County
&
Carlos Vargas-Aburto
Kent State University
Kent, OHIO 44242

ABSTRACT

The workshop met for two hours with approximately 25 participants from the conference. The discussion mainly centered around the two issues of the availability of radiation test facilities in the U.S. and the adequacy of typical radiation measurements to represent accurately space radiation effects. Special concern was expressed about the accuracy of the most commonly used radiation environmental models, AE8 for electrons, and AP8 for protons. The consensus of the workshop participants was that several recommendations be made to the conference as a whole, as a result of the discussions.

RADIATION FACILITIES

1. Available accelerators

It was generally agreed that both electron and proton irradiation facilities were becoming progressively less accessible in the U.S. As a first step in seeing how serious the problem had become, a list of available facilities known to the participants was produced. This is shown in Tables 1 and 2.

Table 1.

| Electron Irradiation Facilities | Maximum Energy or Energy range (MeV) | |
|---|---|-----|
| Boeing Corporation | 1 | |
| Jet Propulsion Laboratory (JPL) | 2.5 | |
| NASA (Goddard) | 2 | |
| Naval Post Graduate School | 20 | 120 |
| Nat'l Institute Standards and Technology (NIST) | 1.5 | |
| U. of Maryland (College Park) | 10 | |
| Wayne State University | 4.7 | |

Table 2.

| Proton Irradiation Facilities | Maximum Energy or Energy range (MeV) |
|---|---|
| Aerospace Corporation | 0.4 |
| Brookhaven | 200 |
| Harvard | 60 |
| Nat'l Institute Standards and Technology (NIST) | ? |
| Jet Propulsion Laboratory (JPL) | 10 |
| Naval Research Laboratory (NRL) | 4.5 |
| U. of British Columbia (*) | 32 500 |
| U. of California (Davis) | 63 |
| U. of Michigan | 3 |
| Wayne State University | 4.7 |
| Western Michigan University | 10 |

* Canada

2. Alternative techniques

There was some discussion on the use of ^{60}Co gamma rays or ^{241}Am alpha particles as alternative radiation sources to electron and proton accelerators. Table 3 lists the ^{60}Co facilities known to the participants. When ^{60}Co gamma rays interact with matter, they mainly generate Compton electrons in low and intermediate Z materials. In high Z materials such as lead, photoelectrons can also become important. The Compton electrons have a spectrum of energies up to ≈ 1 MeV with an average energy of ≈ 0.6 MeV. ^{60}Co gamma rays therefore produce damage that is generally similar in nature to that produced by 1 MeV electrons at an accelerator, except that the Compton electrons are isotropic, not unidirectional. The alpha particles produced as a result of the decay of ^{241}Am can be used as a desktop simulation of the damage effect of protons, so long as due consideration is given to the relative displacement damage dose deposited by the respective particles. In practice, the ^{241}Am source is typically a small disk which is placed ≈ 1 cm from the target. The size of solar cell that can be irradiated depends on the size of the disk. The alpha particles lose energy passing through the air and/or the top part of the cell, and the effective energy of the particle is degraded to ≈ 4 MeV. The problem associated with the use of both ^{60}Co gamma rays and ^{241}Am alpha particles is the general reluctance of the solar cell community to accept the data when 1 MeV electrons and 10 MeV protons are the usual particles employed. In addition, NRC licensing is an issue for ^{241}Am sources used in a laboratory. Some concern was also raised about possible unusual radiation effects that might be produced, especially by ^{60}Co gamma rays.

Table 3.

| Cobalt-60 Irradiation Facilities | Cobalt-60 Irradiation Facilities |
|---|---|
| Aerospace Corporation | Nat'l Institute Standards and Technology (NIST) |
| Jet Propulsion Laboratory (JPL) | Naval Research Laboratory (NRL) |
| NASA (Goddard) | U of Maryland (College Park) |

MEASUREMENTS

1. Testing procedures.

There are two general purposes for ground radiation tests. First, there is the need to provide data back to the producer as new cell technologies are being developed; and secondly, there is the need for data from which to predict cell and array performance for proposed or actual missions. The first need can be met fairly well by performing ground tests in the usual way. That is, the test cell is irradiated at a relatively high dose rate at room temperature by a unidirectional, monoenergetic beam of electrons or protons, in the dark, and at open circuit. At several incremental fluence levels, the irradiation is stopped and the photovoltaic parameters of the cell are measured. However, the workshop participants repeated the concern generally recognized by the radiation effects community that this method of performing ground tests does not adequately represent what actually happens in space. In space, the cells are mostly irradiated at low dose rate, at temperatures that can reach $\approx 60^{\circ}\text{C}$, isotropically by electrons and protons with a wide spectrum of energies, close to short circuit in sunlight. Occasionally, the cells can also be plunged into the dark and drop in temperature way below room temperature. It was not clear to the workshop which, if any (or all), of the environmental parameters really mattered, i.e., do dose rate effects occur or does it matter whether the cell is irradiated at open circuit during tests. If these issues are uncertain for relatively well understood cell types, they are especially a problem for new cell technologies such as multijunction cells and concentrator cells which are designed to operate at high injection levels.

2. Environmental Radiation Models.

The problem of whether the usual ground tests are providing satisfactory radiation data for predicting cell performance in space is compounded by apparent deficiencies in the AP8 and AE8 models. Several space experiments, including CRRES and PASP PLUS indicate that actual cell degradation is about a factor of two less than the models predict. Also, the disagreement with the models was found to vary with the level of shielding on the cells, which indicates that not only is the overall dose wrong but that the proton differential spectrum is also wrong. These results are similar to those found in many operational spacecraft power systems. This fact has prompted some power systems engineers to deliberately reduce the size of photovoltaic arrays below what the models indicate are necessary for a mission, in order to save money. Clearly, this is not a satisfactory situation. However, changing the environment models is not something that can be done easily by the space photovoltaic community, since many other users exist for these models.

3. New Requirements

One particular concern about testing occurs for LILT systems for deep space probes. Cells in these applications will be operating at very low light levels and temperatures. There seems to be very few institutions that have test facilities to accommodate these requirements. In fact, only JPL and Aerospace Corporation could be named during the workshop. There does not appear to be a facility in the U.S. with the range of capabilities similar to what is available in the U.K., at the DRA facilities at Farnborough and Harwell. However, it was generally agreed that the capability developed by Bruce Anspaugh at JPL needed to be supported by the radiation effects community. Bruce's work over the years has consistently provided some of the best data taken on a variety of cell types. Although there does not appear to be any threat that this capability will be lost in the near future, the workshop was insistent that managements be made aware of its overall importance.

RECOMMENDATIONS

The workshop made the following recommendations to the full conference.

1. A comprehensive list of available radiation facilities be developed to include the types of measurements possible, the range of energies available, the cost, the level of availability, and the point of contact.
2. More work be performed as soon as possible to develop acceptable test procedures for new cell technologies such as multijunction, concentrators, and new materials.
3. Strong general support be given to the JPL test facility, and especially Bruce Anspaugh.

SUMMARY OF WORKSHOP ON
CHARACTERIZATION AND TESTING OF NEW CELL TYPES

Dale R. Burger
Jet Propulsion Laboratory
Pasadena, California

and

David J. Brinker
NASA Lewis Research Center
Cleveland, Ohio

542-44
50427
125915
2P

GENERAL

An opening statement was made to the effect that the capture of cell structure and process is an important part of new cell testing since only by knowing what you are dealing with can you decide what a series of test results really mean.

TPV CELLS

The opening statement led into a short discussion of thermophotovoltaic (TPV) cell testing. The spectrum of visible and infrared photons from TPV system emitters will be radically different from the AM0 spectrum. Even at this late date there is difficulty in matching the AM0 spectrum with the various light sources - how then are we to characterize TPV cells, which may be asked to work with spectra created by sources operating at a number of different temperatures with a number of different emitters. The statement was made that spectral response (quantum efficiency) data was the key. This statement was somewhat challenged by the reminder that intensity effects can create non-linear losses at the high fluence of TPV systems.

Finally, there was some discussion of the use of black body sources for characterization. The good news is that black bodies are available which cover the temperature range of space (i.e. radioisotope) heat sources. The bad news is that these black bodies are at most one inch (25 mm) in diameter. Cells can therefore be characterized but strings and arrays cannot.

MULTIJUNCTION CELLS

MultiJunction (MJ) cells was the next area of discussion. This discussion started off with the observation that single junction cells were much less demanding as to spectral match of their test light source to the AM0 spectrum (already we are pining away for the good old days.) Single junction cell testing has the added benefit of the existence of a large database, built up over decades of trial and error.

The MJ cell test problem is twofold. First, the test light source for a combined current-voltage measurement must not contain any unwanted spikes or dips near any of the cell band edges. Second, individual adjustment of each of the double or triple (or quadruple?) light sources is required to properly characterize the performance of each cell (or band gap). Spikes or dips in the band edge regions make proper cell testing nearly impossible. Some dual lamp sources have been built or are being built. A spectrally matched bias light technique needs to be agreed upon, after careful review.

Some agreement was reached on the minimum requirements for MJ cell testing. There must be standard cells of identical construction (this is not as simple as it sounds as cell design and processing is constantly evolving). Since balloon standards are typically flown only once each year, the additional use of aircraft flown standards should be reviewed. The MJ standard cells must be accompanied by standard sub-cells which were calibrated at the same time. Finally, there must be at least one impartial laboratory to act as a clearing house, since the capital expense is likely to be too high for many individual organizations to construct their own facilities.

SUMMARY

There was a strong feeling that an early definition of requirements is needed:

A joint industry/government/academia approach was favored.

A high level of accuracy and confidence in MJ cell testing is required in a short time.

The approach taken for MJ cells can be applied to TPV cells but the need is not quite as urgent.

OPEN ISSUES

A review should be made of the possibility of the use of carbon arc lamps for solar simulators now that modern electronic power conditioning and high speed data collection is available.

Cell strings and arrays testing must also be addressed since the solutions for cell testing may not always scale up.

How will funding be found for all of this?

Solar Power Satellites
summary of a workshop held at SPRAT-XIV

Geoffrey A. Landis
Ohio Aerospace Institute
NASA Lewis Research Center 302-1
21000 Brookpark Rd. Cleveland, OH 44135

543
IN-50428

The concept of solving the Earth's energy crisis by supplying the Earth with solar electricity generated in space and beamed to ground receivers by microwave was proposed by Peter Glaser in 1968 [1]. The concept, referred to as the "Solar Power Satellite" or "SPS," was studied extensively between about 1977 and 1980, by NASA and the U.S. Department of Energy [2,3], and by the National Academy of Sciences [4] and the Office of Technology Assessment [5]. Since these studies were completed fifteen years ago, no official reanalysis of the concept have been done, although there have been a continuous (albeit unfunded) low-level of interest in the subject, as expressed by occasional conferences and workshops [6,7]. Particularly notable (to the present author) is a recent proposed conceptual design which uses thin-film cell technology and integral solid-state microwave elements [8].

The 1980 "reference" concept is shown in cartoon form in figure 1.

Orbit: geosynchronous (35,800 km altitude)

Array: 55 km², using 17% efficient Silicon cells, assumed available at 17¢/watt (1980 dollars)

Transmitter: 1 km² transmitting aperture; 2.45 GHz

Rectenna: 100 km². Microwave power density 23 mW/cm² center, 100 μW/cm² edge.

5 GW electric power produced at the busbar per satellite

Estimated cost: \$100B first unit; \$11B each additional unit (1980 dollars)

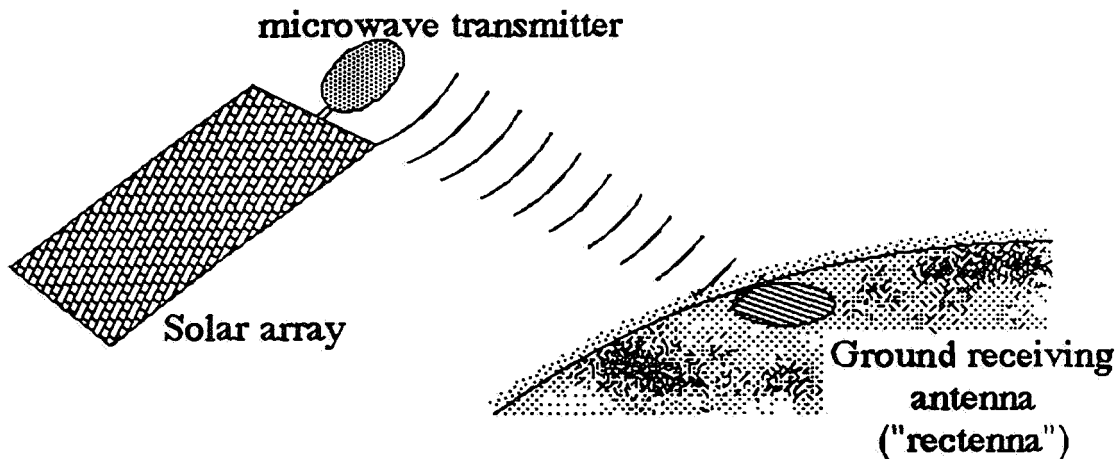


Figure 1
1980 Reference Concept for a Satellite Solar Power System [2]

The Office of Advanced Concepts at NASA recently initiated a re-analysis of the SPS concept. The ground rule for the analysis was that a project of such size (and more particularly, cost) as the 1980 baseline concept is out of the question in today's world. The study questions: (1) have technology improvements since the 1980 studies made SPS concepts more feasible? (2) Are new architectures or concepts for SPS possible which would reduce the cost?

These issues were posed to the workshop conducted at the SPRAT Conference, with the intent of soliciting input from experts on space photovoltaic technology. Note that many of the concerns,

questions, and suggestions generated echo comments from other groups. In the interest of brevity, I report the workshop without attempting to correlate comments to references in the earlier literature.

The first issue brought up at the workshop was the size of the microwave transmitting antenna, which is set by the wavelength and the desire to minimize receiver spot size at the distance of geosynchronous orbit. The immediate question was asked, does transmission have to be by microwaves? Lasers were suggested as an alternative option. Ron Cull discussed his work on analyzing laser transmission, and said that radiators for waste heat rejection are a big problem for lasers, which are not as efficient as microwave transmitters, and which typically require lower operating temperatures. It was pointed out that the Goldstone demonstration of microwave power transmission at 2.5 GHz, 85% efficiency DC in to DC out, is a very impressive practical result.

A tether extending from geosynchronous orbit to the surface to serve as a transmission line was brought up, but quickly dismissed, as the required tensile strength makes it "a very tricky materials problem."

The next question brought up was the operating environment on the cells? The statement was made, "If you can use low-cost screen-printed terrestrial cell technology, OK, but if you have to use space cells, there's no way we can *manufacture* cells in enough quantities." This may require avoiding orbits with significant radiation.

The question was then put forth, what is the minimum project needed to show feasibility and affordability? What is the growth path from there?

The first suggestion was a power relay satellite. The statement was made "we don't have a power generation problem, we have a power distribution problem." It was pointed out that if a microwave power relay satellites could redistribute power, terrestrial arrays e.g., in Australia, or floating in the Atlantic and Pacific Oceans, could send power from the daylit side of the Earth to the users.

The next suggestion was to use a large space mirror for lighting. 30% of the electricity used is used for lighting, why not use sunlight directly? Perhaps not all that big a mirror is needed to do this. On the other hand, there is a big problem if it's cloudy: you don't want a lighting system that only works on sunny days.

The next question addressed was, is it necessary to put the array in orbit? Why not use a balloon (or a raft of balloons) to put an array at 100,000 feet, where it will be above the clouds, and above most of the wind. This might make it possible to use a tether for the power downlink, and it would also make it much easier to pull down, if required, for maintenance. Questions raised were, could a balloon hold up the tether weight? Could a balloon hold up the *array* weight?

It was suggested that there would be great advantages if the solar power satellite constellation could be made in an orbit accessible to the space shuttle. This would make the launch considerably less expensive, and would make it accessible for maintenance. Drag is a problem; you want to put it as high as you can, but trapped protons start getting significant at altitudes above $0.1 R_e$. The objective would be "a constellation of satellites that come over and deliver power, so that there's always another one coming over." This would need a lot of satellites, since most of the time any particular satellite is not over the receiver. The problem gets rapidly worse off the equator: the "Iridium" communications satellite constellation, for example, needs 66 satellites to assure that one is overhead at any time for mid-latitude users, and the communications mission allows a satellite to be usable as far as 80° from overhead. A power beam probably won't be allowed to be used at such low angles. It was noted that storage would help this situation a lot, if a satellite could come by and "dump" accumulated power. It was suggested, can we make hydrogen and use that, either directly as fuel, or as a way to accumulate energy?

It would be "great" if we could configure a system to provide high-value power for peak-shaving. This means the power maximum is at 2-4 PM in the summer (to run air-conditioners).

It was suggested that we could have many small power satellites to beam power to one big antenna at higher orbit, which beams it back down. The advantage of this is that most of the mass is in lower orbit, where it's accessible and repairable, with only a "few" assets in high orbit.

The final question brought up is, what are the showstoppers? The main concern was with launch costs (and associated maintenance costs), and radiation damage. In low orbit, additional concerns were with aerodynamic drag due to residual atmosphere, with the possibility of plasma discharge at the presumably high voltages required for power distribution, and with the need for "lots of receivers and

lots of satellites."

For all orbits, that there could be concerns about microwave link safety. What if it misses? It was noted that even if the concern isn't a scientifically legitimate one, it still will be a factor in getting approval to do the project.

As a final note, one of the participants said that the demand for this is coming. The East Coast is building base electrical power plants again, after a hiatus of almost 20 years due to oversupply, and further demand will be growing down the road.

References

1. P.E. Glaser, "Power from the Sun: Its Future," *Science*, Vol 162, Nov. 11, 1968, pp. 857-861.
2. U.S. Department of Energy, *Final Proceedings of the Solar Power Satellite Program Review*, April 22-25, 1980, Lincoln Nebraska, Conf-800491; NASA TM-84183 (Document N82-22676 through 22767).
3. F.A. Koomanoff and C.E. Bloomquist, "The satellite power system: concept development and evaluation programme." In Glaser, P.E.; Davidson, F.P.; and Csigi, K.I. (eds.); *Solar Power Satellite: The Emerging Energy Option*, pp. 26-59, Ellis Horwood Limited, Chichester England, 1993.
4. National Academy of Sciences, *Electric Power from Orbit: A Critique of a Satellite Power System*, National Academy Press, Washington, DC, 1981.
5. Office of Technical Assessment, *Solar Power Satellites*, Aug. 1981, OTA-E-144, Document N81-77268
6. L. Deschamps (ed), *SPS 91: Power from Space, Second International Symposium*, Societe des Electriciens et des Electroniciens (SEE) and Societe des Ingenieurs at Scientifiques de France (ISF), Paris/Gif-sur Yvette, 27-30 August 1991.
7. A. Brown (ed.), *Proceedings of the First Annual Wireless Power Transmission Conference (WPT '93)*, San Antonio, TX 23-25 Feb. 1993.
8. G.A. Landis and R.C. Cull, "Integrated Solar Power Satellites: An Approach to Low-Mass Space Power," *Space Power*, Vol. 11, No. 3-4, 303-218 (1992). Presented at *SPS 91: Power from Space, Second International Symposium*, 27-30 August 1991; pp. 225-232.

SPRAT XIV, OCTOBER 24-26, 1995
ATTENDANCE LIST

JIM AVERY
(JX Crystals, Inc.)
4408 287th Ave., SE
Fall City, WA 93024

ERIC CLARK
M/S 302-1
NASA LeRC
Cleveland, OH 44135

PERRY BANKSTON
Jet Propulsion Lab
4800 Oak Grove Drive
Pasadena, CA 91109

HENRY CURTIS
M/S 302-1
NASA/LeRC
21000 Brookpark Road
Cleveland, OH 44135

NORRIS BLAKE
(Space Systems)
1078 Normington Way
San Jose, CA 95136

RONALD F. DANIEL
(Lockheed-Martin)
1289 Balbor Ct, #149
Sunnyvale, CA 94086

DAVID BRINKER
M/S 302-1
NASA/LeRC
21000 Brookpark Rd
Cleveland, OH 44135

MICHAEL DASHIELL
AstroPower Inc.
Solar Park
Newark, DE 19716-2000

DALE BURGER
M/S 303-308
Jet Propulsion Lab
4800 Oak Grove Drive
Pasadena, CA 91109

BILL DAVIS
Dept of Electrical Engineering
2015 Neil Avenue
Ohio State University
Columbus, OH 43210

BASAB CHATTERJEE
Dept. of Electrical Engineering
2015 Neil Avenue
Ohio State University
Columbus, OH 43210

VICTORIA DAVIS
S-Cubed
Div. of Maxwell Labs
3398 Carmel Mountain
San Diego, CA 92121

ART CHMIELEWSKI
M/S
Jet Propulsion Lab
4800 Oak Grove Drive
Pasadena CA 91109

RONALD DIAMOND
Spectrolab, Inc.
12500 Gladstone
Sylmar, CA 91342

DONALD CHUBB
M/S 302-1
NASA LeRC
21000 Brookpark Rd
Cleveland, OH 44135

PAUL DILLARD
M/S 81-25
Boeing Aerospace
P. O. Box 3999
Seattle, WA 98124

LOUIS DiNETTA
AstroPower, Inc.
Solar Park
Newark, DE 19716-2000

MARIA FAUR
DRA/MS 302-1
NASA/LeRC
21000 Brookpark Rd
Cleveland, OH 44135

MIRCEA FAUR
Dept. of
Cleveland State U.
Cleveland, OH

DALE C. FERGUSON
MS 302-1
NASA/LeRC
21000 Brookpark Rd.
Cleveland, OH 44135

NAVID FATEMI
MS 302-1
NASA LeRC/Essential Research
21000 Brookpark Road
Cleveland, OH 44135

ROBERT FLOCK
Lockheed-Martin Missiles
& Space
1111 Lockheed Way
Sunnyvale, CA 94088

CRAIG FLORA
M/S 8C-61
Boeing Aerospace
P.O. Box 3999
Seattle, WA

ALEX FREUNDLICH
Space Vacuum Epitaxy Center
M/S #724-SRI
Univ. of Houston
4800 Calhoun
Houston, TX 77204

ED GADDY
Code 734
NASA GSFC
Greenbelt, MD 20771

LINDA GARVERICK
Essential Research

Cleveland, OH

TIM GILLESPIE
Lockheed-Martin
1111 Lockheed Way
Sunnyvale, CA 94088

BRIAN GOOD
M/S 302-1
NASA LeRC
21000 Brookpark Road
Cleveland, OH 44135

CHRIS GOODBODY
Defense Research Agency Command
& Maritime System Group
Space Tech. Dept./Space Sector
Royal Aerospace Establishment
Farnborough Hants GU-14 GTD
United Kingdom

CHANDRA GORADIA
Dept. of

Cleveland State University
Cleveland, OH

DONALD GUIDICE
Code PL/GPSG
Phillips Laboratory
Hanscom AFB, MA 01731-3010

LINDA HALLE
M/S 720
The Aerospace Corp.
13873 Park Center Road
Suite 18
Herdon, VA 22071

MARGARET HANNON
Astropower, Inc.
Solar Park
Newark, DE 19716-2000

PAUL HAUSGEN

ROGER HAWK
U. of Arkansas - Little Rock
Dept. of Applied Science
2801 S. University Ave.
Little Rock, AR 72204

RICHARD HOFFMAN
M/S 302-1
NASA LeRC/Essential Research
21000 Brookpark Road
Cleveland, OH 44135

JAMES HUTCHBY
Research Triangle Institute

RAJ JAIN
M/S 302-1
NASA LeRC/U.of Toledo
21000 Brookpark Road
Cleveland, OH 44135

WILLIAM JAMES
Phillips Lab/USAF

DARREN JOHNSON
PL/VTPC
Phillips Lab/USAF
Kirtland AFB, NM 87117

DAVID KEENER
PL/VTPC
Phillips Lab/USAF
Kirtland AFB, NM 87117

LOUIS KILMER
M/S M2-275
The Aerospace Corp.
P.O. Box 92957
Los Angeles, CA 90009-2957

TED KUBRECHT
Space Vacuum Expitaxy Center
M/S S& R1, #724
University of Houston
Houston, TX 77204-5507

SARAH KURTZ
National Renewable Energy Lab
1617 Cole Blvd.
Golden, CO 80401

GEOFFREY LANDIS
M/S 302-1
NASA LeRC/OAI
21000 Brookpark Road
Cleveland, OH 44135

MIKE LARRO
Optical Coatings Lab. Inst.

CAROL LEWIS
M/S
Jet Propulsion Lab
4800 Oak Grove Road
Pasadena, CA 91109

DAVID LILLINGTON
Spectrolab
12500 Gladstone
Sylmar, CA 91342

ROLAND LOWE
M/S 302-1
NASA LeRC/Essential Research
21000 Brookpark Road
Cleveland, OH 44135

MIKE C. MAUK

LOUIS MAUS
Code PD-14
NASA/MSFC
Huntsville, AL 35812

SCOTT MESSENGER
SFA, Inc.
1401 McCormick Drive
Landover, MD 20785

DREW MEULENBERG
COMSAT Laboratories
22300 Comsat Drive
Clarksburg, MD 20871

SHERIF MICHAEL
Dept. of Electrical & Computer
Engineering
Code 62MI
Naval Post Graduate School
Monterey, CA 93943

JACQUES MOULOUT
Dept. of
Cleveland State University

Cleveland, Oh

DAVID MURPHY
AEC-ABLE Engineering
93 Castilian Drive
Goleta, CA 93117

JOHN MURPHY
Optical Coatings Lab. Inst.

MICHAEL F. PISZCZOR
M/S 302-1
NASA/LeRC
21000 Brookpark Road
Cleveland, OH 44135

STEVE RINGEL
Dept. of Electrical Engineering
Ohio State University
2015 Neil Avenue
Columbus, OH 43210

GEORGE RYBICKI
M/S 302-1
NASA/LeRC
21000 Brookpark Road
Cleveland, OH 44135

TATSUO SAGA
Sharp Corp.
282-1 Hagikami,
Shimjo-cho Kitukutsuragi-gum,
Nara 639-21
JAPAN

DAVID SCHEIMAN
M/S 302-1
NASA LeRC/NYMA
21000 Brookpark Road
Cleveland, OH 44135

JOEL SCHWARTZ
M/S C-369, Bldg. 925
Hughes Space & Communication
P.O. Box 92919
Los Angeles, CA 90009

HARVEY SEREZE
Spire Corp.
One Patriot Park
Bedford, MA 01730

JAMES SEVERNS
Code 6615
Naval Research Labs
Washington, DC 20375

CARLA SIGNORINI
Code XPG
ESA/ESTEC
P.O. Box 299
Noordwick, 2200 AG
THE NETHERLANDS

LUTHER SLIFER, Jr.
7023 Dolphin Road
Lanham, MD 20706

BRIAN SMITH
Spectrolab
12500 Gladstone
Sylmar, CA 91342

TED STERN
Composite Optics, Inc.
9617 Distribution Ave.
San Diego, CA 92020

GEOFFREY SUMMERS
Code 6615
Naval Research Labs
Washington, DC 20375

MICHAEL TIMMONS
Research Triangle Institute

Robert Urbe
Dept. of Electrical Engineering
Kent State University
P.O. Box 5190
Kent, OH 44242

CARLOS VARGAS-ABURTO
Dept. of Electrical Engineering
P.O. Box 5190
Kent State University
Kent, OH 44242

MAURO VIELA
Space Vacuum Epitaxy Center
S & R1 - #724
University of Houston
Houston, TX 77204-5507

FRITZ WALD
ASE Americas, Inc.
4 Suburban Park Drive
Billerica, MA 01821-3980

ROGER WESLER
Center for Microelectronic
Materials & Structures
Yale University
P.O. Box 20824
New Haven, CT 06520-8284

DAVID WILT
M/S 302-1
NASA LeRC
21000 Brookpark Road
Cleveland, OH 44135

STEVE WOJTCZAK
Spire Corp.
One Patriot Park
Bedford, MA 01730

JAMES WOODYARD
Dept. of Electrical Engineering
Wayne State University
Detroit, MI 48201

JANE YATER
MS/302-1
NASA LeRC/DRA
21000 Brookpark Road
Cleveland, OH 44135

| REPORT DOCUMENTATION PAGE | | | Form Approved OMB No. 0704-0188 | |
|--|---|---|------------------------------------|-----------------------|
| Public reporting burden for this collection of information is estimated to average 1 hour per response, including the time for reviewing instructions, searching existing data sources, gathering and maintaining the data needed, and completing and reviewing the collection of information. Send comments regarding this burden estimate or any other aspect of this collection of information, including suggestions for reducing this burden, to Washington Headquarters Services, Directorate for Information Operations and Reports, 1215 Jefferson Davis Highway, Suite 1204, Arlington, VA 22202-4302, and to the Office of Management and Budget, Paperwork Reduction Project (0704-0188), Washington, DC 20503. | | | | |
| 1. AGENCY USE ONLY (Leave blank) | 2. REPORT DATE February 1996 | 3. REPORT TYPE AND DATES COVERED Conference Publication | | |
| 4. TITLE AND SUBTITLE Space Photovoltaic Research and Technology 1995 (SPRAT XIV) | | 5. FUNDING NUMBERS WU-506-41-11 | | |
| 6. AUTHOR(S) Geoffrey Landis, compiler | | | | |
| 7. PERFORMING ORGANIZATION NAME(S) AND ADDRESS(ES) National Aeronautics and Space Administration Lewis Research Center Cleveland, Ohio 44135-3191 | | 8. PERFORMING ORGANIZATION REPORT NUMBER E-10127 | | |
| 9. SPONSORING/MONITORING AGENCY NAME(S) AND ADDRESS(ES) National Aeronautics and Space Administration Washington, D.C. 20546-0001 | | 10. SPONSORING/MONITORING AGENCY REPORT NUMBER NASA CP-3324 | | |
| 11. SUPPLEMENTARY NOTES This document supersedes CP-10108. Responsible person, Geoffrey Landis, organization code 5410, (216) 433-2238. | | | | |
| 12a. DISTRIBUTION/AVAILABILITY STATEMENT Unclassified - Unlimited Subject Categories 76 and 20 This publication is available from the NASA Center for Aerospace Information, (301) 621-0390. | | 12b. DISTRIBUTION CODE | | |
| 13. ABSTRACT (Maximum 200 words) The Fourteenth Space Photovoltaic Research and Technology conference was held at the NASA Lewis Research Center from October 24-26, 1995. The abstracts presented in this volume report substantial progress in a variety of areas in space photovoltaics. Technical and review papers were presented in many areas, including high efficiency GaAs and InP solar cells, GaAs/Ge cells as commercial items, high efficiency multiple bandgap cells, solar cell and array technology, heteroepitaxial cells, thermophotovoltaic energy conversion, and space radiation effects. Space flight data on a variety of cells were also presented. | | | | |
| 14. SUBJECT TERMS Space power; Photovoltaic cells; Solar cells; Solar arrays | | 15. NUMBER OF PAGES 339 | | 16. PRICE CODE A15 |
| 17. SECURITY CLASSIFICATION OF REPORT Unclassified | 18. SECURITY CLASSIFICATION OF THIS PAGE Unclassified | 19. SECURITY CLASSIFICATION OF ABSTRACT Unclassified | 20. LIMITATION OF ABSTRACT | |

**National Aeronautics and
Space Administration**

**Lewis Research Center
21000 Brookpark Rd.
Cleveland, OH 44135-3191**

**Official Business
Penalty for Private Use \$300**

POSTMASTER: If Undeliverable — Do Not Return